WARWICK
THE UNIVERSITY OF WARWICK

A Thesis Submitted for the Degree of PhD at the University of Warwick

Permanent WRAP URL:
http://wrap.warwick.ac.uk/177911

Copyright and reuse:
This thesis is made available online and is protected by original copyright.
Please scroll down to view the document itself.
Please refer to the repository record for this item for information to help you to cite it.
Our policy information is available from the repository home page.

For more information, please contact the WRAP Team at: wrap@warwick.ac.uk

warwick.ac.uk/lib-publications

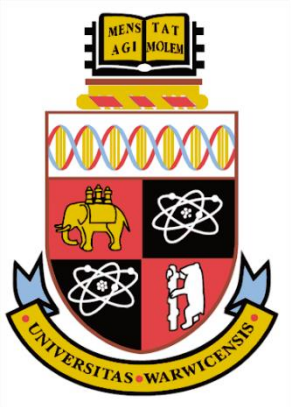

Novel Structured Non-Woven Composite Materials for Broadband Acoustic Damping in Automotive Environments

by

Hiren Padhiar

A thesis submitted in partial fulfilment of the requirements for the degree of

Doctor of Philosophy in Engineering

Warwick Manufacturing Group, University of Warwick

January 2022

Table of Contents

List of Figures

List of Tables

List of Abbreviations

Au Np: Silver nanoparticles

BHT: Butylated hydroxytoluene

BHT: butylated hydroxytoluene

BSD: Backscattering diffraction

$BaTiO_3$: Barium titanite

$BiCl_3$: Bismuth chloride

C: Speed of sound

CNT: Carbon nano tubes

$CeNbO_3$ Cerium niobate

DMAc: Dimethylacetamide

DMF: Dimethylformamide

DMTA: Dynamic mechanical thermal analysis

DSC: Dynamic Scanning Calorimetry

E: Young's modulus

EDS: X-ray spectroscopy

F: Faraday constant

FTIR: Fourier transform infrared spectroscopy

HMW: High molecular weight

KNN: Sodium potassium niobate

$KNbO_3$: potassium niobate

LMW: Low molecular weight

LiCl: Lithium chloride

$LiNO_3$: Lithium nitrate

$MgTiO_3$: Magnesium titanium trioxide

Mv: Molecular viscosity

NRC: Noise reduction constant

NaCl: sodium chloride

$NaNbO_3$: Sodium niobate

OMMT: Organically modified montmorillonite

P0: Reference pressure

PA6: Polyamide-6

PAN: Polyacrylonitrile

PE: Polyester

PEO: Polyethylene oxide

PET: Polyethylene terephthalate

PP: Polypropylene

PS: Polystyrene

PU: Polyurethane

PVA: Polyvinyl acetate

PVC: Polyvinylchloride

PVDF: Polyvinylidene fluoride

PVP: Polyvinylpyrrolidone

PZT: Lead zirconate titanate

Prsm: Root mean square

R: Radium

R: Universal gas constant

SEM: Scanning electron microscopy

Si3N4 Silicon nitride

SiC: Silicon carbide

SiO2: Silicon dioxide

T: Temperature

TBAB: Tetrabutylammonium bromide

TBAC: Tetrabutylammonium chloride

TGA: Thermogravimetric analysis

TPEE: Polyester elastomer

TPU: Thermoplastic polyurethane

TiO2: Titanium dioxide

TiO2: Titanium oxide

WAX: Wide angle X-ray diffraction

XRD: X-ray diffraction

YST: Yttria stabilised zirconia

ZNO: Zinc oxide

Zj: Charge

ZrC: Zinc carbide

cj: Concertation

f: Frequency

qR: Charge density

t: Time

v: Poisson ratio

v: Velocity

α: Alpha polymorph

β: Beta polymorph

γ: Gamma polymorph

γ: Specific heat ratio

γ: Surface area

δ: Sigma polymorph

ε: Epsilon polymorph

ε: Strain

εl: Lateral strain

εt: Longitudinal strain

λ: Wavelength

μj: Electrochemical mobility

ξ: Displacement

ρ: Density

σ: Stress

ϵ0: Relative permittivity

Acknowledgements

I would like to begin by thanking my supervisor Dr Claire Dancer for giving me the opportunity to embark on this journey and providing me with the expertise, motivation, and guidance throughout the process. Most of all I'd like to thank you for the encouragement and reassurance you provided which helped me through the years. I'd like to extend my thanks to Dr Stuart Coles to whom I'm grateful for supporting me during the hard times and providing a different outlook through his expertise.

To Martin Worrall, for his help with technical support within the labs and for providing his advice throughout. A special thanks to Matt Jacobs for his assistance with experimental procedures and assisting with any queries that came up.

Thank you to my colleagues at the Dancer group past and present for their continuous support during my 4 years within the group. A special thanks to Abhijeet Sarangi for his great friendship, and support and Dr Dinesha Dabera for her expertise and assistance but also for helping with any queries. Our group coffee breaks were a blast and helped me through the years. It is something that brought joy to my days at the department. I'd also like to extend my special thanks to Khoa Bui, and Alastair Little, for their friendship and support.

Finally, a special thanks to my parents for all the unconditional love and support they have given me throughout my life. They have always motivated me to strive for big things. My two sisters Devika and Kajol who encouraged me and help on a day-to-day basis, especially during the final stages of the process. Last but by no means least, to my wife Jayna who has continuously been my rock for several years of my studies from undergraduate to my master's and now to my doctorate. Thank you all.

Declaration of Authorship

This thesis is submitted to the University of Warwick in partial fulfilment of the degree of a Doctor of Philosophy. It has been fully composed by myself and has not been submitted to any other higher education institute or university. The work described was carried out between October 2017 – January 2022.

The work presented (including data generated and data analysis) was carried out by the author except in the cases outlined below:

(i) Powder X-ray diffraction measurements were carried out by Dave Walker, Department of Physics, University of Warwick

(ii) Sound absorption measurements were carried out by Matt Jacobs, Austins

Abstract

The electrospinning technique allowed for the formation of piezoelectric composite fibres utilising an electroactive polymer in PVDF and an inorganic salt in KCl and piezoelectric, dielectric and thermally conductive ceramic materials including $NaNbO_3$, $KNbO_3$, $CeNbO_4$, SiC, and Si_3N_4. These fillers were all added to provide control over the average fibre diameters of the PVDF fibres and induce the nucleation of the piezoelectric β polymorph in the PVDF for broadband sound damping applications in the automotive industry.

The addition of the inorganic salt had been demonstrated to assist in the complete removal of beads within the PVDF fibres producing average fibre diameters ranging between 191m – 239 nm. It was also demonstrated that the KCl salt could influence a reduction in the fibre diameter of bead-free fibres with a larger diameter. These fibre diameters were 560 nm – 810 nm. The fibres containing KCl also displayed the highest content of the β polymorph where a value of 99.7 % was obtained with a concentration of 0.8 wt% KCl for the thinner fibres and 86.0 % obtained with a concentration of 0.6 wt% KCl for the thicker fibres. The decrease in fibre diameters for the PVDF / KCl fibres agreed with the increase in the content of the β polymorph within the crystalline phase of the polymer. These results demonstrate that the addition of an inorganic salt can influence the nucleation of the β polymorph and be near phase pure.

The fibre composite mats involving the PVDF, and five ceramic components demonstrated different levels of control over the average fibre diameters of the PVDF. Fibre diameters ranged between 500 nm – 1100 nm for all the fibre mats with the $KNbO_3$ displaying the highest influence on the average fibre diameter. The fibre morphology was dependent on the electrical properties and particle size of the ceramic fillers. Nucleation of the β polymorph was achieved with the addition of all five ceramics with values ranging between 60 % – 74 % with $KNbO_3$ overall assisting to influence the higher values in the content of the β polymorph. The thermal stability of the composite fibre varied with the ceramic type with the niobium oxides decreasing thermal stability and silicon-based ceramics increasing the stability.

In most cases, the PVDF fibre composites enhanced the sound absorption properties of existing sound damping materials with each ceramic type displaying different levels of sound absorption coefficients and resonance peaks. Resonance peaks and overall sound absorption were heavily influenced by the changes in the foamed backing of polyurethane and polyethylene terephthalate with the polyurethane foam-backed setups demonstrating a higher sound absorption coefficient across the entire frequency range. Overall, the PVDF / $KNbO_3$ composite fibres backed with polyurethane foams demonstrated the highest noise absorption

coefficient of 0.52 and a shift in the first resonance peak to lower frequencies of 1250 Hz with an absorption coefficient of 0.90.

Chapter 1 Introduction

1.1 Background

Acoustic sound emissions generated by automotive vehicles have increased the levels of sound pollution, especially in highly populated areas. The primary factors which contribute to the emission of sound from vehicles are the engine, exhaust, tyres, and friction generated by the car body and the wind, whilst secondary emissions are contributed by the glass windows and vibrational movement of the metal sheets.[1] The control measures taken to reduce airborne sound emissions range from, absorbers, barriers, mufflers and silencers.[2] These measures control levels of acoustic sound in line with the current regulations carried out by the government. However, within the years to come, the government aims to set new regulations reducing the amount of sound a car can release into the environment.[3]

Damping of sound waves from an automotive vehicle is difficult as the sound generated, ranges across several frequencies with a varied intensity of decibels.[4,5] The current regulation for sound pressure levels vehicles are allowed to generate is 76 dB; however, by the year 2026, the aim is to decrease this value to 68 dB.[3] It is essential to enhance the sound damping properties of the current foams within vehicles within this timeframe to comply with the set-out regulations. The government aims to stop production of the diesel car by approximately 2030, which could significantly reduce the amount of sound on the roads, as electric cars produce lower levels of sound. However, within these cars it is easier to hear other sources of sound, such as tyre to road, wind to chassis and humming noises.

Studies carried out on viscoelastic materials such as polyurethane (PU) and silicone on their acoustic sound damping properties have shown promise and are effective materials for sound damping applied in automotive vehicles.[6,7] Foams are the current standard material used within several vehicles and are effective at damping sound. However, fibrous materials have also shown great benefit with their damping properties and have the potential to enhance the sound damping of materials within vehicles. Piezoelectric polymers and ceramics are known to have the ability to generate an electrical charge when mechanical stress is applied. Utilising the piezoelectric effect is a promising technique it would allow for the conversion of sound energy into electrical energy and then thermal energy across a wide range of frequencies.[8]

Therefore, within this PhD thesis, the aim is to produce a material that can enhance the acoustic absorption properties of the current foam systems that are deployed within vehicles across the globe. This will be attempted by the formation of piezoelectric polymer fibre mats loaded with piezoelectric and thermally conductive ceramic particles to develop a polymer

composite fibre mat. These materials will act as an additional layer to the current foamed materials to enhance sound absorption properties of the systems across the entire range particularly at the low to medium frequency ranges.

1.2 Research Scope & Strategy

The electrospinning technique has previously allowed for the formation of fibre mats with aligned fibres, non-woven fibres, and composite fibres.[9] The scope of this work is to produce non-woven fibre mats from electroactive polyvinylidene fluoride (PVDF) with the incorporation of inorganic salt specifically KCl and ceramic fillers being sodium niobate ($NaNbO_3$), potassium niobate ($KNbO_3$), cerium niobate ($CeNbO_4$), silicon carbide (SiC), silicon nitride (Si_3N_4). The priority of the thesis is to bring control to the fibre diameters by initially altering the electrospinning and solution parameters, and then adding ceramic filler to fine-tune the fibre diameters and influence the nucleation of the electroactive β polymorph within the PVDF fibres all to produce a non-woven polymer ceramic composite fibre. These fibres will be applied to the front of polyurethane foam to act as a skin to enhance the sound damping properties of the overall system.

The main strategy was to accomplish the formation of a non-woven polymer with fibre diameters of above 1μm alongside the nucleation of the electroactive β in preparation for the addition of KCl and ceramic particles to ensure fibre diameter size was sufficient to fully engulf the ceramic particles. Once the formation of the fibres was accomplished the addition of the fillers could be incorporated to first tune the fibre diameters too small sizes and increase the electroactive properties of the PVDF. Smaller fibre diameters are known to provide more effective sound absorption properties as they provide a higher surface are to mass ratio. This allows for more contact points between the fibres and the sound waves for better sound absorption through vibrational damping and frictional loss.[10] The niobium oxides bring strong piezoelectric properties, while the silicon-based ceramic provides a more thermal conductive approach for effective energy dissipation across the fibre mats. Piezoelectric properties of the ceramic are important within this work as it is known to convert mechanical energy to electrical energy, with studies showing that these properties influence the conversion of sound energy into electrical energy.[11] Once effectively tuned the best performing niobium oxide ceramic was paired with the silicon-based ceramics to bring forward a fibre composite with both piezoelectric and thermal conductive properties for effective conversion of sound energy into electrical energy through the piezoelectric effect and promote effective thermal energy dissipation.

Sound damping materials are most effective with larger mat cross sections as it allows for effective sound absorption at the low-mid frequency ranges of 500 – 2000 Hz.[12] However,

within the electrospinning technique producing a thick enough non-woven mat can be challenging due to the time required to increase thickness. The strategy to provide the extra needed thickness is to use existing foamed materials as a backing to increase thickness, while the electrospun non-woven acts to increase the surface area of the system as seen in Figure 1.1. This could act as a dual-layer system to provide sound absorption across a broadband frequency range.

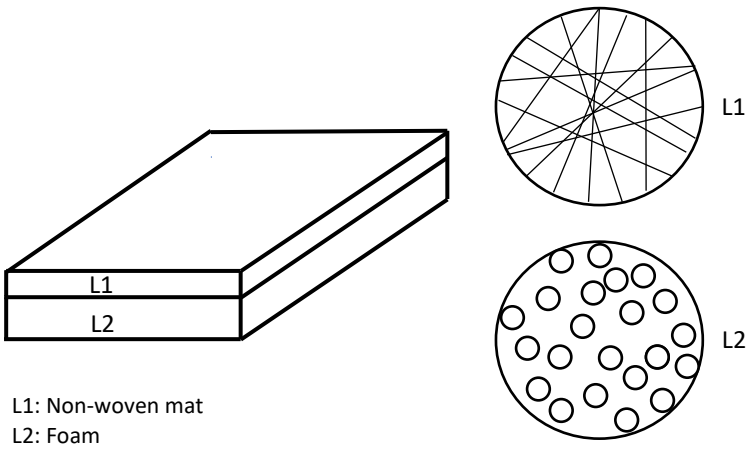

Figure 1.1. Non-woven mat on top of a polymer foam

The main investigated research points were:

(i) Fibre morphology control through alterations to the electrospinning parameters, solution parameters and the addition of KCl and ceramic filler at different concentrations and ceramic types.

(ii) Nucleation of the β polymorph within the PVDF with the addition of KCl or ceramic filler at different concentrations and ceramic types.

(iii) Determining the influence, the points above have on the overall sound damping properties of the material when a ceramic filler is added to the system.

1.3 Thesis Structure

The thesis structure can be seen in Figure 1.2 where the literature review covers 3 main areas including sound waves and the principles of sound waves and how they interact with different mediums, effective sound damping materials, piezoelectric and non-piezoelectric materials, and finally a breakdown of electrospinning and materials produced through the technique. The following chapters are then split into the experimental section including all the

relevant information on the process and steps taken for the development and characterisation of the materials. The remaining chapters are sectioned into parts where initial testing was carried out on PVDF fibres and the addition of KCl to the PVDF fibres. The ceramic addition to the fibres was split into three individual chapters combining the results for each group of ceramic, with the niobium oxides for their electrical properties, the silicon ceramics for their thermal properties, and a combination of the niobium oxide and silicon ceramics for a combination of the two properties as mentioned above. Finally, the last chapter in the thesis will provide a conclusion on the findings of the study and recommendations for future research.

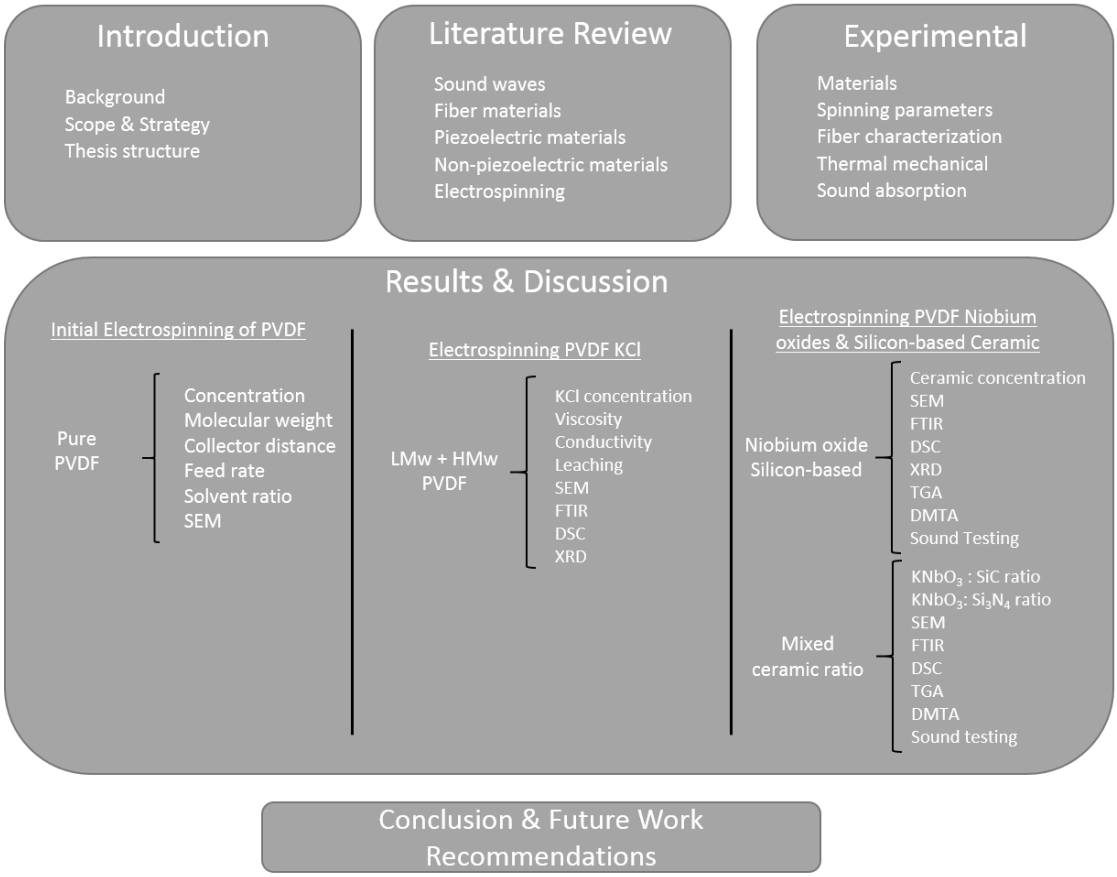

Figure 1.2. The thesis structure highlights sections within chapters.

Chapter 2 Literature Review

2.1 Sound Waves

2.1.1 Longitudinal and Transverse Waves

Sound waves can be categorised into two variants, longitudinal waves, and transverse waves. The differences between these waves are displayed by the movement of the energy across the particles within the medium. Longitudinal waves travel in a longitudinal manner in which particle displacement occurs where the particles are displaced in the same direction as the sound wave is travelling.[13] The sound energy travels across pressure pockets generated through the oscillation of the particles demonstrated by the ripple effect seen in Figure 2.1.

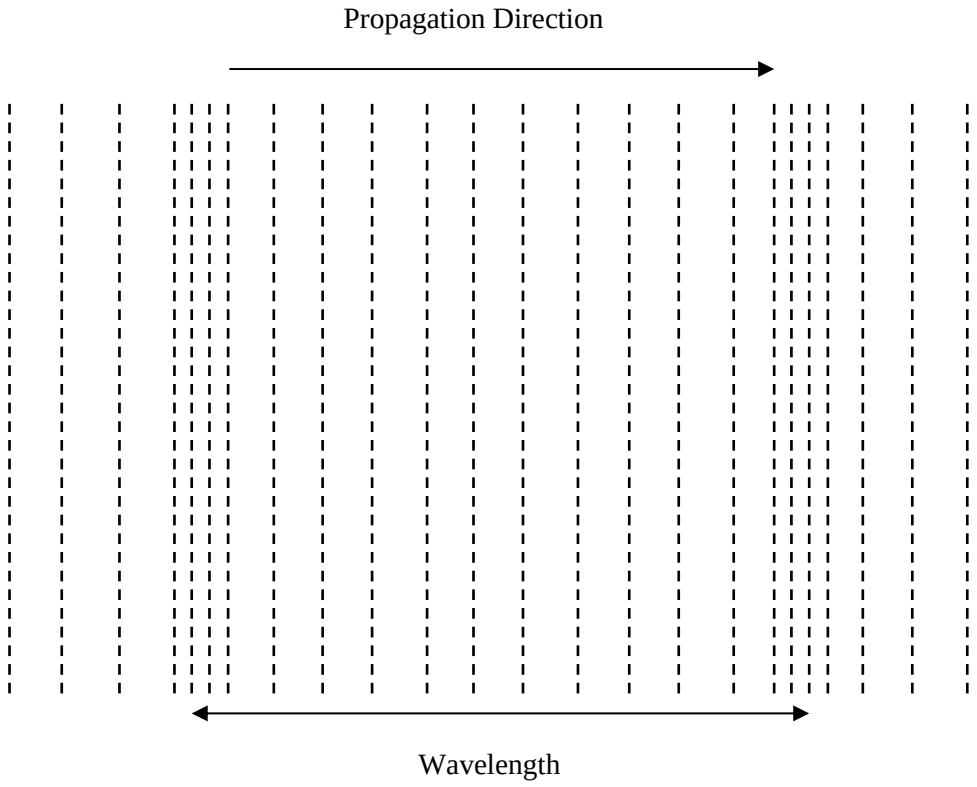

Figure 2.1. Longitudinal wave within pressure pockets in air.

Sound energy requires a medium for the propagation of the energy. Within a vacuum sound energy is unable to travel as there are no particles so the sound is unable to travel through it. In sound waves, the particles do not travel with the wave, but the sound waves use the oscillation of particles as a method to move across a medium, therefore the mechanical and physical properties of the material affect the propagation of the sound waves.[14] There are two

general categories of sound sources. The first is vibrating bodies including vibrating panels, loudspeakers, and piano soundboards. The second category is aerodynamic sources including jet engines, gunshots, and human speech. These types of sound sources have different wavelengths and frequencies; due to the different media, they travel within. These sources of sound energy produce compressive stress on air and liquid mediums, however in solid mediums it acts through shear, bending and compressive stress.[15]

The motion of transverse waves can be represented by the ripples in a pond or by the waves in the sea. The oscillation of transverse waves occurs perpendicular to the direction in which the energy is flowing as demonstrated by the sine curve in Figure 2.2. The direction of oscillating particles occurs in the z – y plane if the flow of energy is moving in the x plane.[16]

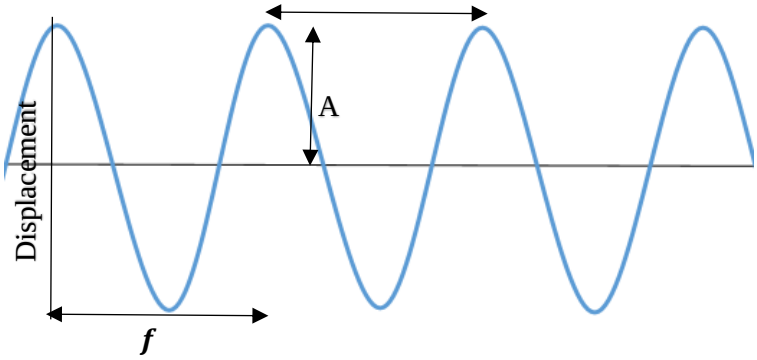

Figure 2.2: Transverse wave

At every half cycle, the sine curve reaches a maximum displacement producing a maximum amplitude A. The frequency of a harmonic wave is described by the equation:

$$f = {}^{1}/_{t} \qquad \text{Eq.1}$$

This demonstrates that the frequency of a wave is the time (t) taken for the completion of one cycle. Using the frequency and the speed of the wave, it is possible to calculate the speed of the wavelength using the equation:

$$\lambda = {}^{v}/_{f} \qquad \text{Eq.2}$$

The sound pressure levels of a wave are how the level of sound is measured. The levels are calculated by analysing the difference between the generated sound pressure and the original sound pressure. The root mean square (RMS) of the calculated values is taken to convert the negative values to positive values. It is possible to use the RMS as the acoustic overpressure alters with the change in time. The use of RMS values is not effective in analysing values across

a large range, hence the use of the decibel (dB).[17] To calculate the dB value of a wave the equation below is used:

$$dB = 20\,log(^{P_{rms}}/_{P_0}) \qquad \text{Eq.3}$$

where P_{rms} is the root mean square of the sound pressure and P_0 is the reference pressure. The dB scale is logarithmic and is used to relate sound pressure to human hearing.[17] The different sound pressured generated from various sources can be observed in Table 2.1.

Table 2.1: The decibel level of different sources of sound.[18]

Decibel level	Sound source
50 – 65	Human Speech
80 – 85	Traffic
95 – 110	Motorcycle
110 – 125	Speaker
150	Fireworks

2.1.2 Sound Waves Travelling Through the Air

When sound waves are travelling through porous material such as foam it will travel through both the air pockets within the material and interact with the solid portion of the foam moving in the form of vibrations. The movement of sound waves through air occurs with the accumulation of low-pressure and high-pressure zones, where the vibrations of sound are produced at the source. The generated sound waves move longitudinally, away from the incident source of the sound. The pressure in the air determines the movement of sound waves. At regions of high pressure, there is a high density of sound waves where the sound begins to dissipate outward towards low-density pressure pockets moving forward. In areas of low pressure, there is a low density of sound waves, this act to move particles closer together. With the variations in density across the medium, the sound waves propagate in the direction in which the sound is travelling. However, when the sound wave is moving through the air, the particles do not move with the waves. Instead, the particles oscillate while the energy travels across the low-pressure and high-pressure regions of the medium.[19]

The most common medium for sound to travel through is air. The velocity of sound within air has shown to be independent of atmospheric pressure, however, it can be varied with the temperature of the medium.[13] In 1942, Hardy *et al*.[20] published the speed of sound as 331.45 ms^{-1}. This was the speed of sound at 0 °C in the dry air of 0 % H_2O and 0.03% CO_2. The

measurements were carried out in an interferometer within a chamber. This measurement was also carried out at 23.82 °C showing a speed of 345.73 ms^{-1}, suggesting that temperature affects the speed of sound in air. In 1986, Wong[21] established a new speed of sound at these conditions of 331.29 ms^{-1}. The study differed with the speed of sound because equipment become technologically more advanced. They also proposed that variations in the speed of sound are due to air humidity and temperature.[22] The speed of sound in air is so fast, the wave itself does not have time to allow for energy loss.[13] The equation concerning the speed of sound in air is:

$$c = \sqrt{(\gamma RT)} \qquad \text{Eq.4}$$

where c is the speed of sound, γ is the specific heat ratio, R is the universal gas constant and T is the temperature. The assumption is that the air the sound is travelling in is an ideal gas and complies with the $PV= nRT$. This equation shows that the speed of sound does not depend on the pressure in the atmosphere.

2.1.3 Sound Waves Travelling Through Solid Materials

To enable the propagation of sound waves, vibrating bodies are required to have a level of inertia, which allows for the movement of momentum from one element to the adjacent element. The vibrating bodies are also required to have a degree of elasticity to allow for the displacement of elements to return to their original positions. For the oscillatory motion to occur within the vibrating body both inertia and elasticity are essential. Vibrations in linear systems occur in either free or forced settings. The free vibrations occur when a force is applied however, the vibration then propagates, and this can be seen in the movement of a stretched-out string. Due to this, the frequency generated is known as the natural frequency. The natural frequency itself is directly related to the inertia and elasticity of the material. In contrast, a forced vibration requires constant energy to be applied to maintain its mode of vibration.[16]

The movement of sound waves through liquid and solid mediums is known as vibroacoustic motion. The movement of a longitudinal sound wave through a solid occurs in the same direction as the displacement of the particles in the solid. However, in a solid with parallel planes, the movement of sound can be different due to the small variations in the material at different points across the medium. The difference in this displacement causes a strain on the material. In this situation, Hooke's law is valid as the longitudinal stress is proportional and parallel to the strain. Young's modulus has a role in the movement of sound in a solid. It is defined as the ratio between the stress and strain of material under constrain and can be expressed as:

$$E = \sigma/\varepsilon \qquad \text{Eq.5}$$

where stress (σ) is the force per unit area and the strain (ε) is the change in length from the original position. It was once considered that Young's modulus was the constant of proportionality in terms of longitudinal waves in solids. However, this is not the case, as Young's modulus is defined as the stress per unit strain of a uniform bar in a fixed position.[23] In a solid material when tension is applied, stress and strain are generated. If the material is not in a fixed position, the stress is zero. This is known as the Poisson contraction. The Poisson's ratio is defined as the ratio between the longitudinal strain and lateral strain on material and can be expressed as:[23]

$$\nu = {}^{\varepsilon_t}/_{\varepsilon_l} \qquad \text{Eq.6}$$

The Poisson's ratio for materials such as steel, glass and rubber is shown in Table 2.2.

Table 2.2: Poisson's ratio for materials

Material	**Poisson ratio**
Steel	0.30
Glass	0.25
Rubber	0.50
Polyurethane	0.26[24]

The displacement of particles in a solid material by a transverse wave is also known as a shear wave. This is the case because, upon application of stress to solid material, a shear response is observed where the deformation of the material occurs with the application of a force. These shear responses are known as shear stresses. The shear stresses allow the transverse motion of waves to travel through solid materials.[14]

When a shear wave moves in the plane of the material, it causes a displacement ξ on the x-axis. The displacement of ξ produces a shear angle γ_{xy}. This shear angle is proportional to the close side x-plane on the side of the samples drawn in Figure 2.3 which is closest to the reader.[25]

$$\gamma_{xy} = \frac{\delta n}{\delta x} \qquad \text{Eq.7}$$

where δn is the displacement in the perpendicular direction and δx is the displacement in the x-axis.

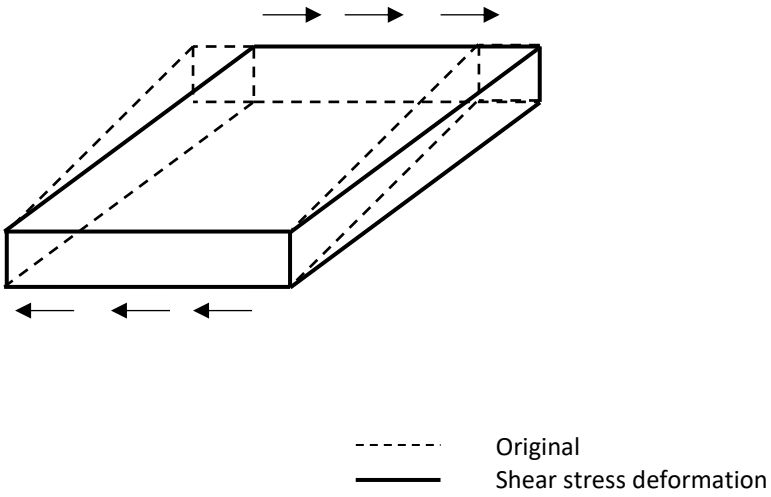

Figure 2.3: The shear deformation of thin material.[25]

The speed of sound is represented by the equation:

$$c=\sqrt{(E / p)} \qquad \text{Eq.8}$$

This equation relates Young's modulus of a material to its density, suggesting that increasing the material stiffness will increase the speed of sound through the material if the density is kept constant. This can also be achieved through the formation of composite materials containing ceramic materials which increase overall material density. Becker and Oberst[26] have shown that increases in the temperature of polymers such as polyvinyl chloride (PVC) reduced the elastic modulus of the material. Concerning the speed of sound in a material equation above, this evidence suggests that the speed of sound through an elastic material, which is heated, would be reduced.

Table 2.3: The speed of sound in different media.[27,28]

Medium	**Speed of sound m.s^{-1}**
Pure water 0 °C	1400
Pure water 25 °C	1470
Polyurethane foam 25 °C	2130
Silicon dioxide[29]	5860

The movement of sound energy through materials, such as porous foam materials is a complex system which has a range of factors affecting the movement of sound. The sound waves move together in the material as sound waves, through the air in the pores of the material, and as mechanical waves through the solid areas of the polymer. This means that the sound absorption of porous materials is related to the elastic and viscoelastic properties alongside the vibroacoustic and acoustic properties of the material.[30] The speed of sound in the cells of the material can be controlled at frequencies above 1000 Hz, this can be achieved by engineering a gradual increase in tortuosity of the material travel further into the material.[31] Overall, the formation of a material that has efficient elastic properties alongside a reasonable pore structure may act effectively as a sound damping material.

2.1.4 Sound Insulation and Absorption

Sound insulation and sound absorption are two like two sides of the same coin and can be distinguished by the fact that sound insulation acts to confine the sound within an enclosed area and sound absorption acts to convert the sound energy into thermal energy. The movement of sound waves through a hollow sphere can assist in representing the two mechanisms. Figure 2.4 demonstrates the interactions of sound energy with a hollow sphere. This mechanism can be applied to several materials not only cellular materials. At each interphase R^1, and R^2 three outcomes for the sound wave will occur those being:

(i) Reflection at the interphase
(ii) Passing through the interphase
(iii) Conversion into thermal energy

At the R^1 interphase reflection of the material occurs which can be associated with insulation of the propagating sound within the confined area. The material entering the solid portion of the materials grey area interacts with the material and experiences viscous loss and thermo-elastic damping.[32] R^2 represents the interaction of the sound energy with the sphere where reflection occurs. Within the porous structure, the reflected sound energy can interact with the incident wave and result in sound cancellation where the waves are out of phase.[33]

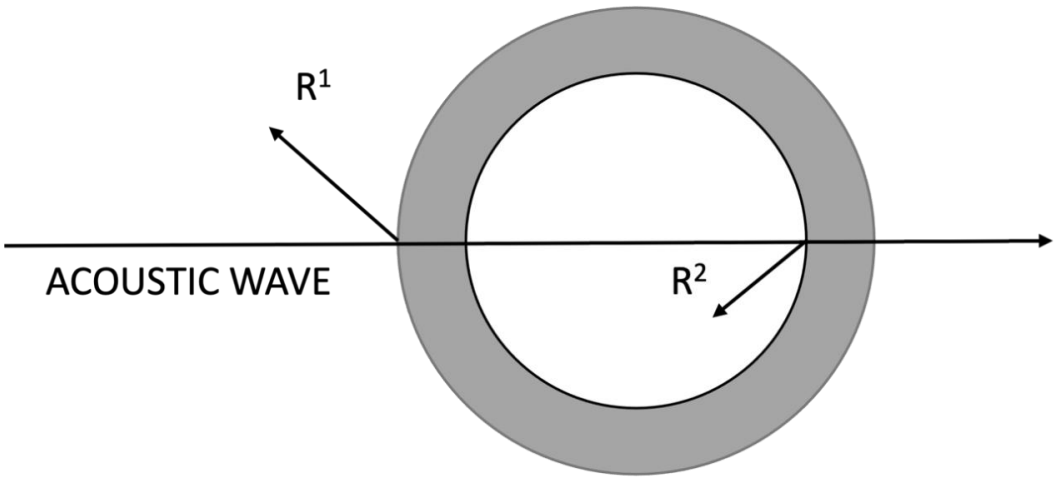

Figure 2.4: The propagation of an acoustic wave through a hollow sphere.

Non-woven mats are materials where the fibres are randomly orientated within the material while woven materials are aligned in a specific pattern.[34] Within non-woven fibre mats, the sound absorption acts in a similar phase where the hollow sphere can be replaced by the pores generated within the non-woven mat. The absorption of sound occurs through two mechanisms. (i) The first is the entanglement of the fibres allowing for a higher degree of friction of the fibres converting the sound energy into thermal energy. (ii) The random packing of the material allows for more points of contact with the incident sound wave and the non-woven fibrous material.[35]

The sound insulation efficiency of an enclosed environment such as an automotive vehicle is influenced by four factors. The first two are the weight and stiffness of the materials used to manufacture the vehicle, and the third and fourth are the airtightness and isolation of the inside of the vehicle.[15] Sound insulation companies have incorporated a variety of mechanisms and materials to aid in the control of the acoustic environment. In terms of car weight, companies are using lighter-weighted materials, which have properties to insulate sound. The advantage of using lighter-weight materials is that it assists in lowering fuel consumption. Materials such as carbon fibre-reinforced composites have been used in these applications as they are lightweight and have good sound insulation properties at lower frequencies in the range of 300 Hz – 600 Hz as lower frequencies are which the human ear can hear.[36] Lead has also shown efficient sound insulation properties, whereby a 5 ft by 5 ft cubic block of lead can absorb 80 dB of sound, however showing decreases in insulation when gaps are present.[15] The use of lead is also unfavourable due to its toxic nature towards humans and industries are reluctant to use such materials.[37]

2.1.5 The Sound Generated by Vehicles

A variety of components in automotive vehicles produce noise and vibration responses to friction. A large fraction of the structure-borne sound is produced in frequencies that are in the low-frequency range of 30 Hz – 500 Hz, whilst frequencies of 500 Hz – 8000 Hz are produced by airborne acoustic sound.[38] The significant parameters that affect the noise and vibration responses are velocity, loading, temperature, and physio-mechanical friction. These parameters affect non-stationary friction joints such as friction clutches and braking systems.[39] Electrical engines and combustion engines work in different ways, producing different amounts of sound. The combustion engine in comparison to the electrical engine produces a significantly louder sound. The sound produced by the combustion engine has lower frequencies and acts to mask other external sounds produced by the car such as air friction and tyre sounds. The electrical engines produce sounds at higher frequencies which masks the external sound much less and so individuals can hear these sounds more. Other sources of noise in a moving car are powertrain noise, road-tyre noise, and wind noise. These are illustrated in Figure 2.5.[40]

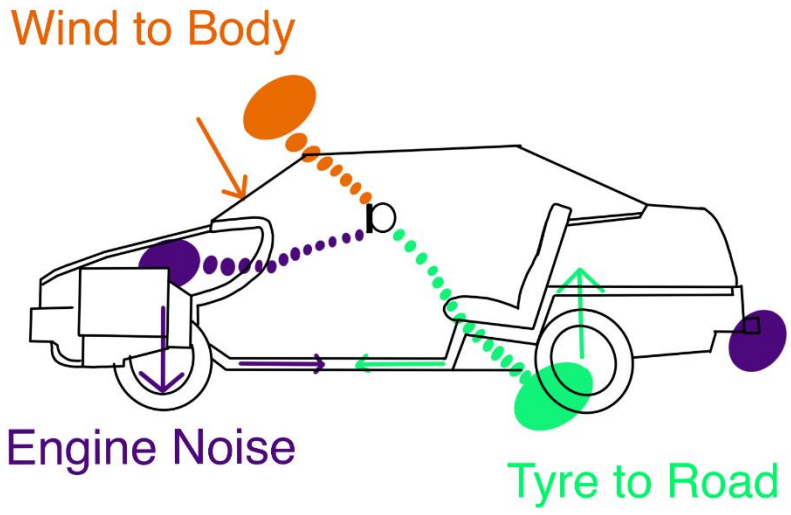

Figure 2.5: Noise paths in an automotive vehicle.[40]

Crèmer[14] explained that noise and vibration in a car's life cycle can be reduced by controlling two variables, these being:

(i) The origin of the sound energy generated
(ii) The movement of the sound energy across the automotive body

The origin of the sound energy and the movement of the energy is represented in Figure 2.5. To control these measures, the automotive industry has added numerous layers of material to

absorb the noise and vibration generated. More details on sound absorption materials are mentioned in the next section 2.2.

The most common diesel engine currently used is the turbocharged diesel engine. Diesel engines are a widely used alternative over their petrol engine counterparts as it has a much better fuel consumption rate, producing lower CO_2 emissions. However, the higher range of parts required in a diesel engine renders it inferior to its petrol engine-based counterpart in terms of sound emission as this causes higher levels of sound energy to be produced by the diesel engine.[41] The three main sources of acoustic sound in diesel engines are:

(i) Mechanical processes – piston slap, brake pads and discs[4,42]

(ii) Combustion[43]

(iii) Fuel injection[43]

The mechanical aspects of sound emission by the engine are generated by piston slap. A piston slap occurs when the direction of the piston's side thrusts and alternates its direction. The amount of noise generated by the piston slap occurs by the piston-cylinder clearance and can be dampened with the use of pressure lubricants. This reduces the amount of sound generated by 2 dB – 3 dB. The pistons in general generate sound waves within the frequency range of 5 Hz – 800 Hz and vary within this range depending on the lubrication applied to the system.[44] Through the use of independent component analysis of the engine noises in diesel cars it has been determined that the engine produces sounds around 2000 Hz.[43] This value combines the frequencies generated by combustion, piston slap, fuel injection, and the exhaust valve.[43] Engine combustion accounts for 80 % of the noise produced in the vehicle. The noise is specifically produced within the cylinders of the car, where the combustion of fuel brings around a change in pressure, which produces noise. The change in pressure also results in the vibration of the cylinders, pistons and engine shell.[43]

The most common brakes used in automotive vehicles are disc brakes. These types of brakes produce a vast range of noise and vibration ranging from 100 Hz – 18000 Hz. This range is broken down into two main categories. First, the low-frequency category of 100 Hz – 1000 Hz includes noise and vibrations described as “brake roughness”, “judder” and “moan” or” groan”. The generation of these low-frequency noises is due to variations in the dimensions of brakes e.g., the thickness and size, or lack of parallel surface of the brake discs. These effects can be caused by thermal implementations or extreme friction of the material. The moans/groans are generated at 150 Hz – 400 Hz, which can be caused by the rigid body oscillation of the calliper and mount within the brakes. The medium-high frequency category of 1000 Hz to 18000 Hz produces noise and vibration called “squeal” or “squeak”. The generation of the squeals tends to occur in the instant before the car comes to a standstill. The

vibrations are produced by the constant rotation of the discs and may also be produced by the bending modes of vibration in the disc shoe assembly.[42] Studies have shown that brake squeal can be produced by modal coupling[45], structural damping, friction-induced damping, and modal damping.[46]

The types of noise and vibrations mentioned earlier for disc brakes can also be categorised by the type of noise and vibration system they produce. This is known as the phenomenological classification system. The phenomenological classification is determined by the vibroacoustic interactions of the brake joints. The classification system has four modes of noise and vibration systems, forced vibration, friction-excited self-oscillations, and resonant oscillations.[47]

With the push to produce more environmentally friendly vehicles, electrically powered cars are being produced. Electric cars have many advantages over traditional combustion engines. The acoustic sound generated by the electrical engine is far lower than the combustion engine. However, as the speeds of the car begin to exceed 30 kph the noise from the friction of the tyres to the road begins to dominate the sound release. Once the speed exceeds 50 kph, the overall levels of sound generated by electric and combustion cars are the same.[48] The frequency range at which trucks produce noise from types ranges from 1200 Hz – 1600 Hz, whilst other road vehicles produce maximum sound levels at 1000 Hz.[49]

With the frequency ranges stated above for several parts of vehicles, it is apparent that a majority of the sound waves generated by vehicles are within the audible frequency range of the human ear. It is thus ideal to produce material that can absorb and convert sound across a broad frequency range for effective conversion of the material. This could be achieved through a range of materials which will be mentioned in 2.2

2.2 Fibre Materials for Sound Damping Applications

There is a whole range of fibrous materials that can be used for effective sound damping material for sound damping applications. These materials can act effectively as their foamed counterparts when a certain thickness of the material is achieved. Generally speaking, foamed materials are effective materials for the damping of sound waves due to their porous nature.[50, 51] However, fibrous materials can achieve the same level of porosity and have the added benefit of a higher surface area to mass ratio for more efficient sound damping properties. This allows the material to provide more points of contact for the sound energy increasing the interactions between the material and sound.[52] With one of mechanisms for sound absorption coming from the friction between the fibres and the air viscous effect.[53] Here the types of sound damping materials have been put into the categories being the naturally occurring fibres and polymer fibres produced mainly from spinning techniques. The alternate mechanism that influences

sound damping with a reduction in fibre diameter is the increase in tortuosity within the material as this increases airflow resistivity in the material increasing loss of energy through the friction between air molecules.[54]

Fibre diameter is a main influencing factor in the sound absorption properties of a material. Shahani *et al*.[55] have demonstrated that a decrease in fibre diameter results in an increase in sound absorption properties at the low-frequency range. Zunaidi *et al*.[56] have also demonstrated that fibres with small fibre diameters will produce better sound absorption across the entire fluency range as seen in Figure 2.6. Mamtaz *et al*.[57] have also shown similar results where a decrease in fibre diameter from 300 nm – 150 nm led to a shift in sound absorption coefficient to lower frequencies from ~ 900 Hz to 700 Hz respectively. The formation of thinner fibres within a material increases its specific surface area and results in larger pores within the same density area. This allows the material to absorb higher quantities of sound as the air molecules have a larger surface area. Thinner fibres will also move more efficiently than larger fibres which allow for better viscous loss in comparison. This information makes fibre diameter an important factor to look at when developing fibrous materials.

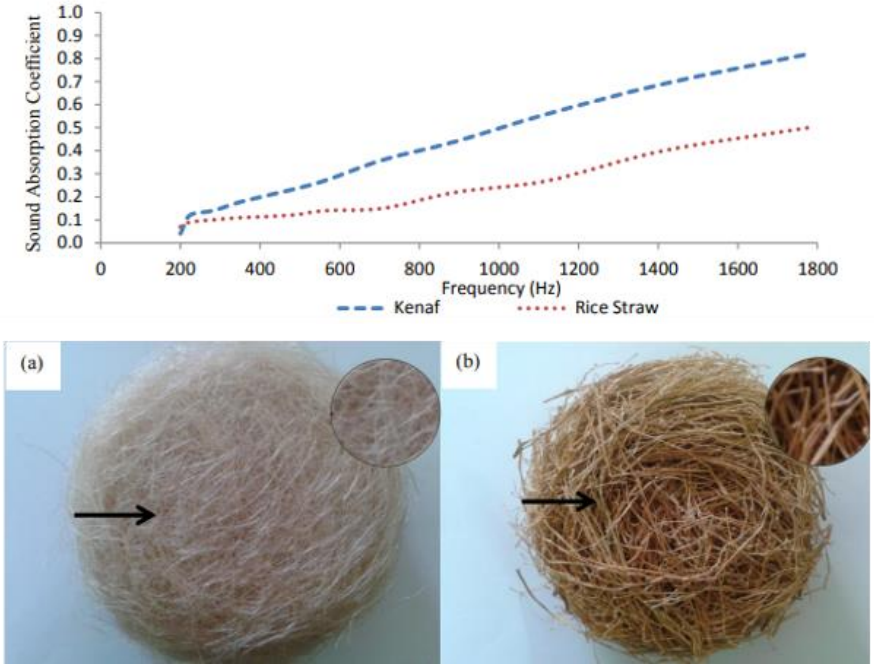

Figure 2.6. The sound absorption properties of kenaf and rice straw with the smaller fibres provide better sound absorption properties. The sound absorption properties of kenaf and rice straw with the smaller fibres provide better sound absorption properties.[56]

2.2.1 Naturally Occurring Fibres

Naturally occurring materials are efficient and environmentally favourable for sound damping applications due to the low processability requirements. The materials can be categorised into three main sections vegetable, animal, and mineral fibres.[58] These governing sections can then be broken down into the subsection of materials seen in Figure 2.7. The use of naturally occurring materials for sound damping applications is owed to the low density, high stability, low price, and low impact on the environment when processing the materials.[59] The sound damping properties of naturally occurring fibres can be seen in Table 2.4.

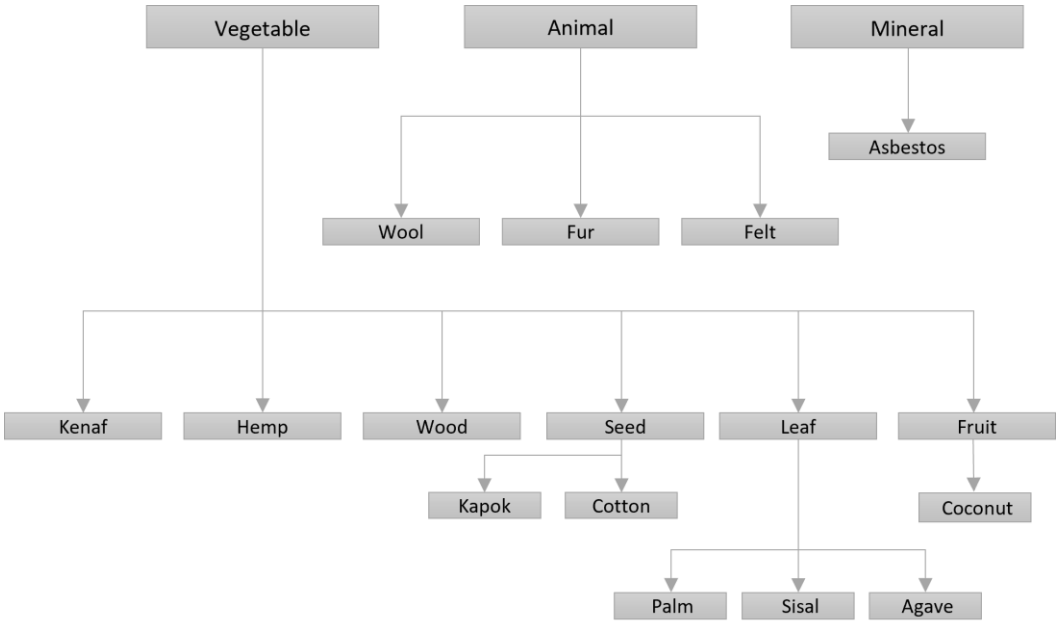

Figure 2.7. Naturally occurring fibres.

Fibres produced from vegetables are highly sought after as these products are easy to grow and have a low environmental impact. Kenaf is a material traditionally used for producing bags within the continents of Asia and Africa and is sourced from bark core wood. Low density, high density, and differing sample diameters of kenaf unbound fibres were analysed. These materials have been shown to produce effective sound absorption properties with changes in the density where both parameters led to an increase in NRC from 0.55 to 0.7.[60] Lim *et al.*[61] studied sound absorption properties of kenaf, specifically analysing the influence of density, material thickness, and a back cavity. Figure 2.8 demonstrates the influence of all these parameters on the absorption coefficient of the material. It specifically demonstrates that an increase in density results in an overall increase in the sound absorption properties within Figure 2.8a. The sample thickness seen within Figure 2.8b demonstrates an increase in sound absorption properties towards the lower frequency range between 500 – 1000 Hz. The increase

in the density and the sample thickness both result in an increase in the sound absorption coefficient as there it leads to an increase in complexity of the pathways sound can travel in and is known as the tortuosity. Figure 2.8 c-d both demonstrate the influence of the air cavity behind the sample. Increasing the back cavity is shown to increase the damping properties at the 500 – 1000 Hz frequency range, with a dip in sound absorption within the middle frequency range. It is suggested that this dip corresponds to frequency associated with the half wavelength. Overall, the material the sample thickness and back cavity show most promise in increasing absorption properties at the low frequency range.

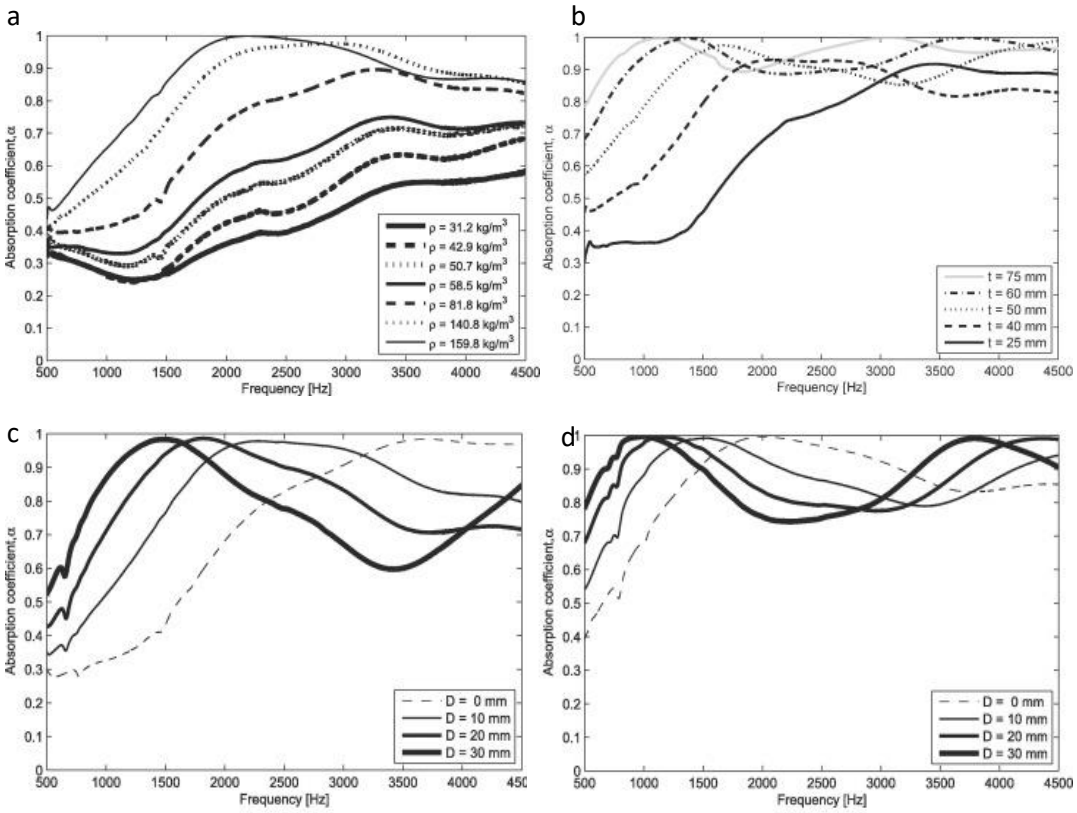

Figure 2.8: Demonstrating the absorption coefficient of kenaf fibres across 500 – 4500 Hz with changes to the density, sample thickness, and varied sample air cavity. (a) density, (b) sample thickness, (c) Sample back cavity with a sample thickness of 20mm, (d) sample back cavity with a sample thickness of 30mm.[61]

Hemp fibres are like jute fibres and require no toxic pesticides or fertiliser making resulting in a low ecological impact. Hui and Fan[62] studied the influence of bulk density, thickness, and an air gap. It was shown that increasing these values led to an increase in the sound absorption coefficient within the range of medium frequency range. Out of the three measurements, an increase in thickness also demonstrated a shift in the absorption coefficient to lower frequency ranges. Leaf-based fibres such as sisal fibres are traditionally used to

produce carpets and ropes, however, there is a lot of excess sisals left over due to the minimum fibre length required to produce these materials. The excess fibres have previously been applied to produce fibre damping materials effective within the mid-high frequency range of 750 Hz – 4000 Hz.[63] The increase in overall mat diameters of sisal fibres of 20 mm, 30 mm and 40 mm had also been shown to increase sound absorption properties and increase the damping properties at the lower frequency range with each increase in mat diameters.[64] This is demonstrated across the board for different types of fibres such as coconut fibres, and palm oil fibres, where sound absorption increases with thicker sample diameters.[65] Seed-based fibres such as kapok are effective sound absorption materials due to the hollow nature of the fibres, which allows for a high porosity of the material reaching a high of 80 % porosity. Xiang *et al*.[35] carried out an extensive study on the influence of bulk density, thickness, and fibre orientations. The study was in line with previous studies carried out on analysing the bulk density and thickness, where increasing these values led to an increase in absorption properties to a point. It was also demonstrated that randomly orientated fibres resulted in a higher sound absorption coefficient due to a higher ratio of fibre entanglement leading to friction between the fibres or the random packing of the fibres allowing for more points of contact in comparison to orientated structures.

Animal fibres are an effective alternative to vegetable fibres as they can be sheared from animals within the farming industry. Wool traditionally used in clothes is also an effective sound damping material, which has been shown to absorb sound within the low-mid frequency range of 500 Hz – 2000 Hz.[60,66,67] Felt is traditionally produced from wool or animal fibres where the material is produced through condensing, matting, and pressing. Fatima and Mohanty[68] produced jute felt materials and demonstrated an effective noise reduction constant of 0.89. The addition of natural rubber to produce a composite material caused a reduction in the noise reduction constant NRC due to a decrease in the porosity of the material.

Mineral fibres such as asbestos have been phased out of use for several applications and are the least desirable material for sound damping applications. The material causes severe lung issues and is not suitable for applications where the fibres may break away from the main body of the material where inhalation of the substance can occur. This leads to complications within the lungs where life-threatening diseases can occur such as lung cancer and asbestosis.[69]

Depending on the fibre type it is difficult to use stand-alone natural fibres for sound damping applications as they do not hold together in position and can easily move apart altering the damping properties of the system. Ideally for use of these materials for industrial sound damping applications binders may be required to ensure the structure of the material is kept intact for the airflow resistivity and porosity to remain unaltered through the use of the material.[70] This can be achieved through the incorporation of polymer materials to produce a

polymer mat filled with natural fibres to produce a composite material.[71] However, the alternative to naturally occurring fibres is spinning polymer fibres. Polymer fibres have been shown to demonstrate efficient sound damping properties and are mentioned in the next section.

Table 2.4. The sound absorption properties of naturally occurring fibres.

Natural fibre name	NRC	Maximum absorption coefficient	Optimal Frequency / Hz	Thickness of Section / mm	Reference
Kenaf	0.60	0.94	2000	60	[60]
Hemp	-	0.97*	400	20	[62]
Sisal	-	0.98*	1600	40	[64]
Coconut husk	-	0.80	578	45	[70]
Coconut coir	-	0.90	4000	50	[65]
Palm oil front	-	0.92	3800	50	[65]
Kapok	0.65	0.98	4000	60	[35]
Jute felt	0.89	-	-	50	[68]

*Values are taken directly from the graphs within the studies.

2.2.2 Polymer Fibres Production Techniques

Polymer fibres are generally obtained through several spinning techniques which can be categorised into melt spinning, and solution spinning materials as seen in Figure 2.9. The use of these techniques allows a level of control of the fibre's morphology through changes to the spinning parameters.[72,73] This allows for the production of fibres with specific characteristics which can be applied for sound damping applications. It is possible to control the fibre diameter through these techniques which in turn provides a level of control over the density, porosity, and airflow resistivity of the material, all contributing factors for sound damping applications. This is expanded more in section 2.5.4.

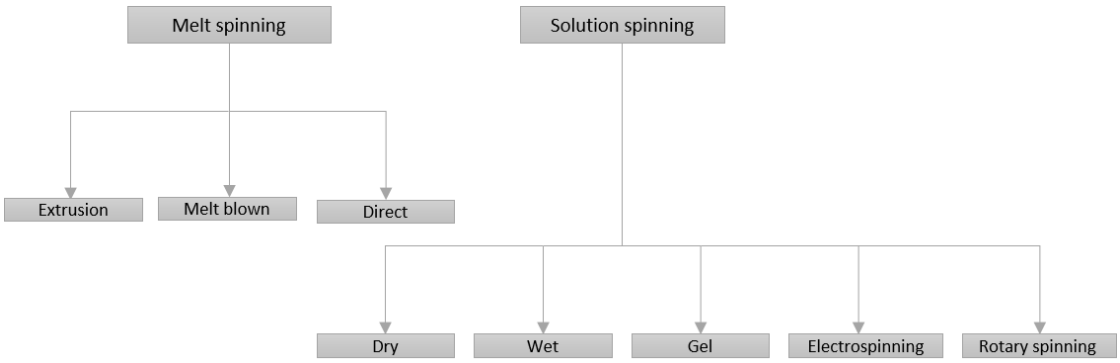

Figure 2.9. Spinning techniques for fibre production.

The melt spinning technique allows thermoplastic polymers to be formed into fibres through heating and extrusion of the materials through a spinneret. It provides for the mixing of materials through the extrusion region of the technique allowing for the formation of composite fibres. Figure 2.10 shows the entire process required to develop fibres using the melt-spinning process. This process is effective at producing a range of fibre diameters for several polymers. This technique can be used for efficient orientation of the polymer chains within the solidification point resulting from rheological forces, air friction and mass inertia.[74] The technique is useful for producing large fibre diameters which has a large range. The average is generally between 10 µm– 12 µm.[75] There have also been reports of fibres being produced with diameters lower than 1 µm. Patnik *et al*.[76] produced PP fibres with a fibre diameter of 794 – 820 nm. However, in general, this technique is more useful for the production of larger fibres above 1 µm than nanofibers.

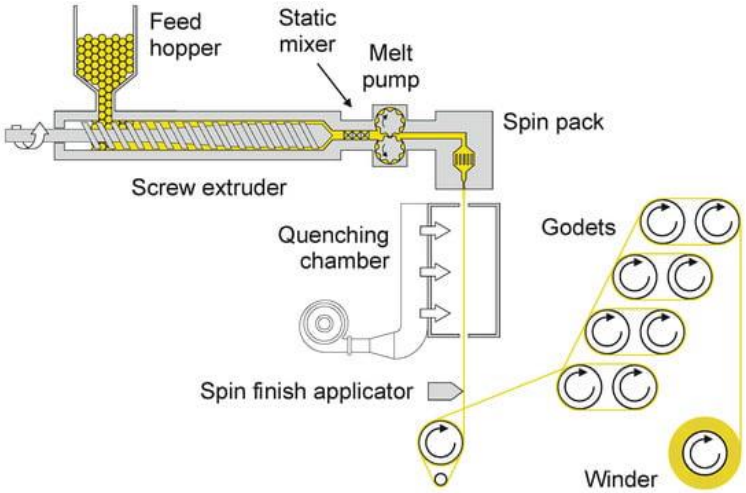

Figure 2.10: The melt spinning process where the polymer is extruded and fibres are produced.[77]

The melt-blown process is similar to the melt-spinning process in which a polymer is heated and melted within an extruder before fibre formation occurs. Within the melt-blown process, the extruded material is released into a stream of high-velocity air. This procures fibre structures which are 10 – 20 cm in length and is deposited on the collector. Polymer fibres with a diameter of 1 – 10 µm are produced during this process which is effective in engulfing ceramic filler particles is required to do so.[78] However, it is still possible to produce fibres of small diameters in the range of 0.3 µm – 0.6 µm.[79] Nayak *et al*.[80] demonstrated the formation of PP fibres lower than 1 µm with PP where diameters of 438 – 755 nm were produced. In general, this technique is used to produce larger fibre diameters over 1 µm.[81,82] Uppal *et al.*[83] have produced fibre diameters as low as 260 nm which could be effective in sound damping applications.

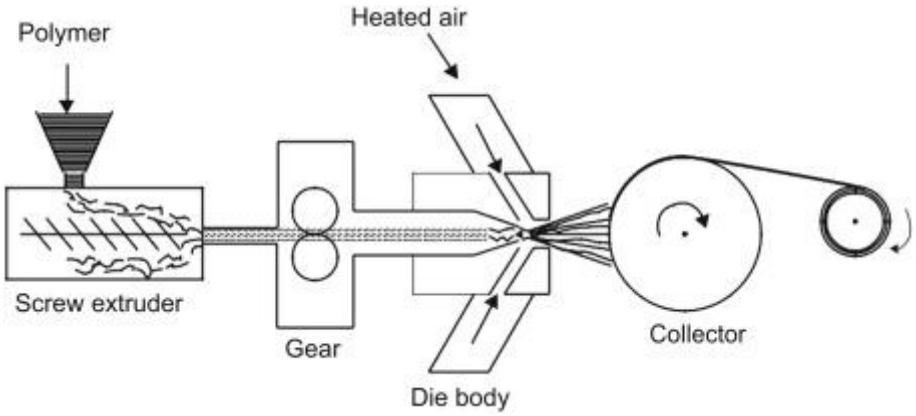

Figure 2.11 The melt-blown process demonstrates how fibres are made[78].

Centrifugal spinning, also known as rotary jet spinning or forcespinning™, is a promising technique which allows the production of fibrous membranes on a large scale with a low-cost factor. The technique utilises a similar centrifugal mechanism used to produce candy floss.[84] The formation of fibres through this technique is achieved by manipulation of the centrifugal force, viscoelastic behaviour, and mass transfer of the prepared solution. Similar to techniques such as electrospinning this technique relies on the elasticity of the solution and the evaporation rate of the solvent within the solution.[85] The added benefit of this technique is its ability to produce fibres in the melt state as well.[86] Vasquez *et al*.[87] produced non-woven PVDF mats demonstrating a fibre diameter of 1242 ± 474 nm at 4000 RPM. Ibtehaj *et al*.[88] recently also produced PVDF fibres utilising this process, with fibre diameters of 1.2 µm with bead-free fibres. Boschetto *et al*.[89] produce PLA fibres and PLa/BaTiO3 composite fibres. These materials were in the large average fibre diameter range of 2.77 ± 1.53 µm and 5.43 ± 2.70 µm for the fibre respectively. Additional polymers have been produced using this technique such as PS[90], PCL[91], PEO[92], and PAN.[93]

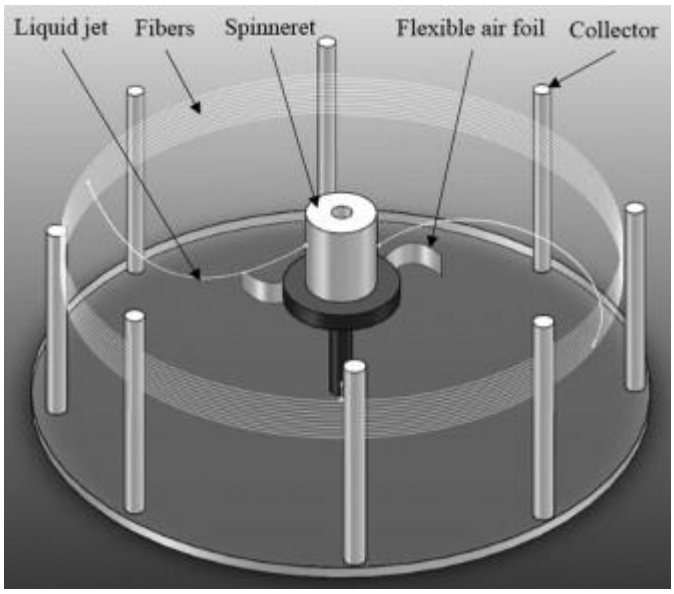

Figure 2.12. Demonstrating the formation of a fibrous mat through the rotary spinning technique.[93]

2.2.3 Polymer Fibres

The alternative to the spinning techniques mentioned above in 2.2.2 is the electrospinning technique which has been extensively researched across a range of materials. The technique requires a dielectric solvent to produce a polymer solution system. Like melt spinning the material is fed through a spinneret, however, instead of heating, an electrostatic field is generated through the application of a high applied voltage which allows for the release of a jet. The technique is explained in more depth within section 2.5.2. The materials mentioned within this section will be mainly focused on those produced from the electrospinning technique.

The sound absorption properties of polymer material have been studied for several synthesised materials, including non-woven polymer systems, and non-woven composite polymer systems. These systems provide effective damping materials due to the high surface area to mass ratio as mentioned previously. Ideally tuning these fibres to certain morphologies can assist in altering the sound damping properties which are mentioned below. Thin non-woven materials have previously been shown to have poor sound damping properties as stand-alone materials due to their thin nature of the material.[94] However, two approaches can be taken to influence and increase the sound damping properties of non-woven materials. The former approach is to increase the spinning times to produce thicker fibres. This approach is beneficial as it does not require the production of secondary material to act as a backing. However, it requires an extended period of spinning with techniques such as electrospinning. The second

options are the incorporation of non-woven materials into the system with a back cavity or foamed backings. This has previously been studied and shown to increase the sound absorption properties of used systems as the non-woven materials increase the surface area of the materials leading to higher points of contact for the sound waves.[94,95]

Lou *et al*.[96] demonstrated the first option by increasing the thickness of a polypropylene/polyester (PP/PE) composite system. The polymer composite demonstrated an overall increase in the absorption coefficient at the lower frequency wave. It was also shown that increasing the density increased the sound absorption coefficient at the mid-high frequency range. In comparison to these fibres, a thin layer of PE 3.5 mm was studied producing an extremely low noise reduction constant. However, the study demonstrated similar results where increasing the density to a certain level of 0.14 $g.cm^{-3}$ increased the absorption properties.[97] In addition to the influence on density, Khan *et al*.[98] demonstrated that increasing the thickness from 0.5 – 1.5 cm increasing the weight of the polyvinylpyrrolidone (PVP), polystyrene (PS), and PVC also influenced the sound absorption coefficient shifting the resonance peak to lower frequencies due to changes in air flow resistivity and velocity. It was also suggested that the surface area and polymer type influenced the sound absorption properties of the material with the materials with higher surface areas absorbing sound more effectively at the lower frequency ranges. Further studies on PVP have recently demonstrated to provide effective sound absorption properties at the low-frequency ranges when the mats are piled above each other to increase the thickness of the material which may be an alternative to an option when electrospinning for several hours is not viable.[99] Kalinova[100] studied the influence of density and nanofiber diameter on the absorption properties of polyvinyl acetate (PVA). It was found that increasing the density of the material led to a shift in the sound absorption coefficient to lower frequencies like in other studies. An increase in nanofiber diameter was also demonstrated to decrease the sound absorption coefficient to lower frequencies. Hui and Fan have shown similar results where a decrease in the fibre diameter increased the sound absorption coefficient of PET fibres.[62] Thermally bonded non-woven polyethylene terephthalate (PET) fibres have previously been shown to be effective sound absorption materials. Lee and Joo[101] Suggested similar results to the studies mentioned previously, in that an increase in the thickness of the PET assisted in increasing the sound absorption properties. It was also suggested that materials with thinner fibres influenced the sound absorption properties of the material due to an increase in mass per unit area.

The second option for producing thicker non-woven mats is to have a back cavity which has previously been shown to enhance the sound damping properties of fibrous materials. It is an economical alternative to the spinning of samples for extended periods or the addition of foams as it reduces the need to manufacture more materials. Liu *et al*.[102] studied the acoustic

absorption performance of polyacrylonitrile (PAN), thermoplastic polyurethane (TPU) and thermoplastic polyester elastomer (TPEE) with a back cavity. The study demonstrated an increase in the sound absorption properties and a shift in the resonance frequency to a lower frequency range for all three materials analysed. The alternative option of having a back cavity has previously been shown to enhance the sound damping properties of fibrous materials.[103] It is an economical alternative to the addition of foams as it reduces the need to manufacture more materials.

In comparison to non-woven fibres containing back cavities, materials backed with a porous bulk material have been shown to perform more effectively across the entire frequency range.[95,104] Attaching non-woven mats to the surface of bulk structures has previously been demonstrated where the attachment of polyamide (PA6) demonstrated a large increase in the sound absorption coefficient at the medium to high-frequency range between 2000 Hz – 3000 Hz. The study demonstrated that porous bulk materials themselves show an increase in sound absorption properties with an increase in thickness in line with the literature. However, the addition of a PA6 electrospun mat to the surface of the 8 mm porous bulk material demonstrated better sound absorption properties.[105] In comparison to non-woven fibres being backed with porous bulk materials the back cavity materials do not perform as effectively across the entire frequency range.[95,104]

The third option is the addition of filler particles into polymers has previously been demonstrated to influence the sound absorption properties of polymer fibre mats. Wu and Chou[94,106] studied the influence of filler on PVDF fibres and correlated it to the piezoelectric effect of the material and the sound absorption coefficient at the low-frequency range of 50 Hz – 250 Hz. It was suggested that the increase in piezoelectric properties due to the addition of carbon nanotubes and graphene nanoparticles occurred because of the materials acting as nucleators. This increase in the piezoelectric properties resulted in an increase in the sound absorption properties at the low-frequency range of 50 Hz– 250 Hz due to the piezoelectric shunt effect. More recently Wu and Chou[107] added silver nanoparticles (Ag-np) to PVDF fibres showing similar results. The materials produced were suggested to influence damping properties similar to the previous composites produced with carbon nanotubes (CNT) and graphene nanoparticles with all the damping values provided in the incorporation of filler particles to polymers previously demonstrated to influence sound absorption properties of polymer fibre mats. The materials produced were suggested to influence damping properties like the previous composites produced with CNT and graphene nanoparticles with all the damping values provided in Table 2.5. Qamoshi and Rasuli[108] incorporated graphene oxide to thin PVP fibres with overall mat thicknesses of between 160 μm – 480 μm. The addition of the graphene particles had shown to increase the absorption coefficient at the 1500 Hz region with

no influence at other frequency ranges. Ciaburro *et al.*[109] studied the influence of mass on the absorption properties of PVP / silica composite fibres. The study demonstrated an increase in the sound absorption coefficient and a shift to lower frequencies of the maximum sound absorption peak.

Ceramic fillers also have the potential to influence the sound damping properties of polymer fibres. Gao *et al.*[110] studied the addition of ceramic filler to PVA fibres. It was suggested that the carbide (ZrC) and titanium dioxide (TiO_2) ceramic fillers influenced the sound damping properties of the PVA differently, where the ZrC influences damping properties at a higher frequency range of 2500 Hz – 3500 Hz, and the TiO_2 influences damping properties at the lower frequency range of 800 Hz – 1500 Hz. The increase in the content of the ceramics led to an increase in the absorption coefficient at these regions respective to the two ceramic fillers. Table 2.5 shows the maximum sound absorption coefficients for a range of non-woven polymers. Overall, the polymers have their maximum damping properties at the frequency range of approximately 1000 Hz – 2000 Hz. In comparison, the natural fibres in Table 2.4 have their maximum sound absorption coefficients at a higher frequency range of 2000-4000 Hz. The sound absorption coefficients in these areas are all similar with both materials demonstrating high coefficients of above 0.8.

Table 2.5. The sound damping properties of non-woven polymer fibres

Polymer Fibre	Absorption Coefficient	Frequency / Hz	Thickness / mm	Fibre Diameter / nm	Ref
PP / PE	-	-	68	-	[96]
PE	0.29*	3000*	3.5	-	[97]
PVP	0.65	2000	24.6	500 – 900	[98]
PVC	0.70	2000	18.0	200 – 350	[98]
PS	0.51	2000	13.3	2000 – 10000	[98]
PET	0.94*	1300*	50	19500	[62]
PVDF / foam backing	0.8	1000*	-	156 ± 13	[94]
PVDF / CNT & foam backing	0.9	1000*	-	138 ± 21	[94]
PVDF / graphene & non-woven backing	0.87	1000	20	169 ± 21	[106]
PVDF / Ag np & foam backing	0.92*	1000*	150	169 ± 21	[107]
PVP / silica	0.99	390*	-	-	[109]
PAN / back cavity	0.92*	1500*	50	400	[102]
TPU / back cavity	0.5*	1000*	50	1000	[102]
TPEE / back cavity	0.89*	1000*	50	1000	[102]
Polyamide 6 / non-woven backing	1.00	3000	8	-	[105]
PVP / graphene oxide	0.40	1500	0.48	-	[108]
PVA / ZrC / needle punch nonwovens	0.99	3143	10	-	[110]
PVA / TiO_2 / needle punch nonwovens	0.65 / 0.99	1000 / 2500	10	-	[110]

*Values are taken directly from the graphs within the articles.

2.2.4 Summary

The reoccurring trend with the studies carried out on fibrous materials can be comprised into the following points:

(i) Standalone thin fibre mats are poor at sound damping and can be enhanced by increasing the thickness of the materials by spinning for longer or by stacking the materials, adding a back cavity, or the addition of a porous bulk backing.

(ii) Altering the type of polymer can influence the sound damping properties of the system.

(iii) Increasing the thickness of the sound absorption system allows for an increase in sound damping properties and allows for better sound absorption at the lower frequency range.

(iv) Increasing the density of the material assists in increasing sound absorption properties. However, materials with extremely high densities will result in a decrease in sound absorption and an increase in sound reflection.

(v) Fibre morphology and orientation have a role in sound absorption with randomly orientated fibres absorbing more sound.

(vi) The addition of filler materials assists in increasing the damping properties, especially at the lower frequency range. With PVDF the piezoelectric shunt effect takes place at 50 Hz – 250 Hz.

(vii) Fibre size is shown to influence the damping of materials. Fibres have demonstrated an increase in sound absorption at the low-frequency range due to an increase in the tortuosity of the material.

With this being said it might be beneficial to produce fibrous material through the electrospinning technique as it has been shown to produce a range of fibres that are effective damping materials. Materials such as PVDF may be effective for sound damping properties, especially at the low-frequency range where it is difficult for sound absorption to occur as mentioned previously. It might also be beneficial to add a piezoelectric filler to the PVDF to increase the piezoelectric properties which may assist in enhancing the sound absorption properties of the material at the low-frequency range. This leads to reviewing current piezoelectric and non-piezoelectric polymer and ceramic materials within the next section.

2.3 Piezoelectric Materials

The outstanding properties of piezoelectric materials have made them desirable for energy harvesting applications as these materials can convert mechanical energy into electrical energy.[111] This is a desirable technique for sound damping applications as when the sound travels through a polymer material it causes deformation of the material. This in turn activates the piezoelectric component of piezoelectric material providing for the conversion of the sound energy into electrical energy. The mechanisms for how the piezoelectric effect takes place are mentioned below. The piezoelectric properties of ceramics and polymers can be seen in Table 2.6 with the ceramic materials demonstrating much higher electroactive properties in comparison to the polymers. Out of the ceramics mentioned PZT displays the overall highest dielectric properties. However, it is not suitable for use due to the toxic nature of the lead within the composition of the ceramic.

Table 2.6. Dielectric and piezoelectric properties of polymers and ceramics.

Material	**Dielectric Constant**	**Piezoelectric Constant / $pC.N^{-1}$**	**Density / $g.cm^{-3}$**	**Ref**
PVDF	-	13	-	[112]
PZT	1000	198	-	[113]
$BaTiO_3$	1700	190	6.02	[114]
$KNbO_3$	580	91.7	4.46	[115] [116]
$NaNbO_3$	480	34.5	4.42	[117] [118]
KNN	420	80	4.15	[119]
KNN - Li	460	240	4.38	[120]
$CeNbO_4$	28	-	5.86	[121]

2.3.1 The Piezoelectric Effect

The theory of piezoelectricity was first proposed in 1880 by J. Curie and P. Curie, with their work on crystal structures where an electrical charge was produced through the application of mechanical stress.[122] They predicted through their knowledge of pyroelectricity, that certain crystal-structured materials under specific conditions would exhibit piezoelectric properties. Thomson[123] also put forward early contributions to the discovery of the piezoelectric effect with his model on the electric crystalline structure laid out the groundwork for the scientific establishment of piezoelectricity. Piezoelectricity is defined as the formation of an electrical

charge across the lattice of a crystalline material when stress is applied as seen in Figure 2.13.[124] This figure demonstrates the application of the mechanical force which induces the formation of the dipoles on the piezoelectric material.

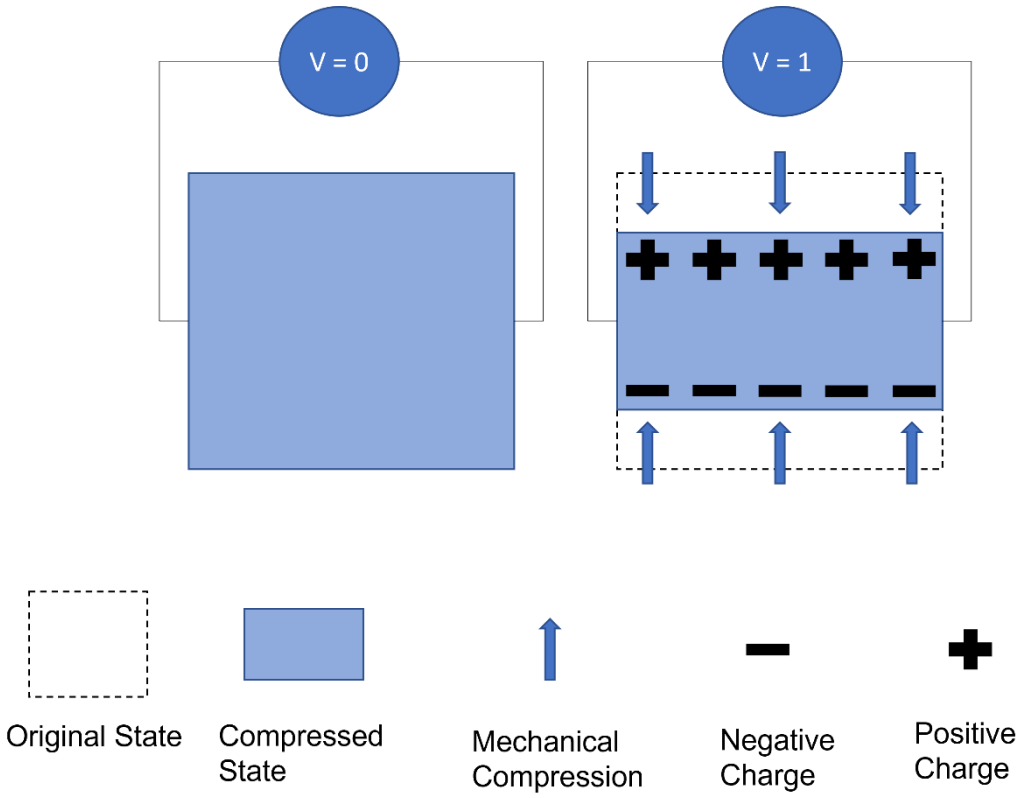

Figure 2.13. Compression of a piezoelectric material demonstrating the piezoelectric effect.

In a regular lattice, the charge distribution of positive and negative charges is neutral. The distribution occurs around a gravitational point, where negative and positive charges face each other. When a force or stress is applied to the material, gravitational points of the charges can be displaced resulting in the formation of dipoles. These dipoles can in turn cause the same charged ions to link producing a polarized material. In this instant, the polarisations allow for the generation of a charge across the material.[125] The permanent alignment of domains however is required for the piezoelectric effect to take place on a higher scale in ceramic materials when mechanical stresses are applied. This is carried out by polarizing the ceramic, where a large DC is applied near the Curie temperature. The Curie temperature is the temperature where the material sees a phase change where it is no longer piezoelectric or ferroelectric. This causes the elongation of the ceramic and the alignment of the domains in the direction of the applied current. Once the applied current is removed from the system, the domains are permanently aligned.[126] The piezoelectric properties of materials begin to diminish once the temperature

exceeds the Curie temperature. The Curie temperature is defined as the temperature at which the material loses its ability to generate an electrical charge.[124] Exceeding the Curie temperature destabilises the alignment of the crystalline domains, which in turn reduces the effects of the piezoelectric properties of the ceramic. Especially for sound damping properties piezoelectric materials when the sound wave travels across the materials the particles begin to oscillate causing vibrations within the material. This results in the deformation of the material, in which the piezoelectric effect takes place and the conversion of the sound energy into electrical energy. The use of piezoelectric materials for acoustic sound damping applications was first established by Forward[127], as a passive approach to the damping of sound vibrations. This made it possible to enhance the acoustic properties of materials with the addition of the piezoelectric effect. Gupta *et al*.[128] have suggested that piezoelectric materials such as lead zirconium titanate (PZT), barium titanate ($BaTiO_3$) and zinc oxide (ZnO) can perform as effective sound absorption materials based on the mechanical energy sound exhibits. Their method of sound conversion suggests that when the mechanical energy of sound hits the crystal on the piezoelectric ceramic it causes a squeezing motion, which acts to apply stress and results in the release of a voltage.

2.3.2 Naturally Occurring Piezoelectric Materials

Potassium sodium tartrate ($KNaC_4H_4O_6 \cdot H_2O$) more commonly known as Rochelle salts, was one of the first salt crystals to undergo electrical analysis and exhibit dielectric properties. It has been deemed the most active naturally occurring crystals discovered.[129] The formation of salt crystals occurs with the seeding of a solution of Rochelle salt and a single crystal.[124] Although Rochelle salt is highly active with high dielectric properties, its drawbacks lie with the Curie temperature of the material. With a Curie temperature of 30 °C, the applications of the salt are limited. The properties are compromised by water moisture contamination. The water moisture dissolves the crystal structure of the salt reducing its dielectric capabilities. However, it also allows for the formation of larger salt crystals.[124,130]

Naturally occurring quartz crystals seen in Figure 2.14 are acquired through mining excavations in the mines of Brazil and Madagascar. The crystal structure of quartz is produced from a continuous tetrahedral structure of Silicon dioxide (SiO_2).[131] On a crystallographic view, the quartz is composed of a 3 – 2 point group of a trigonal structure.[132]

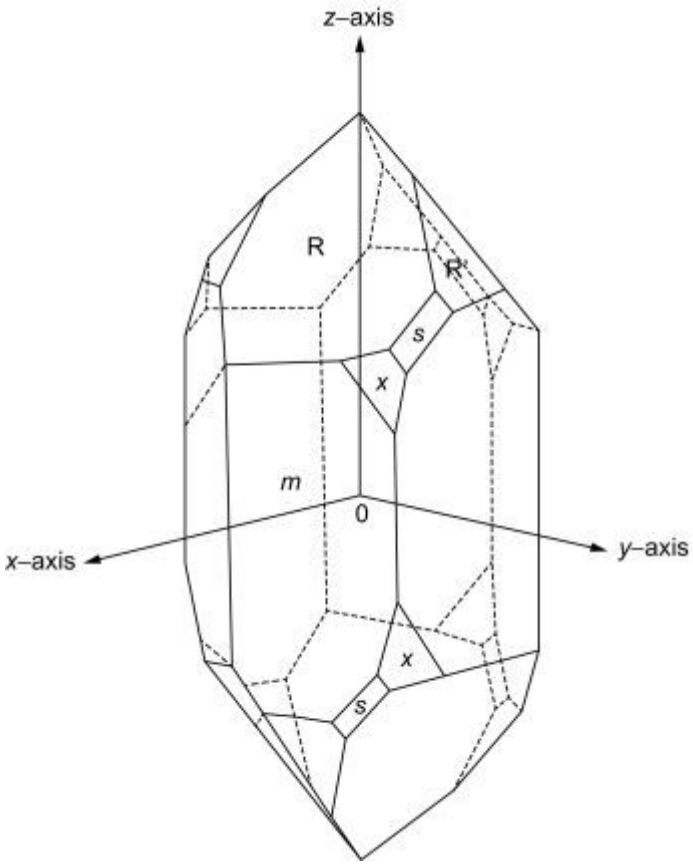

Figure 2.14: Showing a schematic of a quartz crystal with its axis in its piezoelectric state.[132]

P. Curie and J. Curie.[122] studied the piezoelectric properties of quartz crystals and demonstrated that the application of force, to the interface of the quartz crystal, generated an electrical current, bringing about the discovery of the piezoelectric effect. Since its discovery the quartz crystal has been used in applications as a substance detector, detecting small amounts of material in gaseous environments.[133] A wider use of the quartz crystal was in the quartz crystal microbalance, however since then highly advanced weighing equipment has been developed.[134] Naturally occurring piezoelectric materials have their drawbacks, making them not efficient enough for use in real-world applications. However, the use of synthesised ceramic materials with piezoelectric properties has higher electroactive properties and are more stable which make them more desirable for use.

2.3.3 Polyvinylidene Fluoride

PVDF is a semi-crystalline polymer, which has five known polymorphs in the crystalline regions of the polymer. These phases are known as the α, β, γ, δ and ϵ.[135,136,137] Originally these phases were numbered I, II, III, IV, and V respectively, whereas in more recent literature they are denoted in the Greek alphabet. The orientation of the chains can be altered due to the rotation

of the C-C bond and the small atomic radii of the hydrogen and fluorine not sterically hindering the bond orientation. This is usually carried out through external stimuli applied to the PVDF chains.[138] The β and γ polymorphs have been of most interest due to the electroactive nature of these phases displaying piezoelectric and pyroelectric, and dielectric properties.[139] These properties give PVDF potential applications as tactical sensors, shock sensors, dust flux sensors, battery separators, and acoustic transducers.[140,141]

The α polymorph of PVDF has a trans gauge (TGTG') structure of the polymer chains seen in Figure 2.15.[142] The orientation of the polymer chains in the α polymorph results in a net charge of zero as the fluorine and hydrogen atoms are antiparallel to each other. This makes the α configuration a non-piezoelectric phase and spontaneous polarisation does not occur. The α polymorph has a crystalline density of 1.925 g.cm^{-3}.[143] Obtaining the α polymorph is typically carried out through crystallization of melt at temperatures of 160 °C from which samples are cooled at a high rate.[142] Kinetically this phase is the most stable of the 5 conformations and is typically present at room temperature when other phases have not been induced.[142,144]

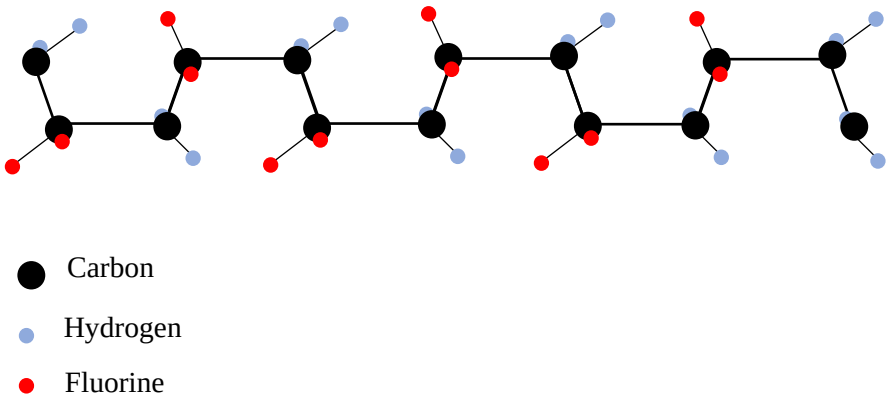

Figure 2.15. The α polymorph configuration of PVDF.

The β polymorph has an all-trans planar zig-zag configuration (TTTT) seen in Figure 2.16.[145] The TTTT configuration of the polymer chains allows results in the alignment of the dipoles across the backbone which gives the polymer an overall net charge.[146,106] This allows for spontaneous polarisation of the polymer to occur displaying the piezoelectric properties of PVDF in the β configuration. Alongside the arrangement of the atoms, the β polymorph is in an orthorhombic configuration, which allows the piezoelectric effect to occur.[147] The β phase has a crystalline density of 1.973 g.cm^{-3}.[143].[145] The TTTT configuration of the polymer chains allows results in the alignment of the dipoles across the chains, this gives the polymer an overall net charge.[146,106] This allows for spontaneous polymerisation of the polymer to occur displaying the piezoelectric properties of PVDF in the β configuration. Alongside the arrangement of the

atoms, the β phase is in an orthorhombic configuration, which allows the piezoelectric effect to occur.[147] The β phase has a crystalline density of 1.973 g.cm^{-3}.[143]

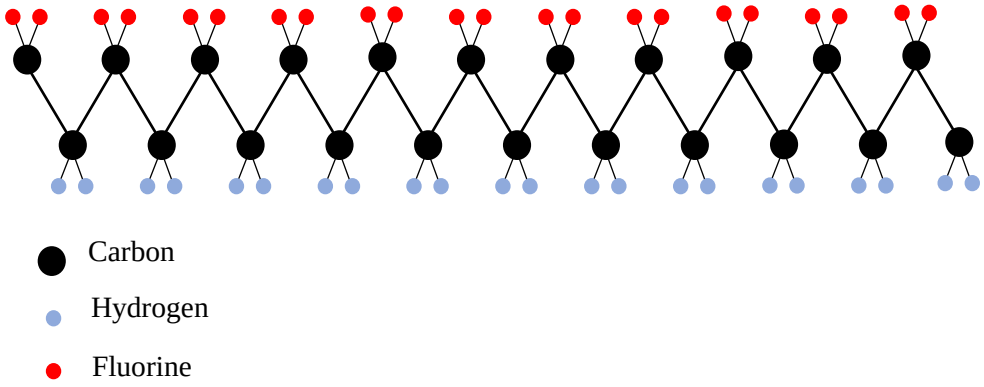

Figure 2.16. The β polymorph conformation of PVDF.[148]

Kawai[149] discovered the piezoelectric properties of PVDF in 1969. During this study, Kawai subjected PVDF films to mechanical forces which lead to the formation of dipoles. It was observed that the application of these mechanical forces led to the formation of a charge and thus the piezoelectricity of PVDF was discovered. In comparison to ceramic materials, PVDF has a low piezoelectric constant with values of 13 pC.N^{-1} that have been analysed.[112]

Several mechanisms can be carried out to induce the nucleation of the β polymorph. The main approach is to mechanically stretch the polymer within the solid state to align the chains from the TGTG configuration to the TTTT configuration.[146,150] Alternatively, hot pressing and hot stretching,[151] solution casting,[152] and poling[112,153] of the polymer can induce the β polymorph. The electrospinning technique has also demonstrated the formation of the β polymorph and is described in depth in section 2.5.6.1.

Mechanical stretching through drawing PVDF has been shown to align the polymer chains into the all-trans configuration. The transformation of the α polymorph to the β polymorph during the drawing process has been shown to occur mainly in areas where the necking of the sample occurs. In these areas, the samples align into fibril structures where approximately 85 % of the region has the presence of the β content and 15 % is the α content.[154] It was also shown that the deformation of the samples at cold drawn temperatures of 82 °C produces a higher content of β polymorph, whilst when the hot drawing temperature of 130 °C produces mainly α phase structures due to the enthalpy relaxation.[154] Similarly Matsushige *et al.*[155] analysed that the formation of the β polymorph through hot drawing did not occur at temperatures above 140 °C.

The melt spinning of PVDF with nano clays has also been demonstrated to induce the formation of the β polymorph with an increase in crystallinity as well. Guo *et al.*[156] demonstrated this and produced fibres with β percentages of 89%.

The orientation of the molecular chains has been shown to influence the piezoelectric properties of unpoled PVDF films. Szewczyk *et al.*[157] produced PVDF fibres for energy harvesting applications and demonstrated that an increase in the orientation of the molecular chains in the β polymorph to 74% resulted in a piezoelectric constant d_{33} of 2.56 pm·V^{-1}. A decrease in the percentage β polymorph to 52% resulted in a d_{33} of 1.65 pm·V^{-1}. Martins *et al.*[158] demonstrate similar results where increasing the percentage β polymorph from 30% to 90% resulted in an increase in the d_{33} to 33 pCN^{-1}. Mohammadia *et al.*[159] had also shown a similar result on PVDF films, where the PVDF film with a percentage β polymorph of 60.2 % resulted in a d_{33} of 28 pCN^{-1}. Increasing the percentage β polymorph to 86.5% results in a d_{33} of 33 pCN^{-1}. Lei *et al.*[160] demonstrate a gradual increase in the piezoelectric response of PVDF fibres from 95 % - 99 % β polymorph with voltages ranging from 150 mV – 175 mV. Gomes *et al*,[161] also show an increase in the piezoelectric properties of PVDF with an increase in the β phase percentage. Here a β polymorph percentage of 80% was achieved with the material demonstrating a d_{33} of 34pCN^{-1}. Overall, the literature suggests that the amount of β polymorph within the PVDF influences the piezoelectric properties of the material and the response provided by these properties.

The γ polymorph has a TTTGTTTG' configuration as seen in Figure 2.17. The TTTG configuration of the γ polymorph allows for the material to experience random polarisation and exhibit electroactive properties.[145] However, its electrical properties are lower than that of the β phase due to the configuration not being all trans and reducing the net polarity of the material.

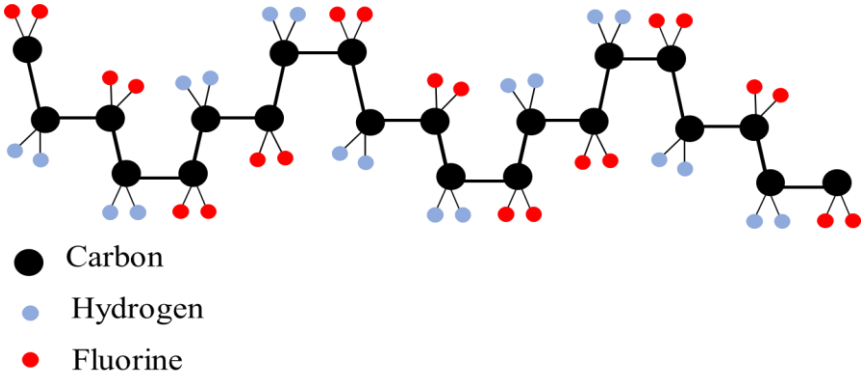

Figure 2.17. The γ phase conformation of PVDF.[148]

2.3.4 Lead Zirconia Titanate

PZT with its efficient dielectric and piezoelectric properties has been applied in a variety of applications such as micro-actuators, sensors and transducers.[162] On an atomic level the structure of PZT is composed of an ABO_3 cubic perovskite arrangement as seen in *Figure 2.18*, where position A is the Pb with valence 2+, position B is the Ti or Zr with valence 4+ and the O^{-2} occupy the face centre.[163,164] PZT is composed of a solid-state solution of lead zirconate and lead titanate.[165] The symmetry of PZT is dependent on the concentration of Ti and Zn in the composition. PZT rich in Ti has a tetragonal structure, whilst PZT rich in Zr has a rhombohedral structure.[166] The phase changes of PZT were observed by Shirane and Suzuki[167] in 1952 at the x = 0.45 composition in the system. Where x is the amount of Ti within the system. However, due to the toxic nature of the Pb within the ceramic, it is undesirable even with the piezoelectric properties it possesses. This leads to the use of alternative materials such as niobic oxides which demonstrate good piezoelectric properties.

Gupta *et al*.[128] have suggested that piezoelectric materials such as lead zirconium titanate, barium titanate and zinc oxide can perform as effective sound absorption materials based on the mechanical energy sound exhibits. Their method of sound conversion suggests that when the mechanical energy of sound hit the crystal on the piezoelectric ceramic it causes a squeezing motion, which acts to apply stress and results in the release of a voltage. Due to the toxic nature of the lead within the material, it is undesirable even with the piezoelectric properties it possesses. This leads to the use of alternative materials such as niobium oxides which demonstrate good piezoelectric properties.[128]

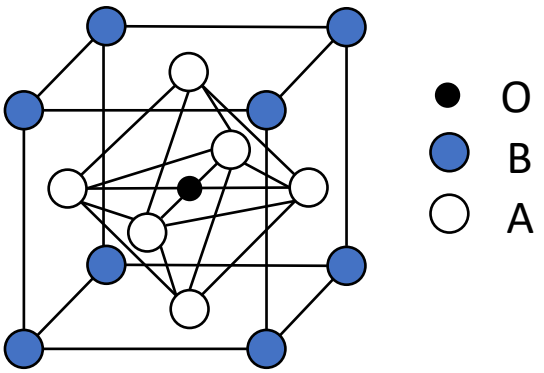

Figure 2.18: ABO_3 perovskite cubic structure of PZT.

2.3.5 Sodium Niobate

As an alternative to PZT, $NaNbO_3$ is a favourable candidate as it displays a good piezoelectric constant and dielectric constant as seen in Table 2.6. E. A. Wood[168] discovered the perovskite structure of $NaNbO_3$ and the phase transitions of the material in 1951. $NaNbO_3$ has an orthorhombic structure at room temperature and has phase transitions at 370 °C and 640 °C of tetragonal and cubic structures respectively. It was later analysed by Cross and Nicholson[169] that 2 further phase transitions at 470 °C and 518 °C were observed with a more revised analysis of the cubic transition at 638 °C. Megaw[170] demonstrated the 7 phases of $NaNbO_3$. The piezoelectric properties of $NaNbO_3$ are displayed by the orthorhombic phase with the reported piezoelectric constant of $NaNbO_3$ being 34.5 pC. N^{-1}.

Matthias and Remeika.[117] analysed the dielectric properties of $NaNbO_3$ and had shown increases in dielectric constants at temperatures of -80 °C, 370 °C and 480 °C, similar to those at which the phase transitions occur. In later studies, Shirane *et al*.[171] reported an increase in dielectric properties at 355 °C, where the phase transition, was in line with previous studies. Studies have shown that the relative dielectric permittivity of materials small degree of dependence on the frequency applied to them. At the phase boundary of tetragonal and orthorhombic at 350 °C, it has been shown that the dielectric constant increases from 634.18 to 649.11 from 10 kHz to 100 kHz respectively.[172]

2.3.6 Potassium Niobate

$KNbO_3$ is another piezoelectric ceramic material belonging to the perovskite family displaying a higher dielectric and piezoelectric constant in comparison to $NaNbO_3$ as seen in Table 2.6. A material with a higher piezoelectric constant could potentially increase the sound damping properties of the material to a higher degree at the lower frequency range as mentioned earlier. Matthias[173] first discovered the material in 1946, where it was known as potassium columbate. It has been reported that $KNbO_3$ demonstrates a piezoelectric constant of 91.7 when within its orthorhombic phase.[116] The crystal structure of $KNbO_3$ generally forms the orthorhombic structure at room temperature with a range of phase changes. The phase changes occur when dramatically cooled down from 418 °C to – 50 °C or heated from -50 °C to 418 °C. At 418 °C, a tetragonal phase is observed and at – 50 °C, a rhombohedral phase is observed.[174] Shirane[175] confirmed the increase in the dielectric constant of $KNbO_3$ at – 50 °C and 225 °C and 435 °C where the phase changes of the materials occurred, suggesting that changes to the crystal structure of $KNbO_3$ lead to better dielectric properties. The cubic structure of $KNbO_3$ has been reported at 434 °C.[117] The properties of $KNbO_3$ are similar to barium titanate, in terms of phase transition orders; however, the phase transitions in $KNbO_3$ occur at higher temperatures in

comparison to barium titanate.[114] B. Yang *et al*.[176] have shown the phase transition are $KnbO_3$ through optical detection techniques, where the results analysed were similar to other studies.

Matthias[117] investigated the dielectric properties of KNbO3, and it was shown that the dielectric constant did not change from 100 °C – 190 °C. Wada *et al*.[177] analysed the piezoelectric properties of single-crystal $KNbO_3$ and found the optimal poling conditions through conventional poling techniques. It was found that temperatures greater than 100 °C, heating, and cooling rates of 1 °C.min^{-1}, poling currents of < 1 µA and soaking times >60 minutes were the most effective conditions for poling. However, the conventional route for poling produced piezoelectric properties where the $KNbO_3$ was not fully poled. The study had shown a two-step poling technique, which gave better results. Later studies on the dependence of particle size on piezoelectric properties had shown that smaller domain crystals had shown an increase in the piezoelectric properties. Where the d_{32} and ϵ_{33}^{T} were 27.8 and 112.6 respectively at 20 µm in domain size and increased to 35.7 and 205.8 respectively for 6.5 µm in domain size.[178]

2.3.7 Cerium Niobate

The piezoelectric properties of $CeNbO_4$ have not been well-researched within the literature suggesting that the ceramic may not display these properties. However, the material displays a moderate dielectric permittivity as seen in Table 2.6. Dielectric ceramics can be promising within the electrospinning technique to assist in producing homogenous fibre diameters. More depth on this is mentioned later in 2.5.8. At room temperature, the stoichiometric oxygen structure of $CeNbO_4$ has a monoclinic fergusonite-type structure. Several studies on the $CeNbO_4$ and the hyper-stoichiometric $CeNbO_{4+\delta}$ structures.[179,180,181] At room temperature, the stoichiometric oxygen structure of $CeNbO_4$ has a monoclinic fergusonite-type structure. Several studies on the $CeNbO_4$ and the hyper-stoichiometric $CeNbO_{4+\delta}$ structures.[179,180,181] The different variants of $CeNbO_{4+\delta}$ include:

(i) $CeNbO_{4.08}$
(ii) $CeNbO_{4.24}$
(iii) $CeNbO_{4.43}$

These variants are all obtained through the oxidation of Ce^{III} to Ce^{IV} which is carried out under air or oxygen at different temperature ranges. The formation of a tetragonal scheelite type has also been demonstrated in the air under a vacuum.[182] Applications for this ceramic are generally within energy generation and storage devices and solid oxide fuel cells due to the ionic conductivity of the material, whereas $CeNbO_{4+\delta}$ is known for its oxygen ion diffusion

efficiency.[181,183] These variants are all obtained through the oxidation of Ce^{III} to Ce^{IV} which is carried out under air or oxygen at different temperature ranges. The formation of a tetragonal scheelite type has also been demonstrated in the air under a vacuum.[182]

2.3.8 Summary

The piezoelectric materials mentioned above all display slight differences in the overall piezoelectric, and dielectric properties and have been demonstrated to have different applications due to their physical and electrical properties. The ceramic materials overall display much better piezoelectric properties than the polymer and would be desirable to influence the piezoelectric properties within a non-woven composite material. However, from the materials mentioned above the naturally occurring crystals are less desirable for the applications of composite materials due to their low Curie temperatures and solubility in water. While the PZT ceramic contains Pb which renders it undesirable for its negative environmental impact. The niobium oxide materials mentioned above are efficient alternatives to the PZT as they display high electroactive properties desirable for the conversion of sound energy into electrical energy at the low-frequency range of 50 Hz – 250 Hz. As mentioned, the electrospinning of PVDF can influence the electroactive phase of the material also potentially assisting in enhancing its sound damping properties within the low-frequency range making this a material of interest.

2.4 Non-Piezoelectric Materials

Non-piezoelectric materials are also of interest in this work. It is widely known that materials such as polyurethane are commercial materials used for damping applications.[184] However, there is still a possibility to look into other ceramic materials which display non-piezoelectric properties. These materials could act effectively as a non-piezoelectric component within the material providing other beneficial properties to the overall material such as enhanced thermal dissipation properties. Non-piezoelectric materials are also of interest in this work. It is widely known that materials such as polyurethane are commercial materials used for damping applications.[184] However, there is still a possibility to look into other ceramic materials which display non-piezoelectric properties. These materials could act effectively as a non-piezoelectric component within the material providing other beneficial properties to the overall material such as enhanced thermal dissipation properties.

2.4.1 Polyurethane Foams

Flexible polyurethane foams are effective at absorbing sound waves; these properties are signified by the elastic properties and morphology of the pores within the material. Acoustic

waves travel through the pores of the material, causing the air particles to vibrate. This vibration allows for energy absorption to occur through viscous and thermal propagation, eluding to the fact that the shaping of the pores determines the overall sound absorption properties of the polyurethane foams.[6,185] As mentioned previously polyurethane is a material that is used within vehicles for damping applications.[186] The use of polyurethane in its foam form is especially desirable as it has acoustic absorption properties, alongside viscoelastic behaviour and low density.[187] However, there may be room to enhance the damping properties of polyurethane foams with the addition of non-woven fibre mats in front of them in some form of dual-damping system.

Polyurethane synthesis occurs with the formation of a urethane linkage between an isocyanate and a polyol.[188] With water being present in the synthesis reactions occur with the isocyanate reacting with the water as well as the polyol. The reaction of the isocyanate and water releases CO_2 which assists in the foaming of the matrix. The structure of polyurethane can be seen in Figure 2.19. To control the cellular structure of the foam, surfactant and catalyst are used. The surfactant and catalyst act to allow for the cellular structure to form by ensuring the growth of bubbles is at an efficient rate in comparison to the rate of formation of the structural formation of cell bubbles.[189] Polyurethane is a polymer that is widely used in the automotive industry, being applied as cushions, seating and sound packing.[186]

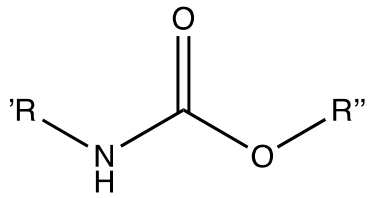

Figure 2.19: Structure of polyurethane.

Pore formation in polyurethane foam occurs in the blowing and gelling phases. The blowing phase produces urea groups, whilst the gelling phase produced urethane groups. The rate at which interactions between the urea and urethane groups occur results in the release of CO_2. The rate of CO_2 release can then be modulated to produce pores with specific diameters.[185] Cell openness within polyurethane foams can be fine-tuned through a range of different methods, a few of these methods consist of spontaneous film rupture, surfactant phase separation, urea precipitation and viscosity rise. Park *et al.*[187] studied the foaming kinetics of polyurethane and had shown that introducing polyethylene glycol (PEG) 2000 to the reaction scheme results in an increase in cell openness. PEG 2000 acts to react with the isocyanate to reduce the molecular weight of the polymer. In doing this the rate of the blowing phase decreases, and the variations between the rates in the two phases result in the reduction of

thickness to the cell walls and allowing for the build-up of CO_2 to rupture of cell walls. Cell openness within polyurethane foams can be fine-tuned through a range of different methods, a few of these methods consist of spontaneous film rupture, surfactant phase separation, urea precipitation and viscosity rise.

2.4.2 Silicon Carbide

SiC is a ceramic material been indicated to not have piezoelectric properties as has extremely low dielectric properties. For sound damping applications, this material may not be effective within 50 Hz – 250 Hz due to the lack of its piezoelectric component. However, it is still of interest as the thermal conductivity of SiC is high in comparison to other ceramic materials. The synthesis of SiC was accidentally carried out by Berzelius in an attempt to produce a synthetic diamond.[190] This formation of SiC would lead to the material being used for several use cases due to its exceptional thermal conductive properties and semiconductor characteristics. The thermal conductivity of the SiC has also been shown to be dependent on the polytype present within the materials, where 4 H has a conductivity of 3.7 $W.cm^{-1}.K^{-1}$ and 6 H had a conductivity ranging between 3.6 – 4.9 $W.cm^{-1}.K^{-1}$.[191] SiC displays several polytypes with the most dominant forms having a hexagonal structure and are denoted as 2 H, 4 H, and 6 H. These hexagonal structures are named in this manner where the H demonstrates the hexagonal structure and the number represents the number of double atomic layers in the structure.[192] The material has also been shown to have a cubic structure which is denoted as β-SiC.[193] The thermally conductive properties of SiC are promising for sound damping applications within piezoelectric materials it effective dispersion of a SiC filler may have the potential to dissipate the thermal energy across the material effectively.

2.4.3 Silicon Nitride

Similar to the SiC mentioned above Si_3N_4 is also not known for its piezoelectric properties and is more known for its high resistance to thermal shock, and mechanical properties allowing for use within the automotive industry for wear and tear parts, and areas of high-temperature parts are required.[194] Si_3N_4 has two crystalline structures being α-Si_3N_4 and β-Si_3N_4. The α-Si_3N_4 has a hexagonal crystal phase where the nitrogen atoms are bonded to three silicon atoms in a trigonal planar configuration. Each silicon atom is bonded tetrahedrally to four nitrogen atoms. The β-Si_3N_4 displays a phenacite structure where trigonal arrangements of the silicon atoms tetrahedrally bond to the nitrogen atoms.[195]

2.4.4 Summary

The non-piezoelectric materials mentioned above have been demonstrated to be of interest for several reasons. It is known that polyurethane is a current material used for sound damping applications within vehicles and is still a desirable material. It has still demonstrated effective sound damping properties and this can still be potentially influenced by the addition of a secondary layer of non-woven materials. The three non-piezoelectric ceramic materials still display a dielectric constant which is of interest within the electrospinning of polymer composite materials as a factor to influence solution dielectric properties. From the three ceramics, the two silicon-based ceramics SiC and Si_3N_4 demonstrate effective thermal conductive properties making these materials useful for thermal energy dissipation across polymer matrix when used as a filler component.

2.5 Electrospinning

The literature so far has demonstrated that non-woven materials are effective at sound damping applications with the use of back cavities, the addition of filler components, and producing thick sample mats. The electrospinning technique is of great interest as it allows for all three areas mentioned to be targeted through the formation of polymer fibres. With this being said it is of interest to look into this process for tunability of the fibre composites to produce a range of fibre diameters which have been shown in 2.2.2 to be effective at sound absorption and reflection across a wide frequency range and in particular the low-frequency range with the piezoelectric effect being induced within piezoelectric polymers.

2.5.1 The History of Electrospinning

Gilbert[196] first analysed the electrostatic interactions of a liquid in the 17th century. The study had shown the manipulation of a liquid droplet into a cone structure when placed on a dry surface. Deformation of the liquid occurred when a rubbed piece of amber was held at a specific distance above the liquid droplet. This work would eventually become a part of the building blocks to understanding that an electrostatic force applied to a liquid droplet has the potential to manipulate the droplet and produce a cone-like structure.

Two centuries passed and Cooley[197] put forward the first patent on electrospinning in 1900. Within the patent, Cooley proposed to use of four types of charged spinning heads. These heads were the traditional spinneret head, a coaxial head, a spinneret with a rotating distributor and the model assisted by air. Many of these models are currently used in modern electrospinning setups to produce an array of different fibre morphologies for several polymers.

During the work, Cooley introduced the use of dielectric solvents rather than a gas medium. The work carried out was used on pyroxylin in an ether solution. The coaxial spinneret was applied to this work with a benzene and toluene solution. This may have been carried out to reduce the early evaporation of the ether leading to clogging of the spinneret.

The technique is widely known to have been advanced by Formhals with a contribution of 22 patents.[198] The early studies Formals conducted on the technique were carried out in the 1930s when the technique was not fully perfected. The drying times of the samples within the work were not ideal due to the short distance between the collector distance and the nozzle.[199,200] This issue was rectified in the 1940s and a new patient was put forth which revised the technical difficulties of his prior inventions by increasing the collector distance. Through these modifications, the formation of fibres was possible for several polymer materials.[201] Taylor[202] carried out his work on the deformation of droplets through the application of an electric field. He analysed the cone structure and had shown the release of a polymer jet from the cone produced. The cone structure produced at the end of the spinneret was named the Taylor cone due to the extensive work carried out by Taylor in the field. In more times that are recent, several groups demonstrated the formation of fibrous materials from multiple polymer materials. Among the groups, Reneker is the most notable who publicised the technique as electrospinning during the 1990s.[203] The most notable work carried out by Reneker *et al*. demonstrated the bending instability of liquid jets within polymer solution systems.[204]

2.5.2 The Process of Electrospinning

The electrospinning process allows for the formation of non-woven polymer fibre mats. These mats display a large surface area to mass ratio due to the fibre produced within the nano-micron range. These properties of electrospun materials can be applied in applications such as filtration systems[205], tissue engineering[206,207], sensors[208,209], drug delivery systems[210,211], and battery separators.[212]

The general setup of an electrospinning system can be seen in Figure 2.20. The technique requires a prepared solution (polymer/solvent system) which is fed through the capillary tube via a syringe at the desired feed rate to produce a droplet at the end of the spinneret. A high voltage is applied to the system which causes deformation to the solution droplet which is known as the Taylor cone.[202] To emit a jet from the Taylor cone a critical voltage is required.[213] During this process, the charge generated on the surface of the droplet acts to repel against one another causing the deformation of the droplet through shear stress. The electrostatic force is directed in the opposite direction of the surface tension, and once the critical voltage is achieved the electrostatic force overcome the surface tension of the Taylor cone and emits the jet. Once the jet is released, a whipping motion is generated as the instability

of the jet occurs under the coulombic forces. During this process, the solvent within the solution system evaporates and deposits a solid polymer fibre on the surface of the collector.[214]

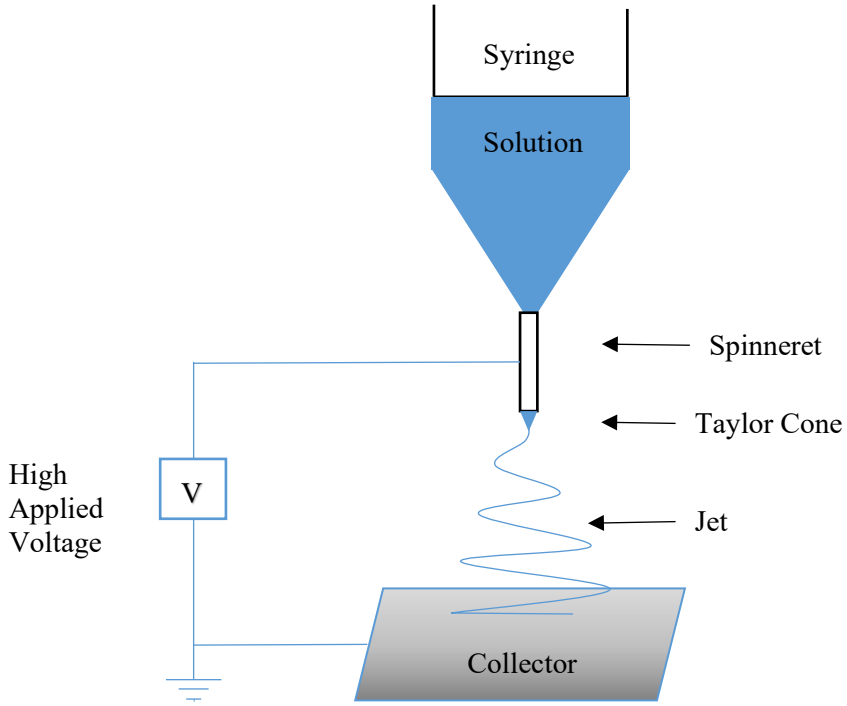

Figure 2.20. An adaptation of the electrospinning process.[215]

2.5.3 The Taylor Cone

Rayleigh[216] theoretically determined that at a specific value of charge, a droplet would be released in the form of a jet. However, the fineness of this jet was dependent on the charge and had an upper limit. The maximum amount of charge a droplet can hold before the formation of a jet can be demonstrated by Rayleigh's equation seen in:

$$q_R = 8\pi(\epsilon_0 \gamma R^3)^{1/2} \qquad \text{Eq.9}$$

where the charge density of a droplet can hold q_R of radius R with a surface tension of γ where the ϵ_0 is the relative permittivity in a vacuum.[217] The applied voltage typically increases with the increase in flow rate. This occurs because a higher voltage is required for the Taylor cone to stay intact and reduce cone instability during spinning.[218] The shape of the Taylor cone has been shown to have an effect on the ideal applied voltage. A larger more convex Taylor cone had a much larger surface area and required a higher voltage to maintain a stable cone. This allows the surface charge of the Taylor cone to be ideal for the formation of the jet.[218] Increasing the voltage to a much higher voltage leads to increased instability in the whipping of the polymer

jet.[219] Taylor[202] established that an angle of 49.3 ° was ideal for the formation of fibres, as the surface tension of the droplet was balanced with the electrostatic force applied to the system.

The increase in applied voltage is suggested to increase the jet thinning of the polymer, as it increases the velocity of the jet and increases the capillary pressure being applied. Combined this causes thinner fibres.[220] Increasing the voltage too high results in the formation of thicker fibre diameters due to the cone shape. Voltages much higher than the critical voltage produce cone shapes with an angle larger than 49.3°. This occurs, as the rate of fibre release from the cone is higher than the feeding rate of the solution.[221] Increasing the voltage leads to an increase in the forces which overcome the surface tension of the droplet, this results in more polymer being ejected from the droplet and leading the thicker fibre diameters.[222] Voltages above the critical voltage can also cause jet splitting where several jets are produced. The fibres repel each other due to the current flowing on the surface of the jets. This causes the fibres to produce larger mats as the jet produces covers a larger area of the collector as a result of the repulsion of fibres.[223]

2.5.4 Electrospinning Parameters Influencing Fibre Morphology

The parameters influencing the morphology of the materials can be categorised into two main sections. The first one is the electrospinning parameters which include the feed rate, collector distance and applied voltage. The second is the solution parameters which include the concentration, molecular weight, surface tension, solvent type, and solvent ratio. It is desired to look at these parameters as they are all known to influence fibre morphology to different extents and have different mechanisms for their influence on the morphology of the electrospun fibres.

2.5.4.1 Polymer Concentration

The polymer concentration within the solution system plays a large role in the transition from the electrospraying process where droplets are formed to the electrospinning process where fibres are formed. A low concentration favours droplet formation while increasing the concentration to above a critical value favours fibre formation.[224] Concentration is linked directly to solution viscosity where when an increase in polymer concentration occurs an increase in the solution viscosity occurs and thus transition from electrospray to electrospinning and further increases lead to the formation of larger average fibre diameters.[225] At high polymer concentrations a sufficient level of polymer chain entanglements is achieved which stops the breakup of the jets and allows for the elongation of the jet to occur effectively and prevents the formation of beaded fibres and smooth fibres can be developed.[226]

Megelski *et al.*[227] studied the influence of concentration on polystyrene and demonstrated the formation of beaded fibres at a concentration of 18 wt% – 30 wt% the removal

of beads occurred at 35 wt% of the polymer in THF solvent with a molecular weight of 190 k mol.g^{-1}. Mit-uppatham *et al*.[228] studied the influence of the concentration of PA-6 demonstrating similar results where the formation of beads occurred at low concentrations with a transition to fibres at higher concentrations. Here the polymer was dissolved in formic acid at several concentrations ranging between 10 % – 34 % w/v, with beaded fibres only forming at 20 w/v% and bead-free fibres occurring at 32 w/v% and above. Increasing the concentration from here demonstrated the formation of thicker fibres. Boland *et al*,[206] demonstrated similar results where an increase in concentration increased the fibre diameter of poly(glycolic acid). The study had shown the diameter of a minimum fibre of 0.11 ± 0.04 μm with a concentration of 1/20 w/v, where beaded fibres were formed. A maximum fibre diameter of 1.19 ± 0.41 μm was seen with an increase in the concentration for 1/7 w/v. The studies mentioned above all show a general trend where the concentration has a large influence on the formation and morphology of fibres across several polymer types. *et al*.[228] studied the influence of the concentration of PA-6 demonstrating similar results where the formation of beads occurred at low concentrations with a transition to fibres at higher concentrations. Here the polymer was dissolved in formic acid at several concentrations ranging between 10 % – 34 % w/v, with beaded fibres only forming at 20 w/v% and bead-free fibres occurring at 32 w/v% and above. Increasing the concentration from here demonstrated the formation of thicker fibres. Figure 2.21 demonstrates the link between polymer concentration and viscosity and the relationship between viscosity and average fibre diameter. An increase in concentration is linked to an increase in average fibre diameter as seen in the figure.

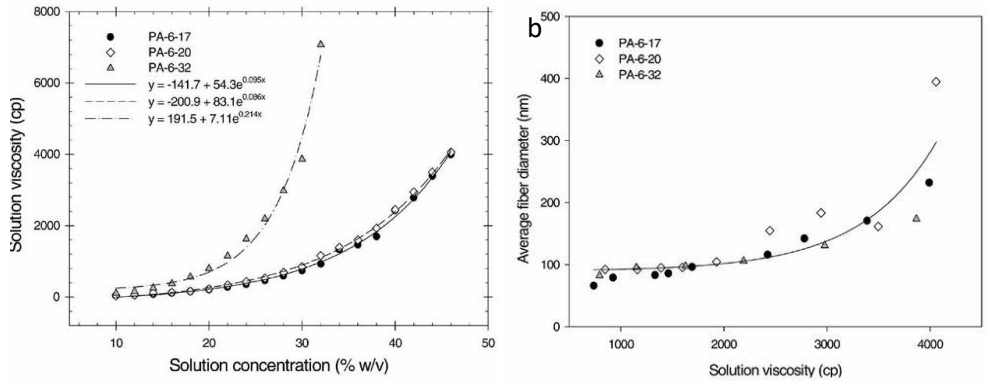

Figure 2.21: Demonstrating an increase in concentration increases viscosity and this influences average fibre diameter. [228]

Boland *et al*,[206] demonstrated similar results where an increase in concentration increased the fibre diameter of poly(glycolic acid). The study had shown the diameter of a minimum fibre of 0.11 ± 0.04 μm with a concentration of 1/20 w/v, where beaded fibres were

formed. A maximum fibre diameter of 1.19 ± 0.41 μm was seen with an increase in the concentration for 1/7 w/v. The studies mentioned above all show a general trend where the concentration has a large influence on the formation and morphology of fibres across several polymer types.

2.5.4.2 Polymer Molecular Weight

The molecular weight plays a similar role to that of the concentrations. It is shown that higher molecular weight polymers require a lower concentration of polymer within the solution system to produce bead-free fibres.[229] The changes in molecular weight result in a change in the solution viscosity of the material which is known to influence the formation of bead-free fibres and influence the average fibre diameters. Polymers with a lower molecular weight have fewer polymer chain engagements due to shorter chains. Larger molecular weight polymers have a higher percentage of entanglements in the chains and thus have a higher viscosity, reducing the formation of beads in the fibres.[230] Mit-uppatham *et al.*[228] had shown a decrease in the critical concentration required for the formation of fibres with an increase in the molecular weight. It was also suggested that an increase in viscosity was demonstrated with an increase in molecular weight however a decrease in concentration was required to maintain a steady viscosity for similar fibre formation. Similar to this study Koski *et al.*[231] demonstrated that increasing the molecular weight while maintaining the concentration of the polymer led to a transition from beaded fibres to bead-free fibres. It was also shown that a higher concentration of polymer was required at the lower molecular weights to produce bead-free fibres. The molecular weight and polymer concentration are parameters that are both linked. Changes to the molecular weight will in turn require changes to the polymer concentration to maintain a certain level of chain entanglements for fibre formation.

2.5.4.3 Solvent

The solvent type, solvent system, and solvent ratio all influence the fibre diameter and surface morphology of the polymer fibres across several fibres. The solvent type depends on the polymer that is chosen to be electrospun. The solvent system and solvent ratio are generally used to alter the volatility of the solution for sufficient solvent evaporation to take place.

Son *et al.*[232] demonstrated the influence of four solvent types on the fibre morphology of PEO. It was shown that solvents with higher dielectric constants produced fibres with thinner average diameters. It was suggested this occurs as the solvents with higher dielectric constants would hold more charge when in solution. This allows the polymer jet to experience a high level of stretching reducing the fibre diameter and bead size. In this case, (dimethylformamide) DMF

produced the thinnest fibres, however, had the highest boiling point. This required a larger collector distance and higher applied voltage to accommodate for fire formation and efficient solvent evaporation. Lee *et al*.[233] demonstrated the influence of solution conductivity on the fibre morphology of poly(ε-caprolactone). A binary solvent system of methylene chloride and dimethylformamide was applied. It was demonstrated that an increase in conductivity and dielectric constant occurred with an increase in the content of DMF ratio in the solution system. This suggested that one of the influencing factors for a decrease in the average fibre diameter was the increase in the electrical properties of the material. The solvent type can also be linked to viscosity and surface tension. Yang *et al*.[234] demonstrated this with the use of three solvents ethanol, dichloromethane and DMF with PVP as the polymer. The solvents altered the viscosity and surface tension of the solution, it was demonstrated that high surface tension and low viscosity resulted in the formation of beaded fibres, while lower surface tensions and higher viscosities did produce bead-free fibres.

Solvent volatility has previously been demonstrated to alter the fibre morphology producing fibres with pores or linear indentation on the surface of the material.[235] The rapid evaporation of the volatile solvent results in the cooling of the surface of the polymer. This causes water moisture to condense on the surface of the fibres creating droplets. These droplets evaporate during the electrospinning process resulting in nanopores on the surface of the fibre.[236] It can also result in the formation of long narrow voids at higher concentrations where solvent evaporation takes place at a lower rate.[237] The volatility of high-temperature solvents can be optimised with the addition of low-volatile solvents creating a binary solvent system. Alternatively, Bognitzki *et al*.[227] suggested rapid phase separation through the rapid evaporation of volatile solvent results in the formation of porous surface morphologies on fibres. The phase separation may occur due to rapid evaporation of the polymer which results in it becoming thermodynamically stable producing a polymer-rich phase and a lean polymer phase. The rich polymer phase solidified before the lean polymer phase which results in the formation of pores and rough surface morphologies of fibres.

2.5.4.4 Applied Voltage

The voltage has been shown to play a large role in the average fibre diameters and the formation of beaded structures within fibres. Generally, a critical voltage is required to emit a polymer jet from the Taylor cone. This is required to produce a strong enough electrostatic field for the release of the polymer jet.[238] It has been suggested that controlling the current of the droplet through changes in the voltage can influence the formation of bead-free fibres. This was demonstrated with PEO, where increasing the voltage from 5.5 kV to 9 kV led to a gradual increase in the current, where a rapid increase in the current between 7 kV – 9 kV was observed.

At this point, a transition from bead-free fibres to beaded fibres occurred. It was also observed that the Taylor cone began to recede into the spinneret itself decreasing in size.[239] Similar to this Zong *et al*.[240] demonstrated that increasing the voltage led to a reduction in the size of the Taylor cone, and fibres of larger diameter and beaded morphologies were produced. The formation of the larger beaded fibres occurs as more polymer is released from the jet causing an increase in the average fibre diameter and size of the beads. To further bring control to the average fibre diameter the electrostatic field can be altered through the addition of secondary components such as an electrostatic lens of the same polarity as the charged jet. This allows for control over the bending instability and in turn, allows for controlled deposition of the jets at the collector alongside a decrease in the average fibre diameters. A reduction in the fibre diameter through this mechanism is thought to be due to an increase in the potential difference between the tip and collector because of the addition of the secondary component.[241]

2.5.4.5 Surface Tension

During the electrospinning process, the electrostatic field is constantly opposing the surface tension of the material to generate an electrostatic jet. The surface tension attempts to reduce the surface area to mass ratio of the jet by producing spheres (beads) from the jet. There then becomes a competition between the surface tension and viscoelastic force which does not favour rapid changes in shape. This phenomenon is known as Rayleigh's instability.[216] To reduce the effects of Rayleigh's instability increasing the viscosity of the material can assist in the formation of smooth fibres occurs.[73] To release a polymer jet from the Taylor cone a critical voltage is required to overcome the surface tension as mentioned in previous chapters. Lee *et al*.[242] have shown that the critical voltage increases with an increase in the surface tension and the two parameters are correlated with each other and the solution conductivity. It was also demonstrated that altering the binary solvent ratio resulted in changes to the overall surface tension. In addition to this Ryu *et al.*[243] demonstrated that an increase in surface tension was also associated with an increase in the concentration and viscosity of the material when the solvent system was kept constant. When the polymer concentration is low the surface tension begins to influence the structure of the fibres resulting in the formation of beads.[239] Overall, it can be said that surface tension is influenced by several parameters and can be controlled depending on which of the mentioned parameters are altered.

2.5.4.6 Feed Rate

The feed rate allows for control over the formation of the jet and the fibre diameter. The feed rate is usually associated with the electrostatic field and works in tangent with the applied

voltage. When the electrostatic field is not strong enough to cause the release of the jet, it has been shown that decreasing the feed rate can assist in the release of a jet.[207] Altering the feed rate to a lower value has been shown to produce thinner fibres, while higher feed rates have been shown to increase the fibre diameter when the other spinning parameters are kept constant. It is suggested that larger droplets allow for the polymer to be carried to the collector at a faster velocity resulting in thicker fibres due to a reduction in the drawing of the jets during the process.[240] Similar studies demonstrated a slower feed rate resulted in ultra-fine fibres, while the higher feed rate resulted in the formation of larger fibres that were beaded. It was suggested the slower feed rate provides longer evaporation times for the solvent to evaporate to avoid the formation of beads.[244] When the feed rate exceeds a critical value the formation of beaded fibres occurs and the control over fibre diameter begins to slip. This occurs as there is insufficient time for the solvent to evaporate and beaded fibres and droplets are deposited at the collector.[227]

2.5.4.7 Collector Distance

The collector distance is a factor that can be controlled to assist in the formation of bead-free fibres and differing fibre diameters. Ki *et al*.[245] demonstrate that increasing the collector distance from 7.5 cm to 20 cm has little influence on the fibre diameter. However, it resulted in the formation of beaded fibres where inadequately charged droplets would reach the collector, which favours the formation of beaded fibres. In contrast, Yuan *et al*.[244] suggest that altering the collector distance does influence fibre diameter, where larger collector distances result in thinner fibres. Similar studies carried out by other groups have also demonstrated that shorter collector distances produce beaded or thicker fibre diameters, while longer collector distances produce thinner fibres.[246]

2.5.4.8 Summary

The parameters mentioned above all play a role in influencing the morphology of the polymer fibres. Fine-tuning these parameters is essential for the formation of bead-free fibres, with the concentration and molecular weight having the largest influence. Both parameters directly alter the viscosity of the solution which is linked to the formation of bead-free fibres. Once the required concentration and molecular weight are chosen and the viscosity is set for fibre formation parameters such as the applied voltage, feed rate, collector distance, and solvent system can be used to tune the fibre to the desirable range of fibre diameters to provide efficient sound damping properties.

2.5.5 Electrospinning PEO

PEO was one of the first polymers that were studied in early research carried out on the electrospinning technique. The polymer is easily dissolved in water and allowed many researchers to apply the electrostatic field to generate the polymer jets and produce the non-woven mats. PEO is generally electrospun in an aqueous solution where the amount of polymer weight required to produce a stable jet depends on the viscosity of the solution. Doshi and Reneker[203] demonstrated the formation of fibres within an aqueous solution with average fibre diameters of 0.05 μm – 5 μm. The work demonstrated that increasing the collector distance resulted in a decrease in the jet diameter because of the stretching and orientation of the polymer within the jet and jet formation would not occur when the viscosity was not within the spinnable range. Using a PEO weight of 1 wt% was shown to produce beaded fibres with the diameters of the fibres ranging between 200 nm – 600 nm with the smallest fibres being 60 nm. Beading distance depended on the diameter of the fibre whereas thinner diameters had beads closer together.[247] Altering the solvent to chloroform resulted in the removal of the beaded fibres and the formation of smooth fibre with a larger diameter of 1 μm – 2 μm. This occurs due to the higher volatility of chloroform in comparison to water, allowing for solvent evaporation to take place before bead formation can occur.[248] Similar to these results Norris *et al*.[249] demonstrated the formation of bead-free fibres with the addition of chloroform as solvent and produced average fibre diameters of 1.6 μm. Megelski *et al*.[227] analysed the influence of solvents on the surface morphology of PEO and demonstrated that the aqueous solution produced smooth fibres, while when acetone and chloroform were applied a rough surface morphology was observed. Like previous work the fibre morphology was thinner for that of the aqueous solution in comparison to the acetone and chloroform producing fibre diameters of 200 nm – 800 nm for the aqueous solution fibres and 800 nm – 1400 nm for the PEO / acetone and PEO / chloroform solutions.

Deitzel *et al*.[239] began to branch out and study in influence of concentration and voltage on the spinnability of PEO. This work demonstrated the window in which effective electrospinning could occur for the concentration, viscosity and surface tension being 4 wt% – 10 wt% 1 P – 20 P and 55–35 $dyn.cm^{-1}$, respectively. It was found that increasing the concentration of the polymer led to an increase in fibre diameter. It also suggests that the bead formation can be controlled by controlling the feed rate and voltage to allow for reduced bending instability at the Taylor cone itself. Drew *et al.*[250] later analysed that viscosity could influence fibre diameter independently of the concentration. The addition of TiO_2 ceramic filler demonstrated an increase in viscosity and was shown to increase the average fibre diameter. It

was also demonstrated the addition of filler resulted in the formation of beaded structures which may have been due to the agglomeration of the particles.

2.5.6 Electrospinning PVDF

Electrospinning PVDF fibres have been shown to produce thin fibre diameters with high surface areas, high porosity and enhanced electrical properties. This allows for non-woven PVDF fibres to be used for several purposes including polymer electrolytes, energy harvesting,[251] battery separators[252] This material is of particular interest for sound damping applications here as its displays piezoelectric properties and can be induced through the electrospinning technique as mentioned in 2.5.6.1. Early studies carried out on electrospinning PVDF were focused mainly on the removal of beaded fibres through changes made to the concentration of the polymer, and altering the ratios of the solvents, mainly DMF or (dimethylacetamide) DMAc and acetone. It was demonstrated by many studies that these two parameters heavily influenced the fibre morphology and altering them could bring control over fibre formation.

One of the earlier electrospinning studies carried out on PVDF was demonstrated by Koombhongse *et al*.[253] on the formation of electrospun ribbons and branched fibres. Within this study a concentration of 20 wt% PVDF was dissolved in a 1:1 ratio of DMF: DMAc and it was found that electrospinning the polymer resulted in the formation of branched fibres of approximately 1 μm in diameter. The process of branched fibres may occur due to the polymer jet splitting as the charges repel each other pulling the original jet into two streams which eventually dry and form branched fibres. Soon after the solvent types were altered to use a differing binary system of acetone and DMF where the fibres produced had fibre diameters of 250 nm. To enhance the physical properties of the non-oven PVDF fibres Choi *et al*.[254] attempted to thermally treat the materials between 150 °C – 160 °C. Thermal treatment of the fibres led to an increase in the fibre diameter, from 400 nm to 510 nm due to shrinkage taking place while heating the mats.

The influence of concentration, acetone, and collector distance on the fibre diameter was later analysed by Zhoa *et al*.[255] This study demonstrated the transition of beaded fibres to ultra-fine fibres through the addition of small quantities of acetone. A ratio of 8:2 DMF to acetone resulted in an average fibre diameter of 172 ± 89 nm. Interestingly it was suggested there was no visible difference in the fibre diameter with an increase in the tip-to-collector distance. Nasir *et al*.[222] demonstrated similar results when analysing the concentration, and collector distance. It was also demonstrated that with PVDF an increase in flow rate led to thinner fibres suggested occurring from a higher flow rate feeding through the jet allowing for more stretching of the fibres. Sanderson *et al*.[256] have also shown similar results where increasing the concentration of PVDF from 15 wt% to 20 wt% lead to a reduction in bead

formation and an increase in fibre diameter drastically from 294 nm to 1 µm respectively. Similarly, other studies have shown that changing concentration had shown similar results to several studies carried out where an increase in concentration increased fibre diameter.[257]

Yee *et al*.[258] analysed altering the ratio of DMF and acetone to increase in volatility of the solution. This resulted in the removal of beaded structures. It was also demonstrated that reducing the spinneret diameter assisted in thinning the fibre diameter and the bead size due to changes in the sizes of the Taylor cone altering the surface tension**.** These studies did not go into depth with a larger range of discrepancies between the solvent ratios. It was later shown by Choi *et al*. analysed the surface morphology of the fibres with changes in the ratio of DMAc: acetone, ranging across a larger ratio depth of 1:1 to 1:9. It was shown that increasing the content of acetone resulted in the formation of porous fibres which was previously analysed by Bognitzki *et al*.[259] The increase in the DMAc in the ratio was shown to increase the viscosity of the material and a decrease in the average fibre diameter was shown. As mentioned in 2.5.4.1 an increase in concentration results in an increase in viscosity and is associated with the formation of larger average fibre diameters. Here it was suggested that the decrease in fibre diameter was associated with the low volatility of the DMAc which allowed for more elongation of the polymer jets.

It is known that altering the solvent ratios can influence the surface tension and viscosity of the solution and enhance the electrospinning parameters of the fibres. A way to alter the surface tension and viscosity can be carried out by changing the chamber temperature. A temperature range between 5 °C – 45 °C has been shown to decrease the surface tension and viscosity of the solution producing thinner fibres.[260] With the concentration and solvent ratios analysed in the early studies carried out on PVDF fibres, the transition to electrospinning parameters was analysed. It was well known that a low concentration would result in beaded fibres, so higher concentrations were applied with a binary solvent system. From here the transition began where fibre diameter was analysed more and attempting to decrease the size of the fibres was to increase the surface area and performance of the materials.[261] demonstrated that altering the voltage, and collector distance could assist in bringing control of fibre distribution. Higher voltages, shorter collector distances and quicker feed rates all demonstrated narrower fibre diameter distributions, with shifts to lower diameters. It was shown that altering the voltage would result in changes being required to the feed rate and collector distance. For the two voltages of 6 kV and 1 kV collector distances of the feed rate of 7 cm, 0.5 $cm^3.h^{-1}$ and 10 kV, 10 cm, 1 $cm^3.h^{-1}$ were required respectively. It was suggested these changes were required to produce optimal charge repulsion for the formation of thin fibres. Similarly, the voltage has shown to decrease in average fibres of PVDF with an increase from 8 kV to 15 kV producing fibres diameters of 884 nm to 514 nm respectively. Where a higher voltage assists in

increasing charge density around the Taylor cone providing for higher elongation of the fibres.[252]

Table 2.7. The electrospinning parameters, fibre morphology, and β content for previous studies on PVDF.

Weight / %	Solvent type	Ratio	Applied voltage / kV	Collector distance / cm	Fibre diameter	β / %	Ref
20	DMAc: acetone	7:3	10 – 15	-	250 nm	-	[212]
25	DMAc	1	10	15	400 nm	-	[254]
15	DMF: acetone	8:2	5	10	172 ± 89 nm	-	[255]
32	DMF: THF	8:2	10 - 12	12	200-300nm	92	[257]
15	DMF: acetone	8:2	15	-	514 nm	-	[252]
28	DMAc	1	12	15	397 nm	-	[262]
10 - 20	DMF	1	7 – 20	15	121 ± 45 nm	75	[263]
12 - 22	DMF: acetone	6:4	15	20	70 ± 17 nm	86.6	[264]
12	DMF: acetone	6:4	11.5-14kV	16	415 ± 139 nm	81.6	[265]
22	Acetone: NMP	5:5	10-12kV	10 – 25	975±17 nm	85	[266]
26	DMF: acetone	6:4	20 kV	15	812±123 nm	68	[267]

2.5.6.1 Influence of Electrospinning on the Electroactive Phase of PVDF

As mentioned previously, the formation of the electroactive β polymorph occurs through several techniques including, hot stretching, solution casting, poling, and mainly mechanical stretching. It is desirable to nucleate the electroactive phase of PVDF to influence the sound damping properties within the low-frequency range of 50 Hz – 250 Hz. Several studies are suggesting that the electrospinning technique can assist in the nucleation of the β polymorph by providing polarisation of the PVDF during the process. However, early studies suggested that the electrospinning technique had little influence on the formation of the β polymorph, and further

treatment was required after the spinning process to induce it.[212,254] It was not until Zhou *et al*.[255] carried out an analysis of the crystal structure of PVDF fibres that led to some understanding of the nucleation of the β polymorph. The study suggested a weakening of the crystallisation of PVDF through DSC thermographs and WAXs analysis. The removal of the α polymorph intensity peak at 18.4 ° was observed in the X-ray diffraction graphs and the remaining intensity peak at 20.0 ° was suggested as the β polymorph. This suggests that electrospinning assists in the nucleation of the β polymorph. In contrast, Choi *et al.*[259] suggested the formation of the γ polymorph was present within the electrospun PVDF. The data suggested a combination of both the α polymorph and the γ polymorph with no indication of the β polymorph being present.

The nucleation of the β polymorph is suggested to occur due to the coulombic force experienced by the polymer jet when the electrostatic field is applied. In comparison to shear forces applied to the polymer solution at the spinneret, it has been suggested that coulombic force is the main influencing factor assisting in the nucleation of the β polymorph.[258] To increase the coulombic force and elongation of the polymer jet, the voltage can be increased within the spinnable range. Studies have shown that increasing the voltage allows for an increase in the charge density around the droplet, assisting in a shift from the α polymorph dominance to β polymorph dominance in the fibres.[268] Andrew and Clarke[263] had shown similar results where increasing the voltage from 10 kV > 15 kV > led to a decrease in fibre diameter and an increase in the percentage of the β polymorph producing a maximum content of 75 %. Gheibi *et al.*[267] had also shown that increasing the voltage also increases the β polymorph content in electrospun PVDF fibres. The high voltage is attributed to an increase in the stretching of the fibres during whipping.

To further enhance the elongation of the fibres the feed rate can be altered. Zheng *et al.*[269] demonstrated a decrease in feed rate from 75 $cm^3.h^{-1}$ to 5 $cm^3.h^{-1}$ resulted in a decrease in the content of the α polymorph, and the lower feed rate resulted in the dominance of the β polymorph. In contrast at a lower feed rate from 1 $cm^3.h^{-1}$ to 4 $cm^3.h^{-1,}$ a very small influence is seen where a slight increase in β content is observed.[270] It has also been demonstrated that there is no linear relationship between the feed rate and the β percentage. Where increasing the feed rate from 0.7 $cm^3.h^{-1}$ to 0.75 $cm^3.h^{-1}$ led to a decrease in the β polymorph formation and increasing the feed rate to 0.8 $cm^3.h^{-1}$ increased the content of the β polymorph. The non-linear relationship between the percentage β polymorph and the feed rate may be due to inconsistency in the fibre morphology, where the beading of the fibres at these lower feed rates may play a role in giving inconsistent β phase percentages.[265]

It was shown that increasing the spinneret diameter from 0.25 mm to 0.50 mm led to a decrease in the content of the β polymorph from 86 % to 53 %. While feed rate demonstrated very little change in the content of the β polymorph.[270] Both parameters act to increase the

elongation of the polymer jet with a decrease in the feed rate and spinneret diameter respectively. Where the lower feed rates and smaller spinneret diameters alter the surface area of the droplet allowing for higher charge density. Zheng *et al.*[269] have shown that four parameters have a large influence on the β phase formation in electrospinning. These parameters include feed rate, solvent, collector distance and temperature. The feed rate influences β polymorph formation at lower feed rates. The understanding is that at lower feed rates less polymer is being ejected from the spinneret and is more influenced by the stretching mechanism occurring during the whipping of the jet. The change in collector distance from a 20 cm to 10 cm distance had shown to increase the β content of the fibres. Baji *et al.*[264] have also shown similar results. Suggesting that the β polymorph is more dominant in fibres with smaller fibre diameters. The work produced fibres of 70 nm in size with β percentages of 86.6 %.

The solvent type is also known to influence the content of the electroactive phases in PVDF. It is shown that solvents with lower volatility produce fibres dominant in the α polymorph. While the addition of high-volatile solvents such as acetone assists in the nucleation of the β polymorph. The suggested mechanism for this is due to an increase in the evaporation rate a lower solidifying temperature is required. This may assist in promoting nucleation of the electroactive phase.[271] Zheng *et al.*[269] also suggested that altering solvent evaporation by changing the temperature within the chamber favours the nucleation of the β polymorph.

2.5.7 Electrospinning PVDF / Salt

The addition of salts to PVDF and other polymers is carried out to assist in providing control over the morphology, and crystallinity, and influence the material absorption properties.[272,273,274,275] It is generally thought that the changes in morphology are associated with the changes in charge density of the material, which occurs with the addition of salt when they dissociate within the solution.[240,276]

Lithium chloride (LiCl) has been proven to influence the morphology of PVDF fibres. At low quantities of 0.004 wt% it had been shown that the formation of beaded fibres can be reduced. However, there is a lower limit in viscosity of 6 wt% where below these beaded fibres begin to form again. This was shown to occur due to the interactions between the salt and the solvent system, which increased the viscosity of the material.[277] The addition of 0.00133 wt% LiCl has also been shown to result in a decrease in fibre diameter from 340 nm to 65 nm. It was demonstrated there is an upper limit in salt content where increasing the value above 0.00133 wt% results in the formation of beaded fibres due to a large increase in viscosity and conductivity.[278] Sahito *et al.*[279] were able to incorporate higher quantities of LiCl into the PVDF fibres of up to 1 wt%. However, increasing the content above this value also resulted in the formation of beaded fibres suggested occurring from overcharging the material resulting in

electron response. Overall the addition of LiCl assists in increasing the electrical conductivity of the solution allowing for better charge density around the polymer jet, this favours the formation of uniform fibres.[280,281]

Sodium chloride (NaCl) addition to PVDF had shown similar results where the addition of the salt resulted in the removal of beaded fibres. Small quantities of 0.2 wt% NaCl were required to produce the complete removal of the beaded fibres in 20 wt% PVDF.[262] The addition of NaCl to PVDF at different ratios has been shown to increase the porosity of the fibres and the ability of the fibres to uptake the volume of toluene. Having a ratio of 1:11 PVDF: NaCl has been shown to produce fires with a 92.5 % porosity which uptakes a volume of 504.2 % of toluene. It has shown that increasing porosity increases the volume of liquid uptake of the materials.[274]

Bismuth chloride ($BiCl_3$) was recently added to PVDF for energy harvesting applications in portable electric devices. This study has shown adding $BiCl_3$ to PVDF fibres increases the β polymorph percentage. The neat electrospun PVDF produced a β-phase percentage of 75.2 %, while the maximum was reached by the membranes containing 7 wt% of the salt with a value of 85.7 %. Fibre diameters had also been shown to increase with the addition of higher quantities of $BiCl_3$ between the 2 wt% - 10 wt% values as the increase in viscosity and conductivity due to the higher saturation of $BiCl_3$.[282] Lithium nitrate ($LiNO_3$) has recently been added to PVDF fibres for applications in electrolyte systems. The addition of the slat has been demonstrated to result in a decrease in the average fibre diameter reaching a size of 222 nm at a loading of 2 wt% of the salt. The addition of the salt was also demonstrated to influence the nucleation of the β polymorph.[283]

The addition of ammonium salts has been demonstrated to influence the fibre morphology where bead removal occurs and influences the nucleation of the β polymorph. Yee *et al*.[258] demonstrated this with the addition of the organic salt tetrabutylammonium chloride (TBAC). This study added 3 wt% of TBAC to the PVDF fibres which were suggested to assist in the removal of beaded fibres and the nucleation of the β polymorph. Benz *et al*.[284] proposed that the addition of TBAC caused the retention of water within the solution where hydrogen bonds were created between the backbone of the PVDF and the water assisting in the alignment of the chains in the β configuration. The formation of tree-like structures has also been demonstrated with the addition of tetrabutylammonium bromide (TBAB) and TBAC, owing to the increase in conductivity of the solution suggested causing slippage of the jet into several streams producing a branched structure.[285]

Table 2.8 The parameters for electrospinning PVDF / salt.

Polymer Weight / %	Salt weight / %	Applied voltage / kV	Collector distance / cm	Fibre diameter / nm	β / %	Ref
6	LiCl 0.004	25 / 28	12 / 15	-	-	[277]
16	LiCl 0.00133	20	20	65	93.6	[278]
22	NaCl 0.6	12	15	~ 80*	-	[262]
10	$BiCl_3$ 7	18	15	356 ± 104	85.7	[282]
19	$LiNO_3$ 2	25	10	222 nm	-	[283]
26	$NiCl_2 \cdot 6H_2O$ 0.5	15	15	80 – 120 nm	92	[273]

*Values are taken directly from a graph.

2.5.8 Electrospinning PVDF / Ceramic Composites

Ceramic materials are known for their electrical properties, dielectric and piezoelectric properties. Incorporating ceramic into polymer material can assist in enhancing the properties and produce a material with higher electroactive performance. As mentioned earlier in the literature review these properties can influence the morphology of the fibres alongside the sound damping materials so it is essential to look at how PVDF interacts with a range of ceramic fillers and the influence of the filler on fibre morphology previously studied.

PZT would be the ideal ceramic of choice due to its desirable electroactive properties. However, as mentioned earlier due to the toxic lead within the ceramic, disposal of the material is difficult and had negative environmental issues. Regardless of these studies have still been carried out to demonstrate the performance PZT can add to PVDF fibres. Chamankar *et al*.[286] have studied the addition of PZT to PVDF and the influence it has on the morphology and piezoelectric properties of the material. The addition of PZT increased average fibre diameters, due to an increase in viscosity. β polymorph formation also increased with an increase in PZT content to a maximum of 70 % with a maximum piezoelectric constant of 22.93 pC. N^{-1}.

Preliminary studies on the addition of $BaTiO_3$ ceramic have shown that the addition of these ceramic materials produces beaded fibres.[287] Similar studies carried out by Chanmal and Jog[288] demonstrated the formation of small fibres ranging between 200 nm – 400 nm with the formation of beaded structures. This work also analysed the nucleation of the β polymorph which demonstrated an increase in the content of the electroactive phase of the PVDF by 18 % with the addition of $BaTiO_3$ ceramic particles. Shu *et al*.[289] have shown the influence of $BaTiO_3$ nanoparticles on the morphology and β-phase content of PVDF fibres. A concentration of 15 wt% was added to PVDF with a combination of graphene. It was shown that a decrease in fibre diameter was observed with the addition of these nanoparticles. PVDF fibres generated fibre diameters in the range of 0.8 μm – 1.2 μm while in contrast, the fibres containing nanoparticles were smaller in the range of 0.4 μm – 0.8 μm. A maximum β polymorph content of 91.1 % was generated with 15 wt% $BaTiO_3$ and 0.15 wt% of graphene. More recently Jiang *et al*.[290] demonstrated similarly resulted where a maximum of 91 % β polymorph was achieved with the addition of 10 wt% $BaTiO_3$ nanoparticles with similar fibre diameters of 1.27 μm.

Another ceramic titanate, barium strontium titanate, has been incorporated into PVDF fibres due to its excellent piezoelectric properties. The addition of these fibres to PVDF materials has been used for energy harvesting applications. Pan *et al*.[291] incorporated barium strontium titanate (BST) into PVDF producing non-woven fibres with diameters of 6.8 μm – 13.7 μm. These materials demonstrated an increase in fibre diameter with the addition and increase in the content of the ceramic and suggested that BST assisted in the nucleation of the β polymorph.

ZnO is another piezoelectric ceramic that has semiconductor properties. Bafqi *et al*.[292] have studied the addition of ZnO particles to PVDF for energy harvesting applications. The fibres produced within this study were bead free with diameters of 757 nm. The addition of ZnO nanoparticles also assisted in increasing the β polymorph content by 7% to 87 %. The addition of the material enhances the piezoelectric properties of the material increasing the output voltage to 2.5x the original value from 315 mV to 1100 mV. It is also possible to grow ZnO rods on the surface of the PVDF fibres through hydrothermal synthesis techniques. Mansouri *et al*.[293] demonstrated that the addition of ZnO particles to PVDF resulted in a decrease in the average fibre diameter of the material as the conductivity of the solution increased with the addition of the ceramic. Kim *et al*.[294] developed PVDF / ZnO composites for nanogenerator applications in wearables. The fibres generated displayed average fibre diameters of 120 ± 100 nm with rod diameters of 183 ± 153 nm. The hydrothermal synthesis of ZnO caused a reduction in the β polymorph in the PVDF from 83.8 % to 80.2 %. However, the piezoelectric response from the material was much larger with the ZnO incorporated with a value of 8361 mV.

SiO_2 of 3 wt% – 7 wt% has previously been added to PVDF fibres to determine its influence on fibre morphology and average fibre diameter. It was shown that the addition of the particles had little influence on the average fibre diameter producing diameters of ~ 490 nm, however, the surface roughness increased with an increase in the content of the ceramic. It was also demonstrated that the addition of SiO_2 resulted in a decrease in the content of the crystalline phase within the material due to it hindering the recrystallisation of the polymer and preserving the amorphous phase.[295] In contrast it was shown that the addition of 10 wt% – 30 wt% SiO_2 to 27 wt% PVDF resulted in a decrease in average fibre diameters with diameters of 310 – 360 nm from the 1.07 μm of the PVDF fibres.[296] Ma *et al*.[297] recently added Si_3N_4 to PVDF fibres for applications as a battery separator in sodium-ion batteries. The addition of Si_3N_4 resulted in fibre diameters of 615 nm and was shown to assist in the nucleation of the β polymorph.

Titanium dioxide (TiO_2) is another ceramic oxide that has previously been added to PVDF. Zhu *et al*.[298] developed a PVDF / TiO_2 composite to enhance the piezoelectric properties of PVDF. The study demonstrated to produce fibres with average diameters of 300 nm – 400 nm. The addition of the ceramic assisted in increasing the piezoelectric constant of the material to a maximum of 30.7 $pC.N^{-1}$ with a loading of 2 wt% with a maximum output voltage of 3.85 Bharath *et al*.[299] analysed the addition of another ceramic oxide in magnesium titanium dioxide ($MgTiO_3$) to PVDF. The study had proven to produce fibres in the range of 200 nm – 300 nm. These fibres produced have shown an β phase percentage of 50 % – 65 % for samples with 0 wt% – 40 wt% $MgTiO_2$. The fibres containing 10 wt% $MgTiO_2$ had a β polymorph percentage of 53%. Higher portions of $MgTiO_2$ produced a higher amount of β polymorph.

Like ceramic oxides, nano clay materials have been demonstrated to influence the morphology of PVDF fibres, alongside the crystal structure. Liu *et al.*[300] electrospun PVDF with organically modified montmorillonite (OMMT). Fibre diameter decreased with the addition of the OMMT, due to a decrease in viscosity. It was also demonstrated the addition of the low amount of nano clay of 1 wt% resulted in an increase in the electroactive phase within the PVDF of 67.5 %. In contrast bentonite, and nano clay addition demonstrated different results. The PVDF fibres from this material resulted in an increase in the average fibre diameter from 577 ± 15 nm to a maximum of 715 ± 56 nm with the addition of the material, this was suggested to occur due to an increase in the viscosity of the solution with the addition and increase in the content of the nano clay. Here the content of β polymorph increased past 1 wt% to 2 wt% with a maximum of ~ 75 %.[301]

Zeolite particles have previously been added to PVDF fibres for high permeability applications for filtration systems. He *et al*.[302] demonstrated that the addition of zeolite to PVDF fibres resulted in an increase in fibre diameter due to an increase in the viscosity of the material. Potentially due to the absorption properties of the zeolite uptaking the solvent. The addition of

these particles also had little influence on the crystal structure producing fibres dominant in the α polymorph. Like this work, Lopes *et al*.[303] demonstrated an increase in fibre diameter as well from 180 nm to 300 nm. However, in contrast, the formation of the β polymorph was suggested. The addition and increase in the concentration of the zeolite did not demonstrate to influence β polymorph nucleation, suggesting the electrospinning process assisted in the nucleation of the electroactive phase over the polymer. Other studies also suggested little difference in fibre diameter in comparison to the PVDF fibres without particles. Average fibre diameters of 350–400 nm were achieved with the addition of 5 wt% zeolites.[304]

As mentioned in sections 2.3.5 and 2.3.6 niobium oxides have exceptional electrical properties and can be used as alternative materials to PZT. Pazhamalai *et al*.[305] incorporate $NaNbO_3$ into PVDF fibres for applications of battery separators and energy harvesting applications. The fibres in this study had diameters of 500 nm with the addition of 10 wt% ceramic. The piezoelectric response was enhanced with the addition of the $NaNbO_3$ from 1.2 V to 4 V at a compressive load of 5 N and 6 V at 10 N compressive force. More recently the fibres were produced and analysed for energy harvesting applications and demonstrated to produce an output of 25V with a compressive force of 10 N.[306]

The alternative ceramic to $NaNbO_3$ is potassium sodium niobate (KNN), which is also known for its piezoelectric properties. Teka *et al*.[307] were one of the first groups to incorporate KNN into PVDF fibres. These fibres were produced for energy harvesting applications, where nucleation of the β polymorph was suggested. The percentage content of the electroactive phase had shown to increase with the addition of the ceramic from 64 % to 68 % respectively. The voltage output of the materials had also been shown to significantly increase with the composite fibres with a value increasing from 50 mV to 1.9 V. In contrast to this study, Bairagi and Ali,[308] suggested that the addition of KNN resulted in a reduction in the content of the β polymorph within the PVDF fibres from a maximum of 97 % to 78 %. However, the addition of the ceramic increased the overall piezoelectric performance of the material producing a maximum output voltage of 17.5 V as in previous studies. To further enhance the piezoelectric properties of the PVDF fibres, a mix of KNN and ZnO nanorods have been developed. The mixed ratio had proven to enhance nucleation of the β polymorph and piezoelectric properties of the material displaying values of 97 % and 25 V respectively.[309]

Table 2.9. PVDF / ceramic fibre processing parameters, morphology, and β content.

Polymer weight / %	Ceramic weight / %	Applied voltage / kV	Collector distance / cm	Fibre diameter	β / %	Ref
10	PZT 1 - 60	20	15	119 – 339 nm	70	[286]
-	$BaTiO_3$ 0.1 – 3	15	15	-	β	[287]
15	$BaTiO_3$	15	15	200 – 400 nm	80	[288]
5	$BaTiO_3$ 5 – 20	10	20	1.06 – 124 μm	91	
26	ZnO 7 - 18	16	17	757	87	[292]
18	SiO_2 3 – 7	18	15	~ 490 nm	β	[295]
27	SiO_2 10 - 30	20	15	310 – 360 nm	α, β, γ	[296]
12	Si_3N_4	15	15	615 nm	β	[297]
20	TiO_2 0.5 – 2	20	5	200 – 300	β	[298]
-	$MgTiO_3$ 10 - 40	12 - 18	14 - 18	200 - 300	65	[299]
20	OMMT 1 - 3	15	15	-	β, γ	[300]
18	Bentonite 0.25 - 2	15	12	577 – 715 nm	75	[301]
-	Zeolite 1 - 5	13	15	570 – 690 nm	α	[302]
20	Zeolite 4 - 32	1.25 kV cm^{-1}	15	180 – 300 nm	84*	[303]
16	Zeolite 5	10	10/12.5	350–400 nm	-	[304]
10	$NaNbO_3$ 10	15	10	500 nm	-	[305]
10	$NaNbO_3$	15	10	100 – 200 nm	-	[306]
25	KNN 5	23	15	-	68	[307]
30	KNN 5	20	20	200 – 300 nm	84	[308]
30	KNN / ZnO 3 / 2	20	20	300 nm	94	[309]

*β%, where the percentage isn't given the appearance of each polymorph, is stated.

2.6 Summary of the Literature

In summary, the electrospinning field is highly saturated with a large range of polymers being spun for a large range of applications. There is a range of non-woven polymers that have been used for sound damping applications due to the high surface area to mass ratio that is obtainable. Non-woven fibres have been chosen as the type of fibre material due to the complex structure produced and small fibre diameters which effective airflow resistivity for sound absorption. These types of fibres also provide the added benefit of tortuosity for effective sound energy dissipation.[310] With this being mentioned electrospinning was utilised to produce the non-woven polymers as it was the only available technique at the time of the study. It should be mentioned that other techniques such as melt spinning are also good options for fibre formation and could be considered in future work. The materials produced using the electrospinning technique have thin sample thicknesses making it difficult for these materials to act effectively as sound damping applications due to the thin nature of the mats where foamed backing provides that needed thickness for effective sound absorption. However, there are still gaps within the field of electrospinning non-woven ceramic composite fibre especially for sound damping applications involving:

(i) Bringing control over the fibre diameters has been demonstrated for a range of titanite ceramics, but there it's a large gap within the field of bringing control to fibre morphology through the addition of niobium oxide and silicon-based materials. Alongside this the nucleation of the electroactive β polymorph within PVDF fibres is yet to be displayed with these materials and if it is possible to do so with the changes in the piezoelectric and dielectric properties of these ceramics display. β polymorph percentages values range between 65 – 94 % β polymorph for materials with fibre sizes of 100 – 1240 nm.

(ii) There is a shortage of studies on the influence of non-woven PVDF ceramic composites on the sound damping applications of a material across a broadband spectrum. Using piezoelectric ceramic materials to overall influence the polymer fibre mat piezoelectric properties for sound absorption at the low-frequency range of 50 Hz – 250 Hz. Current studies are using non-ceramic fillers for sound absorption at this frequency range, and the ceramic fillers used have not explored this area.

(iii) Inorganic salt addition to polymer non-woven fibre has been well studied with these materials producing fibre diameters below 400 nm alongside β polymorph percentages of above 85 %. However, there are still gaps to be filled with the

addition of KCl to PVDF fibres via electrospinning. Understanding, the level of control KCl can provide to the average fibre diameter and its overall influence on the nucleation of the β polymorph within PVDF.

(iv) The mixing of two different ceramic materials to produce an overall material for effective sound damping is not well studied. It is known that ceramic materials can influence the electrospinning technique to different degrees however a mixture of ceramics with two mechanisms taking place during the spinning technique is yet to be fully understood.

2.7 Aims and Objectives

Identifying the gaps within the literature has led to an understanding of which areas require the addition of further study to provide more depth and knowledge to the field as specified above. Based on this there is an exciting potential to utilise the electrospinning technique to produce non-woven polymer ceramic composite fibres for sound damping applications. With a specific interest in attempting to control the fibre size producing fibre diameters of 500 nm and below with the addition of inorganic salt and a range of piezoelectric and dielectric ceramics. If achievable these non-woven polymer ceramic composite materials could act to enhance the current sound damping materials currently used within the automotive industry. Electrospinning has been chosen as the spinning technique as it is the technology available during the time of the study. However, there are still more effective industrial-scale techniques such as melt spinning which can be considered in future work. Here only small sample sizes are needed to analyse the sound damping properties of the material electrospinning was considered sufficient to produce these materials.

Aims:

(i) Develop electrospun fibres of PEO and PVDF with fibres morphologies that are free of beads and within the sub-micron range as these materials have a high surface area to mass ratio which can influence sound damping properties.

(ii) Disperse the niobium oxides, and silicon-based ceramics effectively within the PEO and PVDF fibres to influence the piezoelectric properties of the materials.

(iii) Control the fibre diameter with changes made through the addition of KCl salt, ceramic content, and ceramic type.

(iv) Verify the content of the ceramic filler which has been added to the electrospun fibres.

(v) Nucleate the electroactive β polymorph within the PVDF with the addition of the KCl salt and ceramic fillers.

(vi) Verify if the piezoelectric properties of the electrospun fibre composites assist in increasing the sound damping properties.

Objectives:

(i) Prepare a range of non-woven composite fibres through the electrospinning technique.

(ii) Apply SEM imaging to analyse the structure and confirm the dispersion of each ceramic within the fibres.

(iii) Use techniques such as FTIR, DSC and XRD to confirm the nucleation of the β polymorph within PVDF.

(iv) Determine the thermal-mechanical damping properties of the fibres by using DMTA analysis.

(v) Apply impedance sound testing using impedance tubes across a frequency range of 50 Hz – 6000 Hz.

Chapter 3 Experimental

3.1 Materials

3.1.1 Polyvinylidene Fluoride

The PVDF, grade Kynar 740 was purchased from Arkema. The melt flow rate of the polymer is 1.5 g – 3.0 g 10 min^{-1} (ASTM D1238). The density is 0.96 $g.cm^{-3}$ with a melting temperature ranging between 200 °C – 240 °C as stated on the provided datasheet. The average molecular weight was calculated using gel permeation chromatography (GPC) where a value of 300000 $g.mol^{-1}$ was analysed and denoted the high molecular weight (HMW) variant. The low molecular weight (LMW) PVDF displayed a molecular weight of 190000 $g.mol^{-1}$.

3.1.2 Potassium Chloride

KCl ≥ 99% was purchased from Fisher Scientific.

3.1.3 Niobium Oxide Ceramics

$NaNbO_3$ was purchased from Cerpotech. The ceramic was purchased as a fine white powder with a particle size of ≤ 1 μm and a density of 4.42 $g.cm^{-3}$ and was phase pure with a crystal structure in the orthorhombic perovskite phase. $KNbO_3$ > 99% was purchased from Cerpotech. The ceramic was also purchased as a Fine white powder with a particle size of ≤ 1 μm and a density of 4.62 $g.cm^{-3}$ and was phase pure with a crystal structure in the orthorhombic perovskite phase, Amm2. $CeNbO_4$ was also purchased from Cerpotech. The ceramic was purchased as a fine green powder with a particle size of ≤ 1 μm and was phase pure within its stoichiometric phase $CeNbO_{4.25}$. All the information on the three ceramics was obtained from the company's provided datasheet.

3.1.4 Silicon Ceramics

Alpha SiC, grade UF – 25 was purchased from abcr and produced by Kyocera. The ceramic was purchased as a fine dark grey powder with a density of 3.32 $g.cm^{-3}$ and was in the alpha phase with a particle size of 0.65 μm. Si_3N_4 99.3 %, grade M 11 was purchased from abcr produced by Höganäs. The ceramic was purchased as a fine light grey powder with a particle size of 0.5 μm – 0.7 μm and a density of 3.440 $g.cm^{-3}$ and was in the alpha phase < 90%. The information provided here was obtained from the provided datasheets from both abcr and Höganäs.

3.1.5 Polymer Foams

PET foam was provided by Miers Rubber & Plastic. The density of the foam was 26 – 32 $kg.m^{-3}$. PU foam was also provided by Miers Rubber & Plastic. The density of the foam was 39 – 44 $kg.m^3$ with a cell diameter of 510 μm – 670 μm. All the information on these materials was obtained from the provided datasheet.

3.1.6 General Solvents and Reagents

Dimethylformamide (DMF) > 99 % was purchased from Fisher Scientific. The density of 0.944 $g.cm^{-3}$ and a boiling point of 153 °C. Dimethylacetamide (DMAc) 99 % was purchased from Alfa Aesar. The density of 0.940 $g.cm^{-3}$ and a boiling point of 156 °C – 166 °C. Acetone ACS reagent ≥ 99.5 % was purchased from Sigma Aldrich. The density of 0.701 $g.cm^{-3}$ and a boiling point of 56 °C. The data was provided by the datasheets obtained from the companies the solvents were purchased from.

3.2 Sample Preparation

3.2.1 Ceramic Milling

The Si_3N_4 was milled and freeze-dried to reduce the particle size of the materials due to the agglomeration of the particles. 50 g of the ceramic was placed within 200 cm^3 of distilled water in a round plastic bottle. Yttria-stabilised zirconia (YST) balls were added to the mixture to break down the ceramic particles. The prepared slurry was rotated and mixed on a Capco Ball Mill Model 12 VS for 24 hours. Upon completion of mixing the slurry was placed in a glass beaker. The slurry was then freeze-dried within a FreeZone 2.5 Litre Benchtop Freeze Dryer for 48 hours for the complete removal of the distilled water to produce fine ceramic powder.

3.2.2 Solution Preparation

The pure PVDF solutions were prepared by magnetically stirring the polymer within a singular solvent or a binary solvent system containing either DMF, DMAc or a mixed ratio of DMAc: acetone. The concentration of the PVDF within the solvents ranged between 10 wt% – 30 wt%. The polymer solution system was magnetically stirred for 2 hours at a heated temperature of 60 °C until a clear solution was observed. The LMW PVDF were mixed in a solvent volume of 5 cm^3 – 10 cm^3 while the HMW PVDF was mixed in a solvent volume of 20 cm^3.

Table 3.1. Contents for the LMW PVDF solution system.

Polymer type	Polymer weight / g	DMF volume / cm^3	DMAc volume / cm^3	Acetone volume / cm^3
PVDF 15 wt%	0.71	5	0	0
PVDF 20 wt%	0.94	5	0	0
PVDF 10 wt%	0.86	0	5	5
PVDF 12 wt%	1.04	0	5	5
PVDF 15 wt%	1.30	0	5	5
PVDF 20 wt%	1.78	0	7	3
PVDF 20 wt%	1.75	0	6	4
PVDF 20 wt%	1.73	0	5	5
PVDF 22 wt%	1.90	0	5	5
PVDF 25 wt%	2.23	0	7	3
PVDF 25 wt%	2.20	0	6	4
PVDF 25 wt%	2.16	0	5	5
PVDF 25 wt%	2.12	0	4	6
PVDF 25 wt%	2.09	0	3	7
PVDF 27 wt%	2.33	0	5	5

Table 3.2. Content for the HMW PVDF solution system.

Polymer type	Polymer weight / g	DMAc volume / cm^3	Acetone volume / cm^3
PVDF 15 wt%	2.59	10	10
PVDF 20 wt%	3.46	10	10
PVDF 25 wt%	4.32	10	10
PVDF 26 wt%	4.49	10	10
PVDF 27 wt%	4.67	10	10
PVDF 28 wt%	4.84	10	10
PVDF 29 wt%	5.01	10	10
PVDF 30 wt%	5.18	10	10

3.2.2.1 PVDF / KCl Solution Preparation

The PVDF / KCl solution preparation was carried out like that of the pure PVDF solutions. The KCl salt was added at a weight percentage between 0.2 wt% – 10 wt% to a binary solution system of 1:1 DMA / acetone. It was magnetically stirred for 18 hours at room temperature. The PVDF pellets were then added to the KCl / solvent system and magnetically stirred for 2 hours at a temperature of 60 °C until the polymer was completely dissolved within the system. The LMW PVDF was prepared within 10 cm^3 of solvent while the HMW PVDF was prepared within 20 cm^3 of solvent. The content of PVDF / KCl solutions can be seen in Table 3.3. Contents for the PVDF / KCl solution system.

Table 3.3. Contents for the PVDF / KCl solution system.

Polymer Type	Polymer weight /g	KCl weight / %	KCl weight / g
LMW PVDF 25 wt%	2.16	0.2	0.0043
LMW PVDF 25 wt%	2.16	0.4	0.0086
LMW PVDF 25 wt%	2.16	0.6	0.013
LMW PVDF 25 wt%	2.16	0.8	0.017
LMW PVDF 25 wt%	2.16	1	0.022
LMW PVDF 25 wt%	2.16	2	0.043
LMW PVDF 25 wt%	2.16	3	0.066
LMW PVDF 25 wt%	2.16	5	0.11
LMW PVDF 25 wt%	2.16	10	0.22
HMW PVDF 30wt%	5.18	0.2	0.010
HMW PVDF 30wt%	5.18	0.4	0.021
HMW PVDF 30wt%	5.18	0.6	0.031
HMW PVDF 30wt%	5.18	0.8	0.041
HMW PVDF 30wt%	5.18	1	0.052

3.2.2.2 PVDF / Ceramic Solution Preparation

The PVDF / ceramic solutions were prepared similarly to the PVDF / KCl solutions. The ceramic filler was added between 1 wt% – 10 wt% in a 20 cm^3 binary solvent system with a 1:1 for the DMAc / acetone for all the solutions prepared. The filler was magnetically stirred for 18 hours at room temperature until a cloudy solution was produced. The HMW PVDF of 5.18 g was then added to the solution and magnetically stirred for 2 hours at a temperature of 60 °C until the polymer was fully dissolved in the solvent.

Table 3.4. The content of the ceramic fillers in the HMW PVDF solutions.

Ceramic weight / %	Ceramic weight / g
1	0.052
3	0.155
5	0.259
10	0.518

3.2.3 Electrospinning the Fibres

The electrospun PVDF fibres were produced using a Spraybase electrospun CAT000001 setup composed of a Spraybase 20 kV power supply controller, Spraybase electrospinning platform, Spraybase syringe pump module, 23-gauge spinneret, capillary tube, and a transparent safety cover. The system feeds the polymer solution system through the capillary tube at a specified feed rate. At the spinneret end, an applied voltage is added which causes the deformation of the droplet into a cone-like structure named the Taylor cone. Once the electrostatic force created overcomes the surface tension of the polymer droplet a jet is emitted from the tip which is deposited at the collector.

The electrospinning of the pure PVDF fibres, PVDF / KCl fibres, and PVDF / ceramic fibres was carried out using the general procedure as follows. 5 cm^3 of the PVDF solution was placed in a 5 cm^3 luer lock syringe and connected to the electrospinning set-up. A feed rate ranging between 0.5 $ml.h^{-1}$ – 2 $ml.h^{-1}$ was applied to the system. A collector distance of 10 cm – 15 cm was used. The solution was subjected to an applied voltage range between 6 kV – 20 kV depending on the filler added to the solution system. Once the polymer jet was deposited onto the surface of the aluminium foil it was heated at 40 °C for 24 hours to remove any excess solvent from the system.

3.3 Sample Characterisation

3.3.1 Solution Viscosity Measurements

The viscosity of the solutions produced was analysed using a DV2T Brookfield viscometer. Spindle number 63 was applied to the system, using a rotational rate of 100 RPM for a sustained period of 1 minute. 20 cm^3 of the polymer-solvent solution was used within a medium-sized vial for these measurements to ensure the amount of solution was available to reach the minimum amount required for accurate measurements.

3.3.2 Solution Conductivity Measurements

The solution conductivity was measured using a Thermo Scientific Orion Star A212 Benchtop Conductivity set-up. To carry out measurements an ultra-pure water conductivity sensor was used taking measurements using 20 cm^3 of the prepared PVDF / KCl solutions.

3.3.3 Gel Permeation Chromatography

GPC was carried out on the LMW and HMW PVDF using an Agilent 1260 Infinity II-MDS, with an eluent of DMF with 5mM NH_4BF_4, and a 2 x PLgel Mixed-D column. 1 mg of the PVDF was dissolved in the 3 cm^3 of DMF at 60 °C for 2 hours before being prepared for analysis under the GPC. A flow rate of 1 ml/Min was used.

3.3.4 Scanning Electron Microscopy

The scanning electron microscopy (SEM) technique utilises a high-intensity energy electron beam to produce a high-resolution magnified image. The electrons within the electron beam pass through a column that is loaded with an electromagnetic lens which assists in focusing the beam on the sample stage where the sample is mounted. The sample stage is located within a vacuum chamber where the detectors are located.[311] The system is operated by using the control computer and panel. SEM analysis requires the sample to effectively conduct the incident beam of electrons to avoid charging the sample surface they are coated with a conductive material such as gold-palladium (Au/Pd).[312] When the electrons reach the sample surface excitation of the electrons occurs within the material which results in the release of x-rays or electrons.[311] The types of electrons and X-rays released at different depths within the sample are auger electrons, secondary electrons, backscattered electrons, characteristic X-rays, continuum X-rays, and fluorescent X-rays as seen in Figure 3.1.

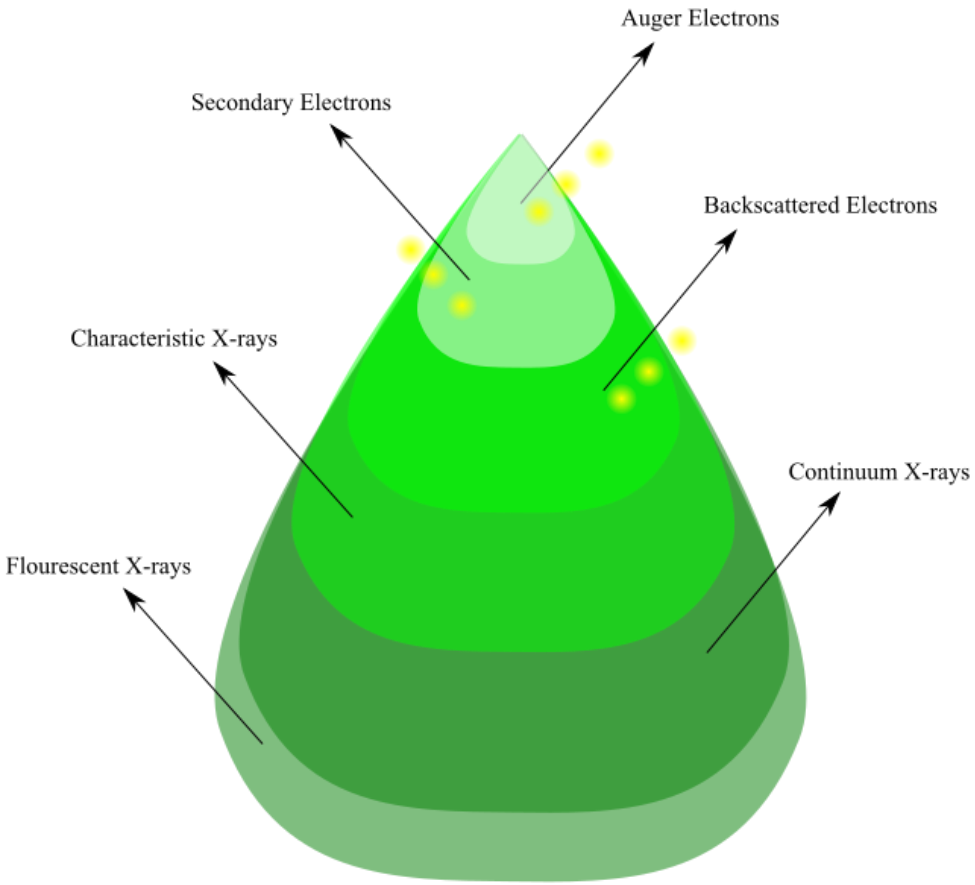

Figure 3.1. Release of Electrons and X-rays at different depths within a sample.

The PVDF fibres electrospun were coated with a thin layer of gold/palladium (Au / Pd) before being mounted on the SEM stage where a conductive carbon tab was used to adhere the fibres to the stub. A Zeiss Sigma scanning electron microscope was used to produce the micrographs. Three probes were used to produce three different images for the prepared samples. An in-lens probe was used at a working distance ranging between 3 mm – 5 mm with a voltage of 5 kV to look at the fibre morphology. Backscattering diffraction (BSD) probe was applied to distinguish between the particles and polymer for certain samples. A working distance of 10 mm was used with a voltage of 10 kV and a high current. This was carried out to distinguish between the particles and polymer within the composite fibre systems. Energy-dispersive X-ray spectroscopy (EDS) was applied to obtain an elemental analysis of the composite fibres to determine the distribution and confirmation of the addition of ceramic particles to the fibres. A working distance of 10 mm was used with a voltage of 10 kV using the EDS probe.

3.3.5 Fourier Transform Infrared

Fourier transform infrared spectroscopy (FTIR) is a rapid analysis technique that allows for the identification of organic, and inorganic materials carried out by applying infrared light to the intended material. A general FTIR setup consists of an IR source, beam splitter, fixed mirror, moving mirror, and a detector seen in Figure 3.2. The IR rays interact with the beam splitter causing partial splitting of the waves where they interact with the corresponding mirrors and reflect towards each other interacting and travelling towards the sample cell and detector. [313,314] Functional groups within the material absorb the infrared beam and vibrate in specific motions, including bending, stretching, rotation, deforming or a combination of vibrations. The absorption and vibration of the peaks can be correlated to specific functional groups and the orientation of polymer chains.[313] This assists in determining the polymorphic structure the PVDF polymers are within.

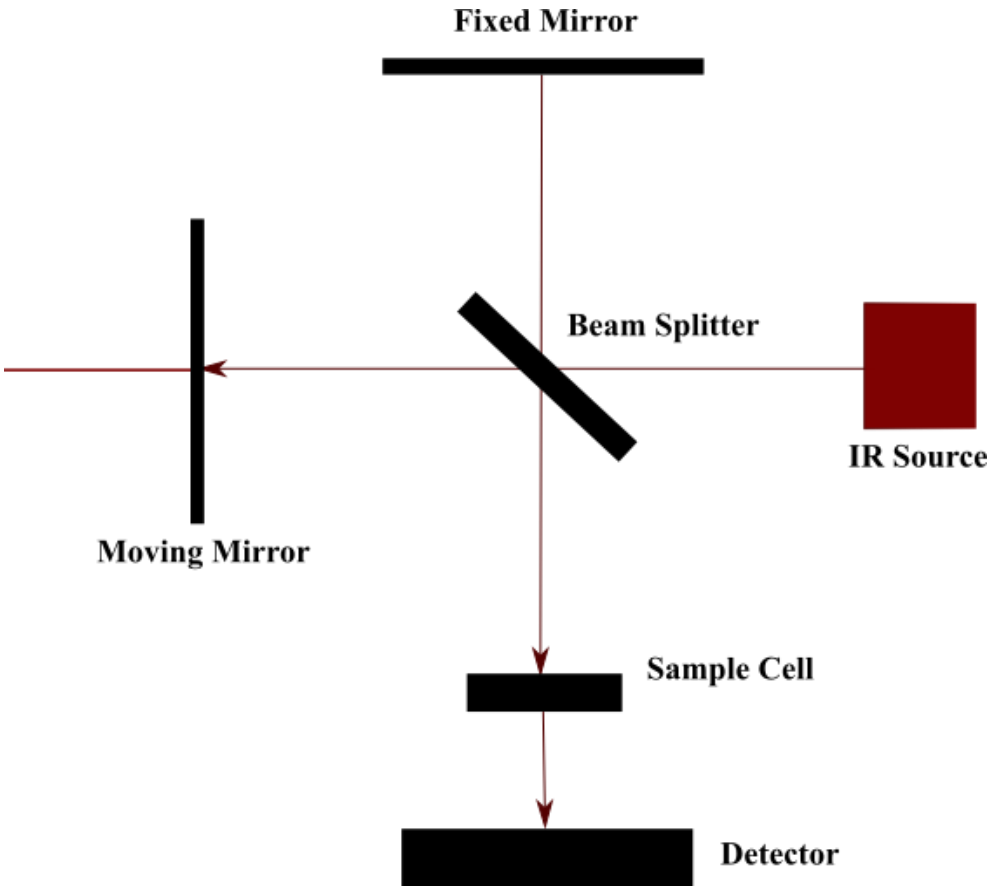

Figure 3.2. Schematic of a general FTIR set-up.

FTIR spectra were measured for all the fibrous samples using a Bruker Tensor 27 instrument across a wavelength range of 500 cm^{-1} – 4000 cm^{-1} with a resolution of 4 cm^{-1}. An

average of 64 scans was recorded for each spectrum with absorbance values being recorded. Quantitative values of the β polymorph were determined by applying the Beer-Lambert law:

$$F_{EA} = \frac{I_{EA}}{\left(\frac{K_{840}}{K_{763}}\right) I_{763} + I_{EA}} X\ 100 \qquad \text{Eq. 10}$$

where I_{EA} represents the intensity of the electroactive component and I_{763} represents the intensity of the α polymorph at the wavelength of 763 cm^{-1}. K_{840} and K_{763} represent the absorption coefficients with values are 7.7 x 10^4 $cm^2.mol^{-1}$ and 6.1 x 10^4 $cm^2.mol^{-1}$ for the β and α polymorphs respectively. [138] Absorbance peak intensity values were taken from the relevant peaks associated with the β and α polymorph to calculate the content of the electroactive phase.

3.3.6 X-ray Diffraction

X-ray diffraction (XRD) is a technique that allows for the characterisation of the crystallographic structure of crystalline materials. The technique is generally used to identify materials or to distinguish the different phases within a material. The incident beam of monochromatic X-rays is directed at the sample where interactions occur. The interactions between the monochromatic X-rays and the crystals within the material result in the diffraction of the X-rays which can be described by Bragg's Law:

$$2dsin\theta = n\lambda \qquad \text{Eq. 11}$$

Where d is the atomic spacing between the planes, θ is the incident angle, n is an integer, and λ is the wavelength of the beam.[315] A majority of the diffracted wave interact with each other resulting in superposition and consequently the destruction of the waves while others specific waves will not superimpose this results in low and high-intensity diffraction patterns. The subsequent diffraction patterns correlate to the specific lattice structure of the material and allow for the analysis of the arrangement of the atoms within the material.[316]

XRD measurements were carried out using a 3rd generation Malvern Panalytical Empyrean equipped with multicore (iCore / dCore) optics and a Pixcel3D detector operating within a 1D scanning mode. A Cu tube was used to give Cu Kα radiation (1.5419 Å) and a beam knife was used to reduce air scatter at the low angles. Scans were carried out in the range of 10 – 80 °2θ with a step size of 0.0263 ° and a counting time of ~ 77 s/step.

3.3.7 Dynamic Scanning Calorimetry

Dynamic scanning calorimetry (DSC) is a technique that allows for the analysis of the energy transfer within the material during the melting and recrystallisation steps of the material with

the changes in psychical or chemical states. It allows for the analysis of the enthalpy of fusion which can be utilised to determine the crystallinity of the material. A general DSC set-up consists of a heated chamber, automated insertion module, purge gas input systems (nitrogen or air), thermocouple, and a reference sample as seen in Figure 3.3.

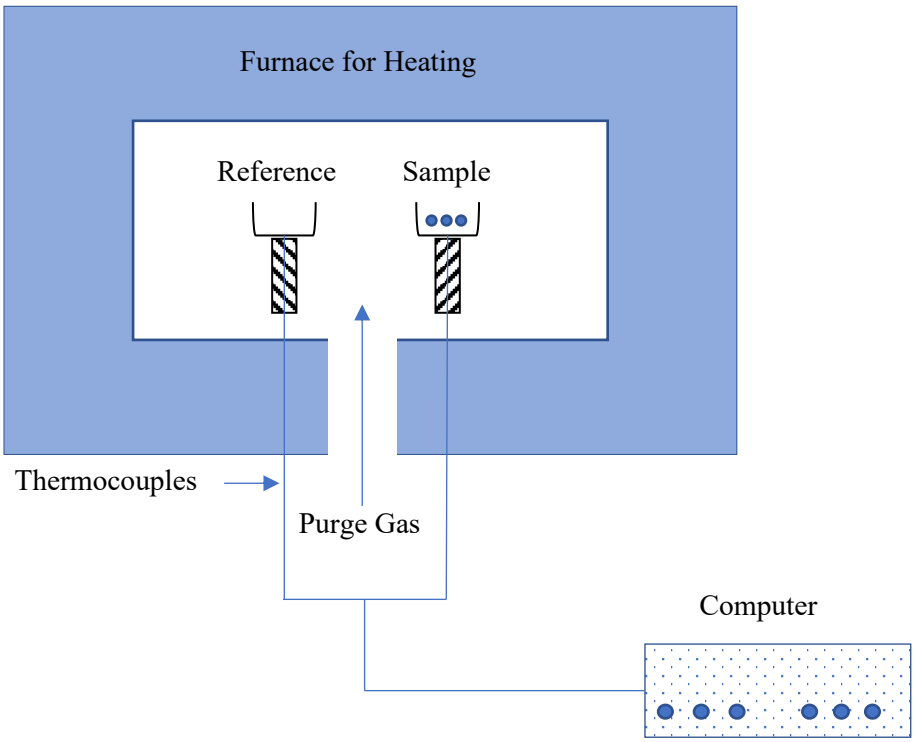

Figure 3.3. Schematic of a general DSC system.

The crystalline content and melt temperatures of the fibrous samples were analysed using a Mettler Toledo STAR1 differential scanning calorimeter. Samples weighing between 5 g – 6 g were weighed out using a Mettler Toledo XS105 dual-range weighing scale and placed within aluminium crucibles of 40 µL in volume. A heating rate of 10 °C.min^{-1} was applied to heat the samples from 25 °C – 180 °C. The samples were cooled from 180 °C – 25 °C at a cooling rate of 10 °C.min^{-1}. The percentage crystallinity of the fibrous mats was determined from:

$$x_c = \frac{\Delta H_f}{\Delta H_0} X\ 100\% \qquad \text{Eq.12}$$

where ΔH_f is the enthalpy of fusion for the material and ΔH_0 is the melting enthalpy of 100 % crystalline PVDF, which is reported to be 104.7 Jg^{-1}.[252] The ΔH_0 was calculated through the plotting the heat flow vs. weight against the time in seconds. The area under the melting of fusion peak was measured to give an enthalpy heat of fusion of the materials.

3.3.8 Thermogravimetric Analysis

Thermogravimetric analysis (TGA) is a technique that allows for the analysis of changes in the physical and chemical properties of a material when a dynamic heating rate is applied. The materials are heated within a furnace where steady air or an inert gas can be pumped into the system. The temperature range exceeds that of which the material is stable to determine the onset degradation temperature and any further degradation steps that occur. It assists in understanding the thermal stability of materials alongside the solid loading of filler within polymer composite systems.

Thermal degradation properties were analysed using a STARe 1 thermal gravitational analyser with an automated sample insertion module. A temperature range of 25 °C – 1000 °C was set with a heating rate of 10 °C.min^{-1} in an inert atmosphere of nitrogen gas. Samples were weighed out between 6 g – 7 g using a Metter Toledo SX105 dual-range weighing scale and placed within an alumina crucible.

3.3.9 Dynamic Mechanical Thermal Analysis

Dynamic mechanical thermal analysis (DMTA) is a sensitive technique that provides information on the viscoelastic properties of a material when oscillatory stress is applied, and the deformation is analysed across a specified temperature run at a constant frequency. A schematic of a general DMTA setup can be seen in Figure 3.4. The DMTA technique provides for effective analysis of the T_g of polymer materials and assists in understanding the molecular motion of the polymer chains with the addition of filler particles, alongside the influence on the damping properties.[317]

The data produced by DMTA analysis provides information on the storage modulus (*E'*), loss modulus (*E''*), and the tan δ. The *E'* represents the elastic properties of the material and the stored energy. While the *E''* represents the viscous properties and energy dissipation across the material.[318] The ratio of these two parameters results in the complex modulus (tan δ) of the material represented in the equations below:

$$E' = \frac{\sigma_0}{\varepsilon_0}\cos\delta \qquad \text{Eq.13}$$

$$E'' = \frac{\sigma_0}{\varepsilon_0}\sin\delta \qquad \text{Eq.14}$$

$$\tan\delta = \frac{E''}{E'} \qquad \text{Eq.15}$$

Where σ_0 represents the peak stress, ε_0 represents the peak strain and δ is the phase difference between the stress and strain.[318]

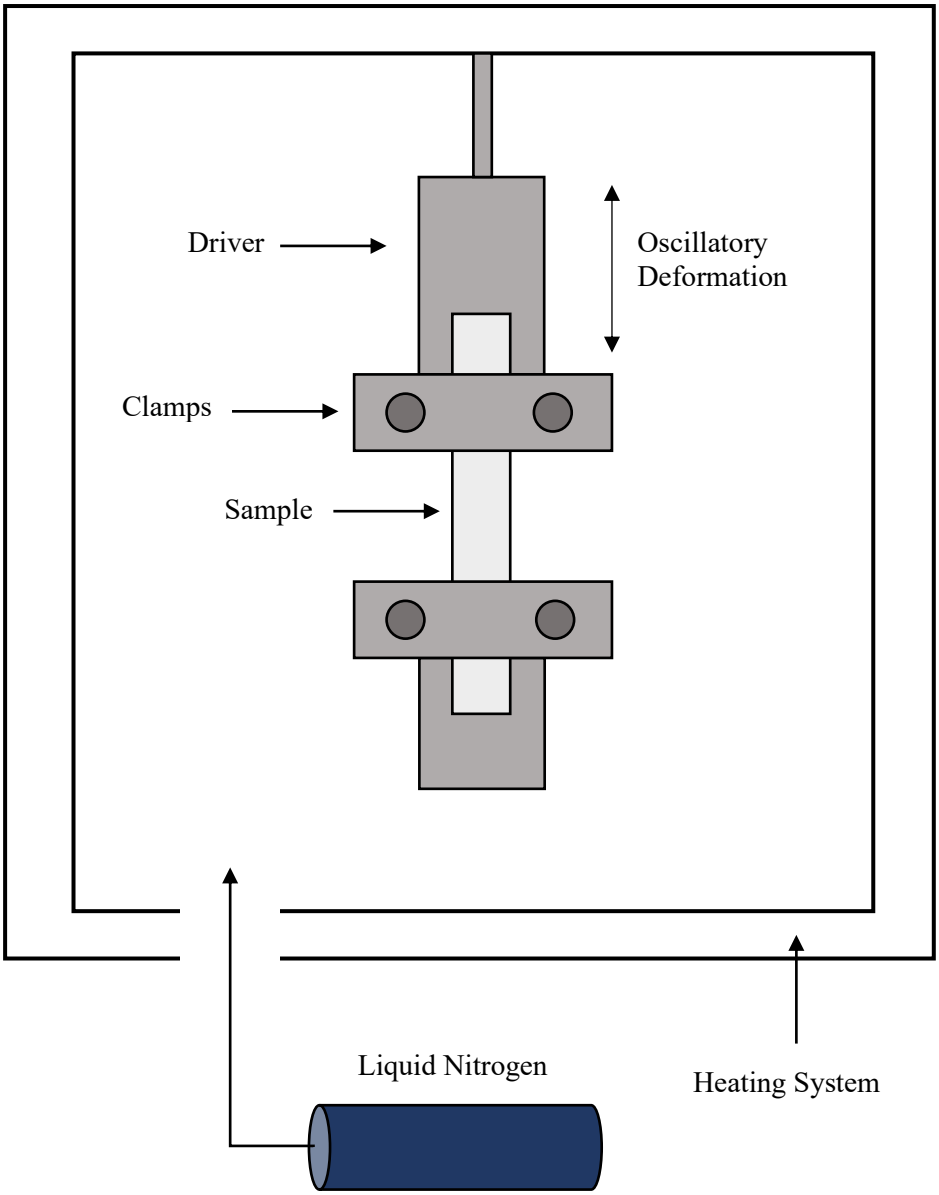

Figure 3.4. Schematic of a DMTA set-up in the tension configuration.

DMTA analysis was carried out using a Tritec 2000 DMA to determine the mechanical damping properties of the prepared samples. The tension configuration was set up which is generally used for thin-film samples. A frequency of 1 Hz was applied, with a displacement of 0.02 mm, and a clamping distance of 7 mm. Measurements were taken across the temperature range of -80 °C to 120 °C was used with a ramp rate of 2 °C.min^{-1}.

3.3.10 Sound Impedance Analysis

The acoustic test system in Figure 3.5 demonstrates the set-up of the impedance tube used to test the absorption coefficient of the materials. The sound source is placed at a certain distance away from the microphones and samples so that plane waves can be generated and directed at the sample. Loudspeakers release a combination of plane and non-plane waves. The non-plane waves will die out at 3 times the diameter of the tube, so the microphones are placed at a distance further away. The generated incident sound wave will interact with the material resulting in absorption and reflection of the wave. The incident wave and reflected wave will begin to interact within the space, resulting in the superimposition of the waves which is the measurable component within the impedance tube and is used to calculate the sound absorption coefficient.[319] The sound absorption coefficient is the ratio of the absorbed sound energy and the incident sound energy and is expressed as:

$$\alpha = \frac{\mathrm{E}}{\mathrm{E_0}} \qquad \text{Eq.16}$$

Where E is the absorbed sound energy, and E_0 is the incident sound energy. The noise reduction constants (NRC) were calculated by averaging out four values at four different frequencies at the low-mid frequency range and were calculated using the equation below:

$$\frac{f_{250}+f_{500}+f_{1000}+f_{2000}}{4} \qquad \text{Eq.17}$$

Where f is the frequency at which the absorption coefficient was taken from. These values provide for accurate measurements of the NRC at the low-frequency range where this work aims to produce materials to perform at.

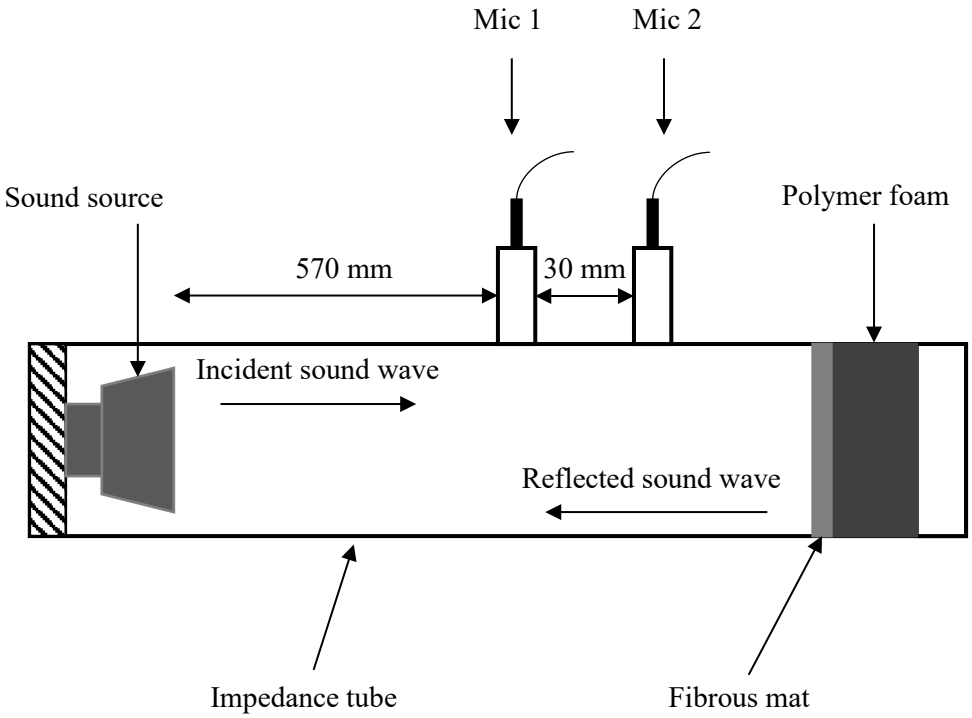

Figure 3.5. Schematic of the impedance tube with the parameters used for testing.

Testing of the materials was carried out using an impedance tube kit type 4206 from Brüel & Kjaer using the ISO 10534-2 standard. The impedance tube has an inner diameter of 29 mm. The microphone was placed 35 mm from the samples, and 570 mm from the sound source with a spacing of 20 mm between microphone 1 and microphone 2. Testing was carried out using a frequency range of 0 Hz – 6400 Hz with a lower frequency limit of 500 Hz and in the 1 / 3-octave band. The environmental conditions were an atmospheric pressure of 101.6 kPa, a temperature of 19.50 °C, relative humidity of 77 %, a sound velocity of 342.94 ms^{-1}, air density of 1.207 $kg.m^{-3}$, and a characteristic impedance air value of 414.0 Pa/(m/s). These parameters were sufficient for reliable acoustic data.

Table 3.5. The material thickness of the foams and the PVDF fibres with the addition of ceramic filler.

Material	Material Thickness/mm
PET	15
PU	35
PVDF / $NaNbO_3$	2.32 ± 0.02
PVDF / $KNbO_3$	2.09 ± 0.01
PVDF / $CeNbO_4$	1.15 ± 0.06
PVDF / SiC	2.7 ± 0.01
PVDF / Si_3N_4	2.65 ± 0.02
PVDF / $KNbO_3$ / SiC	2 ± 0.05
PVDF / $KNbO_3$ / Si_3N_4	2.09 ± 0.01

Chapter 4 Electrospinning PVDF and PVDF / KCl Fibres

4.1 Introduction

The premise of this chapter was to develop uniform fibres with PVDF as the initial stages following the addition of KCl and then later the addition of the niobium oxide and silicon-based ceramic filler. This section is split into two parts, the first including the electrospinning of PVDF fibres, where several electrospinning and solution parameters were analysed and how they influenced fibre morphology. These parameters include the polymer concentration, solvent type, solvent ratio, collector distance, feed rate, and molecular weight. This is well documented within the literature, however, was analysed here as the electrospinning set-up may differ from those used in other studies. PVDF was chosen as the polymer due to its piezoelectric nature with a reported piezoelectric constant of 13 $pC.N^{-1}$.[112] It is known that the piezoelectric effect assists in sound absorption at the low-frequency range of 50 – 250 Hz.[94,106,107]

Following the formation of the PVDF fibres, KCl salt was later added to the fibres to determine its influence on fibre morphology and crystallinity. As mentioned in 2.5.7 the addition of salts has previously been studied and demonstrated to influence the fibre morphology and the crystallinity of the material assisting in the nucleation of the β polymorph. Nucleation of the β polymorph was explored with the addition of KCl for both the LMW and HMW PVDF to enhance the piezoelectric properties of the polymer to potentially increase the sound absorption properties of the material at the low-frequency range. The emphasis of this part of the chapter is to induce a high percentage of β polymorph while producing fibre diameters smaller than 500nm as the smaller fibres have higher absorption coefficients in the lower frequency ranges as seen in Table 2.5.

4.1.1 Preliminary LMW PVDF Mats with DMF

The initial PVDF samples prepared contained 15 wt% in DMF with two collector distances being 12 cm and 15 cm, with a feed rate of 1 ml h^{-1}. These parameters were chosen as they are used in the literature to produce bead-free fibres.[320] The solutions electrospun here produced a membrane-like material that was difficult to remove from the aluminium foil. The weight percent was then increased to 20 wt% and 30 wt% with the collector distance maintained at 12 cm. The samples produced did not have the characteristic look of a fibrous mat where fibres can be observed on the surface of the aluminium foil, rather a film-like structure was observed

instead. These samples were also difficult to remove from the surface of the aluminium foil and were brittle, breaking easily upon removal and so SEM imaging was not carried out. This occurred due to the low concentration of PVDF in the solution, and the high boiling point of DMF. A combination of both parameters led to low entanglement of the polymer jet resulting in the electrospraying, and wet droplets depositing at the collector tip. This led to the droplets merging into a thin layer of PVDF rather than a fibrous mat.

Table 4.1. Electrospinning parameters for the initial LMW PVDF mats with DMF solvent.

PVDF Weight / %	Solvent	Collector Distance / cm	Voltage / kV	Feed Rate / ml h^{-1}	Final Form
15	DMF	12	7.88	1	No Fibres
15	DMF	15	8.56	1	No Fibres
20	DMF	12	7.50	1	No Fibres
30	DMF	12	6.97	1	No Fibres

4.1.2 Preliminary LMW PVDF Mats with DMAc

The solvent type and system were changed to a binary solvent system using DMAc rather than DMF with the second solvent being acetone. The DMF was changed to DMAc as this solvent has lower surface tension and higher viscosity seen in Table 4.2. As mentioned in sections 2.5.4.1 and 2.5.4.5 these parameters can assist in the transition from electrospray to electrospinning and beaded fibres to bead-free fibres.[242] Solvents with lower surface tensions oppose the viscoelastic nature of the polymer solution to a lower degree and have less influence on attempting to increase the surface area of the jet through the formation of spheres. The acetone was mainly added to assist in the complete evaporation of the solvent during the spinning process as it has a much lower boiling point than DMAc as seen in Table 4.2.

Table 4.2. Properties of the used solvents.

Solvent	Boiling point / °C	Dielectric constant	Viscosity	Surface Tension	Electrical conductivity	Resistivity	Ref.
DMF	153	36.70	0.920	12.1	$6.0E^{-2}$	35.0	[321]
DMAc	166	37.80	1.960	11.0	-	43.7	[321]
Acetone	56	20.6	0.308	22.68	0.20	23.3	[321]

The PVDF sample prepared contained 10 wt% of the polymer within a solution of DMAc and acetone at a ratio of 7:3 using a collector distance of 10 cm and a feed rate of 0.5 ml h^{-1}. The produced mats had a translucent thin film look seen in Figure 4.1a. Figure 4.1b displays an SEM image where the electrospun 10 wt% PVDF did not produce a fibrous structure. In place, a smooth surface of the polymer was produced at the low weight percent of PVDF characteristic of the electrospraying process rather than the electrospinning process.[322]

The concentration was increased to try and increase the entanglement between the polymer chains for effective spinning. This is known to produce bead-free fibres.[224,225] Increasing the concentration of polymer to 15 wt% had little effect on the formation of fibres which was unexpected. These mats were similar in structure and no fibres were formed. The collector distance was also gradually increased to allow for a longer time for complete solvent evaporation so the fibres would solidify before depositing on the aluminium foil. Altering the collector distance between 10 cm, 12 cm, and 15 cm did not affect the formation of fibres for these samples. The same type of mat was produced, with a similar brittle nature. This occurred as the concentration of the polymer was not high enough for sufficient chain entanglement. Voltages were also altered to accommodate for the changes in distance, resulting in an increase in the applied voltage with an increase in collector distance seen in Table 4.3. However, these changes had little influence on the formation of fibres, due to the low concentration of PVDF that was added to the solutions leading to spraying rather than spinning.

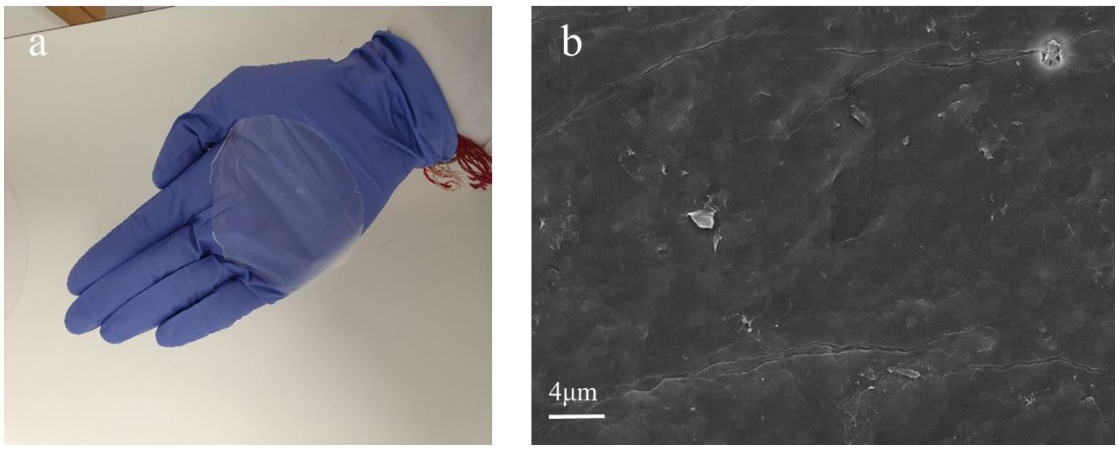

Figure 4.1. (a) Translucent 10 wt% PVDF mat. (b) SEM image of the surface of the 10 wt% PVDF mats showing a smooth surface with no fibre formation.

Table 4.3. Electrospinning parameters for the initial PVDF mats with DMAc: acetone solvent.

PVDF Weight / %	Solvent	Collector Distance / cm	Voltage / kV	Feed Rate / ml.h^{-1}	Final Form
10	DMAc: Acetone	10	7.26	2	No Fibres
15	DMAc: Acetone	10	9.56	2	No Fibres
15	DMAc: Acetone	12	10.07	2	No Fibres
15	DMAc: Acetone	15	10.44	2	No Fibres

4.1.3 Initial Parameter Alterations

Figure 4.2 is demonstrating electrospraying vs electrospinning where the morphology of the materials indicates the different techniques taking place. Figure 4.2a shows the electrospraying process which produces no fibres, while Figure 4.2b displays some fibres but is still demonstrating more electrospraying tendencies. Figure 4.2c displays the fibres with beads which suggest the solution began electrospinning. The concentration of the fibres was increased to 20 wt%, keeping the solvent ratio and collector distance constant with an increased feed rate of 2 ml.h^{-1} seen in Figure 4.2. This had shown slight changes to the morphology of the mats where the formation of droplets was visible on the surface. To further transition to electrospinning, the solvent ratio was altered to allow for complete solvent evaporation to take place more readily during the spinning process. A solvent ratio of 6:4 of DMAc: acetone produced beads with the first formation of very thin fibres. Further altering the solvent ratio to a 1:1 ratio of DMAc: acetone led to the formation of thicker fibres and a reduction in the formation of beads. This was expected as similar results have been demonstrated in the literature where 100% DMF resulted in the formation of no fibres and the addition and increase in acetone resulted in the formation of beaded fibres to then produce fine fibres.[323] These beads were much smaller, and the average fibre diameter was 137 ± 37 nm. The transition from a beaded mat to the initial formation of fibres here was due to the acetone in the system allowing for better evaporation of the binary solvent system. This allowed for the fibres to solidify during the spinning phase and led to a transition from electrospraying to electrospinning and a decrease in the number of beads formed.

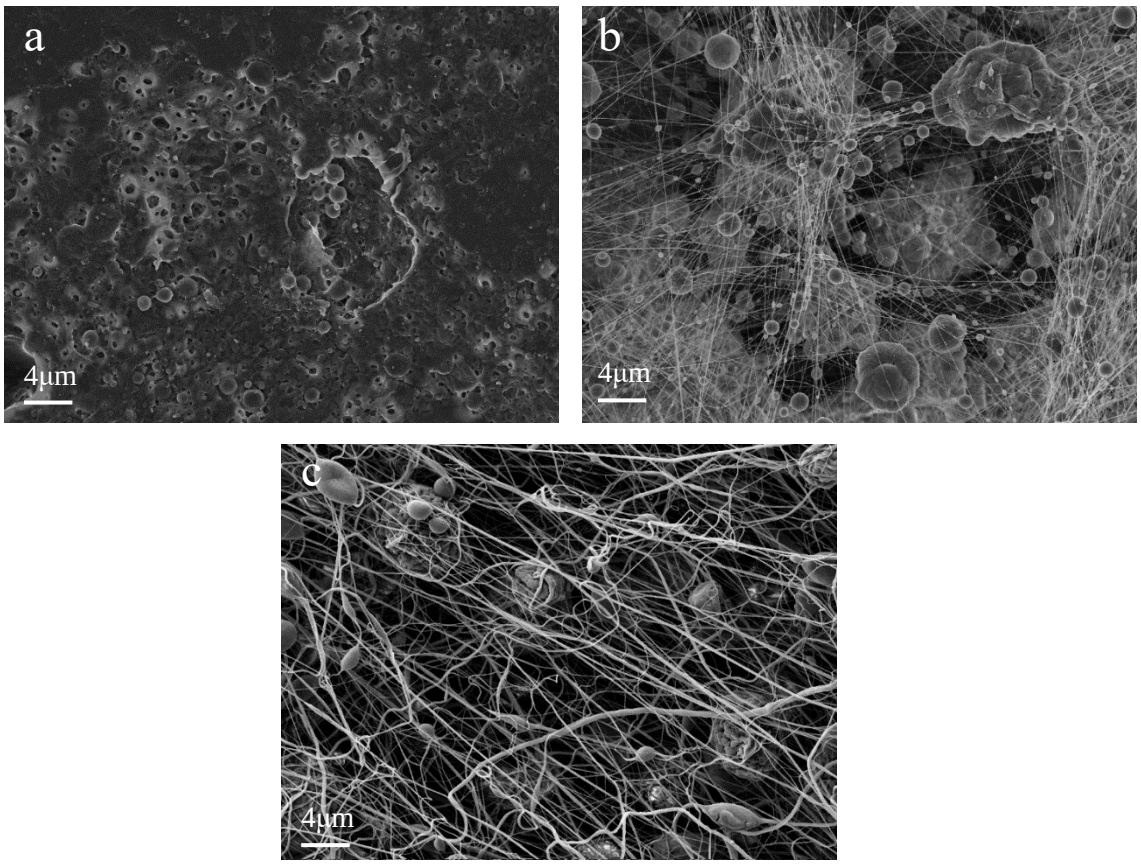

Figure 4.2. (a) 20 wt% PVDF in a DMAc: acetone ratio of 7:3. (b) 20 wt% PVDF in DMAc: acetone ratio of 6:4. (c) 20 wt% PVDF in DMAc: acetone ratio of 1:1. All displaying a transition from electrospraying to electrospinning in the final morphology.

Table 4.4. Electrospinning parameters for 20 wt% with varied solvent ratios.

PVDF Weight / %	**Solvent**	**Solvent ratio**	**Collector Distance / cm**	**Voltage / kV**	**Feed Rate / ml.h^{-1}**
20	DMAc: Acetone	7:3	12	13.72	2
20	DMAc: Acetone	6:4	12	10.78	2
20	DMAc: Acetone	1:1	12	11.0	2

4.1.4 Concentration Adjustments

Following on from the initial changes in the concentration and solvent type it was decided to focus on increasing the concentration to transition to bead-free fibres before altering other parameters to refine the fibre diameter. The concentration of the PVDF was increased at three intervals 22 wt%, 25 wt% and 27 wt%, with a solvent ratio of 1:1, and feed rate of 2 ml.h^{-1}.

Three different collector distances were analysed, however, for comparison to the data in the previous section 4.1.3, a collector distance of 12 cm will be analysed. Further data on the three different collector distances are in section 4.1.5. The concentration of the polymer was carried out to increase polymer chain entanglements to further decrease the bead size and transition from beaded fibres to uniform fibres.

Figure 4.3. demonstrates the change in the morphology of the material with a change in the concentration of the polymer. The fibres produced using these three concentrations had all shown the formation of beads across the fibres. However, the number of beads decreased with the increase in the concentration of polymer in the solution which is in line with previous work.[324] Neo *et al*.[325] have demonstrated similar results where beaded fibres were removed with an increase in the concentration of PVDF in the fibres where 25 wt% of the polymer began to see a removal of the beads with an average fibre diameter of 283 ± 62 nm. The average fibre diameters here were smaller than in the literature for all 3 concentrations showing average fibre diameters of 125 ± 32 nm, 119 ± 29 nm and, 128 ± 48 nm respectively demonstrating little effect on the fibre diameters. These diameters were calculated by analysing the diameter of 100 points across several fibres. The fibre formation of PVDF is heavily influenced by the concentration of PVDF in the solution system. The increase in the concentration of PVDF within the solutions had shown no formation of fibres at the low weight percent loading. An increase in weight percent had shown the transition from electrospraying to electrospinning where fibres were formed however beads were still present. Increasing the weight percent of PVDF in the solutions leads to a higher level of entanglement between the polymer chains and results in an increase in solution viscosity, both related to the removal of beads and an increase in fibre diameters.[226,326] During electrospinning, this reduces the effects of the surface tension attempting to increase the surface area of the solution through producing beads were observed at lower concentrations. At lower weight percentages there are lower levels of entanglement between the polymer chains and the electrospun jet is easily pulled apart forming beaded structures.[324]

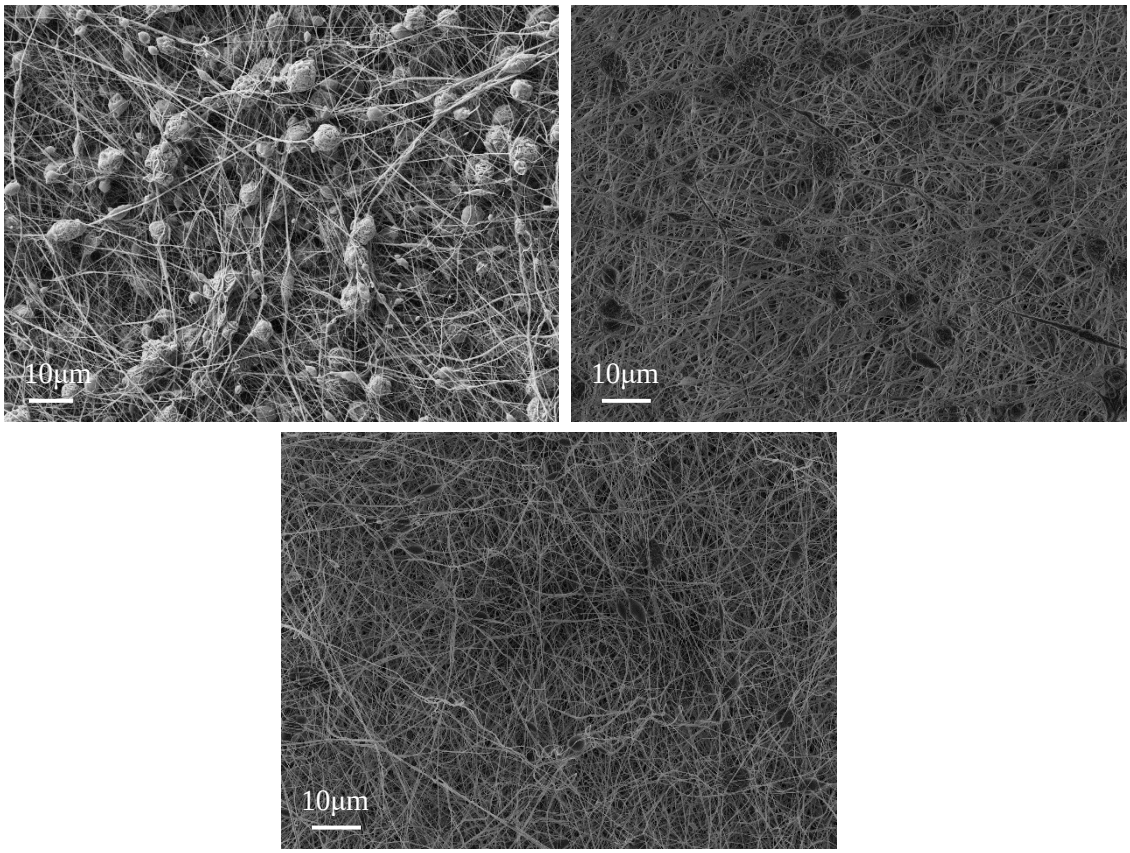

Figure 4.3. (a) 22 wt% PVDF fibres, (b) 25 wt% PVDF fibres, (c) 27 wt% PVDF fibres. Showing the reduction in bead formation with an increase in the concentration of PVDF.

4.1.5 Collector Distance Adjustments

The collector distance was altered with 3 different ranges, including 10 cm, 12 cm, and 15 cm. The samples produced for the 25 wt% at the three collector distances had average fibre diameters of 149 ± 45 nm, 134 ± 31 nm, and 119 ± 29 nm for the different collector distances respectively, showing a decrease in average fibre diameter with an increase in the tip to collector distance. The average fibre diameters were analysed by taking 100 diameter readings across the SEM images and producing an average. The bead formation has been shown to decrease with an increase in the collector distance from 10 cm – 15 cm seen in Table 4.4. This was observed with all the weight percent that were analysed at the three collector distances. The collector distances assisted in determining the required space between the tip and the collector. The formation of beads here decreased with an increase in collector distance as it allowed for a longer interval for complete solvent evaporation and more elongation of the fibres which can reduce the size of the beads.[222] However, the optimal collector distance is required to achieve complete solvent evaporation to assist in the removal of beading. Collector distances were also analysed for the 20 wt% - 27 wt% and can be seen within appendix images Figure 0.1, Figure

0.2, and Figure 0.3. The parameters used for electrospinning these materials are also observed within the appendix in Table 0.1.

Castkova *et al*. [327] had shown similar results where the fibre diameter decreased with an increase in the collector distance and was attributed to the increase in elongation times provided by the larger distance. This is in line with the work here where an increase in the collector distance has shown a gradual decrease in the fibre diameter.

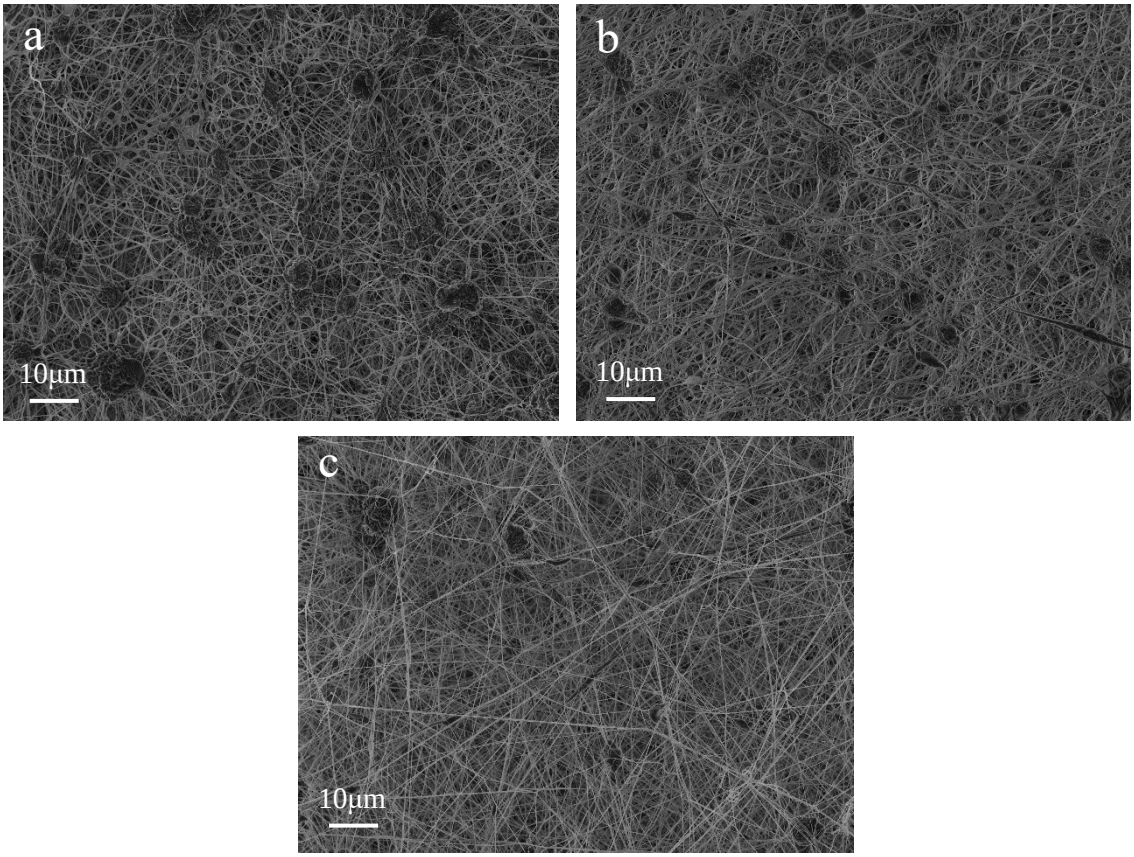

Figure 4.4. (a) 10 cm collector distance 25 wt% PVDF fibres, (b) 12 cm collector distance 25 wt% PVDF fibres, (c) 15 cm collector distance 25 wt% PVDF fibres. Displaying a change in bead formation with an increase in collector distance.

4.1.6 Solvent Ratio Changes

Following on from the changes made to the concentration and the collector distance, a range of DMAc and acetone solvent ratios were analysed, including 7:3, 6:4, 1:1, 4:6 and 3:7 in a concentration of 25 wt% PVDF. These fibres were electrospun using the 15 cm collector distance as it has proven to produce the least beads in section 4.1.5. The voltage was altered to maintain a consistent Taylor cone shape as carried out on all fibres produced previously in the work and the other electrospinning parameters were kept constant. The morphology of the

electrospun fibres produced using the five solvent ratios had shown a transition from the beaded structure to the non-beaded structure from 7:3 – 3:7 respectively. Decreasing the DMAc content and increasing the acetone content in the solvent system had been shown to increase the average fibre diameters seen in Figure 4.5. The average fibre diameters analysed were 107 ± 38 nm, 144 ± 36 nm, 119 ± 29 nm, 257 ± 133 nm, and 347 ± 133 nm respectively. There was a gradual reduction in the number of beads generated with the addition of higher quantities of acetone. The solutions with the highest volume of acetone were difficult to electrospin due to the high volatility of acetone. This resulted in the Taylor Cone solidifying regularly stopping to jet from begin produced. This was also observed with the 1:1 and 4:6 ratios however the solidification occurred less frequently and allowed for sustained periods of sufficient electrospinning. Singh *et al*.[328] also observed a similar result in which at higher concentrations of acetone clogging on the spinneret would occur.

The solvent ratio between DMAc and acetone has shown a large influence on fibre morphology concerning the formation of beading and fibre diameters. Acetone was added to the binary solvent system to increase the evaporation rate due to its lower boiling point in comparison to DMAc, decrease the surface tension of the solution, decrease the viscosity and increase conductivity. This would allow for complete solvent evaporation and stop the formation of wet fibres. Acetone decreases the molecular interactions between the PVDF and solvent, causing a decrease in the shear viscosity of the solution.[323] Typically, a lower solution viscosity will result in the formation of beads in fibres. However, increasing the amount of acetone leads to quicker evaporation of the solvents from the system solidifying the polymer jet before the beading process begins. The average fibre diameters were shown to also increase with the increase in acetone content. This occurs due to the rapid evaporation of acetone reducing the stretching of the jet in the wet state, which reduces the elongation of the overall fibre. This increases fibre thickness.[329] It can also be mentioned that the increase in acetone causes an increase in the conductivity of the solution within a binary system including acetone. As mentioned previously in 2.5.7 increasing the conductivity of the solution has been shown to decrease the formation of beaded fibres. Cozza *et al*.[330] have previously shown similar results where increasing the concentration of the DMF and acetone to 8:2 in the binary system resulted in the formation of beaded structures. While a lower ratio of 7:3 resulted in no beads. Here it was expected that the material would follow a similar principle in which lowering the DMF level would gradually allow for the removal of the beads. However, a ratio of 1:1 was desirable for this solution system. It should be mentioned that the voltages were altered throughout the work to ensure that the Taylor cone released the polymer jet. It is known that surface tension changes with solvent type and so the voltage needs to alter to overcome this variation.[323]

Table 4.5. Electrospinning parameters for 25 wt% PVDF with varied solvent ratios.

PVDF Weight / %	**Solvent**	**Solvent ratio**	**Collector Distance / cm**	**Voltage / kV**	**Feed Rate / ml·h^{-1}**
25	DMAc: Acetone	7:3	15	12.58	2
25	DMAc: Acetone	6:4	15	11.82	2
25	DMAc: Acetone	1:1	15	10.92	2
25	DMAc: Acetone	4:6	15	11.91	2
25	DMAc: Acetone	3:7	15	14.62	2

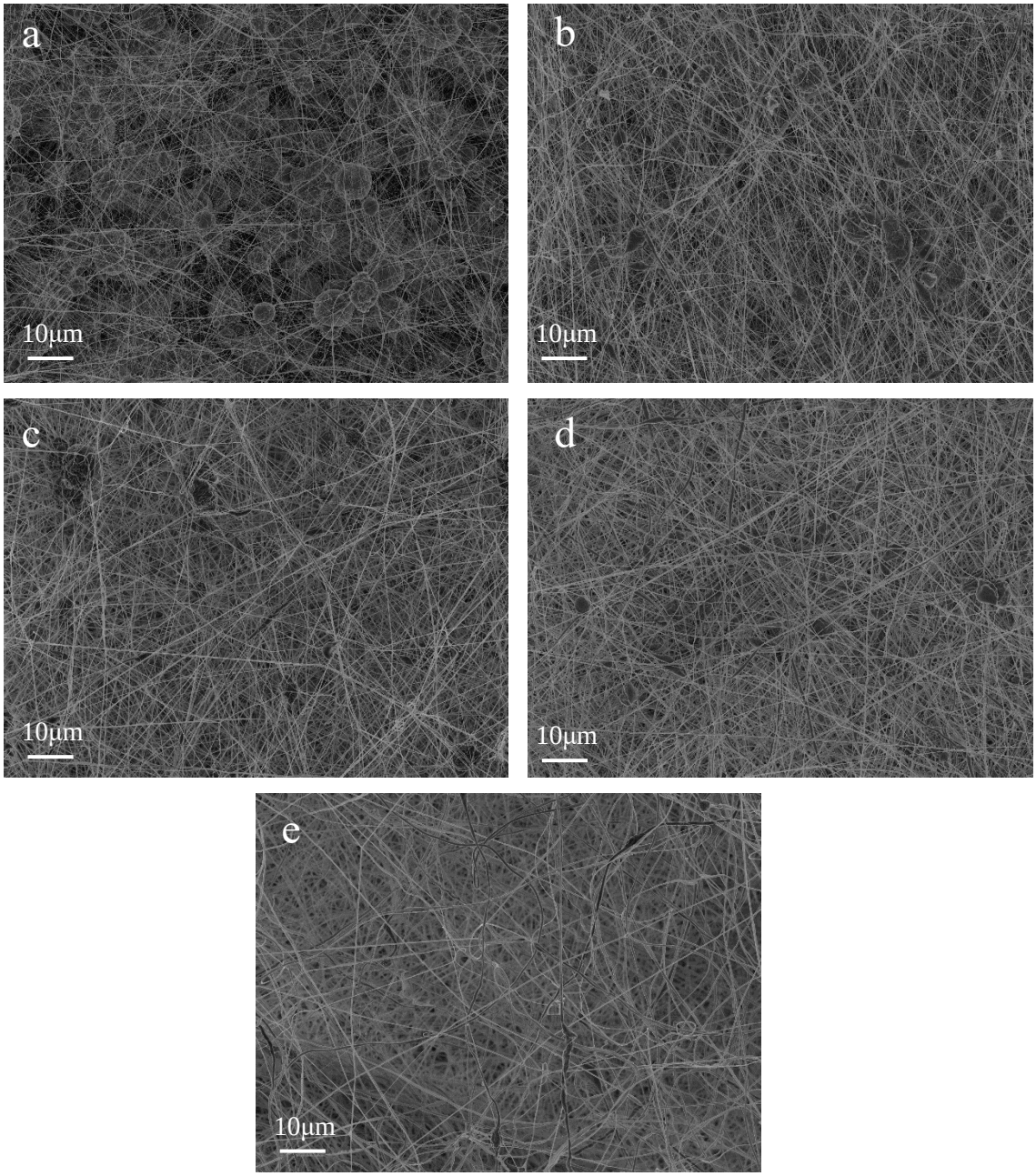

Figure 4.5. (a) 25 wt% PVDF in a 7:3 ratio of DMAc: acetone, (b) 25 wt% PVDF in a 6:4 ratio of DMAc: acetone, (c) 25 wt% PVDF in a 1:1 ratio of DMAc: acetone, (d) 25 wt% PVDF in a 4:6 ratio of DMAc: acetone, and (e) 25 wt% PVDF in a 3:7 ratio of DMAc: acetone. Displaying a reduction in bead formation with the decrease of DMAc and an increase in acetone.

4.1.7 Feed Rate Adjustments

Two solvent ratios were then taken from the previous set of results in section 4.1.6 and analysed using two different feed rates, those being 0.5 $ml.h^{-1}$ and 1 $ml.h^{-1}$. The two solvent ratios applied were the 1:1 and the 6:4 DMAc: acetone variations. These were selected as the formation of beads was minimal and fibres could be electrospun effectively without the need to open the chamber consistently to clean solidified polymer from the Taylor cone. For the 1:1 ratio, the results had shown a decrease in the average fibre diameter with values of 165 ± 79 nm and 90 ± 32 nm at the 0.5 $ml.h^{-1}$ and 1 $ml.h^{-1}$ respectively. The mats spun using both feed rates produced fibres that had the formation of beads seen in Figures 6a and 6b. The second variation of a solvent ratio 6:4 had shown very little change to the fibre morphology, with average fibres of 140 ± 54 nm and 154 ± 69 nm for the 0.5 $ml.h^{-1}$ and 1 $ml.h^{-1}$ feed rates respectively. These fibres had also shown no change in the formation of beads from the previous samples generated in section 4.1.6. This data here is different from that within the literature where a decrease in the feed rate is shown to decrease the fibre diameter and reduce the formation of beads.[240,244] However to overcome this an adjustment to the molecular weight can be carried out to increase the viscosity and polymer chain entanglements for the formation of bead-free beads.

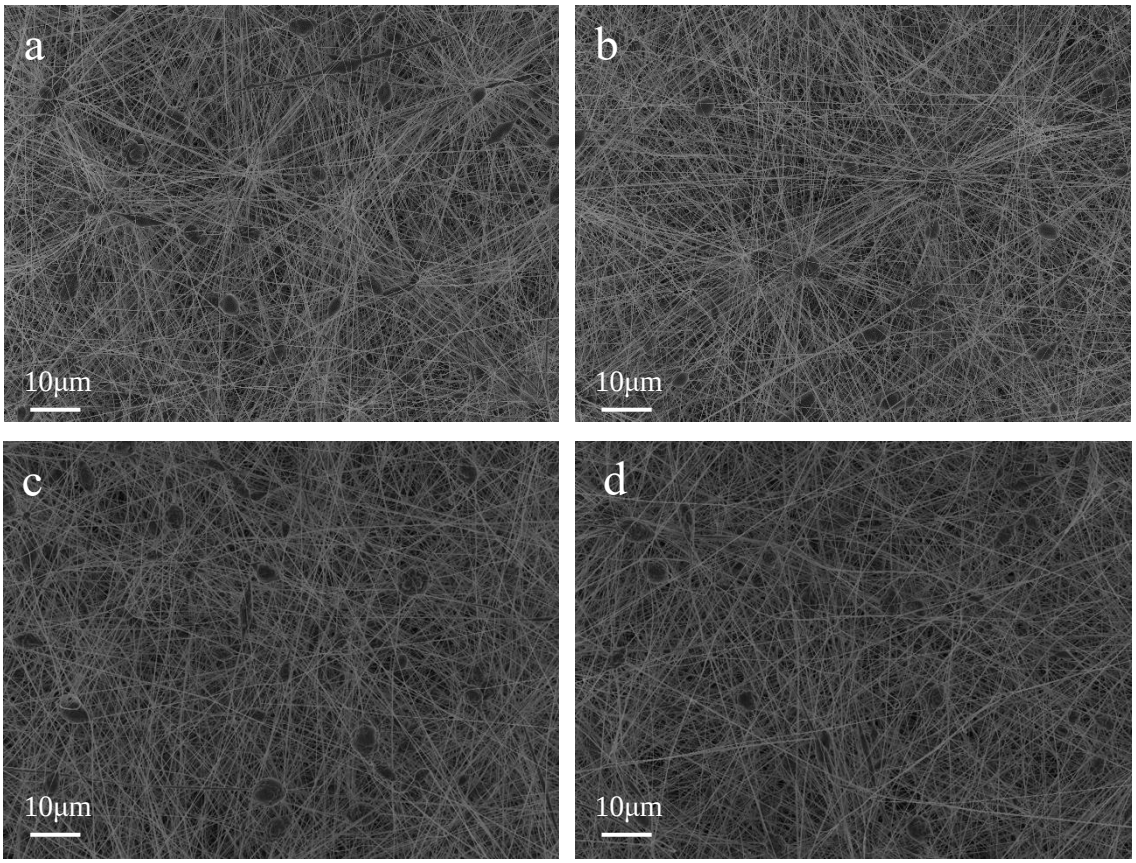

Figure 4.6. (a) 25 wt% PVDF mats with 1:1 DMAc: acetone, and 0.5 ml.h^{-1} feed rate (b) 25 wt% PVDF mat with 1:1 DMAc: acetone, and 1ml.h^{-1} feed rate. (c) 25 wt% PVDF mats with 6:4 DMAc: acetone, and 0.5 ml h^{-1} feed rate (d) 25 wt% PVDF mat with 6:4 DMAc: acetone, and 1 ml h^{-1} feed rate. Showing little change to fibre morphology with changes to the feed rate.

Table 4.6. Electrospinning parameters for 25 wt% with different collector distances.

PVDF Weight / %	**Solvent**	**Solvent ratio**	**Collector Distance / cm**	**Voltage / kV**	**Feed Rate / ml h^{-1}**
25	DMAc: Acetone	1:1	15	10.92	0.5
25	DMAc: Acetone	1:1	15	8.46	1
25	DMAc: Acetone	6:4	15	10.58	0.5
25	DMAc: Acetone	6:4	15	7.88	1

4.1.8 Molecular Weight Adjustments

The changes made to the LMW polymer mainly demonstrated the formation of beaded fibres. It was decided to increase the molecular weight to a higher value to reduce the formation of beaded fibres and produce thicker homogenous fibres in preparation for the addition of the ceramic filler. Kynar 740 PVDF was applied as an HMW variant of the previous LMW polymer. The electrospinning parameters were kept constant from the previous samples with a change to the feed rate. A feed rate of 1 $ml.h^{-1}$ was taken forward and applied for the mats developed here. Eight solutions containing various PVDF concentrations were analysed ranging between 15 wt% – 30 wt% seen in Table 4.7. It was observed that at the lower concentrations of 15 wt% - 26 wt%, the formation of beaded fibres occurred. Increasing the concentration further resulted in the removal of the beads and the formation of smooth fibres. The surface morphology of the bead-free fibres was rough where indentations were observed. A gradual increase in the average fibre diameter was observed with an increase in the polymer concentration seen in figure 7. The average fibre diameters of the HMW PVDF fibres ranged between 99 ± 25 nm – 1342 ± 385 seen in Table 4.7. Zaarour *et al*.[331] displayed similar results where increasing the molecular weight increased the average fibre diameters. In their work, an average fibre diameter was calculated as 1437 ± 167 nm at a molecular weight of 275 kDa at a polymer weight of 28 wt% which is in the experimental error of the fibres produced in fibres produced here.

As mentioned previously a transition from beaded fibres to bead-free fibres occurs due to an increase in the polymer chain entanglements as the concentration increases. When comparing the concentration of the 25 wt% for both molecular weight PVDF the lower molecular weight PVDF has a smaller average fibre diameter than the higher molecular weight PVDF with diameters 90 ± 32 nm and 417 ± 110 nm respectively. This has been shown previously where lower concentrations of polymer are required to produce bead-free fibres when the molecular weight is higher. The formation of rough surface materials may have occurred due to the rapid evaporation of the solvent within the material resulting in phase separation where a rich polymer phase and lean polymer phase are produced. The rich polymer phase solidifies first leaving the lean polymer phase to evaporate after which the evaporation of the solvent results in the surface roughness.[227]

Table 4.7. Electrospinning parameters for HMW PVDF.

PVDF Weight / %	**Solvent ratio**	**Collector Distance / cm**	**Voltage / kV**	**Feed Rate / ml h^{-1}**	**Average Fibre Diameter/ nm**
15	1:1	15	7.50	1	99 ± 25
20	1:1	15	7.24	1	132 ± 35
25	1:1	15	7.03	1	417 ± 110
26	1:1	15	6.78	1	808 ± 244
27	1:1	15	6.88	1	1041 ± 302
28	1:1	15	8.10	1	1206 ± 324
29	1:1	15	7.10	1	1008 ± 332
30	1:1	15	7.14	1	1342 ± 385

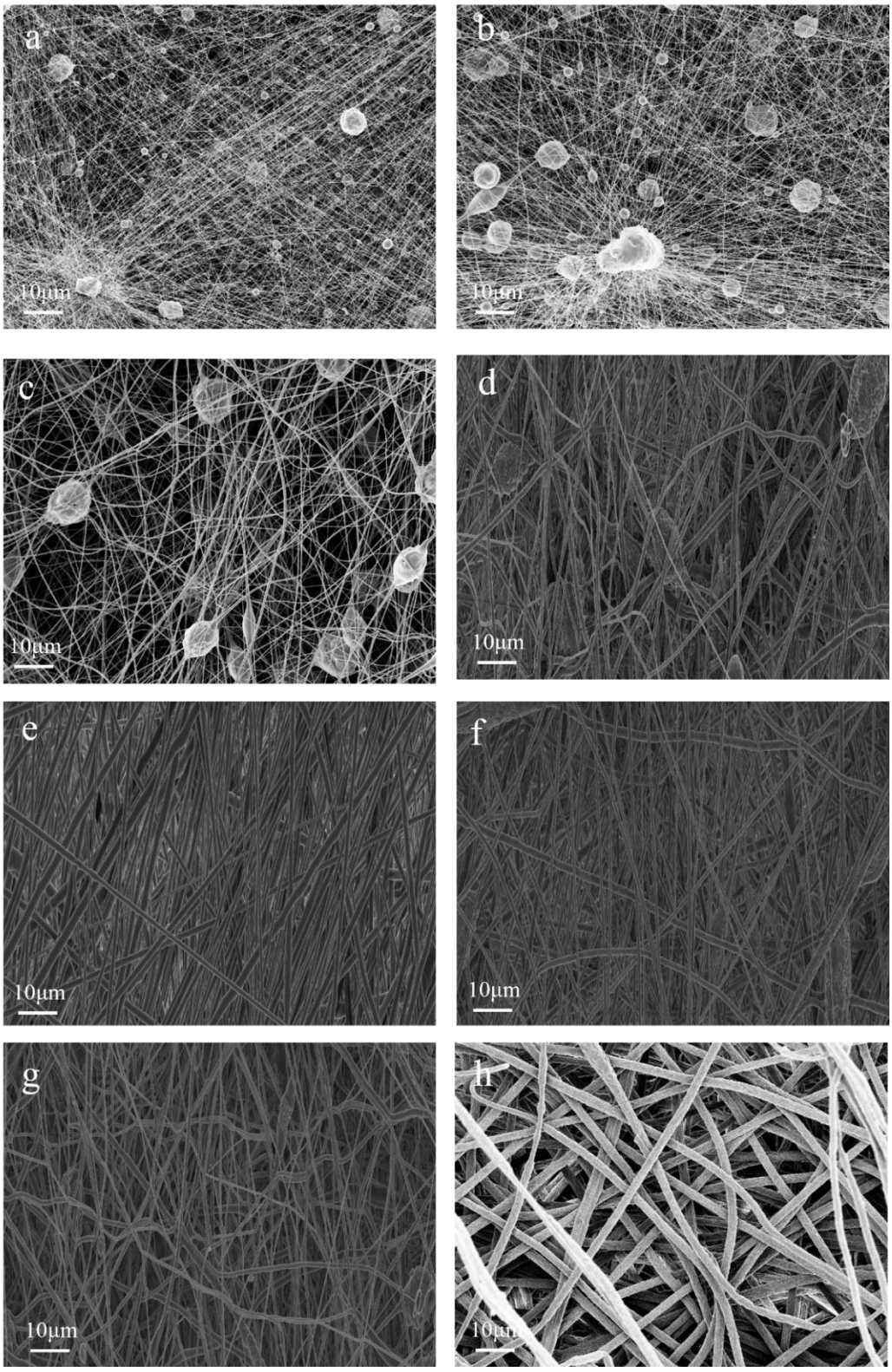

Figure 4.7. (a) 15 wt% PVDF fibres (b) 20 wt% PVDF fibres, (c) 25 wt% PVDF fibres, (d) 26 wt% PVDF fibres, (e) 27 wt% PVDF fibres, (f) 28 wt% PVDF fibres, (g) 29 wt% PVDF fibres, (h) 30 wt% PVDF fibres. Displaying the change in fibre morphology from beaded fibres to thick fibres with the increase in the concentration of PVDF.

4.1.9 Summary

It was found that polymer concentration and molecular weight had the largest influence on the formation of bead-free fibres and influenced the average fibre diameter which was in line with the literature. This has been demonstrated with other polymers such as chitin and PEO, where an increase in these parameters led to the removal of beaded fibres and the increase in fibre diameters.[332,73] This is suggested to occur due to an increase in solution viscosity which has been linked to the removal of beaded fibres and the increase in fibre diameters.[324,325]

The collector distance had shown to reduce bead formation when the tip-to-collector distance was increased by 15 cm producing the fewest beads. This has previously been demonstrated within the literature where Yuan *et al.*[244] displayed a decrease in fibre diameters with the increase in collector distances. Alternative studies had also demonstrated similar results suggesting that the work carried out on collector distance here is in line with the literature.[246]

Alongside these parameters, a solvent ratio of 1:1 had shown efficient fibre formation alongside a feed rate of $1ml.h^{-1}$. A combination of these parameters had been shown to produce effective fibres. All the fibres produced using the LMW PVDF resulted in the formation of beaded fibre morphologies. The fibres produced with the HMW PVDF also produced beaded fibres within the same range. However above 27 wt% concentration and above bead removal were observed. Overall, there was a difference in the size of the fibres produced between the LMW and HMW fibres due to differences in the viscosity of the two solutions.

From the solutions analysed for fibre formation, it was decided to take forward two sets of polymer solutions for the addition of the KCl salt.

(i) 25 wt% LMW PVDF, 15cm collector distance, $1ml/h^{-1}$ feed rate, and 1:1 ratio of DMAc: acetone.

(ii) 30 wt% HMW PVDF, 15 cm collector distance, $1ml/h^{-1}$ feed rate, and 1:1 ratio of DMAc: acetone.

These solution properties were chosen to determine the influence the KCl salt may have on the beaded structures of the LMW PVDF, and the influence the salt would have on thicker fibre diameters of the HMW PVDF. It was also decided to push forward the HMW due to the thicker fibre diameters to ensure the ceramic particles were fully engulfed within the fibres. This section demonstrates similar work to in the literature in an attempt to reproduce bead-free fibres before the addition of filler to the materials. It demonstrates and confirms that the formation of bead-free fibres can be achieved by adjusting the concentration and molecular weight.

4.2 Electrospinning PVDF / KCl Fibres

Continuing from the formation of the PVDF fibres it was decided to utilise the LMW PVDF and HMW PVDF as they displayed two contrasting morphologies at the concentration of 25 wt% and 30 wt% respectively. With the former producing beaded fibres and the latter displaying thick bead-free fibres. Here the addition of KCl was carried out to determine its influence on the fibre morphology and if the removal of beaded fibres would occur due to an increase in solution conductivity of the LMW. The addition of KCl salt was incorporated into the beaded PVDF fibres generated in the previous chapter. This was carried to accomplish to influence the removal of beaded structures which has previously been shown with the addition of LiCl and NaCl mentioned in 2.5.7. The HMW at the specified concentration had already produced homogenous fibre diameters. This was chosen to determine if control over the fibre diameter could be established with the addition of the KCl salt at various concentrations. Overall, the addition of the KCl to both systems was also carried out to influence the formation of the electroactive β polymorph within the PVDF.

4.2.1 Initial LMW PVDF / KCl Fibre Morphology

The initial fibre formation was carried out using the LMW PVDF with a concentration of 25 wt% which was used from here onward on the PVDF / KCl fibrous mats developed until said otherwise. The morphology of the pure PVDF fibres demonstrated beaded fibres with thin fibre diameters and smooth surface morphologies. Here the initial addition of KCl was explored by adding 2 wt% of the salt altering the collector distance with the parameters seen in Table 4.8. The addition of 2 wt% KCl displayed a large change in morphology in comparison to the pure PVDF fibres where the amount of beaded structure significantly reduced at the 10 cm and complete removal of the beads at the 12 cm and 15 cm collector distances as seen in Figure 4.8. In previous literature, it has been shown with PEO and the addition of 0.5 w/v NaCl that the removal of beaded fibres occurs suggested to occur due to a decrease in viscosity and an increase in solution conductivity.[333]

The applied voltage was increased with an increase in collector distance to maintain a stable Taylor cone during the electrospinning process. This led to average fibres being produced with similar average fibre diameters. The increase in collector distance was carried out to decrease the fibre diameter of the material at the 2 wt% concentration of KCl. Average fibre diameters of 263 ± 50 nm, 243 ± 51 nm, and 266 ± 56 nm were analysed for the collector distance respectively seen in Table 4.8. This suggested that the increase in collector distance was offset by the increase of the applied voltage causing no significant change in the average

fibre diameter. With a large removal of the beads from the fibres it was decided to produce a range of different PVDF fibres with several concentrations of KCl within them.

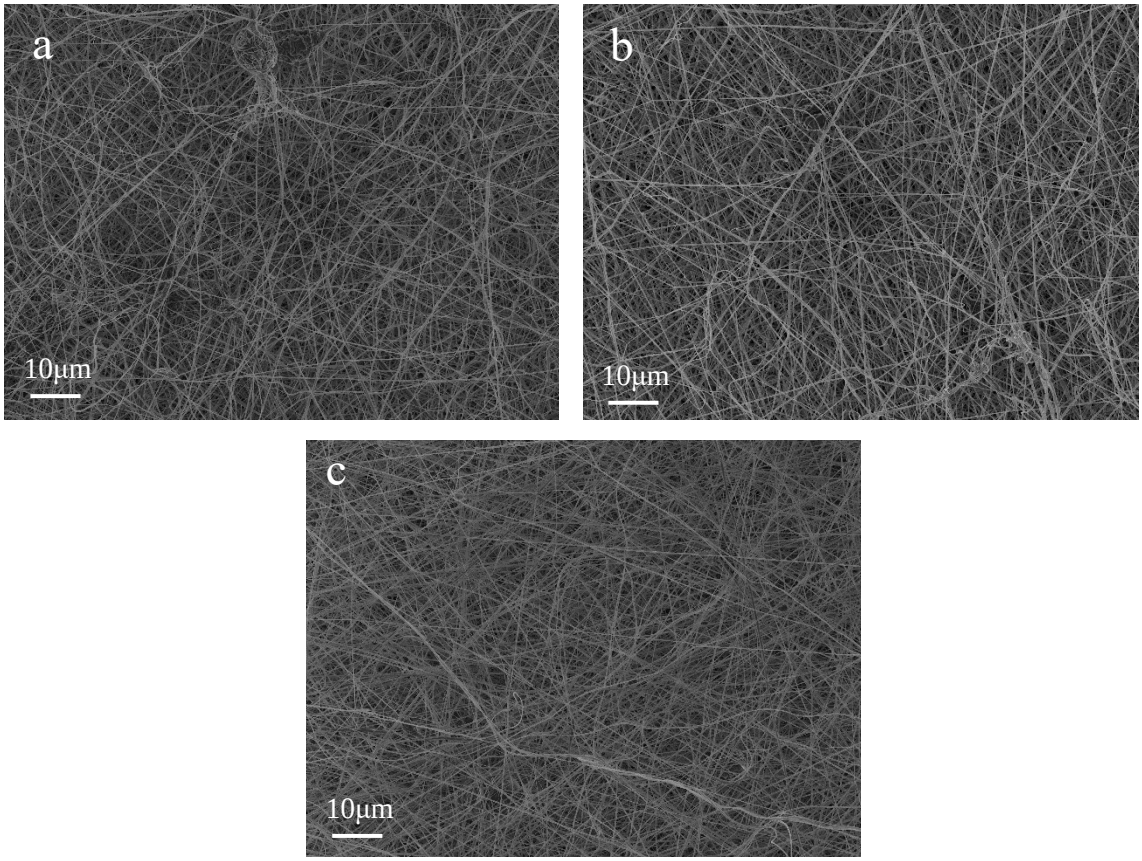

Figure 4.8. SEM images of the PVDF / KCl 2 wt% loading (a) 10 cm collector distance, (b) 12 cm collector distance (c) 15 cm collector distance. Showing little change in fibre morphology with a change in collector distance.

Table 4.8. Electrospinning parameters for the initial PVDF / KCl fibrous mats.

KCl weight / %	**Solvent**	**Collector Distance / cm**	**Voltage / kV**	**Average Fibre Diameter/ nm**
2	DMAc: Acetone	10	14.85	263 ± 50
2	DMAc: Acetone	12	16.06	243 ± 51
2	DMAc: Acetone	15	17.08	266 ± 56

4.2.2 Potassium Chloride Concentration Adjustments

With the initial analysis of the addition of KCl to the LMW PVDF, it was decided to add a range of KCl concentrations to determine the influence of the salt on the fibre morphology. Concentrations ranging from 0.1 wt% - 10 wt% KCl were added to 25 wt% PVDF, with a feed rate of $1ml.h^{-1}$ in an attempt to influence fibre morphology to reduce bead formation and produce thin fibre diameters in comparison to the initial fibres in section 4.2.1.

The fibres were successfully electrospun for all the prepared solutions containing the KCl seen in Figure 4.9. The fibres displayed the complete removal of beads from all the fibres electrospun with rough surface morphologies. As mentioned in 2.5.4.3 the formation of rough surface morphologies with grooves occurs due to the humidity within the chamber. The evaporation of the solvent causes a decrease in temperature close to the fibres which can result in the condensation of water on the surface of the jet. This may result in the formation of the groves that were observed with the PVDF / KCl fibres. The pure PVDF fibres displayed an average fibre diameter of 90 ± 31 nm as mentioned previously. The addition of 0.2 wt% of KCl resulted in an increase in the average fibre diameter to 239 ± 59 nm. Increasing the salt content further to 0.4 wt% had little influence on the average fibre diameter produced diameters of 238 ± 48 nm. From here, the addition of further KCl resulted in average fibre diameters keeping the fibre sizes between 186 nm – 220 nm all within experimental error suggesting little influence of the higher loading of KCl on the PVDF fibres in Table 4.13. These fibres were larger than those produced within the literature with LiCl and NaCl of 65 nm and 80 nm respectively, potentially due to the larger surface area to charge density of the lithium and sodium ions.[278,262]

To further investigate the influence of the KCl on the fibre diameter Gaussian curves were plotted as seen in Figure 4.10. These graphs have shown that most of the fibres counts analysed were within the range of 150 nm – 250nm, with little change in the distribution of the curves/

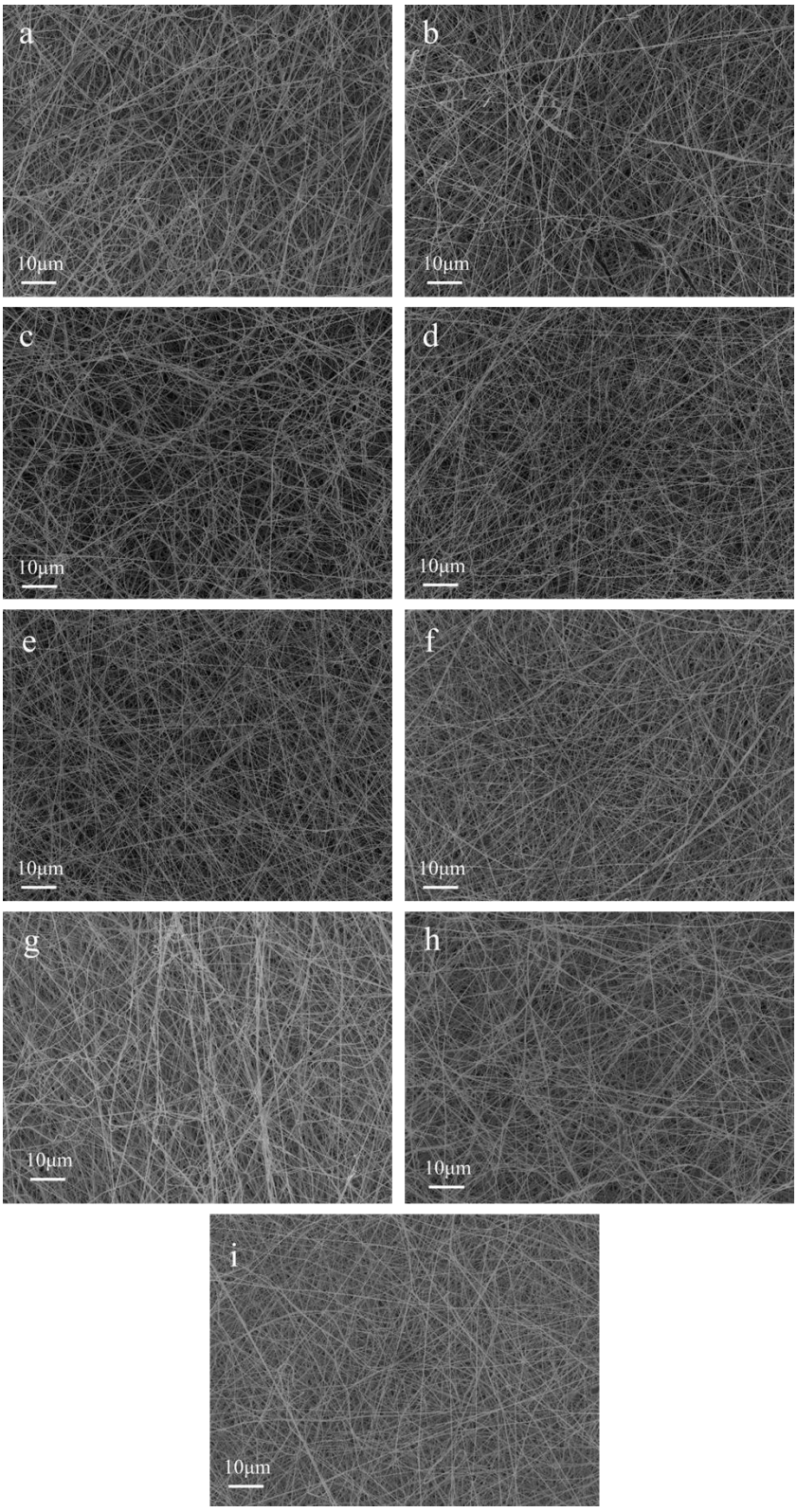

Figure 4.9. SEM images of LMW PVDF/KCl fibres show the influence of KCl on fibre morphology with an increase in its concentration. (a) 0.2 wt% KCl content, (b) 0.4 wt% KCl content, (c) 0.6 wt% KCl content, (d) 0.8 wt% KCl content, (e) 1 wt% KCl content, (f) 2 wt% KCl content, (g) 3 wt% KCl content (h) 5 wt% KCl content, (i) 10 wt% KCl content.

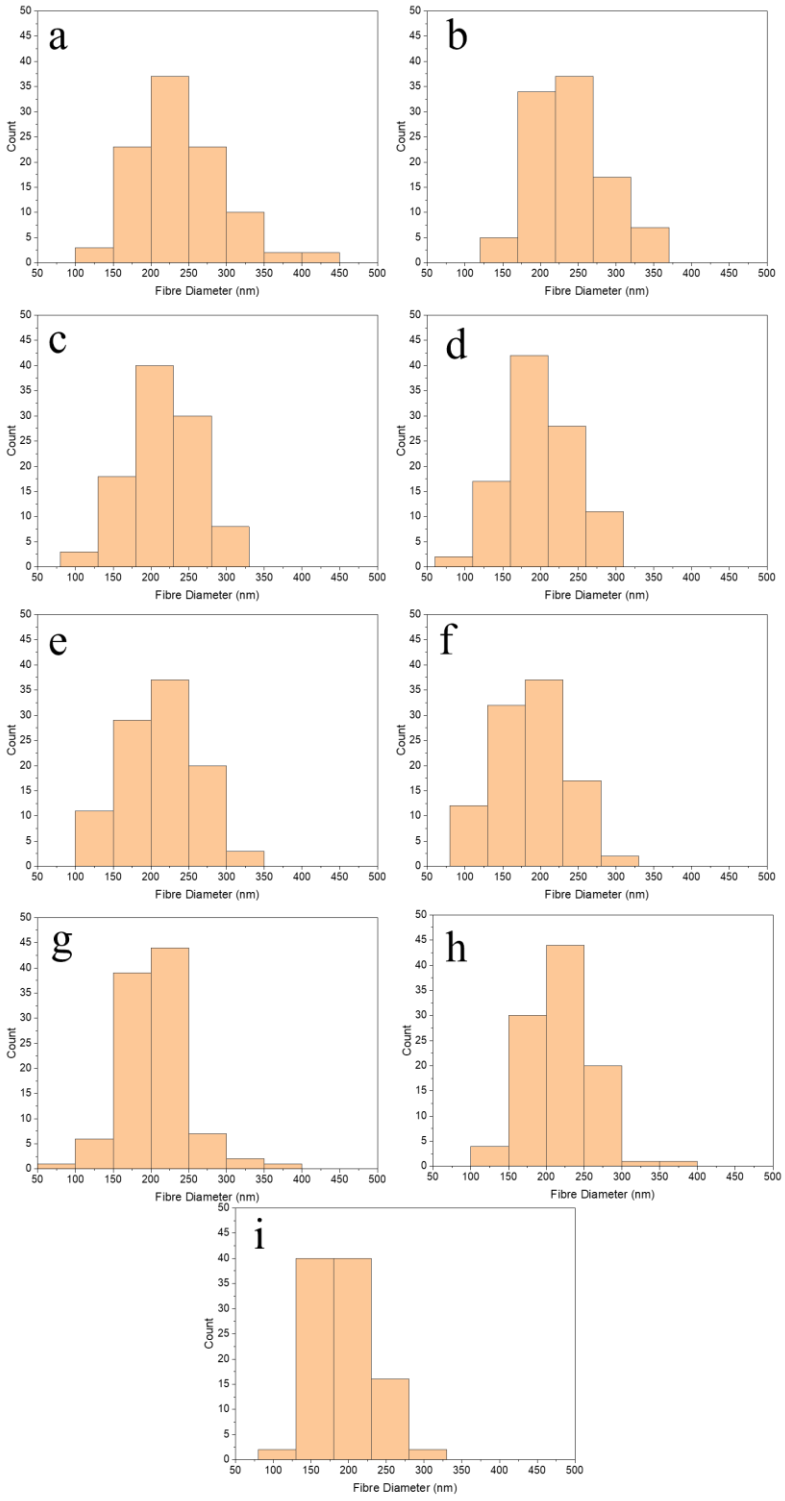

Figure 4.10. The histogram of the LMW PVDF / KCl fibre diameters. (a) 0.2 wt% KCl content, (b) 0.4 wt% KCl content, (c) 0.6 wt% KCl content, (d) 0.8 wt% KCl content, (e) 1 wt% KCl content, (f) 2 wt% KCl content, (g) 3 wt% KCl content (h) 5 wt% KCl content, (i) 10 wt% KCl. Demonstrating little change to the average fibre diameter with the addition of higher quantities of KCl.

Table 4.9. Electrospinning parameters for the LMW PVDF / KCl fibrous mats with 0.2 wt% - 10 wt% KCl salt loading.

KCl weight / %	Solvent	Voltage / kV	Average Fibre Diameter/ nm
0.2	DMAc: Acetone	13.75	239 ± 59
0.4	DMAc: Acetone	13.21	238 ± 48
0.6	DMAc: Acetone	13.46	213 ± 51
0.8	DMAc: Acetone	14.48	200 ± 46
1	DMAc: Acetone	14.34	212 ± 47
2	DMAc: Acetone	14.40	186 ± 46
3	DMAc: Acetone	14.47	204 ± 44
5	DMAc: Acetone	14.36	220 ± 40
10	DMAc: Acetone	16.14	191 ± 39

4.2.3 PVDF / KCl Solution Viscosity

To investigate why the fibre produced increased in diameter with the addition of the KCl the viscosity was analysed. Figure 4.11. demonstrates the change in viscosity with the increase in the concentration of KCl, where overall there is little change in viscosity with the initial addition of the salt however a gradual increase then decreases at higher concentrations. The 25 wt% pure PVDF has shown a viscosity of 139 ± 0.50 cSt. The addition of 0.2 wt% KCl has little influence on the viscosity of the PVDF solution displaying a viscosity value of 138 ± 1.23 cSt. Increasing the salt content to 0.4 wt% - 0.6 wt% had shown to influence the viscosity more, with values increasing to 142 ± 1.47 cSt and 163 ± 3.37 cSt respectively. From here increasing the concentration of the KCl led to a decrease in the viscosity began while increasing the KCl value to 10 wt%. From here, the viscosity began to increase again when 10 wt% KCl was added to the solutions, as seen in Figure 4.11. The changes in viscosity did not alter the average fibre diameter of the materials to a large degree when in previous studies increasing the viscosity has been shown to influence fibre diameter.[278] Here the average fibre diameter increased with the initial addition of 0.2 wt% KCl with little change to the viscosity. Changes to the viscosity concerning the addition of further KCl had shown little influence on the average fibre diameter. This leans towards the suggestion that other parameters during the electrospinning technique had a larger influence on the average fibre diameter rather than the changes in viscosity for the PVDF / KCl samples spun.

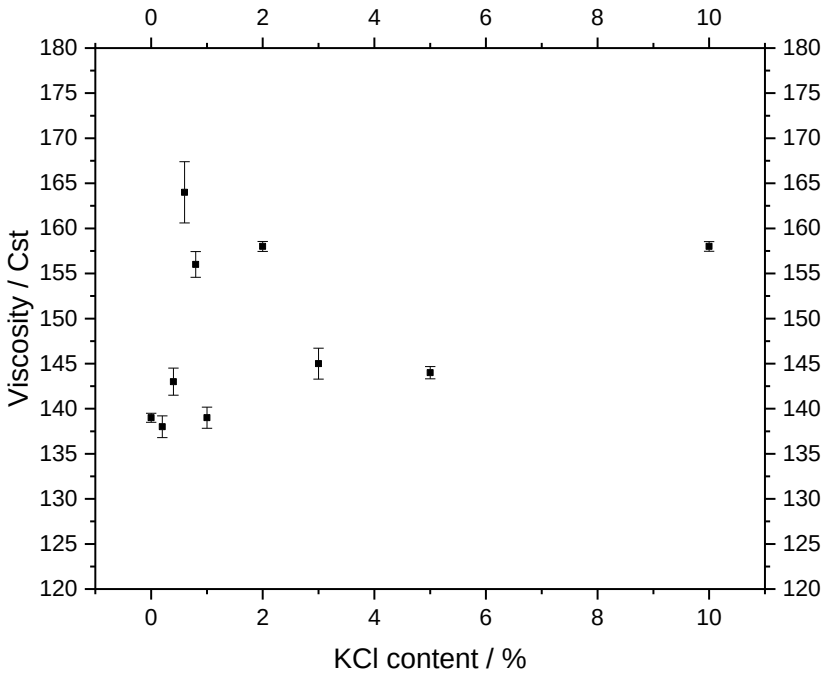

Figure 4.11. Showing the change in viscosity of LMW PVDF / KCl solutions containing 0 wt% - 10 wt% KCl with a change in viscosity with an increase in KCl content.

4.2.4 PVDF / KCL Applied Voltage

With the viscosity of the materials displaying little correlation in the change in the average fibre diameter with the initial addition of the KCl salt, it was then decided to investigate the influence the voltage may have had on the fibre diameters. The critical voltage required to cause deformation of the Taylor cone was increased at three intervals at the 0.2 wt%, 0.8 wt%, and the 10 wt% KCl loadings as the materials did not produce jets if the voltage was not increased. The largest change in the average fibre diameter was observed with the initial addition of 0.2 wt% where the applied voltage increased from 8.46 kV to 13.75 kV. From here increasing the voltage at the 0.8 wt% and 10 wt% loadings did not see a change in the average fibre diameter. As mentioned in 2.5.4.4 an increase in voltage causes the release of higher quantities of the polymer from the Taylor cone resulting in the formation of thicker fibres. The influence on the voltage seems to be more dominant in the lower concentration of KCl of 0.2 wt% rather than at 0.8 wt% and 10 wt% where a further increase in the fibre diameter would be expected as the voltage increases. However, this does not occur, and the average fibre diameters are similar diameters to that of the 0.2 wt% KCl loaded fibres. To further understand why this may be occurring the conductivity of the solutions was analysed.

4.2.5 PVDF / KCl Solution Conductivity

The solution conductivity for the pure PVDF solution in a 1:1 ratio of DMAc: acetone was 1.04 ± 0.06 μs.cm^{-1}. The addition of 0.2 wt% KCl led to an increase in the conductivity to 15.1 ± 0.41 μs cm^{-1}, from here increasing the salt concentration did largely influence the conductivity of the solution. Values were within the range of 14.5 – 15.5 μs.cm^{-1} for all the samples produced from 0.2 wt% - 10 wt% KCl loading, seen in Figure 4.12. The solution conductivity can be calculated by:

$$\sigma = \Sigma F z_j \mu_j c_j \qquad \text{Eq. 18}$$

where F is the Faraday constant, z_j is the charge, μ_j is the electrochemical mobility, and c_j is the concentration of j which is the ion type.[334] According to the solution conductivity equation increasing the salt content leads to an increase in the number of salt ions in the solution system. This, in turn, results in a decrease in the electrochemical mobility of the ions. Alongside this, the charge may be constant due to the formation of neutral ion pairs being formed with high concentrations of salt ions.[335] This leads to no change in the solution conductivity of the solution with the loading of further KCl. It has been shown previously that a much lower loading of LiCl that an increase in the solution conductivity is observed.[278] This suggests that here the concentration of KCl in the solution was too high to see the gradual transition in conductivity which would occur below 0.2 wt%. Overall, there is an increase in conductivity of the solution which could be the reason why the beaded fibres are removed from the material as a higher charge density would form around the Taylor cone associated with the removal of beaded fibres. However, the increase in the average fibre diameter does not seem to be influenced by the conductivity here, rather the increase in voltage may be the main factor influencing fibre diameter over the solution conductivity. It can also be mentioned that further studies on the surface tension of the solutions may provide some understanding of the increase in fibre diameter.

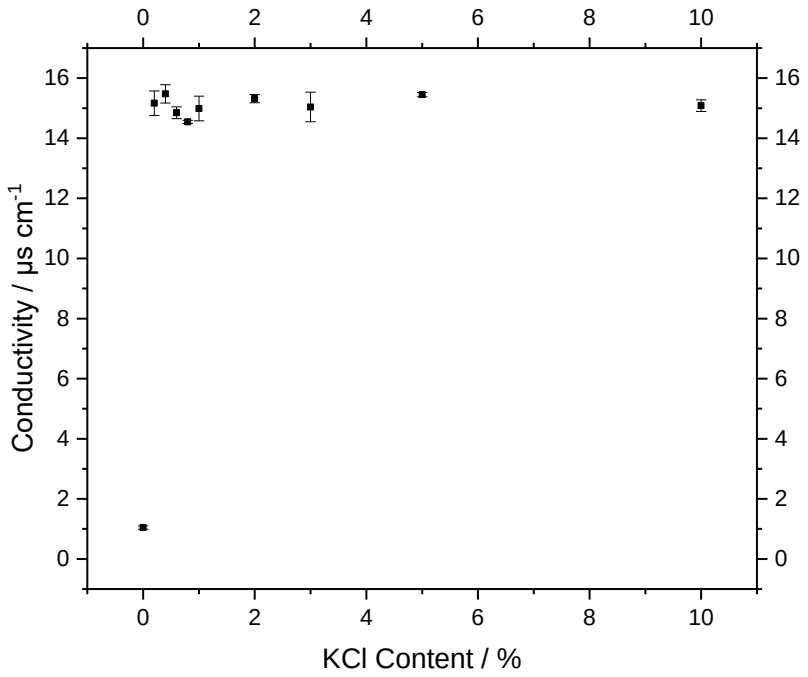

Figure 4.12. The conductivity of LMW PVDF / KCl solutions containing 0 wt% – 10 wt% KCl salt with little change occurring to conductivity with an increase in KCl content.

4.2.6 Leaching the PVDF / KCl Fibres

In an attempt to reduce the average fibre diameters of the PVDF / KCl, it was decided to leach the fibres with distilled water for 24 hours to remove the salt from the surface of the materials. The average fibre diameters for the leached fibres had shown small increases in comparison to the non-leached fibres. It was expected for the fibre diameters to decrease and the formation of pores on the surface of the material as seen in the literature.[336] However, these results were all within experimental error suggesting that there was little influence on the removal of the salt from the surface of the fibres. The average fibre diameters of the PVDF / KCl fibres can be seen in Table 4.10. The morphology of the fibres did not change as seen in Figure 4.13. Generally, the fibre diameters had all displayed similar fibre diameters except the 0.8 wt% which demonstrated a decrease in the fibre diameter. There may have been a higher portion of salt on the surface of the material which could have resulted in the decrease in the fibre morphology. When analysing the surface morphology of the PVDF / KCl loaded with a concentration of 10 wt% of the salt little changed to the surface morphology were observed suggesting there was little removal of the KCl as there was no visual change in surface morphology through the fibres. However, for further analysis surface roughness analysis may be considered to determine

if there was any further change. Further images of the entire range of the leached LMW PVDF / KCl can be seen in the appendix Figure 0.4.

There may have been little change to the average fibre diameter of the non-leached fibres in comparison to the leached fibres however, small changes did occur suggesting that there may have been a potential uptake of water over time causing the fibre to swell producing thicker fibres overall. The little changes to the surface morphology of the fibres also suggest that the KCl salt was not effectively removed from the surface of the fibres as expected. It also suggests that higher quantitates of the KCl were embedded within the fibres which, resulted in little change to the surface morphology of the fibres. This could have occurred due to the samples not being fully dry.

Table 4.10. The average fibre diameter of the leached PVDF / KCl Fibres.

Weight of KCl / %	**Average Fibre Diameters / nm**
0.2	256 ± 65
0.4	259 ± 57
0.6	223 ± 46
0.8	187 ± 46
1	268 ± 54
2	246 ± 57
3	279 ± 67
5	250 ± 55
10	257 ± 67

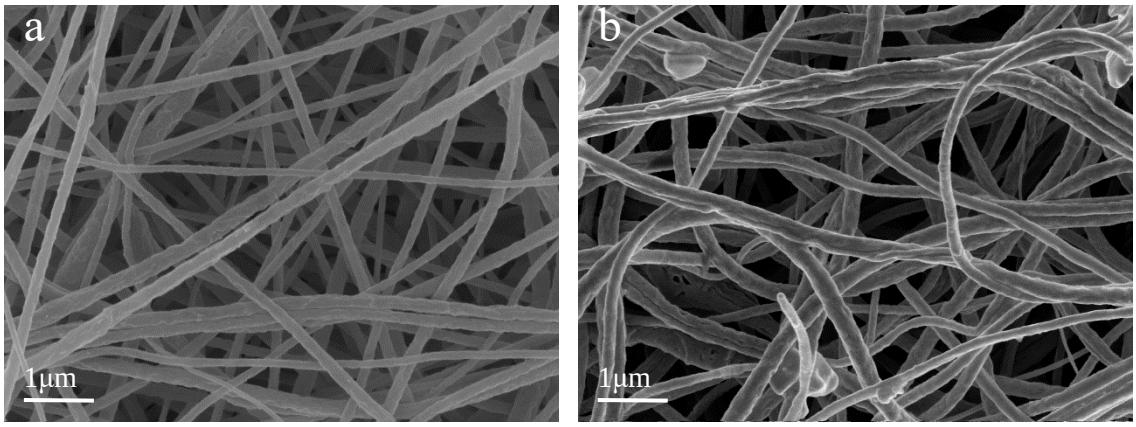

Figure 4.13. Magnified images of PVDF / KCl fibres (a) non-leached 10 wt% KCL (b) Leached. 10 wt% KCl. Displaying changes in the surface morphology once quenched.

4.2.7 FTIR of PVDF / KCl Fibres

The analysis of the electroactive phase of the PVDF was established using FTIR. It was essential to determine the content of the piezoelectric component of the PVDF as it may later play a role in influencing the sound absorption properties at the low-frequency range.

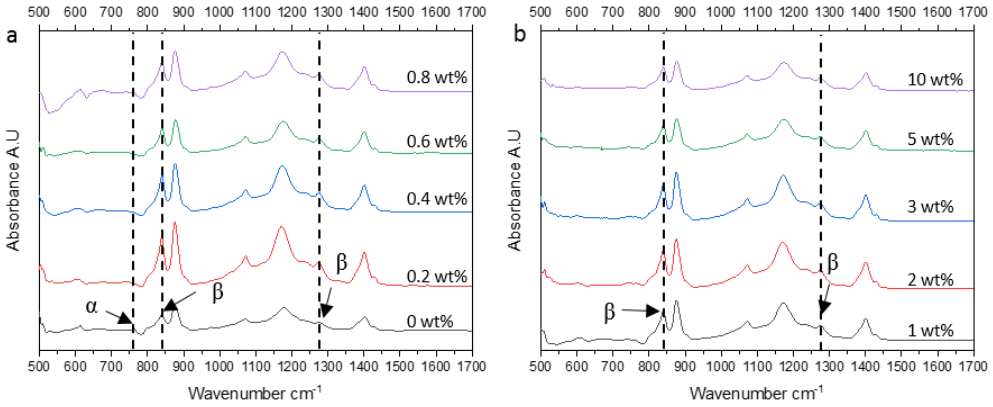

Figure 4.14. demonstrates the change in the peaks associated with the α and β polymorphs with the addition of the KCL filler. The two main polymorphs analysed within the PVDF were the α polymorph displaying intensity peaks at 763 cm^{-1}, 975 cm^{-1}, 1209 cm^{-1}, and 1382 cm^{-1}, and the β polymorph in PVDF displaying intensity peaks at 840 cm^{-1} and 1275 cm^{-1}.[337,338,339,340] Within the PVDF a weak intensity peak representing the α polymorph at 763 cm^{-1} is observed in pure PVDF fibres. Increasing the content of the KCl to 0.2 wt% resulted in a reduction in the intensity of the peak at 763 cm^{-1} suggesting there was a decrease in the content of the α polymorph. While the intensity of the peaks at 840 cm^{-1} and 1275 cm^{-1} of the β polymorph increased with the addition of 0.2 wt% and remained similar throughout the increase in the salt content as seen in

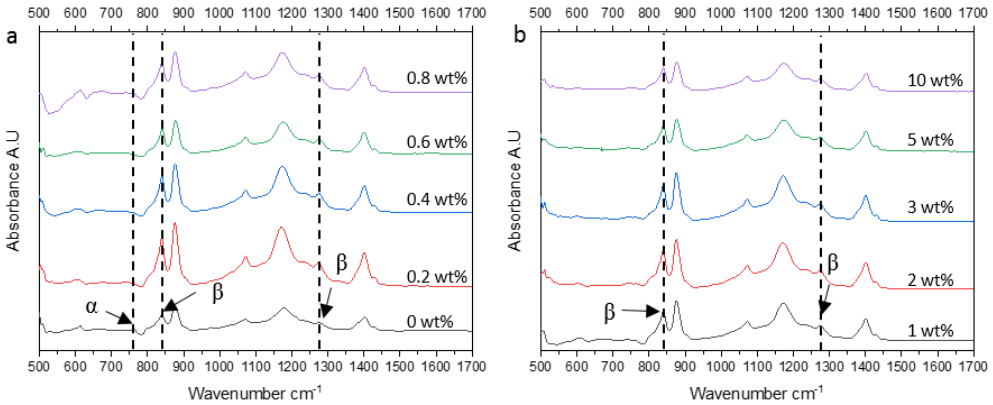

Figure 4.14.

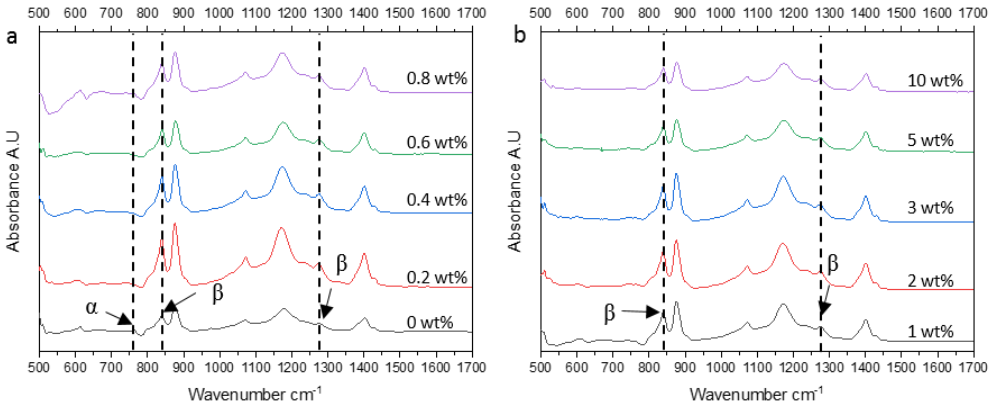

Figure 4.14. The FTIR graphs for LMW PVDF / KCl. (a) 0 wt% - 0.8 wt% KCl, (b) 1 wt% - 10 wt% KCl. Showing the appearance of the peak associated with the β polymorph and removal of α polymorph with the addition of KCl.

To further investigate the quantitative analysis of the β polymorph the Beer-Lambert law was applied as seen in 3.3.5. It has shown that pure PVDF produced the lowest β content with a value of 80.1 %. The initial addition of KCl to the system increased the β phase content by more than 10 % producing a value of 91.8 %. Further increasing the KCl content by 0.8 wt% led to the highest value of the β phase at 99.7 %. The addition of more KCl resulted in a decrease in the β phase percentage with the 1 wt% KCl loading producing a value of 98.8 %. From here a steady decline in the β phase content was seen with an increase in KCl salt. Values of 97.2 %, 87.2 %, 85.6 %, and 85 % were analysed for 2 wt%, 3 wt%, 5 wt%, and 10 wt% KCl loadings respectively seen in Figure 4.15. It could be said that a higher portion of KCl within the material may be acting to hinder the nucleation of the β polymorph within the PVDF. To further investigate this DSC analysis can assist in further analysing the influence of KCl salt on the crystallinity and recrystallisation of the PVDF fibres.

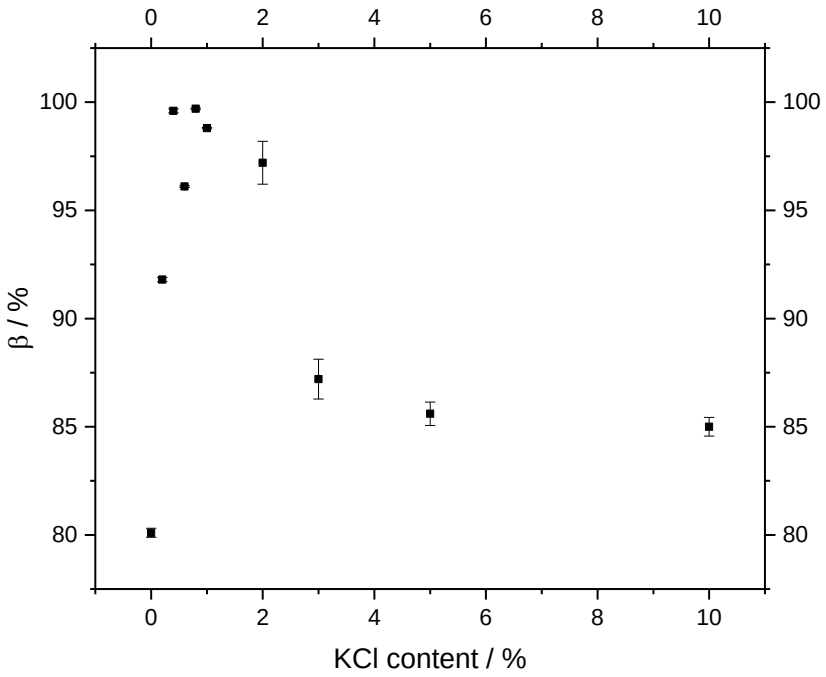

Figure 4.15. The changes in β phase percentage for LMW PVDF fibres with the addition of KCl.

Figure 4.16 is displaying the relationship between the percentage β polymorph and the average fibre diameter. The fibre diameter for all the PVDF / KCL fibres is similar while the content of the β polymorph increases. This suggests that there is no correlation between the two components and that the KCl acts as a nucleator for the nucleation of the β polymorph instead of orientation of the phase through stretching. In general PVDF fibres with lower fibre diameters are known to have higher percentages of the electroactive phase where small fibre diameters of 70 nm produce a β phase percentage of 86.6%.[264] Other studies have also shown that fibre diameters of 107 ± 17 nm produce a β polymorph of 76 %.[341]

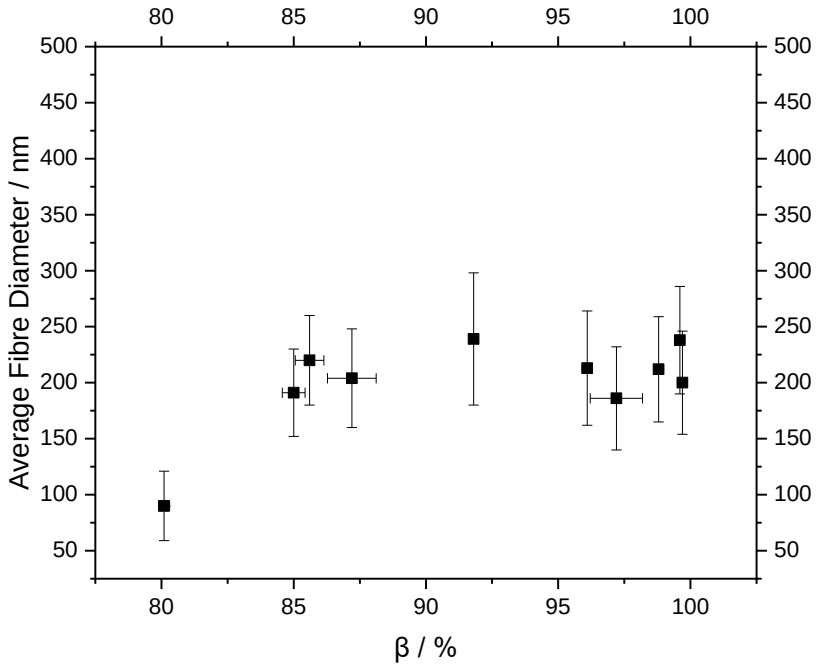

Figure 4.16. The correlation between the beta phase and the average fibre diameter. Displaying no correlation between the two.

It is known that to effectively induce the β polymorph stretching and elongation of the polymer is required to align the polymer chains into the all-Trans TTTT configuration.[258] However, here the PVDF is increasing in beta content with little change to the average fibre diameter. This suggests that the KCl may be interacting with the PVDF solution system to assist in the nucleation of the β configuration. Figure 4.17 represents the interaction between the DMAc solvent, the cations, and the polymer chains, which assists in the nucleation process. The K^+ cations are interacting with the DMAc influencing the solvation of the polymer. It is also acting to orientate the chains in the β configuration by interacting with the fluorine atoms on the backbone of the polymer chain. This could be the factor, which increases the orientation of the β phase.[342]

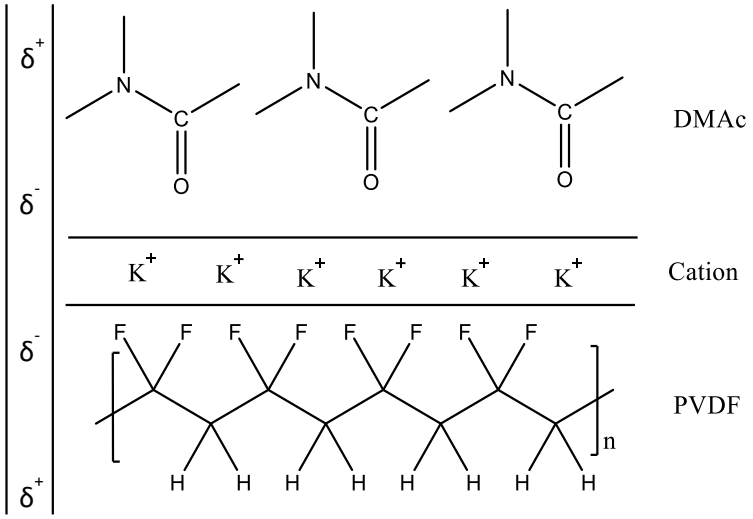

Figure 4.17 The molecular interaction between DMAc, K+ cation, and PVDF where the K^+ ions interact with both the PVDF and DMAc for nucleation of the β polymorph.[342]

4.2.8 DSC of the PVDF / KCl Fibres

To accommodate the FTIR analysis with the increase in the content of the β polymorph it was decided to investigate the crystallinity further using DSC analysis. This would give further information on any changes to the percentage crystallinity which is known to alter with an increase in the β content. Figure 4.18 demonstrates the peak broadening of the melt peaks for the PVDF / KCl salts at all the added concentrations. The melt temperature (T_m) of PVDF is known to be 172 °C and typically represents the dominance of the α phase in PVDF. While a shift to lower melt temperatures of 167 °C represents the dominance of the β phase.[106,143,343] The pure PVDF with 0 wt% KCl had a T_m of 170 °C. The addition of KCl of 0.2 wt% and 0.4 wt% sees the melt peak shift to a lower T_m of 168 °C and 169 °C respectively. Peak broadening becomes more noticeable at the 0.2 wt% and 0.4 wt% loadings showing the overlap of both the α and β melt peaks seen in Figure 4.18. Increasing the content to 0.6 wt% leads to a removal of the peaks, however, a T_m of 168 °C is observed. From here further increasing the KCl content in the fibres leads to T_m ranging between 168 °C – 170 °C seen in Table 4.14. Overall peak broadening occurs for all of the PVDF / KCl fibre mats and is generally associated with the appearance of both the α polymorph and the β polymorph.[344] A shift to lower temperatures was also observed here which is an indication the nucleation of the β polymorph has occurred with the addition of KCl salt.[345]

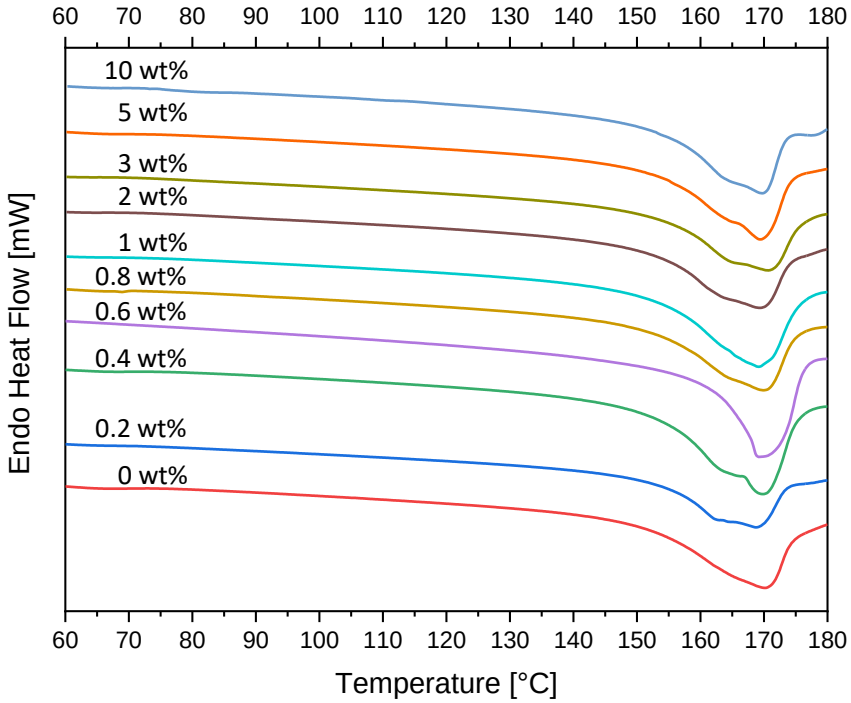

Figure 4.18. The endothermal heat flow graph for the LMW PVDF / KCl fibres with peak broadening representing the α and β polymorph with the addition of KCl.

Figure 4.19 demonstrates the change shift in the recrystallization temperature (T_c) of all the PVDF fibres with KCl salt added. It specifically demonstrates a shift to a higher temperature and the splitting of the peaks. for the pure PVDF was 139 °C. The addition of 0.2 wt% KCl had little influence on the T_c of the materials. Increasing the KCl content to 0.4 wt% and 0.6 wt% began to demonstrate two T_c peaks at 139 °C and 148 °C / 149 °C respectively. With the T_c at higher temperatures becoming the dominant peak at 0.6 wt%. The double T_c did not occur for the fibres containing 0.8 wt% - 3 wt% KCl, melt temperatures for these samples begin to increase ranging between 139 °C – 141 °C seen in Table 4.14. Peak splitting occurs again for the 5 wt% KCl loaded fibres, and much less for the 10 wt% loaded fibres. Table 4.11 displays the T_c of the materials and in particular shows, the two recrystallisation temperatures observed in the PVDF / KCl polymers. A double recrystallisation peak is typically associated with the occurrence of two recrystallisation processes which are found when fillers are present within PVDF. This is where self-nucleation of the polymer occurs alongside heterogeneous nucleation where the filler assists in the nucleation process. This phenomenon occurs due to poor distribution of the filler across the material.[346]

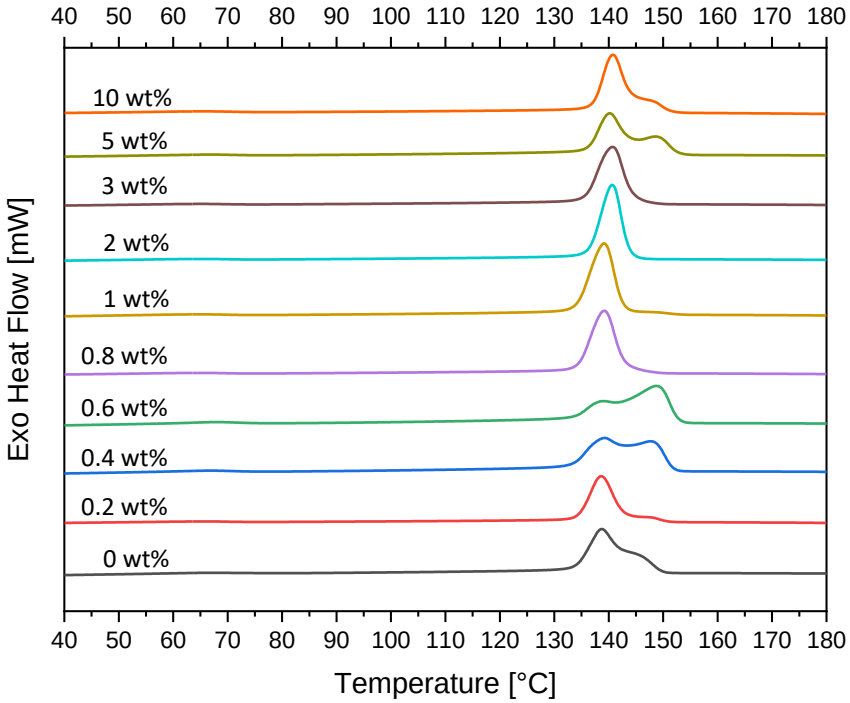

Figure 4.19. The exothermal heat flow graphs for LMW PVDF / KCl fibres. Displaying changes in the recrystallisation temperature with the addition of KCl.

The percentage crystallinity (X_c) of the fibres was calculated using the equation seen in 3.3.7. The pure PVDF fibres had an X_c of 51.7 %. The addition of 0.2 wt% KCl led to an increase in the X_c of the fibres to 53.3 %. From here, the crystallinity increased further up to 0.6 wt% producing an X_c of 55.8 %. The X_c between 0.8 wt% – 3 wt% was steady within the range of 52 % – 55 %. However, increasing the concentration of the KCl to 5 wt% and 10 wt% led to a decrease in the X_c displaying values of 48.9 % and 45.5 % respectively as seen in Table 4.11 The increase in the enthalpy with the addition of KCl suggests the formation of new crystals in the crystalline region of the PVDF.[267] This suggests that the β phase has been further induced with the addition of KCl. However, at higher concentrations, these values decrease and are in line with a decrease in the electroactive phase of the PVDF analysed within the FTIR.

Table 4.11. The DSC data for the LMW PVDF / KCl fibres.

KCl wt%	T_m / °C	T_c / °C	ΔH_f	X_c / %
0	170	139	54.1	51.7
0.2	168	139	55.8	53.3
0.4	169	139 148	58.4	55.8
0.6	168	139 149	59.0	56.3
0.8	169	140	55.8	53.3
1	168	139	55.0	52.5
2	168	141	56.1	53.6
3	170	141	58.0	55.4
5	169	140 149	51.2	48.9
10	169	141	47.6	45.5

*T_c peaks with two temperatures have been stated.

4.2.9 XRD of PVDF / KCl Fibres

To accommodate and enhance the FTIR analysis and the DSC analysis on the nucleation of the β polymorph with the addition of the KCl, XRD analysis was carried out. Figure 4.20 demonstrates the removal of the intensity peaks associated with the α polymorph with the addition of the KCl salt and the increase in the peaks associated with the KCl salt with its addition. The pure PVDF containing 0 wt% KCl has shown intensity peaks at 18.4 ° the reflection of (020) and at 20.8 ° the reflection of (110) and (200).[3] The intensity peak at 18.4 ° is representative of the α polymorph in PVDF, while the intensity peak at 20.8 ° is representative of the β polymorph. The intensity of the peak at 18.4 ° begins to decrease with the addition of KCl and is still observed with an increase in the KCl content suggesting that all the PVDF fibres have some ratio of α phase within them, however, are dominant in the β phase. The weak intensity peak at 36.5 ° represents the (020) reflection of the β phase.[347,345] This intensity peak was displayed in all of the PVDF fibres that were electrospun seen in Figure 4.20. Similar results have been demonstrated with PVDF / ZnO fibres where the formation of the intensity peak representing the β polymorph is present with the addition of the filler.[292] This has also been demonstrated with the addition of nickel chloride hexahydrate salt, where the addition of the salt resulted in a decrease in the intensity of the 18.4 ° intensity peak and an increase in the intensity peak of the β intensity peak.[273]

The intensity peaks representing the KCl begin to appear from 1 wt% loading, from here the intensity of these peaks increases with the addition of further salt. The peak at 28.3 °

represents the (200) reflection and the intensity peak at 40.5 ° represents the (220) both characteristic of the KCl salt within the PVDF.[348,349] This demonstrated that the KCl was loaded within the PVDF material.

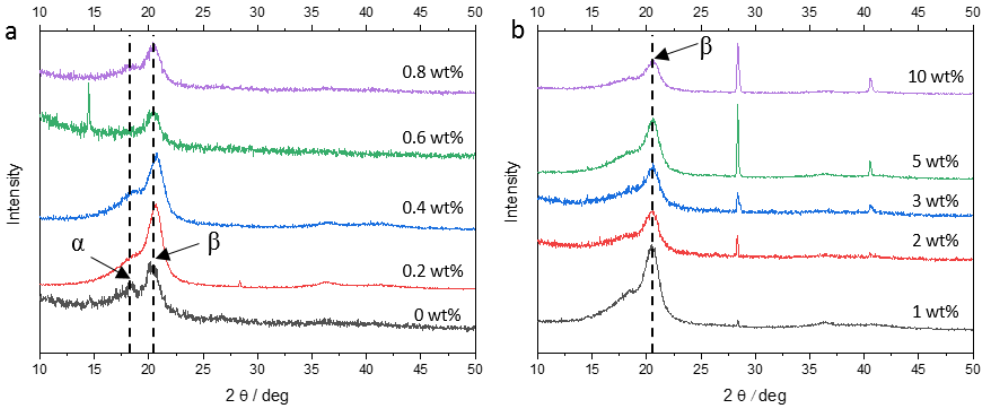

Figure 4.20. XRD partners for the LMW PVDF / KCl fibres displaying the removal of the α peak with the addition of the KCl. (a) 0 wt% - 0.8wt% (b) 1 wt% - 10 wt%.

4.2.10 Summary

The addition of the KCl salt to the LMW PVDF fibres resulted in an initial small increase in the average fibre diameter. While increasing the content of the KCl demonstrated little changes in the average fibre diameter resulting in diameters ranging between 191 nm – 239 nm. These materials were all within the experimental error suggesting that KCl did not influence fibre diameter once increased from 0.2wt% onwards. In comparison to the literature, these fibres were larger than what has been reported for PVDF, where previous studies with the addition of LiCl and NaCl produced fibre diameters of 65 nm and 80 nm respectively.[278,262] This may be due to these materials having a lower concentration of polymer within the system than those here. Leaching of the KCl was not effective in reducing the average fibre diameters with a small shift to higher average fibre diameters. This was suggested to occur due to the potential swelling of the polymer when within the water. The average fibre diameters of the PVDF have been shown to have little influence with the addition of an excess amount of KCl. The only noticeable change was observed with the initial addition of KCl to the fibres. KCl had shown to influence the viscosity and conductivity of the solution, however, this did not have much influence on the average fibre diameter as values were kept within a small diameter range. It was suggested that the initial increase in fibre diameter was influenced by an increase in voltage required to generate cause deformation of the droplet and emit the jet. This may have led to more polymer solution being emitted from the Taylor cone increasing the fibre diameter. It should also be

mentioned again that further analysis on the surface tension of the droplet may be carried out in future to determine if any changes in this value occurred which way influence fibre diameter.

The addition of KCl to the PVDF fibres demonstrated the nucleation of the β polymorph with the proposed molecular interaction seen in Figure 4.17 resulting in the nucleation of the electroactive phase. Magnesium salts have previously been demonstrated to also cause nucleation of the β polymorph with values of ~90%.[350] The new work within the crystallinity studies on the PVDF / KCl polymer demonstrated a maximum β content value calculated at the 0.8 wt% loading of 99.7% producing a pure β phase PVDF. This value was higher than the 93.7% achieved by the addition of LiCl to PVDF in previous studies.[278] This was unexpected as LiCl has a higher charge density than KCl and would influence charge density around the Taylor cone to a higher extent. Higher quantities of KCl loading resulted in the reduction of the β content and a decrease in the overall crystallinity of the PVDF fibres. It was suggested to occur due to a hindrance in the recrystallisation of the polymer due to an increase in the content of the salt. The FTIR, XRD, and TGA all point in the direction of the formation of the β phase, with the intensity peaks of the FTIR and XRD all showing up at the relevant areas, alongside the T_m of the fibres reducing to lower temperatures.

Overall, the new work within this section demonstrates that KCl will influence fibre morphologies by removing beaded structures from fibres with beads, and result in an increase in the average fibre diameter for these smaller fibres. It also assists in the nucleation of the β polymorph for LMW PVDF to produce material which is phase pure in the electroactive phase with fibre diameters ranging between 191 nm – 239 nm. It has also been demonstrated to assist in the nucleation of the β polymorph and provide a content of β polymorph at 99.7% with a low loading of 0.8 wt% which is higher than what has been demonstrated in the literature.

4.3Electrospinning HMW PVDF / KCl Fibres

It was decided to then analyse the influence of KCl on the HMW PVDF fibres which at the higher concentration of 30 wt% did not display any formation of beaded structures. In contrast to the influence, KCl displayed in the removal of beaded fibres for the LMW PVDF it was added here to the HMW to determine if the KCl could reduce the average fibre diameter electrospun PVDF. The crystallinity of the material was also analysed here to determine the influence of KCl on the crystallinity of a polymer with a higher molecular weight and how this may influence the electroactive properties of the material. It was also decided to only add the KCl content from 0.2 wt% – 1 wt% as within the LMW the highest piezoelectric component was observed at the lower concentrations of the KCl rather than the higher. Another reason behind not using the higher concentrations of the salt a decrease in the percentage crystallinity was observed.

4.3.1 KCl Salt Concentration Adjustments

The successful formation of the HMW PVDF / KCl fibres was carried out. The electrospinning for the formation of these fibres was kept the same as the LMW PVDF / KCl fibres with adjustments being made to the applied voltage to maintain a stable Taylor cone. The morphology of the fibres produced was bead free with a rough surface morphology as seen in Figure 4.21. As mentioned previously the formation of rough surface morphologies with groves occurs due to the condensation of water on the surface of the jet which evaporates at a different rate to the binary solvent system causing the formation of indentations and groves. The pure PVDF displayed an average fibre diameter of 1342 ± 385 nm. The initial addition of the KCl at 0.2 wt% to the 30 wt% HMW PVDF fibres had shown to produce average fibre diameters of 560 ± 107 nm. Increasing the content of KCl to 0.4 wt% and 0.6 wt% led to an increase in the average fibre diameter to 620 ± 119 nm and 707 ± 134 nm respectively. From here further increasing the concentration of the KCl to 0.8 wt% resulted in a decrease in the average fibre diameters to 577 ± 120 nm. Further increasing the KCl content to 1 wt% resulted in the fibres once again increasing in average fibre diameters to 810 ± 116 nm. In comparison to previously studied PVDF fibres with salts added to them, these fibres are larger than those mentioned in Table 2.8 with the largest fibres being 365 ± 104 produced by PVDF / $BiCl_3$.[282] The fibres here may be larger as a higher concentration of PVDF was used in comparison to previous studies which use 6 – 22 wt% of the polymer.

This decrease in the average fibre diameter with the addition of the KCl contrasts that of the LMW PVDF / KCl fibres which demonstrated an increase in the average fibre diameter with the initial addition. It can be mentioned that the addition of the KCl led to the removal of beads in the LMW PVDF which would naturally increase fibre diameter. Here there were originally no beads which may have resulted in the KCl influencing the fibres differently by decreasing the average fibre diameter.

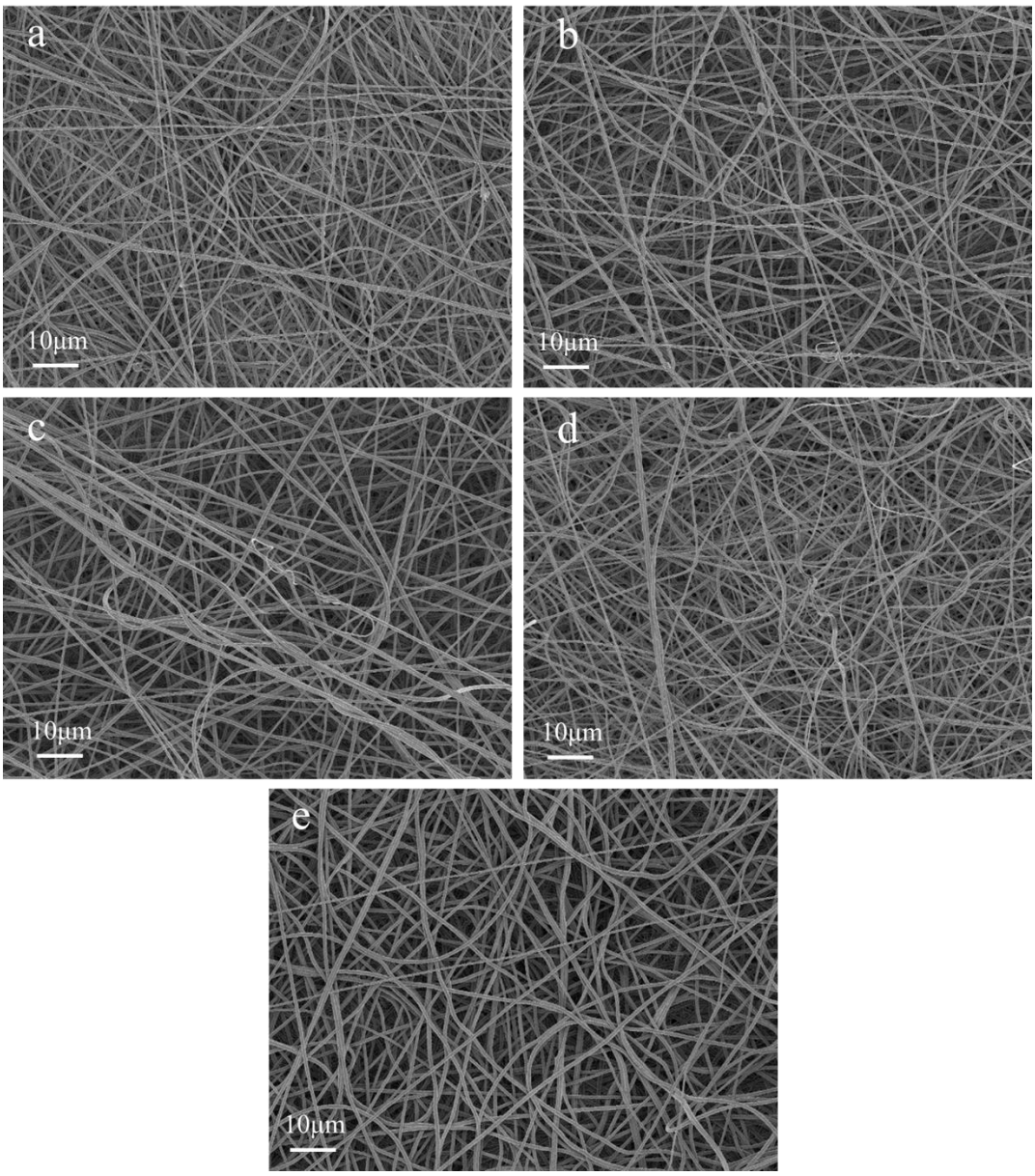

Figure 4.21. Demonstrating HMW PVDF / KCl fibres with no beads on all of the materials produced. (a) 0.2 wt% KCl, (b) 0.4 wt% wt% KCl, (c) 0.6 wt% KCl, (d) 0.8 wt% KCl, (e) 1 wt% KCl

Table 4.12. Electrospinning parameters for the HMW PVDF / KCl 0.2 wt% – 1 wt% fibres.

KCl Weight / %	Applied Voltage / kV	Average Fibre diameter / nm
0	7.14	1342 ± 385
0.2	10.95	560 ± 107
0.4	10.8	620 ± 119
0.6	10.85	707 ± 134
0.8	10.95	577 ± 120
1	9.4	810 ± 116

4.3.2 Solution Viscosity of the HMW PVDF / KCl fibres

To further investigate the PVDF and the influence it had on the decrease in the average fibre diameters it was decided to analyse the viscosity of the PVDF / KCl solutions. The pure PVDF solution had been analysed as 359 ± 7.44 cSt. The addition of the KCl increased the viscosity of the solution. The addition of 0.2 wt% KCl resulted in a viscosity of 749 ± 196 cSt. Increasing the content of KCl to 0.4 wt % – 0.8 wt% resulted in a further increase in the viscosity ranging between 838 cSt – 852 cSt as seen in Table 4.13. In comparison to the LMW PVDF / KCl fibres the viscosity here is higher and produces thicker fibres.

The increase in the viscosity of the solution is associated with an increase in the average fibre diameter due to a higher level of polymer chain entanglements as mentioned in 2.5.4.1.[226] However, here the decrease in the average fibre occurs with the addition of the KCl. This could occur due to the KCl influencing the conductivity of the material which may result in higher charge density on the surface of the Taylor cone resulting in the jet experiencing higher levels of coulombic force resulting in the elongation and stretching of the polymer jet to thinner fibre diameters. It has been previously studied that the addition of salt to polymer solutions during the electrospinning process increases the conductivity of the solution.[278]

Table 4.13. Electrospinning parameters of the HMW PVDF / KCl 0.2 wt% – 1 wt% fibres.

KCl Weight / %	Applied Voltage / kV	Average Fibre diameter / nm	Viscosity / cSt
0	7.14	1342 ± 385	359 ± 7.44
0.2	10.95	560 ± 107	749 ± 196
0.4	10.8	620 ± 119	848 ±126
0.6	10.85	707 ± 134	838 ± 8.13
0.8	10.95	577 ± 120	841 ± 9.61
1	9.4	810 ± 116	852 ± 11.9

4.3.3 FTIR of the HMW PVDF / KCl

Following on from the fibre morphology it was decided to analyse the electroactive phase of the PVDF as mentioned previously. Ideally, it is desired to induce the nucleation of the β polymorph within the PVDF to potentially influence the sound damping properties of the fibres at the lower frequency range. Figure 4.22 is displaying the change in the intensity peaks associated with the α and β polymorphs within the PVDF fibres with the addition of the KCl. The pure PVDF and PVDF / KCl had shown the appearance of both the intensity peaks corresponding to the α polymorph and β polymorph, which demonstrates a reduction in the intensity of the α polymorph and an increase the in the intensity of the peaks associated with the β polymorph. The intensity peak representing the α polymorph at 763 cm^{-1} is weak and barely visible for the pure PVDF and all 5 concentrations of the PVDF / KCl fibres. However, at 973 cm^{-1} is observed and the intensity of the peak begins to increase with the addition of 0.8 wt% and 1 wt% of the KCl salt which suggests that there might be a higher concentration of the α polymorph at the higher concentration of the KCl. The intensity peaks representing the β phase at 840 cm^{-1} and 1275 cm^{-1} are present in all the fibres containing PVDF and the intensity of these peaks remains constant throughout the addition of the KCl salt. This suggests that there is a high ratio of the β phase in the PVDF fibres. Similar results were also obtained with the LMW PVDF / KCl where the intensity of the peaks representing α polymorph decreased with the addition of the KCl and the β polymorph intensity peaks were observed and didn't alter in intensity.

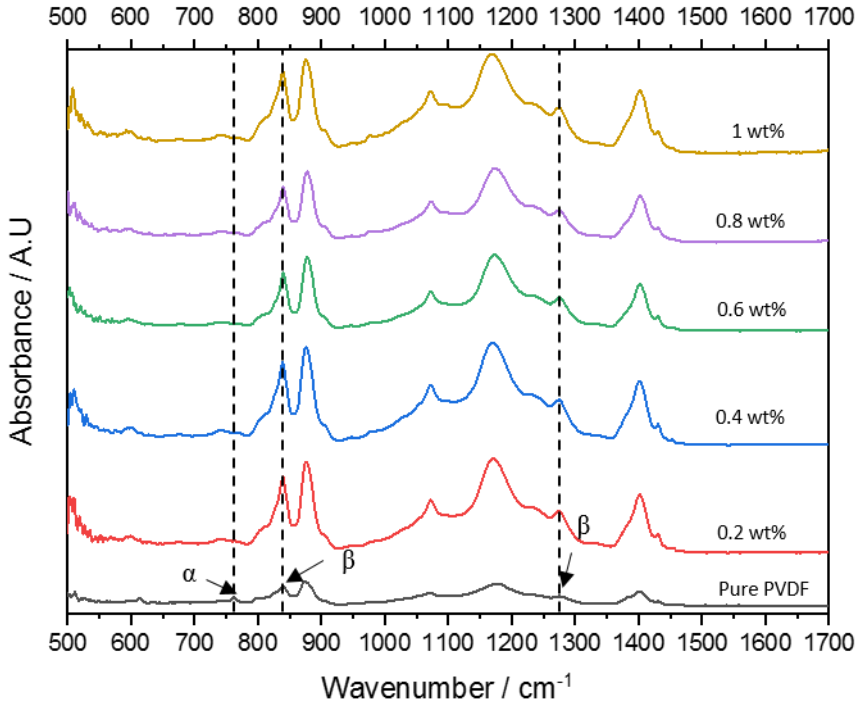

Figure 4.22. FTIR of the HMW PVDF / KCl fibres 0 wt% - 1 wt%. Displaying a removal of the α absorbance peak with the addition of KCl and an increase in the intensity of the β absorbance peak.

To further investigate the content of the β polymorph in the PVDF quantitative analysis was carried out using the Beer-Lambert law seen in 3.3.5. Figure 4.23 demonstrates that the addition of KCl has a large influence on the nucleation of the β phase. The pure PVDF displayed a β content of 56%. The addition of 0.2 wt%, KCl resulted in an increase in the β content to 82 %. The addition of 0.4 wt% and 0.6 wt% resulted in a gradual increase to 84 % and 86 % respectively. Increasing the KCl content any further to 0.8 wt% and 1 wt% resulted in a decrease in the percentage of β phase to 79 % and 76 % respectively. Overall, the HMW fibres demonstrated a lower content of the β polymorph in comparison to that of the LMW fibres. In comparison to the literature, these values are lower than the highest reported PVDF fibres containing LiCl of 93.2%.[278] This would suggest that the HMW PBDF fibres have lower piezoelectric properties than previously reported studies.

It can also be mentioned here that the mechanism of the K^+ ions and the Cl^- ions may play a role in the orientation of the $CH_2 – CF_2$ bonds to assist in aligning the polymer chains in the all-Trans configuration as mentioned in 4.2.7. The decrease in the β polymorph of the fibres created with the HMW fibres in comparison to the LMW fibres can be attributed to the higher level of chain entanglements within the material resulting in difficulty for nucleation of the β polymorph.[351]

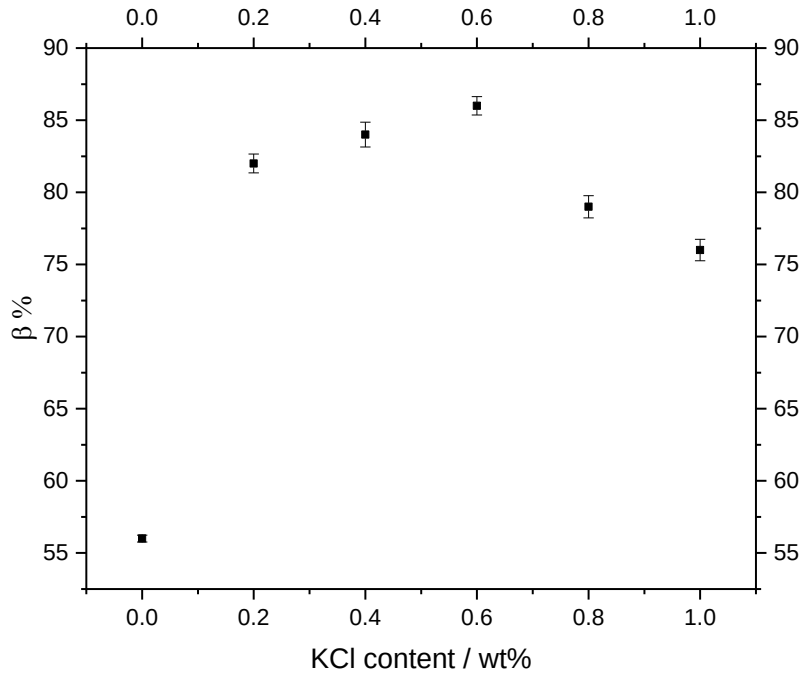

Figure 4.23. Displaying the increase in β phase percentage for the HMW PVDF / KCl fibres with the addition of KCl from 0 wt% - 1 wt%.

Figure 4.24 demonstrates the decrease in fibre diameter with an increase in the content of the β polymorph. This suggests that fibres with lower average diameters display a higher content of the electroactive phase. It is also suggesting a link between smaller fibres and a higher content of the β polymorph which suggests that the addition of KCl may influence orientation of the PVDF chains through stretching where fibre diameters are lower than 600 nm. However, changes in concentration of the KCl does not influence fibre diameter which suggests it is also acting as a nucleator when concentrations are increased to a point up to 0.8wt%

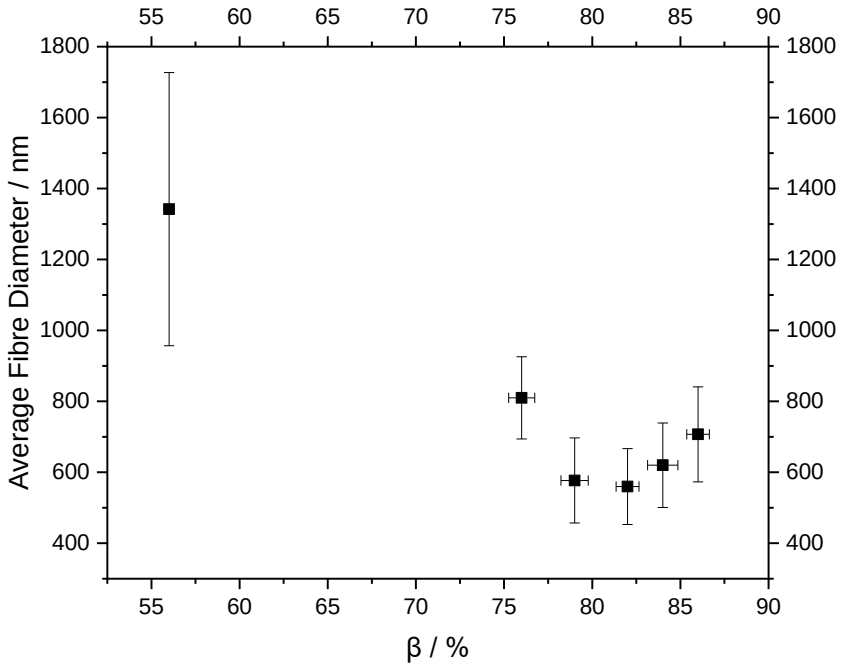

Figure 4.24. The relationship with average fibre diameter and the content of the b polymorph where a decrease in fibre diameter shows an increase in electroactive phase.

4.3.4 DSC of the HMW PVDF / KCl

To further investigate the crystallinity of the HMW PVDF / KCl fibres DSC analysis was carried out as it allows to give different analyses on the nucleation of β polymorph through changes in the T_m and the X_c. The exothermal graph for the PVDF / KCl fibres can be seen in Figure 4.25, which is showing a shift in melt temperature to lower values and the formation of peak broadening and peak splitting for the pure PVDF and the PVDF / KCl fibres. The T_m of the pure PVDF fibres was analysed as 167 °C. The addition of 0.2 wt % KCl led to the splitting of the peak, displaying two melt peaks of 163 °C and 169 °C. The addition of 0.4 wt% KCl resulted in two melt peaks at 162 °C and 166 °C. From here further increasing the KCl content to 0.6 wt% and 0.8 wt% resulted in a T_m of 168 °C. The maximum loading of 1 wt% resulted in peak splitting once again displaying a T_m of 163 °C and 167 °C. As mentioned previously the formation of two T_m peaks is associated with the formation of both the α polymorph and the β polymorph within the PVDF.[344] The decrease in the T_m of the fibres was expected as an increase in the content of the β polymorph was observed. The decrease in temperature is associated with the nucleation of the β polymorph.[345] Similar results were obtained with the LMW PVDF / KCl fibres. The endothermal graph for the PVDF / KCl fibres can be seen in Figure 4.26, where a decrease in the T_c was observed with the addition of the KCl salt between 0.2 wt% – 0.8 wt%.

The pure PVDF displayed a T_c of 141 °C. The addition of KCl of 0.2 wt% - 0.8 wt% resulted in a T_c ranging between 137 °C – 138 °C as seen in Table 4.14. Increasing the content of KCl to the maximum loading of 1 wt% resulted in an increase in the T_c to a value of 141 °C.

Table 4.14. The DSC data for the HMW PVDF / KCl fibres.

KCl wt%	T_m / °C	T_c / °C	ΔH_f	X_c / %
0	167	141	55.5	53.0
0.2	163 169*	138	50.9	48.6
0.4	162 166*	137	54.5	52.1
0.6	168	138	51.5	49.2
0.8	168	138	54.9	52.4
1.0	163 167*	141	54.5	52.1

*These values are the T_m peaks that show splitting.

The X_c of the pure PVDF was analysed as 53.0 %. Overall, the addition of the KCl salt to the HMW PVDF results in a decrease in the crystallinity of the polymer. Other studies on PVDF fibres have shown to produce lower crystallinity values with no filler with values ranging from 42.3 – 39.2%.[252] The addition of the KCl resulted in an overall decrease in the X_c of the polymer. Loading the fibres with 0.2 wt% resulted in an X_c of 48.6 %. From here increasing the content to 0.4 wt% resulted in an increase in the X_c to 52.1 %. The addition of 0.6 wt% KCl resulted in an X_c of 49.2 %. From here increasing the content of the KCl to 0.8 wt% and 1 wt% resulted in an X_c of 52.4 % and 52.1 % respectively. This may have occurred due to the higher charge density of the Taylor cone accelerating the PVDF to the collector at a quicker velocity resulting in less time for crystallisation causing a decrease in the X_c.[352]

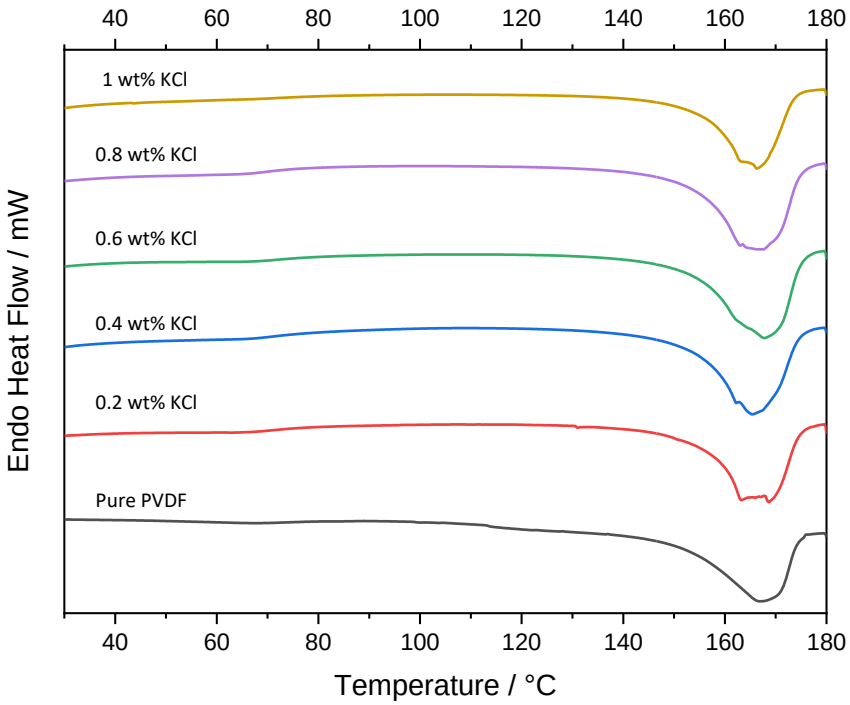

Figure 4.25. Endothermal heat flow of the HMW PVDF / KCl fibres 0 wt% – 1 wt%. Displaying the melt temperatures and peak broadening with the addition of KCl.

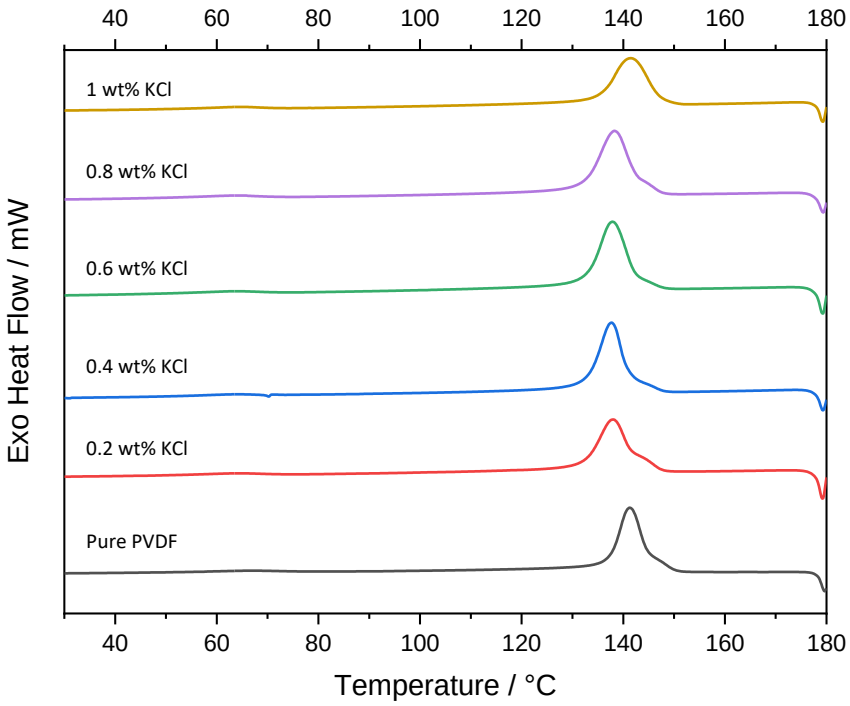

Figure 4.26. Exothermal heat flow of the HMW PVDF / KCl Fibres 0 wt% – 1 wt%. Displaying a shift to lower recrystallisation temperatures with the addition of KCl.

4.3.5 Summary

The addition of KCl to the HMW PVDF fibres had been demonstrated to influence fibre morphology by decreasing the average fibre diameters. Average fibre diameters ranged between 560 nm – 810 nm for the fibres containing the KCl. These were larger than that of the LMW PVDF due to differences in the viscosity of the materials causing different levels of stretching and elongation of the fibres.[324] The nucleation of the β polymorph was also displayed with the addition of the KCl with a maximum of 86 % being obtained with the addition of 0.6 wt% of the inorganic salt. Higher quantities than 0.6 wt% resulted in a gradual decrease in the content of the β polymorph like that seen with the LMW PVDF which demonstrated the same phenomena at 0.8 wt%. These values for the average fibre diameter are higher than what is reported in the literature for a material producing the percentage of β polymorph. The current highest values are produced by the addition of LiCl resulting in a 93.6 % β polymorph content with an 80 nm fibre diameter.[278] Similar to this 80 – 120 nm PVDF fibre with the addition of NiCl2·6H2O resulted in a percentage β polymorph of 92%.[273]

Overall, the content of the β polymorph was lower for the HMW in comparison to the LMW PVDF with the addition of KCl and could be correlated to the difference in the average fibre diameters between the two sets of materials. As mentioned previously thinner fibres experience a higher level of coulombic force which results in the polymer jet experiencing a higher level of elongation and stretching and is associated with nucleation of the electroactive phase.[258] However, here the average fibre diameter does not change drastically when further quantities of salt but the content of the β polymorph varies suggesting that the filler is influencing nucleation of the electroactive phase over alignment through stretching. The DSC data also correlates with the FTIR data suggesting the formation of the β polymorph where peak broadening and splitting occur which suggests the existence of two polymorphs within the PVDF and suggests the formation of the β phase. Here it can be said that the nucleation of the β polymorph is influenced by the KCl salt.

The new findings within this chapter are that the initial addition of KCl salt influences the average fibre diameter and increases the content of the β polymorph within the polymer which has previously not been studied before. This is in line with the LMW polymer however lower values of the electroactive phase are analysed. The solution viscosity is stable across all solutions with KCl within them, however, an increase in the average fibre diameter is displayed contradicting the literature where the increase in viscosity results in an increase in average fibre diameter. Overall, in chapter 4 it can be said that the successful formation of non-beaded fibres has been demonstrated with the addition of KCl and that the salt acted as a nucleator for the increase in the content of the β polymorph.

Chapter 5 Electrospinning PVDF / Niobium Oxides

5.1 Introduction

This chapter involves the formation of non-woven electrospun PVDF mats incorporated with niobium oxide ceramics. The niobium oxide ceramics added to the PVDF fibres were $NaNbO_3$, $KNbO_3$, and $CeNbO_4$. The $NaNbO_3$, $KNbO_3$ was added as a piezoelectric component to not only potentially act as a nucleator but to increase the electroactive nature of the material with the piezoelectric properties of the ceramics. The piezoelectric properties of materials are known to generate electrical energy from the application of mechanical stress.[125] In this work it is important to produce a material which can produce a high voltage output due to its piezoelectric properties as it has been previously mentioned that piezoelectric materials have enhanced sound damping properties in the low-frequency range.[94,106,107] The fibres morphology was also analysed with the addition of these ceramics to determine the influence each type of ceramic had on the surface morphology and average fibre diameters. Alongside this, the ceramics were added to increase the dielectric properties to increase the impact of the polarisation of material and influence nucleation of the β polymorph. In contrast, the $CeNbO_4$ was added as a non-piezoelectric niobium oxide to determine the influence of the electrical properties of the different ceramics on the fibre morphology, crystallinity, and sound damping properties of the fibrous mats. Each of these fillers demonstrates differing properties in piezoelectric and dielectric properties and were chosen specifically to determine their influence on the fibre diameters and nucleation of the electroactive phase of the PVDF.

Following on from the previous chapter the HMW PVDF was applied for these fibres instead of the LMW fibres due to the difference in the average fibre diameter. This was decided as the LMW fibres were much smaller than the ceramic particle sizes which may have led to the ceramic particles protruding the surface which may lead to a morphology like a beaded fibre which is undesirable as it decreases the surface area of the fibres. It has been stated in the literature that a material with a higher surface area to mass ratio will enhance the damping properties of the material.[52] The HMW demonstrated thicker fibres morphologies of 1342 ± 385 nm which would potentially engulf the ceramic particles for homogenous fibres.

5.1.1 Precursor Analysis on the Niobium Oxide Ceramics

Figure 5.1 demonstrates the morphologies of the three-niobium oxide ceramic fillers added to this work. The ceramic particles had an average particle size of 410 ±140 nm, 351 + 134 nm,

and 796 ± 186 nm for the $NaNbO_3$, $KNbO_3$ and $CeNbO_4$ respectively. The values were analysed using SEM images and calculating the particle sizes of the particles at 100 points. These ceramic powders were not milled or treated before analysis and were later used as purchased as the data analysed was in line with the data sheets provided.

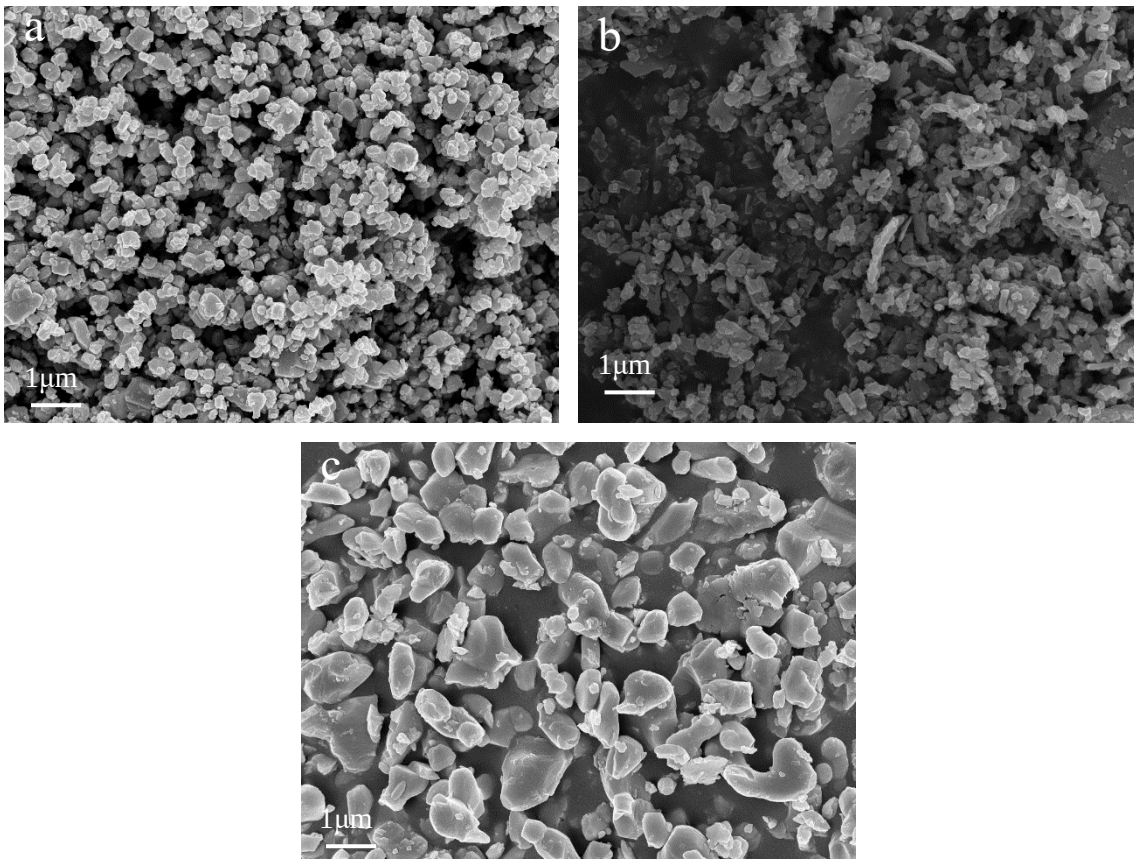

Figure 5.1. SEM images showing the morphology of the niobium oxide ceramics. (a) sodium niobate particles, (b) potassium niobate particles, (c) cerium niobate particles.

5.1.2 PVDF / NaNbO3 Fibre Morphology

Fibres were successfully electrospun from the PVDF / $NaNbO_3$ solutions using a 15cm collector distance, 1 ml/h feed rate and with voltages varying from 8.00 kV – 9.00 kV. These parameters were used as they were shown to produce bead-free fibres in the previous sections. To maintain a consistent Taylor cone across all the solutions and allow the deformation and release of the Taylor Cone. Without altering the applied voltage, the Taylor Cone would not release the jet and so the voltage was adjusted. A minimum voltage was applied for each of the materials and was shown to increase with an increase in the content of the ceramic. A change in the Taylor cone size is known to affect the bending instability and morphology of the fibres and so the voltage was varied to produce a cone similar in size for all the solutions as mentioned in 2.5.3.[218]

SEM images were collected of each composite fibre seen in Figure 5.2a – d. hin fibres were produced with a smooth surface with no appearance of beaded structures on the surface, even with an increase in the content of ceramic. As the ceramic content was increased it was visible to see the ceramic particles protruding from the surface of the polymer fibres. Images using the backscattered electron detector were collected for the 10 wt% $NaNbO_3$ loaded fibres in Figure 5.2f. These images were taken to distinguish where the ceramic filler was distributed across the polymer fibres and if they were agglomerated. The image in Figure 5.2 had shown the distribution of the ceramic particles across the material and showed the protruding ceramic particles on the fibre surface. Figure 5.3 demonstrates the protruding of the ceramic filler from the surface of the polymer. This is seen more frequently at the higher concentration of ceramic as it begins to agglomerate at higher concentrations.

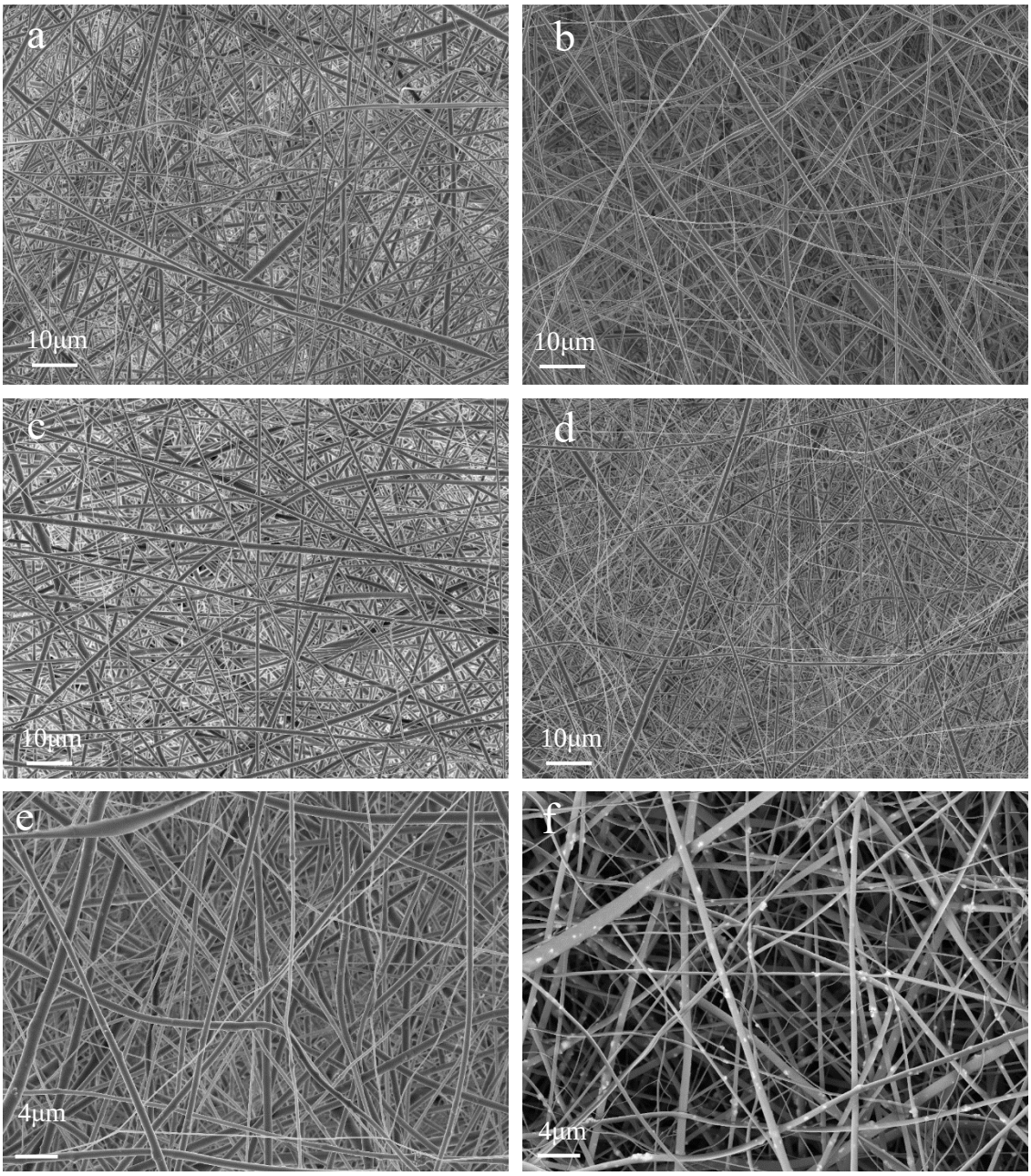

Figure 5.2. SEM images of PVDF / $NaNbO_3$ 1 wt% – 10 wt% displaying surface morphology and $NaNbO_3$ distribution across the fibres. (a) 1 wt% $NaNbO_3$, (b) 3 wt% $NaNbO_3$, (c) 5 wt% $NaNbO_3$, (d) 10 wt% $NaNbO_3$, (e) magnified image of 10 wt% $NaNbO_3$, and (f) BSD elemental imaging of PVDF / $NaNbO_3$ 10wt%

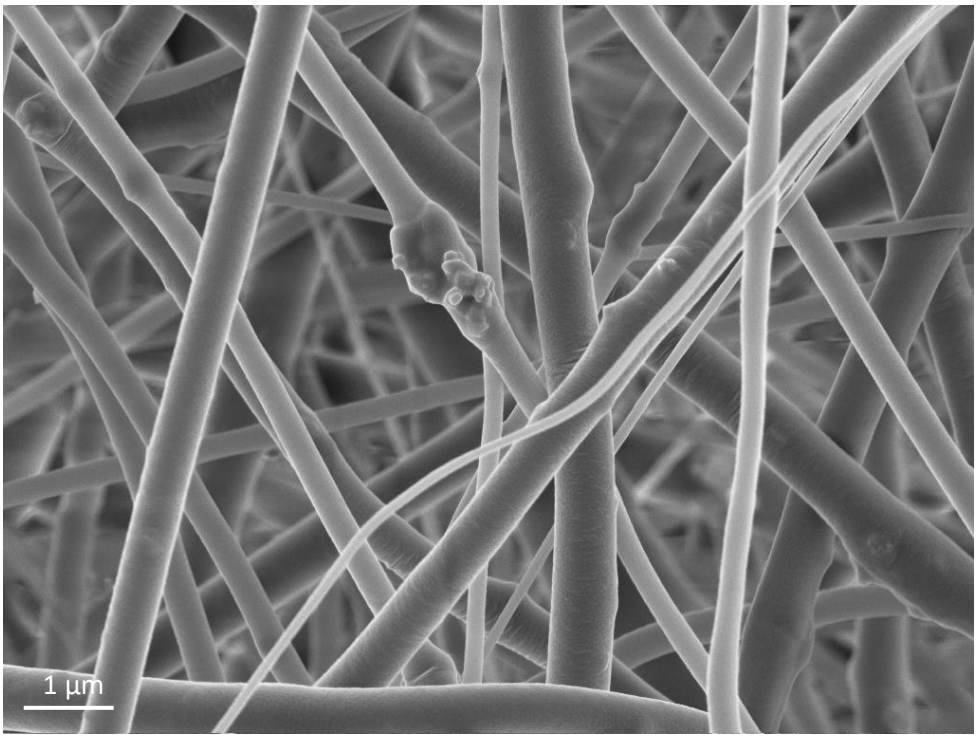

Figure 5.3: SEM image showing the NaNbO3 protruding through the surface of the PVDF fibre.

The average fibre diameters and processing parameters of all the PVDF / $NaNbO_3$ fibres were calculated using ImageJ, a software that allows for an average of several cross sections to be calculated and can be seen in Table 5.1. The pure PVDF fibres had an average fibres diameter of 1342 ± 385 nm with a rough surface morphology as mentioned in 4.1.8. The addition of $NaNbO_3$ led to little decrease in the average fibre diameter where 1 wt% loading $NaNbO_3$ resulted in a slight decrease in the average fibre diameter to 874 ± 253 nm which was in the experimental error of the material. However, further increasing the ceramic content led to further decreases in the average fibre diameter of the material with the highest loading of 10 wt% resulting in an average fibre diameter of 601 ± 183 nm. Overall, the fibres produced within this work were thicker than those produced in previous studies carried out on electrospun PVDF / $NaNbO_3$ fibres where 500nm was observed at a loading of 10 wt%.[305] The high dielectric properties of the ceramic may result in the Taylor cone up take a higher quantity of charge on the surface of the droplet leading to the material experiencing higher bending instability resulting in higher stretching and elongation of the fibres producing thinner fibres.[353] Similar results have also been demonstrated by electrospinning ZnO with PVDF as mentioned in 2.5.8.[292] It may also be due to the piezoelectric component of the ceramic, when shear stress is applied by feeding the material through the spinneret the ceramic may generate its charge increasing charge density further. An increase in charge density then allows for an increase in the stretching of the jet as the charges act to repel each other and stretch the fibre. The increase

in the concentration of ceramic was carried out to determine if the influence of higher quantities of ceramic would increase the effects and produce thinner fibres. This displayed a gradual decrease in the average fibre diameter as seen in Table 5.1 suggesting that increasing the content of ceramic further led to a further increase in charge density at the Taylor cone and assisted in producing thinner fibres.

Table 5.1. The processing parameters and average fibre diameter of the PVDF / $NaNbO_3$ fibres.

$NaNbO_3$ Weight / %	**Applied Voltage / kV**	**Average Fibre diameter / nm**
0	7.14	1342 ± 385
1	8.00	874 ± 253
3	8.50	732 ± 244
5	8.00	782 ± 231
10	9.00	601 ± 183

To assist in determining the control the different contents of ceramic had on the fibre diameter Gaussian curves were plotted as seen in Figure 5.4. The loading of 1 wt% ceramic shows a wide distribution of fibre diameters. Increasing the content of ceramic to 3 wt% led to a shift in the diameters to smaller fibre diameter, with 5 wt% having similar results. The 10 wt% loadings had been shown to decrease the width of the Gaussian curve and push the curve to lower fibre diameters. The progression of the Gaussian distribution from a wide curve to a narrow curve suggests that higher quantities of $NaNbO_3$ influence the spinnability of the fibres producing more homogenous fibre diameters. It also demonstrates that higher quantities of the ceramic give more control over the fibre diameters. This was carried out as it is suggested that polymer mats with thinner fibres are more effective at sound absorption due to the increase in surface area of the fibres allowing for more points of contact as mentioned in 2.2.2. The ability to control the fibre diameter through the addition of the ceramic could later assist in tuning fibre diameters for sound absorption applications through the addition of the ceramics.

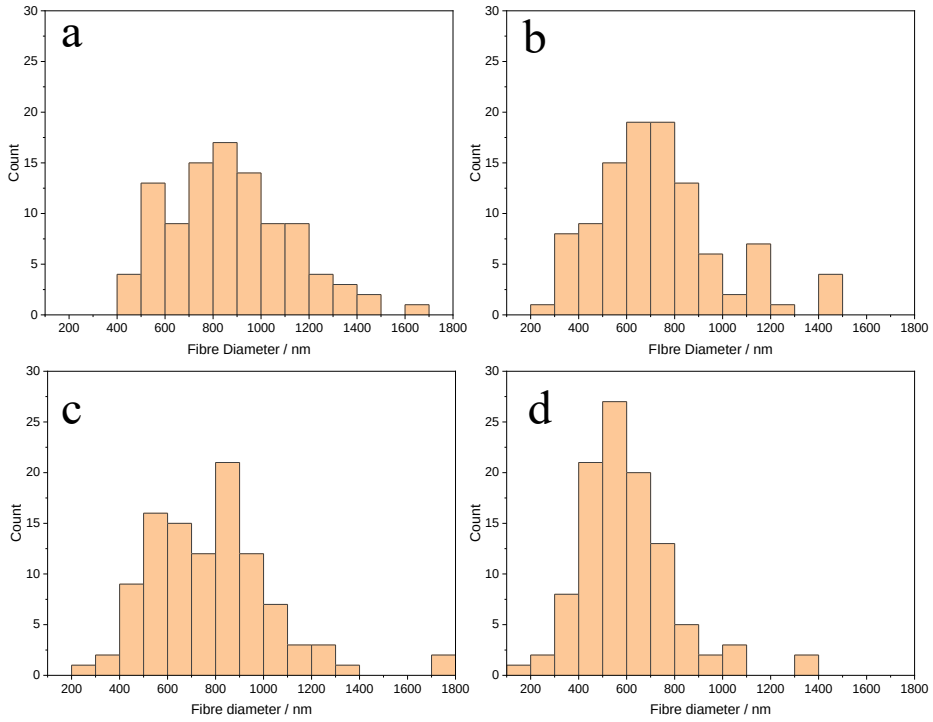

Figure 5.4. The histogram of the PVDF / $NaNbO_3$ fibre diameters displays a shift in the average fibre diameter with an increase in $NaNbO_3$ content. (a) 1 wt% $NaNbO_3$ content, (b) 3 wt% $NaNbO_3$ content (c) 5 wt% $NaNbO_3$ content (d) 10 wt% $NaNbO_3$ content.

The viscosity was then analysed to determine if there was a decrease in this value of the solution which was causing a decrease in the average fibre diameters. However, the viscosity had shown to increase with the initial addition of 1 wt% $NaNbO_3$ resulting in a value of 674 ± 4.72 cSt in comparison to the 359 ± 7.44 cSt of the pure PVDF solutions. The viscosity of the solutions then decreased with the addition of further amounts of $NaNbO_3$ until 10 wt% where an increase in the values was observed, as seen in Table 5.2. Typically it has been demonstrated that the addition of ceramic particles leads to an increase in viscosity and an increase in average fibre diameter.[286] However, here a decrease in fibre diameter is observed with an increase in viscosity with the addition of $NaNbO_3$. As mentioned above the addition of ceramics can influence the charge density of the droplet. In this case, the charge density of the solution may be influencing the fibre diameter to a higher degree than the viscosity to a point where the repulsion of the charges is stronger than the viscoelastic force of the material and pulling the fibres into thinner morphologies.[353]

Table 5.2. $NaNbO_3$ content and the viscosity.

$NaNbO_3$ Weight / %	**Viscosity / cSt**
0	359±7.44
1	674±4.72
3	694±5.73
5	601±15.6
10	734±10.2

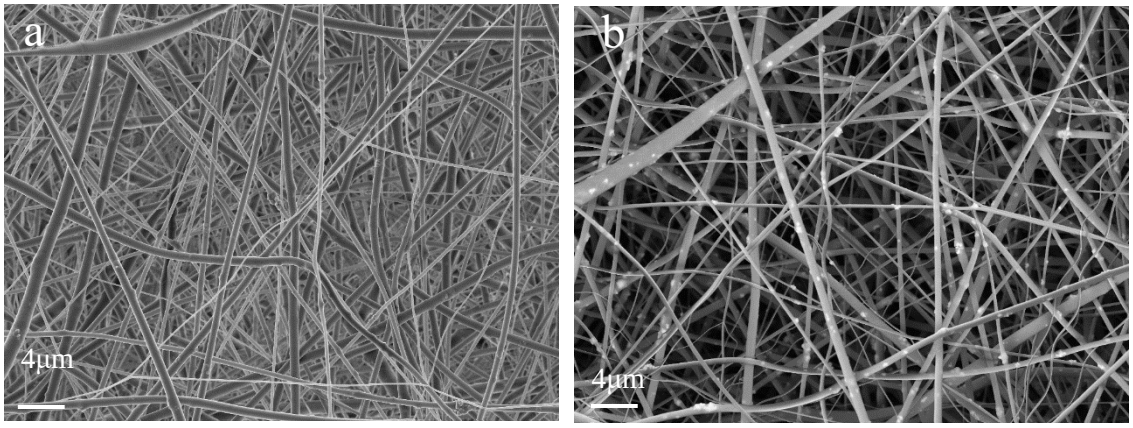

Figure 5.5. (a) SEM image PVDF / $NaNbO_3$ 10wt% showing detail of ceramic particles across the fibres (b) BSD elemental imaging of PVDF / $NaNbO_3$ 10wt%

A magnified image of the PVDF / $NaNbO_3$ fibres can be observed in Figure 5.5a. The fibres produced here have a smooth surface morphology, and areas on the surface where the ceramic particles can be seen protruding through to the surface. To further distinguish between the fibres and the ceramic particles a BSD elemental image was taken as seen in Figure 5.5b. Here it is possible to distinguish the $NaNbO_3$ particles on the surface of the PVDF fibres. The lighter spots represent the ceramic particles and at thinner fibres, it can be seen where the $NaNbO_3$ is protruding through the surface of the material. The protruding of the ceramic particles occurs due to the decrease in average fibre diameter with an increase in the content of ceramic which is seen in Figure 5.3. When loading fibres with larger quantities of ceramic agglomeration of the particles occurs resulting in the protruding effect taking place. The EDS images seen in Figure 5.6 allows for the confirmation of $NaNbO_3$ particles in the PVDF fibres. Figure 29 d – f shows the elements of sodium, niobium, and oxygen respectively, where these particles correlate with each other in all 3 images. This imaging was carried out to accommodate the BSD images in confirming the distribution of the $NaNbO_3$ particles present within the fibre mat and have not denatured during the mixing and electrospinning phases.

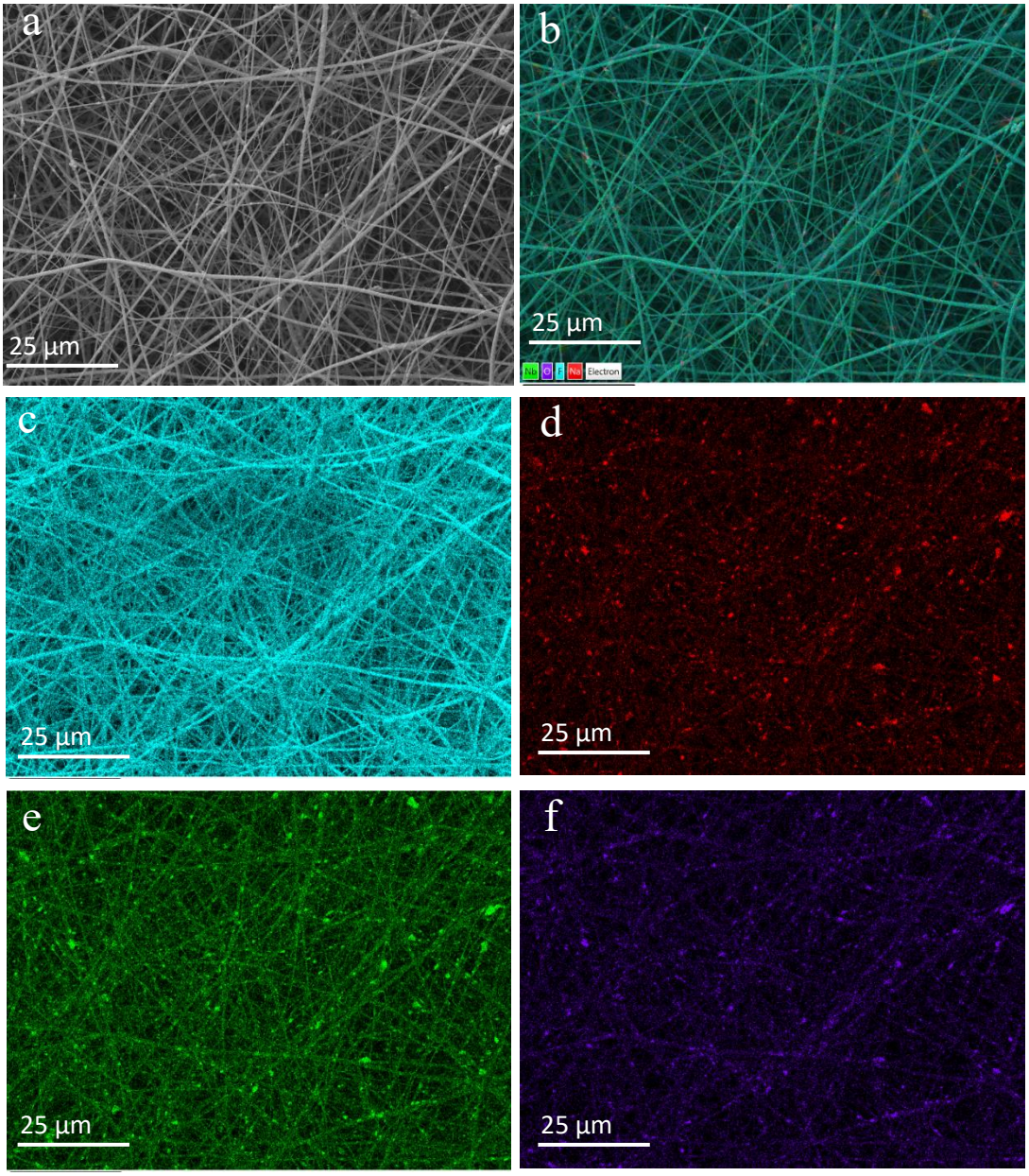

Figure 5.6. EDS of PVDF / $NaNbO_3$ fibre mats with 10 wt% ceramic loadings displaying the distribution of $NaNbO_3$ particles across the fibre mats for the main elements within the material. (a) Original image, (b) Overlapped element image containing Na, O, F and Nb, (c) Fluorine image, (d) Sodium image, (e) Niobium image. (f) Oxygen image.

5.1.3 PVDF / $KNbO_3$ Fibre Morphology

The $KNbO_3$ was added as a ceramic with a larger piezoelectric and dielectric constant of 91.7 $pC.N^{-1}$ and 580 respectively in comparison to 34.5 $pC.N^{-1}$ and 480 for $NaNbO_3$.[115,116,117,118] This was performed to further determine if a ceramic with higher electroactive properties could bring more control to the average fibre diameters. The PVDF / $KNbO_3$ fibres containing 1 wt% – 10

wt% ceramic can be seen in Figure 5.7. The PVDF / $KNbO_3$ fibres had shown a decrease in average fibre diameters with the addition of ceramic. The addition of 1 wt% $KNbO_3$ produced fibres with an average fibre diameter of 435 ± 97 nm. An increase in ceramic content to 3 wt% had little influence on the average fibre diameter producing diameters of 466 ± 144 nm. Increasing the ceramic content to 5 wt% led to a shift in the average fibre diameters to a large average diameter of 592 ± 136 nm. The addition of 10 wt% $KNbO_3$ had shown little influence on the average fibre diameter resulting in a value of 570 ± 139 nm as seen in Table 5.3. Overall, the fibres were similar in diameter with the addition of ceramic. In comparison to the PVDF / $NaNbO_3$ fibre diameter range for PVDF / $KNbO_3$ was much lower between 435 nm – 592 nm and 601 nm – 874 nm respectively. This may occur as the $KNbO_3$ displays a much higher piezoelectric and dielectric constant in comparison to $NaNbO_3$ which would allow for a larger charge density around the Taylor cone. As mentioned previously the increase in charge density allows for the jet to be stretched due to the repulsion of the jets. The higher piezoelectric constant of the $KNbO_3$ also allows for it to generate higher quantities of charge when the same shear stress is applied by the spinneret potentially allowing for it to influence charge density to a higher degree than $NaNbO_3$. In comparison to the literature with PVDF / $NaNbO_3$ fibres, the ones produced here are within a similar fibre diameter range.

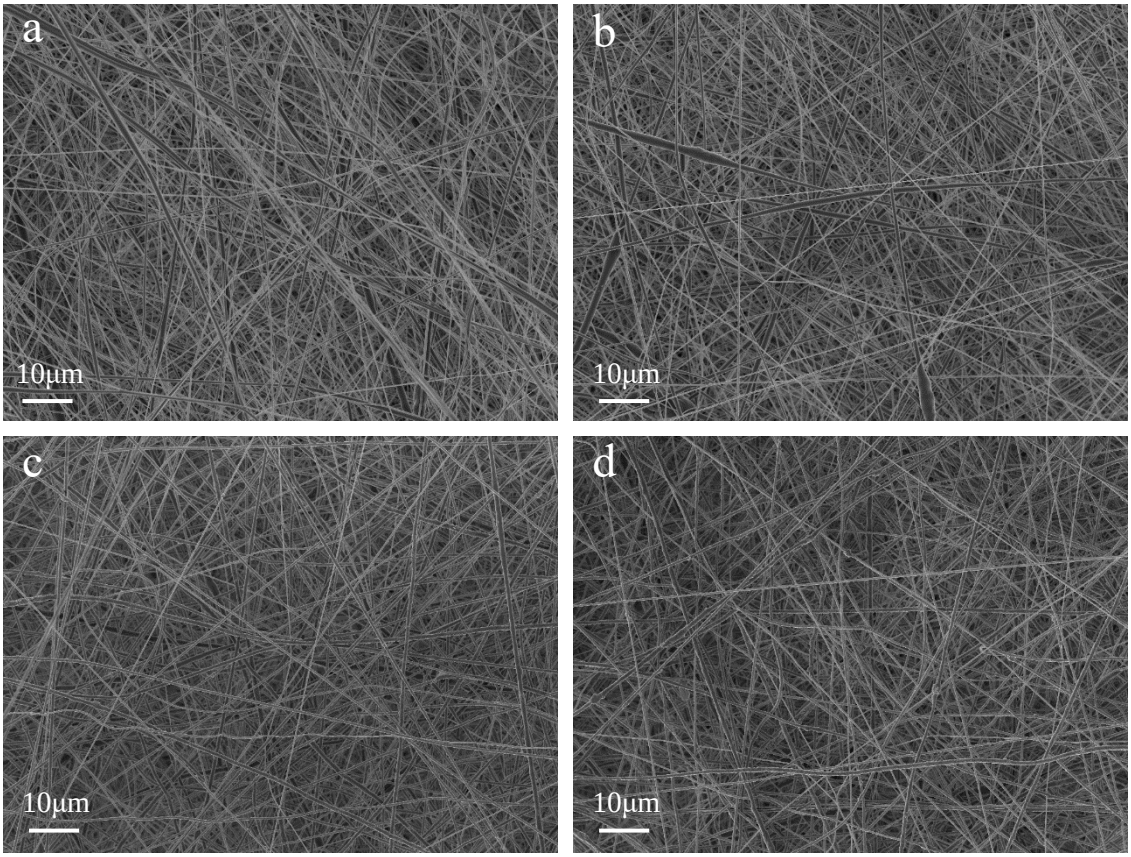

Figure 5.7. SEM images of PVDF / $KNbO_3$ fibres without the formation of beads. (a) PVDF / $KNbO_3$ 1 wt% loading, (b) PVDF / $KNbO_3$ 3 wt% loading, (c) PVDF / $KNbO_3$ 5 wt% loading, (d) PVDF / $KNbO_3$ 10 wt% loading.

Table 5.3. The processing parameters and average fibre diameter of the PVDF / $KNbO_3$ fibres.

$KNbO_3$ Weight / %	**Applied Voltage / kV**	**Average Fibre diameter / nm**
0	7.14	1342 ± 385
1	10.22	435 ± 97
3	9.97	466 ± 144
5	9.20	592 ± 136
10	9.55	570 ± 139

To further investigate the influence of the $KNbO_3$ on the PVDF fibres Gaussian plots were drawn to determine how altering the content of the ceramic pushed the curve seen in Figure 5.8 Unlike the PVDF / $NaNbO_3$ fibres, the PVDF / $KNbO_3$ fibres have a greater degree of control from the initial addition. In contrast, a shift in the Gaussian curve to higher fibre diameters is observed with the addition of higher quantities of $KNbO_3$ and the control over the overall

distribution is maintained. To investigate the reasoning further the viscosity was analysed to determine if there was a gradual increase in the value which may have led to an increase in the fibre diameter.

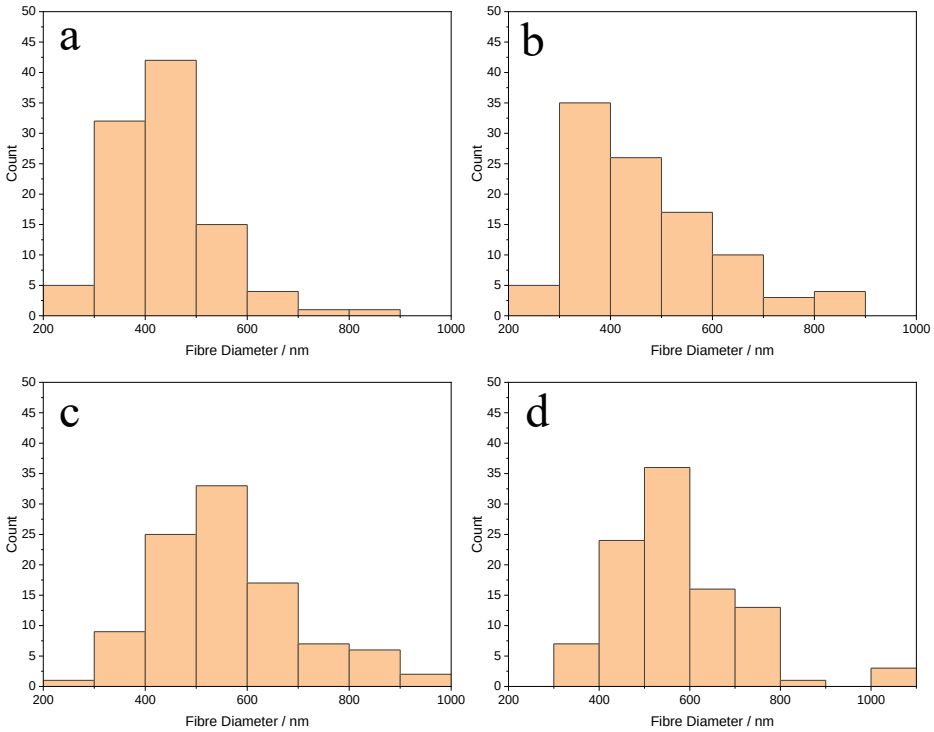

Figure 5.8. The histogram of the PVDF / $KNbO_3$ fibre diameters shows little change to the average fibre distribution. (a) 1 wt% $KNbO_3$ content, (b) 3 wt% $KNbO_3$ content (c) 5 wt% $KNbO_3$ content (d) 10 wt% $KNbO_3$ content.

The viscosity of the PVDF solution increased with the addition of $KNbO_3$ to 421 ± 3.68 cSt increasing from 359 ± 7.44 cSt for the pure PVDF. In comparison to the PVDF / $NaNbO_3$ solution viscosity, the PVDF / $KNbO_3$ demonstrates much smaller values. This could be the difference between why both fibres have differing fibre diameters. As mentioned in 2.5.4.1 the solution viscosity has a large influence on the fibre diameter of electrospun materials.[225] Here the decrease in viscosity coupled with the addition of $KNbO_3$, influencing the charge density of the Taylor cone, may result in the thinner average fibre diameters compared to that of PVDF / $NaNbO_3$. Alongside this, the shift to a higher average fibre diameter when increasing the content of $KNbO_3$ may be due to an increase in the viscosity of the material with an increase in the content of the ceramic.

Table 5.4. $KNbO_3$ content and viscosity.

$KNbO_3$ Weight / %	**Viscosity / cSt**
0	359 ± 7.44
1	421 ± 3.68
3	474 ± 4.04
5	508 ± 4.77
10	483 ± 4.23

The surface morphology of the PVDF / $KNbO_3$ fibres is displayed in Figure 5.9a. The fibres produced have a rough surface morphology contrasting to the PVDF / $NaNbO_3$ fibres which demonstrated smooth surface morphologies. The differences between the fibres may be due to changes in the humidity when the materials were electrospun. These materials were electrospun during different months of the year when changes in temperature and humidity may have occurred. As mentioned in 2.5.4.3 when the solvents evaporate during spinning the surface of the material becomes cooler which may cause the condensation of water on the surface of the material producing ridges and pores, altering the surface morphology to increase the roughness.[236,237] This may have occurred during the spinning of the PVDF / $KNbO_3$ fibres which led to the differences in surface morphology between other fibres. To establish the presence of the ceramic particles within the material BSD was carried out to distinguish between the PVDF fibres and the $KNbO_3$ ceramic particles embedded within them seen in Figure 5.9b. It can be observed the ceramic particles are protruding through to the surface of the PVDF fibres like the PVDF / $NaNbO_3$ fibres.

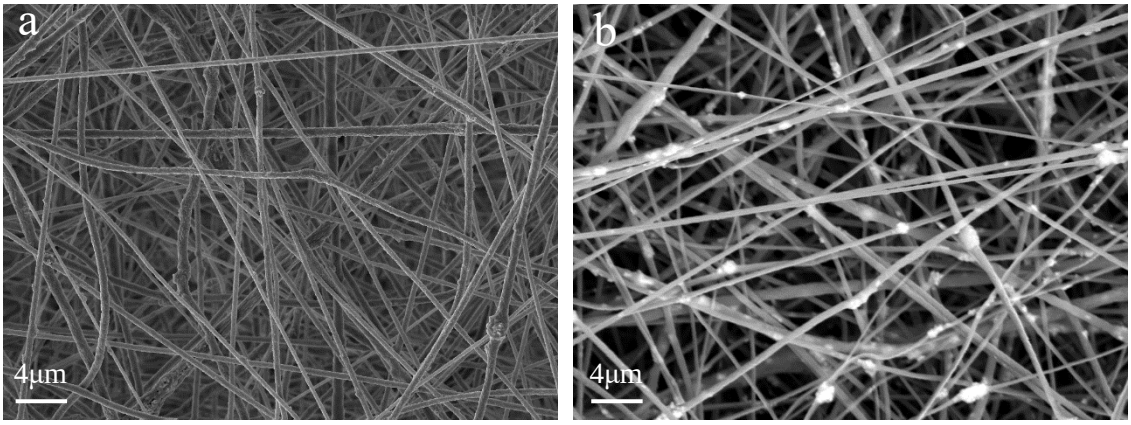

Figure 5.9. (a) Magnified image of PVDF / $KNbO_3$ 10 wt% loading, (b) BSD image of PVDF / $KNbO_3$ 10 wt% loading showing the particles embedded in the fibres.

5.1.4 PVDF / $CeNbO_4$ Fibre Morphology

Like the previous PVDF / niobium oxides fibres, PVDF / $CeNbO_4$ fibres were successfully electrospun demonstrating a smooth fibres morphology visible in Figure 5.10. The fibre surface morphology was like that of the PVDF / $NaNbO_3$ fibres as they were both electrospun a week apart from each other with little changes to humidity and temperature. However, at the higher loading of 5 wt % and 10 wt%, the formation of beaded fibres was demonstrated which did not occur with any of the other PVDF / niobium oxide ceramics at all the weight percentages. This may have occurred due to agglomeration of the larger $CeNbO_4$ particles which were emphasised by the larger particle sizes in comparison to the other niobium oxides.

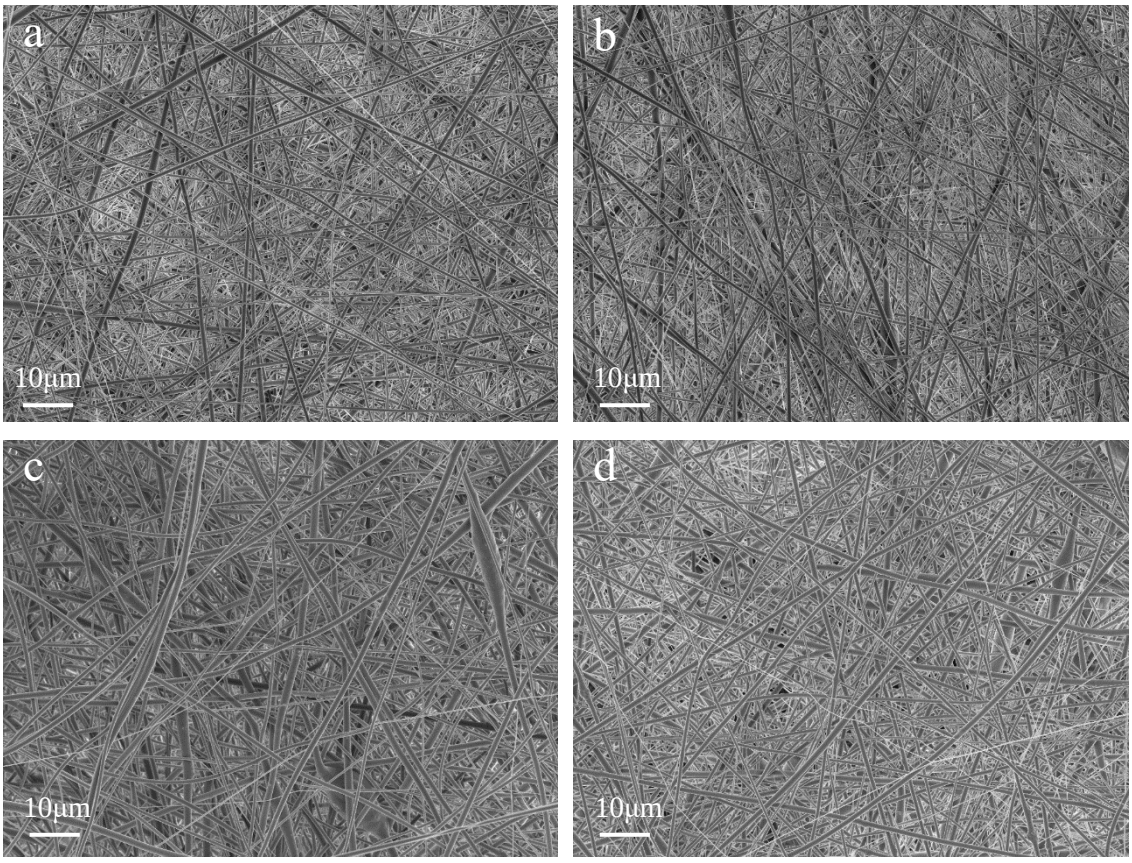

Figure 5.10. SEM images of PVDF / $CeNbO_4$ fibres showing the fibre morphology. (a) PVDF / $CeNbO_4$ 1 wt% loading, (b) PVDF / $CeNbO_4$ 3 wt% loading, (c) PVDF / $CeNbO_4$ 5 wt% loading, (d) PVDF / $CeNbO_4$ 10 wt% loading.

To further analyse the reasoning behind the formation of the beaded fibres EDS imaging was carried out on the 10 wt% $CeNbO_4$ as seen in Figure 5.11a and a magnified image seen in Figure 5.11b. The images assist in determining if the beaded fibres are 100% polymer beads or the formation of ceramic agglomerates covered with polymers. The lighter spots on the material can be distinguished as the ceramic particles with a high count of these materials on the surface.

This points towards to suggestion that the beaded structures at the higher loadings are agglomerates of the ceramic covered with polymer rather than 100% polymer beads.

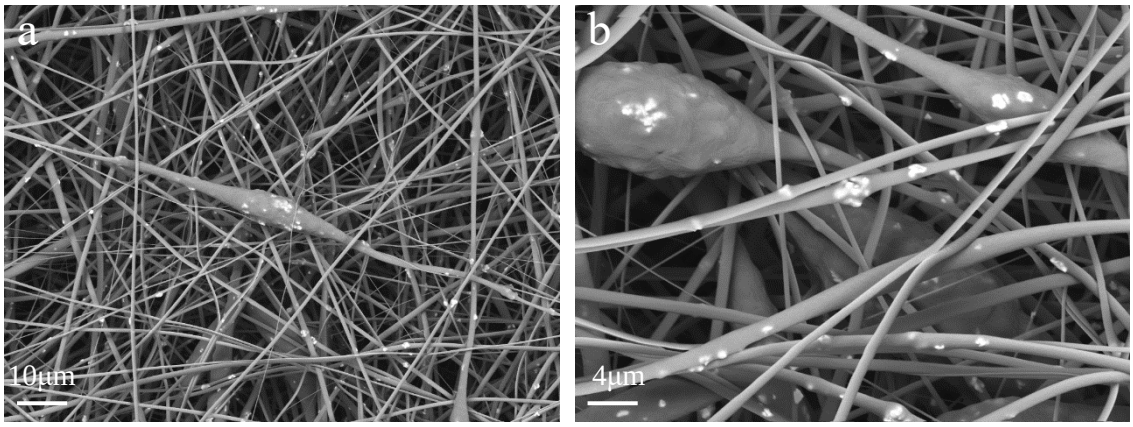

Figure 5.11. (a) BSD image of PVDF / $CeNbO_4$ fibres, (b) 2500x Mag of BSD image of PVDF / $CeNbO_4$ fibres. Displaying the agglomeration of ceramic particles within the beaded structure.

Table 5.5. The processing parameters and average fibre diameter of the PVDF / $CeNbO_4$ fibres.

$CeNbO_4$ Weight / %	**Applied Voltage / kV**	**Average Fibre diameter / nm**
0	7.14	1342 ± 385
1	8.40	617 ± 152
3	8.74	687 ± 218
5	7.28	1023 ± 270
10	7.00	891 ± 219

The average fibre diameters of the pure PVDF fibres displayed an average fibre diameter of 1342 ± 385 nm. The addition of the 1 wt% $CeNbO_4$ resulted in a decrease in the average fibre diameter of 617 ± 152 nm like that demonstrated by the previous PVDF / niobium oxide fibres. Like the addition of $KNbO_3$, increasing the $CeNbO_4$ content in the fibres to 3 wt% resulted in little change to the average fibre diameters with a value of 687 ± 218 nm. Increasing the $CeNbO_4$ content led to average fibre diameters of 1023 ± 270 nm and 891 ± 219 nm for the 5 wt% and 10 wt% ceramic loadings as seen in Table 5.5. The histograms seen in Figure 5.12 demonstrates the influence the $CeNbO_4$ has on the fibre diameters of PVDF. Lower amounts of $CeNbO_4$, 1 wt% and 3 wt% allow for more control over the fibre diameters producing a narrower Gaussian distribution. The increase in the $CeNbO_4$ also shows a gradual shift of the

diameters to larger fibres. At the 5 wt% loadings and above a widening of the distribution occurs suggesting that there is less control over the fibre diameter with higher $CeNbO_4$ content.

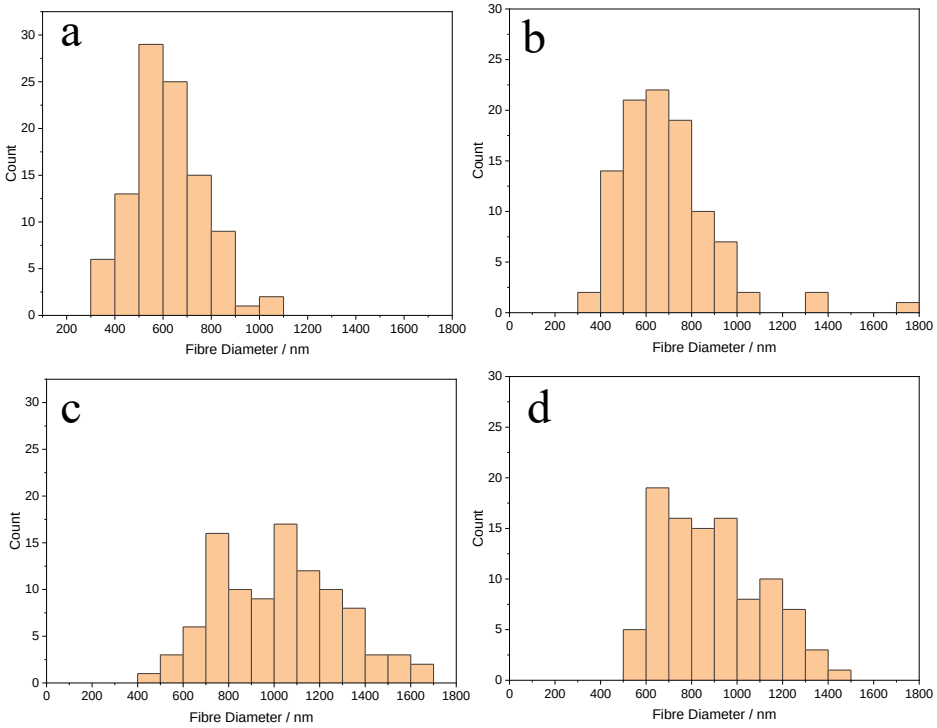

Figure 5.12. The histogram of the PVDF / $CeNbO_4$ fibre diameters shows a shift in average fibre distribution with the addition of ceramic. (a) 1 wt% $CeNbO_4$ content, (b) 3 wt% $CeNbO_4$ content (c) 5 wt% $CeNbO_4$ content (d) 10 wt% $CeNbO_4$ content.

Table 5.6. $CeNbO_4$ weight percent and viscosity of the solution.

$CeNbO_4$ Weight / %	**Viscosity / cSt**
0	359 ± 7.44
1	704 ± 5.34
3	735 ± 2.76
5	860 ± 3.44
10	745 ±11.0

To further investigate the changes in fibre diameter with a change in the content of the ceramic the solution viscosity was analysed as seen in Table 5.6. In comparison to the other PVDF / niobium oxide solutions, the PVDF / $CeNbO_4$ solution has an average viscosity value within a higher range between 700 – 860 cSt. As mentioned in 2.5.4.1 the viscosity heavily influences the fibre diameter and can be suggested here where these PVDF / $CeNbO_4$ display a

higher average fibre diameter ranging between 617 nm – 1023 nm. The viscosity at the higher loading of 5 wt% demonstrates this as the average fibre diameter increases drastically with the increase in viscosity. However, there is still the formation of beaded fibres across the structure even with an increase in viscosity. Previously TiO_2 has been added to PEO, where similar results were demonstrated, and the beaded structures were produced even with an increase in viscosity.[250] It was also suggested that the beaded structures were agglomerates of the ceramic, which also correlates with the BSD images demonstrated within this work. To demonstrate the distribution of the $CeNbO_4$ particles across the fibrous mat EDS imaging was carried out as seen in Figure 5.13. It can be shown that the cerium, niobium, and oxygen atoms in Figure 5.13d, e, and f respectively all correlate together suggesting that the ceramic particles are all intact and distributed across the fibrous mat.

It should also be mentioned that the piezoelectric properties of $CeNbO_4$ are not well studied within the literature, and the dielectric property of the material is not well documented with very few studies providing a real understanding of these properties of the ceramic. However, the $CeNbO_4$ has been shown to influence the average fibre diameter with its initial addition, which suggests that the ceramic has some form of influence on the conductivity of the solution as the viscosity increases and the average fibre diameter decreases at the addition of 1 wt% like the other niobium oxides.

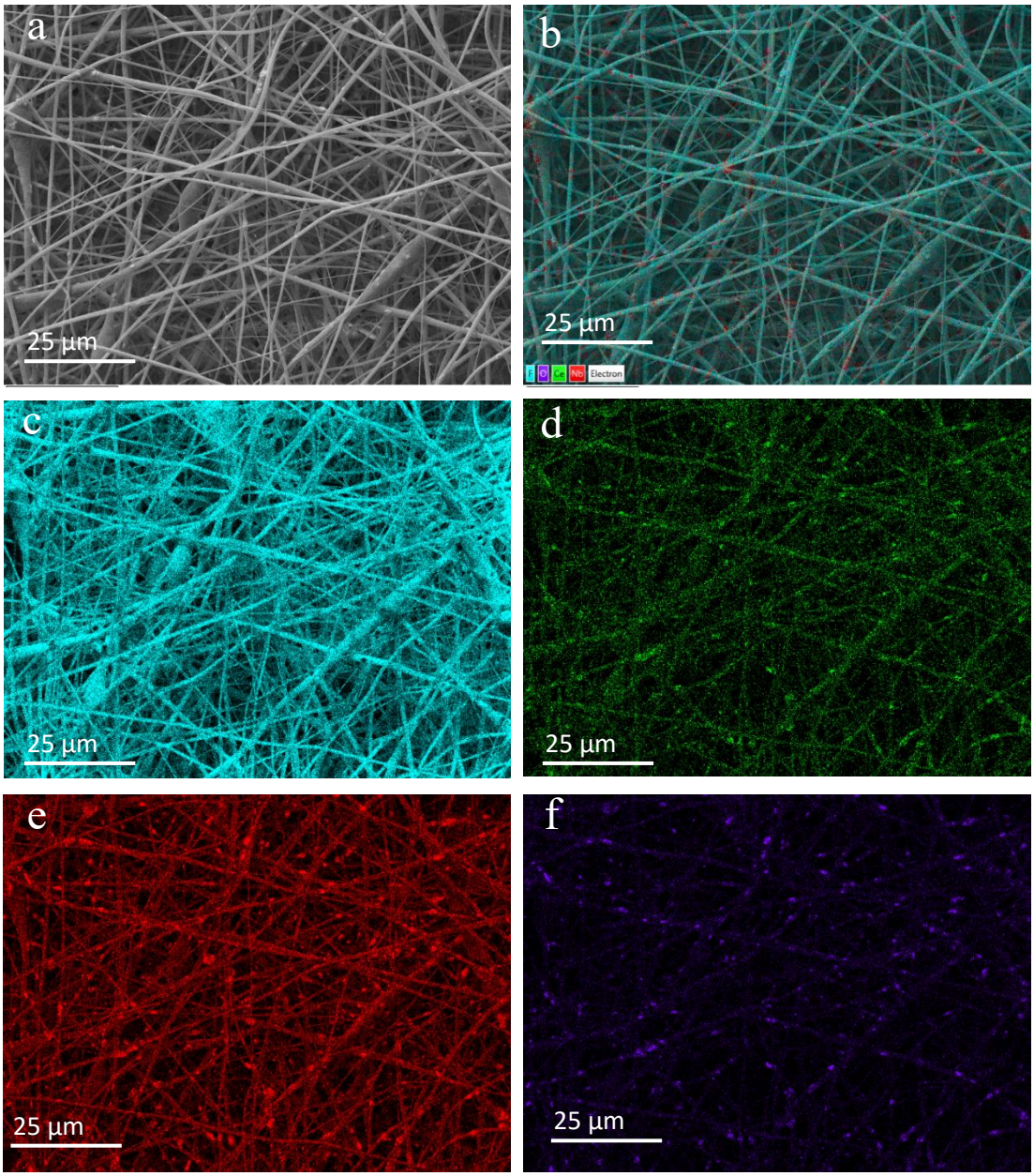

Figure 5.13. EDS of PVDF / $CeNbO_4$ fibre mats with 10 wt% ceramic loadings showing the distribution of $CeNBO_4$ across the fibres. (a) Original image, (b) Overlapped element image containing Ce, O, F and Nb, (c) Fluorine image, (d) Cerium image, (e) Niobium image. (f) oxygen image.

5.1.5 Summary

The addition of $NaNbO_3$, $KNbO_3$, and $CeNbO_4$, had all been shown to produce fibres with varied average fibre diameters. Each ceramic type had been shown to influence the average fibre diameter to a different degree in order of the $KNbO_3$ > $NaNbO_3$ > $CeNbO_4$. At the loading of 5 wt% the ceramic average fibre diameters of 592 ± 136 nm, 782 ± 231 nm, and 1023 ± 270

nm for the $KNbO_3$, $NaNbO_3$, $CeNbO_4$ fibres respectively which were all smaller than that of the pure PVDF with an average fibre diameter of 1342 ± 385 nm. This suggests that the $KNbO_3$ fibres had the largest influence on the fibre diameter, and it was demonstrated that more control over the fibre diameters was observed with the $KNbO_3$ through the histograms generated. The average fibre diameters produced here are in line with the literature for the PVDF / $NaNbO_3$ fibres produced at 500nm. However, other PVDF fibres with niobium oxide fibres demonstrated much small fibre diameters between 100 – 300 nm. [306,307,308,309] The filler particle sizes are similar to that of the PVDF fibre diameter. It could be said that there may be a factor where the filler navigates a level of control to a minimum fibre diameter that is achieved. Upon searching the literature there seems to be little evidence for the rheological influence of particle size on the minimum fibre diameter of composites.

The $NaNbO_3$ and the $KNbO_3$ particles were well dispersed across the PVDF fibres with all the ceramic loadings between 1 wt% – 5 wt%. It was also demonstrated that at the higher loadings of 10 wt% the protruding of the ceramic particles began due to agglomeration of the particles. However, the $CeNbO_4$ fibres demonstrated the formation of beads at the higher loading of 10 wt%, which was uncovered to be the agglomeration of the particles. This was suggested to occur due to the large agglomerate sizes of the $CeNbO_4$ which resulted in the formation of beaded structures where the agglomerates were covered in the polymer. The agglomeration of ceramic particles has been demonstrated previously with the use of $BaTiO_3$ to be added to PVA.[354] The agglomeration and protrusion of filler have also been demonstrated to occur with other fillers such as carbon nanocapsules.[354] It has also been seen in PVDF / $BaTiO_3$ electrospun fibres, where the ceramic resulted in the formation of a beaded structure where the ceramic was agglomerated and areas of ceramic protrusion.[355] Overall, all the studies had shown that the particles were engulfed by the polymer filler similar to this work.

Surface morphology between the three was demonstrated to be different where the PVDF / $NaNbO_3$ and the PVDF / $CeNbO_4$ produced fibres with smooth surfaces. While in contrast the PVDF / $KNbO_3$ produced fibres with rough surface areas. This was suggested to occur due to differences in the humidity and temperature in the electrospun fibres. Where a higher humidity allows for the condensation of water on the surface of the material which can produce pores or groves on the surface during the spinning process.[227]

Overall, the new work within this section demonstrates that the addition of $NaNbO_3$, $KNbO_3$, and $CeNbO_4$ will all initially influence the average fibre diameters of the PVDF with the initial addition of the respective filler. The addition of further quantities of the filler has little influence on the fibre diameter, however, influences the morphology of the fibres. The successful addition of these fillers has been carried out with this being the first report of $KNbO_3$ and $CeNbO_4$ being added to PVDF to the best of my knowledge.

5.2 The Crystallinity of the PVDF / Niobium Oxide Ceramic Fibres

The crystallinity of the PVDF with the addition of ceramic was analysed to determine the influence of different ceramic types on the nucleation of the β polymorph. The different ceramics have been shown to influence the fibre diameter differently with a range of fibre diameters being produced for each ceramic type. It is well known that the conversion of the α polymorph to the β polymorph can be carried out through the stretching and elongation of the polymer to align the polymer chains in the all-trans configuration. Here it was analysed to determine if the addition of the niobium oxide ceramic and increasing the content resulted in changes to the crystal phases within the polymer. The analysis through FTIR was carried out here to gain a quantitative value on the β polymorph within the material, while the DSC was carried out to assist in solidifying the FTIR results in determining if the nucleation of the β polymorph occurred. Overall, the nucleation of the β polymorph within PVDF would assist in enhancing the electroactive properties of the material and potentially assist in increasing the sound-damping properties of the material at the low-frequency range as mentioned in 2.2.2.[94,106,107]

5.2.1 FTIR Analysis of PVDF / $NaNbO_3$ Fibres

The PVDF / $NaNbO_3$ fibres for all the ceramic loadings display both the absorbance peaks for the α and β polymorphs as seen in Figure 5.14 which is showing the increase in the intensity peak associated with the β polymorph and a slight decrease in the intensity peak associated with the α polymorph with an increase in ceramic content. The absorbance peak at 763 cm^{-1} representing the α polymorph is prominent in the 1 wt% $NaNbO_3$ loading. However, the peak begins to decrease with the addition of 3 wt%, 5 wt%, and 10 wt% $NaNbO_3$. The intensity peak at 840 cm^{-1} and 1275 cm^{-1} representing the β polymorph remain constant for the 3 wt% and 5 wt% $NaNbO_3$ loaded fibres. At the maximum loading of 10 wt%, the absorption peak representing the β phase peak begins to decrease again. This suggests that the nucleation of the β polymorph is assisted by the addition of the ceramic particles. Similar results have been demonstrated with the addition of $BaTiO_3$ where a decrease in the intensity of the peak at 761 cm^{-1} representing the α polymorph decreased, and the peak at 840 cm^{-1} was seen to increase in intensity.[355]

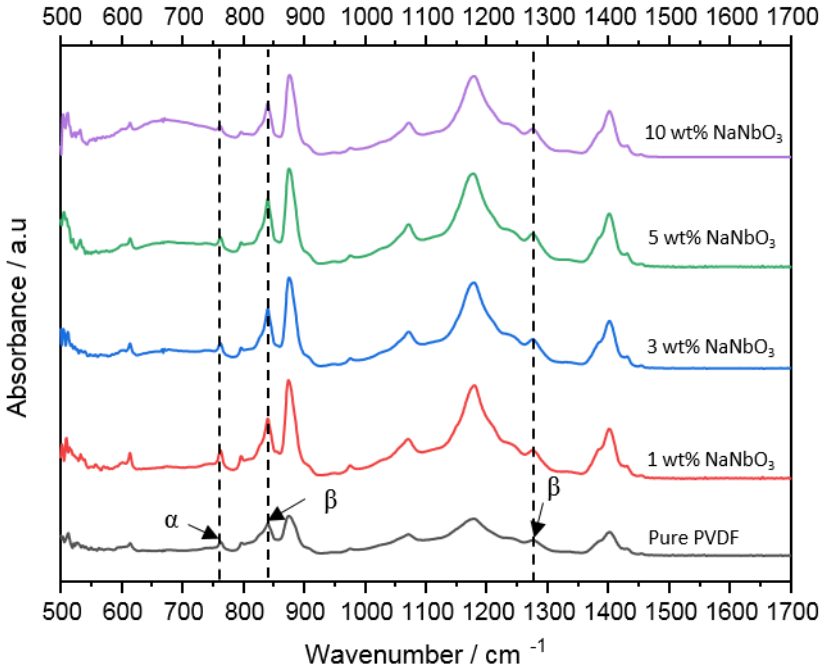

Figure 5.14. FTIR of the PVDF / $NaNbO_3$ fibres 1 wt% – 10 wt%. Displaying the decrease in α peak and increase in β peak intensities with an increase in ceramic.

To analyse the β polymorph the Beer-Lambert law seen in 3.3.5 was applied to determine the content of the electroactive phase in the fibres. The Beer-Lambert law takes into consideration the intensity peaks of the α polymorph and β polymorph to provide a ratio of the two. Figure 5.15 demonstrates the increase in the content of the β polymorph with the addition of the ceramic filler. Pure PVDF fibres have been shown to display a β phase content of 56 % as seen in Figure 5.15. The addition of 1 wt % $NaNbO_3$ led to an increase in the percentage β phase to 64 %. Increasing the ceramic content to 3 wt% and 5 wt% led to an increase in the percentage β phase to 68 % and 67 % respectively. The maximum loading of 10 wt% $NaNbO_3$ led to a decrease in the β phase resulting in a value of 60 %. The addition of small quantities of $NaNbO_3$ may lead to an increase in the dielectric properties of the solution system mentioned earlier. This results in an increase in the bending instability of the jet during spinning allowing for the elongation and stretching of the fibres with fibres decreasing from 874 nm – 601 nm from 1 wt% – 10 wt% content of $NaNbO_3$. Overall, the values demonstrated here are lower than was seen within the literature. PVDF / KNN / ZnO fibres displayed an electroactive phase of 94 %.[309] This is higher than the values in this work which suggests the piezoelectric properties of the fibre produced here may be lower than in previous studies.

During electrospinning, the application of the voltage causes the formation of an electrostatic field as mentioned previously. Polarisation of the dielectric filler occurs which

results in the formation of a small electrostatic field around the filler. The polarised filler in contact with the nearby PVDF would cause the chains to wrap around themselves within the all-trans TTTT configuration. The next layer would wrap around the first layer in the TTTT configuration resulting in the nucleation of the β polymorph.[286] This may be the governing component that is influencing the nucleation of the β polymorph. It could also be said that the dipoles can also be generated through the shear stress applied to the solution causing deformation of the filler resulting in the piezoelectric effect taking place using a similar mechanism as the dielectric phenomena mentioned above as demonstrated with PVDF / $BaTiO_3$ electrospun fibres.[355] Analysis through the DSC may provide a clearer understanding of is this is the case.

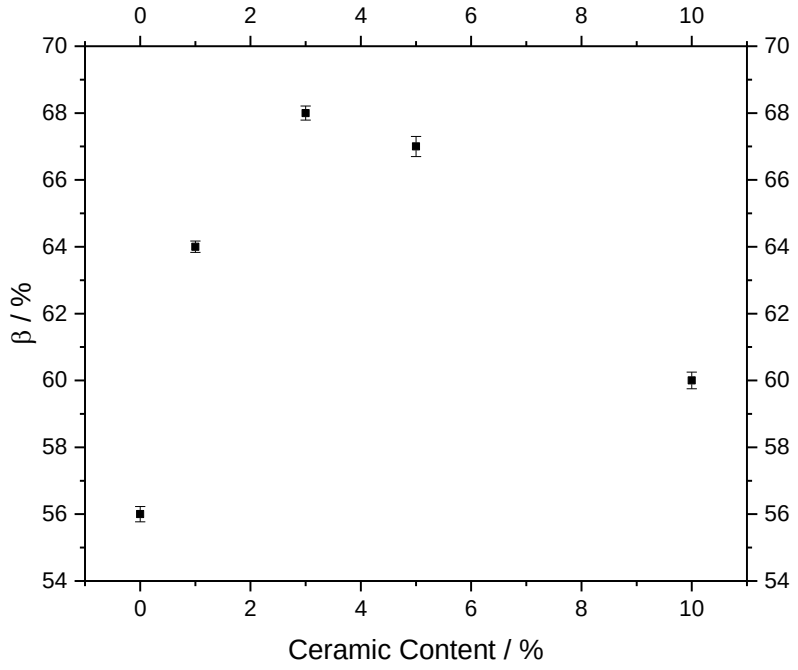

Figure 5.15.The increase in β phase content with the addition of $NaNbO_3$ to the PVDF fibres.

Figure 5.16 demonstrates overall that the fibre diameters are all within experimental error and that a correlation between the average fibre diameter and the percentage of the β phase cannot be made. This suggests that the influence of the ceramic filler is influencing the increase in the nucleation of the β polymorph rather than alignment through the stretching and elongation of the material.

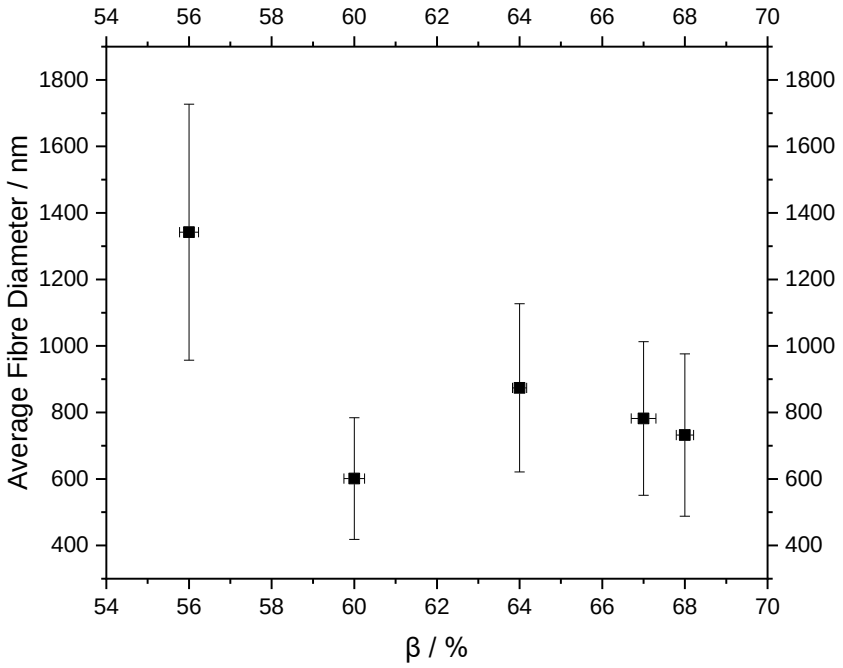

Figure 5.16. The average fibre diameter vs β phase percentage for the PVDF / $NaNbO_3$ fibres. Showing an increase in fibre diameter with a decrease in β content.

5.2.2 DSC Analysis of the PVDF / $NaNbO_3$ Fibres

The melt temperatures of the polymer composites were investigated to accommodate and confirm the nucleation of the β polymorph that was observed in the FTIR data. Figure 5.17 demonstrates the change in the melt temperature and peak broadening with the addition of the $NaNbO_3$ filler. The T_m of the pure PVDF fibres was analysed to be 167 °C. The addition of 1 wt% $NaNbO_3$ led to a decrease in the T_m of the fibres to 166 °C, further increasing the ceramic content in the fibres leading to a lower T_m of 164 °C for the 3 wt% and 5 wt% loaded fibres respectfully. The addition of 10 wt% $NaNbO_3$ led to an increase in the T_m to 165 °C as seen in Figure 5.17 and Table 5.7. The decrease in T_m to between 165 °C – 166 °C alongside the broadening of the melting peak is associated with nucleation of the β polymorph.[344] This is because the two polymorphs are known to have differing melt temperatures and overlap on the DSC. It should also be mentioned that overall it is expected for the T_m to decrease with the adding ceramic filler as impurities within the material would occur lowering the melt temperature.[356]

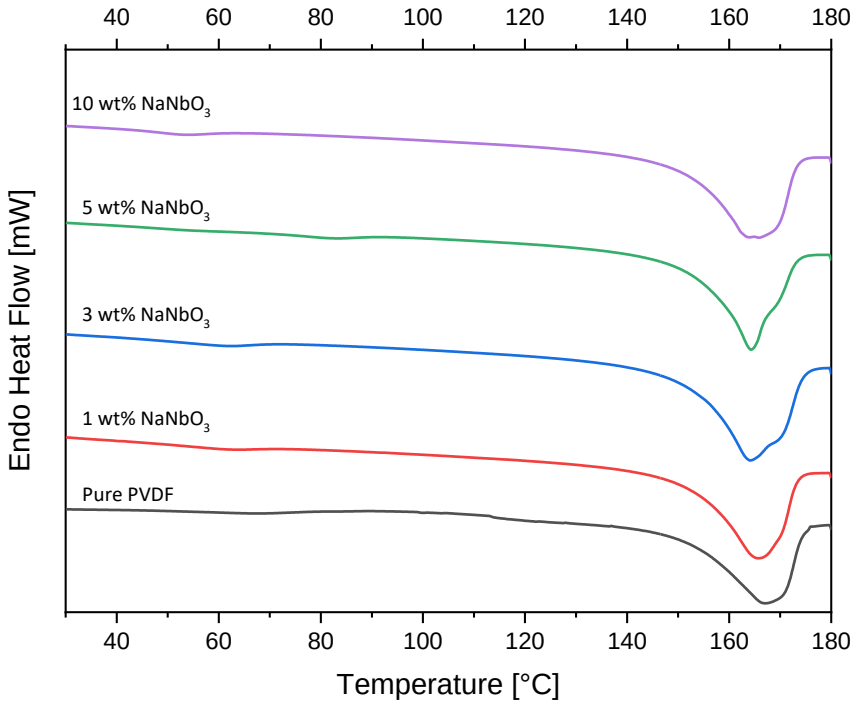

Figure 5.17. Endothermal heat flow for the PVDF / $NaNbO_3$ fibres with a shift to lower melt temperatures with the addition of ceramic.

The T_c of the pure PVDF was analysed to be 141 °C. The addition of $NaNbO_3$ led to a shift in the recrystallisation peaks to lower temperatures as seen in Figure 5.18. The T_c decreased to between 137 °C – 139 °C as seen in Table 5.7 with the lowest temperature being displayed by the highest loading of 10 wt% $NaNbO_3$. The decrease in T_c and T_m of the material is known to be associated with the homogenous distribution of the particles across the composite fibres.[291] This suggests that there are interactions between the PVDF and ceramic articles altering the melt and recrystallisation temperatures of the composite fibres. These interactions could be associated with the polarisation of the filler material which causes the PVDF fibres to wrap around the filler as mentioned in 5.2.1.[286,355] Although the filler may assist in the nucleation of the β polymorph it may also retard the relaxation of the β polymorph due to the interactions between the ion-dipole interactions generated by the ceramic.[300]

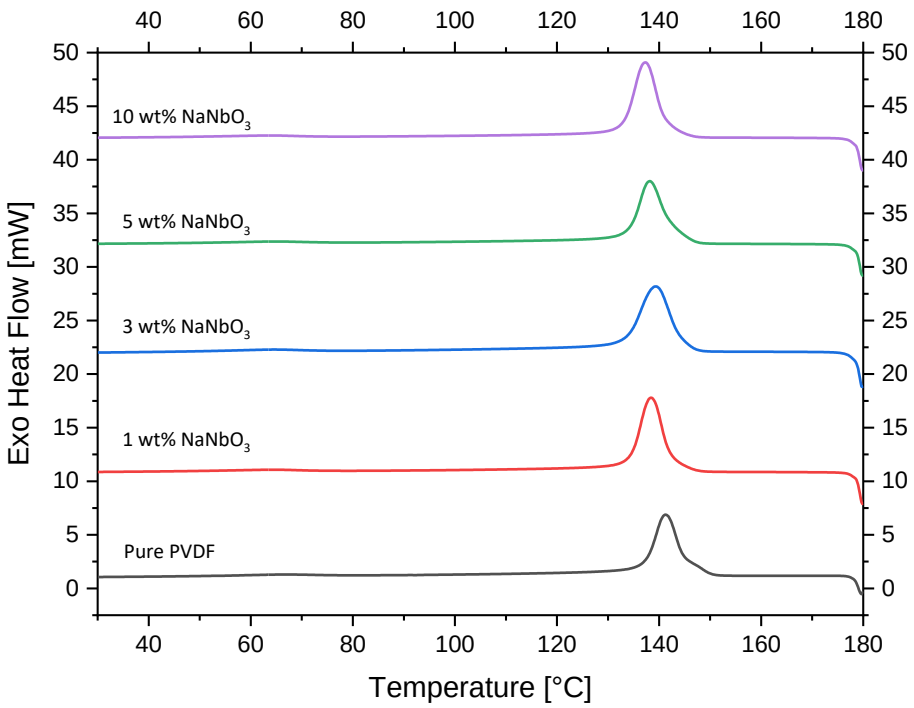

Figure 5.18. Exothermal heat flow for the PVDF / $NaNbO_3$ fibres with a shift to lower recrystallisation temperatures with the addition of ceramic.

shows the decrease in crystallinity of the PVDF composite with the addition of the ceramic filler. The X_c of the pure PVDF was analysed to be 53.0 %. The addition of 1 wt% $NaNbO_3$ led to a decrease in the X_c to 45.9 %. The addition of 3 wt% had little influence on the crystallinity producing an X_c of 45.6 %. The addition of 5 wt% $NaNbO_3$ led to an increase in crystallinity to 46.7 %. The addition of 10 wt% $NaNbO_3$ led to a decrease in the X_c to 44.8 % for the fibres. Generally, an increase in the crystallinity is observed with the addition of ceramic filler as it acts as a nucleator for the nucleation of the β polymorph.[355,357] In comparison to the pure PVDF, the decrease in crystallinity can be associated with the ceramic causing defects to the polymer and restricting the movement of the chains during the recrystallisation phase which reduces the ability of the polymer to recrystallise.[358] This is magnified with the addition of much higher quantities of $NaNbO_3$ addition of 10 wt% leading to a lower crystallinity value potentially due to a higher quantity of ceramic phase within the polymer resulting in more difficulty for chain mobility. It could also be mentioned here that the decrease in crystallinity with an overall addition of the ceramic could be due to the increases in the charge distribution which could accelerate the jet to the collector at a quicker velocity reducing the time available to the recrystallisation which causes a lower content of the percentage crystallinity.

Table 5.7 The DSC data for the PVDF / NaNbO3 fibres.

$NaNbO_3$ wt%	T_m/ °C	T_c / °C	ΔH_f	X_c / %
0	167	141	55.5	53.0
1	166	138	48.1	45.9
3	164	139	47.7	45.6
5	164	138	48.9	46.7
10	165	137	46.9	44.8

Figure 5.19 demonstrates if there are any trends between the average fibre diameter and the crystallinity of the material. It is difficult to make any trends with this graph as the average fibre diameters of the materials are all within the same experimental error range. This occurs with the other PVDF fibres produced with the addition of the niobium oxides where the average fibre diameters are all within the experimental error suggesting there is no trend between these parameters.

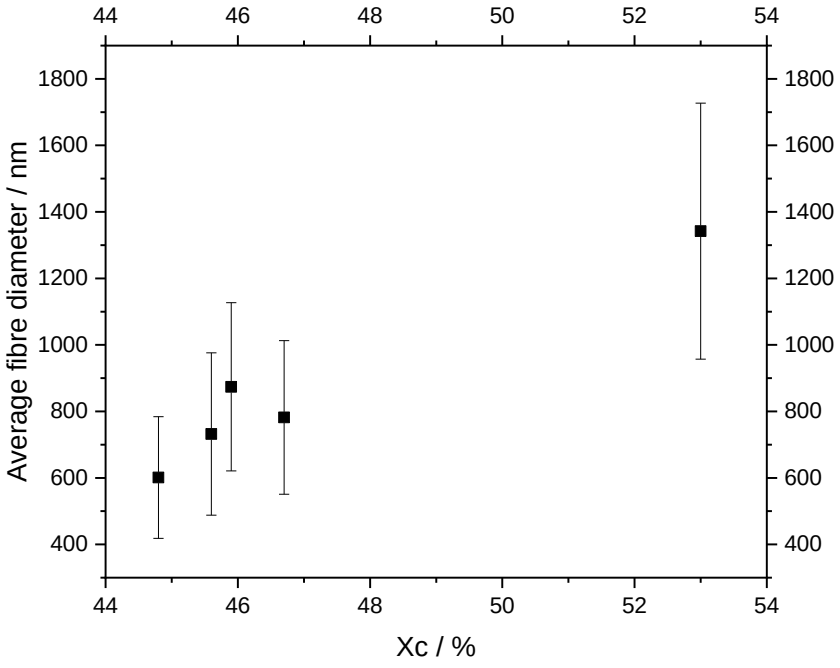

Figure 5.19: The trend between an increase in fibre diameter and an increase in crystallinity.

5.2.3 FTIR of PVDF / $KNbO_3$ Fibres

The FTIR analysis of the PVDF / $KNbO_3$ fibres was carried out to determine if the different electrical properties of the $KNbO_3$ would assist in influencing the nucleation of the β polymorph

to a higher value in comparison to the $NaNbO_3$. Figure 5.20 is showing the decrease in the intensity of the absorbance peaks associated with the α polymorph. The 1 wt% and 3 wt% ceramic loadings have shown the appearance of both the α and β absorbance peaks at 763 cm^{-1} and 840 cm^{-1} respectively as seen in Figure 5.20. All the fibres show the appearance of the absorbance peak at 1275 cm^{-1} which is associated with the β polymorph. The intensity of this peak increase with the addition of 1 wt% $KNbO_3$ and is consistent in intensity with the addition of further quantities of the ceramic. The addition of further quantities of ceramic at 5 wt% began to demonstrate the reduction in the intensity of the absorbance peak of the α polymorph at 763 cm^{-1} alongside the absorbance peak at 975 cm^{-1}. At the highest loading of 10 wt% $KNbO_3$, the intensity of the absorbance peak at 763 cm^{-1} and 975 cm^{-1} are not visible on the spectra. Similar results were obtained with the PVDF / $NaNbO_3$ where increasing the content of the ceramic resulted in a decrease in the α peak and an increase in the β peak. Similar results have been shown with the formation of PVDF / $BaTiO_3$ composite materials.[359]

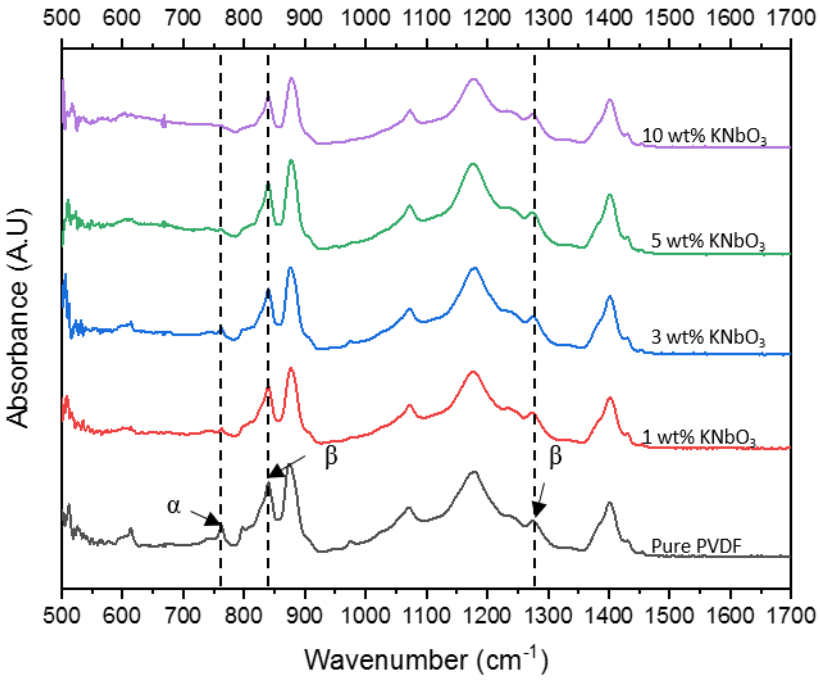

Figure 5.20. FTIR of the PVDF / $KNbO_3$ fibres 1 wt% – 10 wt% showing a decrease in the intensity of the α peak and an increase in the β peak intensity with an increase in ceramic.

To gain quantitative analysis of the content of the β polymorph within the PVDF / $KNbO_3$ fibres the Beer-Lambert law was applied as seen in 3.3.5. Figure 5.21 is displaying the change in the content of the β polymorph with the addition of the $KNbO_3$ filler. The addition of 1 wt% $KNbO_3$ resulted in a β percentage of 70 %, an increase of 14 % from the pure PVDF fibres. Increasing the $KNbO_3$ content in the fibres led to a decrease in the β phase to 67 %.

Further increasing the $KNbO_3$ to 5 wt% resulted in another increase in percentage β content to 73 % producing the highest value for all the PVDF / $KNbO_3$ fibres. The 10 wt% loaded fibres had a percentage β content of 71 %. In comparison to the PVDF / $NaNbO_3$ fibres, the PVDF / $KNbO_3$ fibres overall produced a higher content of the β polymorph. This could have occurred due to two reasons. (i) $KNbO_3$ has a higher dielectric constant than $NaNbO_3$ and would polarise and generate a stronger local electrostatic field when the voltage is applied to the electrospinning set-up. The stronger local electrostatic force would then influence the orientation of the polymer chains nearby in the β configuration. (ii) The higher piezoelectric properties may have allowed for the material to polarise itself through the shear stress applied through the spinneret causing a formation of a local electrostatic field, resulting in a similar phenomenon as the dielectric properties mentioned in point (i).[286,355]

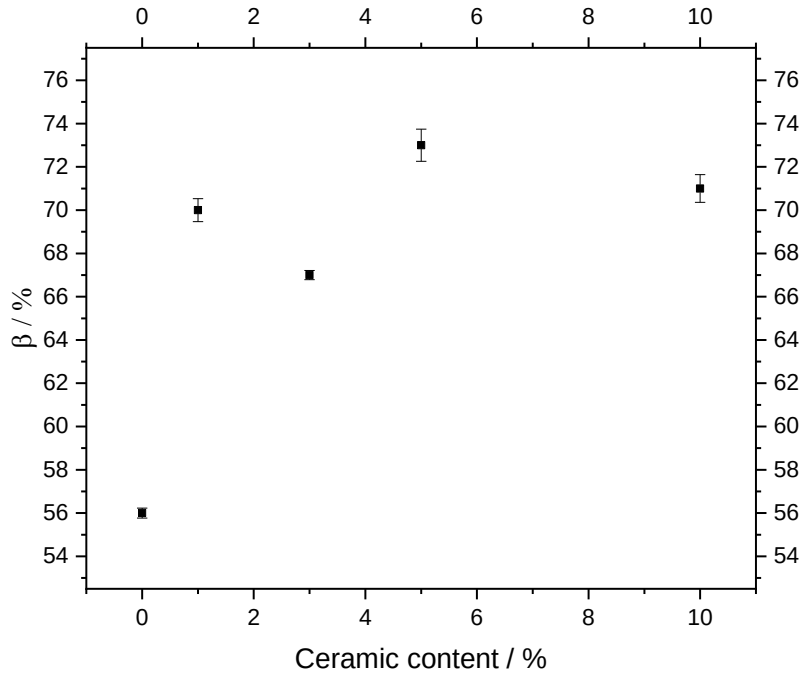

Figure 5.21. The increase in β phase percentage of the PVDF fibres with the addition of $KNBO_3$ 1 wt% – 10 wt%.

Figure 5.22 demonstrates the decrease in the fibre diameter is correlated with an increase in the content of the β polymorph. Here a decrease of approximately 700 nm demonstrates an increase in the content of the β polymorph by 10 – 13 % with fibre diameters ranging between 400 – 600 nm. This suggests that there may be a correlation between a decrease in fibre diameter and an increase in β content. When compared to PVDF / filler materials with a similar fibre diameter

of between 400 – 600 nm values of β content range between 75 – 87 %.[292,301] These values are higher than reported in this work within a similar fibre diameter range.

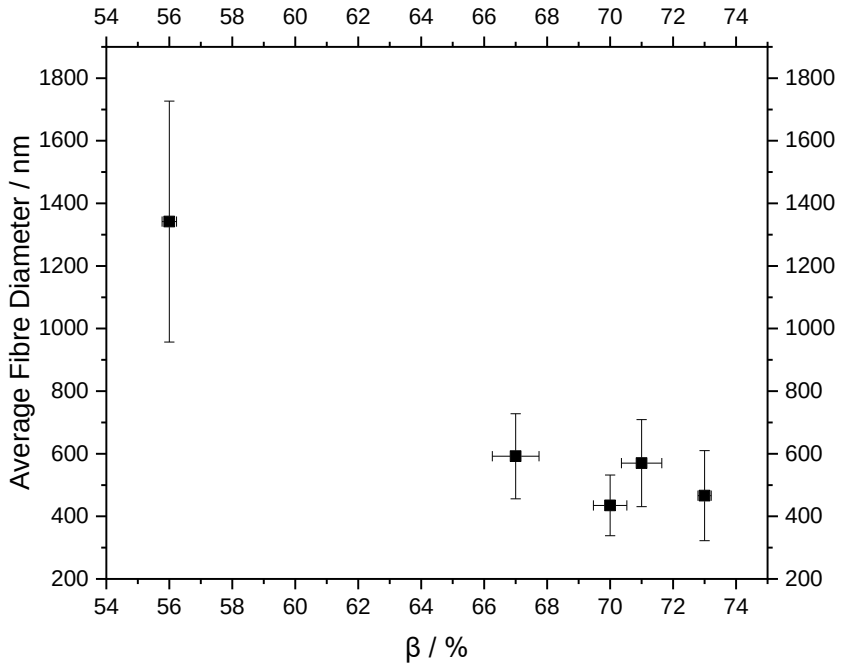

Figure 5.22. The average fibre diameter vs β phase percentage for the PVDF / $KNbO_3$ fibres. Showing an increase in fibre diameter with a decrease in β content.

5.2.4 XRD of PVDF / $KNbO_3$ Fibres

To further investigate the formation of the β polymorph XRD analysis was carried out. This would allow for a second confirmation of the nucleation of the β polymorph and assist in determining if the crystal structure of $KNbO_3$ was affected by the polarity of the solvents used. Overall, Figure 5.23 is displaying the weakening of the peak associated with a polymorph with the addition of the ceramic. It is also demonstrating that the ceramic is within its piezoelectric orthorhombic state which is essential for the piezoelectric properties of the overall material to increase. The pure PVDF fibres show the formation of both the α and β polymorphs in the XRD diffraction peak seen in Figure 5.23. The diffraction peak at 18.4 ° displays the (020) reflection of the α phase. The diffraction peak at 20.4 ° shows the (110) (200) reflections of the β phase. The diffraction peak at 18.4 ° becomes less prominent with the addition of $KNbO_3$ and continues to decrease in intensity at the 5 wt% and 10 wt% loading of the ceramic. This suggests that there is a decrease in the content of the α phase of the PVDF fibres and an increase in the content of the β phase which correlates with the percentage β percentages analysed in the FTIR.

The crystal structure of the $KNbO_3$ can also be determined by the XRD diffraction peaks seen between 20° – 45° from the 10 wt% ceramic content. The cubic, tetragonal, and orthorhombic phases of $KNbO_3$ can be analysed within this range. The splitting of the peak at 45.2° demonstrates the (002) and the (220) reflections which are characteristic of the orthorhombic phase.[360] A gradual increase in these intensity peaks occurs as there is more filler within the system that is being detected. The presence of the orthorhombic phase indicates that the ceramic is not affected by the solvent system during electrospinning and is still in the piezoelectric phase. With $KNbO_3$ being in the piezoelectric state this could also assist in understanding its influence on fibre diameter and nucleation of the β polymorph. The shear stress applied to the polymer during spinning would result in the polarisation of the ceramic through the piezoelectric effect. This would generate a charge on the material that could induce a local electrostatic force like the dielectric polarisation mentioned previously. This would assist in inducing the nucleation of the β polymorph.[286]

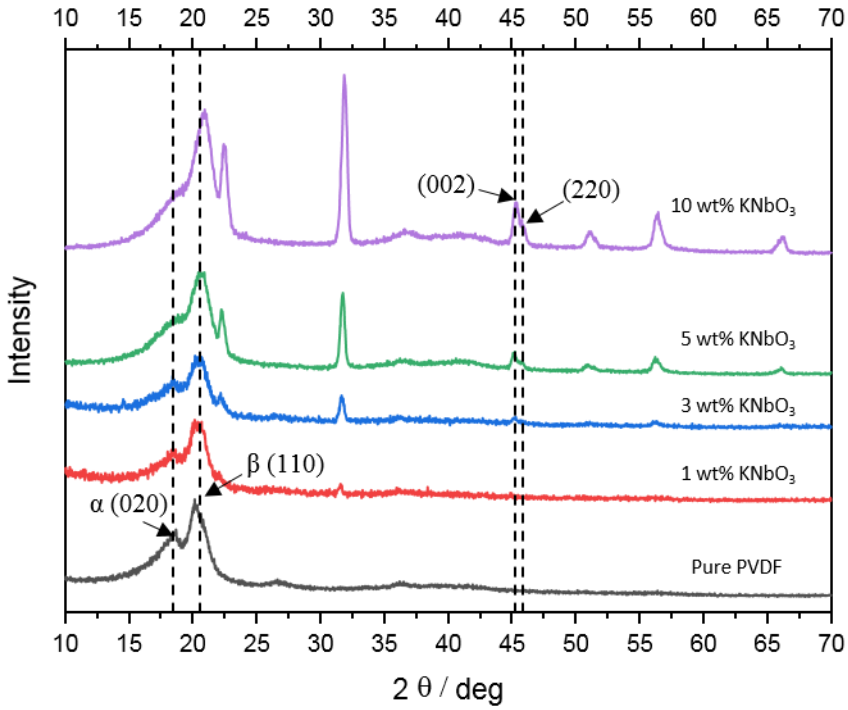

Figure 5.23. XRD of the PVDF / $KNbO_3$ fibres 1 wt% – 10 wt%. Showing a reduction in the intensity of the α peak, and displaying the orthorhombic phase of the $KNbO_3$.

5.2.5 DSC of PVDF $KNbO_3$ Fibres

The DSC of the PVDF / $KNbO_3$ fibres was carried out to determine the influence of the ceramic and increasing its content on the melt temperature, and crystallinity of the PVDF and compare this to the PVDF / $NaNbO_3$ fibres, where the filler had a larger average diameter and lower

electroactive properties. Figure 5.24. is displaying to shift in the melt temperature alongside peak broadening with the addition of the $KNbO_3$ filler. The T_m of pure PVDF states earlier was 167 °C. The addition of 1 wt% $KNbO_3$ led to a shift in the T_m to a higher temperature of 171 °C. The addition of higher quantities of $KNbO_3$ led to a decrease in the T_m of 170 °C, 166 °C, and 164 °C for the 3 wt% 5 wt% and 10 wt% ceramic additions respectively. Peak broadening occurred for the samples containing the ceramics, where it was possible to see two melt peaks overlapping. This suggests the formation of two crystalline phases and indicates the nucleation of the β phase. The melt temperatures were like those of the PVDF / $NaNbO_3$ where a decrease in the T_m was analysed. This was expected as impurities within the material would occur resulting in a lowering in the melt temperature.[356]

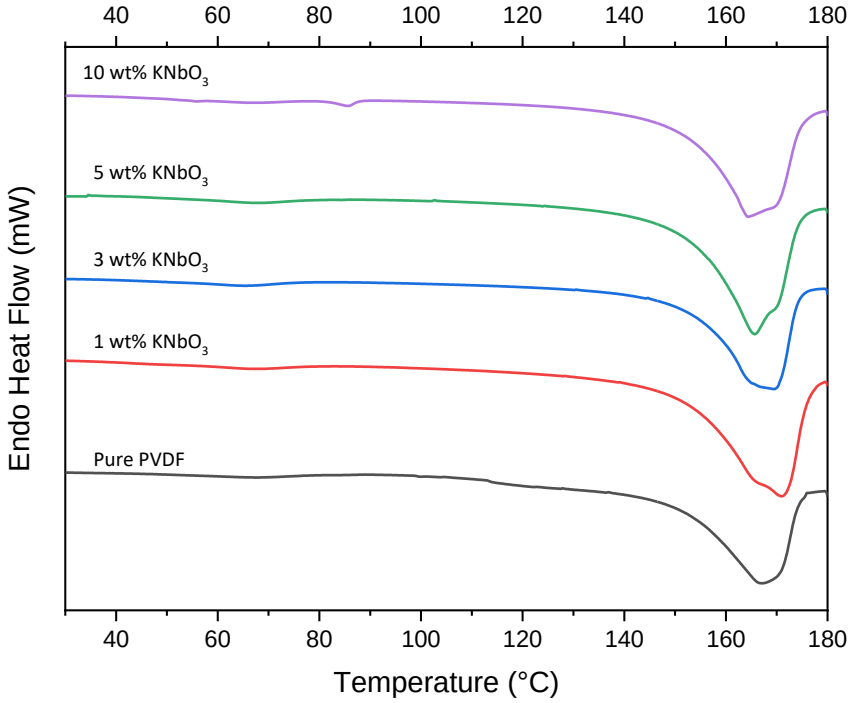

Figure 5.24. Endothermal heat flow of the PVDF / $KNbO_3$ fibres 1 wt% - 10 wt% with a shift to lower melt temperatures with the addition of ceramic.

Figure 5.25 demonstrates the shift in the recrystallisation temperature with the addition of the $KNbO_3$ filler. The T_c of pure PVDF states earlier was 141 °C. The addition of 1 wt% $KNbO_3$ led to an increase in the crystallisation temperature to 144 °C. From here the addition of further $KNbO_3$ led to a decrease in the T_c to 140 °C, 139 °C and 139 °C for the 3 wt% 5 wt% and 10 wt% ceramic addition respectively seen in Table 5.8. As mentioned earlier the decrease in the T_m and T_c occurred due to the homogenous distribution of the ceramic particles across

the fibres.[291] However, for 1 wt% the increase in the T_c and T_m suggests that the ceramic was not well distributed across the fibres.

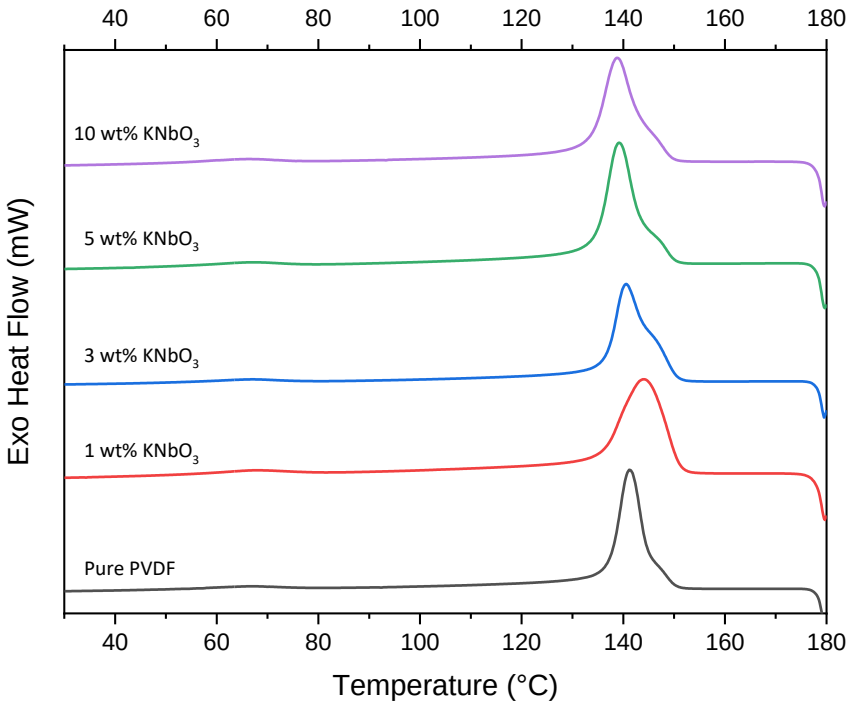

Figure 5.25. Exothermal heat flow of the PVDF / $KNBO_3$ fibres 1 wt% - 10 wt% with an overall shift to lower recrystallisation temperatures with the addition of ceramic.

Table 5.8. DSC data of the PVDF / $KNBO_3$ fibres 1 wt% - 10 wt%.

$KNbO_3$ wt%	**T_m/ °C**	**T_c / °C**	**ΔH_f**	**X_c / %**
0	167	141	55.5	53.0
1	171	144	50.3	48.0
3	170	140	52.4	50.0
5	166	139	49.7	47.5
10	164	139	44.7	42.7

The X_c of pure PVDF mentioned earlier was 53.0 %. The addition of 1 wt% $KNbO_3$ led to a decrease in the X_c to 48.0 %. The X_c then increased with the addition of 3 wt% $KNbO_3$ to 50.0 %. From there the addition of 5 wt% and 10 wt% ceramic led to a decrease in X_c to 47.5 % and 42.7 % respectively. The decrease in X_c at the higher loading of 5 wt% and 10 wt% $KNbO_3$ occurs due to ceramic causing defects to the polymer and restricting the movement of the chains during the recrystallisation phase mentioned earlier. In general, an increase in

crystallinity is associated with the nucleation of the β phase. However, here a decrease in the crystallinity occurs with an increase in the content of the β phase. This suggests that the $KNbO_3$ is influencing the spinnability of the PVDF and influencing the orientation of the polymer chains into the β phase through the elongation and stretching of the jet. As mentioned previously it could also be that the $KNbO_3$ is generating a strong local electrostatic field through its piezoelectric and dielectric properties assisting in the nucleation of the β polymorph.[356] This may still be assisting in the nucleation of the β polymorph even if the crystallinity of the material is decreased due to the hindrance of excess $KNbO_3$.

Overall, the crystallinity of the PVDF / $KNbO_3$ is higher than that of the PVDF / $NaNbO_3$. It has been previously studied that an increase in particle size of $BaTiO_2$ resulted in no change in the crystallinity of PVDF, however, it was suggested that increasing filler content resulted in a decrease in the crystallinity due to hindrance during the recrystallisation process. This was carried out between particle sizes of 10 nm – 500 nm.[361] The fillers in this study have a much larger particle size above 500 nm. To further investigate this the $CeNbO_4$ may assist as it has a much larger particle size in comparison to the $NaNbO_3$ and $KNbO_3$.

5.2.6 FTIR of PVDF $CeNbO_4$ Fibres

Figure 5.26 demonstrates displays the appearance of both the α and β polymorphs at their respective absorbance intensities. The addition of 1 wt% and above led to an increase in the intensity of the absorbance peak at 763 cm^{-1}, and 975 cm^{-1} associated with the α polymorph. The addition of 3 wt% resulted in a further increase in the intensity of the absorption peak at 763 cm^{-1}, and 975 cm^{-1}, and remained consistent for the 5 wt% and 10 wt% fibres. Like the PVDF / $NaNbO_3$ and the PVDF / $KNbO_3$ fibres, the 10 wt % loaded PVDF / $CeNbO_4$ fibres have seen a reduction in the intensity of the absorption peaks at 840 cm^{-1} representing the β polymorph suggesting a reduction in the electroactive phase. This was observed with the PVDF / $KNbO_3$ and the PVDF / $NaNbO_3$ fibres and was expected to occur with the PVDF / $CeNbO_4$ fibres.

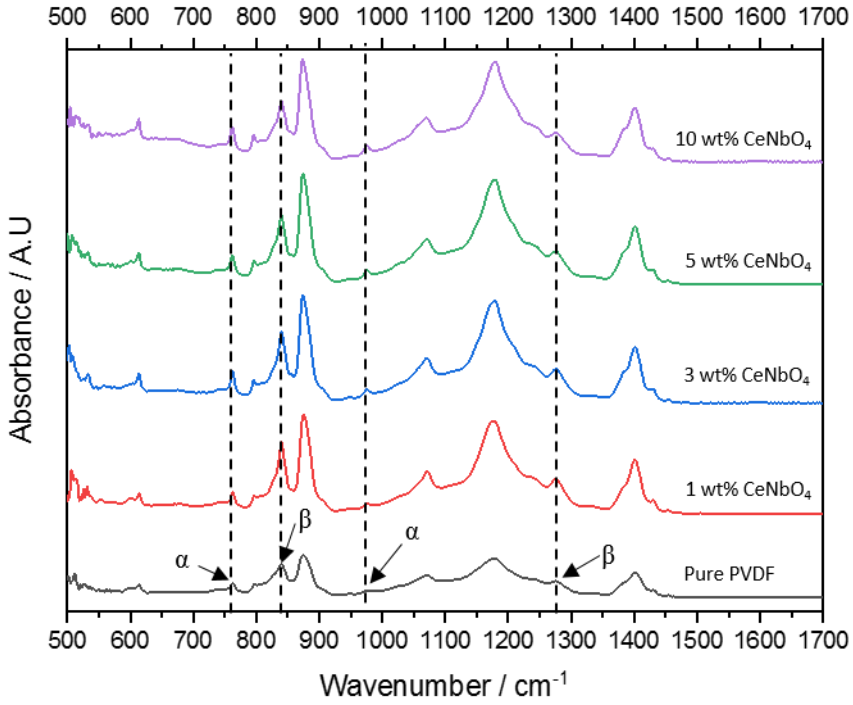

Figure 5.26. FTIR of the PVDF / $CeNbO_4$ fibres 1 wt% - 10 wt% displaying both the α intensity peaks and β intensity peaks.

To further analyse the FTIR data and gain quantitative information on the β polymorph the Beer-Lambert law was applied as seen in 3.3.5. Figure 5.27 displays the change in the intensity peaks associated with the α and β polymorphs. The percentage of the β polymorph had shown to be higher than expected at the lower loading of $CeNbO_4$. The percentage β phase at the lowest loading of 1 wt% $CeNbO_4$ had an unexpected value for the β polymorph with an analysed value of 74 %. Increasing the content of $CeNbO_4$ led to a decrease in the percentage β phase of 67 % for the 3 wt% and 5 wt% ceramic loadings. Further decreases in the percentage β phase were observed at the maximum loading resulting in a value of 61 %. The average fibre diameters of the PVDF / $CeNbO_4$ were like that of the PVDF / $NaNbO_3$ and larger than the PVDF / $KNbO_3$ ranging between 617 nm – 1023 nm, 601 nm – 874 nm and, 435 nm – 592 nm respectively. Overall, the content of the β polymorph of the PVDF / $CeNbO_4$ was like that of the PVDF / $NaNbO_3$ suggesting that the fibre diameter correlated with the nucleation of the electroactive phase. The decrease in the percentage of the β polymorph after the 1 wt% loading may be due to the increase in the content. This may lead to an increase in difficulty in the orientation of the fibres in that all-trans configuration of the β polymorph as mentioned in previous sections. Similar results were also observed with PVDF / BST fibres which had shown a decrease in crystallinity where the ceramic filler agglomerated.[357]

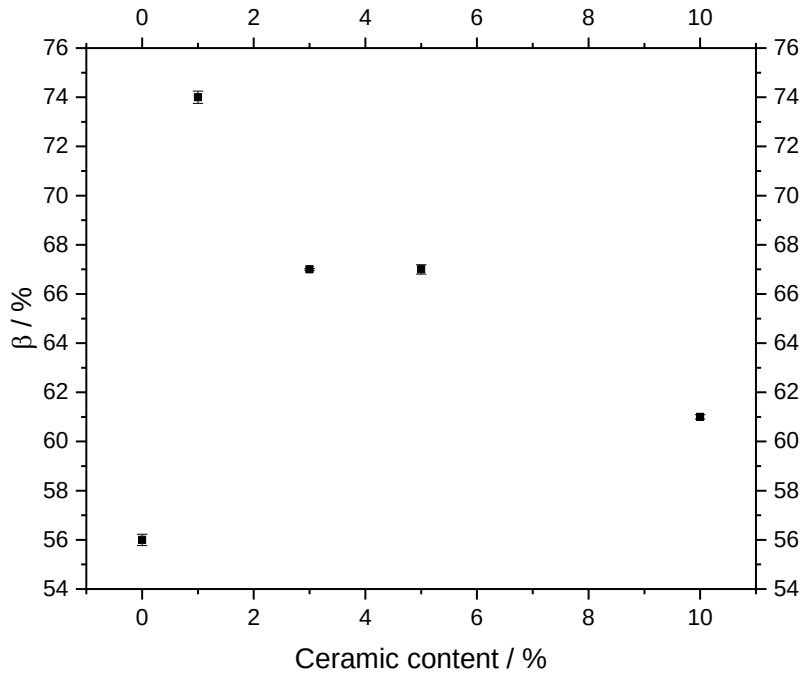

Figure 5.27. The overall increase in β percentage of the PVDF fibres with the addition of $CeNbO_4$ 1 wt% – 10wt%.

Figure 5.28 demonstrates that the average fibre diameters are all within the same experimental error and that there is a general decrease in the average fibre diameter with an increase in the content of the percentage β polymorph. However, because the average fibre diameters overlap in experimental error a correlation between the fibre diameter cannot be made with these samples. However, with the PVDF / $KNbO_3$ fibres, a correlation can be made as the fibre diameter are more uniform and demonstrate a clear decrease in diameter and increase in the content of the electroactive phase. The fibre here has a larger range between 600 – 1000 nm while the PVDF / $KNbO_3$ fibres are smaller at 400 – 600 nm. With a similar content of β polymorph ranging between 66 – 74 %.

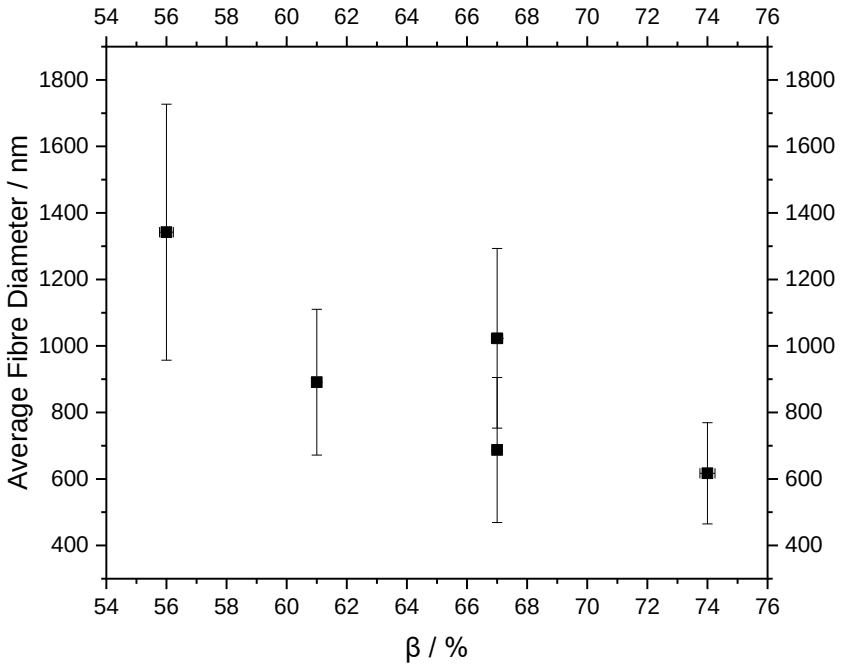

Figure 5.28. The average fibre diameter vs β phase percentage for the PVDF / $CeNbO_4$ fibres. Showing an increase in fibre diameter with a decrease in β content.

5.2.7 DSC of PVDF / $CeNbO_4$ Fibres

The melt temperatures and crystallinity of the PVDF / $CeNbO_4$ fibres were analysed to determine the influence of a larger particle on the recrystallisation of the material and if there was any correlation between this and the nucleation of the β polymorph. The T_m for pure PVDF was 167 °C as seen in Figure 5.29. The addition of 1 wt% $CeNbO_4$ led to an increase in T_m to 168 °C. Increasing the content of $CeNbO_4$ to 3 wt% resulted in a T_m of 164 °C alongside a prominent shoulder peak at 171 °C. The addition of further $CeNbO_4$ of 5 wt% 10 wt% led to an increase in T_m to 166 °C and 167 °C respectively seen in Table 5.9. The formation of a shoulder peak and peak broadening are both associated with the appearance of the β polymorph as mentioned earlier. These results were like those of the PVDF / $KNbO_3$ and PVDF / $NaNbO_3$ which both demonstrated T_m temperatures with a broadening and splitting which suggests the appearance of both the α and β polymorph within the material.[344]

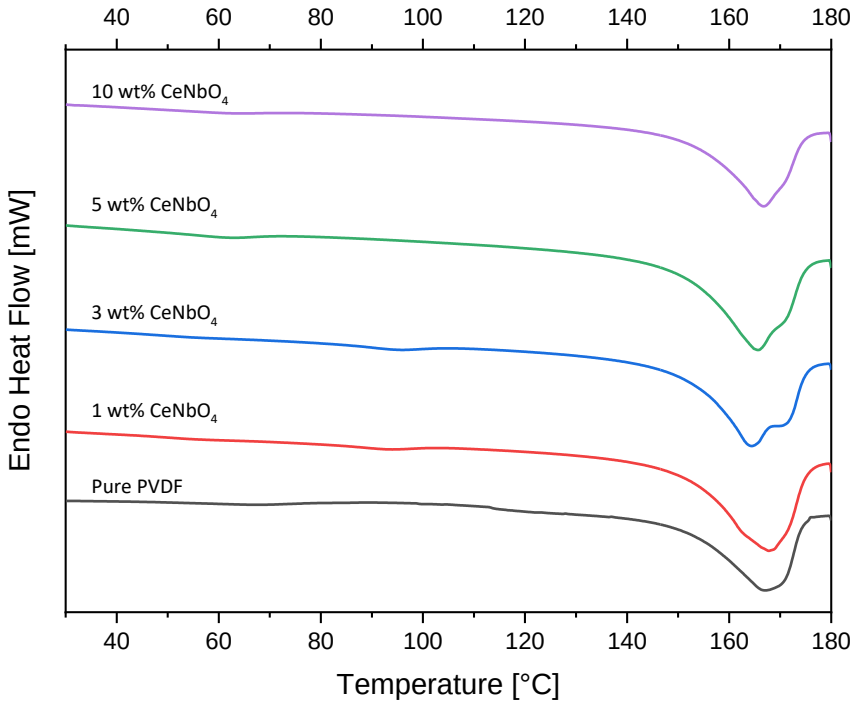

Figure 5.29. Endothermal heat flow of the PVDF / $CeNbO_4$ fibres 1 wt% - 10 wt% with a shift to lower melt temperatures with the addition of $CeNbO_4$.

The T_c of the pure PVDF was 141 °C as seen in Figure 5.30. The addition of 1 wt% $CeNbO_4$ led to a decrease in the T_c. From there the addition of further quantities of the ceramic resulted in a gradual decrease in the T_c, where values of 138 °C, 137 °C, and 137 °C were observed for the 3 wt%, 5 wt%, and 10 wt% ceramic loaded fibres. The decrease in the T_c was also observed with the PVDF / $NaNbO_3$ and PVDF / $KNbO_3$ with similar values being displayed. The decrease in T_c of the composite, mentioned earlier, is associated with the homogenous distribution of the ceramic particles across the PVDF fibres. This distribution across the material causes the PVDF to recrystallise slower as the ceramic is hindering the recrystallisation process.

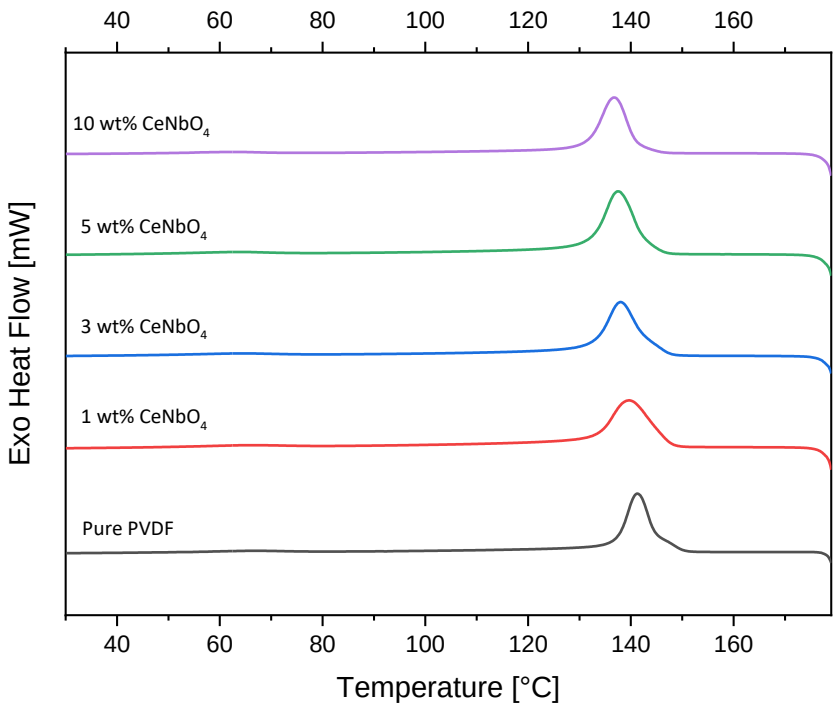

Figure 5.30. Exothermal heat flow of the PVDF / $CeNbO_4$ fibres 1 wt% – 10 wt% with a decrease in recrystallisation temperatures with the addition of $CeNbO_4$.

The X_c of pure PVDF was 53.0 % as in Table 5.9. The addition of $CeNbO_4$ resulted in a decrease in the crystallinity of the material. This was also observed throughout the addition of further quantities of the ceramic. Small changes in the crystallinity of the PVDF / $CeNbO_4$ fibres were observed with a loading of 1 wt% – 5 wt% loading. A large decrease in the crystallinity was observed with the maximum addition of 10 wt%. This resulted in an X_c of 36.5 % which was much lower than those compared to the PVDF / $NaNbO_3$ and the PVDF / $KNbO_3$ samples. This may have occurred due to the larger particle size of the $CeNbO_4$ in comparison to the other two ceramics, resulting in the recrystallisation of the polymer being more difficult. It has also been demonstrated previously that an increase in filler content results in the agglomeration and can cause the material to have lower crystallinity values.[357]

Table 5.9. DSC data for the PVDF / $CeNbO_4$ fibres 1 wt% – 10 wt%.

$CeNbO_4$ wt%	T_m/ °C	T_c / °C	ΔH_f	X_c / %
0	167	141	55.5	53.0
1	168	139	47.5	45.4
3	164	138	46.6	44.5
5	166	137	46.4	44.3
10	167	137	38.2	36.5

5.2.8 Summary

The FTIR data demonstrates an increase in the content of the β polymorph with the addition of all three ceramic fillers. In comparison to previous reports, the values here were lower than what the highest values have been stated. The highest reported figures are demonstrated with a PVDF / KNN / ZnO fibre composite of 94%.[309] The values here are much lower and range between 61 % – 73% with $KNbO_3$ demonstrating the largest influence on the formation of the β polymorph, due to its higher dielectric and piezoelectric properties assisting in the formation of localised dipoles and thus the nucleation of the electroactive phase.[355] Overall, it suggests that the piezoelectric properties of the PVDF with the addition of $KNbO_3$ may be weaker than previously produced PVDF fibres.

The DSC data had been shown to correlate with the FTIR data, which supports two cases. Firstly, the decrease in the melt temperature coupled with the broadening of the endothermal peaks suggests that there is the formation of the β polymorph with the α polymorph still being present within the PVDF. Secondly, the gradual decrease in the X_c for all three sets of the PVDF / niobate fibres with the increase in ceramic content suggests that the recrystallisation of the fibres is hindered by the ceramic particles. The particle size increases from $KNbO_3$ < $NaNbO_3$ < $CeNbO_4$ which sees an overall decrease in the crystallinity. However, the increase in the β polymorph with a decrease in the crystallinity suggests that the ceramic particles are acting as nucleators. Previous studies have shown that a decrease in the crystallinity of PVDF occurs with higher contents of filler due to agglomeration of the filler.[357] Similar results have been demonstrated in this work. It should also be mentioned that a trend cannot be made with fibre diameter and crystallinity as the fibre diameters are all within a similar experimental error range.

It can also be mentioned that the ceramic fillers may have also influenced the PVDF through the dielectric or piezoelectric properties of the ceramics through the formation of the dipole on the surface of the material. The local dipoles generated through the dielectric and piezoelectric properties of the ceramic interact with nearby PVDF polymer chains acting to nucleate the β polymorph as the chains interact with the filler through ion-dipole interactions.[355,357] These

interactions are expected to only occur during the electrospinning technique and not during the recrystallisation within the DSC which could result in a value that may not be true.

The niobium-based ceramic has all shown similarities in its influence on the crystal structure of the PVDF fibres. The initial addition of the ceramic resulted in a large increase in the β polymorph in comparison to the pure PVDF fibres and could not be correlated to the decrease in average fibre diameter as the fibres were all within the experimental error. Overall, the new work within this section demonstrates that the addition of the filler causes a decrease in the crystallinity however the content of the β polymorph increases when $NaNbO_3$, $KNbO_3$ and $CeNbO_4$ are added to PVDF.

5.3 Thermal and Mechanical Properties of the PVDF / Niobium Oxide Fibres

Following on from the nucleation of the β polymorph it was essential to then begin gaining an understanding of the exact loading values of ceramic within the PVDF as some filler may have been left in the vial or syringe or stuck within the spinneret over time. The bulk piezoelectric properties of the composite fibres would come from the ceramic component and is essential to determine how much of the filler was loaded into the fibres. To do this TGA was employed as a technique to assist in confirming the content of the ceramic and provide some understanding of the thermal stability of the material. Following the confirmation of the addition of the niobium oxides through the TGA data, and an understanding of the influence of the ceramic particles on the crystallinity of the PVDF within the previous sections it was then decided to analyse the viscoelastic damping properties of the PVDF / niobium oxide materials using DMTA. This would allow for an understanding of the materials damping properties through analysis of the storage modulus (*E'*), loss modulus (*E''*) and the tan δ concerning the type of ceramic and the content of it added to the PVDF fibres.

5.3.1 TGA of the PVDF / $NaNbO_3$ Fibres

The TGA was used to ensure that the exact loading of the ceramic was carried out. The TGA of the PVDF / $NaNbO_3$ can be seen in Figure 5.31 where two degradation steps are observed. The first degradation step for the pure PVDF occurred at 463 °C, with the second degradation step occurring between 500 °C – 800 °C. The addition of 1 wt% $NaNbO_3$ led to a decrease in the degradation onset temperature to 369 °C. Increasing the content of $NaNbO_3$ to 3 wt% resulted in a degradation onset temperature of 410 °C. The degradation temperature decreased again with the addition of 5 wt% and 10 wt% ceramic content to 374 °C and 387 °C. Overall, a decrease in the degradation of temperature occurs with the addition of the ceramic filler. The

second degradation step for these materials occurred at a lower temperature between 450 °C – 600 °C. The first degradation step of the PVDF fibres is associated with carbon-hydrogen scission, where the formation of hydrogen fluoride occurs. The second degradation step occurs due to the poly(aromatization) of the chains, resulting in the formation of aromatic compounds.[362,363] The decrease in the degradation onset temperature with the addition of ceramic content is associated with the decrease in the order of the polymer chain. This results in less energy being required to cause the degradation of the polymer.[364] Bairagi and Ali[365] demonstrated similar results with PVDF / KNN nanorods where a decrease in the onset degradation temperature was observed with the addition of the ceramic filler suggested to occur due to a decrease in crystallinity of the polymer. Here it is also observed that a decrease in the polymer crystallinity occurs with the addition of the filler which could have influenced the reduction in the onset degradation temperature. It could also be occurring due to the ceramic being a poor thermally conductive material resulting in areas of heat pockets being generated at areas of the polymer causing the material to degrade at a lower temperature.

The residual mass of the pure PVDF fibres was 4.41 % as seen in Table 5.10. Increasing the content of ceramic by 1 wt% resulted in a large increase in the residual mass to 21 %. Increasing the ceramic content to 3 wt% led to a reduction in the residual mass to 17.5 %. Increasing the $NaNbO_3$ content to 5 wt% and 10 wt% resulted in an increase in the residual mass to 23.0 % and 30.7 %. Residual mass in PVDF occurs due to the carbon backbone being stripped of the hydrogen and fluorine atoms. During the degradation of the polymer, HF is released leaving the carbon backbone behind as the residual mass.[366] However, there was still an overall increase in the residual mass with an increase in the content of the ceramic suggesting that the PVDF fibres were loaded with the $NaNbO_3$. It should also be mentioned that during the electrospinning process, the content of the ceramic may alter due to two reasons. (i) The ceramic sediments to the bottom of the syringe during the spinning process may result in lower quantities of it being deposited within the fibres. (ii) The ceramic begins to deposit within areas of the capillary tube and spinneret lowering its content within the fibres.

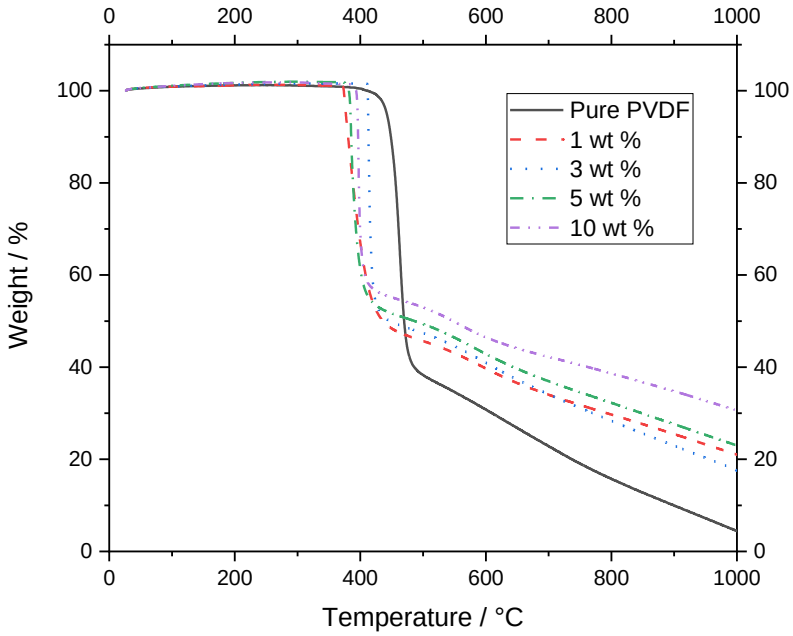

Figure 5.31. TGA of the PVDF / $NaNbO_3$ fibres 1 wt% - 10 wt% showing a decrease in degradation temperature with the addition of $NaNbO_3$.

Table 5.10. The degradation temperature and residual mass percentage of the PVDF / $NaNbO_3$ fibres.

$NaNbO_3$ / wt%	**Degradation Temperature / °C**	**Residual Mass / %**
0	413	4.41
1	369	21.0
3	410	17.6
5	374	23.0
10	387	30.7

5.3.2 DMTA of the PVDF / $NaNbO_3$ Fibres

Dynamic mechanical thermal analysis (DMTA) was applied as it provides information on the damping properties of the materials in an oscillatory fashion across a temperature range. This allows for an understanding of the damping properties of the material in different temperature ranges where it may be applied in real-world applications. Figure 5.32 a–c demonstrates the damping properties of the PVDF / $NaNbO_3$ fibres. It is shown that overall, across the temperature range, the PVDF ceramic composite has similar damping properties to the PVDF fibres. This was unexpected as the literature generally shows an increase in these

damping properties, especially the storage modulus.[367] Zhao *et al*.[368] demonstrated similar results where the increase in storage modulus occurs with the addition of MnO_2 filler, with values ranging between 4.5 – 6.5 GPa. He and Zhang[369] have also added PZT filler to PVDF and displayed storage moduli of 7 – 8 GPa. These values are higher than those proposed in the work below.

Figure 5.32 a demonstrates the decrease in the *E'* across the entire temperature range. Over the entire temperature range, the pure PVDF had a higher *E'* than the 1 wt% and 3 wt% at the lower temperatures below 25 °C. However, at higher temperatures, the 1 wt% – 5 wt% ceramic loaded materials had a higher *E'*. The *E'* of pure PVDF at 0 °C was analysed as 48.8 MPa. Similar results have been demonstrated for PVDF fibres in the literature where the decrease in modulus occurs over the temperature range.[370] The addition of 1 wt% and 3 wt% $NaNbO_3$ resulted in a decrease in the *E'* to 40.3 MPa and 42.3 MPa. Increasing the ceramic content to 5 wt% resulted in an increase in the *E'* to 59.0 MPa, and a further increase in the ceramic content to 10 wt% resulted in a large decrease in *E'* to 19.8 MPa. The changes to the *E'* with changing amounts of $NaNbO_3$ may be associated with three variables. (i) The initial decrease in the *E'* with the addition of the ceramic may be due to a decrease in the crystallinity of the material which results in a lower storage modulus. (ii) The particles at the lower concentrations are acting as a nucleating agent as mentioned in 5.2.1 where the ion-dipole interactions assist in wrapping the polymer chains around the ceramic filler, at the same time hindering the recrystallization of the material by decreasing the chain mobility of the polymer matrix as observed in the DSC data.[355] (iii) The particle size of the $NaNbO_3$ result in lower bond interactions with the chains resulting in sliding and debonding from the polymer resulting in movement of the chains mainly at the higher concentration of 10 wt%.[361] At the temperature range of 50 °C – 100 °C, there is a lot of noise in the data. This occurs due to the slipping of the sample in the clamps at the higher temperature range. Overall, the values demonstrated here are lower than that demonstrated within the literature which are typically upward of 600 MPa and above.[368,369,371] This may occur here as the sample sizes are extremely thin providing for low damping properties and more comparable results larger samples would be required.

Figure 5.32b demonstrates the change in the *E''* with the addition of the $NaNbO_3$ filler to the PVDF. The *E''* of the PVDF / $NaNbO_3$ at 0 °C had shown to initially decrease with the addition of the ceramic from 3.00 MPa to 2.32 MPa for the pure PVDF and 1 wt% loading fibre respectively. The *E''* then began to increase again to 2.71 and 3.60 for the 3 wt% and 5 wt% loaded fibres. Increasing the content of ceramic to the maximum of 10 wt% resulted in a large decrease in the *E''* to 1.37 MPa.

Figure 5.32c displays the tan δ of the PVDF / $NaNbO_3$ and demonstrates the changes in the T_g alongside the damping properties. The tan δ of the PVDF demonstrates several

relaxations across the temperature range. Figure 5.32 shows the initial relaxation at -40 °C is known as the β relaxation and is associated with the glass transition of the amorphous phase of the PVDF where the polymer begins to move from a glassy state to a flexible state.[372,373] The increase in the intensity of the tan δ suggests that the addition of the ceramic filler influenced the damping properties of the material. The T_g of the pure PVDF is displayed as -47 °C, the addition of 1 wt% $NaNbO_3$ had shown little change to the T_g resulting in a value of -47 °C. The addition of 3 wt% – 10 wt% ceramic led to an increase in the T_g to -44 °C, -43 °C, and -43 °C. The increase in the T_g with increases in the ceramic content. This suggests that there is a decrease in the mobility of the polymer chains with the addition of ceramic and a reduction in the free volume of the polymer matrix which occurs with the addition of filler. [374,375]

It can also be mentioned that across testing there was a dip in the E' E'' and tan δ across similar temperatures between -25 °C and -50 °C which occurred to the liquid nitrogen bottle running out which causes temperature fluctuations within the DMTA which is time dependant. To reduce this effect two nitrogen bottle are applied however, there is still unavoidable areas of a rapid decrease.

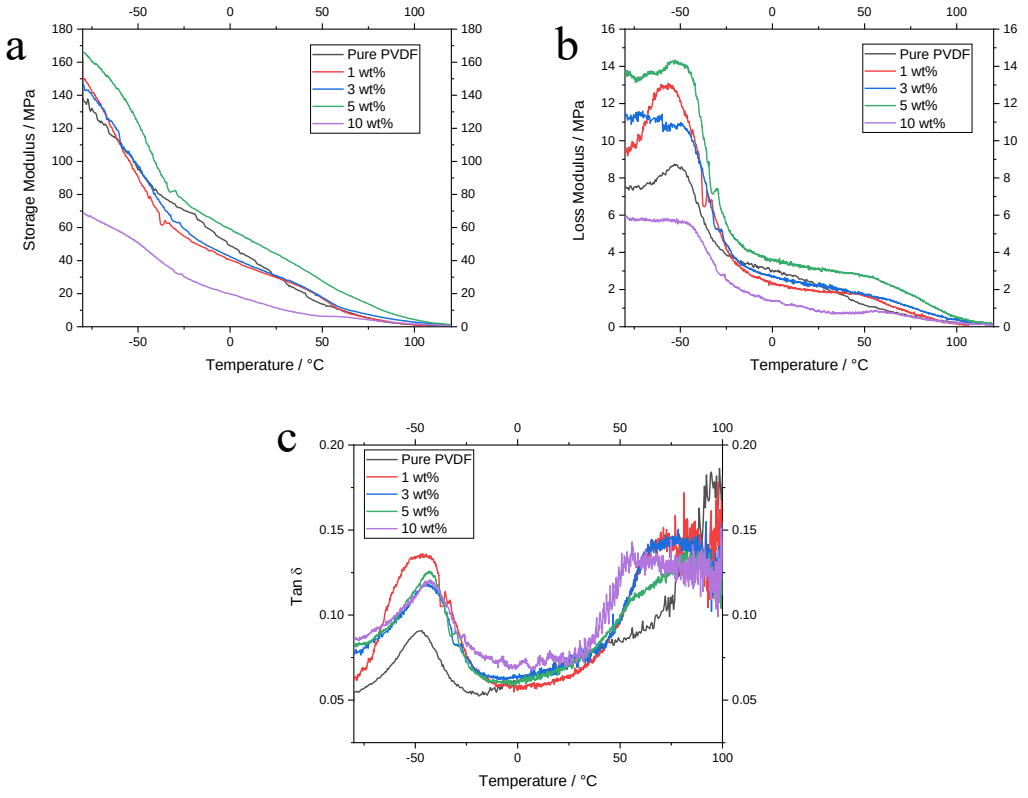

Figure 5.32. DMTA of the PVDF / $NaNbO_3$ fibres 1 wt% - 10 wt% displaying an increase in the damping properties of the material with the addition of $NaNbO_3$.

5.3.3 TGA of the PVDF / $KNbO_3$ Fibres

The TGA of the PVDF / $KNbO_3$ can be seen in Figure 5.33, where two degradation steps are observed for the pure PVDF and PVDF / $KNbO_3$ 3 wt% – 10 wt% and a three-step degradation for the 1 wt% loaded fibre. The onset degradation temperature of pure PVDF was analysed as 413 °C with the second step occurring between 500 °C – 800 °C. The addition of 1 wt% $KNbO_3$ led to a reduction in the onset degradation temperature to 368 °C, with the second degradation step occurring at 404 °C, and the final degradation step occurring at 450 °C – 600 °C. As mentioned in 5.3.1 the decrease in the onset degradation temperature is associated with the decrease in the order of the polymer chains when the ceramic filler is added and a decrease in crystallinity.[364] The PVDF / $KNbO_3$ fibres with 1 wt% of the ceramic filler may have displayed lower loading of the ceramic which resulted in some areas with an efficient order in the polymer chains while some regions with a decrease in the order, leading to two degradation steps between 368 °C – 404 °C. The onset degradation began to increase with the addition of further quantities of $KNbO_3$ resulting in temperatures of 377 °C, 384 °C and 382 °C for the 3 wt%, 5 wt% and 10 wt% loaded fibres respectively. These samples did not show a second degradation step at ~ 400 °C, rather the second degradation step occurred at 450 °C – 600 °C, which is associated with the complex poly (amortization) as mentioned earlier.[362,363] Overall, the thermal stability of the material decreased for the PVDF / $KNbO_3$ fibres and was like that of the PVDF / $NaNbO_3$ fibres suggesting at the two materials have a similar influence on the degradation of the polymer. With the decrease in order of polymer chains and crystallinity already being mentioned. It could be stated that the decrease in degradation temperature could be to do with the poor thermal conductivity the ceramics may have as mentioned in 5.3.1.[364]

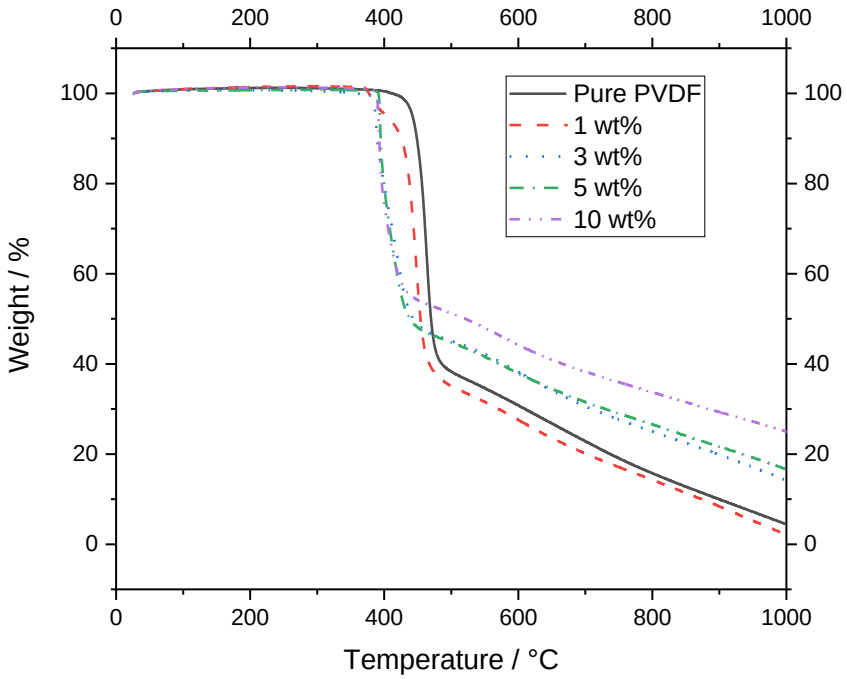

Figure 5.33. TGA of the PVDF / $KNbO_3$ fibres 1 wt% - 10 wt% showing a decrease in the degradation temperature and an increase in final residual percentages with an increase in ceramic content.

The residual mass of the fibres containing 1 wt% $KNbO_3$ decreased from 4.41 % to 2.13 % which may have occurred due to poor loading of the ceramic within the material. This is in line with the double degradation temperature of the PVDF / $KNbO_3$. The addition of further amounts of the ceramic led to a large increase in the residual mass, producing values of 14.1 %, 16.6 % and 25.0 % for the 3 wt%, 5 wt%, and 10 wt% loaded fibres respectively as seen in Table 5.11. Overall, there was a general increase in the residual mass with an increase in the content of the ceramic filler, suggesting that there was a successful and efficient loading of the $KNbO_3$ within the PVDF fibres.

Table 5.11. The degradation temperature and residual mass percentage of the PVDF / $KNbO_3$ fibres.

$KNbO_3$ / wt%	**Degradation Temperature / °C**	**Residual Mass / %**
0	413	4.41
1	368 404	2.13
3	377	14.1
5	384	16.6
10	382	25.0

5.3.4 DMTA of the PVDF / $KNbO_3$ Fibres

Following on from the DMTA analysis of the PVDF / $NaNbO_3$ fibres the PVDF / $KNbO_3$ fibres were analysed for their viscoelastic damping properties to determine if altering the ceramic would demonstrate an influence material. Figure 5.34a displays the storage modulus of the PVDF / $KNbO_3$ fibres where a decrease in the value occurs with an increase in the temperature. As mentioned previously the pure PVDF displayed an *E'* at 0 °C of 21.1 MPa. The addition of 1 wt% $KNbO_3$ led to an increase in the *E'* to 69.9 MPa. Increasing the ceramic content to 3 wt% and 5 wt% resulted in further increases in the *E'* to 76.3 MPa and 83.0 MPa. The *E'* began to decrease with an increase in the ceramic content to the maximum 10 wt% loadings, displaying values of 80.2 MPa. Overall, there was an increase in the *E'* with an increase in the content of the $KNbO_3$ between 1 wt% – 5 wt%. In comparison to the PVDF / $NaNbO_3$ fibres, the PVDF / $KNbO_3$ fibres analysed, demonstrated a higher *E'* and a similar increase in the *E'* with an increase in the content of the ceramic from 1 – 5 wt% then a decrease at the 10 wt%. The overall higher *E'* of the PVDF / $KNbO_3$ fibres in comparison to the PVDF / $NaNbO_3$ fibres may have occurred due to the stronger nucleation properties of the $KNbO_3$ in comparison to the $NaNbO_3$ resulted in a higher conversion of the α to the β polymorph as shown in 5.2.3 and the higher crystallinity of the PVDF / $KNbO_3$ in comparison to that of the PVDF / $NaNbO_3$ fibres. A combination of both parameters has previously been shown to increase the *E'* of PVDF.[376] It can also be mentioned that a higher *E'* is also due to hindrance in the movement of the polymer chains due to the addition of the ceramic as mentioned previously. The PVDF / $KNbO_3$ follow the trend of the literature where the addition of filler to PVDF increases the storage modulus to above 4.5 GPa and is associated with the decrease in free volume within the amorphous region.[368,369] This suggests that the materials produced here have lower damping properties than those produced in the literature.

Figure 5.34b displays the loss modulus over the temperature range where a higher value is seen with the addition of the $KNbO_3$. The *E''* at 0 °C had shown to increase with the addition of $KNbO_3$ producing values of 3.56 MPa, an increase of 0.56 MPa. The maximum *E''* was observed with the 3 wt%, displaying a value of 4.31 MPa. Increasing the ceramic content to 5 wt% and 10 wt% led to a decrease in the *E''* to 3.76 MPa and 3.44 MPa respectively. At the higher temperature of 50 °C, an initial increase in the *E''* was observed displaying a value of 2.99 MPa. Increasing the content of ceramic from here resulted in little change to the *E''* displaying values of 3.51 MPa, 3.45 MPa and 3.63 MPa for the 3 wt% – 10 wt% fibres respectively.

Figure 5.34c displays the tan δ which demonstrates a change in the T_g alongside the damping properties of the material. The tan δ of the fibres had shown little change in the intensity of the β relaxation with the initial addition of 1 wt%, 5 wt% and 10 wt% $KNbO_3$, suggesting that these amounts of ceramic had little influence on the damping factor of the material. However, increasing the content of the ceramic to 3 wt% increased the intensity β relaxation peak of the tan δ. In comparison to the PVDF / $NaNbO_3$ which has shown an increase in the damping factor, the PVDF / $KNbO_3$ fibres demonstrated little change. However, the damping factor is a ratio of the *E'' / E'* which both respectively demonstrate overall higher values for the PVDF / $KNbO_3$ than the PVDF / $NaNbO_3$ suggesting it has higher damping properties. Changes in the T_g were observed with the addition of the ceramic with the initial loading of 1 wt% decreasing the T_g to -61.6 °C. From here the addition of 3 wt% and 5 wt% $KNbO_3$ led to an increase in the T_g producing values of -57.5 °C and -43.4 °C. A shift to a higher temperature was observed with the 10 wt% loaded fibres displaying a value of -46.4 °C. The decrease and increase in the T_g at the interval can be explained by two contrasting effects. (i) A reduction in the T_g can be associated with an increase in the free volume of the matrix due to the packing difficulty of the chains within the amorphous region.[368] (ii) An increase in T_g as mentioned previously due to the decrease in mobility of the chains close to the ceramic filler.[377] The data suggests that for the 1 and 3 wt% the former of the two is the dominant effect and the latter is more dominant for the higher content of the $KNbO_3$. However, it cannot confirm if there is a change to these regions and advanced microscopy could be considered to look further into the interactions between the PVDF and ceramic. It can also be said that there may be some form of issues with thermal transfer within the material which could be interfering with the temperature of the material leading to shifts in the temperature range seen more strongly in the *E''* as well as the tan δ.

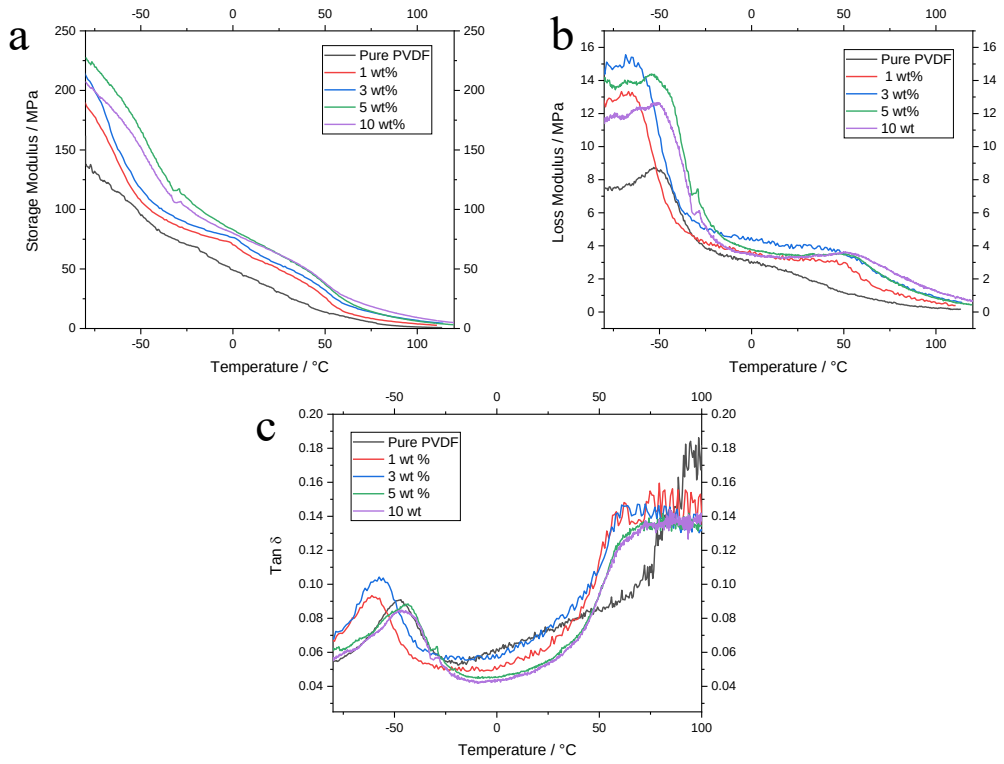

Figure 5.34. DMTA of the PVDF / $KNbO_3$ fibres 1 wt% - 10 wt%, showing an overall increase in damping properties with an increase in ceramic content.

5.3.5 TGA of the PVDF / $CeNbO_4$ Fibres

The degradation onset temperature of pure PVDF fibres was analysed as 463 °C as mentioned previously. The addition of 1 wt% $CeNbO_4$ led to a decrease in the degradation onset temperature to 340 °C. Increasing the content of ceramic from here at little influence on the degradation temperature resulting in temperatures ranging between 350 °C – 355 °C as seen in **Error! Reference source not found.**. The thermal stability of the PVDF / $CeNbO_4$ fibres was m uch lower than that in comparison to the PVDF / $NaNbO_3$ fibres and the PVDF / $KNbO_3$ fibres. As mentioned previously the onset degradation temperature is known to decrease with a decrease in the order of the polymer chains.[364] This may be influenced by the larger particle size of the $CeNbO_4$ which causes a further decrease in the order of the chains and results in a decrease in the thermal stability of the material. Overall, the crystallinity of the PVDF / $CeNbO_4$ was lower than that of the other PVDF / niobium oxides which could have also influenced the degradation of the material resulting in a lowering of the onset degradation temperature as mentioned in 5.3.1. The $CeNbO_4$ may also have lower conductive properties than the other niobium oxides which causes areas within the PVDF to degrade much more quickly as the energy is not being dissipated across the material effectively.

The residual mass had shown a similar increase in mass as analysed by the samples containing $NaNbO_3$ and $KNbO_3$. These samples had all shown to increase drastically in mass with the addition of 1 wt% $CeNbO_4$ resulting in a residual mass of 21.4 %. From here a gradual increase in mass was observed with the addition of further amounts of the ceramic, with a maximum residual mass being produced by the 10 wt% $CeNbO_4$ of 32.1 % as seen in Table 5.13 The increase in the content of the residual mass aligns with an increase in the content of the ceramic as expected and demonstrated by the other PVDF / niobium fibres. It also suggests there was successful loading of the $CeNbO_4$ into the PVDF fibres.

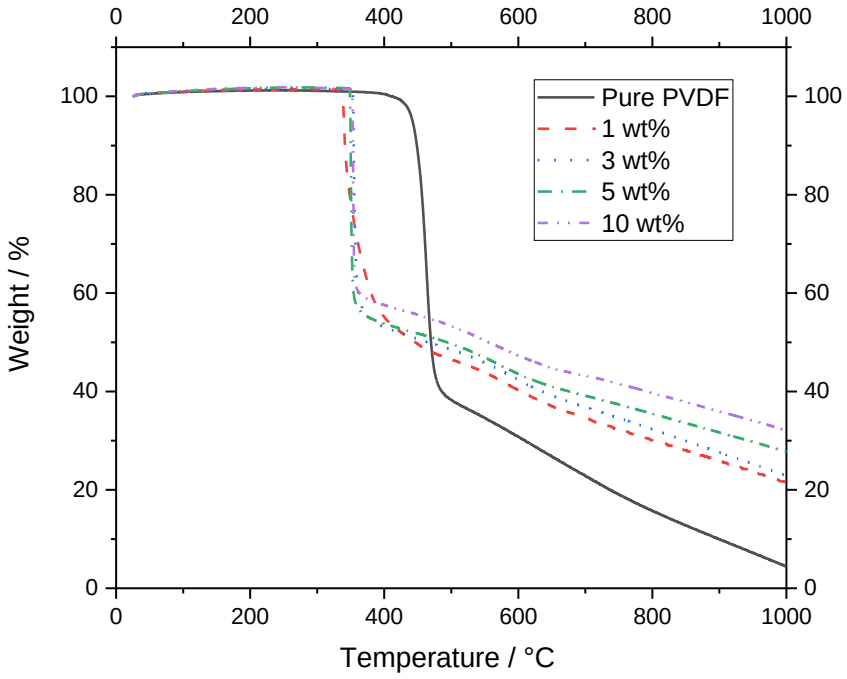

Figure 5.35. TGA of the PVDF / $CeNbO_4$ fibres 1 wt% - 10 wt% showing a decrease in degradation temperature and an increase in residual percentages with the addition of $CeNbO_4$.

Table 5.12 The degradation temperature and residual mass percentage of the PVDF / CeNbO4 fibres.

$CeNbO_4$ / wt%	Degradation Temperature / °C	Residual Mass / %
0	463	4.41
1	335	21.4
3	352	22.9
5	348	27.8
10	351	32.1

5.3.6 DMTA of the PVDF / $CeNbO_4$ Fibres

Following the DMTA analysis of the PVDF / $NaNbO_3$ fibres and the PVDF / $KNbO_3$ fibres, the PVDF / $CeNbO_4$ fibres were analysed. Figure 5.36a demonstrates the change in storage modulus with the addition of the $CeNbO_4$ across the temperature range where a gradual decrease in the value is observed. These fibres displayed a much lower *E'* in comparison to the other PVDF / niobium oxide fibres. The *E'* at 0 °C containing 1 wt% $CeNbO_4$ was drastically lower than that of the pure PVDF fibres, displaying a value of 6.56 MPa, which was a decrease of 42.24 MPa. The addition of 3 wt% led to a further decrease in *E'* to 3.48 MPa. Increasing the content of $CeNbO_4$ to 5 wt% and 10 wt% led to an increase in the *E'* to 10.3 MPa and 10.6 MPa. The low *E'* was not expected as the addition of ceramics generally causes an increase in the *E'* as it hinders the movement of the polymer chains.[367] The increase in storage modulus with the addition of the ceramic occurs due to a decrease in the free volume within the amorphous region of the polymer. However, the PVDF / $CeNbO_4$ fibres display a lower crystallinity than the other PVDF / niobium oxide ceramics which may have led to a larger decrease in the *E'*. Alongside this, the larger particle size may result in more slippage and debonding of the chains with the ceramic causing a lower *E'* as mentioned with the PVDF / $NaNbO_3$ 5.3.2.[361] This may allow for a movement of the polymer chains at the higher loading of ceramic resulting in its decrease here. Alongside this, the overall damping property of the PVDF / $CeNbO_4$ is lower than that for other PVDF composite materials demonstrated in the literature which display storage moduli of 4.5 GPa and above.[369,368]

The *E''* at 0 °C had shown to decrease with the addition of the $CeNbO_4$ particles, resulting in a value of 0.58 MPa, a decrease of 2.42 MPa from the pure PVDF fibres. Increasing the ceramic content to 3 w% resulted in a decrease in the *E''* to 0.32 MPa. Increasing the $CeNbO_4$ to 5 wt% resulted in an increase in the *E''* to 0.68 MPa, and at 10 wt% a decrease in the *E''* was observed with a value of 0.54 MPa.

The tan δ of the pure PVDF fibres was much lower than that of the fibre containing the $CeNbO_4$ as seen in Figure 5.36c. This suggests that the PVDF / $CeNbO_4$ fibres are performing

as better damping materials. However, this can be deceptive as the tan δ is the ratio of the *E''* / *E'* and when the values individually vary largely it can suggest a material is damping more effectively. When looking at the overall values on all three graphs it can be said that the pure PVDF overall displays more effective *E''* and *E'*. The T_g of the pure PVDF was -47 °C. The addition of the $CeNbO_4$ resulted in an increase in the T_g displaying values of -40.2 °C and -39.0 °C for the ceramic loading of 1 wt% and 3 wt% respectively. Increasing the content of ceramic to 5 wt% and 10 wt% resulted in the T_g decreasing to -41.3 °C and -42.1 °C. This trend contrasts that of the PVDF / $NaNbO_3$ which demonstrated an increase in the T_g with an increase in the ceramic content. Overall, in comparison to the pure PVDF, there is an increase in the T_g. However, when comparing the loading of the $CeNbO_4$ within the polymer there is a decrease in the T_g is observed with an increase in the content of the ceramic. It can also be mentioned here that the SEM images within 5.1.4 demonstrate agglomeration of the ceramic particles with polymer covering the surface to produce bead-like structures. This might play a role in decreasing the T_g with the increase in ceramic as the agglomerates may not be as well distributed allowing for some movement of the chains with an increase in the content of the ceramic. It could also be that the large particle size of the $CeNbO_4$ and large agglomerate size could cause an increase in slippage and debonding of the ceramic within the chains allowing a small increase in chain movement.[361] Overall, the Tan δ is in line with what is expected to occur with the addition of filler. Zhao *et al.*[368] demonstrate an increase in the Tan δ with the addition of MnO_2 filler and is associated with the decrease in molecular movement of the chain within the amorphous region.

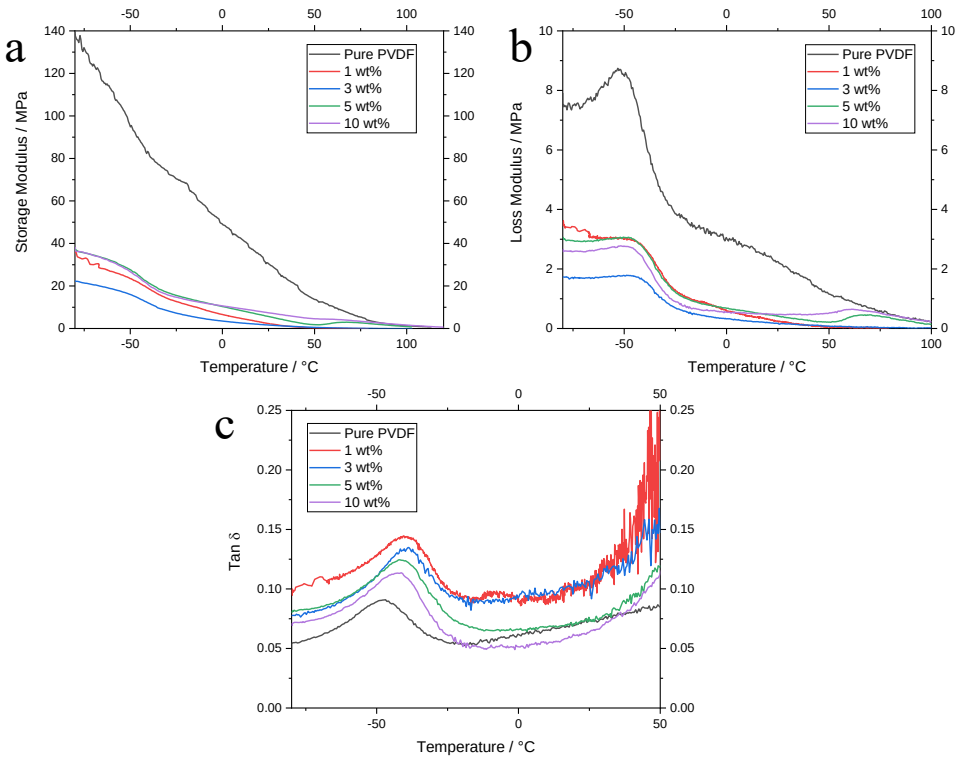

Figure 5.36. DMTA of the PVDF / $CeNbO_4$ fibres 1 wt% – 10 wt% showing a decrease in overall damping properties with the addition of the $CeNbO_4$.

5.3.7 Summary

The addition of the three types of niobium oxide ceramic particles had shown a reduction in the thermal stability of the PVDF. A decrease in the degradation temperature of 463 °C to 340 °C – 413 °C for the PVDF / niobium oxide ceramic occurred. The PVDF / $NaNbO_3$ and PVDF / $KNbO_3$ fibres had all displayed similar onset degradation temperatures, where a decrease in the value was displayed for both. While the PVDF / $CeNbO_4$ fibres displayed an overall larger decrease in the onset degradation temperature. This overall decrease in the degradation temperatures of the PVDF / niobium oxide fibres was suggested to occur due to an increase in the defects occurring within the polymer matrix due to the addition of the ceramic and a decrease in crystallinity.[364] It could be said that the PVDF / $CeNbO_4$ displayed a larger decrease in the onset degradation temperature due to the larger particle size of the $CeNbO_4$ which could have resulted in a higher degree of defects within the material. Bairagi and Ali[365] demonstrated similar results with PVDF / KNN nanorods. Here a decrease in the onset degradation temperature was observed and suggested to occur due to a decrease in the crystallinity of the polymer. In addition to this, the overall decrease in degradation temperatures and a reduction in thermal stability could be due to the poor thermal conductivity of the ceramic materials which

causes areas of the polymer to heat up with poor energy dissipation across the entire material. This results in a lower degradation of the material. It should also be mentioned here that the successful loading of the niobium ceramic was carried out for all three sets of ceramics as an increase in residual mass was observed with an increase in the content of the ceramic fillers.

Overall, the damping properties of the PVDF / $CeNbO_4$ have been displayed to be weaker than that of the PVDF / $NaNbO_3$ fibres and the PVDF / $KNbO_3$ fibres. As mentioned in 5.3.2 the particle size of the ceramic may influence the mechanical performance of the fibres. The increase in particle size reduces the connectivity of the polymer matrix and increases the level of defects in the polymer matrix and resulting in a decrease in the mechanical performance of the fibre composite. Out of the three PVDF / niobium oxide materials, the PVDF / $KNbO_3$ fibres demonstrated the highest damping properties, potentially due to the higher crystallinity of the material, and small particle size as mentioned above. However, there are still more studies required with this material on the interfacial interactions between the polymer and the ceramic as there is an odd decrease in the T_g at the lower loading of ceramic which suggests an increase in the mobility of the polymer chains with the addition of a ceramic. The materials produced here all display low damping properties in comparison to the literature where values of 4.5 – 8 GPa and above are generally reported for PVDF / composite materials. This may occur due to the thin sample sizing within this work which may result in lower damping values[368,369]

The new work demonstrated within this section demonstrates that the damping properties of PVDF can be enhanced with the addition of $KNbO_3$ ceramic filler. It also demonstrates that $NaNbO_3$ has little influence on the damping properties and that $CeNbO_4$ produces a material with poor damping properties. Overall, it also demonstrates that the degradation temperatures of the PVDF decrease with the addition of the ceramics.

5.4 Sound Testing of PVDF / Niobium Oxide Fibres

Following on from the characterisation of the electroactive phase of the PVDF and the viscoelastic damping properties it was decided to use the PVDF containing 5 wt% of the ceramics as it provided high values for the β polymorph, and the content of the ceramic could act as a secondary component for the piezoelectric effect to take place. It can also be mentioned that the higher loading of 10 wt% was not added for two reasons (i) The viscoelastic damping properties of the 10 wt% were lower than the 5 wt% for all three of the PVDF / niobium oxide materials. (ii) The size of the electrospun mat was small and difficult to fit within the impedance tube for accurate measurements. Alongside this, two foamed backings were used to assist in increasing the sound absorption properties of the material with PET being the low-density variant and PU being the high-density variant. These two materials were used as it is mentioned within the literature that density is a large factor in increasing the damping properties and it was

essential to determine this here.[61] Alongside this PU is used on a commercial level for sound damping within vehicles. Within the automotive industry, foamed materials are currently used and are effective at damping sound. However, as mentioned in 2.2.2 the addition of non-woven porous material may assist in influencing the sound damping properties of the overall system.

5.4.1 PET / PVDF / Niobium Oxide Fibre Sound Testing

The PET / PVDF / niobium oxide system was produced by cutting the samples into the side of the tub and placing them on top of each other in the order of PET at the back and the PVDF / niobium oxide fibre mat in front of it. The standalone PET foam displays a very low sound absorption coefficient across the entire frequency range in comparison to the dual sound damping system of the PET with the fibrous mats added to the front. A frequency range of 0 – 6400 Hz was analysed as this is range as it is in the audible hearing range. The highest absorption coefficient is achieved at 6000 Hz with a value of 0.44. Similar results for PET foam have previously been demonstrated with a maximum sound absorption coefficient of 0.42 observed at 6000 Hz.[378] To increase the sound absorption properties, the PVDF fibres were added to the surface of the material. However, this resulted in the formation of a double resonance peak rather than an increase in sound absorption coefficient across the entire frequency range with a drastic increase in damping properties with the addition of a small amount of PVDF / niobium oxide fibres. A drastic increase in the damping properties with the addition of the fibre mats could be that the fibres assist in increasing the tortuosity of the system. This increase in tortuosity has previously been shown to increase the damping properties of a material. Khan *et al*.[98] demonstrated a similar result where the addition of a fibrous mat to the front of a foamed backing increased the damping properties of the material. It was suggested to occur due to an increase in tortuosity of the system and in turn, increased airflow resistivity of the material enhancing the damping properties. An increase in air flow resistivity causes more friction between the air molecules are increase the absorption of the sound energy.[54]

Figure 5.37 demonstrates the sound absorption constant of the PET film and the PET film with the PVDF fibre composite attached to the front of it. It Is demonstrating poor damping properties of the standalone PET and the formation of a double resonance peak with the addition of the PVDF fibre composites. The first resonance peak was observed between 1000 Hz – 1500 Hz and a secondary peak occurred at approximately 5000 Hz. The addition of ceramic to the fibres had shown changes in the absorption coefficient at the lower frequency range peak, the PVDF / $KNbO_3$ and the PVDF / $NaNbO_3$ have a lower absorption coefficient than the pure PVDF and the PVDF / $CeNbO_4$ fibres. At the higher frequency absorption peak, the PVDF / $KNbO_3$ and the PVDF / $NaNbO_3$ have a higher intensity peak in comparison to the pure PVDF and PVDF / $CeNbO_4$. The formation of a double resonance peak has previously been

demonstrated by sound damping materials which have a back cavity behind the bulk material which has suggesting to occur due to the frequency selected sound absorption as a result of sound resonance.[103] The porous nature of the PET may be causing the material to act similarly to an air cavity resulting in the formation of the double resonance peak. It has been suggested that the airspace between a fibrous mat and the rigid backing of the impedance tub generates a resonance structure which leads to the creation of the double resonance peak.[379] This may be the factor that is causing the formation of the two peaks.

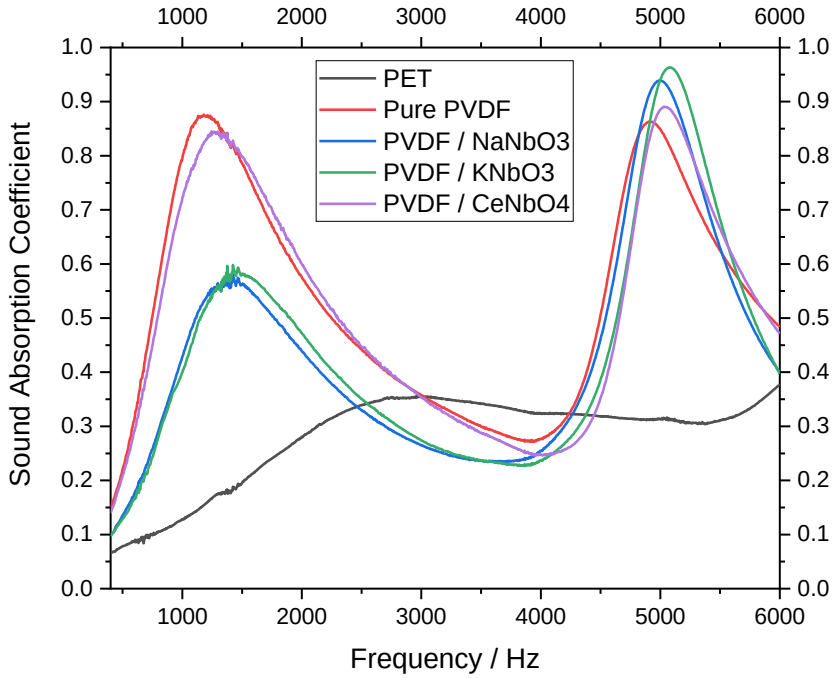

Figure 5.37. Sound absorption coefficient vs. frequency of the PET / PVDF / niobium oxide fibres showing two main resonance peaks and an increase in damping properties with the addition of a PVDF fibre mat.

To further analyse the influence the fibres demonstrated on the sound absorption properties of the sound damping system the average fibre diameters were plotted with the noise reduction constant (NRC) values. Figure 5.38 demonstrates the change in absorption coefficient with the changes in fibre diameter. Here the increase in fibre diameter demonstrates an increase in the NRC. As expected, the PET foam alone demonstrated a low NRC value of 0.12. The addition of pure PVDF resulted in the highest NRC values. The addition of the PVDF / niobium mat resulted in a decrease in the NRC with the PVDF / $NaNbO_3$, PVDF / $KNBO_3$, and PVDF / $CeNnO_4$ displaying values of 0.28, 0.28, and 0.40 respectively. The average fibre diameters also correlated with the decrease in low-frequency absorption where a decrease in the fibre diameter led to a decrease in the NRC values. This is unexpected as a decrease in fibre diameter is

typically associated with an increase in the sound absorption properties of a material due to an increase in the surface area of the material increasing tortuosity of the material increasing the airflow resistivity.[54,62,100,101] This provides the sound wave with more points of contact when entering the material for effective sound absorption. The decrease in the NRC may have occurred due to an increase in reflection of the sound when hitting the surface of the material resulting in a lower content of the sound being absorbed by the material.

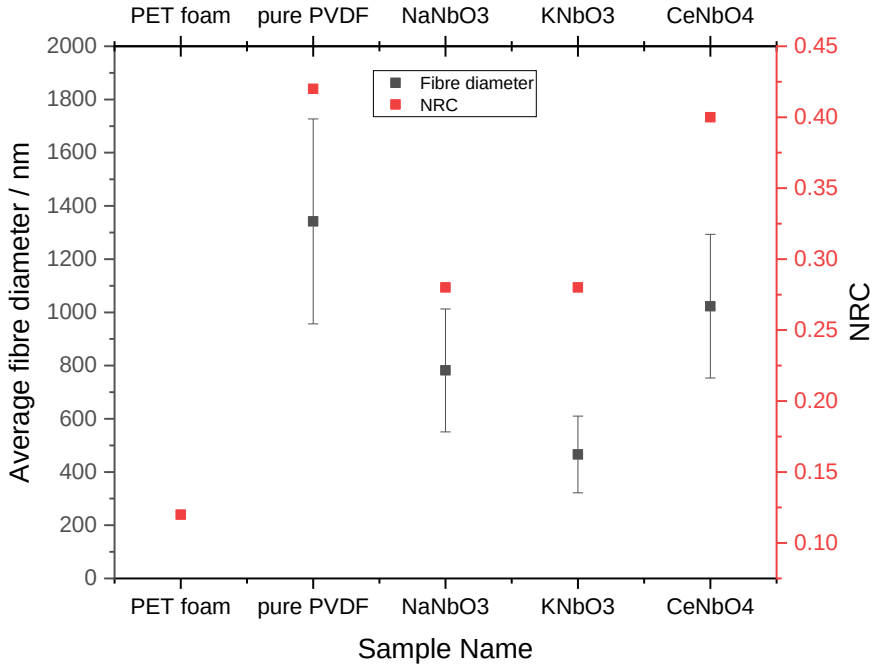

Figure 5.38. The trend between the average fibre diameter and noise reduction constant (NRC) for the PET foam, pure PVDF, and PVDF / niobium oxide fibres.

The relative thickness also demonstrates a contrasting result to what is expected. The PET/PVDF/$CeNbO_4$ decreases in thickness in comparison to the other samples and an increase in the NRC is observed. It was expected for the PET / PVDF / $CeNbO_4$ to have weaker damping properties as the literature demonstrates that decreasing sample thickness results in a decrease in the damping properties.[96,97] The samples are all electrospun using the same volume of solution. It could be mentioned that the material may have a higher volume of fibres within the small area. It has previously been shown that increasing the density of the material results in an increase in the tortuosity of the material resulting in a higher level of airflow resistivity.[61] This may occur here as the same volume of fibres is condensed into a smaller area and impacts the tortuosity of the material as a result of this the material performs better at the lower frequency range.

Table 5.13. The percentage thickness ratio of each component within the PET/PVDF/niobium oxide composite system.

Sample name	PET Relative Thickness %	PVDF/Ceramic Relative Thickness %
PET / PVDF	93.9	6.1
PET / PVDF / $KNbO_3$	93.3	6.7
PET/ PVDF / $NaNbO_3$	93.9	6.1
PET / PVDF / $CeNbO_4$	96.5	3.6

5.4.2 PU / PVDF / Niobium Oxide Fibre Sound Testing

Following on from testing the dual sound damping material with PET foam as the backing it was decided to alter the backing to a PU which had a higher density to prevent the foam from acting as a back cavity and more like a traditional sound-absorbing material used within vehicles. Figure 5.39 demonstrates the sound absorption coefficient of the analysed PU foams and the PU / PVDF / niobium oxides. It displays similar sound damping properties across the entire frequency range.

Figure 5.39 demonstrates the sound absorption coefficient of the PU / PVDF / niobium oxide system across the entire frequency range, where the damping properties are similar for all systems and a shift to lower frequencies for the fibres containing $KNbO_3$. The standalone PU foams analysed here display 3 resonance peaks at 650 Hz – 1400 Hz, 1400 Hz – 2000 Hz, and 5000 Hz – 6000 Hz. The initial resonance peak at 650 Hz – 1400 Hz had shown to rapidly increase the absorption coefficient. Within this range, a maximum coefficient of 0.77 is achieved as seen in Table 0.3. At the second resonance peak at 1400 Hz – 2000 Hz, a maximum absorption coefficient of 0.80 is achieved within this range. The absorption coefficient then begins to decrease before increasing and levelling off between 5000 Hz – 6000 Hz. The PU foams overall demonstrated a more effective sound absorption coefficient in comparison to that of the PET foams. This occurs due to the difference in the density of the foams. As mentioned in 2.2 the density of a material is shown to influence the damping properties and is shown within these results, with the PU demonstrating more effective sound damping properties across the entire frequency range while the PET displayed poor sound absorption properties.[61] Similar results are shown for PU foams in the literature where the material performs most effectively between the frequency range of 1000 – 2000 Hz, with maximum absorption coefficients of 0.6 – 0.9.[51,187,380,] This demonstrates that the PU foam chosen for this work is effective at sound absorption and in line with previous studies.

To increase the surface area of the PU foams the pure PVDF and PVDF / niobium oxide fibres were added to the system. The addition of the pure PVDF fibres on the surface of the PU increased the maximum sound absorption at the lower frequency range between 650 Hz – 1400 Hz. A maximum sound absorption coefficient was achieved at 1400 Hz with a value of 0.84. A shift to lower frequencies was observed for the second absorption coefficient at the higher frequency range. The addition of the PVDF / $NaNbO_3$ fibrous mat resulted in an overall increase in the sound absorption coefficient in comparison to the PU and the pure PVDF. The maximum peak of the sound absorption coefficient at the lower frequency shifted to the right to 1600 Hz displaying a coefficient value of 0.88. The sound absorption at the second frequency range had demonstrated an increase, alongside the third resonance peak shifting to a lower frequency range which was also observed by all of the dual PU/PVDF fibre systems. In comparison, the addition of the PVDF / $KNbO_3$ fibres has been shown to shift the first resonance peak to a lower frequency range of 1250 Hz displaying an increase in the absorption coefficient to 0.90. The resonance peak at the higher frequency range has been shown to produce the highest sound absorption value from the five samples analysed. While the addition of PVDF / $CeNbO_4$ was like that of the pure PVDF with the absorption peak at the lower frequency range overlapping that of the pure PVDF, displaying a sound absorption coefficient of 0.84. At the higher frequency range, the PVDF / $CeNbO_4$ had shown to display a lower sound absorption coefficient in comparison to the pure PVDF. These materials perform within a similar range to those within the literature. The addition of filler has been shown to produce a narrower range of sound absorption coefficients at 1000 Hz ranging from 0.8 – 0.92. [94,106,107] This suggests that the materials here may perform similarly to those within the literature.

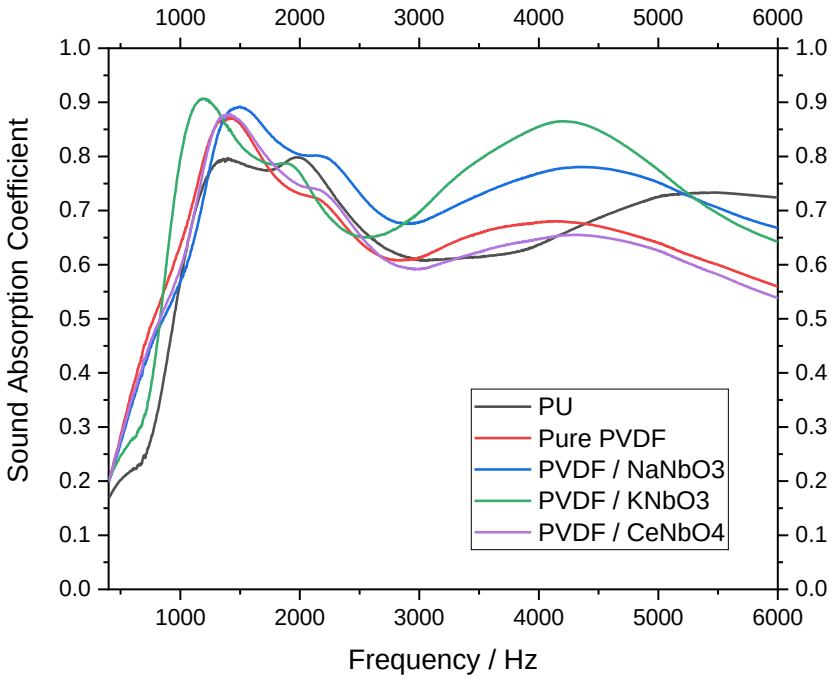

Figure 5.39. Sound absorption coefficient vs. frequency of the PU / PVDF / niobium fibres showing several resonance peaks and an overall increase in sound damping properties with the addition of niobium oxides.

Table 5.14. demonstrates the relative thickness of the materials. The changes in the thickness of the PVDF composite fibre have little influence on the damping properties of the PVDF. The absorption coefficient is similar across the entire frequency range and only PVDF / $KNbO_3$ fibres have a shift to a lower frequency range. This suggests that fibre diameter is influencing the shift in the absorption coefficient to the lower frequency range as expected.

Table 5.14. The percentage thickness ratio of each component within the PU/PVDF/niobium oxide composite system.

Sample name	PU Relative Thickness %	PVDF/Ceramic Relative Thickness %
PU / PVDF	87.8	12.2
PU / PVDF / $NaNbO_3$	86.6	13.3
PU/ PVDF / $KNbO_4$	87.9	12.1
PU / PVDF / $CeNbO_4$	92.8	7.2

The NRC values for the pure PVDF can be seen in Figure 5.40. The PU foam displayed an NRC of 0.42. The addition of the pure PVDF fibres resulted in an increase in the NRC to 0.44. In an attempt to further enhance the NRC, the pure PVDF was replaced with the PVDF / $NaNbO_3$ which had shown little influence on the NRC producing a value of 0.44. The PVDF / $KNbO_3$ had shown the greatest influence on the NRC producing a value of 0.52. While the PVDF / $CeNbO_4$ had shown a reduction in the NRC to 0.43 in comparison to the pure PVDF fibres. It should be mentioned here that the NRC value was an average of 4 frequencies 500 Hz, 1000 Hz, 1500 Hz and 2000 Hz.

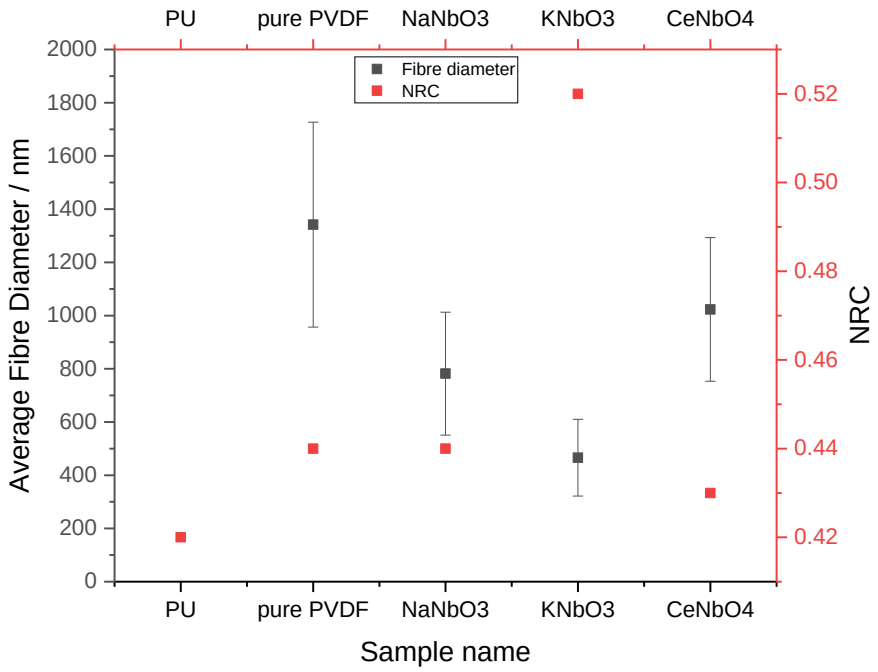

Figure 5.40. The trend between the NRC and average fibre diameters where a decrease in fibre diameter shows an increase in NRC for the PU, Pure PVDF and PVDF / niobium composite fibres.

The average fibre diameter was analysed against the NRC to further determine the influence of the change in fibre diameter on the sound damping properties of the material. The pure PVDF had an average fibre diameter larger than all of the PVDF / niobium oxide materials. However, the NRC values suggest that the addition of the $NaNbO_3$ and the $CeNbO_4$ has little influence on the sound absorption properties. Overall, the sound absorption properties of the PVDF / $NaNbO_3$ and PVDF / $CeNbO_4$ are much better than the pure PVDF fibres across the entire frequency range. While the PVDF / $KNbO_3$ display the smallest fibres of those analysed here it can be seen that this material also demonstrates the highest NRC and overall better sound

absorption properties across the entire frequency range. It can be said that the average fibre diameter plays a role in the overall sound absorption properties of the material. However, there is still further study required here as it cannot be fully confirmed in the average fibre diameters are the sole component influencing the sound absorption properties.

The piezoelectric properties of the PVDF / $KNbO_3$ fibres may also have a role in increasing the NRC of the material alongside the mechanical properties which were demonstrated to be much higher than that of the other PVDF / niobium oxide fibres The increase in the absorption coefficient and NRC with the addition of the fibrous mats with and without the addition of the ceramic may be associated with the increase in the surface area of the materials. The readily moving fibres allow for effective energy dissipation across the material when the acoustic energy begins to enter the material. The sound energy is then converted to thermal energy by the drag experienced between the vibrating air particles and the fibre surface.[107] The thinner fibres within the PVDF / niobium oxides have a higher surface area than the pure PVDF fibres, this provides more points of contact for the sound waves to interact with the fibres and results in increasing the conversion of the sound energy.[52,53] It also influences the tortuosity of the material where smaller fibres increase the airflow resistivity of the material resulting in loss of energy through frictional forces with the air particles within the fibre mats.[54,98]

5.4.3 Summary

The sound absorption coefficient for the PET in comparison to the PU was different with the PET demonstrating maximum values of 0.44 and the PU displaying maximum values of 0.80 at contrasting ends of the analysed frequency. These values were both in line with what was expected from them and are similar to the values demonstrated of 0.42 and 0.6 – 0.9 from previous studies on both the stand-alone PET and PU respectively.[51,187,378,381] For both systems, it was apparent that the addition of the pure PVDF demonstrated an improved absorption coefficient due to an increase in surface area the fibre mats bring to the dual set-up. The addition of the ceramic to the fibres displayed effective sound absorption across the entire frequency range when added to the PU and demonstrated little influence when added to the PET with a decrease in the absorption coefficient as seen with the fibre containing $NaNbO_3$ and $KNbO_3$. This decrease may have been associated with an increase in the reflection of the sound waves, reducing the sound absorption properties of the first resonance frequency in the PET / PVDF / $NaNbO_3$ or $KNbO_3$ fibres. The increase in the NRC of the PVDF / $CeNbO_4$ was unexpected as it produced a thinner mat. It was expected that this system would demonstrate lower damping properties at the low-frequency range. However, this was not the case and a higher NRC was displayed. This may have occurred due to a higher quantity of fibres being compacted into a

smaller volume area increasing material density. This leads to an increase in the tortuosity of the material and in turn results in an increased air flow resistivity. This increase in air flow restively results in higher frictional force between air particles resulting in the material absorbing higher quantities of sound energy. [54,62,100,101]

The NRC values for the PET also demonstrated a much lower value than the PU with 0.13 and 0.42. In both cases, the addition of the pure PVDF fibres led to an increase in the absorption coefficient across the entire frequency range, with the PU-backed fibres displaying higher absorption coefficients in comparison to the PET-backed fibres. The standout material from those analysed containing the niobium oxides was the PU / PVDF / $KNbO_3$ which demonstrated the highest NRC values of 0.52 and a shift to the lower frequency range of 1250 Hz. This may have occurred due to a decrease in the fibre diameter of the material which increased the surface area of the fibres. This allowed for more points of contact between the fibres and sound resulting in more sound absorption through frictional forces between fibres. [52,53]

Overall, it can be said that the addition of the PVDF / niobium oxide fibre mats increased the sound absorption properties for the PU foams across the entire frequency range and increases the sound absorption properties at the low and high-frequency range within the PET foams displaying two resonance peaks. It should also be mentioned that the confirmation of the piezoelectric effect taking place cannot be made here as the frequency range in which the effect takes effect is below the frequency range analysed within this material due to the impedance tube being too narrow in diameter for reliable results.

The new work within this chapter demonstrates that the addition of a fibrous PVDF / niobium oxide composite mat can enhance the damping properties of PET and demonstrates a double resonance peak. It also demonstrates that the addition of the fibrous PVDF / niobium oxide composite mat to PU assists in increasing the damping properties in the lower frequency range.

Chapter 6 Electrospinning PVDF / Silicon Ceramics

6.1 Introduction

Following on from the niobium oxide ceramic materials specifically known for their electroactive properties two types of silicon-based ceramics were added to the pure PVDF fibres to produce a polymer composite fibrous mat. The silicon ceramic powders added were SiC and Si_3N_4 where 1 wt% – 10 wt% was added to the fibres. These ceramics were added to determine the influence low dielectric non-piezoelectric ceramic particles would have on the morphology, crystallinity, thermal-mechanical properties, and acoustic damping properties of the polymer fibres in comparison to the niobium oxides.

SiC and Si_3N_4 are known for their high thermal conductivity properties, where both have previously been displayed to enhance the thermal conductivity of PVDF. The addition of SiC to PVDF films has previously been shown to enhance the thermal conductivity of the material.[382] This has also been demonstrated with the addition of Si_3N_4 to PVDF fibres enhancing the piezoelectric properties of PVDF fibres alongside increasing the thermal conductivity of the materials.[297] It is desirable to add SiC and Si_3N_4 as fillers as an increase in the thermal conductivity properties of the material could potentially influence the thermal energy dissipation of the acoustic sound across the material when the conversion of the acoustic energy to thermal energy occurs. These materials were analysed here to decide on which ceramic would be taken forward in the next set of tests where the silicon-based ceramic would be paired with the $KNbO_3$ for a PVDF / mixed ratio composite system to balance out the properties demonstrated by the raw materials for a balance between the electroactive phase of the PVDF, and the thermal properties of the silicon-based ceramics and the piezoelectric properties of the $KNbO_3$.

6.1.1 Precursor Analysis on the Silicon Ceramics

The ceramic particles had an average particle size of 865 ± 268 nm and 758 ± 204 nm for the SiC and the Si_3N_4 powders respectively. The particle sizes were analysed by taking particle value values from 100 different points across the SEM image. When analysing these values against the SEM images in Figure 6.1a – b, the particle sizes of the ceramic powders were similar to each other and within the same experimental error. The morphology of the particles was drastically different from each other, where the SiC had a typical morphology for ceramic particles, while the Si_3N_4 displayed a flat morphology seen in Figure 6.1a, and Figure 6.1b

respectively. The Si_3N_4 particles were milled before use due to the agglomeration of the particles where the ceramic particle size exceeded 100 μm as seen in Figure 6.1c. The SiC particles were not milled as the powder was fine and ready for use, while in contrast, the Si_3N_4 powder had agglomerated as seen in Figure 6.1c.

In comparison to the particle sizes of the niobium oxides, the silicon-based ceramics were larger in average particle size where the $NaNbO_3$ and $KNbO_3$ particles of 410 ± 140 nm and 351 ± 134 nm respectively and a similar particle size to the $CeNbO_4$ of 796 ± 185 nm.

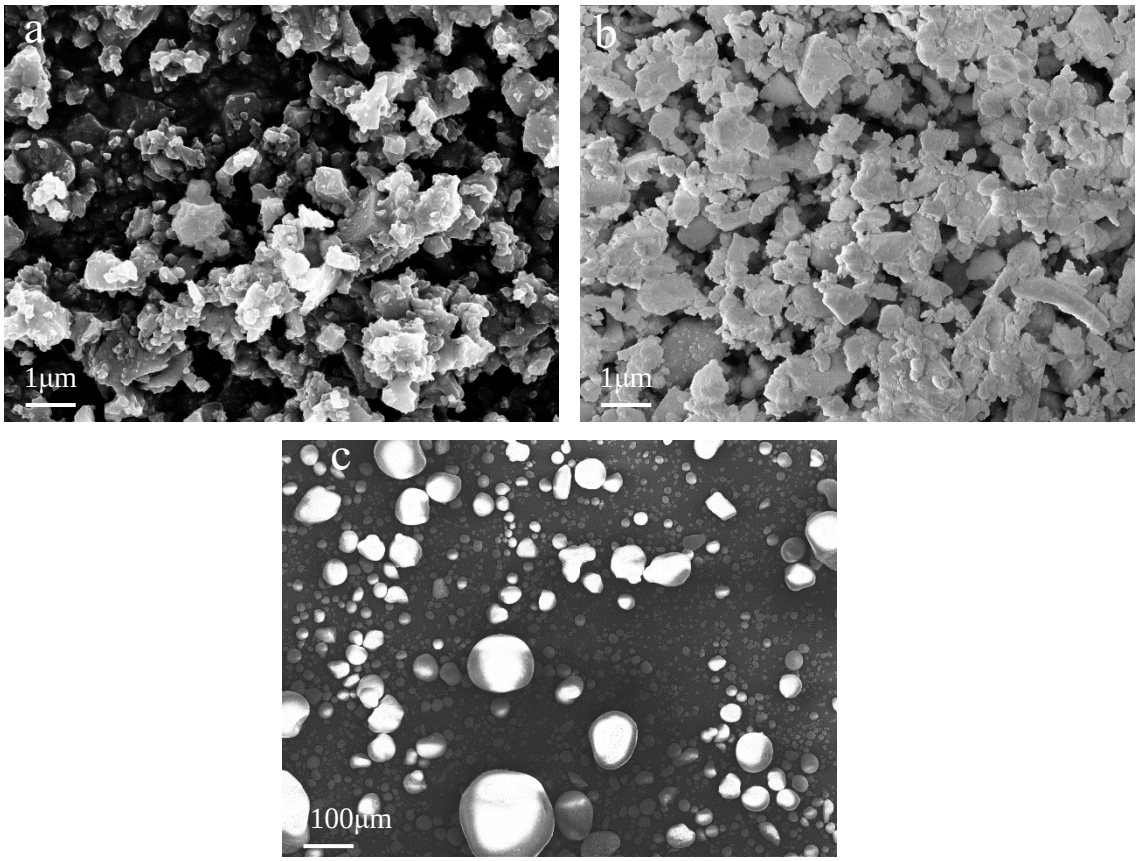

Figure 6.1. The morphology of the silicon-based ceramic particles. (a) SiC, (b) Milled Si_3N_4, (c) Pre-milled Si_3N_4.

6.1.2 PVDF / SiC Fibre Morphology

The successful formation of electrospun PVDF / SiC fibres was achieved where all parameters were kept constant in line with the PVDF / niobium oxide fibres. The voltage was altered with the addition of the SiC to ensure a stable Taylor cone was maintained for effective electrospinning. Figure 6.2 displays the morphology of the PVDF / SiC fibres for all of the wt% added to the polymer. The fibres produced in Figure 6.2a and Figure 6.2b are smooth and with a bead-free morphology. The PVDF / SiC fibres produced in Figure 6.2c and Figure 6.2d display the formation of beaded structures at the higher loading of the 5 wt% – 10 wt% SiC ceramic.

This may have resulted from the agglomeration of the SiC particles at the higher loading of the ceramic like what occurred with the PVDF / $CeNbO_4$ fibres at the higher loadings of the ceramic filler. This has also been demonstrated with the addition of $BaTiO_3$ to PVDF where agglomeration of filler resulted in the formation of beads on the fibres.[355] Suggesting that a similar agglomeration of filler may have occurred in this work.

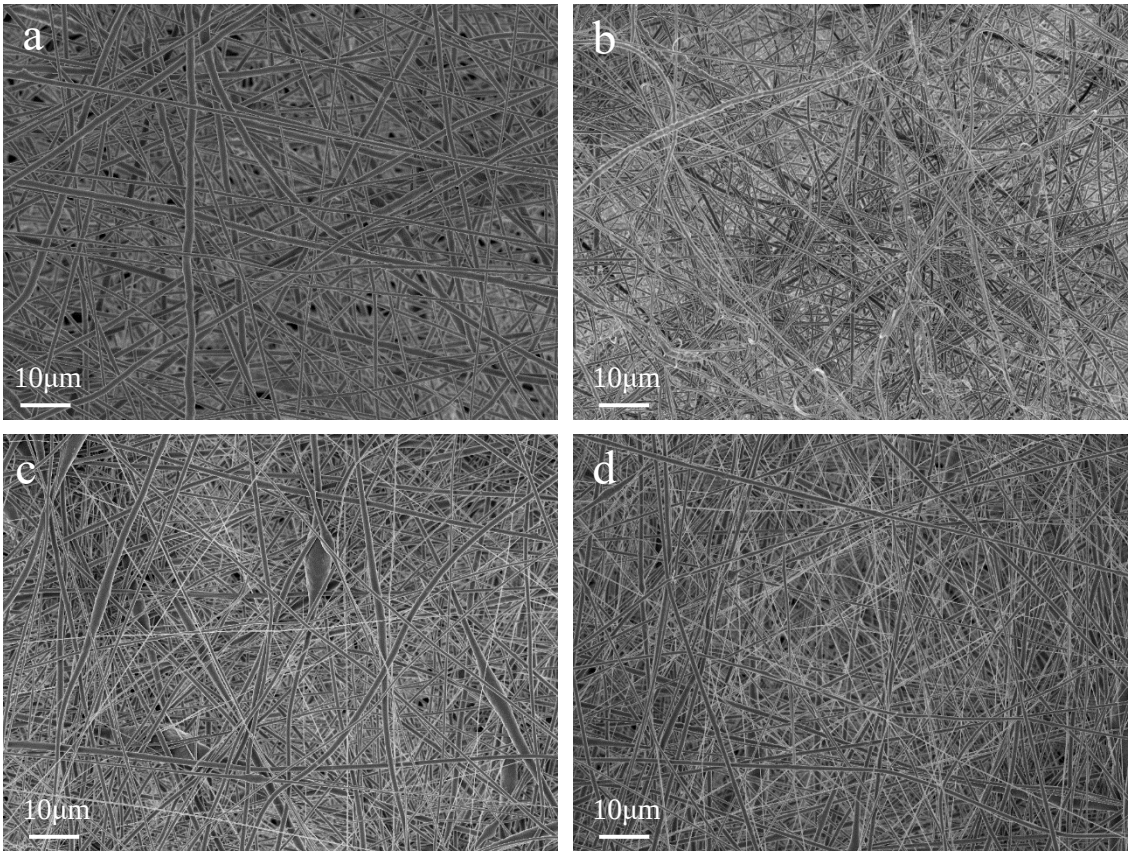

Figure 6.2. SEM images of the PVDF / SiC 1 wt% – 10 wt% displaying the fibre morphologies. (a) 1 wt% SiC, (b) 3 wt% SiC, (c) 5 wt% SiC (d) 10 wt% SiC.

To analyse the beaded structures further and determine if they were agglomerates of SiC covered in the polymer EDS imaging was carried out as seen in Figure 6.3. The beaded structures can be seen to have high quantities of green spotting which was marked as the silicon atoms of the ceramic. This suggests that these beaded areas are agglomerated SiC particles that have been covered by the PVDF polymer. The formation of these beaded structures could have occurred due to the large particle size of the SiC alongside the higher loading quantity where agglomeration of the ceramic particles would produce large agglomerates which could be covered by the polymer producing the beaded structure. The structure of the beads is like that of those observed in the PVDF / $CeNbO_4$ with an irregular structure which could also indicate a similar scenario.

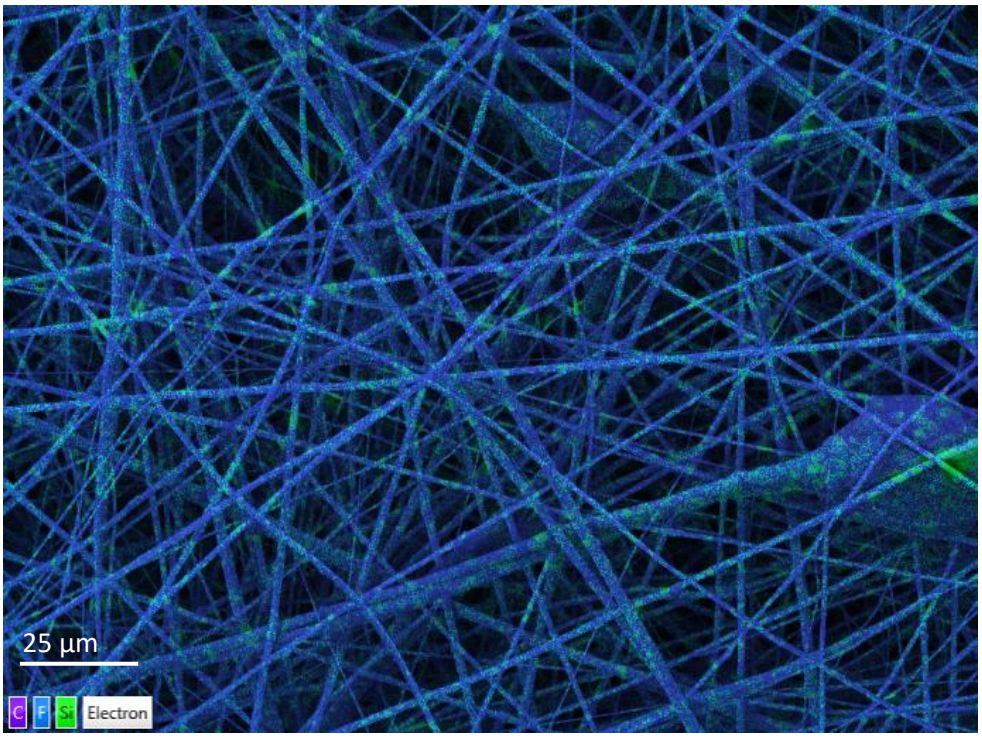

Figure 6.3. EDS image of the PVDF / SiC 10 wt% fibres showing the distribution of the SiC across the material and high concentrations at beaded zones.

The average fibre diameters of the materials were calculated using ImageJ. The average fibre diameter of the pure PVDF was 1342 ± 385 nm as mentioned previously. The average fibre diameters of the PVDF / SiC had been shown to decrease with the addition of the 1 wt% SiC, displaying a diameter of 969 ± 211 nm. The addition of 3 wt% SiC led to an increase in the average fibre diameter resulting in a value of 1158 ± 301 nm. From there the addition of higher quantities of SiC, 5 wt% and 10 wt%, led to a decrease in the average fibre diameter producing diameters of 691 ± 266 nm and 657 ± 245 nm respectively as seen in. These results are different to the niobium oxide ceramics where generally the average fibre diameter increase with an increase in the ceramic loading with the PVDF / $KNbO_3$ fibres and the PVDF / $CeNbO_4$ fibres. It is more in line with the PVDF / $NaNbO_3$ fibres where the ceramic content increase correlated with a decrease in average fibre diameters. The fibres produced here are within a similar fibre diameter to those produced using Si_3N_4 in the literature of 615 nm.[297] However, they are larger than those produced with niobium oxide materials ranging between 100 nm – 500 nm. [306,307,308,309]

Table 6.1. The processing parameters and average fibre diameters of the PVDF / SiC fibres.

SiC Weight / %	Applied Voltage / kV	Average Fibre Diameter / nm
0	7.14	1342 ± 385
1	6.50	969 ± 221
3	6.66	1158 ± 301
5	6.65	691 ± 266
10	6.69	657 ± 245

To further investigate the influence of the SiC on fibre diameter, the viscosity of the solutions was analysed as seen in Table 6.2. These results were also like the PVDF / niobium oxide solutions where the initial addition of the ceramic led to an increase in the viscosity and a decrease in the average fibre diameter. The SiC is known to have a low dielectric constant reported as low as 2.71.[383] However, this could still influence the dielectric properties of the solution and assist in influencing charge density around the Taylor cone producing thinner fibres even with an increase in solution viscosity. Increasing the content of the ceramic led to a gradual increase in viscosity. The ceramic content of interest is at 5 wt% and above where the trend is not followed as it should. Here a decrease in the average fibre diameter occurs with an increase in the content of ceramic. This could occur as higher quantities of the ceramic increase the conductivity of the solution further and influence the stretching of the polymer jet to a higher degree than the lower quantities for the PVDF / SiC fibres. It could also occur due to the dielectric properties of the ceramic resulting in the formation of localised polarisation with the application of the electrostatic field. This could increase the coulombic forces experienced by the polymer jet resulting in higher levels of elongation and stretching of the fibres as mentioned previously to occur with the PVDF / niobium oxide fibres. It should also be mentioned here that the formation of the beads could lead to thinner fibres due to a higher portion of the polymer being used to engulf the ceramic agglomerates producing thin fibres around the beaded areas.

Table 6.2. The weight percent of SiC and solution viscosity.

SiC Weight / %	Viscosity / cSt
0	359 ± 7.44
1	672 ± 1.37
3	718 ± 2.48
5	707 ± 2.60
10	721 ± 2.01

The control over the fibre diameters distribution with the addition of the ceramic was analysed using the Gaussian distributions as seen in Figure 6.4. The distribution of the fibre diameters is like that of the PVDF / $NaNbO_3$ and PVDF / $CeNbO_4$ where a wide distribution of the fibre diameters is seen across a large range. The distribution width does not vary much depending on the content of the ceramic, however, shifts to a diameter lower range from 5 wt% content onward. As mentioned previously this may occur due to the higher content of ceramic influencing the conductivity of the solution and allowing for a higher charge density or the polarisation of the material influencing elongation and stretching of the fibres. This allows for the shift in the fibre diameters to lower diameters, however, does not narrow the distribution seen in the PVDF / $KNbO_3$ fibres. This suggests that there is overall some control provided with the addition and increase in the content of the SiC however if a narrow distribution is required it is difficult to achieve an increase in the content of this ceramic.

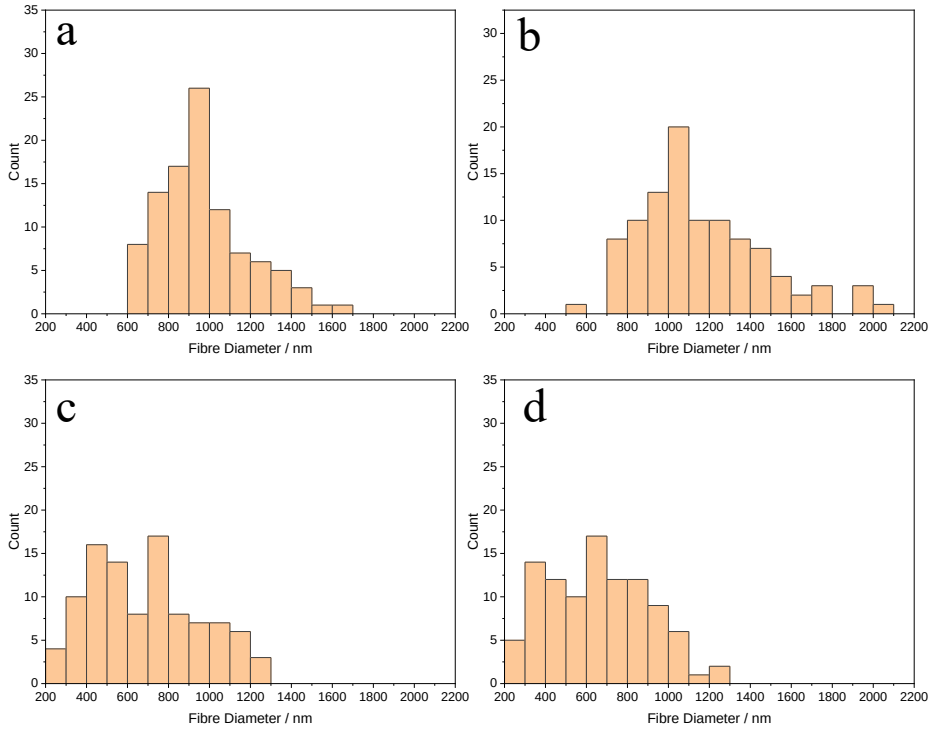

Figure 6.4. The histogram shows a shift in fibre distribution of the PVDF / SiC fibre to smaller diameters. (a) 1 wt% SiC content, (b) 3 wt% SiC content (c) 5 wt% SiC content (d) 10 wt% SiC content.

6.1.3 PVDF / Si_3N_4 Fibre Morphology

The successful formation of PVDF / Si_3N_4 fibres was carried out where the spinning parameters were kept in line with those used for the PVDF / SiC, with changes to the applied voltage to produce a stable Taylor cone for efficient electrospinning. The morphology of the PVDF / Si_3N_4 fibres can be seen in Figure 6.5. These fibrous mats displayed the formation of beaded fibres across all four of the ceramic loadings. The particle size of the Si_3N_4 was much larger than that of the PVDF / SiC and the PVDF / niobium oxide materials which may have resulted in the agglomerate size being much larger and producing beaded structures across the material even at the lower loading of the ceramic filler. This is evident within the EDS image seen in Figure 6.6 showing the distribution of the Si_3N_4 particles across the fibre mats. It displays the formation of the beaded structures which have a high spotting of the green-marked Si atoms. This suggests that the beaded structures could be agglomerated Si_3N_4 particles that have been covered in the PVDF polymer, like that observed in the PVDF / SiC and the PVDF / $CeNbO_4$ beaded fibres at the higher ceramic loading.

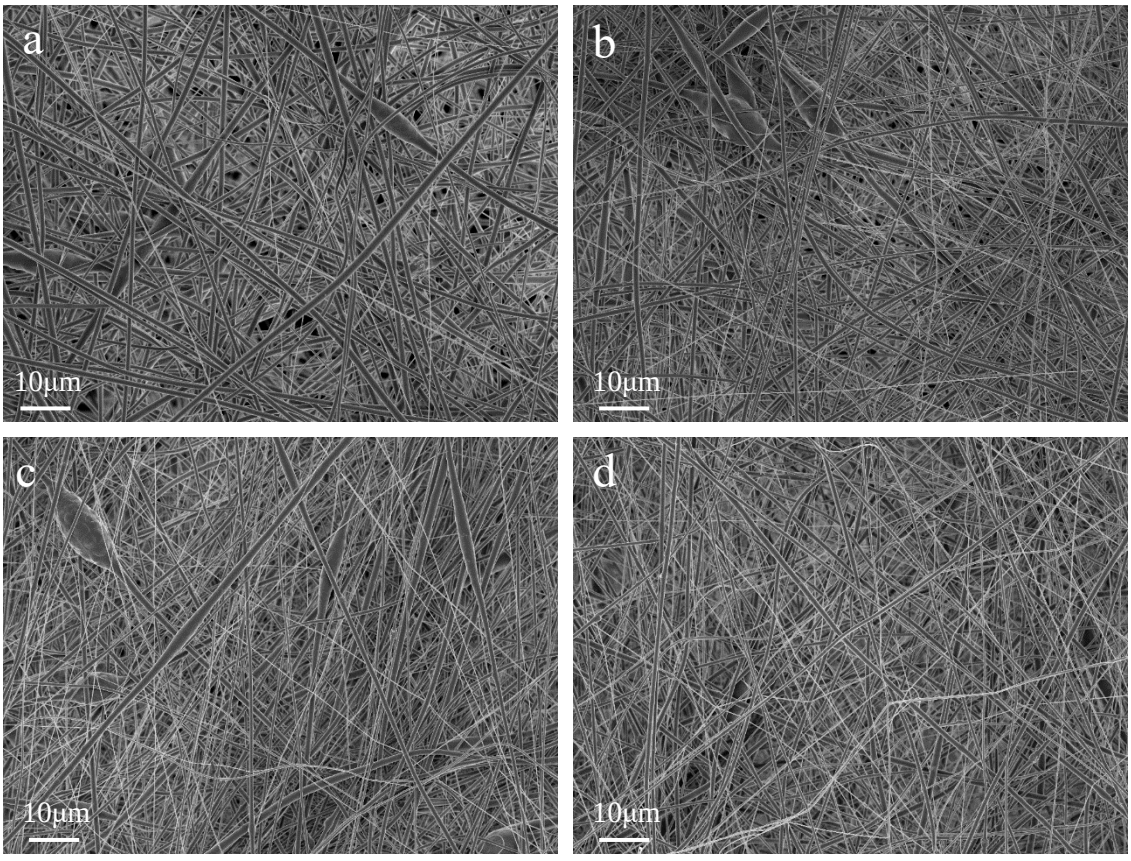

Figure 6.5. SEM images of PVDF / Si_3N_4 1 wt% – 10 wt% displaying the fibre morphology with beaded structures within the fibres. (a) 1 wt% Si_3N_4, (b) 3 wt% Si_3N_4, (c) 5 wt% Si_3N_4, (d) 10 wt% Si_3N_4.

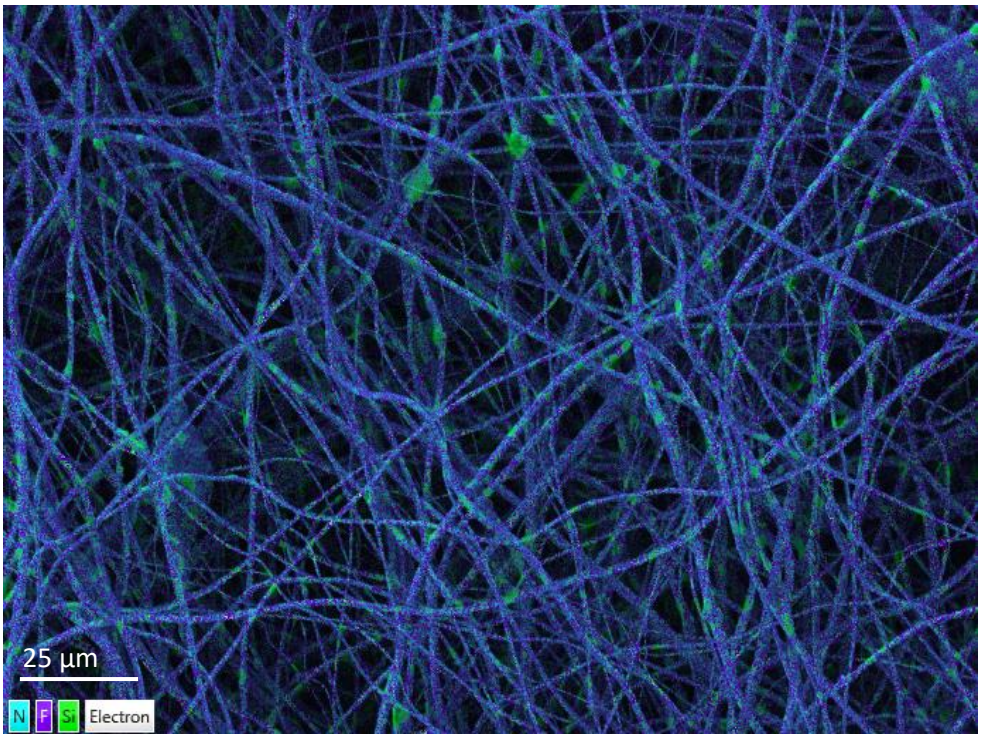

Figure 6.6. The EDS of the PVDF / Si_3N_4 10 wt% content fibres shows the distribution of Si_3N_4 across the material and at protruding zones.

The pure PVDF fibres displayed an average fibre diameter of 1342 ± 385 nm as mentioned previously. The average fibre diameters of the PVDF / Si_3N_4 fibres were within the experimental error with the addition of the ceramic in comparison to the pure PVDF fibres. The addition of 1 wt% Si_3N_4 resulted in an average fibre diameter of 966 ± 294 nm. The addition of 3 wt% Si_3N_4 resulted in a further decrease in the average fibre diameter producing values of 753 ± 257 nm. While further increasing the content of the Si_3N_4 to 5 wt% and 10 wt% resulted in little change to the average fibre diameters producing values of 764 ± 274 nm, and 715 ± 247 nm respectively as seen in Table 6.3. The decrease in the overall average fibre diameters at higher concentrations with the addition of the Si_3N_4 may be associated with the dielectric properties of the material which have previously been reported as 7.9.[384] This may increase in dielectric properties of the overall solution like the other materials and assist in decreasing the average fibre diameter through an increase in charge density around the Taylor cone. In comparison to the PVDF / SiC fibres, the PVDF / Si_3N_4 fibres are similar in diameter. They are also in line with the average fibre diameters of PVDF / Si_3N_4 fibres produced previously of 615 nm.[297]

Table 6.3. Processing parameters and average fibre diameters for PVDF / Si3N4.

Si_3N_4 Weight / %	**Applied Voltage / kV**	**Average Fibre diameter / nm**
0	7.14	1342 ± 385
1	6.30	966 ± 294
3	6.71	753 ± 257
5	7.01	764 ± 274
10	7.26	715 ± 247

To further investigate the influence of the Si_3N_4 on the fibre diameters it was analysed against the viscosity of the material as seen in Table 6.4. The addition of 1 wt% ceramic resulted in a large increase in the viscosity of the material and a decrease in average fibre diameter as demonstrated by all the previous solutions studied here. This was suggested to occur due to an increase in the dielectric properties of the solution with the addition of the ceramic. From here the addition of further quantities of ceramic had little influence on the viscosity which ranged between 690 cSt – 719 cSt. However, the average fibre diameter of the material gradually decreased suggesting that the Si_3N_4 was influencing the fibre diameter. The increase in solution viscosity is typically associated with a reduction in the formation of beaded structures. However here the increase in viscosity from the pure PVDF to the ceramic-loaded materials led to the formation of beads. As mentioned in 5.1.4 this was shown previously with the incorporation of TiO_2 to PEO fibres where the beaded structures were suggested to be agglomerates of the ceramics.[250] In this work the same could be mentioned and occurs at the lower content of the Si_3N_4 due to the larger particle size and larger agglomerates forming.

Table 6.4. The weight percent of Si_3N_4 and solution viscosity.

Si_3N_4 Weight / %	**Viscosity / cSt**
0	359 ± 7.44
1	719 ± 1.00
3	690 ± 0.66
5	695 ± 9.22
10	729 ± 7.47

The histogram seen in Figure 6.7 demonstrates that the addition of Si_3N_4 results in little control over the average fibre diameter, where a wide gaussian distribution is observed. The overall curve shifts to lower diameters; however, a wide curve is still observed. This suggests that the addition of higher quantities of the Si_3N_4 particles assists in giving control to produce

lower fibre diameters; however, does not assist in producing a homogenous fibre diameter. In comparison to the PVDF / SiC fibres, the PVDF / Si_3N_4 fibres have demonstrated a lower level of control over the fibre diameter. This may be due to the increase in the larger particle size and particle agglomeration of the Si_3N_4 particles which had a negative influence on fibre formation.

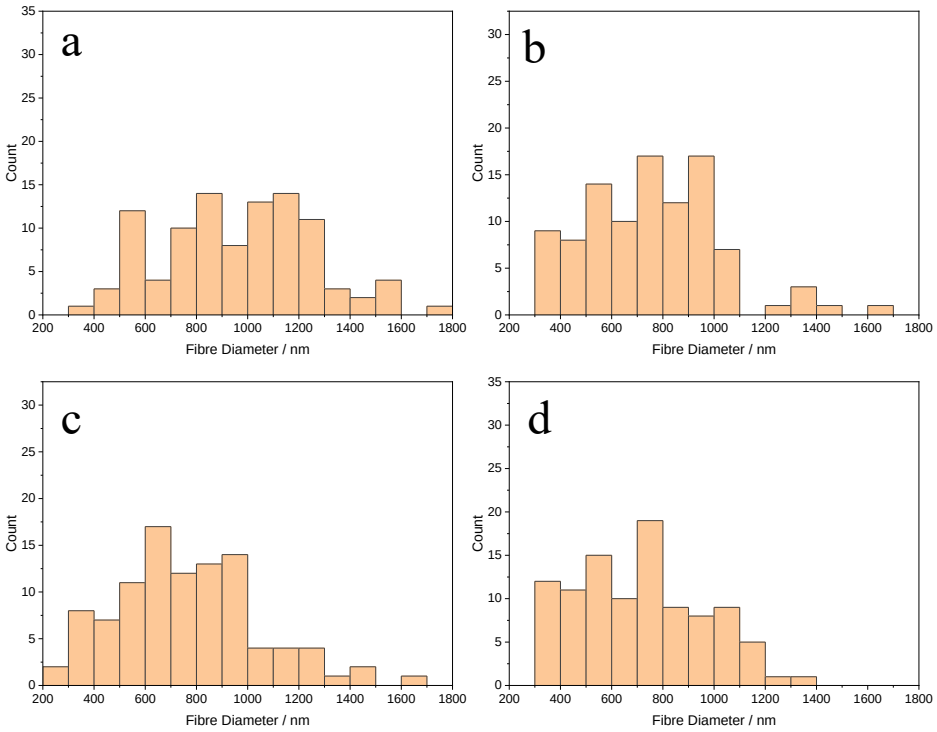

Figure 6.7. The histogram of the PVDF / Si_3N_4 fibre diameters shows little shift in the average fibre distribution. (a) 1 wt% Si_3N_4 content, (b) 3 wt% Si_3N_4 content (c) 5 wt% Si_3N_4 content (d) 10 wt% Si_3N_4 content.

6.1.4 Summary

The PVDF / SiC and the PVDF / Si_3N_4 fibres show similar morphologies where the formation of beads occurs in both cases. The PVDF / SiC fibres demonstrated the formation of beaded fibres at the 5 wt% and 10 wt% loadings only. The PVDF / Si_3N_4 fibres displayed beading for all the fibres produced from 1 wt% - 10 wt% ceramic loading. This may have occurred due to the agglomeration of particles that occurs which were covered by the polymer demonstrated in the EDS images. The Si_3N_4 has a similar particle size to SiC which results in larger bead formation even at the lower loading of ceramic where the agglomerated ceramic is covered in the PVDF polymer. This also occurred with the PVDF / $CeNbO_4$ fibres at the ceramic loading. Similar agglomeration of particles has been displayed previously with the addition of $BaTiO_3$ to PVA materials.[354] Similar studies have also been demonstrated with the addition of

$BaTiO_3$ to PVDF at high loadings.[355] Suggesting that agglomeration of ceramics can occur at higher loadings. The new work within this section demonstrates that the addition of SiC and Si_3N_4 can produce fibre diameters smaller than 1 μm and can assist in a reduction in the overall average fibre diameter with its initial addition. It also demonstrates that the addition of these types of fillers results in the formation of a beaded structure which may be agglomerated filler within the fibres as seen in the EDS images provided for each system.

Increasing the content of the ceramic in the PVDF / SiC fibres resulted in a decrease in the average fibre diameters while for the PVDF / Si_3N_4 there was little change in the average fibre diameter. At the highest weight loading the PVDF / SiC and the PVDF / Si_3N_4 produce fibres with diameters of 657 ± 245 nm and 715 ± 247nm respectively with the SiC demonstrating a similar influence over fibre diameter than the Si_3N_4. These values are in line with the average fibre size of PVDF / Si_3N_4 produced in previous work of 615 nm.[297] When compared to previous materials produced using niobium oxide filler the particle sizes are much larger in comparison to those ranging between 100 – 500 nm.[306,307,308,309] Both ceramic particles have a very low dielectric constant, which may influence the spinnability of the material. These fibre diameters are also in a similar range as the particle size of the filler. However, in this case, several areas of agglomeration are observed. The particle size may act to control the minimum fibre diameter that can be produced. However, as mentioned in the previous section there is little evidence to suggest that there is rheological influence with the addition of filler sizes on the minimum fibre diameter of the composites. The increase in electrical conductivity of the material due to the addition of the ceramic particles may result in thinning of the fibres when higher quantities of the ceramic are added as mentioned earlier with the PVDF / niobium oxide fibres. It may also be that the formation of beaded fibres led to some of the polymer not being distributed across the entire fibre effectively resulting in lower fibre diameter. Overall, it can be said that there is a reduction in control of the fibre diameter distribution with the addition of the PVDF / silicon-based fibres in comparison to the PVDF / niobium oxide fibres as the Gaussian distributions are across a much wider range for the PVDF / silicon-based fibres.

6.2 The Crystallinity of the PVDF / Silicon Ceramic Composite Fibres

The information provided by the fibre morphology demonstrated a decrease in the average fibre diameter with the addition of silicon-based ceramics. As mentioned previously in 2.5.6.1 elongation and stretching of the polymer chains produces smaller fibre diameters and are associated with the nucleation of the β polymorph. With this being said it would be interesting to determine the influence the silicon-based ceramics displayed on the crystallinity of the

material. The silicon-based materials demonstrate a low dielectric constant in comparison to the niobium oxides. As mentioned in the crystallinity of the PVDF / niobium oxides, the dielectric constant may play a role in the orientation of the polymer chains. Here it was studied to determine if there was a difference in the influence on the nucleation of the β polymorph when a ceramic with a lower dielectric constant was added to the fibres.

6.2.1 FTIR of PVDF / SiC Fibres

To determine the influence of the SiC on the electroactive phase of the PVDF FTIR analysis was carried out. Figure 6.8 demonstrates the appearance of both the peaks associated with the α polymorph and the β polymorph, with the intensity of the peaks associated with the β polymorph increasing with the addition of the ceramic. The FTIR of the PVDF / SiC fibres seen in Figure 6.8 has shown three strong absorbance peaks at 614 cm^{-1} and 763 cm^{-1}, and 795 cm^{-1} all three representing the appearance of the α polymorph. The intensity of these peaks representing the α polymorph remains constant with an increase in the SiC content, suggesting there is little change in the ratio between the α polymorph and β polymorph. The same can be mentioned about the absorbance peaks at both representing the β polymorph at 840 cm^{-1} and 1275 cm^{-1}, where no change to the intensity of these peaks is observed. Overall, this suggests that the values in the percentage of the electroactive phase within the PVDF / SiC at all the loadings of the ceramic may be similar. The literature demonstrates a decrease in the peaks associated with the α polymorph with the addition of a filler.[355] Sheth *et al*.[385] also demonstrate this with the addition of SiC to PVDF films, where the intensity of the peaks at 763 cm^{-1} decreases with the addition of the filler. Here there is no decrease in the intensity peak of the α polymorph at 763 cm^{-1} which contrasts that from previous work and the PVDF / niobium ceramics make in the previous chapter and what is displayed in the literature. This suggests that the SiC here has little influence on the nucleation of the β polymorph. To gain further understanding quantitative analysis of the polymorphs needs to be carried out.

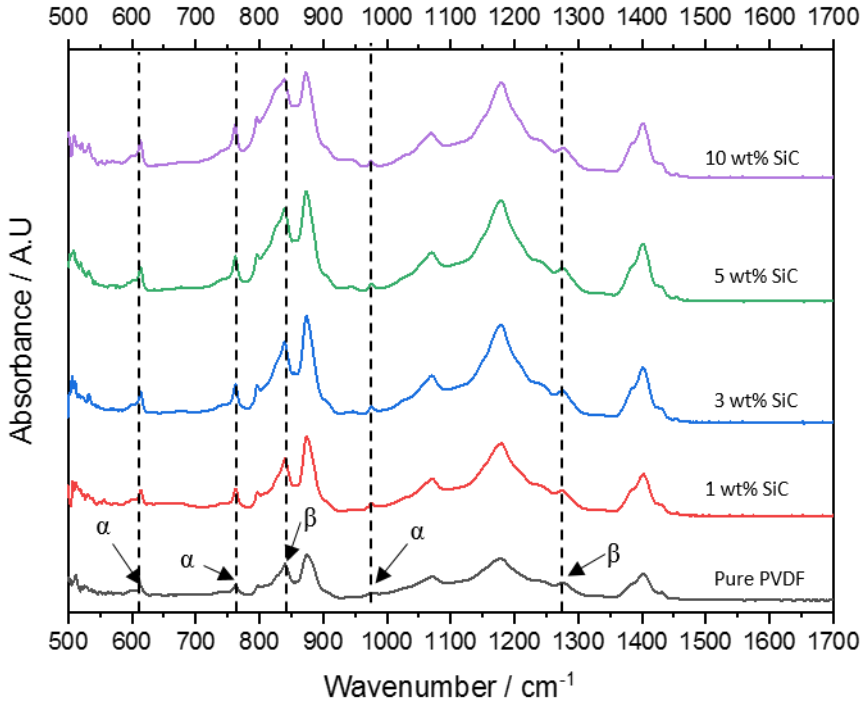

Figure 6.8. The FTIR of the PVDF / SiC 1 wt% - 10 wt% content displays the relevant intensity peaks for the α polymorph and β polymorph.

The Beer-Lambert law as seen in 3.3.5 was applied for quantitative analysis of the β polymorph. The content of the β polymorph in the PVDF fibres can be seen in Figure 6.9 which displays a general increase in the content of the β polymorph with the addition of the ceramic and from there little change in the content of the electroactive phase. The addition of 1 wt% SiC leads to an increase in the percentage of the β phase in comparison to the pure PVDF fibres. Further increasing the content of the SiC in the fibres had little influence on the percentage β phase. Values ranging between 61 % – 63 % were analysed for these fibres. The highest loading of the ceramic resulted in the lowest content of the β polymorph. The average fibre diameter of the PVDF / SiC ranged between 657 nm – 1158 nm with the highest loading of the ceramic resulting in the smallest average fibre diameter. These average diameters were like that of the PVDF / $CeNbO_4$ which ranged between 617 nm – 1023 nm. The content of the β polymorph should be similar for both materials if it was determined by the average fibre diameter. However, the PVDF / SiC demonstrates an overall lower range between 61 % – 63 % in comparison to the 61 % – 74 % range of the PVDF / $CeNbO_4$.

As mentioned previously, when the electrostatic field is generated through the application of the voltage, dielectric ceramics become polarised. The polarised ceramics created a local electrostatic field which then assists in the nucleation of the β polymorph where the PVDF chains wrap around the ceramic in the all-trans TTTT configuration.[286] The lower

dielectric constant of the SiC may result in this effect having a lower influence on the nucleation of the polymer chains resulting in lower content of the β polymorph in comparison to the other PVDF / ceramic composite fibres analysed here. Previous studies in PVDF / SiC particles have demonstrated an increase in the content of β polymorph to a maximum of 93% with the addition of 2.5 wt% ceramic. This work has a lower value which could be due to a higher concentration of polymer (30 wt%) used in comparison to the 18wt% used with that study. The higher concentration of polymer provides a higher polymer chain entanglement which makes it more difficult for nucleation of higher quantities of the β polymorph.[351]

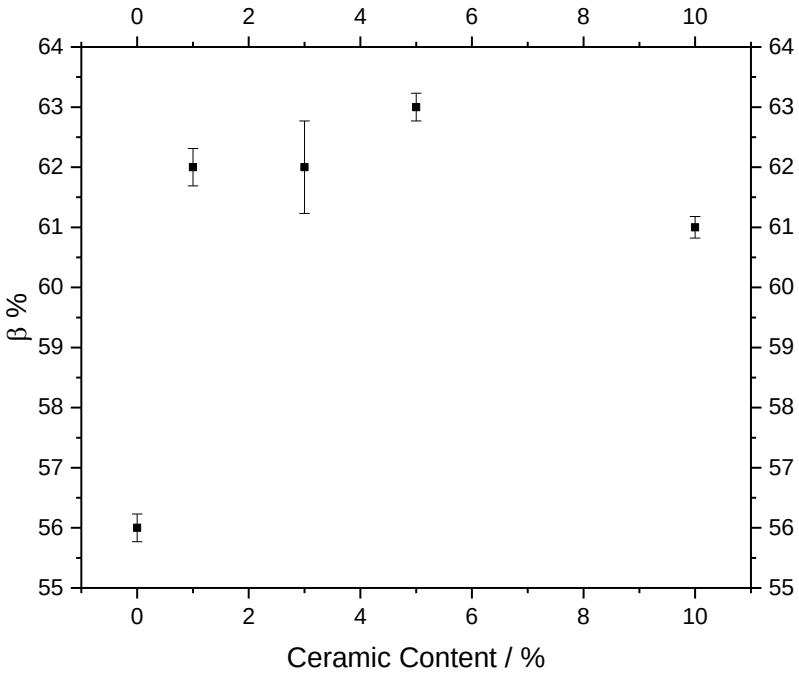

Figure 6.9. The increase β phase percent for the PVDF fibres with the addition and increase in SiC content of 1 wt% – 10 wt%. Displaying an initial increase in the β polymorph with the addition of SiC.

Figure 6.10 demonstrates that there is no real correlation between the average fibre diameter and the increase in the content of the electroactive β polymorph. The increase in the amount of the β polymorph occurs with the addition of the filler, however, the average fibre diameters are within the same experimental error suggesting that there is little correlation between the two components.

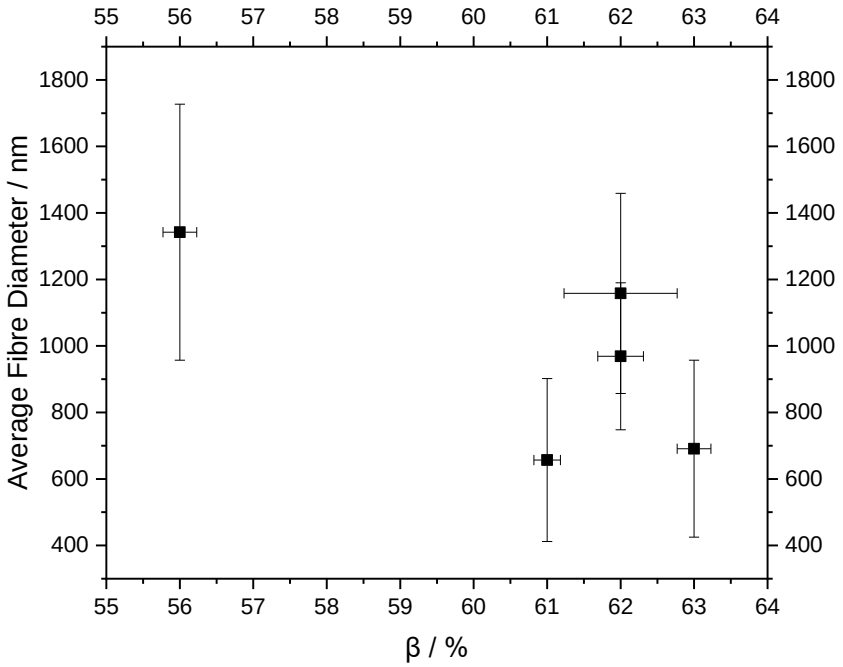

Figure 6.10.The average fibre diameter vs β phase percentage for the PVDF / SiC fibres. Showing an increase in fibre diameter with a decrease in β content all within experimental errors.

6.2.2 DSC of the PVDF / SiC Fibres

The thermal analysis through DSC was carried out on the PVDF / SiC fibres to assist in confirming the nucleation of the β polymorph within the PVDF fibres. Figure 6.11 demonstrates the melt peaks of the PVDF / SiC fibres where peak splitting does not occur with no shift in the peaks. The T_m of the pure PVDF was analysed as 167 °C. The addition of 1 wt% SiC resulted in little change to the T_m showing a small increase to 168 °C. The addition of 3 wt% SiC led to a decrease in the T_m to 166 °C. Further increasing the content of SiC to 5 wt% and 10 wt% resulted in a T_m of 167 °C for both composite fibres respectively. Peak broadening and overlapping of the PVDF / SiC samples were not observed which is associated with the nucleation of the β polymorph.[344] However, the temperature of the T_m is within the range associated with the formation of the β polymorph. The change in the T_m is also associated with the change in lamella thickness. Here the melt temperatures did not alter suggesting that there was little change in the thickness of the lamella.[386] Overall, a similar melt temperature suggests that SiC has little influence on the nucleation of the β polymorph.

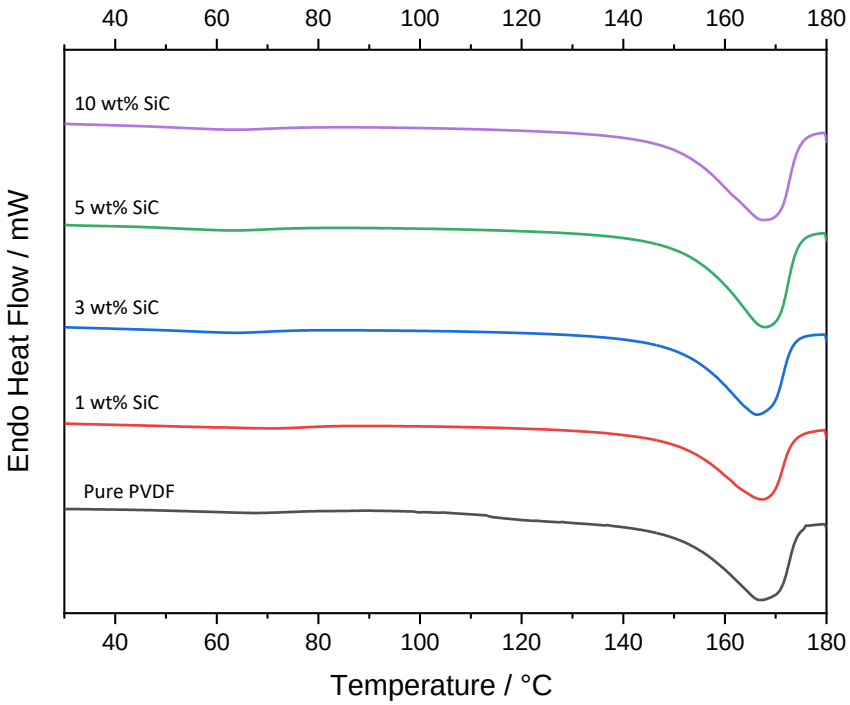

Figure 6.11. Endothermal heat flow for the PVDF / SiC fibres 1 wt% – 10 wt% showing an overall shift in the melt temperatures.

The exothermal peaks for the pure PVDF and PVDF / SiC can be observed in Figure 6.12 where a shift to lower temperatures is demonstrated. The T_c of the pure PVDF was analysed as 141 °C. The addition of 1 wt% SiC demonstrated an overlapping of two T_c peaks, with the dominant peak on the left demonstrating a recrystallisation temperature of 138 °C. The addition of 3 wt% SiC leads to a decrease in the T_c to 137 °C. While the addition of 5 wt% and 10 wt% resulted in a further decrease in the T_c to 136 °C respectively. The double T_c peak of the 1 wt% may be associated with the occurrence of both self-nucleation and heterogenous nucleation due to poor distribution of the filler across the material at the lower loading.[346] To analyse this further TGA analysis may assist to determine if efficient loading of the ceramic was carried out at the 1 wt% concentration.

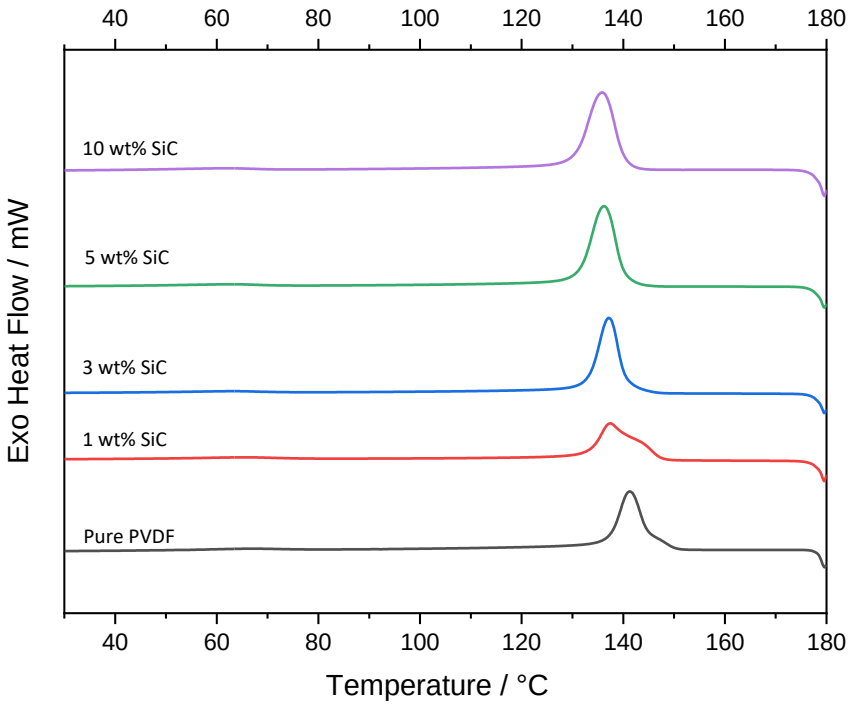

Figure 6.12. The Exothermal heat flow for the PVDF / SiC fibres 1 wt% – 10 wt% shows a decrease in the recrystallisation temperature.

The X_c of the pure PVDF was analysed to be 53.0 % as seen in Table 6.5 where a decrease in crystallinity is observed with the addition of filler. The X_c of the fibres containing 1 wt% SiC was analysed as 45.4 %. The addition of 3 wt% and 5 wt% SiC resulted in an increase in the X_c to 46.2 % and 46.0 % respectively. However, increasing the content of the SiC to 10 wt% results in a decrease in the X_c resulting in a value of 43.7 %. The decrease in the X_c for the PVDF / SiC fibres can be associated with defects occurring in the material. It can also be associated with a reduction in the mobility of the polymer chains, which results in an increased difficulty in the recrystallisation of the material which reduces the overall crystallinity as mentioned with the PVDF / niobium fibres.[355,357] This effect occurs to a higher degree when the higher loading of 10 wt% is added to the materials resulting in a larger decrease in the X_c and is observed with all the PVDF / niobium oxide fibres. It is thought to occur due to agglomeration of the particles which further hinders the ability of PVDF to crystallise.[357]

Table 6.5. The DSC data for the PVDF / SiC fibres 1 wt% – 10 wt%.

SiC wt%	T_m / °C	T_c / °C	ΔH_f	X_c / %
0	167	141	55.5	53.0
1	168	138	47.5	45.4
3	166	137	48.4	46.2
5	168	136	48.2	46.0
10	168	136	45.8	43.7

6.2.3 FTIR of the PVDF / Si_3N_4 Fibres

The FTIR of PVDF / Si_3N_4 seen in Figure 6.13 has shown three strong absorbance peaks at 614 cm^{-1} and 763 cm^{-1}, and 795 cm^{-1} all three representing the α polymorph. Increasing the content of Si_3N_4 to above 3 wt% resulted in a decrease in the intensity of the intensity peak at 763 cm^{-1}. The two β polymorph absorbance peaks at 840 cm^{-1} and 1275 cm^{-1} are also present for all the PVDF / Si_3N_4 fibres, with the intensity of these peaks remaining constant throughout with the addition of higher quantities of the ceramic. The appearance of both the absorbance peaks associated with the α and β polymorph suggests that the fibres contain both crystal structures. It also suggests that there is an increase in the content of the β polymorph due to the α polymorph peak at 763 cm^{-1} beginning to decrease. Similar results were obtained with the PVDF / SiC fibres which demonstrated little change in the content of the electroactive phase with an increase in the content of the ceramic. Here we expect a similar result as the intensity of the α polymorph at 763 cm^{-1} does not decrease with the addition of the ceramic as it has previously been demonstrated in the literature.[355]

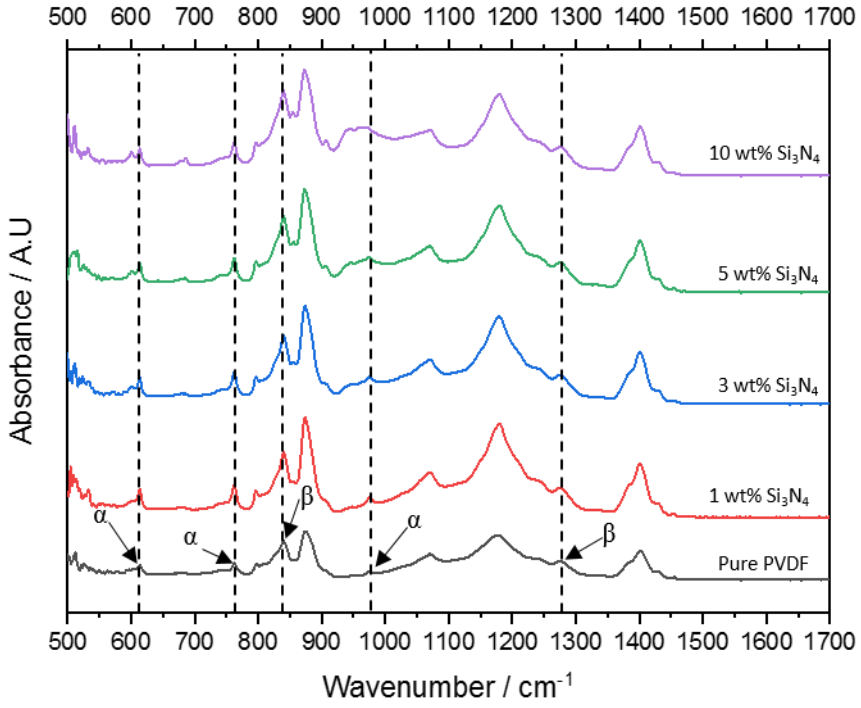

Figure 6.13. FTIR of the PVDF / Si_3N_4 fibres 1 wt% – 10 wt% displaying both the intensities representing the α polymorph and the β polymorph.

The Beer-Lambert law seen in 3.3.5 was applied to gain quantitative data on the content of the PVDF / Si_3N_4 fibres to compare with the PVDF / SiC fibres. Figure 6.14 demonstrates the increase in the content of the β polymorph with the addition of the Si_3N_4 filler. The pure PVDF has shown a β polymorph percentage of 56 %. The addition of 1 wt% Si_3N_4 resulted in a large increase in the β polymorph to 62 %. The addition of 3 wt% and 5 wt% resulted in an increase in β polymorph percentage to 66 % and 65 % respectively. The maximum loading of 10 wt% Si_3N_4 led to a further increase in the β polymorph to 67%. Overall, the PVDF / Si_3N_4 displayed a higher content of the β polymorph in comparison to the PVDF / SiC. The fibre diameters of the PVDF / SiC were 657 nm – 1158 nm which were closely related to that of the PVDF / Si_3N_4 with values ranging between 715 nm – 966 nm. The main difference between the ceramics was the dielectric constant with Si_3N_4 demonstrating a higher value than SiC. The ion-dipole interactions between the material generated by the polarisation of the ceramic through the application of an electrostatic field could have influenced the nucleation of the β polymorph. The PVDF / Si_3N_4 fibres displayed a similar average fibre diameter and β polymorph content to those, which also suggests that the ion-dipole interactions between the fibre diameters are an influencing factor for the orientation of the polymer chains.[387] It is also in line with previous work carried out on PVDF fibres incorporated with Si_3N_4. However, quantitative comparisons between this work and the previous study cannot be made as values of the β polymorph were

not generated. The highest value of β polymorph demonstrated previously is at 94% produced by the addition of KNN / ZNO to PVDF. These values are much higher than those within this work and could be attributed to the higher dielectric properties of KNN at 420 in comparison to Si_3N_4.[119]

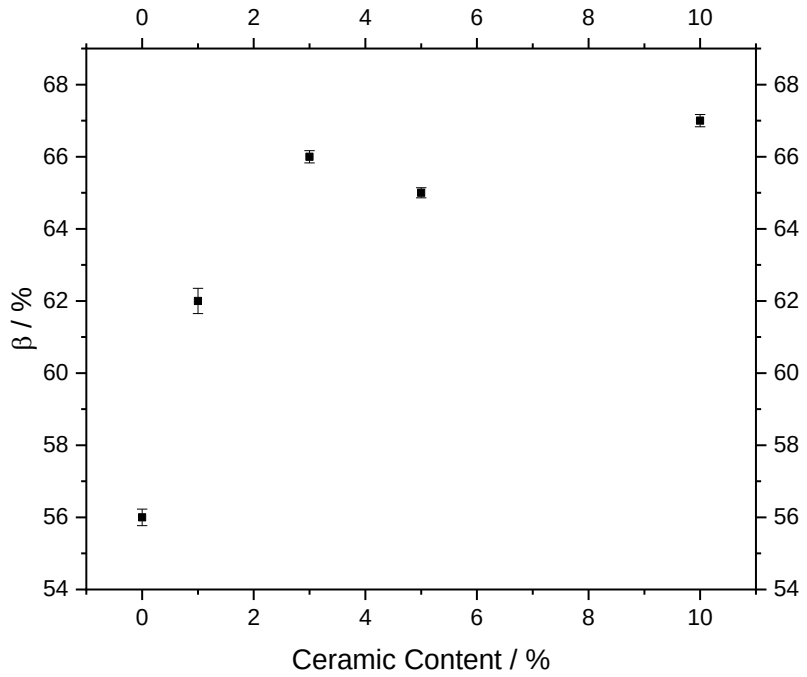

Figure 6.14. The increase in β phase percent for the PVDF fibres with the addition and increase of Si_3N_4 content from 1 wt% – 10 wt%.

Figure 6.15 demonstrates a gradual decrease in the fibre diameter within the experimental error and an increase in the content of the β polymorph. Overall, it can be said that as the average fibre diameter is similar for all of the materials produced, then a correlation between the average fibre diameter and the content of the β polymorph cannot be made. This suggests that the ceramic filler here has less influence on the alignment of the fibres through stretching of the jet and more influence on nucleation as there is still an increase in the content of the electroactive phase with the addition of the filler.

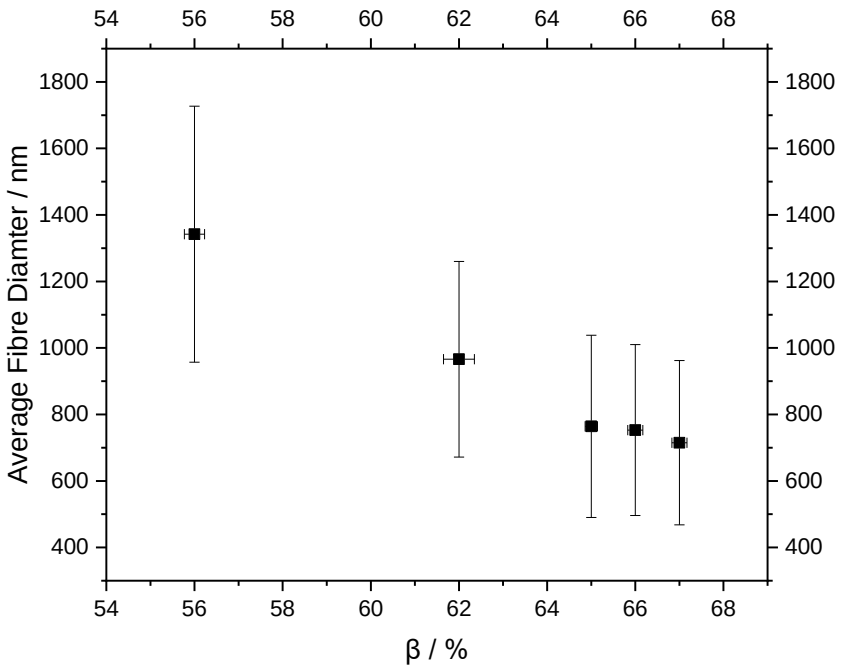

Figure 6.15. The average fibre diameter vs β phase percentage for the PVDF / Si_3N_4 fibres. Showing an increase in fibre diameter with a decrease in β content.

6.2.4 DSC of the PVDF / Si_3N_4 Fibres

The thermal properties of PVDF / Si_3N_4 were analysed to assist in confirming the nucleation of the β polymorph with the FTIR data and to compare with the PVDF / SiC fibres as both have previously demonstrated effective thermal properties. The T_m of the pure PVDF was 167 °C as seen in Table 6.6. The addition of 1 wt% Si_3N_4 had shown a decrease in the T_m to 166 °C. The addition of further content of the ceramic resulted in little change to the T_m producing values within the range of 165 °C – 166 °C as seen in Table 6.6. Unlike with the PVDF / SiC fibres melt peaks, there was peak broadening of the PVDF / Si_3N_4 fibres seen in Figure 6.16. The values of the content of the β polymorph were also higher in that of PVDF / Si_3N_4 which suggests that peak broadening and splitting occur in the materials with a higher content of the β polymorph in comparison to the α polymorph.

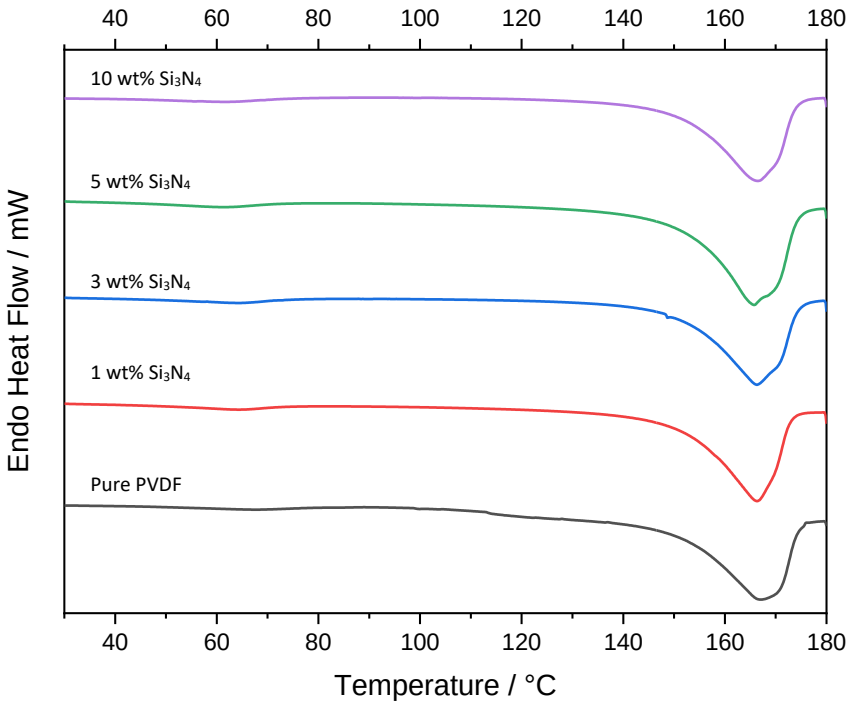

Figure 6.16. Endothermal heat flow for the PVDF / Si_3N_4 fibres 1 wt% - 10 wt% showing a decrease in the melt temperatures with the addition of the Si_3N_4.

Figure 6.17 displays the T_c of the PVDF / Si_3N_4 fibres where a shift to lower temperatures is observed. The T_c of the pure PVDF was 141 °C as seen in Table 6.6. The addition of 1 wt% Si_3N_4 resulted in a decrease in the T_c to 138 °C. The addition of further quantities of Si_3N_4 resulted in the T_c remaining between 137 °C – 138 °C. The decrease in the T_c is associated with an even distribution of the filler across the material. However, a decrease in T_c is observed here even with an agglomeration of the Si_3N_4 materials which suggests that the distribution of the filler still acts to reduce the T_c by slowing the rate of recrystallisation. This has been observed with most of the fibres produced containing ceramic filler. Previous studies have mentioned that the agglomeration of particles and a reduction in dispersion demonstrates a decrease in the T_c.[387] However, as mentioned previously the analysis of the recrystallisation carried out through the DSC analysis may be different to that which occurs within the electrospinning process as the polymer is recrystalising from solution with the assistance of a dielectric ceramic which may be influencing orientation and recrystallisation of the material.

The X_c of the pure PVDF fibres was 53.0 % as seen in Table 6.6. The addition of 1 wt% Si_3N_4 resulted in a decrease in the X_c to 45.7 %. From here the X_c had shown to decrease to 40.6 % with the addition of 3 wt% Si_3N_4. An increase in the X_c was observed with the addition of 5 wt% to 45.5 %. The addition of the maximum 10 wt% Si_3N_4 resulted in a decrease to 41.5 %.

Overall, the crystallinity of the PVDF / Si_3N_4 is lower than that of the PVDF / SiC as mentioned with the niobium oxide materials there was a slight decrease in crystallinity with an increase in the particle size of the filler from $KNBO_3$ < $NaNbO_3$ < $CeNbO_4$. Similar results are seen here where the particle size of the Si_3N_4 is larger than that of the SiC and an overall decrease in the crystallinity is overall with the addition of Si_3N_4 to the SiC, suggesting that particle size may influence recrystallisation of the filler alongside increasing the content of the ceramic.

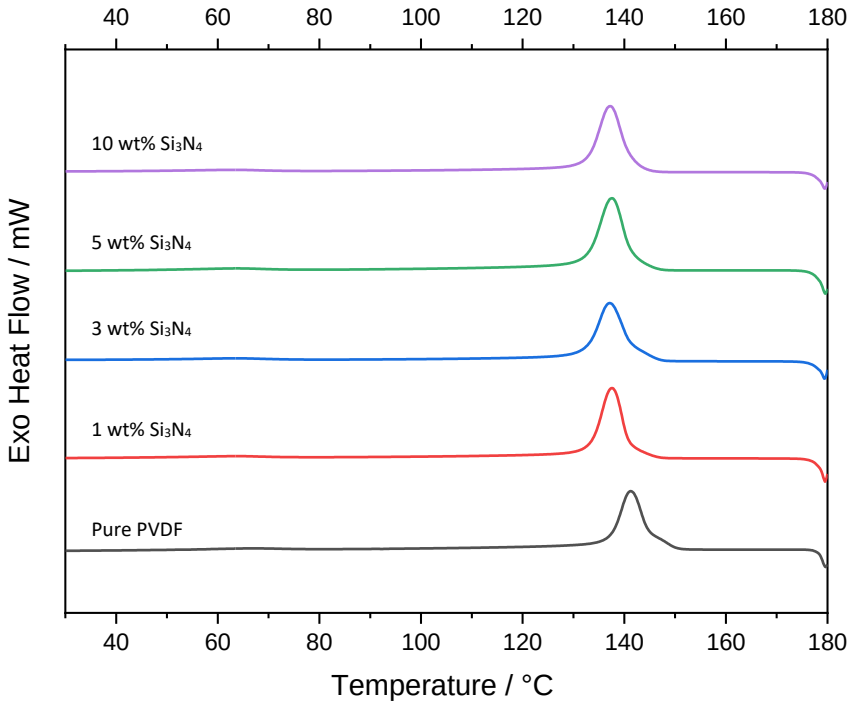

Figure 6.17. Exothermal heat flow for the PVDF / Si_3N_4 fibres 1 wt% – 10 wt% with a decrease in the recrystallisation temperature.

Table 6.6. DSC data for the PVDF / Si_3N_4 fibres 1 wt% – 10 wt%.

Si_3N_4 wt%	**T_m/ °C**	**T_c / °C**	**ΔH_f**	**X_c / %**
0	167	141	55.5	53.0
1	166	138	47.8	45.7
3	166	137	42.5	40.6
5	165	138	47.6	45.5
10	166	137	43.5	41.5

6.2.5 Summary

The percentage of the β polymorph was overall lower for the PVDF / SiC fibres in comparison to the PVDF / Si_3N_4 fibres with values ranging between 61 % – 63 % and 62 % – 67 % respectively. This was suggested to occur due to the difference in the dielectric properties of the materials which may have assisted in the nucleation of the electroactive phase in PVDF. As mentioned earlier SiC displays a lower dielectric constant the Si_3N_4 which would result in a weaker polarisation of the material when an electrostatic field is applied. This could lead to weaker ion-dipole interactions between the polymer and ceramic resulting in a lower content of the β polymorph in PVDF / SiC. Overall, the average fibre diameters were similar between the two sets of composite fibres which suggests that the difference in dielectric properties may have been the influencing factor. In comparison to the PVDF / niobium oxide fibres, the content of the β polymorph of the PVDF / SiC was much lower and the PVDF / Si_3N_4 was within a similar range. The FTIR data suggests so far, that Si_3N_4 acts as a more effective nucleating agent for the β polymorph in comparison to that of the SiC. In comparison to the content of β percentage in previously studied PVDF / ceramic fibres the materials here have a much lower percentage of the electroactive phase. The highest reported figures are demonstrated with a PVDF / KNN / ZnO fibre composite of 94%.[309] It has also been shown that the addition of SiC to PVDF resulted in an increased content of the β polymorph to 93%. This suggests that the SiC and Si_3N_4 fillers are not influencing the nucleation of the β polymorph in comparison to what has previously been reported. This could be due to the higher concentration of PVDF within the material resulting in higher molecular chain entanglements reducing the ability for the nucleation of the electroactive phase.[351]

The dielectric properties of the material would not be expected to be active in a DSC environment. This means the recrystallisation within the DSC may be different to what the PVDF would experience within the electrospinning set-up. This could result in the recrystallisation temperatures being lower suggesting that there is a hindrance in recrystallisation. However, the polarisation of the ceramic during the electrospinning process may still act to assist in the nucleation of the β polymorph and would not occur within the DSC so this aspect is not analysed. The average fibre diameter of the fibres is all within the experimental error range suggesting they are similar in size. Here an increase in the content of the β polymorph is observed with little change to the average fibre diameter which suggests that the filler is assisting in nucleating the β polymorph over alignment through stretching within the spinning phase.

Overall, the work in this section demonstrates that the addition of SiC and Si_3N_4 to the PVDF fibres can induce nucleation of the β polymorph by increasing it from 56% to 61% and

above. However, this is not as significant of an increase in comparison to when niobium oxide ceramics were added in previous chapters. It can also be mentioned that increasing the number of ceramic fillers results in a decrease in the X_c which is in line with reports within the literature as agglomeration occurs with these materials and hinders the crystallisation process.[358,359]

6.3 Thermal and Mechanical Properties of PVDF / Silicon Ceramic Fibres

The thermal and mechanical properties of the PVDF / silicon-based fibre composites were analysed to determine if the silicon-based ceramics could enhance the thermal stability of the composite fibres. As mentioned in 2.4.2 and 2.4.3 the silicon-based ceramics display good thermal conductive properties for ceramic materials. A potential increase in thermal stability due to effective thermal dissipation of the silicon-based may assist in providing better thermal energy dissipation within the composite fibres during the sound damping testing within later chapters. So, it is of interest to determine if there are any changes to the changes in thermal stability of the materials with the addition of silicon-based ceramics where higher temperatures are observed for degradation. It would then be of interest to analyse the thermal-mechanical properties to determine if there is an increase in the damping properties which could be linked to the increase in the thermal stability due to better dissipation of the thermal energy across the material.

6.3.1 TGA of the PVDF / SiC Fibres

The thermal degradation of the pure PVDF and PVDF / SiC fibres shows a two-step degradation process as seen in Figure 6.18. The two degradation steps of the material are associated firstly with the carbon-hydrogen scission and secondly, with a poly(aromatization) step as mentioned in 5.3.1.[362,363] The pure PVDF had shown a degradation onset temperature of 413 °C and a second degradation between 500 °C – 800 °C. The addition of 1 wt% SiC led to a reduction in the onset temperature to 409 °C. Increasing the content of the ceramic to 3 wt%, 5 wt%, and 10 wt% resulted in a gradual increase in the degradation temperature producing temperatures of 424 °C, 428 °C and 431 °C respectively as seen in Table 6.7. These results were contrasting with the PVDF / niobium composite fibres as an overall decrease in the onset degradation temperature for all three sets of ceramic was observed. The increase in the thermal onset temperature with the addition of 3 wt% - 10 wt% SiC suggests that the ceramic is increasing the thermal stability of the PVDF fibres. Cao *et al*.[388] demonstrated similar results with the addition of pristine SiC to PVDF, where an increase in the degradation temperature occurred. This was suggested to occur as the SiC acted to allow for more efficient internal heat

transformation. It is also suggested that this occurs due to interactions between the ceramic filler and the polymer, assisting in increasing the thermal ability of the material.[361] The residual mass of the pure PVDF is shown as 4.41 %. The addition of 1 wt% SiC leads to an increase in the residual mass to 6.01 %. Increasing the content of ceramic led to an increase in the residual mass as expected seen in Table 6.7. This suggests that the successful addition of the filler was demonstrated for all the weight percentages added to the PVDF fibres.

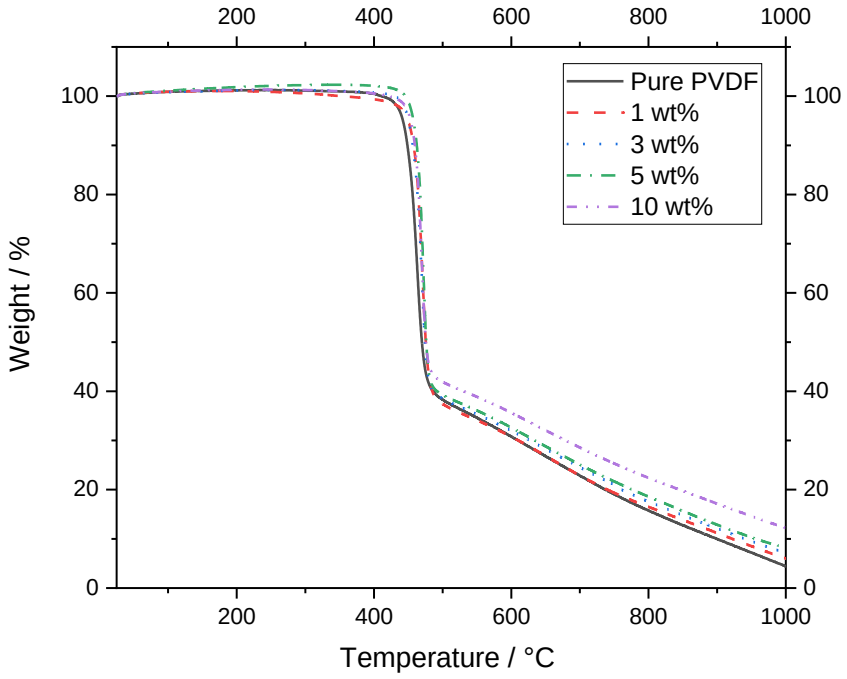

Figure 6.18. TGA of the PVDF / SiC fibres 1 wt% – 10 wt% showing an increase in the degradation temperature and residual mass with the increase in SiC content.

Table 6.7. TGA data for the PVDF / SiC fibres 1 wt% – 10 wt%.

SiC / wt%	**Degradation Temperature / °C**	**Residual Mass / %**
0	413	4.41
1	409	6.02
3	424	7.16
5	428	8.36
10	431	12.3

6.3.2 DMTA of the PVDF / SiC Fibres

The PVDF / SiC fibres were expected to work effectively as damping materials due to their thermal conductive properties which may assist in thermal dissipation across the material. In comparison to the PVDF / $KNbO_3$ fibres which overall displayed the highest damping properties, the PVDF / SiC materials displayed weaker damping properties. Figure 6.19a demonstrates the change in the storage modulus with the addition of the SiC filler. As mentioned previously the pure PVDF has been shown to display the highest *E'* across most of the temperature range analysed. The *E'* at 0 °C was 48.8 MPa as mentioned previously. Here the PVDF / SiC containing 1 wt% was not analysed due to the weak nature of the material which led to consistent breakage during the clamping process of the technique. Inefficient clamping led to slippage and unreadable data for this sample. The addition of 3 wt% SiC to the ceramic resulted in a decrease in the *E'* to 26.14 MPa. Increasing the content of the SiC to 5 wt% resulted in a large decrease in the *E'* to 4.16 MPa, from here doubling the content of the SiC resulted in an increase in the *E'* to 34.9 MPa. The overall decrease in the *E'* of the PVDF / SiC material may have been due to the decrease in the crystallinity of the PVDF as mentioned in 5.3.2 alongside debonding of the filler from the PVDF allowing for movement of the chains.[361] Overall the damping properties of the PVDF / SiC were much lower than what is reported within the literature. Here values range from 600 MPa up to 8 GPa depending on the polymer / ceramic composite system.[369,368] Figure 6.19b displays the change in the loss modulus with the addition of SiC to the PVDF. The *E''* followed a similar trend in which at 0 °C, the pure PVDF displayed the highest values followed by the 10 wt% > 3 wt% > 5 wt%.

Figure 6.19c displays the shift in the T_g and the damping properties with the addition of the filler where a shift to a higher temperature is observed. The tan δ of the fibres had shown to increase in intensity suggesting that the addition of the ceramic assisted in enhancing the damping properties of the material. However, the tan δ is a ratio of the *E'* and *E''*, which results in a deceiving intensity of damping factors peak. The 5 wt% shows the highest tan δ however, displays the lowest *E'* and *E''*. The T_g of the pure PVDF was analysed as -47 °C. The addition of the SiC ceramic increased the T_g of the materials. Incorporating 3 wt% SiC resulted in a T_g of -44.4 °C. The addition of 5 wt% and 10 wt% SiC resulted in a T_g of -42.8 °C, and -45.2 °C respectively. The overall increase in the T_g is associated with a decrease in the mobility of the polymer chains as mentioned previously in 5.3.2.[374,375] This was also observed with the PVDF / $CeNbO_4$ fibres.

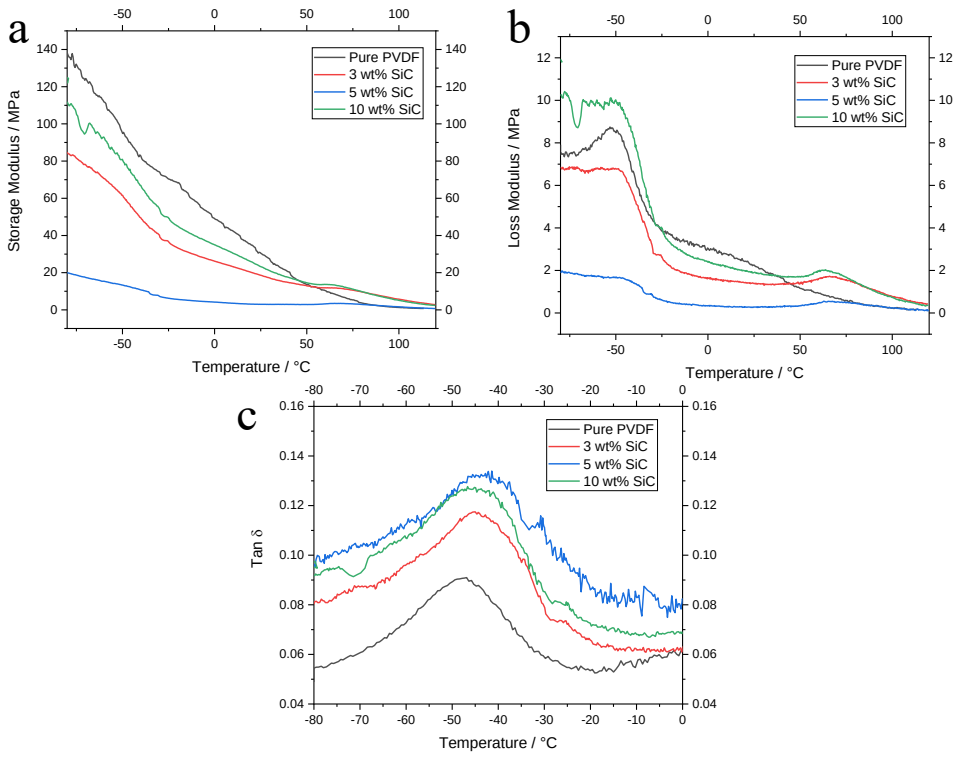

Figure 6.19. DMTA of the PVDF / SiC fibres 1 wt% - 10 wt% showing a decrease in damping performance with the addition of SiC.

6.3.3 TGA of the PVDF / Si_3N_4 Fibres

The pure PVDF displayed a two-step degradation process as seen in Figure 6.20. The first degradation step is associated with the carbon-hydrogen scission and then secondly with a poly(aromatization) step as mentioned in 5.3.1.[362,363] The pure PVDF had shown a degradation onset temperature of 413 °C and a second degradation between 500 °C – 800 °C. Interestingly the PVDF / Si_3N_4 composite fibres only demonstrate a single degradation step. The second degradation step may have been reduced due to the Si_3N_4 particles hindering the process of poly(aromatization) due to the large particle size. The addition of 1 wt% Si_3N_4 had shown to increase the onset temperature to 416 °C. The addition of 3 wt% - 10 wt% of the Si_3N_4 ceramic had little influence on the degradation temperature from here producing onset temperatures between 410 °C – 414 °C as seen in Table 6.8. Overall, it suggests that increasing the content of the Si_3N_4 has little influence on the thermal stability of the material. This was the only polymer that has shown little difference in the onset degradation temperature of the PVDF. This could have occurred due to agglomerates of the ceramic begin displayed and poor distribution of the ceramic across the polymer mats resulting in little influence on the degradation of the material in comparison to the PVDF / niobium fibres and the PVDF / SiC fibres. Ma *et al.*[297]

display an increase in the degradation temperature of PVDF fibres containing Si_3N_4 with the values increasing to approximately 480 °C. It was expected that the addition of Si_3N_4 may have a similar influence and did not. This may have occurred due to agglomeration of the Si_3N_4 within the material leading to a lower influence on the internal thermal heat transformation.[388] Table 6.8 displays the increase in residual mass with the addition of the filler. The residual mass for the pure PVDF was 4.41 %. The addition of 1 wt% Si_3N_4 resulted in an increase in the residual mass to 11.0 %. Increasing the content to 3 wt% resulted in a further increase to 18.6 %. The addition of 5 wt% and 10 wt% has similar residual masses of 20.3 % and 19.9 %. The amounts of residual mass for the 5 wt% and the 10 wt% suggest that the loading of the two was similar. This may have occurred as the Si_3N_4 has a large particle size which may have caused the agglomerates to be stuck are regions within the electrospinning set-up. This could have resulted in a decrease in the content of the ceramic entering the final fibres. Alternatively, the Si_3N_4 particles could have sediment at the bottom of the syringe resulting in a lower loading of the ceramic overall.

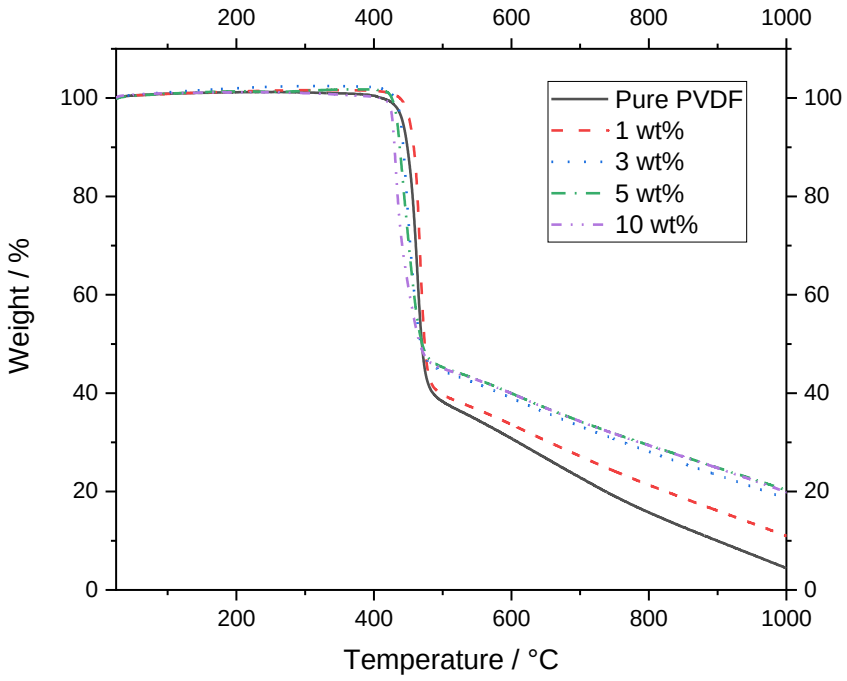

Figure 6.20. The TGA of the PVDF / Si_3N_4 fibres 1 wt% – 10 wt% shows little change to the degradation temperature and an increase in residual mass with the addition of Si_3N_4.

Table 6.8 The TGA data for the PVDF / Si3N4 fibres 1 wt% – 10 wt%.

Si_3N_4 / wt%	Degradation Temperature / °C	Residual Mass / %
0	413	4.41
1	416	11.0
3	411	18.6
5	414	20.3
10	410	19.9

6.3.4 DMTA of the PVDF / Si_3N_4 Fibres

The PVDF / Si_3N_4 fibres demonstrated a similar result in comparison to the PVDF / SiC fibres. Figure 6.21a displays the change in the storage modulus with the addition of the Si_3N_4 filler with a decrease as the temperature increased. As mentioned previously the pure PVDF demonstrate the *E'* of the pure PVDF fibres at 0 °C was analysed as 48.8 MPa. This was also the highest *E*' across the temperature range. The addition of 1 wt% Si_3N_4 resulted in a decrease in the *E*' to 28.9 MPa. The addition of 3 wt% has little influence on the *E*' of the fibres resulting in a small increase to 30.8 MPa. The addition of 5 wt% and 10 wt% Si_3N_4 resulted in a further decrease in the *E*', where similar values of 11.6 MPa and 10.3 MPa were analysed respectively. In comparison to the other analysed fibres, the PVDF / Si_3N_4 demonstrates the highest level of beading, this was observed higher at the highest loading of ceramics 5 wt% and 10 wt%. It could be suggested that the agglomeration of the particles led to a higher level of slippage and debonding of the ceramic with the polymer leading to a gradual decrease in the *E'*.[361]

Figure 6.21b shows the change in the loss modulus with the addition of the Si_3N_4 filler for the PVDF fibres. The *E*'' of the pure PVDF fibres has shown to be like the of the PVDF / Si_3N_4 1 wt% fibres as seen in Figure 6.21b. The. The *E''* of the pure PVDF fibres at 0 °C was analysed as 3.00 MPa. The addition of Si_3N_4 resulted in a gradual decrease in the *E*'' with an increase in the content of the ceramic within the fibres. The 1 wt% PVDF / Si_3N_4 fibre had shown to produce the highest *E*'' of 2.33 MPa out of the ceramic loaded fibres. The lowest *E*'' was produced by the 10 wt% PVDF / Si_3N_4 fibre, resulting in a value of 0.77 MPa.

Figure 6.21c demonstrates the shift in the T_g to higher temperatures and an increase in the damping factor with the addition of the filler. The T_g of the pure PVDF fibres was analysed at -47 °C as seen in Figure 6.21c. The addition of 1 wt% Si_3N_4 resulted in an increase in the T_g of the PVDF to -44.2 °C. Increasing the content of the Si_3N_4 to 3 wt% and 5 Wt% had little influence on the T_g producing a value of -44.0 °C and -44.2 °C. The addition of the maximum content of 10 wt% Si_3N_4 resulted in an increase in the T_g to -42.8 °C. The increase in the T_g is

typically associated with a decrease in the mobility of the polymer chains with the addition of an increase in filler. It can also be associated with a reduction in the free volume which occurs when the filler is added to the polymer matrix.[374,375] Similar results were observed with the PVDF / SiC and the PVDF / $CeNbO_4$ where the addition of the ceramic filler increased the T_g.

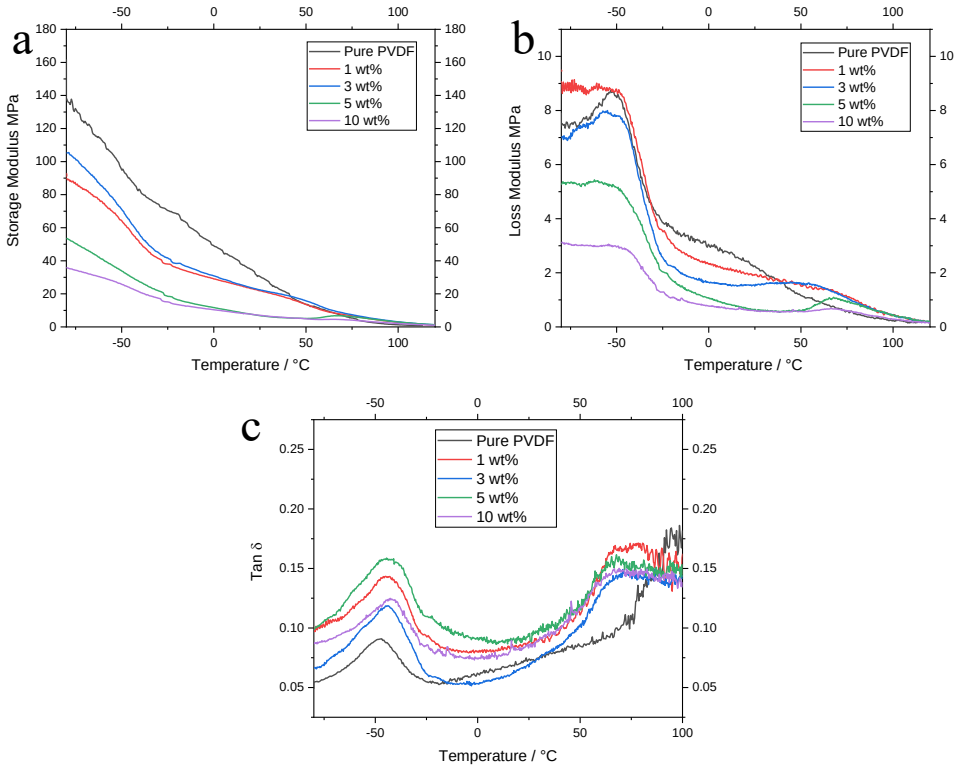

Figure 6.21. DMTA of the PVDF / Si_3N_4 fibres 1 wt% - 10 wt% showing an overall decrease in the damping properties with the addition of Si_3N_4.

6.3.5 Summary

Overall, the thermal stability of the PVDF / SiC fibres was higher than that of the PVDF / Si_3N_4. It could be suggested that with the PVDF / SiC there was better interaction with the polymer and potentially a lower level of defects as the onset temperature increased. Alternatively, the PVDF / Si_3N_4 demonstrate little change to the onset degradation temperature in comparison to the pure PVDF fibres, suggesting there is little change in the matrix of the PVDF. This could have occurred due to the agglomeration of the ceramic across the matrix and resulting in a lower level of defects.[356] The PVDF / niobium ceramics all demonstrated a lower onset degradation temperature in comparison to the PVDF / silicon-based fibres. The main factor for this could be due to the ceramic causing a higher degree of defects to the polymer matrix due to better dispersion of the ceramic across the material. Alternatively, the thermal stability of SiC and Si_3N_4 might be higher than that of the niobium oxides and assists in more efficient dissipation

of the heat across the fibre mats resulting in better thermal stability for the PVDF / silicon-based fibres. This would lead to fewer areas acting as heat zones which could assist in increasing the overall degradation temperatures. Overall, when compared to the literature it is shown that the addition of SiC and Si_3N_4 enhances the thermal stability of the material and shifts the degradation temperature to higher values.[297,388] Here we observe this with the PVDF / SiC material and less so with the PVDF / Si_3N_4. This was unexpected as the PVDF / Si_3N_4 was expected to have a similar increase and to be in line with previous studies.

The DMTA results for both PVDF / SiC fibres and the PVDF / Si_3N_4 fibres suggest that the addition of the ceramic particles results in a decrease in the damping performance of the materials. Overall, the values demonstrated for the *E'* are considerably lower than what is reported in the literature. Here values ranged between 40 – 140 MPa. While within the literature studies have shown much higher *E'* ranging between 600 MPa – 8 GPa.[369,368] It also suggests that the materials are experiencing a decrease in chain mobility due to the addition of the ceramic as the T_g increases for all the PVDF / silicon ceramic fibres produced. Here the free volume within the amorphous region of the material occurs resulting in a decrease in chain mobility.[374,375] Overall, in comparison to the PVDF / $NaNbO_3$ and PVDF / $KNbO_3$, the PVDF / silicon-based materials were much displayed lower *E'* and *E''* potentially due to changes in particle size which may influence fibre properties. It could also be mentioned here that the PVDF / SiC and PVDF / Si_3N_4 fibres were more susceptible to beaded fibres rather than smooth fibre diameters. This may have some form of influence on the decrease in damping properties as the beads within the fibres may alter have the material performs during deformation. There is further work that could be done here to determine if the difference between the bead and bead-free fibres with ceramic loading is the main factor influencing a decrease in the overall thermal-mechanical properties.

Overall, the work within this section demonstrates that each filler influences the thermal stability of the material differently with SiC increasing thermal stability and Si_3N_4 having no influence on these properties. The damping properties of the materials also are shown to decrease with the addition of the filler with the *E'* and *E''* decreasing with the addition of the fillers.

6.4 Sound Testing of the PVDF / Silicon Fibres

The PET foams had shown to have poor acoustic absorbance properties across the frequency range analysed as seen in Figure 6.22 and mentioned in 5.4.1. The addition of the pure PVDF fibres or PVDF / niobium oxide fibres displayed a double resonance peak. The addition of the silicon fibres was carried out to determine if the absorption coefficient at the mid-frequency range could be increased to have an overall effective sound absorption coefficient across the

entire frequency range like that produced by the PU-backed systems and if there was a shift in the two resonance peaks if the sound absorption within the mid-range could not be increased. The PVDF / silicon-based fibres could influence the energy dissipation of the sound energy which may assist in the effective conversion of the sound energy across the entire frequency range due to the higher thermal conductivity the silicon-based ceramics demonstrates in comparison to the niobium oxide materials.

6.4.1 PET / PVDF / Silicon Fibres

As mentioned previously in 5.4.1 the maximum sound absorption coefficient of the PET foams was analysed as 0.44 at 6000 Hz. The poor absorption performance from the PET is associated with the low density of the material and is in line with other PET foams within the literature displaying maximum absorption coefficients of 0.42.[378] This allows for the sound to enter and travel through the foam easily due to the large pores within the foam which have a lower surface area. This reduces the number of interactions the sound waves have with the material resulting in lower absorption of the sound energy. It is known that materials with a higher density will enhance damping properties, especially in the low-frequency range.[97,100]

Figure 6.22 displays the sound absorption coefficient for the PET and PET / silicon-based composite materials. It is demonstrating an increase in sound damping properties with the addition of the fibre mats to the surface of the PET similar to how the PVDF / niobium oxides acted. At the low-frequency range, there is a difference in the absorption coefficient in the order of Si_3N_4 < SiC < pure PVDF with values of 0.5, 0.65 and 0.87 respectively. While at the higher frequency range, there is little change in the sound absorption coefficient with values ranging between 0.82 – 0.86. The formation of the double resonance peak has been associated with similar results carried out by having a back cavity behind bulk material. The back cavity acts to produce an area for frequency-selected sound absorbance due to sound resonance.[103] Similar to as mentioned in the previous chapters the PET may act similarly to the air cavity forming the double resonance peak. The rigid backing acts as a resonance structure which causes the formation of the double resonance peak.[379] These materials are shown to perform weaker than those in the literature at the low-frequency ranges. Materials which demonstrate a back cavity have sound absorption properties at the lower frequency range between 0.89 – 1.[102,105] Here the materials are shown to perform with the low-frequency range with an absorption coefficient between 0.5 – 0.89. Overall, it suggests that the materials here would perform to a lower standard than those produced previously at the low-frequency range.

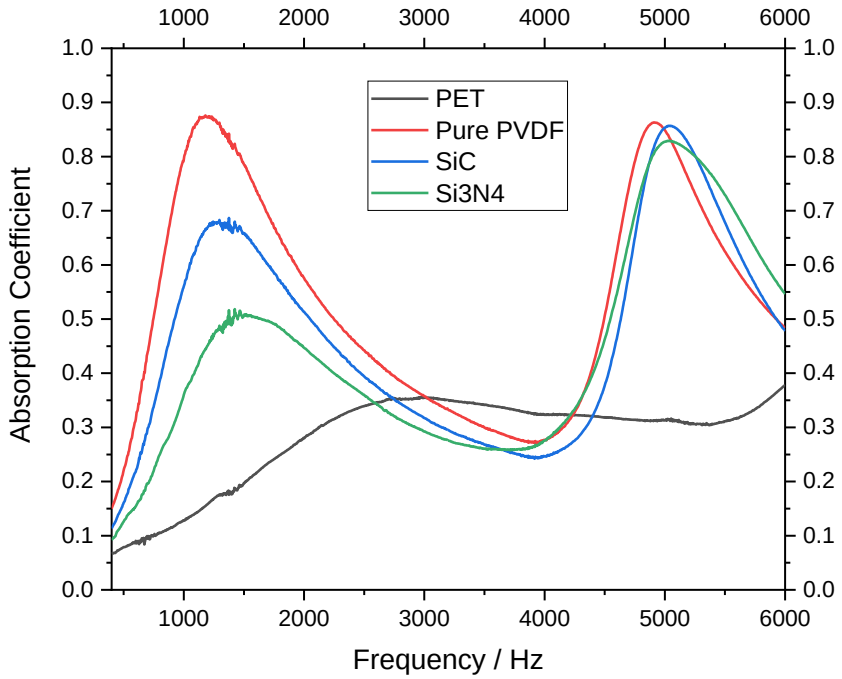

Figure 6.22. Sound absorption coefficient vs. frequency of the PET / PVDF / silicon fibres showing two main resonance peaks.

Table 7.9 displays the relative thickness of the PET foam and the PVDF / silicon-based fibres. The thickness values are all similar to each other with changes occurring to the sound absorption properties at the low-frequency range. This suggests that within these samples the thickness is not showing a large influence on the difference in the absorption coefficients. The addition of a fibre material does however influence the damping properties of the material overall at the low and high-frequency ranges. This can be associated with an increase in the tortuosity of the system which in turn increases airflow resistivity and the air particles within the system experience a high level of friction between each other absorbing more sound energy.[54]

Table 6.9. The percentage thickness ratio of each component within the PET/PVDF/silicon composite system.

Sample name	PET Relative Thickness %	PVDF/Ceramic Relative Thickness %
PET / PVDF	93.9	6.1
PET / PVDF / SiC	92	8
PET/ PVDF / Si_3N_4	92.4	7.6

Figure 6.25 demonstrates the change in average fibre diameter with the NRC. Here a general decrease in the average fibre diameter displays an increase in the NRC. However, the average fibre diameters are within the experimental error of each other making it difficult to draw an accurate comparison. Overall, it can be said that there is an influencing factor which is resulting in a decrease in the NRC of the material with the addition of the filler. The pure PVDF displayed the best acoustic performance within the NRC range displaying a value of 0.42. The addition of the PVDF / silicon-based composite fibres had shown a reduction in the NRC values, with PVDF / SiC and PVDF / Si_3N_4 displaying values of 0.33 and 0.24 respectively. These values were like that of the PVDF / niobium oxide fibres containing either $NaNbO_3$ or $KNbO_3$, which suggests that a similar influence on sound reflection may have occurred at the lower frequency resonance peak resulting in a lower amount of sound absorption by the material.

The average fibre diameters for the PVDF / silicon-based composite fibres were shown to decrease in comparison to the pure PVDF fibres as mentioned in 6.1.1. Similar results were observed with the PVDF / $NaNbO_3$ and PVDF / $KNbO_3$ fibres which suggest that the fibres demonstrated a similar mechanism of sound reflection which may be linked to the average fibre diameters of the fibres. It can be mentioned here that the morphology of the fibres here displayed a beaded structure.

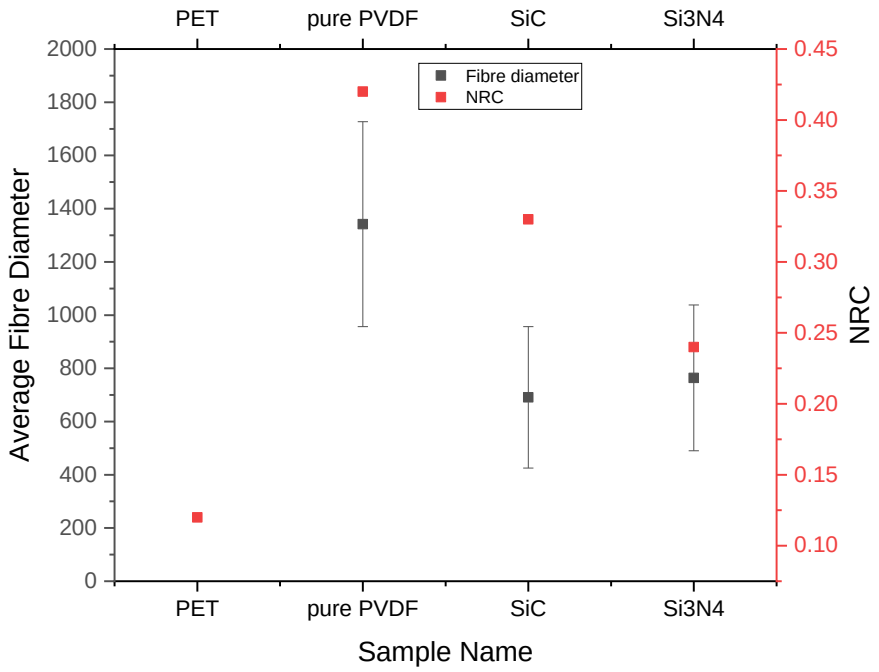

Figure 6.23. Average fibre diameter vs NRC of the PET foam, pure PVDF fibre, and PVDF / silicon-based fibres showing the trend between NRC and average fibre diameter.

6.4.2 PU / PVDF / Silicon Fibres

Following on from the sound testing on the PU / PVDF / niobium oxide composite fibres, the PVDF / silicon-based fibres replaced the PVDF / niobium oxide fibres for analysis due to the potential influence on thermal conductivity which may increase the energy dissipation properties of the material to determine if this assists in influencing overall sound absorption. As mentioned in 5.4.2 the PU foams have shown a rapid increase in the absorption coeffect between 650 Hz – 1400 Hz as seen in Figure 6.24. The frequency range displayed a maximum value of 0.77 Hz as seen in Table 0.6. The addition of pure PVDF fibres to the surface of the material resulted in an increase in the absorption coefficient to 0.84 at the frequency of 1400 Hz as seen in 5.4.2. The values demonstrated here for the maximum sound absorption coefficient for PU are within a similar range for previous studies carried out on PU which ranges between 0.6 – 0.9. This demonstrates that the PU within this work is showcasing a similar form of sound absorption properties. [187,380,389]

The addition of PVDF / SiC to the system resulted in little change to the maximum absorption coefficient at 1400 Hz, displaying the same value of 0.84. The absorption coefficient across the entire frequency range was closely related between the pure PVDF fibres and the PVDF / SiC fibres. This suggests that the addition of the SiC had little influence on the acoustic performance of the material. In comparison to the pure PVDF fibres. The addition of Si_3N_4 to the PVDF fibres resulted in a small shift of the acoustic coefficient to a higher frequency range of 1500 Hz displaying a maximum absorption coefficient of 0.88. Overall, the materials are performing with similar sound damping properties across the entire frequency range. The slight increase in damping properties with the addition of the fibre mats may occur due to an increase in tortuosity of the system which is provided by the fibre mat. The increased tortuosity leads to a higher level of airflow resistivity and increase friction between air particles within the material increasing sound absorption.[54,98] When compared to materials in the literature which have filler added to them the materials here are forming within a similar capacity at a similar frequency range. At the 1000 Hz frequency range materials have been shown to produce maximum absorption coefficients of 0.8 – 0.92.[94,106,107] The materials within this work demonstrate values within this range at 0.84 – 0.88. This suggests that the materials produced within this section can perform to a similar standard as those previously developed.

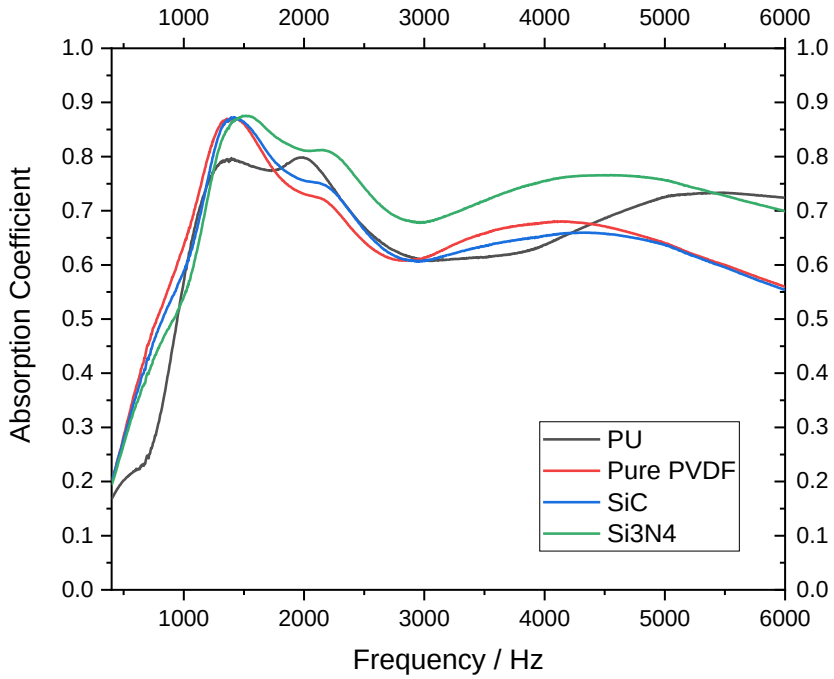

Figure 6.24. Sound absorption coefficient vs. frequency of the PU / PVDF / silicon fibres showing an increase in sound absorption with the addition of a fibrous material.

Table 6.10 demonstrates the relative thickness of the PU foam and the PVDF / silicone-based ceramic fibres. Here the relative thicknesses for the PU/PVDF are approximately 3 % lower than that of the PVDF / SiC and PVDF / Si_3N_4 systems. However, when comparing the three systems across the entire frequency range it can be said that the thickness of the samples has little influence on the damping properties at the low-frequency range with the damping properties being within the 0.84-0.88 absorption coefficient range.

Table 6.10. The percentage thickness ratio of each component within the PU/PVDF/silicon composite system.

Sample name	PU Relative Thickness %	PVDF/Ceramic Relative Thickness %
PU / PVDF	87.8	12.2
PU / PVDF / SiC	84.4	15.6
PU / PVDF / Si_3N_4	85	15

Figure 6.25 demonstrates the NRC values for all of the systems. These values are all within a similar range of 0.42 – 0.44 suggesting that the materials would all perform similarly

on a larger scale. The addition of the pure PVDF had been shown to enhance the NRC to a higher value of 0.44. The addition of SiC and Si_3N_4 to the PVDF fibres had shown no changes in the NRC resulting in a value of 0.43 respectfully. These results were similar to those calculated for the PVDF / $NaNbO_3$ and the PVDF / $CeNbO_4$. However, a similar correlation was observed with the PVDF / niobium oxide and PVDF / silicon-based fibres where a decrease in the average fibre diameter demonstrated a decrease in the NRC. This may occur as smaller fibres have a higher surface area and provide more points of contact for the sound waves which increased the interactions between the fibres and the sound waves increasing vibration and conversion of the energy.[54,98]

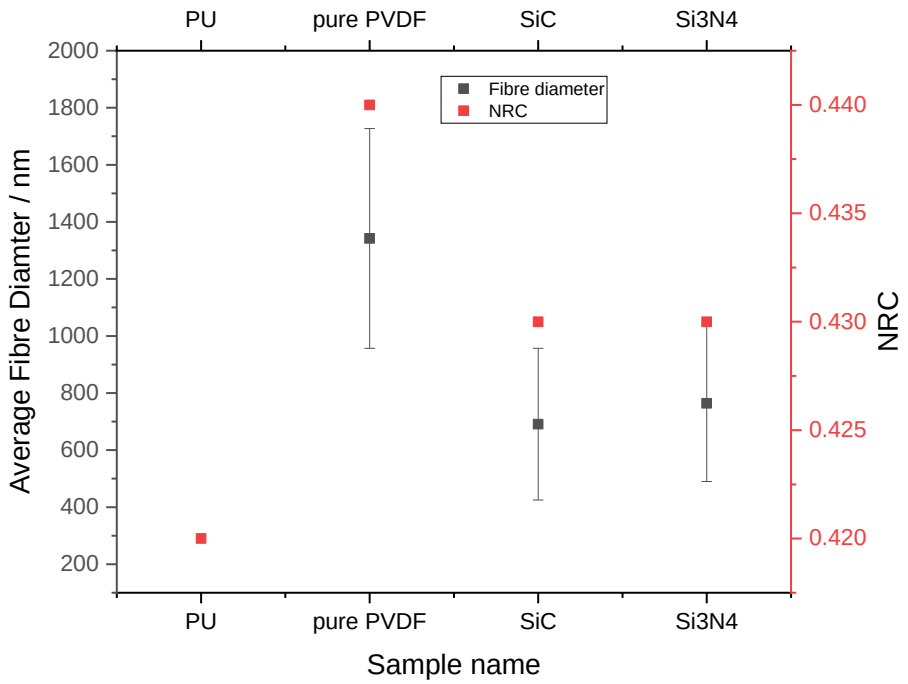

Figure 6.25. Average fibre diameter vs NRC of the PU foam, pure PVDF fibre, and PVDF / silicon-based fibres. Showing similar NRC values with similar average fibre diameters.

6.4.4 Summary

The results obtained for the PVDF / silicon-based ceramics with both the PU-backed and PET-backed fibres were like those obtained by the PVDF / niobium oxide fibres in both systems except for the PU / PVDF / $KNbO_3$ fibres which were outperforming the other fibre mats. As mentioned previously the standalone PET foam has demonstrated similar damping properties to what has been seen within the literature where values of 0.42 maximum absorption

coefficients were observed as opposed to the similar 0.44 demonstrated in this work at 6000 Hz.[378]

Firstly, changing the type of ceramic within the PET-backed system did not influence the sound absorption properties within the mid-frequency range and displayed a decrease in the lower frequency range with the addition of the PVDF / silicon-based fibres potentially due to these materials reflecting the sound waves. This was also observed with the PVDF / niobium oxide materials containing either $NaNbO_3$ or $KNbO_3$. The similarities between the materials were that the average fibre diameters seemed to correlate whereas a decrease in the average fibre diameter resulted in a decrease in the absorption coefficient at the lower frequency resonance peak. Overall, the materials performed as they were expected to form where a double resonance peak was expected. This has previously been demonstrated in the literature with porous fibre composites. With absorption coefficient resonance peaks reaching 0.85 at the low-frequency range and high-frequency range similar to what was demonstrated here.[379] This suggests that the PET / PVDF fibre composites are acting similarly to the systems that have been reported previously.

Secondly, the addition of the PU backing demonstrates much better sound absorption properties across the entire frequency range in comparison to the PET with the addition of the pure PVDF and PVDF / silicon-based fibres, similar to the PVDF / niobium oxide fibres. This suggests that changing the type of ceramic from a niobium oxide to a silicon-based ceramic with a higher thermal conductivity does not increase the damping properties of the material and that the PVDF morphology of the PVDF fibres demonstrates a larger influence on the sound damping properties of the material rather than the ceramic itself as a decrease in the average fibre diameter has overall demonstrated to increase the damping properties of the PU / silicon-based and PU / niobium based fibres across the entire frequency range in comparison to the pure PVDF fibres. Overall, it can be said that the addition of the PVDF / silicon-based fibres demonstrated to increase the sound absorption properties over the entire frequency range of the PU back foams which are generally used within the automotive industry for sound damping applications.

The new work within this section demonstrates that the addition of a silicon-based filler in SiC or Si_3N_4 has little influence on the sound damping properties of PVDF fibres. It demonstrates a similar NRC value ranging between 0.43 – 0.44 and across the entire frequency range a similar trend in the damping properties is observed when added to the PU foams. It also demonstrates similarities to the literature with the addition of the fibre mat to PET where it acts as a back cavity. However, this has not been analysed with the addition of a PVDF / Silicon-based fibre material.

Chapter 7 Electrospinning PVDF / Niobium Oxide / Silicon Ceramics

7.1 Introduction

In this chapter, a mixed ratio of ceramic was added to pure PVDF fibres to enhance the piezoelectric properties and the thermal conductivity properties of the polymer fibre composite electrospun. To achieve these properties, the addition of the $KNbO_3$ in a mixed ratio of either SiC or $Si3N_4$ was incorporated into the pure PVDF fibres. $KNbO_3$ was chosen as it demonstrated the highest influence on the nucleation of the β polymorph in PVDF and has the highest piezoelectric and dielectric properties out of the niobium oxides. While SiC and Si_3N_4 were added to enhance the thermal conductivity of the material. Ideally, a mixture of the $KNbO_3$ and SiC or Si_3N_4 would produce a final material with both increased piezoelectric and thermally conductive properties. It is important to enhance the thermal conductivity of the material for better thermal energy dissipation across the material when the sound energy is converted into thermal energy through the frictional forces between fibres. The mixed ratios of the $KNbO_3$ with either the SiC or Si_3N_4 were analysed to determine the influence of the ceramics on the morphology of the PVDF fibres, alongside the influence on the crystallinity, thermal-mechanical properties, and acoustic absorption properties. As mentioned in previous chapters the addition of SiC and Si_3N_4 has previously been shown to enhance the thermal conductivity of PVDF.

The previous chapters discussed the influence of the niobium oxide ceramics on the electroactive β polymorph of the PVDF. It was analysed that $KNbO_3$ assisted in aligning the polymer chains in the all-trans TTTT configuration of the β polymorph with the biggest influence coming from the 5 wt% concentration of the ceramic. Here the addition of $KNbO_3$ was carried out to influence the orientation of the polymer chains and nucleate the β polymorph. This led to the decision to take $KNbO_3$ forward to the mixed ratio stage above the other niobium oxide ceramics. SiC was demonstrated in enhancing thermal stability while Si_3N_4 had little influence on the thermal stability of PVDF. They have also been shown in previous chapters to influence the β polymorph. The fibre morphology of the PVDF / silicon-based ceramic is undesirable due to the beaded structure. Here the addition of $KNbO_3$ was carried out to influence fibre morphology and assist in the removal of the beads but still provide the needed piezoelectric properties.

7.1.1 PVDF / $KNbO_3$ / SiC Fibre Morphology

The successful formation of fibres was carried out by mixing the ratios of $KNbO_3$ and SiC within the solutions. The parameters were kept constant throughout the process with little changes being made to the applied voltage to produce a stable Taylor cone for efficient electrospinning. Figure 7.1 show the fibre morphology of the materials which was demonstrated to be smooth with no bead formation for the 1:1 and 7:3 ratio mats and the formation of a small number of beaded structures in the 9:1 ratio of $KNbO_3$: SiC. In comparison to the PVDF / $KNbO_3$ fibres and PVDF / SiC fibres, the morphology of the fibres electrospun here is closely related to the PVDF / $KNbO_3$ fibres as expected at the lower quantities of the SiC within the mixture. However, at the 1:1 ratio, the fibre diameters remained like that of the PVDF / $KNbO_3$ rather than that of the larger PVDF/ SiC fibres. This suggests that $KNbO_3$ had a larger influence on fibre morphology than SiC. It could be due to the piezoelectric and dielectric properties of the $KNbO_3$ influencing the fibre diameter to a higher degree than the properties of the SiC.[218] Alternating the ratios did not have a large influence on the range of the average fibre diameters where diameters of 544 nm – 557 nm were analysed using ImageJ where 100 fibre diameters were analysed and seen in Table 7.1. In comparison to the pure PVDF fibres of 1342 ± 385 nm, these mixed ratio fibres were expected to be smaller and follow the trends of the previous ceramics studied in this work. As the fibre diameters did not change with a decrease in the content of the $KNbO_3$ it could be suggested that the influence on the ceramic remains similar to the fibre diameter when with a lower ratio within the mixture. In comparison to the literature, the fibre diameters here are within the range where most of the PVDF / niobium oxide materials of 100 – 500 nm.[306,307,308,309]

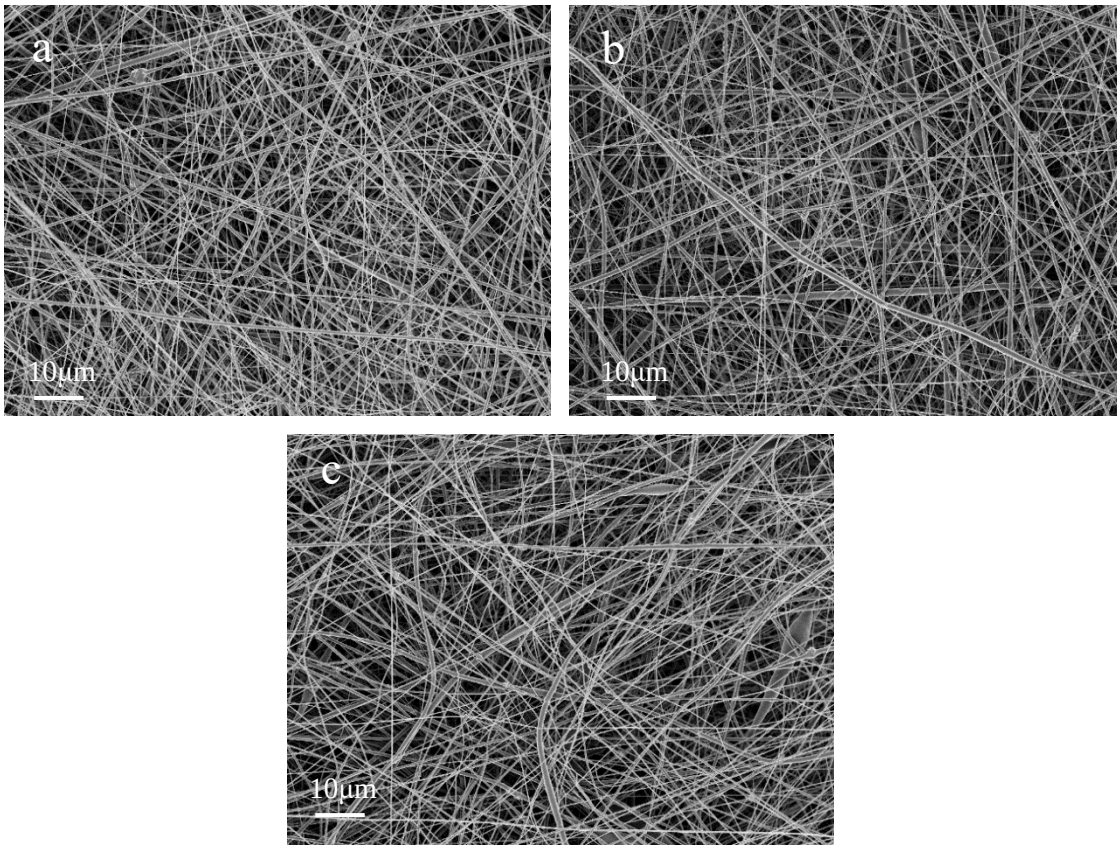

Figure 7.1. The SEM images of the PVDF / $KNbO_3$ / SiC fibres (a) 1:1 (b) 7:3 (c) 9:1 display the morphology of the fibres.

Table 7.1. The processing parameters and average fibre diameters of the PVDF / $KNbO_3$ / SiC fibres.

$KNbO_3$: SiC Ratio	Applied Voltage / kV	Average Fibre diameter / nm
0	7.14	1342 ± 385
1:1	9.50	550 ± 212
7:3	9.30	544 ± 192
9:1	9.10	557 ± 199

To further determine the influence of altering the ratios of the fibre diameters, Gaussian distributions were analysed seen in Figure 7.2 which shows the distribution of the average fibre diameters. The change in the ratio of the PVDF / $KNbO_3$ / SiC had shown little influence on a shift in the gaussian curve. This suggests that altering the $KNbO_3$ and SiC content in the fibres shows little influence on changes to the fibre diameter. When comparing the PVDF / SiC fibres and PVDF / $KNbO_3$ fibres to the ones analysed here it can also be mentioned that the addition

of $KNbO_3$ has a larger influence on the average fibre diameter than SiC as the average fibre diameter is 650 nm – 1100 nm and 540 nm – 560 nm for the fibres respectively.

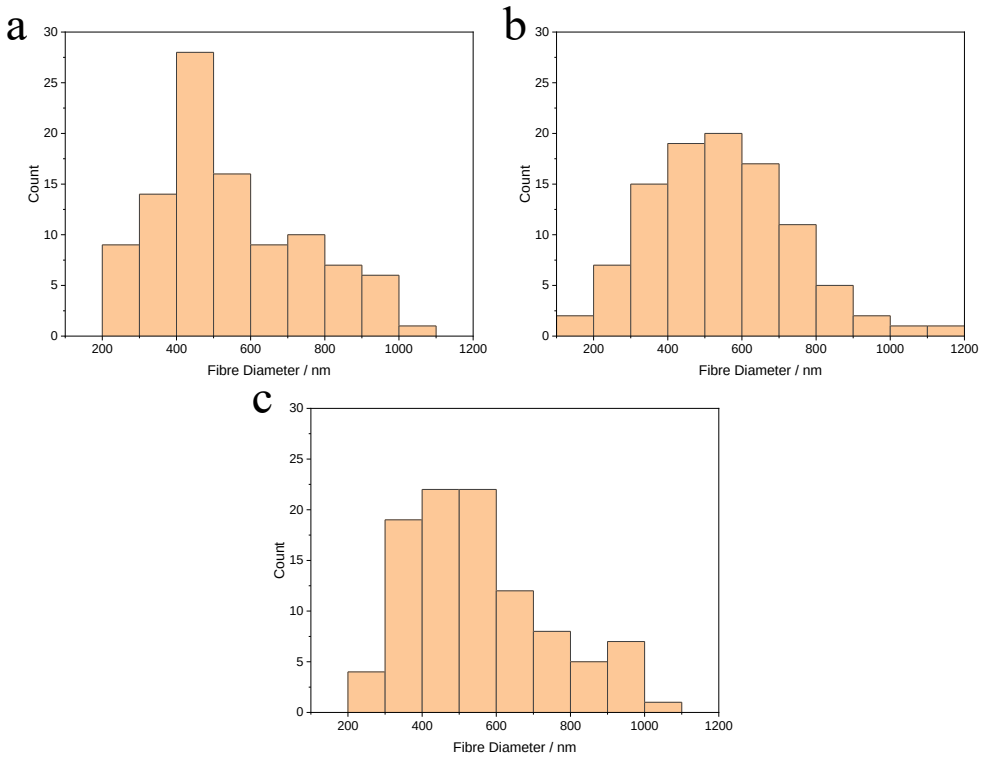

Figure 7.2. The histogram of the PVDF / $KNbO_3$ / SiC fibres (a) 1:1 (b) 7:3 (c) 9:1 shows the influence of ceramic content on the fibre diameter distribution.

Table 7.2. Mixed ratio $KNbO_3$: SiC ceramic weight and solution viscosity.

$KNbO_3$: SiC Ratio	**Viscosity / cSt**
0	359 ± 7.44
1:1	713 ± 1.31
7:3	724 ± 1.82
9:1	754 ± 0.85

The viscosity was analysed to determine if there was a decrease in viscosity at the 9:1 ratio to see if the formation of the few beads was a result of this. However, the viscosity of the 9:1 ratio was higher than that of the 1:1 and 7:3 which did not have beaded fibres. As mentioned previously in 5.1.4 the beads on fibres that contain filler and have seen an increase in viscosity may have been agglomerates of the filler covered in the polymer. It can also be mentioned that an increase in the viscosity from 1:1 < 7:3 < 9:1 was observed with little changes to the average

fibre diameter suggesting that the ceramic material played a role in influencing fibre elongation by influencing the electrical properties of the solution and increasing charge density around the Taylor cone. The $KNbO_3$ has a much larger dielectric constant than that of the SiC. So as the viscosity of the material increases so do the dielectric properties of the solution with the increase in $KNbO_3$. This would allow for the solution to generate a higher charge density due to local polarisation as the dielectric properties of the solution would increase resulting in the jet experiencing higher levels of coulombic force.[218]

The distribution of the $KNbO_3$ and the SiC with a ratio of 1:1 can be seen in the EDS images in Figure 7.3. The $KNbO_3$ is distributed evenly across the fibrous mats. Figure 7.3d – e shows that the K, Nb, and O atoms correlate together and are distributed across the entire fibrous mat. Figure 7.3f shows silicon within the material and demonstrates that the SiC has shown agglomeration at points across the fibrous mat. However, the formation of beads is not observed within Figure 7.3a, while the PVDF / SiC fibres spun in previous chapters have the formation of beads at 5 wt% and 10 wt%. This demonstrates that the addition of $KNbO_3$ acts to assist in decreasing the number of beads and in some cases the complete removal of the formation of beading to a point. It should also be mentioned that there are lower quantities of the SiC within these fibres which may also contribute to less agglomeration of the particles within the fibres.

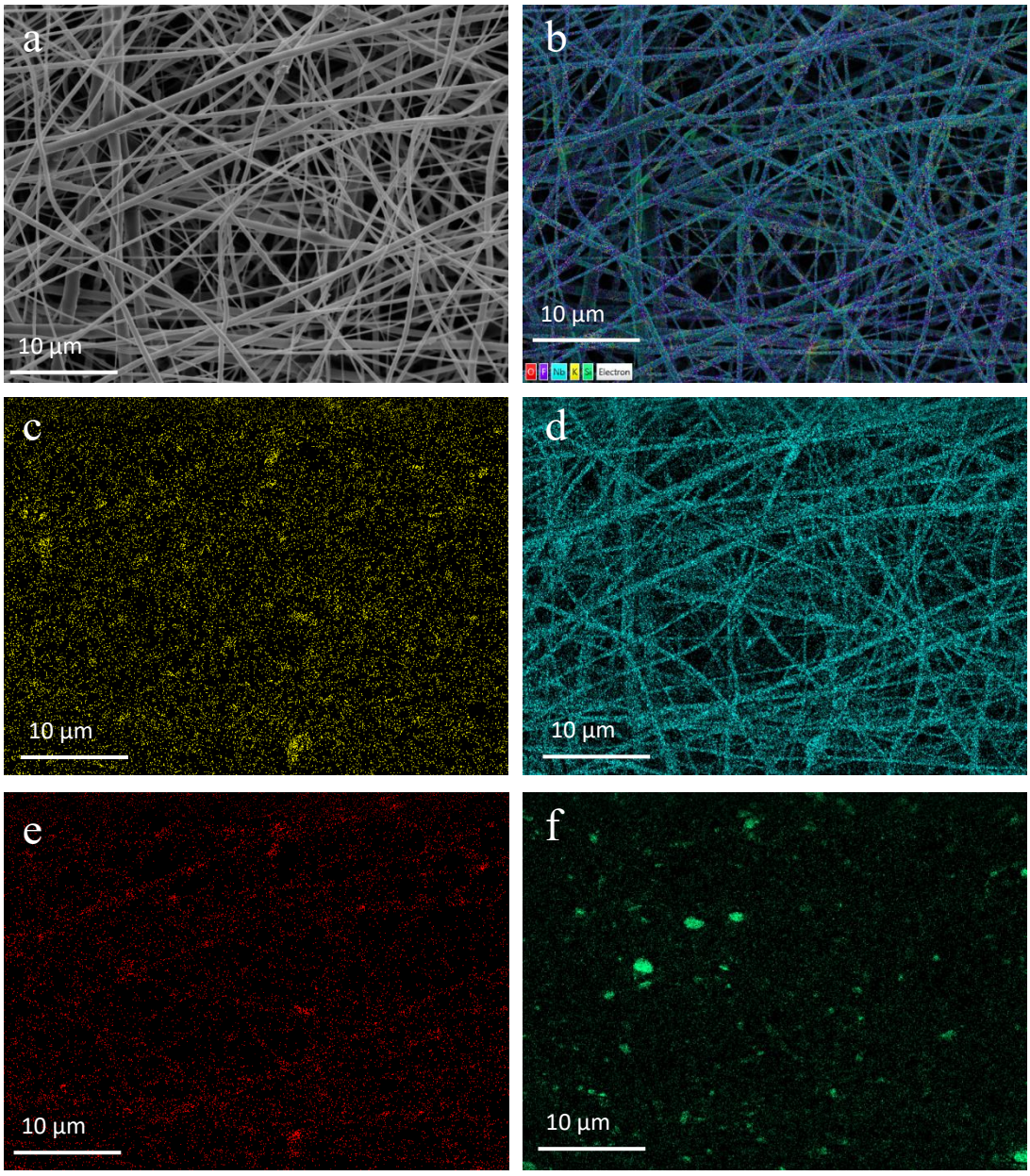

Figure 7.3. The EDS image of the PVDF / $KNbO_3$ / SiC fibres shows the distribution of the ceramic across the fibre mat. (a) Original SEM image, (b) Overlaid image, (c) Potassium, (d) Niobium, (e) Oxygen, (f) Silicon.

7.1.2 PVDF / $KNbO_3$ / Si_3N_4 Fibre Morphology

The successful formation of PVDF / $KNbO_3$ / Si_3N_4 was carried out with the same parameters used with the previous PVDF / ceramic materials with the applied voltage being altered to produce a stable Taylor cone for effective electrospinning. Figure 7.4. displays the morphology of the PVDF / $KNbO_3$ / Si_3N_4 fibres for all of the mixed ratios, where little change to the morphology is observed. The surface morphology of the PVDF / $KNbO_3$ / Si_3N_4 was smooth

with a bead-free structure with ceramic particles protruding through the surface of the fibres. The average fibre diameters of these fibres range between 420 nm – 507 nm which was much smaller than that of the pure PVDF at 1342 ± 385 nm as seen in Table 7.3. In comparison to the PVDF / $KNbO_3$ / SiC fibres which ranged between 544 nm – 557 nm, here these fibres were smaller. The difference in the dielectric properties of the Si_3N_4 and SiC may have resulted in the difference in the fibre diameters, where the Si_3N_4 displays a higher dielectric constant than that of the SiC. As mentioned previously with the application of the electrostatic field the dielectric ceramics create a local electrostatic field which may assist in influencing the elongation and stretching of the fibres to produce thinner fibres.[218] The higher dielectric properties of the Si_3N_4 in comparison to the SiC may have assisted in increasing the elongation and stretching forces on the fibres resulting in thinner average fibre diameters. Overall, these fibres are also in a similar range to those reported within the literature for PVDF filled with niobium oxide ceramics of 100 – 500 nm diameters.[306,307,308,309] These fibres are also a similar size to the PVDF / Si_3N_4 that has previously been demonstrated where fibre diameters of 615 nm are displayed.[297] This suggests that the fillers used here follow the same principles as those used within the literature where they influence the fibre diameter when added to PVDF.

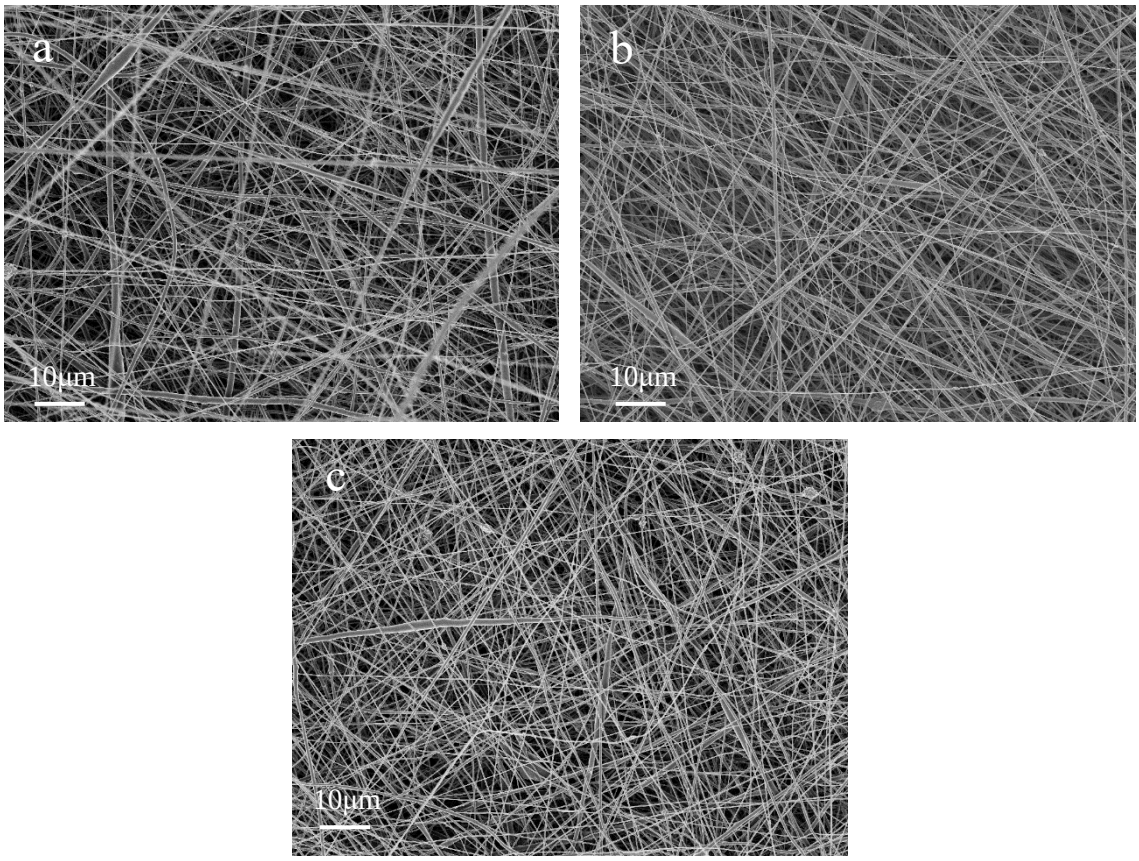

Figure 7.4. SEM images of the PVDF / $KNbO_3$ / Si_3N_4 fibres (a) 1:1 (b) 7:3 (c) 9:1 showing the morphology of the fibres.

Table 7.3 The processing parameters and average fibre diameters of the PVDF / $KNbO_3$ / Si_3N_4 fibres.

$KNbO_3$: Si_3N_4 Ratio	**Applied Voltage / kV**	**Average Fibre Diameter / nm**
0	7.14	1342 ± 385
1:1	9.40	507 ± 136
7:3	9.20	476 ± 155
9:1	8.60	420 ± 117

The histogram in Figure 7.5 demonstrated a shift in the gaussian curve to lower fibre diameters with an increase in the $KNbO_3$ and a decrease in the Si_3N_4 content within the fibres. This shows that altering the ratio of the ceramic content in the mixture allows for control over which region the fibre diameter can be analysed. The shift in the fibre diameter with an increase in the $KNbO_3$ may occur due to the higher dielectric constant of the ceramic in comparison to the Si_3N_4, were mentioned earlier the $KNbO_3$ assists in increasing the dielectric properties of

the electrospun solution. This in turn allows a higher charge density on the surface of the fibres to allow for a higher degree of elongation and stretching of the fibres to thinner diameters. It could also be lower quantities of the Si_3N_4 entering the material in general as the particles may be blocked within the spinneret or sediment at the bottom of the syringe over time due to the larger particle size as mentioned previously.

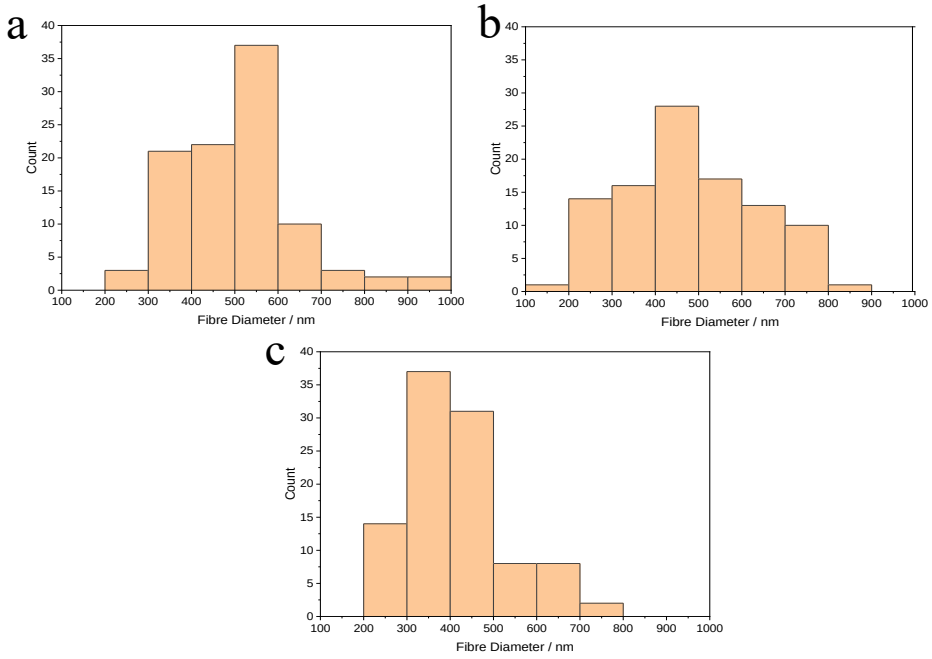

Figure 7.5. Histogram of the PVDF / $KNbO_3$ / Si_3N_4 fibres (a) 1:1 (b) 7:3 (c) 9:1 showing a shift in the fibre diameter distribution.

To investigate the average fibre diameters further the influence of the viscosity was carried out. It had shown contrasting results to the mixed ratio with SiC where those fibres had shown an increase in viscosity which had little influence on the fibre diameter. Here the viscosity did not vary as much with changes in the ratio of the ceramics and the average fibre had shown to decrease with an increase in the content of the $KNbO_3$. This also points in the direction of the $KNbO_3$ influencing the fibre diameter even with a change in the second type of ceramic added to the system. The differences in the interaction between the silicon-based ceramics and the solvent–polymer system may differ leading to differences in viscosity. Overall, the $KNbO_3$ has been demonstrated to allow for more control over the fibre diameters.

Table 7.4 Mixed ratio $KNbO_3$: Si_3N_4 ceramic weight and solution viscosity.

$KNbO_3$: Si_3N_4 Ratio	Viscosity / cSt
0	359 ± 7.44
1:1	720 ± 5.78
7:3	722 ± 2.76
9:1	721 ± 4.21

To determine the distribution of the ceramic across the fibre mats, EDS imaging was carried out as seen in Figure 7.6. Figure 7.6 c – e shows the K, Nb, and O atoms representing the $KNbO_3$ where all three elements correlate to the same areas where the ceramic particles are located on the image. The distribution of the $KNbO_3$ is seen across several areas of the fibres, with small areas of agglomerates formed by the ceramic. However, the agglomerates are small and do not produce large beads as seen in the PVDF / SiC and PVDF / Si_3N_4 fibres. Figure 7.6f represents the silicon within the Si_3N_4 and demonstrates several areas where the ceramic is distributed across the fibres. The areas shining in the ceramic are around 1 μm 2 μm which is larger than the size of the Si_3N_4 particle size of 758 ± 204 nm seen in the SEM images which demonstrates a degree of agglomeration occurring.

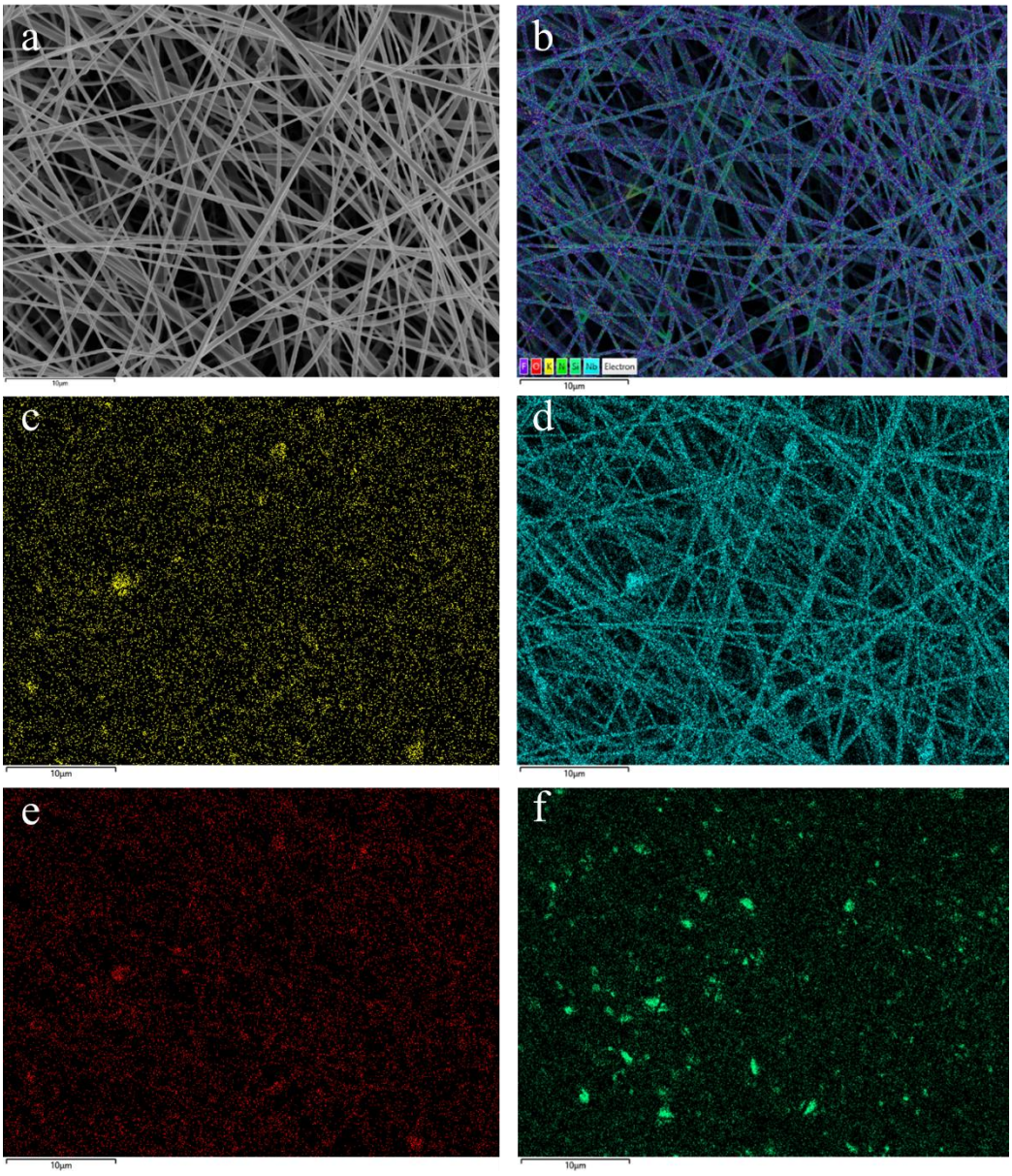

Figure 7.6. EDS image of the PVDF / $KNbO_3$ / Si_3N_4 fibres showing the distribution of the ceramic across the fibre mats. (a) Original SEM image, (b) overlaid image, (c) Potassium, (d) Niobium, (e) Oxygen, (f) Silicon.

7.1.3 Summary

The addition of the mixed ratios of the $KNbO_3$ / SiC and the $KNbO_3$ / Si_3N_4 both influenced the average fibre diameter of the material, where the addition of the ceramic led to a decrease in the overall diameter of the fibres. However, altering the ratio of the $KNbO_3$ / SiC had shown little influence on control over the average fibre diameter. In contrast the $KNbO_3$ / Si_3N_4 had shown to provide more control over the average fibre diameter allowing for small fibres to be produced with an increase in the content of the $KNbO_3$ and a decrease in the Si_3N_4. This may have been

due to the higher dielectric properties of the Si_3N_4 in comparison to the SiC which would allow for the overall dielectric properties of the solution to be higher.[218] As mentioned previously the increase in the dielectric constant of the solution allows for higher levels of polarization which assists in increasing the charge density of the jet. This in turn will allow the material to experience a higher level of coulombic forces for more elongation and stretching of the fibre jets and could allow for more homogenous fibre diameters.[286] The fibre diameters for the PVDF / SiC ranged between 540 – 500 nm and the PVDF / Si_3N_4 ranged between 420 – 510 nm. When compared to the literature the fibre diameters produced here are in line with both those produced by PVDF / niobium oxide fibres and PVDF / Si_3N_4 ranging from 100 – 600 nm for all variations.[297,306,307,308,309] This suggests that mixing the ratios of the fillers can assist in bringing control to fibre diameters. It can also be mentioned that the fibre diameters are smaller than that of the ceramic filler, especially for the Si_3N_4 which suggests that the fillers here are influencing fibre diameter and not limiting the diameters to a similar size of the particle size.

In comparison to the PVDF / SiC and the PVDF / Si_3N_4 fibres, the addition of $KNbO_3$ assisted in a reduction in the formation of beads in the PVDF / $KNbO_3$ / SiC fibres, and the complete removal of beads in the PVDF / $KNbO_3$ / Si_3N_4 fibres. This suggests that the $KNbO_3$ is acting to assist the silicon-based ceramic particles from agglomerating and in turn reduces and removes the formation of large beads in the fibrous mats. However, the exact mechanism for why this is occurring is unknown. It can also be mentioned that there are lower quantities of the silicon-based ceramic within these solutions which could have resulted in less agglomeration of the particles for better dispersion across the fibres.

The viscosity of the solutions varied between the two systems. The $KNbO_3$ / SiC resulted in an increase in the viscosity with changes to the ratio, while in contrast the $KNbO_3$ / Si_3N_4 had shown no changes in the changes to the viscosity with changes to the ratio of the ceramics. In the case of the $KNbO_3$ / SiC, the viscosity increased, and the average fibre diameter remained constant. While with the $KNbO_3$ / Si_3N_4 the viscosity remained constant and a shift to smaller fibre diameters was observed with an increase in the $KNbO_3$ concentration. This suggests that $KNbO_3$ is the dominant ceramic influencing the average fibre diameter over silicon-based ceramics. Overall, it can be said that the mixing of the $KNbO_3$ and silicon-based fibres demonstrate good control over the fibre diameters, assists in the removal of beaded fibres to produce fibres with higher surface area to mass ratios which is good for sound damping applications, and good dispersion of the filler is demonstrated for both sets of fibres electrospun.

Overall, the new work within this section demonstrates that the addition of a mixed ratio of ceramic filler can influence the average fibre size and result in a decrease in this value in comparison to pure PVDF fibres. It also demonstrates a reduction in the formation of beaded structures which was previously seen with solely silicon-based ceramic within the fibres. It

demonstrates that the $KNbO_3$ has a larger influence on the morphology and fibre diameters of the PVDF as no beaded structures are observed alongside fibre diameters in closer diameters to those produced in the previous chapter with the addition of only $KNbO_3$.

7.2 The Crystallinity of the PVDF / Niobium / Silicon Ceramic Fibres

7.2.1 FTIR of the PVDF / $KNbO_3$ / SiC Fibres

From the previous FTIR data of the PVDF / $KNbO_3$ fibres and the PVDF / SiC fibres, there is a large difference between the content of the β polymorph within both fibre composites, with the PVDF / $KNbO_3$ displaying a much higher content in the electroactive phase that the PVDF / SiC with values ranging between 67 % – 73 % and 61 % – 63 % respectively. The idea behind the addition of SiC to the mixture was to increase the thermal properties of the material as mentioned previously. However, this may result in a decrease in the content of the electroactive phase, and FTIR analysis was carried out to determine if this was the case.

The FTIR of the PVDF / $KNbO_3$ / SiC fibres as seen in Figure 7.7 demonstrates the appearance of both the absorbance peaks associated with the α polymorph and the β polymorph for all the mixed ceramic ratios electrospun. It then demonstrates a decrease in the intensity of the absorbance peak at 763 cm^{-1} with an increase in the content of $KNbO_3$. The intensity in the absorbance peaks representing the α polymorph at 614 cm^{-1} and 763 cm^{-1}, and 795 cm^{-1} remain constant for the 1:1 and 7:2 ratios, with a decrease in intensity for the 9:1 ratio. The absorbance peaks representing the β polymorph at 840 cm^{-1} and 1275 cm^{-1} remain constant in intensity for all the mixed ratio fibres produced. The trend within this work is showing that increasing the amount of $KNbO_3$ reduces the intensity peak and is in line with the work here where the $KNbO_3$ standalone in PVDF demonstrated that decrease in the α polymorphs intensity peak while the SiC had a strong peak throughout at the same peak. The decrease in intensity of the α polymorph has previously been demonstrated with the addition of $BaTiO_3$ to PVDF and has been associated with an increase in the content of the β polymorph.[355] Here it was expected that similar results would occur with the 9:1 ratio of $KNbO_3$:SiC as there is a higher loading of $KNbO_3$ in comparison to the SiC.

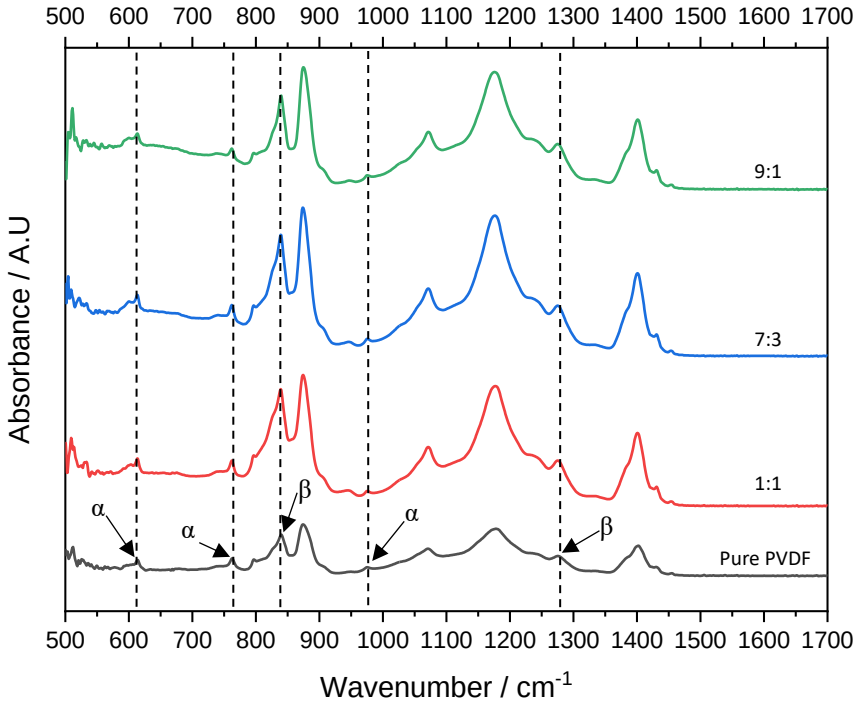

Figure 7.7. The FTIR of the PVDF / $KNbO_3$ / SiC fibres with mixed ceramic ratios of 1:1, 7:3, and 9:1 shows the intensity peaks representing the α polymorph and β polymorph.

The Beer-Lambert law 3.3.5 was applied for quantitative analysis of the β polymorph. The percentage β polymorph in the pure PVDF fibres had shown to be 56 % as previously mentioned and seen in Figure 7.8. The mixed ratio of 1:1 of $KNbO_3$: SiC resulted in an increase in the content of the β polymorph to 67 %. Altering the ratios to increase the content of the $KNbO_3$ and decrease the SiC to 7:3 and 9:1 led to a decrease in the percentage β phase to 65 % for both composite fibres respectively. In comparison to the PVDF / SiC fibres, the PVDF / $KNbO_3$ had been shown to produce higher ratios of the β polymorph. At 10 wt% SiC, the value of the β polymorph is 61 % here the maximum value reached is 6 % higher at 67 %. The average fibre diameter of the PVDF / $KNbO_3$ / SiC was closely related to that of the PVDF / $KNbO_3$ as mentioned in 7.1.1. The addition of the SiC ceramic may hinder nucleation of the electroactive phase and could be due to its low dielectric properties which may result in an overall decrease in nucleation performance of the $KNbO_3$ potentially through competition for ion-dipole interactions with the polymer chains in the PVDF.[286] Overall altering the ratio of the two ceramics has little influence on the content of the β polymorph. However, when comparing these values to those of the PVDF / SiC ranging between 61 % – 63% it can be said that $KNbO_3$ assists in increasing the nucleation of the β polymorph. In comparison to previous studies, the content of the β polymorph is lower than that produced by PVDF / KNN / ZnO and PVDF / Si_3N_4 which displayed values of 94 % and 93 % respectively.[297,309] This suggests that the fillers

used here are displaying less influence on nucleation of the β polymorph in comparison to previous studies.

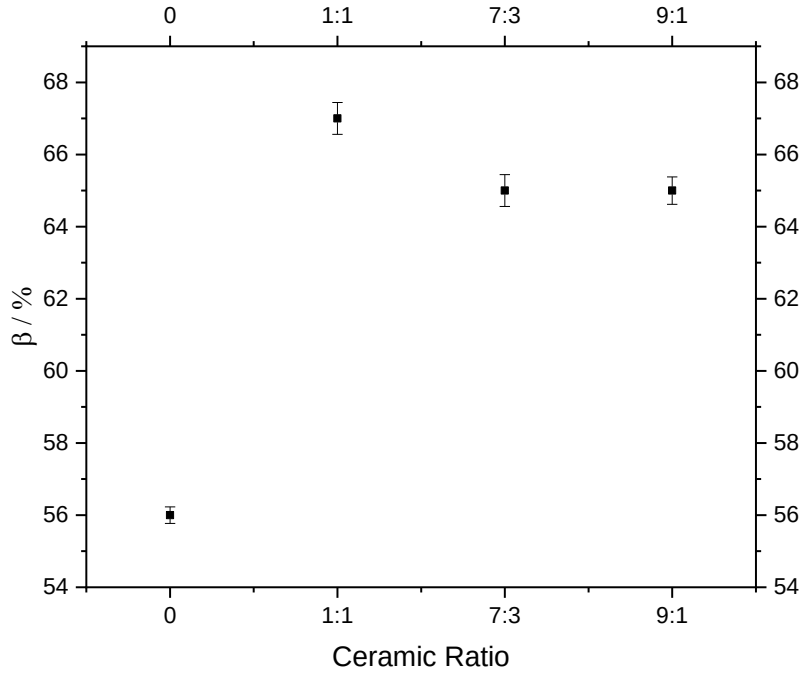

Figure 7.8. The increase in the β phase content of the PVDF fibres with the addition of a mixed ratio of / $KNbO_3$ / SiC of 1:1, 7:3, and 9:1.

Figure 7.9 demonstrates the average fibre diameter and its correlation to the percentage β polymorph. Here it demonstrates that a decrease in the average fibre diameter to below 600nm influences the increase in the content of the β polymorph. In comparison to the PVDF / $KNbO_3$ fibres previously analysed a similar result is obtained here, even with the addition of SiC which previously demonstrated no correlation between average fibre diameter and the content of percentage β polymorph within its system. This suggests that within these systems the $KNbO_3$ has a more dominant influence on influencing the percentage β polymorph and that there is a correlation between the average fibre diameter and electroactive phase. It may only have relevance when the fibre diameter is below 600 nm.

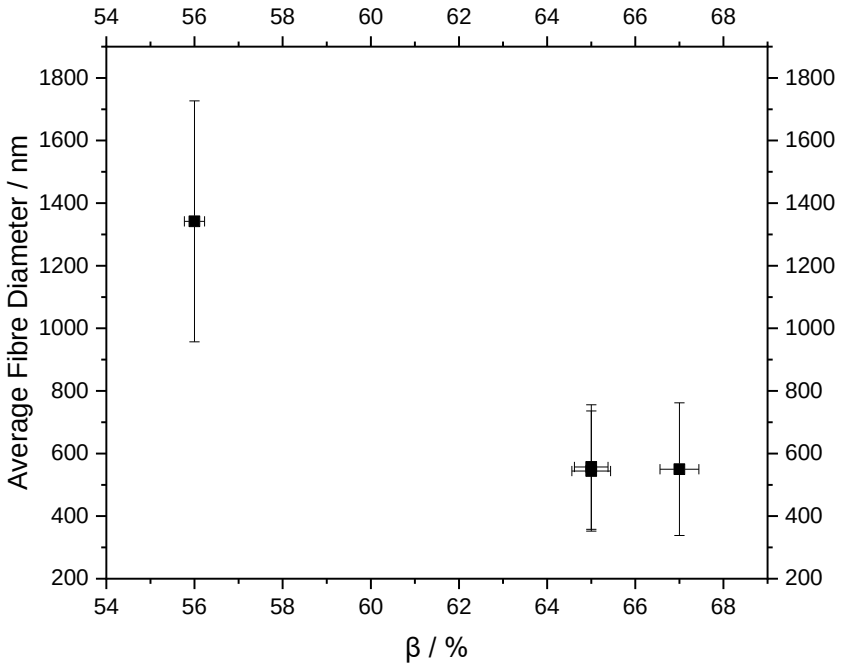

Figure 7.9. The average fibre diameter vs β phase percentage for the PVDF / $KNbO_3$ / SiC fibres. Showing a decrease in initial fibre diameter and an increase in β polymorph content.

7.2.2 DSC of the PVDF / $KNbO_3$ / SiC Fibres

The thermal properties of the mixed ratio fibre composite of PVDF / $KNbO_3$ / SiC to accommodate the FTIR result in the nucleation of the β polymorph and determine the influence mixing two types of ceramic has on the percentage crystallinity. Figure 7.10 is showing a shift in the melt temperature of the PVDF with the addition of the ceramic fillers. It also demonstrated the broadening of the peaks where it can be seen that two peaks within proximity have overlapped. This is typically associated with the nucleation of the β polymorph in the material.[344] The T_m of the pure PVDF was analysed to be 167 °C as seen in Table 7.5. The addition of the mixed ratio of 1:1 resulted in a shift in the melt temperature to the higher temperature of 169 °C for both fibrous mats electrospun. While the addition of the mixed ratio of 7:3 and 9:1 in a melt temperature of 166 °C for both composite fibrous mats respectively. The addition of PZT to PVDF has also demonstrated a melt temperature of around 168 °C which was reported to be associated with the nucleation of the β polymorph.[390] Throughout the work here the materials have all demonstrated a melt temperature around this area with peak broadening. Where it has occurred in the PVDF / niobium fibres an increase in the content of the β polymorph has been observed.

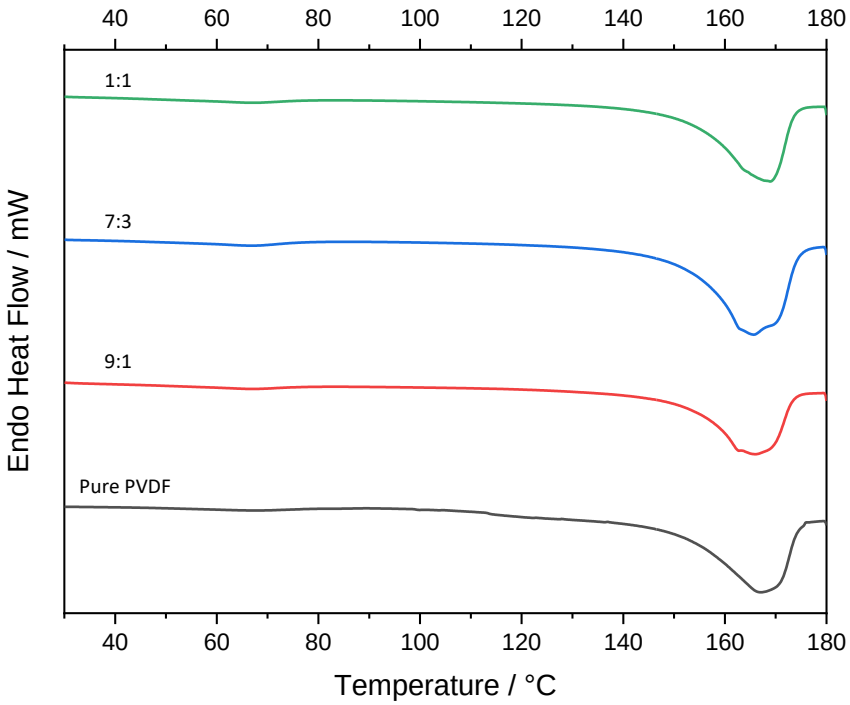

Figure 7.10. Endothermal heat flow for the PVDF / $KNbO_3$ / SiC fibres 1:1, 7:3, and 9:1 showing a shift to lower temperatures of the melting points with the addition of a dual ceramic filler.

Figure 7.11 displays the T_c of the fibres where a shift to lower temperatures is observed with the addition of the filler. The T_c of the pure PVDF was analysed as 141 °C. The addition of the mixed ratio of 1:1 resulted in a shift of the T_c to a lower temperature of 137 °C. Altering the ratio of the ceramic to 7:3 and 9:1 resulted in a further shift to a lower temperature of 136 °C. This shift in the T_c to lower temperatures suggests the ceramic particles are well dispersed across the fibrous mats as mentioned previously for the PVDF / niobium oxides and the PVDF / silicon ceramics. This acts to hinder the recrystallisation of the material which then occurs at a lower temperature.

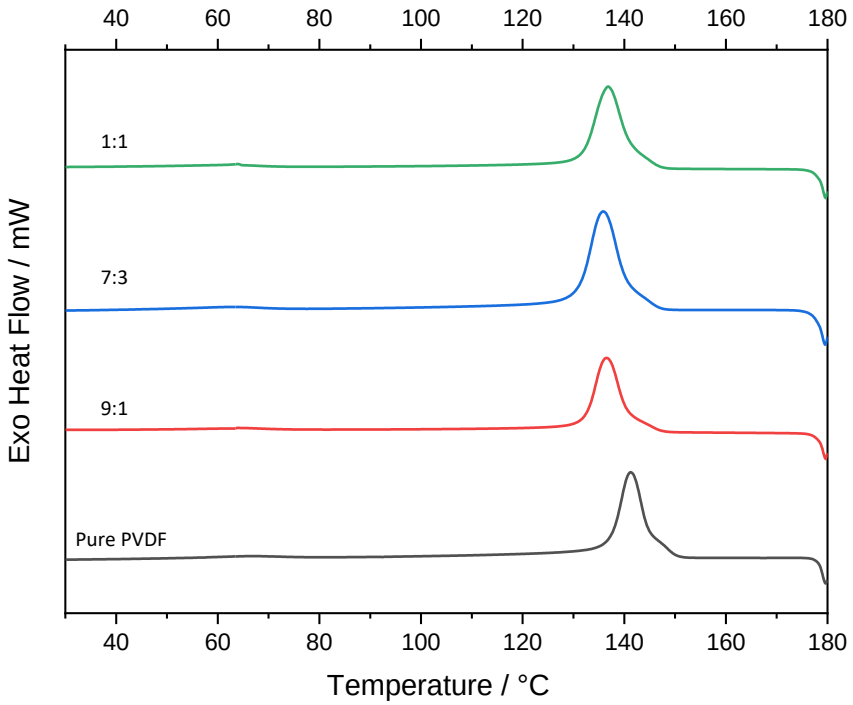

Figure 7.11. Exothermal heat flow for the PVDF / $KNbO_3$ / SiC fibres 1:1, 7:3, and 9:1 showed a decrease in recrystallisation temperatures with the addition of a dual ceramic component.

The X_c of the pure PVDF has been analysed as 53.0 %. The addition of the mixed ratio of ceramic has resulted in a decrease in the X_c for all the composite mats electrospun. The mixed ratio of 1:1 displayed the lowest X_c of 42.3 %. Altering the ratio to 7:3 and 9:1 resulted in a gradual increase in the X_c, producing values of 43.7 % and 45.6 % respectively. The gradual increase in the X_c of the materials can be attested to the change in the free volume within the polymer matrix. There is an increase in the free volume due to the changes in ratio with an increase in the $KNbO_3$. The smaller particle size of the $KNbO_3$ may allow for more movement of the chains in comparison to the SiC during recrystallisation and results in a higher crystallinity being produced. These differences in crystallinity align with the DSC data on the PVDF / $KNbO_3$ fibres and the PVDF / SiC fibres where the difference in crystallinity is higher overall for the PVDF / $KNBO_3$ fibres in comparison to the PVDF / SiC fibres. Here an increase in the content of the SiC causes a decrease in the X_c which aligns with the idea that the particle sizes may influence the crystallinity of the material through the hindrance of chain mobility.

Table 7.5. DSC data for the PVDF / $KNbO_3$ / SiC fibres 1:1, 7:3, and 9:1.

Ceramic Ratio	T_m / °C	T_c / °C	ΔH_f	X_c / %
0	167	141	55.5	53.0
1:1	169	137	44.3	42.3
7:3	166	136	45.8	43.7
9:1	166	136	47.7	45.6

7.2.3 FTIR of the PVDF / $KNbO_3$ / Si_3N_4 Fibres

From the previous data on the PVDF / SiC and PVDF/ Si_3N_4, it was observed that the Si_3N_4 demonstrated a higher content in the β polymorph. This led to the addition of the Si_3N_4 to the system to determine how it would influence the orientation in comparison to the SiC within the mixed ratio system. Figure 7.12 demonstrates the FTIR of the PVDF / $KNbO_3$ / Si_3N_4 where the formation of both the α polymorph and the β polymorph for all the mixed ceramic ratios electrospun. The intensity peaks of the peaks at 614 cm^{-1}, 763 cm^{-1}, and 795 cm^{-1} represent the α polymorph remaining constant for all the mixed ratio samples with little change. The absorbance peaks at 840 cm^{-1} and 1275 cm^{-1} represent the β polymorph remaining constant for all the mixed ratio ceramic fibres electrospun. This was also observed with the PVDF / $KNbO_3$ / SiC at the same analysed ratios which suggests that a similar trend may be followed with the ceramics here. The addition of $BaTiO_3$ to PVDF has previously demonstrated contrasting results where the peaks associated with the α polymorph decrease with the addition of the ceramic.[355] Here no change is observed and could be associated with a higher content of the α polymorph within the material. To further clarify the content of the β is lower than expected quantitative analysis was carried out.

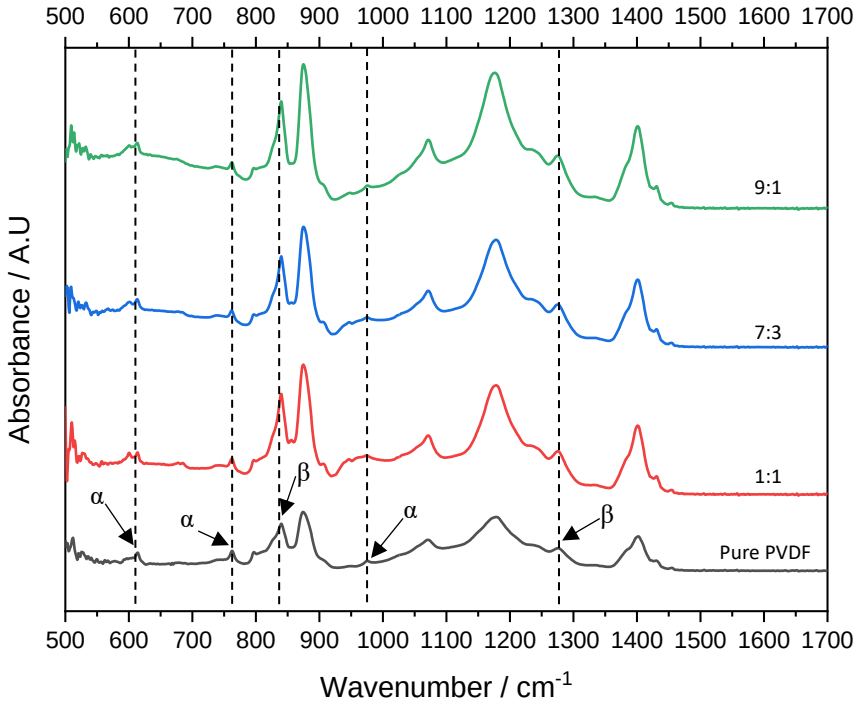

Figure 7.12. FTIR of the PVDF / $KNbO_3$ / Si_3N_4 fibres 1:1, 7:3, and 9:1 displaying the intensity peaks representing the α polymorph and the β polymorph.

The Beer-Lambert law was applied to gain a quantitative value on the content of the β polymorph. Figure 7.13 displays the change in the percentage β polymorph with the addition of the mixed ratio filler. Pure PVDF had been shown to produce a percentage β phase of 56 %. The addition of the mixed ratio of $KNbO_3$ / Si_3N_4 of a 1:1 ratio resulted in a percentage β phase of 69 %. Altering the ratio to 7:3 resulted in a decrease in the percentage β phase to 67 %. Further altering the ratio to 9:1 led to another reduction in the β phase content to 65 %. In comparison to the PVDF / Si_3N_4 fibres, the addition of $KNbO_3$ resulted in a small increase in the β polymorph. An increase of 2 % is observed with these fibres in comparison to the PVDF / Si_3N_4 at the 10 wt% ceramic loadings. The fibre diameters between the PVDF / $KNbO_3$ / SiC and PVDF / $KNbO_3$ / Si_3N_4 demonstrated thin fibre diameters with the PVDF / $KNbO_3$ / Si_3N_4 displaying an overall smaller average fibre diameter. When comparing the content of the β polymorph between the two sets of mixed ratios there is little change overall in the content of the β polymorph between the two. The content of the β polymorph here is lower than that which is reported in the literature. Values of 94 % and 93% have been reported with the addition of KNN / ZnO and Si_3N_4 respectively.[297,309] This would suggest that the piezoelectric properties of the materials here may be weaker than those produced by those within the literature.

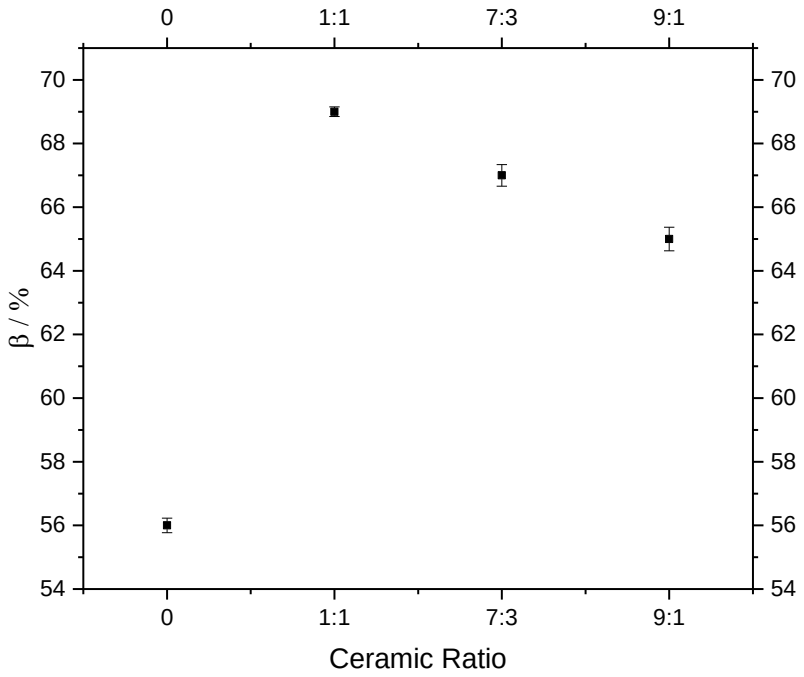

Figure 7.13. The increase in the β phase percentage of the PVDF fibres with the addition of $KNbO_3$ / Si_3N_4 at ratios of 1:1, 7:3, and 9:1.

Figure 7.14 demonstrates the correlation between the average fibre diameter and the percentage β polymorph. Here it can be seen that a decrease in the average fibre diameter increases the content of the electroactive phase. This was also observed with the PVDF / $KNbO_3$, and PVDF / $KNbO_3$ / SiC. This is in line with the literature demonstrating that the addition of a filler can reduce the average fibre diameter and influence the nucleation of the β polymorph.[289]

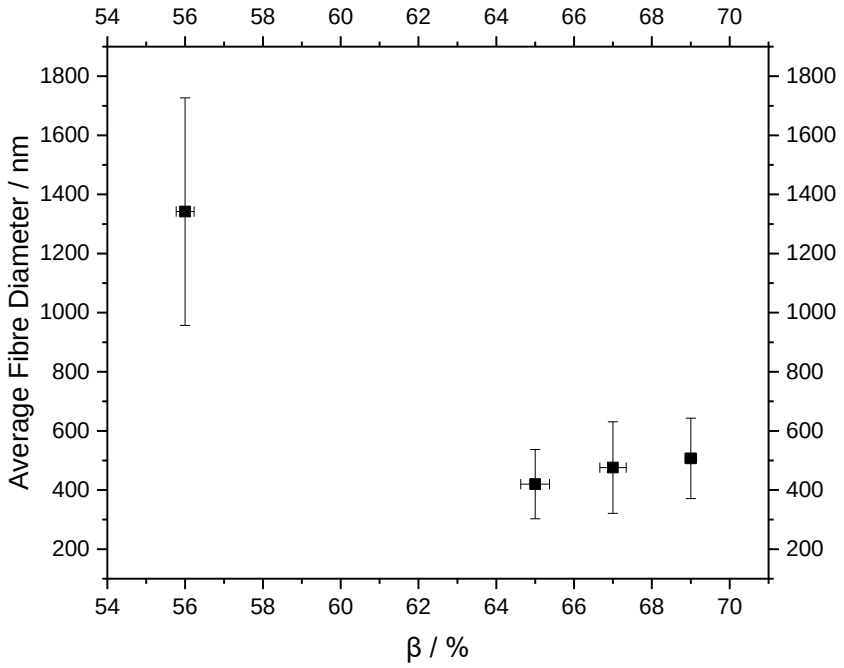

Figure 7.14. The average fibre diameter vs β phase percentage for the PVDF / KNbO3 / Si_3N_4 fibres. Showing a decrease in initial fibre diameter and an increase in β polymorph content.

7.2.4 DSC of the PVDF / $KNbO_3$ / Si_3N_4 Fibres

The FTIR data suggested that nucleation of the β polymorph occurs with the addition of the mixed ratios. An increase in the β polymorph occurred with a decrease in $KNbO_3$ and an increase in the Si_3N_4 weight percent led to an increase in the content of the β polymorph. It would be interesting to use the DSC data to back up the FTIR data and determine the level of crystallinity within the material. It was mentioned before even with a decrease in the content of the β polymorph if the crystallinity of the material increases the overall piezoelectric properties of the PVDF itself may still be similar.

Figure 7.15 displays the shift in the melt temperatures and the splitting/peak broadening of the melt temperatures with the addition of the mixed ratio of filler. The T_m of the pure PVDF was analysed to be 167 °C as seen in Table 7.6. The addition of the mixed ratio of ceramic 1:1 led to a decrease in the T_m to 164 °C. Altering the ratio to 7:3 does not influence the melt temperature resulting in the same value of 164 °C. At the ratio of 9:1, an increase in the T_m to 165 °C was observed. The lower peak is displayed at 166 °C – 167 °C with the formation of a shoulder peak displayed close to 170 °C. This suggests the presence of both the α polymorph and the β polymorph which is in line with the FTIR data analysed previously.

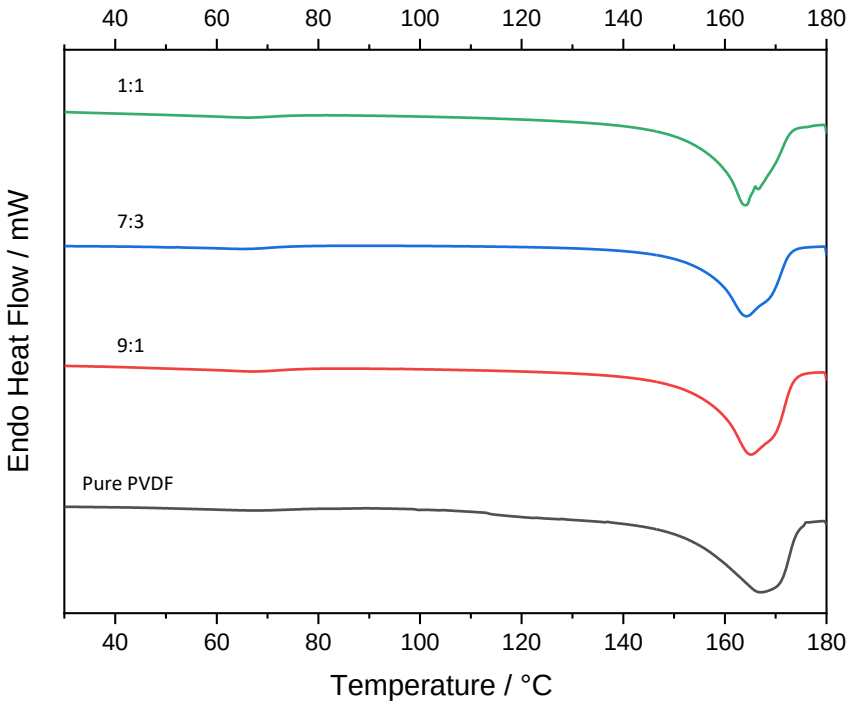

Figure 7.15. The endothermal heat flow of the PVDF / $KNbO_3$ / Si_3N_4 fibres 1:1, 7:3, and 9:1 shows a decrease in the melt temperature with the addition of ceramic.

Figure 7.16 displays the shift in the T_c of the PVDF mixed ratio fibres to lower temperatures. The T_c of the pure PVDF was analysed as 141 °C. The addition of the ceramic filler resulted in a decrease in the T_c as seen in Figure 7.13. The addition of the mixed ratio of 1:1 resulted in a T_c of 138 °C. Altering the ratio to 7:3 had no influence on the T_c producing the same value of 138 °C. The ratio of 9:1 resulted in a T_c of 136 °C. The decrease in T_c is associated with the distribution of the ceramic across the material. It also suggests that the ceramic is hindering the recrystallization of the material as it is recrystallizing at a lower temperature than that of the pure PVDF. This is expected as the same results were obtained by the PVDF / niobium oxide fibres and the PVDF / silicon-based fibres.

The X_c of the pure PVDF was analysed as 53.0 %. The addition of the mixed ratio of 1:1 resulted in a decrease in the crystallinity of the material to 42.9 %. Altering the mixed ratio to 7:3 and 9:1 resulted in a gradual increase in the X_c producing values of 43.7 % and 47.9 % respectively. In comparison to the PVDF / $KNbO_3$ / SiC, a similar increase in the X_c is observed. This may occur due to the same phenomena where there is an increase in free volume within the material which allows for the chains to recrystallise due to a reduction in the hindrance of the polymer chains. However, when comparing these results to the FTIR results it shows that there is an increase in the content of the β polymorph with a decrease in the crystallinity. In terms of the electroactive properties of the PVDF itself, it could be said that a decrease in the β

polymorph with an increase in the crystallinity could result in a similar output of charge by the PVDF when the piezoelectric ceramic is not considered.

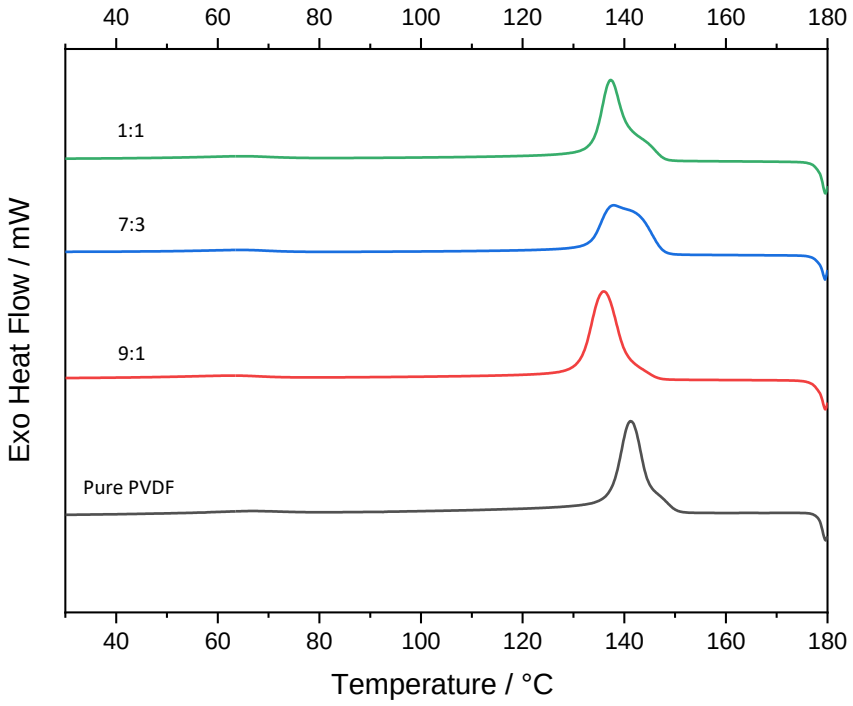

Figure 7.16. The exothermal heat flow of the PVDF / $KNbO_3$ / Si_3N_4 fibres 1:1, 7:3, and 9:1 shows a shift to lower recrystallisation temperatures with the addition of the mixed ratio of ceramics.

Table 7.6. The DSC data for the PVDF / $KNbO_3$ / Si_3N_4 fibres 1:1, 7:3, and 9:1.

Ceramic Ratio	**T_m / °C**	**T_c / °C**	**ΔH_f**	**X_c / %**
0	167	141	55.5	53.0
1:1	164	138	44.9	42.9
7:3	164	138	45.7	43.7
9:1	165	136	50.1	47.9

7.2.5 Summary

The PVDF / $KNbO_3$ / SiC fibres and PVDF / $KNbO_3$ / Si_3N_4 fibres displayed similarities in the crystallinity of the polymer with the changes in the ratio of the ceramics. It was analysed that a mixed ratio of 1:1 resulted in the highest content of the β polymorph for both composite fibre mats. Increasing the content of the $KNbO_3$ and decreasing the silicon-based ceramics with the

ratio of 7:3 and 9:1 had shown to decrease the content of the β polymorph within the PVDF fibres. This was unexpected as the PVDF / $KNbO_3$ fibres display a higher percentage β polymorph in comparison to the fibres produced in this section. Further analysis of the interactions between the mixed ratio of ceramic fillers may be required for a better understanding of why this may be occurring. Overall, the content of the β polymorph within these materials is lower than that reported in the literature. The highest value is reported with the addition of KNN / ZnO at a value of 94% and the addition of SiC at a value of 93%.[309,351]

To further investigate these values of the β polymorph content the DSC was employed. The increase in crystallinity of the PVDF with the changes in the ratio of the ceramic for both systems may offset the β polymorph values analysed in the FTIR. A gradual increase in the crystallinity with a decrease in the β polymorph may result in an overall similar volume of the electroactive phase within the material, potentially resulting in a similar piezoelectric output. It should also be mentioned that the increase in the crystallinity occurred for both materials where higher quantities of the $KNbO_3$ ceramic were within the material. Overall, it may have occurred as the silicon-based ceramics displayed a much higher particle size than the $KNbO_3$ which may have increased the hindrance of chain recrystallisation with its increase in content. The overall piezoelectric properties of the material would however be higher at the 9:1 ratio for both ceramics as there would be a higher content of the $KNbO_3$ within the material. However, further piezoelectric studies are required for confirmation.

The new work within this section demonstrates that the mixed ratio of $KNbO_3$ / SiC or Si_3N_4 can assist in influencing the nucleation of the β polymorph. It also demonstrates that changing the ratios between 1:1 – 9:1 has little influence on the control of the amount of the β polymorph within the PVDF fibres. Overall, it suggests that $KNbO_3$ has a larger influence on the nucleation of the β polymorph as the percentages are more closely related to the previously produced PVDF / $KNbO_3$ fibres.

7.3 Thermal and Mechanical Properties of PVDF / $KNbO_3$ / Silicon Fibres

The previous values on the stability of the PVDF fibres with the addition of $KNbO_3$ and the silicon-based ceramics all contrasted in result with the PVDF / $KNbO_3$ fibres displaying a decrease in onset degradation temperatures. The PVDF / SiC displayed an increase in onset degradation temperature, and the PVDF / Si_3N_4 displayed little influence on the onset degradation temperature. Here it would be interesting to see how a mixture of the ceramics could influence the thermal stability of the material, alongside if effective loading of the ceramic filler is carried out. As mentioned previously the increase in thermal onset degradation may

occur due to better heat dissipation across the material. This is beneficial for sound damping applications as it may then allow for effective heat dissipation across the material when the sound energy is absorbed.

Following on from the previous analysis on the viscoelastic damping properties of the PVDF / $KNbO_3$ and the PVDF / silicon-based ceramics the same properties were analysed here to determine the influence adding SiC or Si_3N_4 would have on the overall properties. As analysed previously in 5.3.3, 6.3.2, and 6.3.4 it was shown that the PVDF / $KNbO_3$ fibres demonstrated higher damping properties than that of the PVDF / SiC fibres and Si_3N_4 / fibres respectively. As mentioned previously silicon-based ceramic has been added to enhance the thermal stability properties. However, for the DMTA analysis, it was the aim to add the silicon-based ceramic filler without reducing the damping properties of the overall material. Here it is of interest to see if the damping properties of the composite can be kept high with the addition of both ceramic components which demonstrates to influence of these properties differently.

7.3.1 TGA of the PVDF / $KNbO_3$ / SiC Fibres

The degradation of the PVDF / $KNbO_3$ / SiC fibres can be seen in Figure 7.17, where a two-step degradation process takes place like the PVDF / niobium and PVDF / silicon fibres analysed in 5.3 and 6.3. The pure PVDF displayed a degradation onset temperature of 413 °C. The addition of the mixed ratio of ceramics resulted in an overall reduction in the thermal onset temperature of the materials as seen in Figure 7.17. The 1:1 ratio displayed a degradation temperature of 401 °C. Altering the ratio to 7:3 resulted in a decrease in the onset degradation temperature to 391 °C. The 9:1 mixed ratio resulted in an increase in the onset degradation temperature to 410 °C in comparison to the other two mixed ratios. The second degradation step for the pure PVDF has shown to take place between 500 °C – 800 °C, while with the addition of the ceramic particles, this degradation step was shifted to the lower range of 450 °C – 600 °C. The second degradation step is associated with a complex poly(aromatization) step.[362,363] Previously it has been reported that the degradation step decreases with the addition of niobium oxide ceramics and has shown to increase with the addition of SiC.[365,388]This suggests that the influence of the $KNbO_3$ outweighs the thermal stability properties the SiC can provide for the material. In comparison to the PVDF / $KNbO_3$ and the PVDF / SiC, it could be that the mixture of the two materials influences the thermal stability of the material, as the onset degradation temperatures specified for all three PVDF / mixed ratios are between those of the values displayed by the unmixed PVDF / $KNbO_3$ and the PVDF / SiC.

The displayed residual masses of the PVDF / $KNbO_3$ / SiC fibres for all three mixed ratios had shown to increase with the addition of the ceramics which was expected as this occurred with the addition of the ceramic in earlier chapters. The residual mass from the 1:1 –

7:3 was similar at 22.7 % and 24.3 % respectively as seen in Table 7.7. However, the 9:1 mixed ratio demonstrated a decrease in the residual mass with also an increase in the thermal onset temperature was characteristic of the PVDF / SiC fibres. It could be said that the PVDF loaded with a 9:1 ratio demonstrated a lower content of the $KNbO_3$ within the mix which led to the SiC having a larger influence on the onset degradation shifting it to a higher temperature. Overall, it can be mentioned that the ceramic fillers have been successfully added to the PVDF fibres. However, determining the exact content of each ceramic within the mixture cannot be established with the data provided.

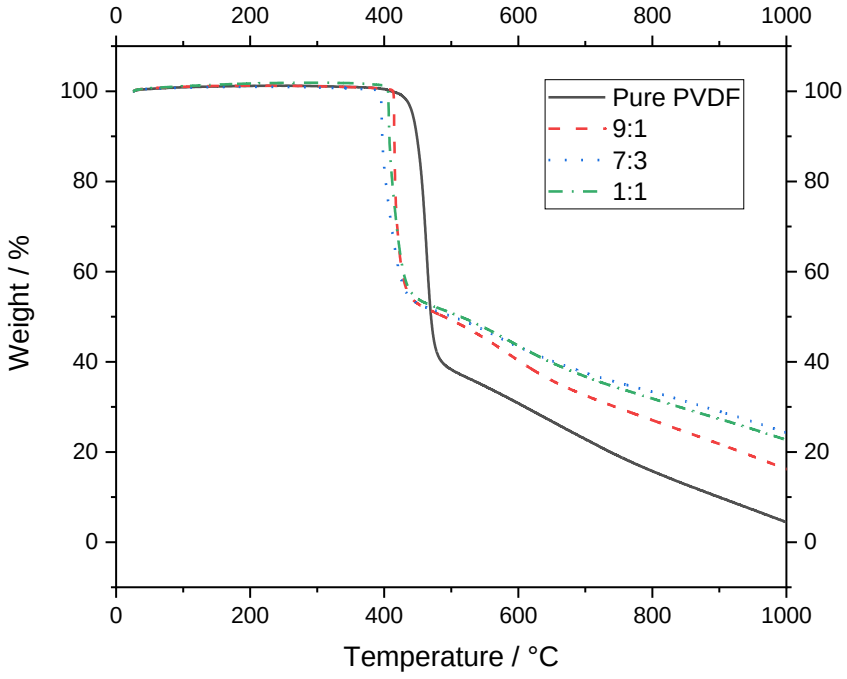

Figure 7.17. The TGA graph for the PVDF / $KNbO_3$ / SiC fibres 1:1, 7:3, and 9:1 shows a decrease in the degradation temperature and an increase in residual mass with the addition of ceramic.

Table 7.7. The TGA data of the PVDF / KNbO3 / SiC fibres 1:1, 7:3, and 9:1.

$KNbO_3$ / SiC Ratio	**Degradation Temperature / °C**	**Residual Mass / %**
0	413	4.41
1:1	401	22.7
7:3	391	24.3
9:1	410	16.2

7.3.2 DMTA of the PVDF / $KNbO_3$ / SiC Fibres

Following on from the previous analysis on the viscoelastic damping properties of the PVDF / $KNbO_3$ and the PVDF / SiC the properties were analysed for the mixed ratio to determine if mixing the ratios of ceramic within the PVDF led to changes to the damping properties. The pure PVDF had shown a high *E'* in comparison to all the PVDF / $KNbO_3$ / SiC fibres as seen in Figure 7.18a. It also displayed the highest *E'* out of these fibres produced here displaying a value of 48.8 MPa at 0 °C. The addition of ceramic resulted in a decrease in the *E'*, with the 1:1 and 7:3 ratios displaying similar values of a value of 21.2 MPa and 19.4 MPa respectively. The 9:1 ratio had a higher *E'* at 48.7 MPa close to that of the pure PVDF fibres. In comparison to the *E'* of the PVDF / $KNbO_3$ fibres at the maximum loading of 10 wt%, 80.2 MPa, the mixed ratio is much lower. This may have occurred due to the addition of the SiC to the system which has previously been shown in 6.3.2 to decrease the materials *E'* due to the decrease in crystallinity alongside the debonding of the ceramic allowing for sliding of the movement of the chains. It can also be mentioned that the SiC has less influence on the nucleation of the β polymorph due to its low dielectric properties which may have resulted in a decrease in the wrapping of the polymer chains around the filler allowing the chains to move more freely in comparison to the PVDF / $KNbO_3$ fibres this may have assisted in causing the reduction in the *E'* within the PVDF / $KNbO_3$ / SiC fibres.[286] When compared to the literature the values demonstrated here are also much lower than was reported. The addition of MnO_2 or PZT to PVDF displayed a large increase in the damping properties, especially the storage modulus.[374] *E'* values of 4.5 – 8 GPa were demonstrated with the addition of the filler and could be attributed to the larger material diameters of the material tested in comparison to the thinner materials diameters here.[375,369]

The *E''* of the pure PVDF was seen to be the highest out of the fibres electrospun Figure 7.18b. At 0 °C the *E''* for the pure PVDF was 3.00 MPa. The addition of the PVDF / $KNbO_3$ / SiC resulted in a decrease in the *E''* for all three of the mixed ratios. The 1:1, 7:3 and 9:1 ratios displayed values of 1.59 MPa, 1.28 MPa, and 2.54 MPa, at 0 °C for the fibres respectively.

Figure 7.18c displays the shift in the T_g to higher temperatures and an increase in the damping factor. The tan δ of the fibres had shown to increase in intensity from the pure PVDF < 9:1 < 7:3 < and the 1:1, suggesting that the 1:1 ratio has the highest damping performance out of the four electrospun fibrous mats. However, as mentioned previously the damping factor is a ratio of the *E'' / E'* and these values should be taken into consideration when there are large differences between them respectively. The T_g of pure PVDF fibres was analysed at -47 °C. The addition of the mixed ratio of $KNbO_3$ and SiC led to an increase in the T_g, where the 1:1, 7:3 and 9:1 ratio displayed a T_g of -42.2 °C, -42,9 °C, and -44.05 °C respectively. The increase in the T_g occurs due to the reduction in the free volume within the polymer matrix which results in a decrease in the mobility of the polymer chains.[374,375] The SiC has a larger particle size than the $KNbO_3$ which results in a decrease in the free volume within the polymer matrix with an increase in the content of the SiC. This leads to a gradual increase in the T_g as mentioned in previous chapters.

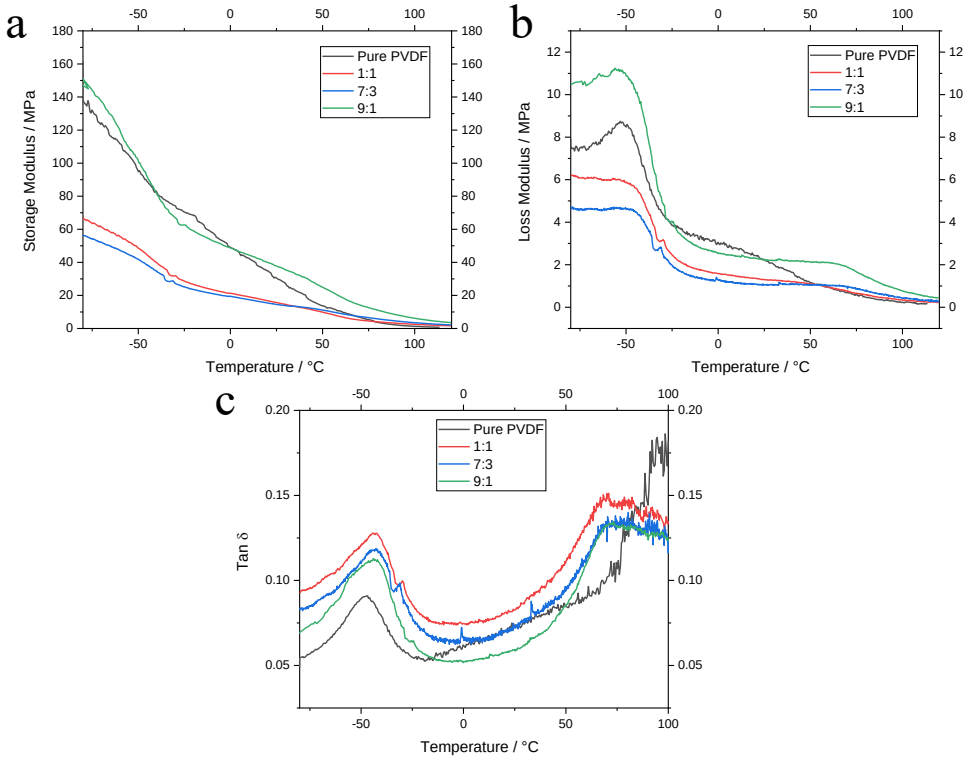

Figure 7.18. The DMTA of the PVDF / $KNbO_3$ / SiC fibres 1:1, 7:3 and 9:1 showed an overall decrease in damping properties of the material with the addition of ceramic.

7.3.3 TGA of the PVDF / $KNbO_3$ / Si_3N_4 Fibres

The degradation of the PVDF /$KNbO_3$ / Si_3N_4 fibres can be seen in Figure 7.19, where a two-step degradation process takes place like the PVDF / $KNbO_3$ / SiC, and the previous PVDF / ceramic composite fibres electrospun as seen in 5.3 and 6.3 where the 2nd degradation step is associated with a complex poly(aromatization) step.[362,363] The pure PVDF has displayed an onset degradation temperature of 413 °C. The addition of the mixed ratios of $KNbO_3$ / Si_3N_4 resulted in a decrease in the thermal stability as seen in Figure 7.19 of the material like that which occurred with the $KNbO_3$ / SiC mixed ratio fibres. The 1:1 mixed ratio displayed an onset degradation temperature of 396 °C. The mixed ratio of 7:3 and 9:1 displayed an increase in the onset degradation temperature to 402 °C and 405 °C respectively. In comparison to the PVDF / $KNbO_3$ / SiC, the onset degradation temperatures were within a similar range suggesting that changing the type of silicon-based ceramic within the material has little influence on the overall thermal stability. However, it does demonstrate that altering the ratio of the ceramic can have some influence on thermal stability as the values produced here are higher than that of the PVDF / $KNbO_3$ which demonstrated an onset degradation temperature range of 368 °C – 384 °C. It has been previously studied that the addition of niobium oxide materials to PVDF results in a decrease in degradation temperature due to a decrease in material crystallinity which is also observed here.[365] It was expected that the degradation temperature would not decrease with the addition of Si_3N_4 as it has previously been reported to increase the degradation temperatures.[388] Overall, this suggests that the $KNbO_3$ influences the degradation temperature to a higher degree than the Si_3N_4.

The residual masses of the pure PVDF were analysed as 4.41 %. The addition of the ceramic materials all displayed an increase in the residual mass as expected which suggests the successful addition of the mixed ratio of $KNbO_3$: Si_3N_4 was carried out. Like the PVDF / $KNbO_3$ / SiC fibres, a similar trend was observed with the PVDF / $KNBO_3$ / Si_3N_4 fibres where a gradual increase occurred with the 1:1 and 7:3 ratios. While the 9:3 ratio had shown a decrease in the residual mass. However, the decrease was not as large with the PVDF / $KNbO_3$ / Si_4N_4 fibres which may be due to efficient quantities of the $KNbO_3$ entering the system in comparison to the PVDF / $KNbO_3$ / SiC at the 9:1 ratio.

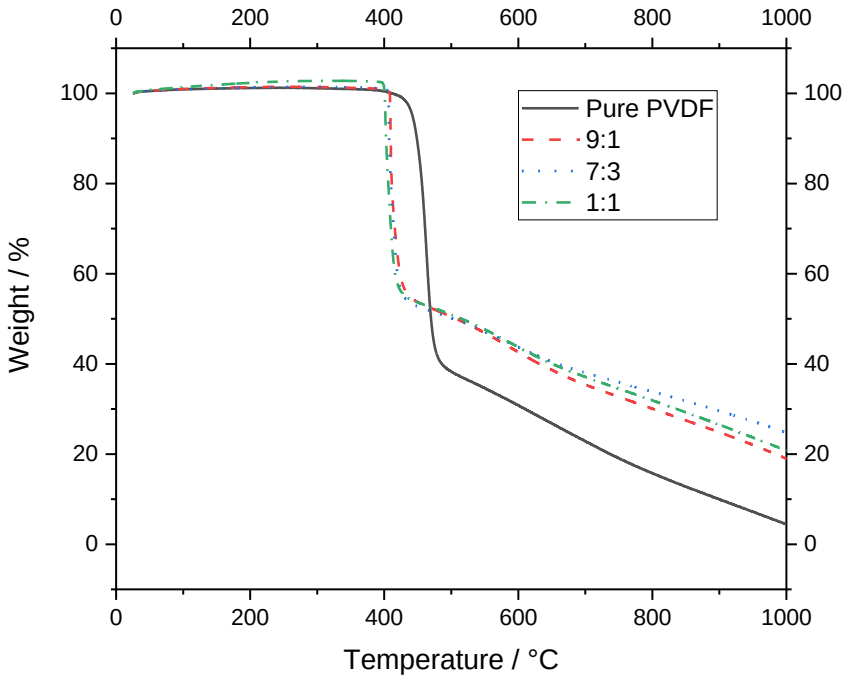

Figure 7.19. The TGA graph for the PVDF / $KNbO_3$ / Si_3N_4 fibres 1:1, 7:3, and 9:1 shows a decrease in the degradation temperature and an increase in residual mass with the addition of ceramic.

Table 7.8. The TGA data of the PVDF / $KNbO_3$ / Si_3N_4 fibres 1:1, 7:3, and 9:1.

$KNbO_3$: Si_3N_4 Ratio	**Degradation Temperature / °C**	**Residual Mass / %**
0	413	4.41
1:1	396	20.8
7:3	402	24.8
9:1	405	19.0

7.3.4 DMTA of the PVDF / $KNbO_3$ / Si_3N_4 Fibres

Following on from the PVDF / $KNbO_3$ / SiC fibres the PVDF / $KNbO_3$ / Si_3N_4 fibres display contrasting results, where the 9:1 mixed ratio displays the lowest *E'* while the 1:1 and 7:3 mixed ratios display higher *E'*. Figure 7.20a displays the change in storage modulus across the temperature range where a decrease is observed for all materials. The pure PVDF, 1:1, and 7:3 fibres displayed similar *E'* across the entire temperature range as seen in Figure 7.20a with *E'* values of 48.8 MPa, 53.4 MPa, and 50.7 MPa at 0 °C respectively. The 9:1 ratio displayed a

much lower *E'* of 20.9 MPa. In comparison to the PVDF / $KNbO_3$ / SiC fibres, these fibres produced here displayed a higher *E'* suggesting a greater level of rigidity in the material due to a decrease in mobility of the polymer chains due to the addition of the ceramic.[361] However, the 9:1 demonstrates an increase in crystallinity which is associated with an increase in rigidity and an increase in *E'* which does not occur here. The *E''* of the pure PVDF was analysed as 3.00 MPa at 0 °C. The addition of the mixed ratio of 1:1 led to an increase in the *E''*, displaying a value of 3.26 MPa. Altering the ratio to 7:3 and 9:1 resulted in a gradual decrease in the *E''* of the fibres displaying values of 2.84 MPa, and 1.51 MPa at 0 °C respectively. Here the values of the *E'* are lower than what is reported in the literature for PVDF fibres with the addition of filler such as MnO_2 and PZT. These materials have *E'* ranging between 4.5 – 8 GPa could be due to the larger material diameters of the material tested in comparison to the thinner materials' diameters here.[374,375]

The tan δ peak of the pure PVDF was displayed as lower than that of the PVDF / $KNbO_3$ / Si_3N_4 fibres for all the three mixed ratios as seen in Figure 7.20c where a shift in the T_g is observed. This demonstrates that the addition of ceramic fillers assists in increasing the viscoelastic damping properties of the overall fibres. The increase in the tan δ occurs from the ratio of 7:3 < 1:1 < 9:1, suggesting that the 9:1 mixed ratio fibre displays the highest damping properties. However, as mentioned previously it should be mentioned that when there is a large difference in the *E''* and *E'* it may produce misleading values. The T_g of the pure PVDF was analysed as -47 °C as mentioned previously. The addition of the mixed ratio of $KNbO_3$ / Si_3N_4 resulted in a shift in the T_g to higher temperatures of -44.0 °C, -44.5 °C, and -43.3 °C for the 1:1, 7:3, and 9:1 fibres respectively. As mentioned previously the increase in the T_g is associated with the decrease in the mobility of the chains with the addition of the ceramic filler.[374,375]

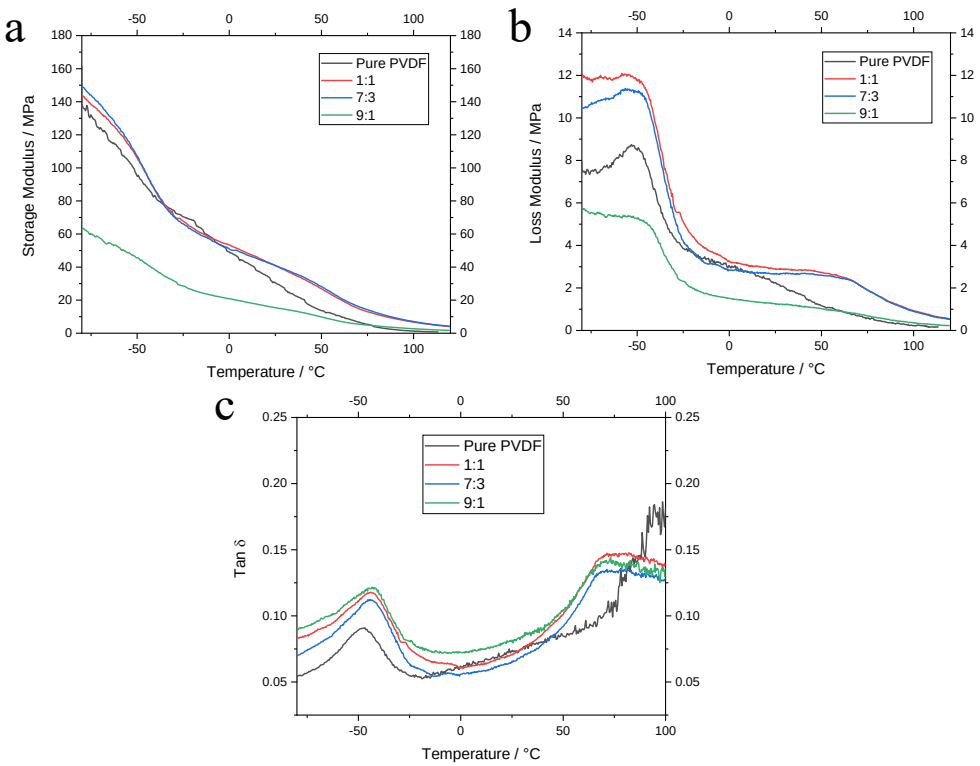

Figure 7.20. DMTA of the PVDF / KNbO3 / Si_3N_4 fibres 1:1, 7:3 and 9:1 showing the viscoelastic damping properties with the addition of ceramic.

7.3.5 Summary

The PVDF / $KNbO_3$ / SiC fibres and the PVDF / $KNbO_3$ / Si_3N_4 fibres all displayed similar onset degradation temperatures ranging from 390 °C – 410 °C. Overall a gradual increase in the onset temperature was observed with an increase in the content of the $KNbO_3$ suggesting that better thermal stability was achieved by altering the mixed ratio. However, in comparison to pure PVDF, the addition of the ceramic resulted in a reduction in the thermal stability of the material. As mentioned previously this occurs due to the defects which occur within the material with the addition of the ceramic particles and an increase in crystallinity when comparing the ceramic loaded PVDF fibres.[365] Overall, it can be said that the successful addition of the mixed ratios of ceramic was carried out, and the thermal stability of the materials was in between the values demonstrated by the unmixed PVDF / $KNbO_3$, PVDF / SiC, and PVDF / Si_3N_4 fibres. With this being said these materials may provide for effective heat dissipation during sound testing when the sound energy is converted into thermal energy through the friction of the fibres. Previously within the literature, it has been demonstrated that with the addition of silicon-based materials thermal heat transformation increases and degradation values increase. [297,388] It was expected that with the addition of the silicon-based filler in combination with the $KNbO_3$ that

an increase in the degradation temperatures would also occur. However, this did not occur and suggests that the $KNbO_3$ has a larger influence on the thermal stability of the material over SiC and Si_3N_4

The damping properties of the PVDF / $KNbO_3$ / SiC fibres and the PVDF / $KNbO_3$ / Si_3N_4 fibres had been shown to contrast each other. The tan δ increase in intensity from 9:1 < 7:3 < 1:1 for the PVDF / $KNbO_3$ / SiC fibres and then displaying ad 9:1 > 7:3 > 1:1 for the PVDF / $KNbO_3$ / Si_3N_4 fibres. Both systems seem to be very complex with contrasting intensities in the tan δ. However, as mentioned previously it should be pointed out that the tan δ is a ratio of the *E''* / *E'* and can provide misleading information used solely to determine the level of damping when the individual values of the *E'* and *E''* are largely different. However, it can still be mentioned here that the increase in T_g analysed using the tan δ values overall suggests that there is a hindrance of chain mobility with the addition of the ceramic filler, which correlated with the DSC data showing hindrance of the ceramic during recrystallisation. The increase in the T_g with the addition of the fillers demonstrates a decrease in free volume within the material and a decrease in chain mobility. [374,375] It should also be mentioned here that further study on the interfacial interactions between the ceramic and polymer could be analysed for more understanding of mixing the ratios of the $KNbO_3$ and the SiC or Si_3N_4.

The new work within the section demonstrates that the addition of a mixed ratio of ceramic fillers does not influence the degradation properties of the material and damping properties as expected with a decrease in the degradation values and little change to the damping performance. Overall, there is still a shift in the T_g to a higher temperature which demonstrates that the filler is distributed across the material hindering chain mobility.

7.4 Sound Testing of the PVDF / Niobium / Silicon Ceramic Fibres

Following on from the characterisation and viscoelastic damping analysis of the PVDF / $KNbO_3$ / silicon-based fibres it was determined to use the 1:1 mixed ratio of the ceramics for both the $KNBO_3$ / SiC and $KNbO_3$ / Si_3N_4 variations. It was decided to choose these materials as they both demonstrated a high value to nucleate the β polymorph in the PVDF at the 1:1 ratio and having an equal combination of a piezoelectric ceramic and thermally conductive ceramic could bring the best of both properties into the PVDF fibres. It is already demonstrated that the standalone PVDF / $KNbO_3$ fibres and PVDF / silicon-based fibres have differences in their sound damping properties, with the former displaying the higher NRC and absorption coefficient across the entire frequency range. This addition of $KNbO_3$ to the PVDF / silicon-based fibres may potentially enhance the damping properties of that material at the lower frequency range and produce a material that is effective in sound damping and energy dissipation.

7.4.1 PET / PVDF / $KNbO_3$ / Silicon-based Fibre Sound Testing

The PET foam as mentioned previously had shown poor acoustic performance across the frequency range analysed as seen in Figure 7.21. The maximum absorption coefficient achieved by the PET foam was 0.44 at 6000 Hz. These values are similar to the literature for PET fibres within the same frequency range where a sound absorption coefficient of 0.42 at 6000 Hz was analysed.[378]

Figure 7.21 demonstrates the absorbance coefficient of the PET alongside the PET / mixed ratio filler fibres. It demonstrates that with the addition of the fibre mats, the formation of the double resonance peak occurs which was seen in the previous fibre mats added to the PET in this work. The first occurs between 1000 Hz – 1500 Hz and the second occurs at 4500 Hz – 5000 Hz. The appearance of a double resonance peak has previously been studied and demonstrated to occur due to a back cavity or rigid backing. The systems act as an air cavity behind the fibres and act as a resonance structure which causes the formation of double resonance peaks.[103,379]

The pure PVDF fibres displayed the highest absorption coefficient at the first resonance peak at 1000 Hz – 1500 Hz. The addition of the mixed ratio PVDF / KNbO3 / SiC fibres and the PVDF / $KNbO_3$ / Si_3N_4 fibres both demonstrated a decrease in the first resonance peak in comparison to the pure PVDF back with PET. This was like the previous PVDF / niobium oxide and PVDF / silicon-based fibres. It was suggested this occurred due to the material causing reflection of the sound where the sound does not enter the material and is not absorbed effectively. At the higher frequency resonance peak, the pure PVDF fibres and the PVDF /

$KNbO_3$ / Si_3N_4 displayed similar absorption coefficients, while the PVDF / $KNbO_3$ / SiC fibres displayed a much higher absorption coefficient demonstrating that some control to the resonance peak can be carried out by altering the type of ceramic within the material. The formation of the double resonance peak occurred due to the highly porous PET acting as a back cavity as mentioned in 5.4.1.[103,379] In comparison to the PVDF / $KNbO_3$ and PVDF / silicon-based fibres, these fibres here demonstrate an overall display of a higher sound absorption coefficient at both the lower and higher resonance peaks. This may have occurred due to less reflection and more absorption occurring with these fibres in comparison to those single ceramic polymer composites. Previously studied materials have demonstrated absorption coefficients ranging between 0.89 – 1 at the low-frequency range. [102,105] The materials within this work demonstrate absorption coefficients ranging between 0.6 – 0.9 with the PVDF filled fibres demonstrating within the lower part of that range at 0.6 – 0.7. This suggests that the PVDF / Sic or Si_3N_4 fibre mats may not perform as well as those previously used at the low-frequency ranges.

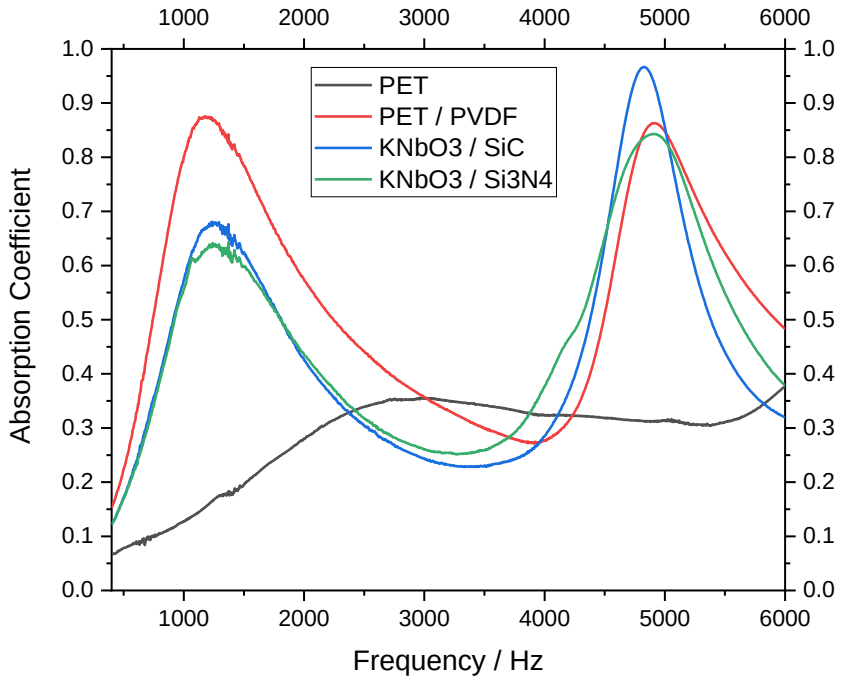

Figure 7.21. The sound absorption coefficient vs. frequency of the PET / PVDF / $KNbO_3$ / SiC or Si_3N_4 fibres shows two main resonance peaks.

The NRC values of the pure PVDF were much higher than that of the PET foams and PVDF / $KNbO_3$ / silicon-based fibres as seen in Figure 7.22 where a decrease in the average fibre diameter resulted in a decrease in the NRC. Due to the high porosity of the PET foams, the NRC values and absorption coefficient across the entire frequency range were low

displaying a value of 0.13. The pure PVDF fibres displayed an NRC value of 0.42, while the addition of the mixed ratio of 1:1 $KNbO_3$ / SiC or $KNbO_3$ / Si_3N_4 displayed the same NRC values of 0.31 respectively. These values were similar to those analysed by the fibres containing a single type of ceramic. The change in the NRC was not observed with the change in the type of the ceramic from SiC to Si_3N_4. To further analyse this the average fibre diameter was plotted with the NRC values to determine if there was a correlation between the two values. As mentioned in 5.4.1 and 6.4.1 the decrease in average fibre was associated with a decrease in the absorption coefficient with the PVDF / niobium oxide and PVDF / silicon-based fibres backed with PET respectively. The same results were obtained here, where a decrease in the average fibre diameter resulted in a decrease in the NRC value. The two mixed ratio fibres here display similar average fibre diameters and are suggested to have similar sound absorption properties at the lower frequency range where the NRC was analysed.

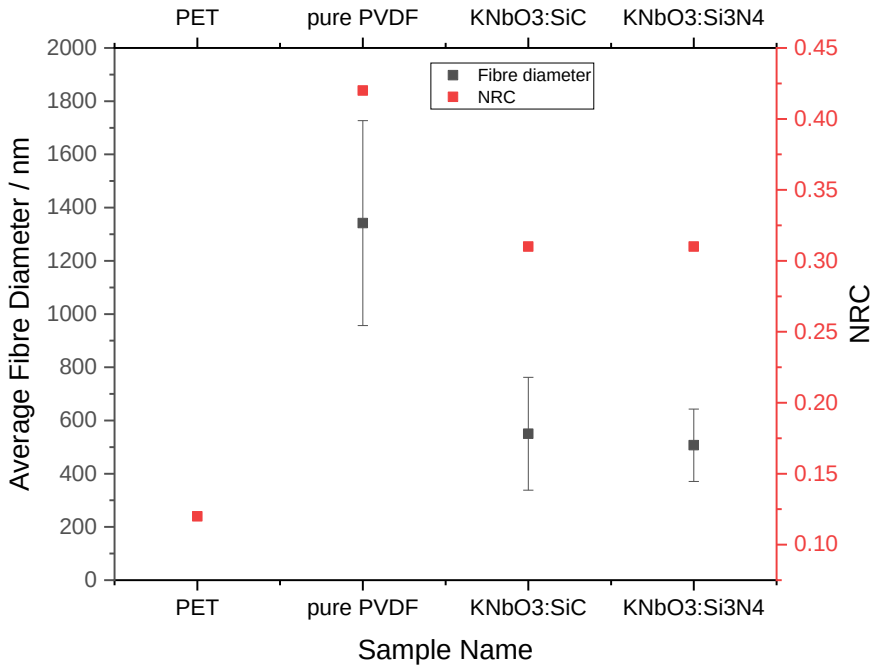

Figure 7.22. The trend between the average fibre diameters and the NRC values for the PET, pure PVDF and PVDF / $KNbO_3$ / SiC or Si_3N_4 fibres.

Table 7.9 demonstrates the relative thickness of the materials. Here the relative thickness of the ceramic within the material is similar for all the materials. Overall, the sound damping properties of the material are similar across the entire frequency range. The thickness of the ceramic filler does not correlate with an increase in the NRC of the systems as the relative thickness is all within 1 – 2 % of each other.

Table 7.9. The percentage thickness ratio of each component within the PET/PVDF/ niobium oxide/silicon ceramic composite system.

Sample name	PET Thickness %	PVDF/Ceramic Thickness %
PET / PVDF	93.9	6.1
PET / PVDF / SiC / $KNbO_3$	94.2	5.8
PET/ PVDF / Si_3N_4 $KNbO_3$	92.6	7.4

7.4.2 PU / PVDF / $KNbO_3$ / Silicon Ceramic Fibre Sound Testing

The change in the foam type was carried out as previously mentioned to increase the absorption properties of the material across the entire frequency range due to the increase in density of the material.[96] Figure 7.23. demonstrates the sound absorption coefficient of the PU and the PU / $KNbO_3$ / Silicon-based fibres across a frequency range of 400 – 6000 Hz. It demonstrates that there is an increase in damping performance at the low-frequency range and similar damping properties across the remaining frequency range. The PU foam displays three resonance peaks with the first occurring with a rapid increase from 650 Hz – 1400 Hz and reaching a maximum absorption coefficient of 0.77 as mentioned previously. The absorption coefficient then began to decrease and increase once again where it reached a maximum absorption coefficient of 0.80 at 2000 Hz for the second resonance peak and the final resonance peak is observed at 5000 Hz. The addition of the pure PVDF fibres to the surface of the PU mat resulted in an increase in the absorption coefficient at the first resonance peak at 650 Hz – 1400 Hz frequency range while the second resonance peak decreases. The final resonance peak at the higher frequency range shifts to a lower frequency range reaching a maximum of 0.84 as mentioned previously. The absorbance coefficient at the first resonance peak is in line with what is expected to occur for materials of this type. Materials analysed within the literature demonstrate a sound absorption coefficient of 0.8 – 0.92 within the same range.[94,106,107] This suggests that the materials here may perform similarly to those demonstrated previously.

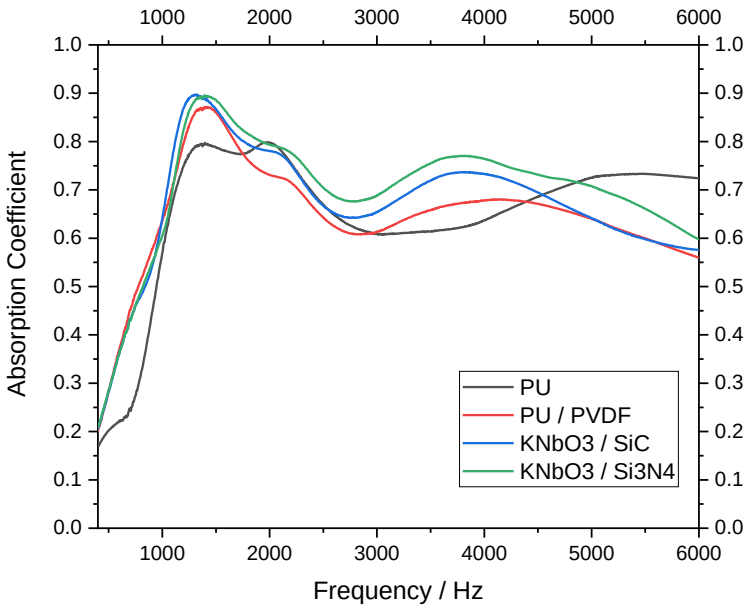

Figure 7.23. Sound absorption coefficient vs. frequency of the PU / PVDF / $KNbO_3$ / SiC or Si_3N_4 fibres showing an overall increase in sound absorption properties with the addition of the ceramics.

Table 7.10 demonstrates the relative thickness of the materials. The PVDF / ceramic mats are all within 3 % size of each other and the damping properties of the entire system are similar across the board for these 3 samples. This suggests that the small difference in thickness does not influence the damping properties. However, the addition of the fibre mats in general does demonstrate the increase in damping properties at the low-frequency range.

Table 7.10. The percentage thickness ratio of each component within the PU/PVDF/niobium oxide/silicon composite system.

Sample name	PU Relative Thickness %	PVDF/Ceramic Relative Thickness %
PU / PVDF	87.8	12.2
PU / PVDF / SiC	88.4	11.6
PU / PVDF / Si_3N_4	85.4	14.6

The addition of the mixed ratio of ceramics resulted in an increase in the absorption coefficient at 1300 Hz – 1400 Hz. The PVDF / $KNbO_3$ / SiC displayed a maximum absorption coefficient of 0.89 at 1300 Hz while the PVDF / $KNbO_3$ / Si_3N_4 achieved the same absorption coefficient of 0.89 at a higher frequency of 1400 Hz. Overall, the fibre diameters of the PVDF

/ $KNbO_3$ / SiC were similar to the PVDF / $KNbO_3$ / Si_3N_4. This may have resulted in a similar sound absorption coefficient across the entire frequency range. The increased sound absorption properties with the addition of the PVDF / ceramic fibres may be due to the increase in tortuosity of the system which increases the airflow resistivity and in turn, increases the friction between air particles within the material absorbing a higher content of sound energy.[54,98] It should also be mentioned that an increase in surface area would also occur with the addition of fibrous material. This allows for more points of contact between the sound wave and the material increasing friction between materials and absorbing sound.[52,53]

The NRC values for the PU foam were lower than that of the PU foam with the fibrous mats covering the front as expected and seen in Figure 7.24. The PU foam displayed an NRC value of 0.42. The addition of the pure PVDF resulted in an increase in the NRC value to 0.44. The incorporation of the 1:1 mixed ratio of $KNbO_3$ / SiC and $KNbO_3$ / Si_3N_4 led to an increase in the NRC to 0.45 for both fibrous mats respectively. Overall, there is not a large change in the noise reduction constant due to the second resonance peak in the PVDF filled with ceramic being lower at 2000 Hz as it has shifted to a higher frequency. However, it should still be said that the addition of the mixed ratio of the ceramics has little influence on the shift in sound absorption coefficient at the first resonance peak. Figure 7.24. demonstrates the average fibre diameter and NRC, where a decrease in the average fibre diameter increases the NRC. However, the values are not significantly different.

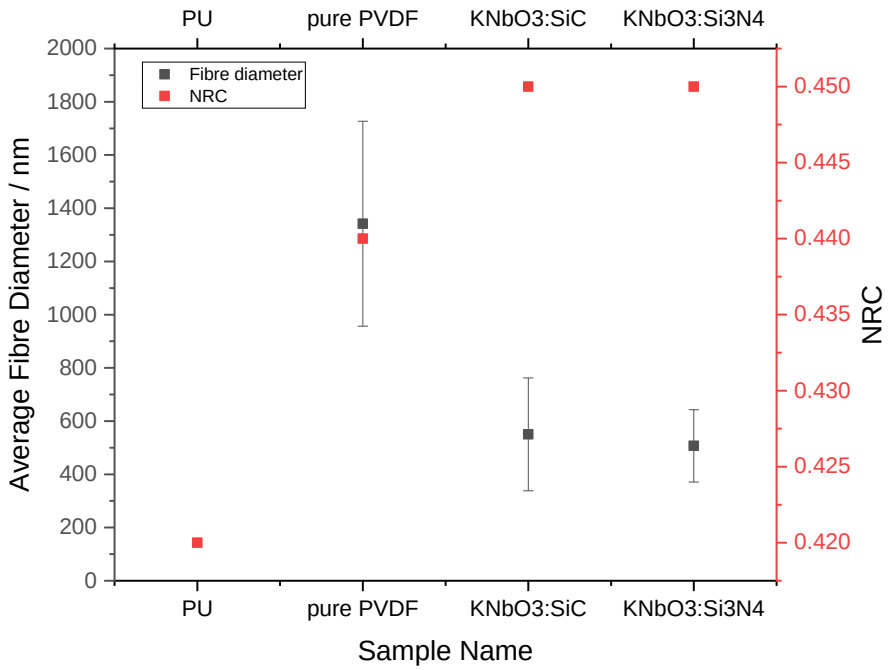

Figure 7.24. The trend between the average fibre diameter and the NRC values for the PU, Pure PVDF and PVDF / KNbO3 / silicon composite fibres.

7.4.3 Summary

The sound absorption properties of the PVDF / $KNbO_3$ / silicon-based fibres demonstrated similar results to all of the other PVDF / ceramic fibres analysed using PET as the backing foams. When comparing the two composites here it was shown that the composites with SiC performed better at the low-frequency resonance peak than the composite fibres with Si_3N_4 due to lower levels of reflection and higher absorption. However, when cross-comparing to the PVDF / silicon-based variants alone it could be said that the addition of $KNbO_3$ increased the influence of the absorption at the lower resonance peak. Overall, the mixing of the ceramic did not influence the absorption coefficient within the mid-frequency range and the material was performed similarly to previous PVDF / ceramic fibres. When compared to values from the literature these materials perform within similar parameters of a double resonance peak however at the first peak the performance of the material is lower than in other studies. Absorption coefficients of 0.89 – 1 are observed with similar damping systems.[102,105] Here the materials demonstrated absorption coefficients ranging between 0.6 – 0.9 at a similar frequency range. This suggests that the material produced within this work would perform to a lower standard than those produced previously.

The mixed ratio composite fibres backed with the PU foams demonstrated effective sound damping properties in comparison to the pure PVDF fibres added to the foams. These

materials demonstrated absorption coefficients of 0.77 – 0.84 at the low-frequency range. Overall, the fibres produced demonstrated similar sound damping properties across the entire frequency range. It can be said that with the addition of the fibre mats, an increase in damping properties at the low-frequency range was demonstrated. It was suggested to occur due to an increase in the thickness of the material and an increase in the surface area of the system. Both components provide for initially an increase in tortuosity with the influence of airflow resistivity of the system and an increase in points of contact between the sound wave and fibres. Of the system. [52,53,54,98] However, in comparison to the PU / PVDF / $KNbO_3$ fibres, the addition of the silicon ceramic at a mixed ratio did not perform better across the frequency range. This could be due to the PVDF / $KNbO_3$ fibres displaying great crystallinity, viscoelastic damping properties, and higher piezoelectric properties. However, distinguishing how each one of these properties influences the sound damping properties of the PVDF will require further testing. When compared to the literature these materials have performed within a similar frequency range as those previously studied which are within the range of 0.8 – 0.92 Hz.[94,106,107] Here the materials with the addition of the composite perform at 0.8 – 0.84 Hz with the standalone PU foam demonstrating a maximum sound absorption coefficient at 0.77 within the low-frequency range at 1000 Hz. This suggests that the materials here will perform similarly to those which have previously been studied in the literature.

The new work within this section demonstrates that the mixing of different types of SiC or Si_3N_4 with $KNbO_3$ to produce a mixed ratio of ceramic filler in the PVDF has little influence on the sound damping properties of the material. It also demonstrates that the addition of a PVDF fibre mat to the surface of a PET or PU foam will enhance the damping properties of the standalone materials and affect rigid porous material differently from flexible PU foams.

Chapter 8 Conclusions and Future Work

8.1 Conclusions

This thesis aimed to bring control to the fibre morphology, disperse ceramic filler to the polymer and increase the content of the electroactive phase in the PVDF polymers. This was accomplished through the addition of KCl salt and a range of piezoelectric ceramics of $NaNbO_3$, and $KNbO_3$, and non-piezoelectric ceramics of $CeNbO_4$, SiC, and Si_3N_4 all possessing some form of dielectric properties with the silicon-based ceramic providing the thermally conductive properties. Each component brought forward differing properties which may have influenced the polymer's morphology and electroactive phases and required analysis. A range of concentrations of filler was added 1 wt%, 3 wt%, 5 wt%, and 10 wt% of the ceramic were added to the PVDF solutions, electrospun using the same parameters.

Electrospinning the LMW and HMW PVDF with KCl salt had successfully demonstrated to influence the PVDF differently with the LMW displaying the complete removal of beaded fibres with an increase in average fibre diameter, and the HMW demonstrating a reduction in fibre diameter to its fibres which originally had no beads present. It analysed that the addition of KCl could both remove beads from small fibre and bring control to large fibre diameters with its addition. The average fibres analysed for both materials ranged from 186 nm – 239 nm and 560 nm – 810 nm respectively with both sets of PVDF / KCl materials. In comparison to fibres with the addition of salts, these fibres are much larger. Previous studies produced fibres with a diameter ranging between 60 – 350 nm. [262,273,278,282,283] These are in line with the LMW fibres and lower than the HMW fibres, as the HMW fibres were produced using a higher concentration of polymer alongside a higher average molecular weight. The viscosity of the solutions had little influence on the fibre diameter for both cases, especially with the HMW where an increase in solution viscosity with the addition of salt demonstrated a stronger influence on fibre diameter which could have occurred due to the increase in solution conductivity with its addition. Alongside this, the crystallinity of both sets of PVDF / KCl demonstrated the nucleation of the β polymorph. Maximum β phase contents were achieved at a concentration of 0.8 wt% KCl with 99.7 % and a concentration of 0.6 wt% KCl with 86 % for the LMW and HMW PVDF respectively. Differences associated with the higher concentration of polymer in the HMW hinder the nucleation of higher quantities of the β polymorph due to higher levels of chain entanglements.[351] The maximum reported content of the β polymorph was 93.6 % for PVDF with the addition of LiCl.[278] This means the materials produced with the LMW may have a higher piezoelectric response. It is also correlated with the

fibre diameters, where smaller fibre diameters have a higher content of the β polymorph. The specific contribution to knowledge from this area was:

(i) The addition of KCl brings control to the surface morphology and average fibre diameters of the electrospun LMW and HMW PVDF.

(ii) The nucleation of the β polymorph can be achieved with the addition of KCl across all concentrations with some cases a phase pure of the β polymorph can be achieved within the PVDF fibres.

For the PVDF / ceramic materials electrospun using the HMW PVDF, it was demonstrated that each ceramic type had different influences on the fibre morphology in terms of average fibre diameters and surface morphology. Overall, the initial addition of ceramic led to a slight decrease in average fibre diameter in comparison to the pure PVDF fibres which demonstrated a value of 1342 ± 385 nm. It was also analysed that each ceramic provided a different level of control to the average fibre diameter with the addition of the 4 concentrations of ceramic. The $NaNbO_3$ and $CeNbO_4$ had an increase in fibre diameter with the increase in the concentration of the ceramic. While the $KNbO_3$, SiC, and Si_3N_4 demonstrated a decrease in the fibre diameter with an increase in the content of the ceramic. Overall, the fibre diameters ranged between 600 – 1100 nm, for the fibres with the addition of $NaNbO_3$, $CeNbO_4$, SiC, and Si_3N_4. Those produced with the addition of $KNbO_3$ were between 400 – 600 nm. When compared to the literature these values are generally larger than those produced by similar ceramics. With fibre ranging between 100 – 500 nm for niobium oxide fillers and 615 nm for Si_3N_4 fillers. Alongside this, the overall change in fibre diameters could potentially be linked to the different dielectric constants of the materials. The overall average fibre diameters of the PVDF generally increase from the $KNbO_3$ < $NaNbO_3$ < $CeNbO_4$ < SiC < Si_3N_4 which is in line with the decrease in the dielectric constant of the material. The fibre morphology was also different with differing ceramics. The PVDF / $KNbO_3$ demonstrated a rough surface, while the other PVDF / ceramics demonstrated smooth surface morphologies. Differences in beaded structures were observed with the larger particle size ceramics with confirmation through the EDS and BSD imaging that the beads formed were agglomerates of the ceramic particles covered in PVDF polymer. The main point with this was that an increase in viscosity with the addition of ceramic was seen and a decrease in average fibres was displayed. This leads to an indication that the dielectric ceramics here influence fibre morphology more stronger than an increase in viscosity.

Distinct crystalline differences are observed with an increase in the ceramic content and the changes in the ceramic type. Firstly, the nucleation of the β polymorph is shown to occur with the electrospinning technique produced a 56 % content for the pure PVDF. The addition

of all 5 ceramics demonstrates a further increase in the content of the β polymorph with an overall increase across all concentrations of 1 wt% - 10 wt%. The content of the β polymorph ranged between 61 % – 74% for all the materials with PVDF / $CeNbO_4$ 1 wt% displaying the highest values of 74 % and overall, the PVDF / $KNbO_3$ fibres provided the highest content across all 4 ceramic concentrations ranging between 67 % - 73 %. The average fibre diameter was plotted against the β % and demonstrated that the orientation of the fibres did not influence the average fibre diameter as the diameters were within a similar range. This pointed in the direction that the filler acted as a nucleator rather than influence orientation through stretching of the fibres. Overall, the crystallinity of all the fibres demonstrated a decrease with the addition of ceramic with the highest concentration of 10 wt% causing a reduction in crystallinity across all the fibres containing ceramic due to hindrance of the recrystallisation of the fibres created by a high concentration of the ceramic. These materials produced a lower content of the electroactive phase than what has been demonstrated in the literature for ceramic fillers. Previous studies have produced a percentage β polymorph ranging between 65 – 94 %, with the highest value being produced by a KNN / ZnO mixed ratio of ceramic. Overall, the materials produced in this work are on the lower end of the scale in terms of the percentage β polymorph with the addition of filler. This suggests that the piezoelectric properties of the material may not be as effective as the previous work.

The thermal stability of the materials decreased with the addition of all the niobium oxides with a large decrease in the onset degradation temperature suggested to occur due to the fillers causing a decrease in the order of the polymer chains and a decrease in crystallinity. The PVDF / Si_3N_4 displayed little change to the thermal stability while the PVDF / SiC displayed an increase in thermal stability with higher degradation onset temperatures of 409 °C – 431 °C. This suggests that out of all the ceramic fillers, SiC provides the best performance for increased thermal stability. The thermal mechanical properties of the fibres varied across all the materials varied. In most cases, there was a shift in the T_g to higher temperatures indicating the hindrance of molecular chain movement with the addition of the ceramics. The PVDF / $KNbO_3$ demonstrated the highest damping properties in terms of the *E'* and *E''* displaying values of 83.0 MPa and 3.76 MPa at a ceramic concentration of 5 wt%. Overall, it can be said that the different ceramics added to the PVDF fibres varied in their influence on the thermal-mechanical properties. Further studies on this are required to gain a better understanding of the interfacial interactions between ceramic and PVDF to determine why the interactions between the ceramic and filler are causing the decrease in mechanical performance. These values produced by the materials here are much lower than what was expected with the literature producing values ranging between 600 MPa – 8 GPa.[369,368] Overall, demonstrating that the damping properties

displayed by the fibres produced in this work are weaker than those produced in previous reports.

The sound absorption resonance peaks depended heavily on the type of foamed backing applied. In all cases, the addition of the non-woven fibres and composite fibres all demonstrated an increase in the sound absorption properties of the foams across a broadband frequency range. PU foam-backed fibres demonstrated better sound absorption coefficients across the frequency range in comparison to the PET foam-backed fibres displaying 2 large resonance peaks. Overall, the setup of interest was the PU / PVDF / $KNbO_3$ demonstrating the highest absorption coefficient and displaying the highest NRC of 0.52 with a maximum absorption coefficient of 0.90 at 1250 Hz. Figure 8.1 demonstrates the different types of sound absorption materials and shows that the materials produced in this work will perform similarly to natural and polymer fibres that have previously been developed at the frequency range of 1000 Hz. Most polymer fibres perform between absorption coefficient values of 0.4 – 0.95, while those within this work are between 0.4 – 0.85. This suggests that the material here can perform similarly with slightly reduced properties.

Mixing the $KNbO_3$ with the SiC or Si_3N_4 demonstrated similar results with both silicon-based fibres. The PVDF fibres were largely influenced by the $KNbO_3$ over the silicon-based fibres where more control over the average fibre diameter and the crystallinity of the material due to its higher piezoelectric, dielectric properties and smaller particle size of the niobium oxide. Average fibre diameters ranged between 544 nm – 557 nm and 420 nm – 507 nm for the SiC and Si_3N_4 variants respectively. Thermal and thermal-mechanical properties were still weaker than the pure PVDF for these fibres. However thermal stability did increase in comparison to the PVDF / $KNbO_3$ fibres. Sound damping of these materials was very similar at the lower frequency range with the same NRC of 0.45 being displayed and the PU / PVDF / Si_3N_4 demonstrating higher sound absorption coefficients across the entire frequency range with the smaller average fibres demonstrating to influence sound damping across the entire frequency range. The specific contributions to knowledge from this area were:

(i) The fibre morphology of the PVDF can be controlled with the addition of niobium oxide and silicon-based ceramic filler, with the type of ceramic providing different levels of control.

(ii) Nucleation of the β polymorph in electrospun PVDF can be achieved with the addition of niobium oxide ceramics and silicon-based ceramic.

(iii) The effects of a piezoelectric ceramic with high dielectric properties can be mixed with a ceramic that has poor fibre morphology control and weaker nucleation

properties to promote the nucleation of the β polymorph and provide for more control over fibre diameters.

Overall, it can be said that the addition of KCl and ceramic filler assist in the nucleation of the β polymorph and bring control to the average fibre diameters which are dependent on the concentration of the filler and the type of filler. The outstanding PVDF / ceramic fibre composite is the PVDF / $KNbO_3$ fibre mats displayed the highest influence on the overall control of the fibre diameters, nucleation of the β polymorph, thermal-mechanical properties and sound absorption properties with the PU foam backing from all the PVDF / ceramic composite fibres produced.

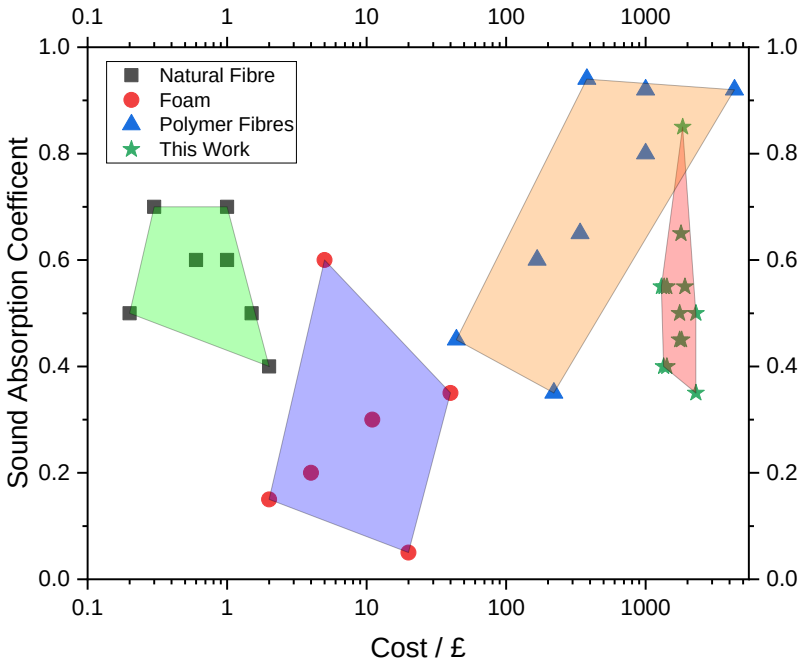

Figure 8.1. Comparison of sound absorption properties of different materials against the cost of the materials.[35,62,64,68,96,97,98,102,105,381,391,392,393,394,395]

Figure 8.1 is displaying the sound properties of materials analysed for sound absorption properties and their cost to produce through the purchase of the raw materials on up to 1kg worth of material. When comparing the materials' cost and the sound damping properties at 1000 Hz it is seen that overall, the formation of the materials within this study has a higher cost value due to specialist ceramic particles added to the material. It also performs within a similar sound absorption range as the natural fibres and the polymer fibres. The graph suggests that it may be viable to use other materials which are cheaper to obtain similar sound absorption

properties resulting in the materials produced in this work displaying a less cost-effective outlook when attempting to scale up.

The electrospinning process itself is difficult to scale up for mass production. This is due to the time required to produce a set of mats large enough to fit within the interior of vehicles. For mass production on an entire line of automotive vehicles, it would be difficult to produce the required amount of material. However, if the materials produced could be used for specialist vehicles where a small number of the vehicle are launched then it may be an option to use the electrospinning technique to produce a fibre mat. The main limitation for production here would be firstly hitting the targets for the amount of polymer fibre required and secondly the solvent use which evaporates into the environment and on a large scale this may have large negative implications for the environment. Currently, PU foams are the standard for sound damping applications within the industry and there are still improvements that can be made. On a commercial level, the technique is not yet used to produce sound damping material. It is more used within industries for air filtration membranes, water filtration membranes, and face masks.[396] There is still the option of using the electrospinning technique and using polymers which are more cost-effective than PVDF to reach similar sound absorption properties at a lower cost.

8.2 Recommendations for Future Work

There is still interest in further inducing the nucleation of the β polymorph with the combination of KCl and $KNbO_3$ within the PVDF fibres. It was demonstrated within this thesis that the KCl influences the nucleation of the β polymorph within the PVDF to a higher degree than the ceramic. With its addition to the PVDF / $KNbO_3$ fibres, it may provide for further nucleation of the β polymorph and enhance the piezoelectric properties of the material further. Overall, this increase in β content with a piezoelectric ceramic within the material may provide for a higher level of sound absorption within the 50 Hz – 250 Hz area which is known to represent the piezoelectric shunt effect which needs further analysis and is another recommendation to provide further knowledge to the field.

For the PVDF / ceramic composite fibre materials, the degree of crystallinity was observed to decrease with the addition of the ceramic materials. However, there was an increase in the nucleation of the β polymorph. It would be especially interesting to look at the PVDF / silicon-based fibres as they are not piezoelectric and determine how much influence the decrease in crystallinity of the and increase in the β polymorph by 2 % – 3 % had on the overall piezoelectric properties of the material and if there is any change in the values at all. The PVDF / silicon-based fibre composite materials were also demonstrated to influence the thermal stability of the material when analysed under the TGA with the SiC providing an increase in

thermal degradation. It would be of interest to determine the thermal diffusion and conductivity of this fibre composite as it may provide for more effective thermal energy dissipation across the material.

There is still potential to determine the influence of beaded fibres on both the thermal-mechanical properties of the fibres and the sound damping properties. It was seen here that the PVDF / SiC and PVDF / Si_3N_4 and PVDF / $CeNbO_4$ fibres were much lower than that of the bead-free PVDF / $NaNbO_3$ and PVDF / $KNbO_3$. It would be of interest to produce a set of fibre samples with a specific loading of ceramic with bead and bead-free structures to determine the influence of beaded structures on these properties.

The piezoelectric properties of $CeNbO_4$ are yet to be analysed within the literature with the main studies carried are on the oxygen diffusion properties of the material. It would be beneficial to produce pellets for analysis of the piezoelectric constant. This would allow for a more coherent understanding of the influence the piezoelectric properties of the ceramics have on the average fibre diameters of PVDF if the material is piezoelectric. This would assist in providing a more coherent case for the piezoelectric properties of the niobium ceramics influencing the properties of the PVDF fibres. It would also be beneficial to determine the piezoelectric properties of the PVDF / ceramic fibre mats analysed to link to the sound damping properties at the 50 Hz – 250 Hz range when tested.

For the analysis of the PU / PVDF / niobium oxide fibres, PU / PVDF / silicon-based fibres, and the PU / PVDF / $KNbO_3$ / silicon-based fibres the piezoelectric influence of the polymer or the ceramic components could not be analysed within this work due to the small size of the impedance tube. It would still be a contribution to the field to investigate the sound absorption coefficient of these foam / non-woven composite mats at the lower frequency range between 50 Hz – 250 Hz where the piezoelectric properties of the electroactive components within the systems may demonstrate an increase in the absorption coefficient. The diameters of the larger impedance tubes are likely to be too large for fibres PVDF loaded with $NaNbO_3$ or $KNbO_3$ as they've shown to produce very small diameters. It would be interesting to alter the electrospinning parameters of the set-up to attempt to increase the diameter of these fibres so they can be placed within the larger impedance tube for sound absorption testing to take place.

For the PVDF / $KNbO_3$, it would be interesting to alter the electrospinning parameters at the ceramic loading of 5 wt% to produce a range of fibres with different fibre diameters. It was unclear if the smaller average fibre diameter of the PVDF / $KNbO_3$ fibres were the cause of the increase in NRC in the first resonance peak to a lower frequency range. The change in the average fibre diameter across a large range could assist in determining if the changes in these values alter the sound absorption properties of the material. Alongside attempting to alter the fibre diameter of the materials it would also be beneficial to analyse the dielectric properties

of the solutions with an increase in the content of the ceramic, as there was a decrease in the fibre diameter with an increase in viscosity. This might provide a better understanding of if the ceramic is influencing the dielectric properties enough to reduce the average fibre diameters.

References

1 A. Nick, U. Becker and W. Thoma, Improved acoustic behavior of interior parts of renewable resources in the automotive industry, *J. Polym. Environ.*, 2002, **10**, 115–118.

2 M. D. Rao, Recent applications of viscoelastic damping for noise control in automobiles and commercial airplanes, *J. Sound Vib.*, 2003, **262**, 457–474.

3 E. Parliament and Council of the European Union, Regulation (EU) No 540/2014, *J. Eur. union*, 2014, 131–195.

4 S. D. Haddad and H. L. Pullen, Piston slap as a source of noise and vibration in diesel engines, *J. Sound Vib.*, 1974, **34**, 249–260.

5 G. Cerrato, Automotive Sound Quality – Powertrain, Road and Wind Noise, *Sound Vib.*, 2009, **43**, 16–24.

6 H. Bahrambeygi, N. Sabetzadeh, A. Rabbi, K. Nasouri, A. M. Shoushtari and M. R. Babaei, Nanofibers (PU and PAN) and nanoparticles (Nanoclay and MWNTs) simultaneous effects on polyurethane foam sound absorption, *J. Polym. Res.*, , DOI:10.1007/s10965-012-0072-6.

7 A. Abbad, M. Ouisse and N. Dauchez, Acoustic performances of silicone foams for sound absorption, *J. Cell. Plast.*, 2017, **1**, 1–21.

8 S. Bauer and F. Bauer, in *Piezoelectricity*, Springer, Berlin, Heidelberg, 2008, pp. 157–177.

9 N. Bhardwaj and S. C. Kundu, Electrospinning: A fascinating fiber fabrication technique, *Biotechnol. Adv.*, 2010, **28**, 325–347.

10 Y. Tao, M. Ren, H. Zhang and T. Peijs, Recent progress in acoustic materials and noise control strategies – A review, *Appl. Mater. Today*, , DOI:10.1016/j.apmt.2021.101141.

11 C. H. Zhang, Z. Hu, G. Gao, S. Zhao and Y. D. Huang, Damping behavior and acoustic performance of polyurethane/lead zirconate titanate ceramic composites, *Mater. Des.*, 2013, **46**, 503–510.

12 Z. Du, D. Yao, Y. Xia, K. Zuo, J. Yin, H. Liang and Y. P. Zeng, The sound absorption properties of highly porous silicon nitride ceramic foams, *J. Alloys Compd.*, 2020, **820**, 1–7.

13 G. Porges, *Applied Acoustics*, peninsula publishing, London, 1st edn., 1977.

14 L. Cremer, M. Heckl and B. A. T. Petersson, *Structure-borne sound: Structural vibrations and sound radiation at audio frequencies*, 2005.

15 P. Lord and F. L. Thoman, *Noise measurement and control*, Heywood & Company LTD, London, 1st edn., 1963.

16 M. P. Norton, *Fundamentals of Noise and Vibration Analysis for Engineers*, 1989, vol. 88.

17 R. Padhye and R. Nayak, *Acoustic Textiles*, singapore: Springer, 1st edn., 2016.

18 E. Daniel, Noise and hearing loss: A review, *J. Sch. Health*, 2007, **77**, 225–31.

19 H. Ohanian, *Principles of physics*, W.W.Norton & Company, First edit., 1994.

20 H. C. Hardy, D. Telfair and W. H. Pielemeier, The velecity of sound in air, 1942, **226**, 226–233.

21 G. S. K. WONG, Speed of Sound in Standard Air, *J. Acoust. Soc. Am.*, 1986, **79**, 1359–1366.

22 G. S. K. Wong and T. F. W. Embleton, Variation of the speed of sound in air with humidity and temperature, *J. Acoust. Soc. Am.*, 1985, **77**, 1710–1712.

23 F. FAHY and P. GARDONIO, *Sound and structural vibration; Radiation, Transmission and Response*, 2007.

24 P. J. Blatz and W. L. Ko, Application of Finite Elastic Theory to the Deformation of Rubbery Materials, *Trans. Soc. Rheol.*, 1962, **6**, 223–251.

25 A. Nilsson and B. Liu, *Vibro-acoustics*, 2012, vol. 1.

26 B. V. G. W. and H. Oberst, uber das dynamiseh-elastisehe Verhalten linearer, vernetzter und gefullter Kmaststoffe, *Kolloid Zeitschrift*, 1956, **148**, 6–16.

27 V. A. Del Grosso and C. W. Mader, Speed of Sound in Pure Water, *J. Acoust. Soc. Am.*, 1972, **52**, 1442–1446.

28 Wiley, *Properties and Behavior of Polymers, 2 Volume Set*, John Wiley & Sons, 2012.

29 K. D. Sattler, *Handbook of Nanophysics. 1. Principles and Methods*, 2010, vol. 1.

30 P. Göransson, Tailored acoustic and vibrational damping in porous solids - Engineering performance in aerospace applications, *Aerosp. Sci. Technol.*, 2008, **12**, 26–41.

31 Y. J. Kang and J. S. Bolton, Sound transmission through elastic porous wedges and foam layers having spatially graded properties, *J. Acoust. Soc. Am.*, 1996,

102, 3319–3332.

32 X. Wang and T. J. Lu, Optimized acoustic properties of cellular solids, *J. Acoust. Soc. Am.*, 1999, **106**, 756–765.

33 J. Z. Liang and B. Zhu, Estimation of sound transmission loss of polymer/hollow microsphere composites, *J. Compos. Mater.*, 2015, **50**, 2137–2142.

34 I. M. Hutten, *Handbook of Nonwoven Filter Media*, 2015.

35 H. F. Xiang, D. Wang, H. C. Liua, N. Zhao and J. Xu, Investigation on sound absorption properties of kapok fibers, *Chinese J. Polym. Sci.*, 2013, **31**, 521–529.

36 Z. Zhang and Y. Du, Sound insulation analysis and optimization of anti-symmetrical carbon fiber reinforced polymer composite materials, *Appl. Acoust.*, 2017, **120**, 34–44.

37 S. Srianujata, Lead - The toxic metal to stay with human., *J. Toxicol. Sci.*, 1998, **23**, 237–240.

38 N.-C. Park, Y.-C. Kim and C.-R. Park, The effect of additives on sound absorption coefficient of polyurethane foam, *J. korean ind. Eng. Chem.*, 1997, **8**, 197–203.

39 V. P Sergienko and S. N Bukharov, *Noise and vibration in friction systems*, springer international publishing, 2015.

40 M. N. Dassi, A. Gaudin, Z. Abbadi, L. Gagliardini, C. Pézerat and F. Gautier, in *11th International Conference on Engineering Vibration*, 2015, pp. 2–6.

41 E. G. Giakoumis, A. M. Dimaratos and C. D. Rakopoulos, Experimental study of combustion noise radiation during transient turbocharged diesel engine operation, *Energy*, 2011, **36**, 4983–4995.

42 S. K. Rhee, P. H. S. Tsang and Y. S. Wang, Friction-induced noise and vibration of disc brakes, *Wear*, 1989, **133**, 39–45.

43 W. Li, F. Gu, A. D. Ball, A. Y. T. Leung and C. E. Phipps, A study of the noise from diesel engines using the independent component analysis, *Mech. Syst. Signal Process.*, 2001, **15**, 1165–1184.

44 J. Skorecki and B. . Fielding, Identification of mechanical sources of noise in a diesel engine: Sound originating from piston slap, *Inst. Mech. Eng.*, 1969, **184**, 859–874.

45 J. Flint and J. Hulten, Lining-Deformation-Induced Modal Coupling As Squeal Generator In A Distributed Parameter Disc Brake Model, *J. Sound Vib.*, 2002,

254, 1–21.

46 G. Fritz, J.-J. Sinou, J.-M. Duffal and L. Jézéquel, Effects of damping on brake squeal coalescence patterns – application on a finite element model, *Mech. Res. Commun.*, 2007, **34**, 181–190.

47 H. Jacobsson, Aspects of Disc Brake Judder, *Proc. Inst. Mech. Eng. Part D J. Automob. Eng.*, 2003, **217**, 419–430.

48 E. Verheijen and J. Jabben, Effect of electric cars on traffic noise and safety, *Public Health*, 2010, 29.

49 U. Sandberg, Tyre/ road noise - Myths and realities, *Inter-noise 2001*, 2001, 22.

50 R. K. M. Chu, H. E. Naguib and N. Atalla, Synthesis and characterization of open-cell foams forsound absorption with rotational molding method, *Polym. Eng. Sci.*, 2009, **49**, 1744–1754.

51 C. Zhang, J. Li, Z. Hu, F. Zhu and Y. Huang, Correlation between the acoustic and porous cell morphology of polyurethane foam: Effect of interconnected porosity, *Mater. Des.*, 2012, **41**, 319–325.

52 M. Tascan and E. A. Vaughn, Effects of Total Surface Area and Fabric Density on the Acoustical Behavior of Needlepunched Nonwoven Fabrics, *Text. Res. J.*, 2008, **78**, 289–296.

53 X. Tang and X. Yan, *Compos. Part A Appl. Sci. Manuf.*, 2017, 101, 360–380.

54 M. J. M. Nor, M. Ayub, R. Zulkifli, N. Amin and M. H. Fouladi, Effect of different factors on the acoustic absorption of coir fiber, *J. Appl. Sci.*, 2010, **10**, 2887–2892.

55 F. Shahani, P. Soltani and M. Zarrebini, The analysis of acoustic characteristics and sound absorption coefficient of needle punched nonwoven fabrics, *J. Eng. Fiber. Fabr.*, 2014, **9**, 84–92.

56 N. H. Zunaidi, W. H. Tan, M. S. A. Majid and E. A. Lim, Effect of physical properties of natural fibre on the sound absorption coefficient, *J. Phys. Conf. Ser.*, 2017, **908**, 1–7.

57 H. Mamtaz, M. Hosseini Fouladi, M. Z. Nuawi, S. Narayana Namasivayam, M. Ghassem and M. Al-Atabi, Acoustic absorption of fibro-granular composite with cylindrical grains, *Appl. Acoust.*, 2017, **126**, 58–67.

58 D. Chandramohan and Marimuthu, A review on natural fibers, *Int. J. Res. Rev. Appl. Sci.*, 2011, **8**, 194–206.

59 D. Chandramohan and Marimuthu, A review on natural fibers, *Int. J. Res. Rev. Appl. Sci.*, 2011, **8**, 194–206.

60 U. Berardi and G. Iannace, Acoustic characterization of natural fibers for sound absorption applications, *Build. Environ.*, 2015, **94**, 840–852.

61 Z. Y. Lim, A. Putra, M. J. M. Nor and M. Y. Yaakob, Sound absorption performance of natural kenaf fibres, *Appl. Acoust.*, 2018, **130**, 107–114.

62 Z. Hui and X. Fan, Sound Absorption Properties of Hemp Fibrous Assembly Absorbers, *J. Text. Soc.*, 2009, **65**, 191–196.

63 L. J. Azevedo and M. Nabuco, in *International Congress on Noise Control Engineering 2005, INTERNOISE 2005*, 2005, vol. 3, pp. 1894–1899.

64 C. C. B. da Silva, F. J. H. Terashima, N. Barbieri and K. F. de Lima, Sound absorption coefficient assessment of sisal, coconut husk and sugar cane fibers for low frequencies based on three different methods, *Appl. Acoust.*, 2019, **156**, 92–100.

65 M. N. Yahya, M. Sambu, H. A. Latif and T. M. Junaid, in *IOP Conference Series: Materials Science and Engineering*, 2017, pp. 1–7.

66 K. O. Ballagh, Acoustical properties of wool, *Appl. Acoust.*, 1996, **48**, 101–120.

67 D. J. Oldham, C. A. Egan and R. D. Cookson, Sustainable acoustic absorbers from the biomass, *Appl. Acoust.*, 2011, **72**, 350–363.

68 S. Fatima and A. R. Mohanty, Acoustical and fire-retardant properties of jute composite materials, *Appl. Acoust.*, 2011, **72**, 108–114.

69 M. Lippmann, Asbestos exposure indices, *Environ. Res.*, 1988, **46**, 86–106.

70 M. Hosseini Fouladi, M. Ayub and M. Jailani Mohd Nor, Analysis of coir fiber acoustical characteristics, *Appl. Acoust.*, 2011, **72**, 35–42.

71 Y. S. Munde, R. B. Ingle and I. Siva, Vibration damping and acoustic characteristics of sisal fibre–reinforced polypropylene composite, *Noise Vib. Worldw.*, 2019, **50**, 13–21.

72 A. Charuchinda, R. Molloy, J. Siripitayananon, N. Molloy and M. Sriyai, Factors influencing the small-scale melt spinning of poly(ε-caprolactone) monofilament fibres, *Polym. Int.*, 2003, **52**, 1175–1181.

73 H.Fong, I.Chun and D.H.Reneker, Beaded nanofibers formed during electrospinning, *Polymer (Guildf).*, 1999, **40**, 4585–4592.

74 R. Beyreuther and R. Vogel, Spinnability of polymer melts - A complex problem

in basic research, *Int. Polym. Process.*, , DOI:10.3139/217.960154.

75 J. D. Bronzino, D. J. Mooney and R. S. Langer, in *Biomedical Engineering*, 2000.

76 A. Patnaik and R. D. Anandjiwala, An optimized melt spinning process to increase the productivity of nanofiber materials, *J. Ind. Text.*, 2016, **45**, 1026–1037.

77 R. Hufenus, Y. Yan, M. Dauner and T. Kikutani, Melt-spun fibers for textile applications, *Materials (Basel).*, 2020, **13**, 1–32.

78 B. S. Gupta and J. V. Edwards, in *Advanced Textiles for Wound Care*, Elsevier, 2019, pp. 55–104.

79 M. Wehmann and W. J. G. McCulloch, *Melt blowing technology*, 1999.

80 R. Nayak, I. L. Kyratzis, Y. B. Truong, R. Padhye, L. Arnold, G. Peeters, M. O'Shea and L. Nichols, Fabrication and characterisation of polypropylene nanofibres by meltblowing process using different fluids, *J. Mater. Sci.*, 2013, **48**, 273–281.

81 Y. Lee and L. C. Wadsworth, Structure and filtration properties of melt blown polypropylene webs, *Polym. Eng. Sci.*, 1990, **30**, 1413–1419.

82 B. T. Grafe, K. Graham, D. Co and P. O. Box, Polymeric Nanofibers and Nanofiber Webs : A New Class Of Nonwovens, *Int. Nonwovens J.*, 2003, **5**, 1–7.

83 R. Uppal, G. Bhat, C. Eash and K. Akato, Meltblown nanofiber media for enhanced quality factor, *Fibers Polym.*, 2013, **14**, 660–668.

84 L. Ren, R. Ozisik and S. P. Kotha, Rapid and efficient fabrication of multilevel structured silica micro-/nanofibers by centrifugal jet spinning, *J. Colloid Interface Sci.*, 2014, **425**, 136–142.

85 L. Ren, R. Ozisik, S. P. Kotha and P. T. Underhill, Highly efficient fabrication of polymer nanofiber assembly by centrifugal jet spinning: Process and characterization, *Macromolecules*, 2015, **48**, 2593–2602.

86 K. Shanmuganathan, Y. Fang, D. Y. Chou, S. Sparks, J. Hibbert and C. J. Ellison, Solventless high throughput manufacturing of poly(butylene terephthalate) nanofibers, *ACS Macro Lett.*, 2012, **1**, 960–964.

87 B. Vazquez, H. Vasquez and K. Lozano, Preparation and characterization of polyvinylidene fluoride nanofibrous membranes by forcespinning™, *Polym. Eng. Sci.*, 2012, **52**, 2260–2265.

88 K. Ibtehaj, M. H. Hj Jumali and S. Al-Bati, A novel facile preparation method of self-polarized Poly(vinylidene fluorides) nanofiber for high-performance piezoelectric nanogenerator, *Polymer (Guildf).*, 2020, **208**, 1–8.

89 F. Boschetto, H. N. Doan, P. P. Vo, M. Zanocco, W. Zhu, W. Sakai, K. Kinashi, E. Marin and G. Pezzotti, Effect of BaTiO3 on the aging process of PLA fibers obtained by centrifugal spinning, *Mater. Today Chem.*, 2021, **20**, 1–14.

90 L. Wang, J. Shi, L. Liu, E. Secret and Y. Chen, Fabrication of polymer fiber scaffolds by centrifugal spinning for cell culture studies, *Microelectron. Eng.*, 2011, **88**, 1718–1721.

91 Z. McEachin and K. Lozano, Production and characterization of polycaprolactone nanofibers via forcespinning^{TM} technology, *J. Appl. Polym. Sci.*, 2012, **126**, 473–479.

92 K. Sarkar, C. Gomez, S. Zambrano, M. Ramirez, E. De Hoyos, H. Vasquez and K. Lozano, Electrospinning to Forcespinning^{TM}, *Mater. Today*, 2010, **13**, 12–14.

93 Y. Lu, Y. Li, S. Zhang, G. Xu, K. Fu, H. Lee and X. Zhang, Parameter study and characterization for polyacrylonitrile nanofibers fabricated via centrifugal spinning process, *Eur. Polym. J.*, 2013, **49**, 3834–3845.

94 C. M. Wu and M. H. Chou, Polymorphism, piezoelectricity and sound absorption of electrospun PVDF membranes with and without carbon nanotubes, *Compos. Sci. Technol.*, 2016, **127**, 127–133.

95 H. F. Xiang, S. X. Tan, X. L. Yu, Y. H. Long, X. L. Zhang, N. Zhao and J. Xu, Sound absorption behavior of electrospun polyacrylonitrile nanofibrous membranes, *Chinese J. Polym. Sci. (English Ed.*, 2011, **29**, 650–657.

96 C. W. Lou, J. H. Lin and K. H. Su, Recycling Polyester and Polypropylene Nonwoven Selvages to Produce Functional Sound Absorption Composites, *Text. Res. J.*, 2005, **75**, 390–394.

97 Y. na, J. Lancaster, J. Casali and G. Cho, Sound Absorption Coefficients of Micro-fiber Fabrics by Reverberation Room Method, *Text. Res. J.*, 2007, **77**, 330–335.

98 W. S. Khan, R. Asmatulu and M. B. Yildirim, Acoustical Properties of Electrospun Fibers for Aircraft Interior Noise Reduction, *J. Aerosp. Eng.*, 2012, **25**, 376–382.

99 J. Avossa, F. Branda, F. Marulo, G. Petrone, S. Guido, G. Tomaiuolo and A.

Costantini, Light Electrospun Polyvinylpyrrolidone Blanket for Low Frequencies Sound Absorption, *Chinese J. Polym. Sci. (English Ed.*, 2018, **36**, 1368–1374.

100 K. Kalinová, Nanofibrous resonant membrane for acoustic applications, *J. Nanomater.*, 2011, **1**, 1–6.

101 Y. E. Lee and C. W. Joo, Sound Absorption Properties of Thermally Bonded Nonwovens Based on Composing Fibers and Production Parameters, *J. Appl. Polym. Sci.*, 2004, **92**, 2295–2302.

102 H. Liu, D. Wang, N. Zhao, J. Ma, J. Gong, S. Yang and J. Xu, Application of electrospinning fibres on sound absorption in low and medium frequency range, *Mater. Res. Innov.*, 2014, **18**, 888–891.

103 T. Yang, X. Xiong, M. Venkataraman, R. Mishra, J. Novák and J. Militký, Investigation on sound absorption properties of aerogel/polymer nonwovens, *J. Text. Inst.*, 2019, **110**, 196–201.

104 G. Iannace, Acoustic properties of nanofibers, *Noise Vib. Worldw.*, 2014, **45**, 29–33.

105 T. Ulrich and J. P. Arenas, Sound absorption of sustainable polymer nanofibrous thin membranes bonded to a bulk porous material, *Sustain.*, 2020, **12**, 1–15.

106 C. M. Wu and M. H. Chou, Sound absorption of electrospun polyvinylidene fluoride/graphene membranes, *Eur. Polym. J.*, 2016, **82**, 35–45.

107 C. M. Wu and M. H. Chou, Acoustic–electric conversion and piezoelectric properties of electrospun polyvinylidene fluoride/silver nanofibrous membranes, *Express Polym. Lett.*, 2020, **14**, 103–114.

108 K. Qamoshi and R. Rasuli, Subwavelength structure for sound absorption from graphene oxide-doped polyvinylpyrrolidone nanofibers, *Appl. Phys. A Mater. Sci. Process.*, 2016, **122**, 1–7.

109 G. Ciaburro, G. Iannace, J. Passaro, A. Bifulco, D. Marano, M. Guida, F. Marulo and F. Branda, Artificial neural network-based models for predicting the sound absorption coefficient of electrospun poly(vinyl pyrrolidone)/silica composite, *Appl. Acoust.*, 2020, **169**, 107472.

110 B. Gao, L. Zuo and B. Zuo, Sound absorption properties of spiral vane electrospun PVA/nano particle nanofiber membrane and non-woven composite material, *Fibers Polym.*, 2016, **17**, 1090–1096.

111 H. Li, C. Tian and Z. D. Deng, Energy harvesting from low frequency applications using piezoelectric materials, *Appl. Phys. Rev.*, 2014, **1**, 1–20.

112 G. T. Davis, J. E. McKinney, M. G. Broadhurst and S. C. Roth, Electric-field-induced phase changes in poly(vinylidene fluoride), *J. Appl. Phys.*, 1978, **49**, 4998–5002.

113 A. Chaipanich, Dielectric and piezoelectric properties of PZT-cement composites, *Curr. Appl. Phys.*, 2007, **7**, 537–539.

114 B. Jaffe, W. Cook and H. Jaffe, *Piezoelectric Ceramics*, 1971, vol. 41.

115 K. Matsumoto, Y. Hiruma, H. Nagata and T. Takenaka, Piezoelectric properties of pure and Mn-doped potassium niobate ferroelectric ceramics, *Jpn. J. Appl. Phys.*, 2006, **45**, 4479–4483.

116 H. Nagata, K. Matsumoto, T. Hirosue, Y. Hiruma and T. Takenaka, Fabrication and electrical properties of potassium niobate ferroelectric ceramics, *Jpn. J. Appl. Phys.*, 2007, **46**, 7084–7088.

117 B. T. Matthias and J. P. Remeika, Dielectric properties of sodium and potassium niobates, *Phys. Rev.*, 1951, **82**, 727–729.

118 C. Bessaguet, E. Dantras, C. Lacabanne, M. Chevalier and G. Michon, Piezoelectric and mechanical behavior of NaNbO3/PEKK lead-free nanocomposites, *J. Non. Cryst. Solids*, 2017, **459**, 83–87.

119 L. Egerton and D. M. Dillon, Piezoelectric and Dielectric Properties of Ceramics in the System Potassium-Sodium Niobate, *J. Am. Ceram. Soc.*, 1959, **42**, 438–442.

120 E. D. Hollenstein Matthew Damjanovic, Dragan, Setter, Nava, Piezoelectric properties of Li- and Ta-modified (K0.5Na0.5)NbO3 ceramics, *Appl. Phys. Lett.*, 2005, **87**, 182905.

121 Z. Zhang, C. Xu and Q. Liu, Microwave dielectric properties of RENbO4 (RE=Y, Yb,Ce) ceramics, *Key Eng. Mater.*, 2010, **434**–**435**, 217–220.

122 J. Curie and P. Curie, Development, via compression, of electric polarization in hemihedral crystals with inclined faces, *Bull. la Soc. Minerol. Fr.*, 1880, **3**, 90–93.

123 M. Trainer, Kelvin and piezoelectricity, *Eur. J. Phys.*, 2003, **24**, 535–542.

124 J. P. Shields, *Basic Piezoelectricity*, w.foulshan & co. ltd, 1966.

125 A. Arnau and D. Soares, in *Piezoelectric Transducers and Applications*, 2008,

pp. 1–38.

126 L. APC International, *Piezoelectric ceramics : principles and applications.*, Mackeyville, PA : APC International, 2011, second edi., 2011.

127 R. L. Forward, Electronic damping of vibrations in optical structures, *Appl. Opt.*, 1979, **18**, 690.

128 A. Gupta, V. Goel and V. Yadav, Conversion of sound to electric energy, *Int. J. Sci. Eng. Res.*, 2014, **5**, 2146–2149.

129 C. B. Sawyer and C. H. Tower, Rochelle salt as a dielectric, *Phys. Rev.*, 1930, **35**, 269–273.

130 Y. Xu, *Ferroelectric materials and their applications*, 1991.

131 W. G. Cady, *Piezoelectricity*, Dover Publications INC, New York, 1965.

132 Y. Saigusa, in *Advanced Piezoelectric Materials*, 2017, pp. 171–203.

133 Y. Shou-Zhuo and M. Zhi-Hong, Frequency properties of a piezoelectric quartz crystal in solutions and application to total salt determination, *Anal. Chim. Acta*, 1987, **193**, 97–105.

134 C. Lu and A. W. Czanderna, *Applications of Piezoelectric Quartz Crystal Microbalances*, 1984.

135 M. Kobayashi, K. Tashiro and H. Tadokoro, Molecular Vibrations of Three Crystal Forms of Poly(vinylidene fluoride), *Macromolecules*, 1975, **8**, 158–171.

136 S. Weinhold and J. B. Lando, The Crystal Structure Of Phase Iv Of Poly(Vinylidene Fluoride), *Ferroelectrics*, 1980, **30**, 95.

137 A. J. Lovinger, Annealing of Poly(vinylidene fluoride) and Formation of a Fifth Phase, *Macromolecules*, 1982, **15**, 40–44.

138 X. M. Cai, T. P. Lei, D. H. Sun and L. W. Lin, A critical analysis of the alpha, beta and gamma phases in poly(vinylidene fluoride) using FTIR, *Rsc Adv.*, 2017, **7**, 15382–15389.

139 W.-K. Lee and C.-S. Ha, Miscibility and surface crystal morphology of blends containing poly(vinylidene fluoride) by atomic force microscopy, *Polymer (Guildf).*, 1998, **39**, 7131–7134.

140 S. B. Lang and S. Muensit, *Appl. Phys. A Mater. Sci. Process.*, 2006, 85, 125–134.

141 Q. X. Chen and P. a Payne, Industrial applications of piezoelectric polymer transducers, *Meas. Sci. Technol.*, 1995, **6**, 249–267.

142 W. W. Doll and J. B. Lando, Polymorphism of Poly(vinylidene Fluoride). III. The Crystal Structure of Phase II, *J. Macromol. Sci. Part B*, 1970, **4**, 309–329.

143 R. Gregorio, and M. Cestari, Effect of crystallization temperature on the crystalline phase content and morphology of poly(vinylidene fluoride), *J. Polym. Sci. Part B Polym. Phys.*, 1994, **32**, 859–870.

144 D. C. Bassett, *Developments in Crystalline Polymers—1*, 1982.

145 R. Hasegawa, Y. Takahashi, Y. Chatani and H. Tadokoro, Crystal Structures of Three Crystalline Forms of Poly(vinylidene fluoride), *Polym. J.*, 1972, **3**, 600–610.

146 J. Humphreys, I. M. Ward, E. L. Nix, J. C. McGrath and T. Emi, A study of the drawing behavior of polyvinylidene fluoride, *J. Appl. Polym. Sci.*, 1985, **30**, 4069–4079.

147 P. Holstein, U. Scheler and R. K. Harris, Semicrystallinity and polymorphism in PVDF: A solid-state 19F n.m.r. investigation, *Polymer (Guildf).*, 1998, **39**, 4937–4941.

148 T. Wu, H. Jin, S. Dong, W. Xuan, H. Xu, L. Lu, Z. Fang, S. Huang, X. Tao, L. Shi, S. Liu and J. Luo, A flexible film bulk acoustic resonator based on β-phase polyvinylidene fluoride polymer, *Sensors*, 2020, **20**, 1–11.

149 H. Kawai, The Piezoelectricity of Poly (vinylidene Fluoride), *Jpn. J. Appl. Phys.*, 1969, **8**, 975–976.

150 M. C. Branciforti, V. Sencadas, S. Lanceros-Mendez and R. Gregorio, New technique of processing highly oriented poly(vinylidene fluoride) films exclusively in the β phase, *J. Polym. Sci. Part B Polym. Phys.*, 2007, **45**, 2793–2801.

151 V. T. Rathod, D. R. Mahapatra, A. Jain and A. Gayathri, Characterization of a large-area PVDF thin film for electro-mechanical and ultrasonic sensing applications, *Sensors Actuators, A Phys.*, 2010, **163**, 164–171.

152 J. P. Luongo, Far-infrared spectra of piezoelectric polyvinylidene fluoride, *J. Polym. Sci. Part A-2 Polym. Phys.*, 1972, **10**, 1119–1123.

153 V. Sencadas, C. M. Costa, V. Moreira, J. Monteiro, S. K. Mendiratta, J. F. Mano and S. Lanceros-Méndez, Poling of ß-poly(vinylidene fluoride): Dielectric and IR spectroscopy studies, *E-Polymers*, 2005, 1–12.

154 T. C. Hsu and P. H. Geil, Deformation and transformation mechanisms of

poly(vinylidene fluoride) (PVF2), *J. Mater. Sci.*, 1989, **24**, 1219–1232.

155 K. Matsushige, K. Nagata, S. Imada and T. Takemura, The II-I crystal transformation of poly(vinylidene fluoride) under tensile and compressional stresses, *Polymer (Guildf).*, 1980, **21**, 1391–1397.

156 Z. Guo, E. Nilsson, M. Rigdahl and B. Hagström, Melt spinning of PVDF fibers with enhanced β phase structure, *J. Appl. Polym. Sci.*, 2013, **130**, 2225–3025.

157 P. K. Szewczyk, A. Gradys, S. K. Kim, L. Persano, M. Marzec, A. Kryshtal, T. Busolo, A. Toncelli, D. Pisignano, A. Bernasik, S. Kar-Narayan, P. Sajkiewicz and U. Stachewicz, Enhanced Piezoelectricity of Electrospun Polyvinylidene Fluoride Fibers for Energy Harvesting, *ACS Appl. Mater. Interfaces*, 2020, **12**, 13575–13583.

158 P. Martins, C. Caparros, R. Gonçalves, P. M. Martins, M. Benelmekki, G. Botelho and S. Lanceros-Mendez, Role of nanoparticle surface charge on the nucleation of the electroactive β-poly(vinylidene fluoride) nanocomposites for sensor and actuator applications, *J. Phys. Chem. C*, 2012, **116**, 15790–15794.

159 B. Mohammadi, A. A. Yousefi and S. M. Bellah, Effect of tensile strain rate and elongation on crystalline structure and piezoelectric properties of PVDF thin films, *Polym. Test.*, 2007, **26**, 42–50.

160 T. Lei, L. Yu, G. Zheng, L. Wang, D. Wu and D. Sun, Electrospinning-induced preferred dipole orientation in PVDF fibers, *J. Mater. Sci.*, 2015, **50**, 4243–4347.

161 J. Gomes, J. S. Nunes, V. Sencadas and S. Lanceros-Mendez, Influence of the β-phase content and degree of crystallinity on the piezo-and ferroelectric properties of poly(vinylidene fluoride), *Smart Mater. Struct.*, , DOI:10.1088/0964-1726/19/6/065010.

162 H. Kueppers, T. Leuerer, U. Schnakenberg, W. Mokwa, M. Hoffmann, T. Schneller, U. Boettger and R. Waser, PZT thin films for piezoelectric microactuator applications, *Sensors Actuators, A Phys.*, 2002, **97**–**98**, 680–684.

163 N. Izyumskaya, Y. I. Alivov, S. J. Cho, H. Morkoç, H. Lee and Y. S. Kang, *Crit. Rev. Solid State Mater. Sci.*, 2007, 32, 111–202.

164 S. Teslic, T. Egami and D. Viehland, Local atomic structure of PZT and PLZT studied by pulsed neutron scattering, *J. Phys. Chem. Solids*, 1996, **57**, 1537–1543.

165 N. J. Donnelly, T. R. Shrout and C. A. Randall, Addition of a Sr, K, Nb (SKN)

combination to PZT(53/47) for high strain applications, *J. Am. Ceram. Soc.*, 2007, **90**, 490–491.

166 T. R. Shrout and S. J. Zhang, Lead-free piezoelectric ceramics: Alternatives for PZT?, *J. Electroceramics*, 2007, **19**, 111–124.

167 G. Shirane and K. Suzuki, Crystal Structure of Pb(Zr-Ti)O3, *J. Phys. Soc. Japan*, 1952, **7**, 333.

168 E. a. Wood, Polymorphism in Potassium Niobate, Sodium Niobate, and other ABO3 Compounds, *Acta Crystallogr.*, 1951, **4**, 353–362.

169 L. E. Cross and B. J. Nicholson, LV. The optical and electrical properties of single crystals of sodium niobate, *London, Edinburgh, Dublin Philos. Mag. J. Sci.*, 1955, **46**, 453–466.

170 H. D. Megaw, The Seven Phases of Sodium Niobate, *Ferroelectrics*, 1974, **7**, 87–89.

171 G. Shirane, R. Newnham and R. Pepinsky, Dielectric properties and phase transitions of NaNbO3 and (Na,K)NbO3, *Phys. Rev.*, 1954, **96**, 581–588.

172 K. Singh, V. Lingwal, S. C. Bhatt, N. S. Panwar and B. S. Semwal, Dielectric properties of potassium sodium niobate mixed system, *Mater. Res. Bull.*, 2001, **36**, 2365–2374.

173 B. T. Matthias, New ferroelectric crystals, *Phys. Rev.*, 1949, **75**, 1771.

174 E. Palik, *Handbook of Optical Constants of Solids*, 1985.

175 G. Shirane, H. Danner, A. Pavlovic and R. Pepinsky, Phase transitions in ferroelectric $KNbO_3$, *Phys. Rev.*, 1954, **93**, 672–673.

176 B. Yang, P. D. Townsend and M. Maghrabi, Optical detection of phase transitions in potassium niobate, *J. Mod. Opt.*, 2001, **48**, 319–331.

177 S. Wada, A. Seike and T. Tsurumi, Poling treatment and piezoelectric properties of potassium niobate ferroelectric single crystals, *Japanese J. Appl. Physics, Part 1 Regul. Pap. Short Notes Rev. Pap.*, 2001, **40**, 5690–5697.

178 S. Wada, K. Muraoka, H. Kakemoto, T. Tsurumi and H. Kumagai, in *Japanese Journal of Applied Physics, Part 1: Regular Papers and Short Notes and Review Papers*, 2004, vol. 43, pp. 6692–6700.

179 J. G. Thompson, R. L. Withers and F. J. Brink, Modulated Structures in Oxidized Cerium Niobates, *J. Solid State Chem.*, 1999, **143**, 122–131.

180 S. J. Skinner and Y. Kang, X-ray diffraction studies and phase transformations

of CeNbO 4+δ using in situ techniques, *Solid State Sci.*, 2003, **5**, 1475–1479.

181 R. D. Bayliss, S. S. Pramana, T. An, F. Wei, C. L. Kloc, A. J. P. White, S. J. Skinner, T. J. White and T. Baikie, Fergusonite-type CeNbO4+δ: Single crystal growth, symmetry revision and conductivity, *J. Solid State Chem.*, 2013, **204**, 291–297.

182 S. J. Skinner, I. J. E. Brooks and C. N. Munnings, Tetragonal CeNbO4 at 1073 K in air and in vacuo, *Acta Crystallogr. Sect. C Cryst. Struct. Commun.*, 2004, **60**, i37–i39.

183 S. S. Pramana, T. Baikie, T. An, M. G. Tucker, J. Wu, M. K. Schreyer, F. Wei, R. D. Bayliss, C. L. Kloc, T. J. White, A. P. Horsfield and S. J. Skinner, Correlation of Local Structure and Diffusion Pathways in the Modulated Anisotropic Oxide Ion Conductor CeNbO4.25, *J. Am. Chem. Soc.*, 2016, **138**, 1273–1279.

184 M. Ates, S. Karadag, A. A. Eker and B. Eker, Polyurethane foam materials and their industrial applications, *Polym. Int.*, 2022, **71**, 1157–1163.

185 G. Soto, A. Castro, N. Vechiatti, F. Iasi, A. Armas, N. E. Marcovich and M. A. Mosiewicki, Biobased porous acoustical absorbers made from polyurethane and waste tire particles, *Polym. Test.*, 2017, **57**, 42–51.

186 S. Chen and Y. Jiang, The acoustic property study of polyurethane foam with addition of bamboo leaves particles, *Polym. Compos.*, , DOI:10.1002/pc.24078.

187 J. Hyuk Park, K. Suh Minn, H. Rae Lee, S. Hyun Yang, C. Bin Yu, S. Yeol Pak, C. Sung Oh, Y. Seok Song, Y. June Kang and J. Ryoun Youn, Cell openness manipulation of low density polyurethane foam for efficient sound absorption, *J. Sound Vib.*, 2017, **406**, 224–236.

188 M. F. Sonnenschein, *Polyurethanes: Science, Technology, Markets, and Trends*, 2014.

189 R. Verdejo, R. Stämpfli, M. Alvarez-Lainez, S. Mourad, M. A. Rodriguez-Perez, P. A. Brühwiler and M. Shaffer, Enhanced acoustic damping in flexible polyurethane foams filled with carbon nanotubes, *Compos. Sci. Technol.*, 2009, **69**, 1564–1569.

190 J. J. Berzelius, Untersuchungen über die Flussspathsäure und deren merkwürdigsten Verbindungen, *Ann. Phys.*, 1824, **77**, 169–230.

191 G. L. Harris, *Properties of Silicon Carbide*, IET, illustrate., 1995.

192 J. Fan and P. K. Chu, *Silicon Carbide Nanostructures: Fabrication, Structure, and Properties*, Springer New York LLC, 2014, vol. 483–484.

193 A. Taylor and D. S. Laidler, The formation and crystal structure of silicon carbide, *Br. J. Appl. Phys.*, 1950, **1**, 174–181.

194 R. Lad, in *Handbook of surface science*, 1996, pp. 185–229.

195 F. L. Riley, Silicon nitride and related materials, *J. Am. Ceram. Soc.*, 2000, **83**, 245–265.

196 W. Gilbert, De Magnete, Magneticisque Corporibus, et de Magno Magnete Tellure (Translated by P. Fleury Mottelay), *London, Peter Short.*, , DOI:10.1109/ISCID.2013.212.

197 J. Cooley, Improved methods of and apparatus for electrically separating the relatively volatile liquid component from the component of relatively fixed substances of composite, *Pat. GB*, 1900, 8.

198 N. Tucker Ph.D., J. J. Stanger MSc, M. P. Staiger Ph.D., H. Razzaq Ph.D. and K. Hofman Ph.D., The History of the Science and Technology of Electrospinning from 1600 to 1995, *J. Eng. Fiber. Fabr.*, 2012, 63–73.

199 A. Formhals, 1934, 1,975,504.

200 A. Formhals, Methods and apparatus for Spinning, *Lett. Pat.*, 1944, **2,349,950**, 1–5.

201 A. Formhals, 1940, 2,187,306.

202 G. I. Taylor, Electrically Driven Jets, *Proc. R. Soc. A Math. Phys. Eng. Sci.*, 1969, **313**, 453–475.

203 J. Doshi and D. H. Reneker, Electrospinning process and applications of electrospun fibers, *J. Electrostat.*, 1995, **35**, 151–160.

204 D. H. Reneker, A. L. Yarin, H. Fong and S. Koombhongse, Bending instability of electrically charged liquid jets of polymer solutions in electrospinning, *J. Appl. Phys.*, 2000, **87**, 4531–4547.

205 P. Gibson, H. Schreuder-Gibson and D. Rivin, Transport properties of porous membranes based on electrospun nanofibers, *Colloids Surfaces A Physicochem. Eng. Asp.*, 2001, **187**–**188**, 469–481.

206 E. D. Boland, G. E. Wnek, D. G. Simpson, K. J. Pawlowski and G. L. Bowlin, Tailoring tissue engineering scaffolds using electrostatic processing techniques: A study of poly(glycolic acid) electrospinning, *J. Macromol. Sci. - Pure Appl.*

Chem., 2001, **38**, 1231–1243.

207 J. A. Matthews, G. E. Wnek, D. G. Simpson and G. L. Bowlin, Electrospinning of collagen nanofibers, *Biomacromolecules*, 2002, **3**, 232–238.

208 X. Wang, C. Drew, S. H. Lee, K. J. Senecal, J. Kumar and L. A. Samuelson, Electrospinning technology: A novel approach to sensor application, *J. Macromol. Sci. - Pure Appl. Chem.*, 2002, **39**, 1251–1258.

209 X. Wang, C. Drew, S. H. Lee, K. J. Senecal, J. Kumar and L. A. Samuelson, Electrospun Nanofibrous Membranes for Highly Sensitive Optical Sensors, *Nano Lett.*, 2002, **2**, 1273–1275.

210 E. R. Kenawy, G. L. Bowlin, K. Mansfield, J. Layman, D. G. Simpson, E. H. Sanders and G. E. Wnek, Release of tetracycline hydrochloride from electrospun poly(ethylene-co-vinylacetate), poly(lactic acid), and a blend, *J. Control. Release*, 2002, **81**, 57–64.

211 J. Zeng, X. Xu, X. Chen, Q. Liang, X. Bian, L. Yang and X. Jing, Biodegradable electrospun fibers for drug delivery, *J. Control. Release*, 2003, **92**, 227–231.

212 S. W. Choi, S. M. Jo, W. S. Lee and Y. R. Kim, An electrospun poly(vinylidene fluoride) nanofibrous membrane and its battery applications, *Adv. Mater.*, 2003, **15**, 2027–2032.

213 J. Fernández de la Mora, The effect of charge emission from electrified liquid cones, *J. Fluid Mech.*, 1992, **243**, 561–574.

214 T. Lin and X. Wang, *NEEDLELESS ELECTROSPINNING OF NANOFIBERS - Technology and Applications*, 2013.

215 Y. Zheng, in *Bioinspired Design of Materials Surfaces*, 2019, pp. 99–146.

216 Lord Rayleigh, XX. On the equilibrium of liquid conducting masses charged with electricity, *London, Edinburgh, Dublin Philos. Mag. J. Sci.*, 1992, **14**, 184–186.

217 J. Fernández de la Mora, The effect of charge emission from electrified liquid cones, *J. Fluid Mech.*, 1992, **243**, 561–574.

218 C. Wang, C. H. Hsu and J. H. Lin, Scaling laws in electrospinning of polystyrene solutions, *Macromolecules*, 2006, **39**, 7662–7672.

219 M. M. Hohman, M. Shin, G. Rutledge and M. P. Brenner, Electrospinning and electrically forced jets. II. Applications, *Phys. Fluids*, 2001, **13**, 2221–2236.

220 C. P. Carroll and Y. L. Joo, Axisymmetric instabilities of electrically driven viscoelastic jets, *J. Nonnewton. Fluid Mech.*, 2008, **153**, 130–148.

221 C. Zhang, X. Yuan, L. Wu, Y. Han and J. Sheng, Study on morphology of electrospun poly(vinyl alcohol) mats, *Eur. Polym. J.*, 2005, **41**, 423–432.

222 M. Nasir, H. Matsumoto, T. Danno, M. Minagawa, T. Irisawa, M. Shioya and A. Tanioka, *J. Polym. Sci. Part B Polym. Phys.*, 2006, 44, 779–786.

223 M. M. Demir, I. Yilgor, E. Yilgor and B. Erman, Electrospinning of polyurethane fibers, *Polymer (Guildf).*, 2002, **43**, 3303–3309.

224 P. K. Baumgarten, Electrostatic spinning of acrylic microfibers, *J. Colloid Interface Sci.*, 1971, **36**, 71–79.

225 Z. Jun, H. Hou, A. Schaper, J. H. Wendorff and A. Greiner, Poly-L-lactide nanofibers by electrospinning - Influence of solution viscosity and electrical conductivity on fiber diameter and fiber morphology, *E-Polymers*, 2003, **3**, 9.

226 C. J. Buchko, L. C. Chen, Y. Shen and D. C. Martin, Processing and microstructural characterization of porous biocompatible protein polymer thin films, *Polymer (Guildf).*, 1999, **40**, 7397–7407.

227 S. Megelski, J. S. Stephens, D. Bruce Chase and J. F. Rabolt, Micro- and nanostructured surface morphology on electrospun polymer fibers, *Macromolecules*, 2002, **35**, 8456–8466.

228 C. Mit-Uppatham, M. Nithitanakul and P. Supaphol, Ultrafine electrospun polyamide-6 fibers: Effect of solution conditions on morphology and average fiber diameter, *Macromol. Chem. Phys.*, 2004, **205**, 2327–2338.

229 J. S. Lee, K. H. Choi, H. Do Ghim, S. S. Kim, D. H. Chun, H. Y. Kim and W. S. Lyoo, Role of molecular weight of atactic poly(vinyl alcohol) (PVA) in the structure and properties of PVA nanofabric prepared by electrospinning, *J. Appl. Polym. Sci.*, 2004, **93**, 1638–1646.

230 V. Jacobs, R. D. Anandjiwala and M. Maaza, The influence of electrospinning parameters on the structural morphology and diameter of electrospun nanofibers, *J. Appl. Polym. Sci.*, 2010, **115**, 3130–3136.

231 A. Koski, K. Yim and S. Shivkumar, Effect of molecular weight on fibrous PVA produced by electrospinning, *Mater. Lett.*, 2004, **58**, 493–497.

232 W. K. Son, J. H. Youk, T. S. Lee and W. H. Park, The effects of solution properties and polyelectrolyte on electrospinning of ultrafine poly(ethylene oxide) fibers, *Polymer (Guildf).*, 2004, **45**, 2959–2966.

233 K. H. Lee, H. Y. Kim, M. S. Khil, Y. M. Ra and D. R. Lee, Characterization of

nano-structured poly(ε-caprolactone) nonwoven mats via electrospinning, *Polymer (Guildf).*, 2003, **44**, 1287–1294.

234 Q. Yang, L. I. Zhenyu, Y. Hong, Y. Zhao, S. Qiu, C. E. Wang and Y. Wei, Influence of solvents on the formation of ultrathin uniform poly(vinyl pyrrolidone) nanofibers with electrospinning, *J. Polym. Sci. Part B Polym. Phys.*, 2004, **42**, 3721–3726.

235 J. Lin, B. Ding, Y. Jianyong and Y. Hsieh, Direct fabrication of highly nanoporous polystyrene fibers via electrospinning, *ACS Appl. Mater. Interfaces*, 2010, **2**, 521–528.

236 M. Srinivasarao, D. Collings, A. Philips and S. Patel, Three-dimensionally ordered array of air bubbles in a polymer film, *Science (80-.).*, 2001, **292**, 79–83.

237 R. Balgis, H. Murata, T. Ogi, M. Kobayashi and L. Bao, Enhanced Aerosol Particle Filtration Efficiency of Nonwoven Porous Cellulose Triacetate Nanofiber Mats, *ACS Omega*, 2018, **3**, 8271–8277.

238 H. Zhuo, J. Hu, S. Chen and L. Yeung, Preparation of polyurethane nanofibers by electrospinning, *J. Appl. Polym. Sci.*, 2008, **109**, 406–411.

239 J. M. Deitzel, J. Kleinmeyer, D. Harris and N. C. Beck Tan, The effect of processing variables on the morphology of electrospun nanofibers and textiles, *Polymer (Guildf).*, 2001, **42**, 261–272.

240 X. Zong, K. Kim, D. Fang, S. Ran, B. S. Hsiao and B. Chu, Structure and process relationship of electrospun bioabsorbable nanofiber membranes, *Polymer (Guildf).*, 2002, **43**, 4403–4412.

241 J. M. Deitzel, J. D. Kleinmeyer, J. K. Hirvonen and N. C. Beck Tan, Controlled deposition of electrospun poly(ethylene oxide) fibers, *Polymer (Guildf).*, 2001, **42**, 8163–8170.

242 K. H. Lee, H. Y. Kim, H. J. Bang, Y. H. Jung and S. G. Lee, The change of bead morphology formed on electrospun polystyrene fibers, *Polymer (Guildf).*, 2003, **44**, 4029–4034.

243 Y. J. Ryu, H. Y. Kim, K. H. Lee, H. C. Park and D. R. Lee, Transport properties of electrospun nylon 6 nonwoven mats, *Eur. Polym. J.*, 2003, **39**, 1883–1889.

244 X. Y. Yuan, Y. Y. Zhang, C. Dong and J. Sheng, Morphology of ultrafine polysulfone fibers prepared by electrospinning, *Polym. Int.*, 2004, **53**, 1704–

1710.

245 C. S. Ki, D. H. Baek, K. D. Gang, K. H. Lee, I. C. Um and Y. H. Park, Characterization of gelatin nanofiber prepared from gelatin-formic acid solution, *Polymer (Guildf).*, 2005, **46**, 5094–5102.

246 T. Wang and S. Kumar, Electrospinning of polyacrylonitrile nanofibers, *J. Appl. Polym. Sci.*, 2006, **102**, 1023–1029.

247 R. Jaeger, H. Schönherr and G. J. Vancso, Chain packing in electro-spun poly(ethylene oxide) visualized by atomic force microscopy, *Macromolecules*, 1996, **29**, 7634–7636.

248 R. Jaeger, M. M. Bergshoef, C. Martín I Batlle, H. Schönherr and G. J. Vancso, Electrospinning of ultra-thin polymer fibers, *Macromol. Symp.*, 1998, **127**, 141–150.

249 I. D. Norris, M. M. Shaker, F. K. Ko and A. G. MacDiarmid, Electrostatic fabrication of ultrafine conducting fibers: Polyaniline/polyethylene oxide blends, *Synth. Met.*, 2000, **114**, 109–114.

250 C. Drew, X. Wang, L. A. Samuelson and J. Kumar, The Effect of Viscosity and Filler on Electrospun Fiber Morphology, *J. Macromol. Sci. - Pure Appl. Chem.*, 2003, **40**, 1415–1422.

251 B. J. Hansen, Y. Liu, R. Yang and Z. L. Wang, Hybrid nanogenerator for concurrently harvesting biomechanical and biochemical energy, *ACS Nano*, 2010, **4**, 3647–3652.

252 K. Gao, X. Hu, C. Dai and T. Yi, Crystal structures of electrospun PVDF membranes and its separator application for rechargeable lithium metal cells, *Mater. Sci. Eng. B Solid-State Mater. Adv. Technol.*, 2006, **131**, 100–105.

253 S. Koombhongse, W. Liu and D. H. Reneker, Flat polymer ribbons and other shapes by electrospinning, *J. Polym. Sci. Part B Polym. Phys.*, 2001, **39**, 2598–2606.

254 S. S. Choi, Y. S. Lee, C. W. Joo, S. G. Lee, J. K. Park and K. S. Han, Electrospun PVDF nanofiber web as polymer electrolyte or separator, *Electrochim. Acta*, 2004, **50**, 339–343.

255 Z. Zhao, J. Li, X. Yuan, X. Li, Y. Zhang and J. Sheng, Preparation and properties of electrospun poly(vinylidene fluoride) membranes, *J. Appl. Polym. Sci.*, 2005, **97**, 466–474.

256 E. Smit, U. Buttner and R. D. Sanderson, Continuous yarns from electrospun fibers, *Polymer (Guildf).*, 2005, **46**, 2419–2423.

257 G. Zhong, L. Zhang, R. Su, K. Wang, H. Fong and L. Zhu, Understanding polymorphism formation in electrospun fibers of immiscible Poly(vinylidene fluoride) blends, *Polymer (Guildf).*, 2011, **52**, 2228–2237.

258 W. A. Yee, M. Kotaki, Y. Liu and X. Lu, Morphology, polymorphism behavior and molecular orientation of electrospun poly(vinylidene fluoride) fibers, *Polymer (Guildf).*, 2007, **48**, 512–521.

259 S. W. Choi, J. R. Kim, Y. R. Ahn, S. M. Jo and E. J. Cairns, Characterization of electrospun PVdF fiber-based polymer electrolytes, *Chem. Mater.*, 2007, **19**, 104–115.

260 F. Huang, Q. Wei, J. Wang, Y. Cai and Y. Huang, Effect of temperature on structure, morphology and crystallinity of PVDF nanofibers via electrospinning, *E-Polymers*, 2008, **8**, 1–8.

261 N. Chanunpanich, B. Lee and H. Byun, A study of electrospun PVDF on PET sheet, *Macromol. Res.*, 2008, **16**, 212–217.

262 K. P. Matabola and R. M. Moutloali, The influence of electrospinning parameters on the morphology and diameter of poly(vinyledene fluoride) nanofibers- Effect of sodium chloride, *J. Mater. Sci.*, 2013, **48**, 5475–5482.

263 J. S. Andrew and D. R. Clarke, Effect of electrospinning on the ferroelectric phase content of polyvinylidene difluoride fibers, *Langmuir*, 2008, **24**, 670–672.

264 A. Baji, Y. W. Mai, Q. Li and Y. Liu, Electrospinning induced ferroelectricity in poly(vinylidene fluoride) fibers, *Nanoscale*, 2011, **3**, 3068–3071.

265 S. Gee, B. Johnson and A. L. Smith, Optimizing electrospinning parameters for piezoelectric PVDF nanofiber membranes, *J. Memb. Sci.*, 2018, **563**, 804–812.

266 J. Bae, I. Baek and H. Choi, Efficacy of piezoelectric electrospun nanofiber membrane for water treatment, *Chem. Eng. J.*, 2017, **307**, 670–678.

267 A. Gheibi, R. Bagherzadeh, A. A. Merati and M. Latifi, Electrical power generation from piezoelectric electrospun nanofibers membranes: electrospinning parameters optimization and effect of membranes thickness on output electrical voltage, *J. Polym. Res.*, , DOI:10.1007/s10965-014-0571-8.

268 E. Öğüt, O. S. Yördem, Y. Z. Menceloğlu and M. Papila, in *Behavior and Mechanics of Multifunctional and Composite Materials 2007*, 2007, pp. 1–10.

269 J. Zheng, A. He, J. Li and C. C. Han, Polymorphism control of poly(vinylidene fluoride) through electrospinning, *Macromol. Rapid Commun.*, 2007, **28**, 2159–2162.

270 C. Ribeiro, V. Sencadas, J. L. G. Ribelles and S. Lanceros-Méndez, Influence of processing conditions on polymorphism and nanofiber morphology of electroactive poly(vinylidene fluoride) electrospun membranes, *Soft Mater.*, 2010, **8**, 274–287.

271 Z. Jianfen, H. Aihua, L. Junxing and H. C. C, Polymorphism Control of Poly(vinylidene fluoride) through Electrospinning, *Macromol. Rapid Commun.*, 2007, **28**, 2159–2162.

272 K. Arayanarakul, N. Choktaweesap, D. Aht-ong, C. Meechaisue and P. Supaphol, Effects of poly(ethylene glycol), inorganic salt, sodium dodecyl sulfate, and solvent system on electrospinning of poly(ethylene oxide), *Macromol. Mater. Eng.*, 2006, **291**, 581–591.

273 D. Dhakras, V. Borkar, S. Ogale and J. Jog, Enhanced piezoresponse of electrospun PVDF mats with a touch of nickel chloride hexahydrate salt, *Nanoscale*, 2012, **4**, 752–756.

274 F. Chen, Y. Lu, X. Liu, J. Song, G. He, M. K. Tiwari, C. J. Carmalt and I. P. Parkin, Table Salt as a Template to Prepare Reusable Porous PVDF–MWCNT Foam for Separation of Immiscible Oils/Organic Solvents and Corrosive Aqueous Solutions, *Adv. Funct. Mater.*, , DOI:10.1002/adfm.201702926.

275 Z. Mokhtari-Shourijeh, L. Montazerghaem and M. E. Olya, Preparation of Porous Nanofibers from Electrospun Polyacrylonitrile/Polyvinylidene Fluoride Composite Nanofibers by Inexpensive Salt Using for Dye Adsorption, *J. Polym. Environ.*, 2018, **26**, 3550–3563.

276 T. Uyar and F. Besenbacher, Electrospinning of uniform polystyrene fibers: The effect of solvent conductivity, *Polymer (Guildf).*, 2008, **49**, 5336–5343.

277 Y. Liao, R. Wang, M. Tian, C. Qiu and A. G. Fane, Fabrication of polyvinylidene fluoride (PVDF) nanofiber membranes by electro-spinning for direct contact membrane distillation, *J. Memb. Sci.*, 2013, **425**–**426**, 30–29.

278 F. Mokhtari, M. Shamshirsaz and M. Latifi, Investigation of β phase formation in piezoelectric response of electrospun polyvinylidene fluoride nanofibers: LiCl additive and increasing fibers tension, *Polym. Eng. Sci.*, 2016, **56**, 61–70.

279 I. A. Sahito, F. Ahmed, Z. Khatri, K. C. Sun and S. H. Jeong, Enhanced ionic mobility and increased efficiency of dye-sensitized solar cell by adding lithium chloride in poly(vinylidene fluoride) nanofiber as electrolyte medium, *J. Mater. Sci.*, 2017, **52**, 13920–13929.

280 F. Russo, C. Ursino, E. Avruscio, G. Desiderio, A. Perrone, S. Santoro, F. Galiano and A. Figoli, Innovative poly (Vinylidene fluoride) (PVDF) electrospun nanofiber membrane preparation using DMSO as a low toxicity solvent, *Membranes (Basel).*, 2020, **10**, 17.

281 S. Santoro, I. Vidorreta, I. Coelhoso, J. C. Lima, G. Desiderio, G. Lombardo, E. Drioli, R. Mallada, J. Crespo, A. Criscuoli and A. Figoli, Experimental evaluation of the thermal polarization in direct contact membrane distillation using electrospun nanofiber membranes doped with molecular probes, *Molecules*, 2019, **24**, 13.

282 C. Chen, Z. Bai, Y. Cao, M. Dong, K. Jiang, Y. Zhou, Y. Tao, S. Gu, J. Xu, X. Yin and W. Xu, Enhanced piezoelectric performance of BiCl3/PVDF nanofibers-based nanogenerators, *Compos. Sci. Technol.*, , DOI:10.1016/j.compscitech.2020.108100.

283 S. Janakiraman, A. Surendran, S. Ghosh, S. Anandhan and A. Venimadhav, A new strategy of PVDF based Li-salt polymer electrolyte through electrospinning for lithium battery application, *Mater. Res. Express*, , DOI:10.1088/2053-1591/aaf369.

284 M. Benz, W. B. Euler and O. J. Gregory, The role of solution phase water on the deposition of thin films of poly(vinylidene fluoride), *Macromolecules*, 2002, **35**, 2682–2688.

285 Z. Li, Y. Xu, L. Fan, W. Kang and B. Cheng, Fabrication of polyvinylidene fluoride tree-like nanofiber via one-step electrospinning, *Mater. Des.*, 2016, **92**, 95–101.

286 N. Chamankar, R. Khajavi, A. A. Yousefi, A. Rashidi and F. Golestanifard, A flexible piezoelectric pressure sensor based on PVDF nanocomposite fibers doped with PZT particles for energy harvesting applications, *Ceram. Int.*, 2020, **46**, 19669–19681.

287 J. J. P.-H. Corral-Flores, Verónica, E. Torres-Moye, J. Romero-García, D. Bueno-Baqués and ERonald F. Ziolo, Preparation of electrospun barium titanate

- Polyvinylidene fluoride piezoelectric membranes, *Mater. Sci. Forum*, 2010, **644**, 33–37.

288 C. V. Chanmal and J. P. Jog, Electrospun PVDF/BaTiO3 nanocomposites: Polymorphism and thermal emissivity studies, *Int. J. Plast. Technol.*, 2011, **15**, 1–9.

289 K. Shi, B. Sun, X. Huang and P. Jiang, Synergistic effect of graphene nanosheet and BaTiO3 nanoparticles on performance enhancement of electrospun PVDF nanofiber mat for flexible piezoelectric nanogenerators, *Nano Energy*, 2018, **52**, 153–162.

290 J. Jiang, S. Tu, R. Fu, J. Li, F. Hu, B. Yan, Y. Gu and S. Chen, Flexible Piezoelectric Pressure Tactile Sensor Based on Electrospun BaTiO3/Poly(vinylidene fluoride) Nanocomposite Membrane, *ACS Appl. Mater. Interfaces*, 2020, **12**, 33989–33998.

291 C. T. Pan, S. Y. Wang, C. K. Yen, A. Kumar, S. W. Kuo, J. L. Zheng, Z. H. Wen, R. Singh, S. P. Singh, M. T. Khan, R. K. Chaudhary, X. Dai, A. Chandra Kaushik, D. Q. Wei, Y. L. Shiue and W. H. Chang, Polyvinylidene Fluoride-Added Ceramic Powder Composite Near-Field Electrospinned Piezoelectric Fiber-Based Low-Frequency Dynamic Sensors, *ACS Omega*, 2020, **5**, 17090–17101.

292 M. S. Sorayani Bafqi, R. Bagherzadeh and M. Latifi, Fabrication of composite PVDF-ZnO nanofiber mats by electrospinning for energy scavenging application with enhanced efficiency, *J. Polym. Res.*, , DOI:10.1007/s10965-015-0765-8.

293 S. Mansouri, T. F. Sheikholeslami and A. Behzadmehr, Investigation on the electrospun PVDF/NP-ZnO nanofibers for application in environmental energy harvesting, *J. Mater. Res. Technol.*, 2019, **8**, 1608–1615.

294 M. Kim, Y. S. Wu, E. C. Kan and J. Fan, Breathable and flexible piezoelectric ZnO/PVDF fibrous nanogenerator for wearable applications, *Polymers (Basel).*, 2018, **10**, 15.

295 Y. J. Kim, C. H. Ahn, M. B. Lee and M. S. Choi, Characteristics of electrospun PVDF/SiO2 composite nanofiber membranes as polymer electrolyte, *Mater. Chem. Phys.*, 2011, **127**, 137–142.

296 X. Xiong, Q. Li, X. C. Zhang, L. Wang, Z. X. Guo and J. Yu, Poly(vinylidene fluoride)/silica nanocomposite membranes by electrospinning, *J. Appl. Polym.*

Sci., 2013, **129**, 1089–1095.

297 X. Ma, F. Qiao, M. Qian, Y. Ye, X. Cao, Y. Wei, N. Li, M. Sha, Z. Zi and J. Dai, Facile fabrication of flexible electrodes with poly(vinylidene fluoride)/Si3N4 composite separator prepared by electrospinning for sodium-ion batteries, *Scr. Mater.*, 2021, **190**, 153–157.

298 J. Zhu, H. Sun, Y. Xu, T. Liu, T. Hou, L. Liu, Y. Li, T. Lin and Y. Xin, Preparation of PVDF/TiO2 nanofibers with enhanced piezoelectric properties for geophone applications, *Smart Mater. Struct.*, 2019, **28**, 1–7.

299 R. S. Bharath, T. Chakraborthy, H. Nhalil, B. Masin, K. Ashok, H. Sreemoolanadhan, C. Oommen and S. Elizabeth, Synthesis and evaluation of PVDF-MgTiO3 polymer-ceramic composites for low-: K dielectric applications, *J. Mater. Chem. C*, 2019, **7**, 4484–4496.

300 Y. L. Liu, Y. Li, J. T. Xu and Z. Q. Fan, Cooperative effect of electrospinning and nanoclay on formation of polar crystalline phases in poly(vinylidene fluoride), *ACS Appl. Mater. Interfaces*, 2010, **2**, 1759–1768.

301 A. A. Shah, Y. H. Cho, S. E. Nam, A. Park, Y. I. Park and H. Park, High performance thin-film nanocomposite forward osmosis membrane based on PVDF/bentonite nanofiber support, *J. Ind. Eng. Chem.*, 2020, **86**, 90–99.

302 T. He, W. Zhou, A. Bahi, H. Yang and F. Ko, High permeability of ultrafiltration membranes based on electrospun PVDF modified by nanosized zeolite hybrid membrane scaffolds under low pressure, *Chem. Eng. J.*, 2014, **252**, 327–336.

303 A. C. Lopes, C. Ribeiro, V. Sencadas, G. Botelho and S. Lanceros-Méndez, Effect of filler content on morphology and physical-chemical characteristics of poly(vinylidene fluoride)/NaY zeolite-filled membranes, *J. Mater. Sci.*, 2014, **49**, 3361–3370.

304 D. H. Kang and H. W. Kang, Surface energy characteristics of zeolite embedded PVDF nanofiber films with electrospinning process, *Appl. Surf. Sci.*, 2016, **387**, 82–88.

305 P. Pazhamalai, K. Krishnamoorthy, V. K. Mariappan, S. Sahoo, S. Manoharan and S. J. Kim, A High Efficacy Self-Charging MoSe2 Solid-State Supercapacitor Using Electrospun Nanofibrous Piezoelectric Separator with Ionogel Electrolyte, *Adv. Mater. Interfaces*, , DOI:10.1002/admi.201800055.

306 P. Pazhamalai, V. K. Mariappan, S. Sahoo, W. Y. Kim, Y. S. Mok and S. J. Kim,

Free-standing pvdf/reduced graphene oxide film for all-solid-state flexible supercapacitors towards self-powered systems, *Micromachines*, 2020, **11**, 1–13.

307 A. Teka, S. Bairagi, M. Shahadat, M. Joshi, S. Ziauddin Ahammad and S. Wazed Ali, Poly(vinylidene fluoride) (PVDF)/potassium sodium niobate (KNN)–based nanofibrous web: A unique nanogenerator for renewable energy harvesting and investigating the role of KNN nanostructures, *Polym. Adv. Technol.*, 2018, **29**, 2537–2544.

308 S. Bairagi and S. W. Ali, Influence of High Aspect Ratio Lead-Free Piezoelectric Fillers in Designing Flexible Fibrous Nanogenerators: Demonstration of Significant High Output Voltage, *Energy Technol.*, , DOI:10.1002/ente.201900538.

309 S. Bairagi and S. W. Ali, A hybrid piezoelectric nanogenerator comprising of KNN/ZnO nanorods incorporated PVDF electrospun nanocomposite webs, *Int. J. Energy Res.*, 2020, **44**, 5545–5563.

310 M. Kucuk and Y. Korkmaz, Sound absorption properties of bilayered nonwoven composites, *Fibers Polym.*, 2015, **16**, 941–948.

311 J. I. Goldstein, D. E. Newbury, J. R. Michael, N. W. M. Ritchie, J. H. J. Scott and D. C. Joy, *Scanning Electron Microscopy and X-Ray Microanalysis*, Springer, New York, NY, Fourth Edi., 2018.

312 P. Echlin, *Handbook of Sample Preparation for Scanning Electron Microscopy and X-Ray Microanalysis*, First Edit., 2009.

313 C. Outline, *Methods for Assessing Surface Cleanliness*, 2019, vol. 12.

314 P. R. Griffiths and J. A. de Haseth, in *Fourier Transform Infrared Spectrometry*, Second Edi., 2006, pp. 19–55.

315 P. W. H. Bragg and W. L. Bragg, The reflexion of X-rays by crystals, *Proc. R. Soc. Lond. A*, 1913, **17**, 428–438.

316 B. Fultz and J. M. Howe, *Transmission electron microscopy and diffractometry of materials*, Fourth Edi., 2013.

317 L. H. Sperling, *Introduction to Physical Polymer Science: Fourth Edition*, 2005.

318 K. K. Mahato, K. Dutta and B. C. Ray, in *New Materials in Civil Engineering*, 2020, pp. 221–271.

319 N. Hiremath, V. Kumar, N. Motahari and D. Shukla, An Overview of Acoustic Impedance Measurement Techniques and Future Prospects, *Metrology*, 2021, **1**,

17–38.

320 Z. He, F. Rault, M. Lewandowski, E. Mohsenzadeh and F. Salaün, Electrospun PVDF nanofibers for piezoelectric applications: A review of the influence of electrospinning parameters on the β phase and crystallinity enhancement, *Polymers (Basel).*, 2021, **13**, 174.

321 M. A. Jahangir, T. M. Rumi, A. Wahab, M. A. Rahman and Z. Bin Sayed, Poly Lactic Acid (PLA) Fibres: Different Solvent Systems and Their Effect on Fibre Morphology and Diameter, *Am. J. Chem.*, 2017, **2017**, 177–186.

322 L. M. M. Costa, R. E. S. Bretas and R. Gregorio, Effect of Solution Concentration on the Electrospray/Electrospinning Transition and on the Crystalline Phase of PVDF, *Mater. Sci. Appl.*, 2010, **01**, 247–252.

323 Y. J. Hwang, S. Choi and H. S. Kim, Structural deformation of PVDF nanoweb due to electrospinning behavior affected by solvent ratio, *E-Polymers*, 2018, **18**, 339–345.

324 G. Eda and S. Shivkumar, Bead-to-fiber transition in electrospun polystyrene, *J. Appl. Polym. Sci.*, 2007, **106**, 475–487.

325 Y. P. Neo, S. Ray, A. J. Easteal, M. G. Nikolaidis and S. Y. Quek, Influence of solution and processing parameters towards the fabrication of electrospun zein fibers with sub-micron diameter, *J. Food Eng.*, 2012, **109**, 645–651.

326 N. Okutan, P. Terzi and F. Altay, Affecting parameters on electrospinning process and characterization of electrospun gelatin nanofibers, *Food Hydrocoll.*, 2014, **39**, 19–26.

327 K. Castkova, J. Kastyl, D. Sobola, J. Petrus, E. Stastna, D. Riha and P. Tofel, Structure–properties relationship of electrospun pvdf fibers, *Nanomaterials*, 2020, **10**, 1–19.

328 R. K. Singh, S. W. Lye and J. Miao, Holistic investigation of the electrospinning parameters for high percentage of β-phase in PVDF nanofibers, *Polymer (Guildf).*, , DOI:10.1016/j.polymer.2020.123366.

329 R. Casasola, N. L. Thomas, A. Trybala and S. Georgiadou, Electrospun poly lactic acid (PLA) fibres: Effect of different solvent systems on fibre morphology and diameter, *Polymer (Guildf).*, 2014, **55**, 4728–4737.

330 E. S. Cozza, O. Monticelli, E. Marsano and P. Cebe, On the electrospinning of PVDF: Influence of the experimental conditions on the nanofiber properties,

Polym. Int., 2013, **62**, 41–48.

331 B. Zaarour, L. Zhu and X. Jin, Controlling the surface structure, mechanical properties, crystallinity, and piezoelectric properties of electrospun PVDF nanofibers by maneuvering molecular weight, *Soft Mater.*, 2019, **17**, 181–189.

332 S. Haider, Y. Al-Zeghayer, F. A. Ahmed Ali, A. Haider, A. Mahmood, W. A. Al-Masry, M. Imran and M. O. Aijaz, Highly aligned narrow diameter chitosan electrospun nanofibers, *J. Polym. Res.*, 2013, **20**, 1–11.

333 K. Arayanarakul, N. Choktaweesap, D. Aht-ong, C. Meechaisue and P. Supaphol, Effects of poly(ethylene glycol), inorganic salt, sodium dodecyl sulfate, and solvent system on electrospinning of poly(ethylene oxide), *Macromol. Mater. Eng.*, , DOI:10.1002/mame.200500419.

334 J. Du and X. Zhang, Role of polymer-salt-solvent interactions in the electrospinning of polyacrylonitrile/iron acetylacetonate, *J. Appl. Polym. Sci.*, 2008, **109**, 2935–2941.

335 P. G. Bruce, Ion association in polymer electrolytes: transport and materials optimization, *Synth. Met.*, 1991, **45**, 267–278.

336 Y. Wang, B. Wang, G. Wang, T. Yin and Q. Yu, A novel method for preparing electrospun fibers with nano-/micro-scale porous structures, *Polym. Bull.*, 2009, **63**, 259–265.

337 J. S. Andrew and D. R. Clarke, Enhanced ferroelectric phase content of polyvinylidene difluoride fibers with the addition of magnetic nanoparticles, *Langmuir*, 2008, **24**, 8435–8438.

338 X. Cai, T. Lei, D. Sun and L. Lin, A critical analysis of the α, β and γ phases in poly(vinylidene fluoride) using FTIR, *RSC Adv.*, 2017, **7**, 15382–15389.

339 L. He, J. Sun, X. Wang, C. Wang, R. Song and Y. Hao, Facile and effective promotion of β crystalline phase in poly(vinylidene fluoride) via the incorporation of imidazolium ionic liquids, *Polym. Int.*, 2013, **62**, 638–646.

340 A. Salimi and A. A. Yousefi, Analysis Method: FTIR studies of β-phase crystal formation in stretched PVDF films, *Polym. Test.*, 2003, **22**, 699–704.

341 X. Chen, C. Tougne, T. Jiang, M. Espindola-Rodriguez, Q. Zhao, Q. Jia, H. Mendil-Jakani, J. Jiang and W. Zhang, Highly oriented PVDF molecular chains for enhanced material performance, *Polymer (Guildf).*, 2022, **261**, 125366.

342 Y. K. A. Low, L. Y. Tan, L. P. Tan, F. Y. C. Boey and K. W. Ng, Increasing

solvent polarity and addition of salts promote β-phase poly(vinylidene fluoride) formation, *J. Appl. Polym. Sci.*, 2013, **128**, 2902–2910.

343 S. G. Lee, K.-S. Han, C. W. Joo, J. K. Park, S.-S. Choi and Y. S. Lee, in *Electrochimica Acta*, 2004, vol. 50, pp. 339–343.

344 S. Satapathy, S. Pawar, P. K. Gupta and K. B. RVarma, Effect of annealing on phase transition in poly(vinylidene fluoride) films prepared using polar solvent, *Bull. Mater. Sci.*, 2011, **34**, 727–733.

345 N. Moazeni, M. Sadrjahani, A. A. Merati, M. Latifi and S. Rouhani, Effect of stimuli-responsive polydiacetylene on the crystallization and mechanical properties of PVDF nanofibers, *Polym. Bull.*, 2020, **77**, 5373–5388.

346 F. He, J. Fan and S. Lau, Thermal, mechanical, and dielectric properties of graphite reinforced poly(vinylidene fluoride) composites, *Polym. Test.*, 2008, **27**, 964–970.

347 T. Lei, X. Cai, X. Wang, L. Yu, X. Hu, G. Zheng, W. Lv, L. Wang, D. Wu, D. Sun and L. Lin, Spectroscopic evidence for a high fraction of ferroelectric phase induced in electrospun polyvinylidene fluoride fibers, *RSC Adv.*, 2013, **3**, 24952–24958.

348 F. Samavat, E. Haji Ali, S. Solgi and P. Taravati Ahmad, KCl Single Crystals Growth with Mn, Ag and In Impurities by Czochralski Method and Study of Impurities Influence on Their Properties, *Open J. Phys. Chem.*, 2012, **02**, 185–188.

349 M. Agarwal, S. K. Garg, K. Asokan, D. Kanjilal and P. Kumar, Facile synthesis of KCl:Sm3+ nanophosphor as a new OSL dosimetric material achieved through charge transfer between the defect states, *RSC Adv.*, 2017, **7**, 13836–13845.

350 S. Jana, S. Garain, S. Sen and D. Mandal, The influence of hydrogen bonding on the dielectric constant and the piezoelectric energy harvesting performance of hydrated metal salt mediated PVDF films, *Phys. Chem. Chem. Phys.*, 2015, **17**, 17429–17436.

351 M. Rasoolzadeh, Z. Sherafat, M. Vahedi and E. Bagherzadeh, Structure dependent piezoelectricity in electrospun PVDF-SiC nanoenergy harvesters, *J. Alloys Compd.*, 2022, **917**, 165505.

352 O. Ero-Phillips, M. Jenkins and A. Stamboulis, Tailoring Crystallinity of Electrospun Plla Fibres by Control of Electrospinning Parameters, *Polymers*

(Basel)., 2012, **4**, 1331–1348.

353 S. Garain, S. Jana, T. K. Sinha and D. Mandal, Design of in Situ Poled Ce3+-Doped Electrospun PVDF/Graphene Composite Nanofibers for Fabrication of Nanopressure Sensor and Ultrasensitive Acoustic Nanogenerator, *ACS Appl. Mater. Interfaces*, 2016, **8**, 4532–4540.

354 H. A. Ávila, M. M. Reboredo, M. Castro and R. Parra, Nanofibers obtained by electrospinning of BaTiO3 particlesdispersed in polyvinyl alcohol and ethylcellulose, *Mater. Res.*, , DOI:10.1590/S1516-14392013005000061.

355 C. Mota, M. Labardi, L. Trombi, L. Astolfi, M. D'Acunto, D. Puppi, G. Gallone, F. Chiellini, S. Berrettini, L. Bruschini and S. Danti, Design, fabrication and characterization of composite piezoelectric ultrafine fibers for cochlear stimulation, *Mater. Des.*, 2017, **122**, 206–219.

356 L. Lee, S. J. Park and S. Kim, Effect of nano-sized barium titanate addition on PEO/PVDF blend-based composite polymer electrolytes, *Solid State Ionics*, 2013, **234**, 19–24.

357 C. T. Pan, S. Y. Wang, C. K. Yen, A. Kumar, S. W. Kuo, J. L. Zheng, Z. H. Wen, R. Singh, S. P. Singh, M. T. Khan, R. K. Chaudhary, X. Dai, A. Chandra Kaushik, D. Q. Wei, Y. L. Shiue and W. H. Chang, Polyvinylidene Fluoride-Added Ceramic Powder Composite Near-Field Electrospinned Piezoelectric Fiber-Based Low-Frequency Dynamic Sensors, *ACS Omega*, 2020, **5**, 17090–17101.

358 Y. M. Song, Z. Di Zhao, W. X. Yu, B. Li and X. F. Chen, Morphological structures of poly(vinylidene fluoride)/montmorillonite nanocomposites, *Sci. China, Ser. B Chem.*, 2007, **50**, 790–796.

359 H. Abdolmaleki and S. Agarwala, PVDF-BaTiO3 nanocomposite inkjet inks with enhanced β-phase crystallinity for printed electronics, *Polymers (Basel).*, 2020, **12**, 1–12.

360 N. Kumada, T. Kyoda, Y. Yonesaki, T. Takei and N. Kinomura, Preparation of KNbO3 by hydrothermal reaction, *Mater. Res. Bull.*, 2007, **42**, 1856–1862.

361 S. F. Mendes, C. M. Costa, C. Caparros, V. Sencadas and S. Lanceros-Méndez, Effect of filler size and concentration on the structure and properties of poly(vinylidene fluoride)/BaTiO3 nanocomposites, *J. Mater. Sci.*, 2012, **47**, 1378–1388.

362 G. Botelho, S. Lanceros-Mendez, A. M. Gonçalves, V. Sencadas and J. G. Rocha, Relationship between processing conditions, defects and thermal degradation of poly(vinylidene fluoride) in the β-phase, *J. Non. Cryst. Solids*, 2008, **354**, 72–78.

363 M. L. O'shea, C. Morterra and M. J. D. Low, Spectroscopic studies of carbons. XVII. Pyrolysis of polyvinylidene fluoride, *Mater. Chem. Phys.*, 1990, **26**, 193–209.

364 Z. Mirzazadeh, Z. Sherafat and E. Bagherzadeh, Physical and mechanical properties of PVDF/KNN composite produced via hot compression molding, *Ceram. Int.*, , DOI:10.1016/j.ceramint.2020.10.199.

365 S. Bairagi and S. W. Ali, A unique piezoelectric nanogenerator composed of melt-spun PVDF/KNN nanorod-based nanocomposite fibre, *Eur. Polym. J.*, 2019, **116**, 554–561.

366 M. M. Hirschler, Effect of oxygen on the thermal decomposition of poly(vinylidene fluoride), *Eur. Polym. J.*, 1982, **18**, 463–467.

367 K. Osińska and D. Czekaj, Thermal behavior of BST//PVDF ceramic-polymer composites, *J. Therm. Anal. Calorim.*, 2013, **113**, 69–76.

368 Q. Zhao, L. Yang, K. Chen, Y. Ma, Q. Peng, H. Ji and J. Qiu, Flexible textured MnO2 nanorods/ PVDF hybrid films with superior piezoelectric performance for energy harvesting application, *Compos. Sci. Technol.*, 2020, **199**, 108330.

369 Q. He and A. Zhang, Effect of microwave irradiation on crystalline structure and dielectric property of PVDF/PZT composite, *J. Mater. Sci.*, 2008, **43**, 820 823.

370 U. Montanari, D. Cocchi, T. M. Brugo, A. Pollicino, V. Taresco, M. Romero Fernandez, J. C. Moore, D. Sagnelli, F. Paradisi, A. Zucchelli, S. M. Howdle and C. Gualandi, Functionalisable epoxy-rich electrospun fibres based on renewable terpene for multi-purpose applications, *Polymers (Basel).*, 2021, **13**, 1804.

371 R. Song, D. Yang and L. He, Effect of surface modification of nanosilica on crystallization, thermal and mechanical properties of poly(vinylidene fluoride), *J. Mater. Sci.*, 2007, **42**, 8408–8417.

372 A. J. Lovinger and T. T. Wang, Investigation of the properties of directionally solidified poly(vinylidene fluoride), *Polymer (Guildf).*, 1979, **20**, 725–732.

373 G. Ceccorulli, M. Pizzoli, M. Scandola, G. C. Alfonso and A. Turturro, Dynamic mechanical relaxations of poly(vinylidene fluoride)-poly(vinylpyrrolidone) blends, *Polymer (Guildf).*, 1989, **7**, 1251–1256.

374 V. Goodarzi, M. Kokabi, M. Razzaghi Kashani and A. Reza Bahramian, Prediction of long-term mechanical properties of PVDF/BaTiO3 nanocomposite, *J. Appl. Polym. Sci.*, 2014, **131**, 1–8.

375 S. Ganguli, A. K. Roy and D. P. Anderson, Improved thermal conductivity for chemically functionalized exfoliated graphite/epoxy composites, *Carbon N. Y.*, 2008, **46**, 806–817.

376 A. Gebrekrstos, S. Biswas, A. V. Menon, G. Madras, P. Pötschke and S. Bose, Multi-layered stack consisting of PVDF nanocomposites with flow-induced oriented MWCNT structure can supress electromagnetic radiation, *Compos. Part B Eng.*, 2019, **116**, 749–757.

377 P. Russo, D. Acierno, C. Leonelli and A. Corradi, Mechanical and dynamic-mechanical behavior and morphology of polystyrene/perovskite composites: Effects of filler size, *Surf. Coatings Technol.*, 2011, **10**, 1017–1022.

378 J. Zhang, Y. Shen, B. Jiang and Y. Li, Sound absorption characterization of natural materials and sandwich structure composites, *Aerospace*, 2018, **5**, 75.

379 Y. Xu, W. Li, M. Zhu, X. Yue and M. Wang, Novel porous fiber-based composites with excellent sound-absorbing and flame-retardant properties, *J. Wood Chem. Technol.*, 2020, **40**, 285–293.

380 M. Bandarian, A. Shojaei and A. M. Rashidi, Thermal, mechanical and acoustic damping properties of flexible open-cell polyurethane/multi-walled carbon nanotube foams: Effect of surface functionality of nanotubes, *Polym. Int.*, 2011, **60**, 475–482.

381 M. Bandarian, A. Shojaei and A. M. Rashidi, Thermal, mechanical and acoustic damping properties of flexible open-cell polyurethane/multi-walled carbon nanotube foams: Effect of surface functionality of nanotubes, *Polym. Int.*, 2011, **60**, 475–482.

382 B. Wang, X. H. Yin, D. Peng, R. H. Lv, B. Na, H. S. Liu, X. B. Gu, W. Wu, J. L. Zhou and Y. Zhang, Achieving thermally conductive low loss PVDF-based dielectric composites via surface functionalization and orientation of sic nanowires, *Express Polym. Lett.*, 2020, **14**, 2–11.

383 X. Li, T. K. S. Wong, Rusli and D. Yang, Structural and electronic properties of low dielectric constant carbon rich amorphous silicon carbide, *Diam. Relat. Mater.*, 2003, **12**, 963–967.

384 H. Du, Y. Li and C. Cao, Effect of temperature on dielectric properties of Si3N 4/SiO2 composite and silica ceramic, *J. Alloys Compd.*, 2010, **503**, L9–L13.

385 J. Sheth, Devendra Kumar, V. K. Tiwari and P. Maiti, Silicon carbide-induced piezoelectric b-phase in poly(vinylidene fluoride) and its properties, *J. Mater. Res.*, 2012, **27**, 1838–1845.

386 K. Nakagawa and Y. Ishida, Annealing effects in poly(vinylidene fluoride) as revealed by specific volume measurements, differential scanning calorimetry, and electron microscopy, *J. Polym. Sci. Part B Polym. Phys.*, 1973, **11**, 2153–2171.

387 Y. Wu, S. L. Hsu, C. Honeker, D. J. Bravet and D. S. Williams, The role of surface charge of nucleation agents on the crystallization behavior of poly(vinylidene fluoride), *J. Phys. Chem. B*, 2012, **116**, 7379–7388.

388 X. Cao, W. Zhao, X. Gong, D. Zhang, Q. Su, J. Zha, X. Yin, W. Wu and R. K. Y. Li, Mussel-inspired polydopamine functionalized silicon carbide whisker for PVDF composites with enhanced dielectric performance, *Compos. Part A Appl. Sci. Manuf.*, 2021, **148**, 106468.

389 C. Zhang, J. Li, Z. Hu, F. Zhu and Y. Huang, Correlation between the acoustic and porous cell morphology of polyurethane foam: Effect of interconnected porosity, *Mater. Des.*, 2012, **41**, 319–325.

390 T. Greeshma, R. Balaji and S. Jayakumar, PVDF phase formation and its influence on electrical and structural properties of PZT-PVDF composites, *Ferroelectr. Lett. Sect.*, 2013, **40**, 41–55.

391 R. Verdejo, C. Saiz-Arroyo, J. Carretero-Gonzalez, F. Barroso-Bujans, M. A. Rodriguez-Perez and M. A. Lopez-Manchado, Physical properties of silicone foams filled with carbon nanotubes and functionalized graphene sheets, *Eur. Polym. J.*, 2008, **44**, 2790–2797.

392 S. Ersoy and A. El-Hafid, Investigation of sound properties of High Density Polyethylene / Styrene Butadiene Rubber polymer composites, *Vibroengineering Procedia*, 2013, **1**, 77–80.

393 P. Peças, H. Carvalho, H. Salman and M. Leite, Natural fibre composites and their applications: A review, *J. Compos. Sci.*, 2018, **2**, 66.

394 J. M. Kopania, W. Zakrzewicz, P. Kubiak, A. Mrowicki, M. Głogowski, J. Gralewski, G. Bogusławski, K. Wójciak and P. Gaj, The Properties of Materials

and Structures of Fluted PVC Panels for the Transmission of Airborne Sound, *Appl. Sci.*, 2022, **12**, 1–20.

395 R. Jian, P. Shahi, M. Semeniuk, J. Tan, W. Yang and M. Sain, Acoustic Absorption Properties of Polystyrene-Pyrolytic Pinus Resinosa Composite Foams Prepared by Torsion-Induced Extrusion, *Macromol. Mater. Eng.*, 2022, **307**, 2100622.

396 A. Nadaf, A. Gupta, N. Hasan, N. Fauziya, S. Ahmad, P. Kesharwani and F. J. Ahmad, Recent update on electrospinning and electrospun nanofibers: current trends and their applications, *RSC Adv.*, 2022, **12**, 23808–23828.

Appendix

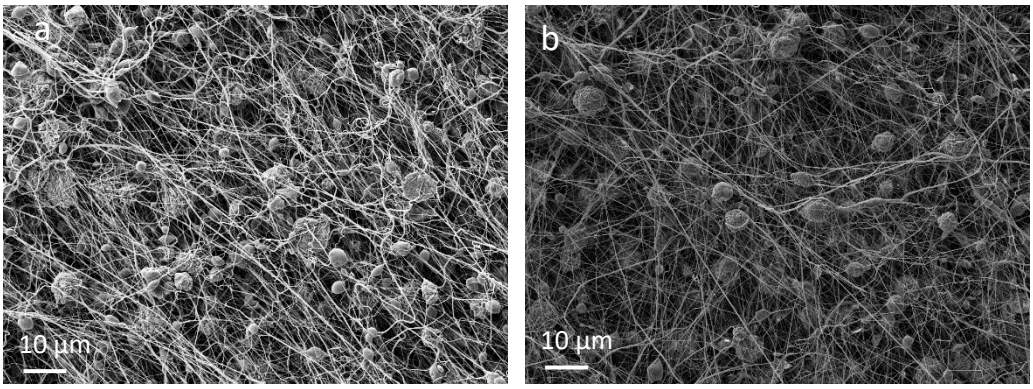

Figure 0.1. SEM images of the LMW PVDF 20 wt% at (a):10 cm, and (b) 15 cm collector distance

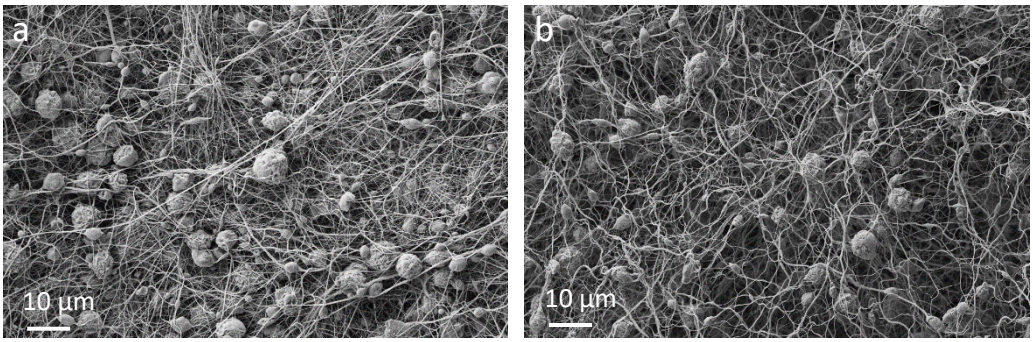

Figure 0.2. SEM images of the LMW PVDF 22 wt% at (a):10 cm, and (b) 15 cm collector distance

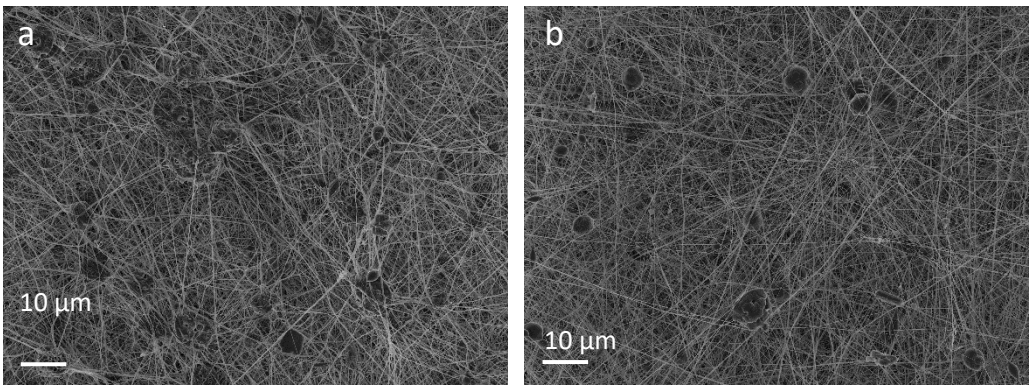

Figure 0.3: SEM images of the LMW PVDF 27 wt% at (a):10 cm, and (b) 15 cm collector distance

Table 0.1. Electrospinning parameters for 15 wt% – 27 wt% with differing tip to collector distances.

PVDF Weight / %	**Solvent**	**Solvent ratio**	**Collector Distance / cm**	**Voltage / kV**	**Feed Rate / ml h^{-1}**
15	DMAc: Acetone	1:1	10	9.56	2
15	DMAc: Acetone	1:1	12	10.07	2
15	DMAc: Acetone	1:1	15	10.44	2
20	DMAc: Acetone	1:1	10	10.44	2
20	DMAc: Acetone	1:1	12	11.00	2
20	DMAc: Acetone	1:1	15	11.00	2
22	DMAc: Acetone	1:1	10	10.81	2
22	DMAc: Acetone	1:1	12	10.42	2
22	DMAc: Acetone	1:1	15	9.59	2
25	DMAc: Acetone	1:1	10	8.81	2
25	DMAc: Acetone	1:1	12	9.83	2
25	DMAc: Acetone	1:1	15	10.20	2
27	DMAc: Acetone	1:1	10	10.61	2
27	DMAc: Acetone	1:1	12	12.48	2
27	DMAc: Acetone	1:1	15	15.74	2

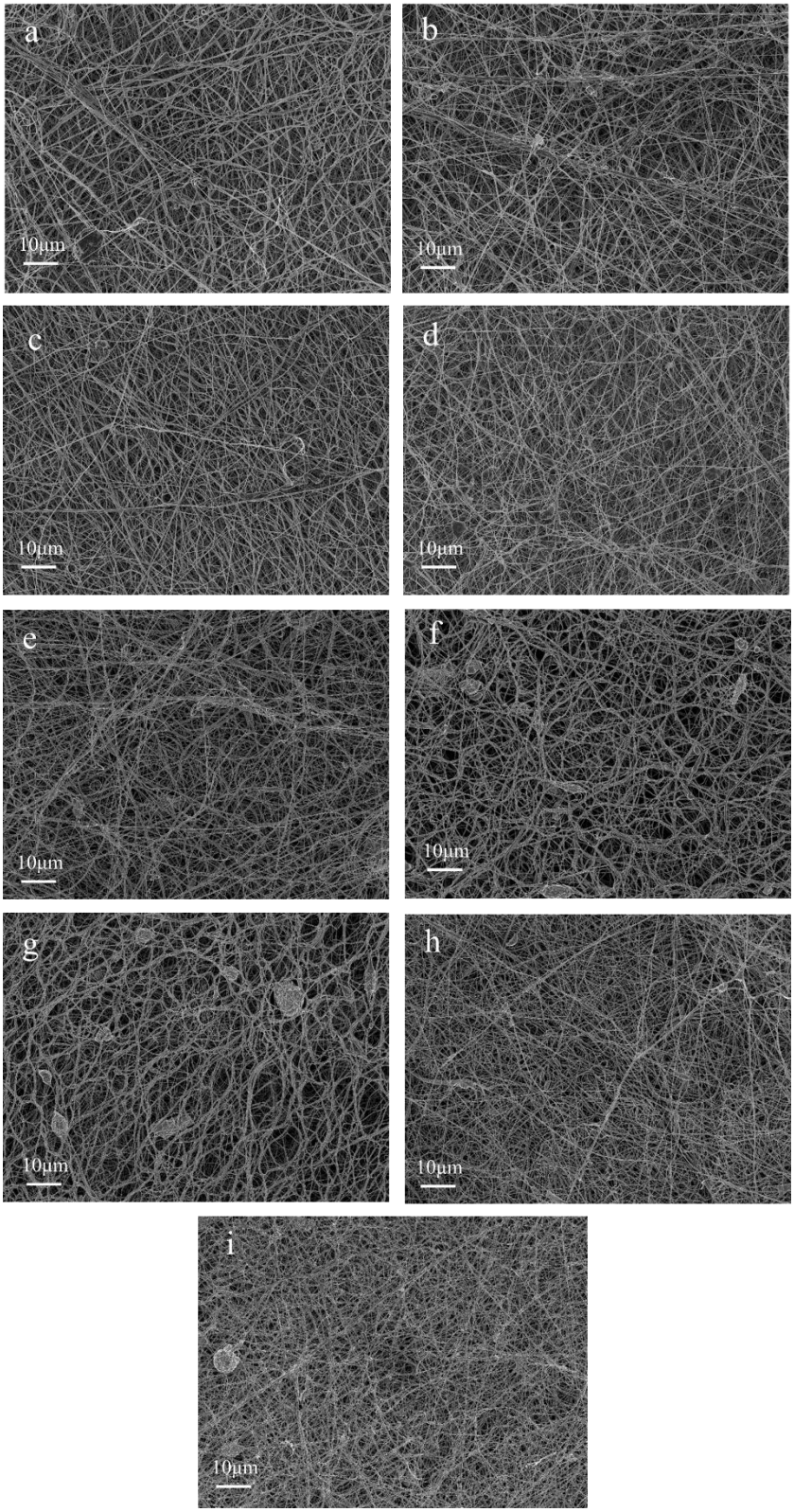

Figure 0.4. SEM images of LMW leached PVDF / KCl fibres. (a) 0.2 wt% KCl content, (b) 0.4 wt% KCl content, (c) 0.6 wt% KCl content, (d) 0.8 wt% KCl content, (e) 1 wt% KCl content, (f) 2 wt% KCl content, (g) 3 wt% KCl content (h) 5 wt% KCl content, (i) 10 wt% KCl content.

Table 0.2. Sound absorption coefficient values from 400 Hz – 6000 Hz of the PET / PVDF / niobium oxide fibres.

Sample	PU	Pure PVDF	$NaNbO_3$	$KNbO_3$	$CeNbO_4$
400 / Hz	0.07	0.15	0.10	0.10	0.14
500 / Hz	0.08	0.22	0.14	0.13	0.21
630 / Hz	0.08	0.35	0.20	0.18	0.32
800 / Hz	0.11	0.57	0.29	0.28	0.51
1000 / Hz	0.13	0.79	0.43	0.40	0.72
1250 / Hz	0.17	0.87	0.55	0.54	0.84
1600 / Hz	0.21	0.74	0.54	0.57	0.76
2000 / Hz	0.28	0.58	0.44	0.47	0.60
2500 / Hz	0.34	0.44	0.33	0.35	0.45
3150 / Hz	0.35	0.34	0.25	0.26	0.33
4000 / Hz	0.32	0.28	0.25	0.24	0.25
5000 / Hz	0.31	0.85	0.94	0.94	0.89
6000 / Hz	0.44	0.44	0.33	0.29	0.39

Table 0.3. Sound absorption coefficient values from 400 Hz – 6000 Hz of the PU / PVDF / niobium Fibres 5 wt%.

Sample	PU	Pure PVDF	$NaNbO_3$	$KNbO_3$	$CeNbO_4$
400 / Hz	0.17	0.20	0.20	0.20	0.20
500 / Hz	0.20	0.28	0.27	0.25	0.28
630 / Hz	0.22	0.40	0.37	0.28	0.38
800 / Hz	0.32	0.51	0.47	0.44	0.48
1000 / Hz	0.57	0.64	0.57	0.80	0.59
1250 / Hz	0.77	0.83	0.78	0.90	0.83
1600 / Hz	0.78	0.83	0.88	0.80	0.84
2000 / Hz	0.80	0.73	0.80	0.77	0.75
2500 / Hz	0.67	0.64	0.73	0.65	0.66
3150 / Hz	0.61	0.63	0.69	0.73	0.60
4000 / Hz	0.64	0.68	0.77	0.86	0.65
5000 / Hz	0.73	0.64	0.75	0.78	0.63
6300 / Hz	0.72	0.54	0.66	0.61	0.52

Table 0.4. Sound absorption coefficient values from 400 - 6000 Hz of the PET / PVDF / silicon-based fibres.

Sample	PET	pure PVDF	SiC	Si_3N_4
400 / Hz	0.07	0.15	0.11	0.09
500 / Hz	0.08	0.22	0.16	0.13
630 / Hz	0.08	0.35	0.24	0.17
800 / Hz	0.11	0.57	0.39	0.25
1000 / Hz	0.13	0.79	0.56	0.36
1250 / Hz	0.17	0.87	0.68	0.47
1600 / Hz	0.21	0.74	0.63	0.50
2000 / Hz	0.28	0.58	0.51	0.45
2500 / Hz	0.34	0.44	0.39	0.36
3150 / Hz	0.35	0.34	0.30	0.28
4000 / Hz	0.32	0.28	0.25	0.28
5000 / Hz	0.31	0.85	0.85	0.83
6000 / Hz	0.44	0.44	0.42	0.48

Table 0.5. Sound absorption coefficient values from 400 - 6000 Hz of the PET / PVDF / silicon-based fibres.

Sample	PET	pure PVDF	SiC	Si_3N_4
400 / Hz	0.07	0.15	0.11	0.09
500 / Hz	0.08	0.22	0.16	0.13
630 / Hz	0.08	0.35	0.24	0.17
800 / Hz	0.11	0.57	0.39	0.25
1000 / Hz	0.13	0.79	0.56	0.36
1250 / Hz	0.17	0.87	0.68	0.47
1600 / Hz	0.21	0.74	0.63	0.50
2000 / Hz	0.28	0.58	0.51	0.45
2500 / Hz	0.34	0.44	0.39	0.36
3150 / Hz	0.35	0.34	0.30	0.28
4000 / Hz	0.32	0.28	0.25	0.28
5000 / Hz	0.31	0.85	0.85	0.83
6000 / Hz	0.44	0.44	0.42	0.48

Table 0.6. Sound absorption coefficient values from 400 - 6000 Hz of the PU / PVDF / silicon-based fibres.

Sample	PU	pure PVDF	SiC	Si_3N_4
Weight / g/m^2		241.6		
400 / Hz	0.17	0.20	0.20	0.19
500 / Hz	0.20	0.28	0.28	0.27
630 / Hz	0.22	0.40	0.38	0.36
800 / Hz	0.32	0.51	0.49	0.45
1000 / Hz	0.57	0.64	0.59	0.54
1250 / Hz	0.77	0.83	0.81	0.78
1600 / Hz	0.78	0.83	0.84	0.87
2000 / Hz	0.80	0.73	0.76	0.81
2500 / Hz	0.67	0.64	0.66	0.74
3150 / Hz	0.61	0.63	0.62	0.69
4000 / Hz	0.64	0.68	0.65	0.75
5000 / Hz	0.73	0.64	0.64	0.76
6300 / Hz	0.72	0.54	0.53	0.68

Table 0.7. Sound absorption coefficient values from 400 Hz – 6000 Hz of the PET / PVDF / $KNbO_3$ / silicon-based fibres

Sample	PET	Pure PVDF	$KNbO_3$ / SiC	$KNbO_3$ / Si_3N_4
400 / Hz	0.07	0.15	0.12	0.12
500 / Hz	0.08	0.22	0.17	0.17
630 / Hz	0.08	0.35	0.25	0.25
800 / Hz	0.11	0.57	0.39	0.38
1000 / Hz	0.13	0.79	0.57	0.55
1250 / Hz	0.17	0.87	0.68	0.64
1600 / Hz	0.21	0.74	0.59	0.57
2000 / Hz	0.28	0.58	0.43	0.44
2500 / Hz	0.34	0.44	0.31	0.32
3150 / Hz	0.35	0.34	0.24	0.25
4000 / Hz	0.32	0.28	0.28	0.38
5000 / Hz	0.31	0.85	0.86	0.83
6000 / Hz	0.44	0.44	0.30	0.37

Table 0.8. Sound absorption coefficient values from 400 - 6000 Hz of the PU / PVDF / $KNbO_3$ / Silicon fibres

Sample	PU	PVDF	SiC	Si_3N_4
Weight / g/m^2		241.6		
400 / Hz	0.17	0.20	0.20	0.19
500 / Hz	0.20	0.28	0.28	0.27
630 / Hz	0.22	0.40	0.38	0.36
800 / Hz	0.32	0.51	0.49	0.45
1000 / Hz	0.57	0.64	0.59	0.54
1250 / Hz	0.77	0.83	0.81	0.78
1600 / Hz	0.78	0.83	0.84	0.87
2000 / Hz	0.80	0.73	0.76	0.81
2500 / Hz	0.67	0.64	0.66	0.74
3150 / Hz	0.61	0.63	0.62	0.69
4000 / Hz	0.64	0.68	0.65	0.75
5000 / Hz	0.73	0.64	0.64	0.76
6300 / Hz	0.72	0.54	0.53	0.68